CO_2 Capture by Aqueous Absorption
Summary of Third Quarterly Progress Reports 2010

by Gary T. Rochelle

Supported by the Luminant Carbon Management Program

and the

Industrial Associates Program for CO_2 Capture by Aqueous Absorption

Department of Chemical Engineering

The University of Texas at Austin

November 1, 2010

Introduction

This research program is focused on the technical obstacles to the deployment of CO_2 capture and sequestration from flue gas by alkanolamine absorption/stripping and on integrating the design of the capture process with the aquifer storage/enhanced oil recovery process. The objective is to develop and demonstrate evolutionary improvements to monoethanolamine (MEA) absorption/stripping for CO_2 capture from coal-fired flue gas. The Luminant Carbon Management Program and the Industrial Associates Program for CO_2 Capture by Aqueous Absorption supports 17 graduate students. These students have prepared detailed quarterly progress reports for the period July 1, 2010 to September 30, 2010. Also attached are 12 papers prepared for presentation at GHGT-10 in Amsterdam.

Conclusions

Thermodynamics and Rates

The unhindered carbamate (4-carboxyl-2-methylpiperazine) accounts for 80 to 95% of the carbamate of 2-methylpiperazine as the CO_2 loading increases from 0.11 to 0.33 mol/mol alkalinity. At a loading of 0.33, the hindered carbamate is about 1/6 of the unhindered carbamate and only 3% of the 2MPZ is present as dicarbamate.

In 3.75 m PZ/3.75 m 1-methylpiperazine/0.5 m 1,4-dimethylpiperazine, the rate of CO_2 absorption at 40 °C is practically the same as in 8 m PZ. The solution capacity (P_{CO2}^* = 0.5 to 5 kPa at 40 °C) is 0.88 mol CO_2/kg solution, compared to 0.79 for 8 m PZ.

The CO_2 solubility in 3.75 m PZ/3.75 m 1-methylpiperazine/0.5 m 1,4-dimethylpiperazine is given by:

$$\ln P_{CO2} = (34.4 \pm 0.2) + \frac{-10597 \pm 81}{T} + (7627 \pm 177) \cdot \frac{\alpha}{T}$$

At the mid-loading where P_{CO2} is 1.5 kPa at 40°C, the ΔH_{abs} is 70±1 kJ/mol CO_2 for the blend.

At 120 °C, the amine volatility in 6.2 m MEA is 167 and 108 Pa at 0.38 and 0.48 loading; at 140 °C, the volatility of 6.3 m MEA is 332 Pa at 0.46 loading.

The amino acid blend, 5 m K^+Taurate/3 m K^+Homotaurate, provides rate of absorption that is competitive with MEA and a competitive heat of absorption of 75–80 kJ/mol. However, this solvent and other amino acids have consistently provided CO_2 capacity (0.2–0.35 mol/kg solvent) that is substantially less than 7 m MEA (0.5).

The volatility of an amine in water is not correlated directly with its pure boiling point. UNIFAC-DMD theory was seen to overestimate the volatilities of most amines studied with the exception of MEA.

Amine Henry's constants are in the order: MDEA < DGA® < PZ < 2-MPZ < MAPA < EDA < MEA < 1,2 Diaminopropane < 1-MPZ < AMP.

The apparent activity coefficient, partial pressure of methyl-amino-propane amine (MAPA), liquid mass transfer coefficient, and viscosity were compared with ethylenediamine (EDA). EDA with CO_2 is less volatile than MAPA with CO_2 and MAPA is more viscous than EDA. EDA has a higher CO_2 partial pressure than MAPA; however the liquid mass transfer coefficient for MAPA is higher than EDA at lower CO_2 partial pressure.

MAPA degrades faster than MEA at stripper conditions and there was complete oxidative degradation of MAPA in the low gas flow oxidative experiment after 5 days. Inhibitor A was shown to reduce the oxidative degradation, but MAPA still degrades faster than MEA.

Modeling

The interheated stripper provided the lowest equivalent work. With 8 m PZ it is 30.9 kJ/mol. With 9 m MEA it is 34.2 kJ/mol CO_2.

With both MEA and PZ, greater complexity in the stripper usually resulted in better energy efficiency due to a closer approach to a reversible process. The improvement over the simple stripper depended on the solvent, rich loading, and reboiler temperature, but the interheated column consistently required 4.8% to 7.8% less equivalent work.

8 m PZ consistently had a lower energy requirement than 9 m MEA when using a rich loading which accounted for the faster reaction rate of PZ in the absorber. The simple stripper and complex configurations with packed columns demonstrated substantial improvement of 9%-11% better energy performance with PZ. The multi-stage flash configurations were 3%-4% better with PZ.

Increasing the stripping temperature of 8 m PZ from 120°C to 150°C reduced the work requirement by 1% to 3%.

Pilot plant results show that it is possible to obtain 90% removal using 6.1 m of Mellapak 2X packing and 8 m PZ.

Reconciled pilot plant results demonstrate model capability of simulating absorber operation. Loadings and removal fraction were matched (less than 0.03 difference). Temperature profiles were adequately determined and the temperature bulge location was closely approximated. The interfacial area factor used was equal to 0.98 showing an adequate prediction of the effective area using Tsai et al.(2008)

When the absorber operates close to the critical L/G, intercooling is capable of generating an increase in CO_2 removal as high as 12%. Intercooling eliminates the mass transfer pinch and lowers overall absorber temperature leading to higher removal and richer rich loadings (Figures 16 & 17)

The critical L/G region for this system is near 4 mol/mol for 90% removal. It can be determined by following the location of the discontinuity in the constant removal curve.

The observed critical L/G was closely predicted using the equation in Plaza et al. (2009).

CO_2 venting improves profits over inflexible capture by up to 10% but is uneconomical at high CO_2 prices.

Solvent storage improves profits over inflexible capture from 29% at \$30/tCO_2 to 9% at \$100/tCO_2.

For the current case study, the most valuable solvent storage system is only large enough to exploit 15–30 minutes of high prices each day.

In the measurement of k_g with 42 inches of packing, the end effects account for about 24% of the total NTU.

The pressure drop of one-inch plastic Pall rings is approximately 1.3 times that of RSR # 0.5, 3.1 times that of Flexipac 1.6 Y HC, 3.5 times that of RSP 250, and 11.4 times that of Mellapak 2X.

The effective fractional mass transfer area of one-inch plastic Pall rings is smaller than metal packings.

Pilot plant testing at comparable conditions (gas rate = 350 cfm, L/G ~ 3.6, 90% CO_2 removal, absorber intercooling to 40 °C) demonstrates a specific heat duty for 8 m piperazine (1171 Btu/lb CO_2) that is 20% less than 9 m MEA (1435 Btu/lb CO_2).

Solvent Management

The thermal degradation rate of piperazine is first order in piperazine with 4 to 12 m PZ.

Morpholine (Mor) is highly resistant to thermal degradation. A solution of 8 Mor lost only 17% of the initial amine after 15 weeks of degradation at 175 °C, less than a comparable 8 m PZ experiment.

Hexamethylenediamine (HMDA) degrades readily at 175 °C losing 80% of the initial amine within 15 weeks.

When a solution of 8 m PZ loaded with 0.3 mole $^{13}CO_2$ per mole alkalinity was degraded at 175 °C , all of the formate formed contained the ^{13}C, demonstrating that the formate is derived from CO_2.

The addition of 500 mM formate to 8 m PZ did not strongly affect the oxidation of PZ or generation of degradation products. In this experiment, formate quickly established an equilibrium with formyl amides. Formate is not an oxidation inhibitor and is not oxidized to CO_2.

The addition of 500 mM formaldehyde to 8 m PZ created stable, dense, white foam that persisted through the oxidation experiment.

Oxidation of 8 m PZ with a rich loading of 0.42 mole CO_2 per mole alkalinity proceeded more slowly than a lean loading experiment (0.26 mole CO_2 per mole alkalinity).

The foaminess coefficient for oxidized 8 m PZ solutions does not accurately represent degradation. The measurement is not repeatable and is a function of the amount of time between the end of an experiment and the foaminess test.

Mass Spectrometry detects dinitrosopiperazine (DNPZ) with a major peak at 115 and at a collision energy of 30 breaks DNPZ to peaks at 56 and 85. .

Dinitrosopiperazine can be measured by LC-MS using a reverse phase column, with a UV detection limit of 9e-5 mmol/kg.

The reaction of nitrite with 8 m loaded piperazine is first order in nitrite with a rate constant of 0.36 hr^{-1} at 60 ^oC. The activation energy is 50 kJ/mol.

Less than 4 e-4 mmol/kg dinitrosopiperazine is produced from the reaction of 50 mM nitrite with 8 m loaded piperazine at 60 ^oC.

When loaded with 0.39 mol CO_2/mol alkalinity, 3.75 m PZ/3.75 m 1MPZ/0.5 m 1,4 DMPZ is free of solid precipitates at room temperature. A zero loading this blend precipitates below 33 ^oC, compared to 43 ^oC for 8 m PZ.

was developed; the heat of absorption of CO_2 is given by the derivative of that expression. In the following equations P_{CO2} is in Pa, T is in K and α is the CO_2 loading.

$$\ln P_{CO2} = (34.4 \pm 0.2) + \frac{-10597 \pm 81}{T} + (7627 \pm 177) \cdot \frac{\alpha}{T}$$

At the mid-loading where P_{CO2} is 1.5 kPa at 40 °C, the ΔH_{abs} is 70±1 kJ/mol CO_2 for the blend.

Temperature and pressure calibrations were conducted with the high temperature-pressure vapor liquid equilibrium apparatus. 7 m MEA was used as the solvent for a test run. Better temperature control was achieved with the oil bath, so vapor condensation was avoided. At 120 °C, the volatility of 6.2 m MEA is 167 and 108 Pa at 0.38 and 0.48 loading; at 140 °C, the volatility of 6.3 m MEA is 332 Pa at 0.46 loading.

4. Amine Volatility *p. 60*

by Thu Nguyen

The volatilities of 10 amines in water were measured using the FTIR and expressed as amine Henry's constants. Regarding the intrinsic amine volatility in water, it was determined that: MDEA < DGA® < PZ < 2MPZ < MAPA < EDA < MEA < 1,2 Diaminopropane < 1MPZ < AMP. Most importantly, it was found that the volatility of an amine in water does not necessarily track the pure amine boiling point. An empirical correlation was successfully developed to estimate the amine Henry's constant at 40 ˚C by accounting for molecular group contributions: ln $H_{amine,40\,°C}$ = [4.19 (±0.09)] – [1.65(±0.17)](N) – [0.21(±0.07)](NH) – [1.55(±0.17)](R-O-R) + [0.7(±0.08)](Non Cyclic C-CH_3) + [2.63(±0.21)](Cyclic N-CH_3). Predictions of amine volatilities in water by UNIFAC-DMD theory (in Aspen Plus®) overestimated measured values, by up to an order of magnitude, for most of the amines studied except for MEA.

At conditions at the top of the absorber (~40 ˚C and nominal lean loading), the amine volatilities are: 7 m MEA: 2.7 Pa; 8 m PZ: 0.78 Pa; 7 m MDEA/2 m PZ blend: 0.49 Pa/0 Pa, respectively. The amine heats of solution at their respective nominal lean loadings (~500 Pa P_{CO2}) were estimated to be: 7 m MEA: 10.2 kJ/mol; 8 m PZ: -37.1 kJ/mol; 7 m MDEA/2 m PZ: --1.5kJ/mol/-74.6 kJ/mol, respectively. PZ in the blend is even less volatile than 8 m PZ.

5. Modeling MDEA/PZ Thermodynamics, Hydraulics, and Kinetics p. 73

by Peter Frailie

The goal of this study is to evaluate the performance of an absorber/stripper operation that utilizes MDEA/PZ. Before analyzing unit operations and process configurations, thermodynamic, hydraulic, and kinetic properties for the blended amine must be satisfactorily regressed in Aspen Plus®. The approach used in this study is first to construct separate MDEA and PZ models that can later be reconciled via cross parameters to model accurately the MDEA/PZ blended amine. This study is currently in the process of finalizing the MDEA/PZ model based on thermodynamic, hydraulic, and kinetic data. Separate MDEA and PZ models have been finished that accurately predict VLE, heat capacity, unloaded amine volatility, CO_2 activity coefficient, and CO_2 absorption rate over operationally significant temperature, amine concentration, and loading ranges. All available thermodynamic and hydraulic data for 7 m MDEA/2 m PZ and 5 m MDEA/5 m PZ have also been regressed. The goal for the next quarter

is to improve MDEA/PZ CO_2 absorption rate predictions and begin modeling an absorption/stripping/compression process.

6. N-methyl-1,3-propanediamine (MAPA) for CO_2 capture p. 83

by Solrun Johanne Vevelstad

Supported by the SOLVit project, NTNU

Several thermal and oxidative degradation experiments were performed with 9 m N-methyl-1,3-propanediamine (MAPA). The samples were analyzed for degradation products using anion IC, cation IC, amino acid IC, IC-MS, LC-MS, GC-MS and MS-MS. Alkalinity and total inorganic carbon were also measured. The thermal samples were analyzed for metals. Amine volatility of 9 m MAPA was measured using hot gas FTIR. Chen measured CO_2 solubility and liquid mass transfer coefficient in the wetted-wall column (8 m MAPA). Viscosity of 9 m MAPA was measured at different loadings at 40 °C.

The degradation experiments show that MAPA degrades faster than MEA. Under oxidative conditions, complete degradation was obtained after 5 days in the low gas flow apparatus, with stainless steel metals mixture. Inhibitor A was shown to reduce the amine loss to 35–37%. Most of the degradation products from thermal and oxidative experiments were not identified and quantified. However, it is believed that one of the main thermal degradation compounds is 1-methyltetrahydro-2(1H)-pyrimidone (*N*-methyl-*N*,*N*'-trimethyleneurea). In oxidation at low gas flow without Inhibitor A, formate was produced at 2.4 mol /kg solution.

Apparent activity coefficient, partial pressure of MAPA, liquid mass transfer coefficient and viscosity were compared with ethylenediamine (EDA). EDA loaded with CO_2 is less volatile than loaded MAPA. MAPA is more viscous than EDA. EDA had a higher CO_2 partial pressure than MAPA; however, the liquid mass transfer coefficient for MAPA was higher than EDA at lower CO_2 partial pressure.

7. Modeling Stripper Performance for CO_2 Capture by Amines p. 117

by David Van Wagener

Five stripper flowsheets with varying levels of complexity were simulated in Aspen Plus® using 9 m MEA and 8 m PZ. The configurations included a 1-stage flash, 2-stage flash, simple stripper, adiabatic lean flash, and interheated column. Many specifications were implemented to allow adequate comparison between the configurations. These constants included constant rich loading, isothermal stripping at 120 °C or 150 °C, a 5 °C temperature approach on all cross exchangers, equimolar vapor production on each stage, 5 m of packing, a final CO_2 pressure of 150 bar, and rich and lean pump outlet pressures which matched the destination vessel pressure and added 50 kPa for pressure drop and additional pressure for the elevation gain of the packing. Although the absorber was not modeled, the rich loadings used for the two solvents accounted for the faster CO_2 reaction rate of PZ in the absorber. A compressor correlation similar to that used in previous work was utilized to avoid convergence issues of the MCOMP block in stripper simulations. The goal of the simulations was to obtain energy consumption estimates in the stripper when running CO_2 capture with concentrated PZ. A rough estimate had previously been calculated with a first generation Aspen Plus® model. The new rigorous model in Aspen Plus® has just been completed, and these are its first results in the stripper.

The simulations demonstrated that increased configuration complexity improved the efficiency of the stripper by 5–8%, depending on the solvent, operating temperature, and rich loading. The most improvement over the simple stripper was observed with the interheated column. The improvements were attributed to better reversibility of the more complex flowsheets. Furthermore, 8 m PZ consistently had a lower energy requirement than 9 m MEA. Configurations with packed columns exhibited improvements in energy consumption of 9%–11%. The base case configuration and solvent was a simple stripper with 9 m MEA, and its energy requirement was 36.1 kJ/mol CO_2. Using the simple stripper with 8 m PZ at its maximum temperature of 150 °C showed an energy requirement of 33.1 kJ/mol CO_2, and improvement of 3.0 kJ/mol CO_2. The most energy efficient configuration, an interheated column, provided an energy requirement of 34.2 kJ/mol CO_2 and 30.9 kJ/mol CO_2 for 9 m MEA and 8 m PZ, respectively. These numbers demonstrate a 14% improvement of the interheated column with 8 m PZ at 150 °C over the base case.

8. CO_2 Absorption Modeling Using Aqueous Amines p. 126

by Jorge M. Plaza

Data from the November 2008 pilot plant campaign were analyzed using the 5deMayoV1 model. 14 data points were studied. The only variable parameter was the interfacial area. It was reduced 2% from the value generated using Tsai et al. (2008). Two data points were discarded due to noticeable variations in the final reconciled data. Results show that it is possible to obtain 90% removal using 6.1 m of Mellapak 2X packing and concentrated PZ. The model is capable of simulating absorber operation. Loadings and removal fraction were matched (less than 0.03 difference). Temperature profiles were adequately traced and the temperature bulge location was closely approximated.

The validated model was used to test intercooling with 8 m PZ. Absorber performance was evaluated with respect to changes in L/G and lean loading. As in previous work, intercooling was most effective in the critical L/G region. For the studied system, the critical L/G is approximately 4 and intercooling is capable of increasing absorber removal by as much as 12%.

The critical L/G equation gave a close approximation to the critical L/G. It predicted 4.2 (mol/mol) for 90% and 4.4 (mol/mol) for 80% removal.

9. Electric Grid-Level Implications of Flexible CO_2 Capture Operation *p. 137*

by Stuart Cohen, Department of Mechanical Engineering. Supported by the EPA STAR Fellowship Program and the Luminant Carbon Management Program

Co-supervised by Prof. Michael Webber

Flexible post-combustion absorption/stripping that vents carbon dioxide (CO_2) or stores rich solvent at partial or zero load is investigated for its ability to improve profits by operating in response to volatile electricity prices. A versatile mixed-integer linear programming optimization model is created to maximize annual profits at a coal-fired facility with CO_2 capture. The model includes constraints on minimum/maximum load, ramp limits, startup behavior, and minimum up and down time for the base plant, absorption, and stripping equipment.

The first comprehensive analysis using the model was reported in the GHGT-10 paper "Optimal operation of flexible post-combustion CO_2 capture in response to volatile electricity prices." This analysis considered a nominal 500 MW coal-fired facility in the Electric Reliability Council of Texas (ERCOT) grid using an amine scrubbing unit with 7 m monoethanolamine (MEA). The analysis concluded the following:

- CO_2 venting improves profits over inflexible capture by up to 10% but is uneconomical at high CO_2 prices.
- Solvent storage improves profits over inflexible capture from 29% at \$30/tCO_2 to 9% at \$100/tCO_2.
- CO_2 emissions reductions are significant with flexible capture above any CO_2 price required to justify operating CO_2 capture (~\$30/tCO_2).
- Profit improvements with flexibility are achieved for any reasonable capture system response time.
- For the current case study, the most valuable solvent storage system is only large enough to exploit 15–30 minutes of high prices each day.

Future work will investigate the tradeoff between model accuracy and computation time when more accurate constraints are added. Sensitivity to several power, CO_2 capture, and electricity system parameters will be studied, especially in the context of solvent storage system design.

10. Measurement of Packing Liquid Phase Film Mass Transfer Coefficient *p. 148*

by Chao Wang

(also supported by the Process Science and Technology Center)

In this quarterly report, end effects for associated mass transfer measurements were considered. End effects account for about 20% of k_G measurement when using a short packed bed of approximately 42 inches. The area and k_L measurements utilize a ten-foot packed bed and, as a result, the end effects appear to be negligible.

In this quarter, a new packing, 1-inch plastic Pall ring, was studied. This plastic packing has the advantages of low cost, light weight construction, and resistance to breakage.

The Pall ring is an economic and versatile industrial standard packing with well-known performance characteristics. Pressure drop, liquid hold-up, and mass transfer effective area were measured this quarter. Gas and liquid phase film mass transfer coefficients will be measured in November 2010. Next quarter, the performance characteristics of the Raschig Super Ring #0.7 will be examined, and in January 2011, the performance characteristics of 1-inch metal Pall rings will be studied.

11. Pilot Plant Testing of Advanced Process Concepts using Concentrated Piperazine *p. 156*

by Dr. Eric Chen

Supported by the CO_2 Capture Pilot Plant Project of the Process Science and Technology Center

and by NRGEnergy Contract with DOE

Pilot plant testing of 8 m piperazine in a two-stage heated flash with absorber intercooling is planned for fall of 2010. In this reporting period, mechanical fabrication of the two-stage flash

pilot skid was completed. Process and utility piping and instrumentation tie-ins of the skid into the pilot plant were also completed. A gross leak check of the skid and tie-in piping and configuration of the primary skid instrumentation with the DeltaV control system was completed. Troubleshooting of the skid using water is currently underway. A small absorber intercooling skid was fabricated and retrofitted onto the pilot absorber at the UT Pickle Research Center. Absorber intercooling test were completed for 9 molal MEA (35 wt %) and 8 molal piperazine (42 wt %).

Absorber intercooling tests using the simple stripper configuration were completed for 9 m MEA and 8 m piperazine. The packing in the absorber and stripper was Sulzer Mellapak 2X and Raschig-Jaeger RSP 250 (new version), respectively. The test matrix for the 12 MEA runs was structured such that for a given gas and liquid rate and lean loading, the absorber was first operated with the intercooler off and then on. The conditions for MEA testing varied over the following ranges:

lean loading = 0.2 to 0.36 mol CO_2/mol MEA
gas rate = 350 to 500 cfm
L/G ratio (mass basis) = 2 to 6
absorber intercooling to 40 °C,
stripper temperature = 115 °C
stripper pressure = 1.5 to 2.2 bar.

A total of 13 runs were completed for piperazine. The test matrix for piperazine was structured to achieve 90% CO_2 removal for a given lean loading and gas rate. The liquid rate was adjusted to maintain 90% CO_2 removal. The addition test conditions were:

lean loading = 0.22 to 0.30 mol CO_2/mol total alkalinity
gas rate = 350 to 750 cfm
L/G ratio (mass basis) = 2.6 to 5.8
absorber intercooling to 40 °C
CO_2 removal = 90%
stripper temperature = 120 °C
stripper pressure = 2.1 to 2.7 bar.

Three runs at 350 cfm and variable L/G were completed without absorber intercooling for comparison.

At a gas rate of 350 cfm, L/G ~ 3.6, 90% CO_2 removal, and absorber intercooling to 40 °C, the specific heat duty for piperazine (1171 Btu/lb CO_2) was 20% less than MEA (1435 Btu/lb CO_2). The piperazine runs demonstrated a 6.5% reduction of specific heat duty with absorber intercooling for a given L/G ratio (gas rate = 350 cfm, L/G range = 2.5 to 4.5, and 90% CO_2 removal). The MEA runs showed that at low (2.1) and high (5.8) L/G, absorber intercooling did not have any effect on specific heat duty.

A HAZOP was conducted for the skid to identify potential hazards and worst case scenarios with the operators and technical staff at SRP. No major design and safety flaws were found. Additional interlocks will be built into the control system setup to address some of the minor safety concerns.

Two MicroMotion 7829 online viscometers and the associated flow chambers were donated by Emerson Process Management and installed on the skid. The viscometers measure viscosity, density, and temperature and will be used to determine online amine concentration and CO_2

loading through the viscosity and density measurements, respectively. There are currently some issues with getting the inputs from the viscometers into the DeltaV. These are being resolved.

Troubleshooting of the two-stage flash skid using water is currently underway and has already identified a few issues. The steam control valves were specified to fail-close but upon installation were found to be fail-open. This will need to be rectified for safety reasons. The liquid level control valve on the low pressure vessel was found to be too small, resulting in an upper flow limit of 18 gpm. A by-pass around the low pressure liquid control valve will be installed to fix the problem. Finally, it was determined that the electronics of variable speed drive (VSD) on the high pressure pump was not working properly. The pump drive will need to be sent back to the manufacture for repair or replacement.

The preliminary stages of skid troubleshooting haves also shown that startup of the skid will require pressurizing the two gas-liquid separator tanks because there are no pumps downstream of each tank to pump the solvent back to the main pilot unit. However, the liquid flow issue disappears once the solvent has been heated and pressure begins to build. Aside from these issues, control of the gas pressures, liquid levels, and flash temperatures seems to work well with the water tests. A heat loss test for the skid will need to be completed before the piperazine campaign with two-stage flash begins.

The schedule for startup of the two-stage flash campaign will be contingent on the replacement of the pump VSD. The lead time is currently unknown. At this time, start-up is tentatively scheduled for late November or early December.

Detailed reporting of this activity is limited to sponsors of the CO_2 Capture Pilot Plant Project and does not appear in this report to Luminant sponsors.

12. MDEA/PZ Degradation in Cycled Solvents *p. 158*

by Fred Closmann

(also supported by the Process Science & Technology Center)

7 m methyldiethanolamine (MDEA) was degraded in three separate experiments in the Integrated Solvent Degradation Apparatus (ISDA) during the quarter. We measured a formate production rate of 0.15 mM/hr in the ISDA with the thermal reactor maintained at 90 °C and 7 m MDEA dosed with 100 mM Inh A, which indicated that the oxidative degradation inhibitor was not effective at this temperature. When we utilized a headspace gas of 98% air/2% O_2 and maintained the thermal reactor at 90 °C, we measured a formate production rate of 0.04 mM/hr, compared to 0.12 mM/hr when we utilized a 98% O_2/2% CO_2 gas at comparable conditions. When we stripped dissolved oxygen from the solvent immediately downstream of the oxidative reactor using a 2 L/min N_2 gas purge in 7 m MDEA cycled from 55 to 120 °C in the ISDA, we reduced the formate production rate to 0.047 mM/hr. The rate without stripping was 0.31 mM/hr, indicating that stripping of dissolved oxygen is a practical solution to reducing oxidative degradation in absorber/stripper configurations.

The formate production rate in 8 m piperazine (PZ) (0.3 moles CO_2/mole alk) was 0.05 mM/hr, compared to 0.31 mM/hr measured in 7 m MDEA when cycled from 55 to 120 °C. When the thermal reactor temperature was reduced to 90 °C, the formate production rate was 0.013 mM/hr in 8 m PZ. We measured an ethylenediamine (EDA) production rate of 0.17 mM/hr in 8 m PZ, and a PZ loss rate of ~5%/wk.

When 7 m MDEA was treated with 0.35 m tetramethylammonium chloride (quat), loaded to 0.2 moles CO_2/mole alk, and thermally degraded at 150 °C for up to 30 days in the absence of oxygen in the thermal cylinder headspace, we detected monoethanolamine (MEA), diethanol ethylamine, and dimethyl ethanolamine (DMEA). We did not detect bicine or diethanolamine (DEA), both of which are detected in cycling experiments, confirming that these are primarily oxidative degradation products of MDEA.

We improved our oxidative degradation model for the ISDA using a plug-flow reactor model, and estimated energies of activation (Ea) for the production of DEA, formate, and bicine of 85,000, 91,000, and 100,000 kJ/mol*K.

13. Thermal Degradation and Oxidation of Concentrated Piperazine (PZ) *p. 175*

by Stephanie Freeman

The concentration of PZ does not have a strong effect on the thermal degradation rate of 8 m PZ, indicating the rate is first order in amine loss. The concentration of formate and formyl amides increases directly with increased PZ and CO_2 concentration. The equilibrium between formate and formyl amides does not have a consistent trend between 4, 8, and 12 m PZ.

The concentration of ethylenediamine produced is consistent in degraded 4, 8, and 12 m PZ within the error limits of the cation IC, indicating that it is not a direct function of PZ or CO_2 concentration.

In 12 m PZ, the formyl amides quantified through alkaline amide reversal track with N-formyl PZ measured directly with cation IC for the first six weeks of degradation at 175 °C. The N-formyl PZ then reaches an equilibrium concentration and the total formyl amides continue to increase.

Morpholine (Mor) is highly resistant to thermal degradation. A solution of 8 Mor lost only 17% of the initial amine after 15 weeks of degradation at 175 °C, less than a comparable 8 m PZ experiment. Mor and piperidine are the only amines screened so far that are more resistant to thermal degradation than concentrated PZ. Hexamethylenediamine (HMDA) degrades readily at 175 °C losing 80% of the initial amine within 15 weeks.

A solution of 8 m PZ loaded with 0.3 mole $^{13}CO_2$ per mole alkalinity was degraded at 175 °C to show that formate is produced from CO_2 directly. ^{13}C NMR results of background samples and degraded PZ solutions confirmed the hypothesis that the carbon in formate is the same carbon as in the CO_2 molecule.

The addition of 500 mM formate to 8 m PZ did not strongly affect the oxidation of PZ or generation of degradation products. In this experiment, formate quickly established an equilibrium with formyl amides. Formate is not an oxidation inhibitor, and total formate was conserved, disproving the hypothesis that formate is being oxidized to CO_2.

The addition of 500 mM formaldehyde to 8 m PZ created stable, dense, white foam that persisted throughout the oxidation experiment. The foam likely decreased oxygen mass transfer rates, reducing the production of degradation products.

Oxidation of 8 m PZ with a rich loading of 0.42 mole CO_2 per mole alkalinity proceeded more slowly than a lean loading experiment (0.26 mole CO_2 per mole alkalinity). The result of the

rich loading experiment was confounded by the increased CO_2 concentration, but reduced oxygen concentration.

The foaminess coefficient for oxidized 8 m PZ solutions does not accurately represent degradation. The measurement is not repeatable and is a function of the amount of time between the end of an experiment and the foaminess test.

14. Oxidative Degradation of Amino Acid Salts *p. 208*

by Alex Voice

Amino acids are shown to degrade oxidatively at rates comparable to other amines used in CO_2 capture. Ammonia (NH_3) production from a variety of amine and neutralized amino acid solutions was measured under moderate conditions representative of those in an absorber for CO_2 capture.

6 m potassium glycinate (GLY) degraded the most rapidly, showing a steady state rate of 6.25 mmol/kg/hr of NH_3 in the presence of 0.4 mM Fe^{2+}, 0.1 mM Cr^{3+}, and 0.05 mM Ni^{2+} at 80 °C. Under the same conditions, 7 m monoethanolamine (MEA) produced ammonia at a rate of 3.44 mmol/kg/hr. The rates for 5 m potassium taurinate (TAU), 3 m potassium taurinate/5 m potassium homotaurinate (HTAU), and sarcosine (SAR) were 0.62, 0.43, and 0.12 mmol/kg/hr, respectively.

The effect of metal salts and Inhibitor A was also assessed for these amino acids. Metals increased the ammonia production rate of GLY, TAU, TAU/HTAU, and MEA. No significant effect was observed for SAR. Inhibitor A decreased the NH_3 production rate for MEA, TAU, TAU/HTAU, but actually increased the rate for GLY.

15. Nitrosamine Formation in CO_2 Capture by Piperazine *p. 225*

by Mandana Ashouripashaki

Secondary amines may react with nitrite to produce carcinogenic products called nitrosamines. Piperazine (PZ) is an amine of interest in our study and nitrosation products of PZ are N-nitrosopiperazine and N-N, dinitrosopiperazine (DNPZ).

A method for detecting and measuring dinitrosopiperazine (DNPZ) has been developed. A calibration curve with a sensitivity analysis of 6e-5 mmol/kg by liquid chromatography followed by mass spectrometry (LC-MS) has been obtained.

After considering methods of establishing the probability of DNPZ presence, the kinetics of reaction between loaded PZ and nitrite are under investigation. Primary results show a first order reaction in nitrite in loaded PZ. However the amount of DNPZ produced is very small. Additional experiments will address the possible catalytic effects of formaldehyde and other degradation products on PZ nitrosation.

16. Thermal Reclaiming *p. 237*

by Steven Fulk

In this quarter, concentrated, loaded piperazine (PZ) solutions created last quarter using a simple heated-beaker evaporator were analyzed using a variety of techniques. Two solutions were created; the first was 8 m PZ with 0.3 molCO_2/ mol alkalinity, and the second was 8 m PZ with 0.3 mol CO_2/ mol alkalinity plus 250 mM formic acid. Total Inorganic Carbon (TIC) and cation

chromatography analysis showed the solution containing formic acid had 1.4 mol PZ/kg solution and 0.02 mol CO_2/mol alkalinity less than the solution with no formic acid. The difference is hypothesized to be the formate/amine/formamide equilibrium reaction. Anion chromatography showed less formate than predicted from a mass balance on the non-volatile species in the concentrated solution. Formamide reversal using NaOH is needed to confirm the hypothesis.

Goals for next quarter include performing three experiments. First, thermal degradation experiments using stainless steel bombs will analyze degradation characteristics of concentrated amine solutions. Second, liquid-liquid equilibrium experiments will be conducted on amines and inhibitor mixtures. Finally, a thermal reclaiming apparatus with continuous FTIR vapor sampling constructed this quarter will be used to reclaim aqueous amine solutions. Liquid and vapor samples will be analyzed for composition.

17. Amine Reclaiming by Solids Precipitation *p. 248*

by Humera Abdul Rafique

The solubility of potassium sulfate (K_2SO_4) in piperazine (PZ) solution increases with increasing loading because of a greater concentration of carbamate and protonated amine in the system. The solubility decreases with a decrease in temperature. The solubility of K_2SO_4 is lower in PZ than in MEA when determined using the solid solubility experimental procedure, i.e., the solubility decreases in organic solutions with greater organic concentrations.

It has been determined that the \ solubility window for CO_2 in PZ solutions is between 0.3 and 0.46 mol CO_2/mol alkalinity (Freeman, 2008). In order to determine the loading limit of the PZ solutions, experiments are being carried out to determine the solubility of hydrated protonated piperazine carbamate by initially preparing the crystals and using the solid solubility method to determine the solubility.

A qualitative analysis to determine the solubility envelope of CO_2 loaded 3.9 m PZ/3.9 m 1MPZ/0.2 m 1,4 DMPZ and 3.75 m PZ/3.75 m 1MPZ/0.5 m 1,4 DMPZ blended solutions at varying temperatures was performed. A maximum CO_2 loading of 0.41 and 0.39 was obtained for the two blends, respectively, at room temperature without any solid precipitation. At zero loading, both the blends are solids (piperazine hexahydrate, $PZ.6H_2O$) up to 33 °C compared to PZ, which melts at 43 °C at zero loading.

Attachments:

Papers and Posters presented at GHGT-10

Speciation Study & Rate Measurement of Piperazine Derivatives

Quarterly Report for July 1– September 30, 2010

by Xi Chen

Supported by the Luminant Carbon Management Program

Department of Chemical Engineering

The University of Texas at Austin

November 1, 2010

Abstract

Quantitative ^{1}H and ^{13}C NMR studies were performed on CO_2-loaded 2-methylpiperazine (2MPZ) solutions at loadings of 0.10, 0.28, and 0.33 mol CO_2/mol alkalinity and 40 °C. Unhindered carbamate is the dominant carbamate species and it increases quickly with loading, while hindered carbamate and dicarbamate only exist at low concentrations. At 0.33 loading, the ratio of hindered and unhindered carbamate is about 1:6.

3.75 m piperazine (PZ)/3.75 m 1-methylpiperazine (1MPZ)/0.5 m 1,4-dimethylpiperazine (DMPZ) was tested using the wetted wall column (WWC). Results show that it has the same absorption/desorption rate as 8 m PZ from 40 to 100 °C and has a 10% higher CO_2 capacity than 8 m PZ.

Introduction

In the previous quarterly report, a quantitative NMR study was done for 2MPZ at loading 0.33. In this quarter, an additional NMR study was conducted for the loadings of 0.10 and 0.28 to get the speciation profile in the operating range of CO_2 loading. The NMR data will be incorporated into later modeling work.

A thermal degradation study by Freeman showed that the blend of PZ/1MPZ/DMPZ at the right ratio is stable at high temperature due to inherent chemical equilibrium. This optimal ratio is believed to be around 3.75/3.75/0.5. Therefore, this blend was tested in the WWC. Molecular structures of the three components are shown in Figure 1.

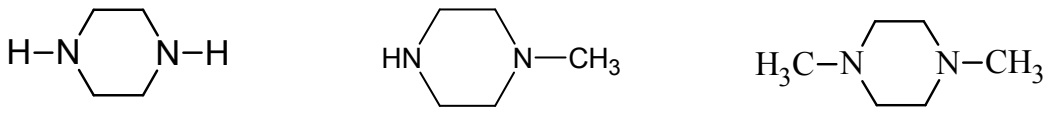

PZ **1MPZ** **1,4-DMPZ**

Figure 1: Molecular structure of PZ, 1MPZ, and 1,4-DMPZ

Experimental Methods

Experimental apparatus, procedures, and analytical methods for the WWC experiment have been described in previous reports and will not be repeated here. PZ (anhydrous, 99%, Sigma-Aldrich), 2MPZ (99%, AK Sci., Inc., Mountain View, CA), 1,4-dimethylpiperazine (99%, Acros Organics, Geel, Belgium), $^{13}CO_2$ (99.9%, Cambridge Isotope Laboratories, Inc, PA), and deionized water (Millipore, Direct-Q) were used as received in this study.

The procedure for preparation of NMR samples is the same as that described in the previous report.

Results and Discussion

The molecular structures of different 2MPZ and CO_2 related species are shown in Figure 2. The carbon and hydrogen atoms are labeled with numbers to differentiate them. Hydrogen atoms share the same number with the carbon to which they attach. The atom labeling is consistent with that used in the previous report.

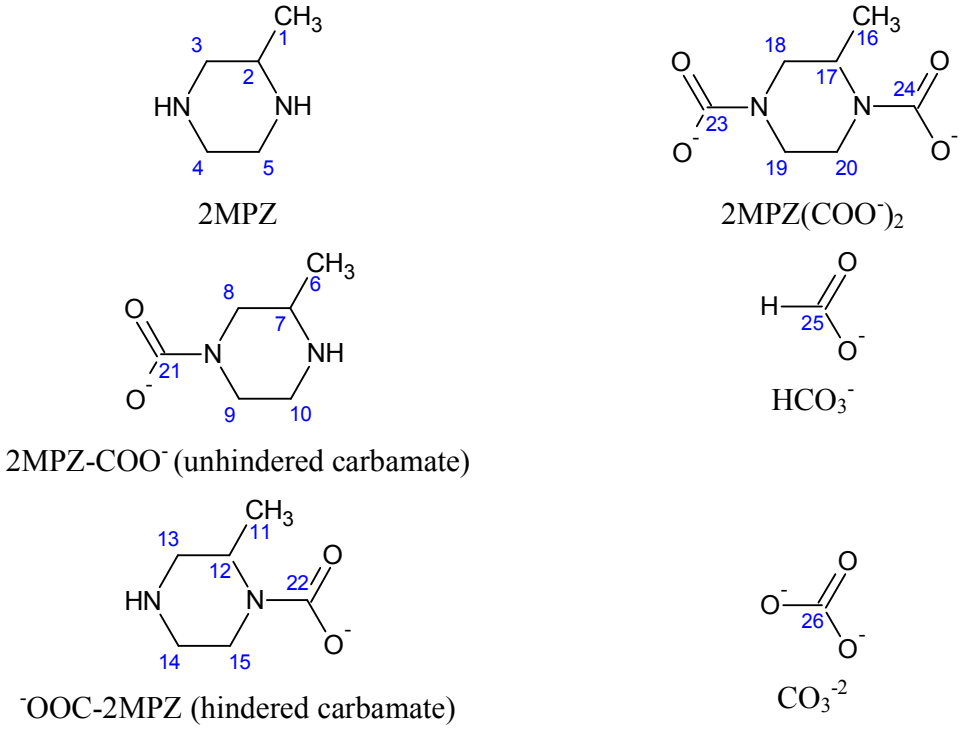

Figure 2: Molecular structure of 2MPZ and different products from reactions between CO_2 and 2MPZ aqueous solution. The products shown can alternatively be protonated.

The ^{13}C NMR spectrum in the up field is shown in Figure 3. Thepeak for $^{-}$OOC-2MPZ/$^{-}$OOC-2MPZH^{+} shifted significantly with CO_2 loading due to the change in pH value. However, not as much shift is observed for the 2MPZ-COO^{-}/$^{+}$H2MPZ-COO^{-} peak. This might indicate that protonation preferentially occurs on the unhindered amino group. No chemical shift with loading is found for dicarbamate.

Unknown peaks show up in the far upfield, which are suspected to be impurity amines in 2MPZ. They would form carbamate after reacting with CO_2.

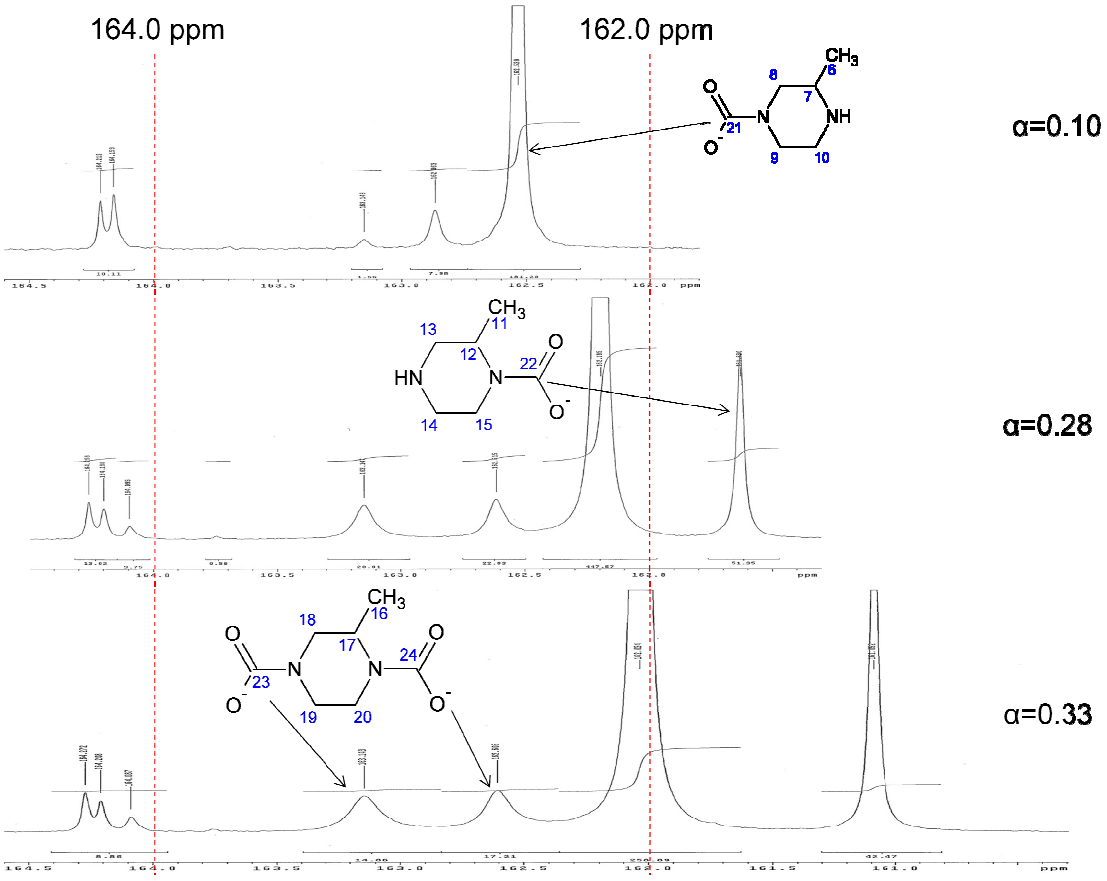

Figure 3: ^{13}C NMR Spectra from 160 to 165 ppm for 8 m 2MPZ, α = 0.10, 0.28 and 0.33 mol/mol alkalinity, T = 40 °C.

The ^{13}C NMR spectra in downfield are shown in Figure 4. At lean loading of 0.1 mol/mol$_{alk}$, only two small peaks are seen. The other two peaks corresponding to unhindered carbamate are probably imbedded under other peaks. Unequal areas of the peaks also indicate peak overlap. Since the amount of hindered carbamate and dicarbamate is too small, the response from them is probably lost in the background noise. As CO_2 loading increases, the peaks start to split and more peaks are seen in the spectra. At loading of 0.33, there are 4 peaks from 2MPZ/2MPZH$^+$ and 4 peaks from 2MPZCOO$^-$/H2MPZCOO.

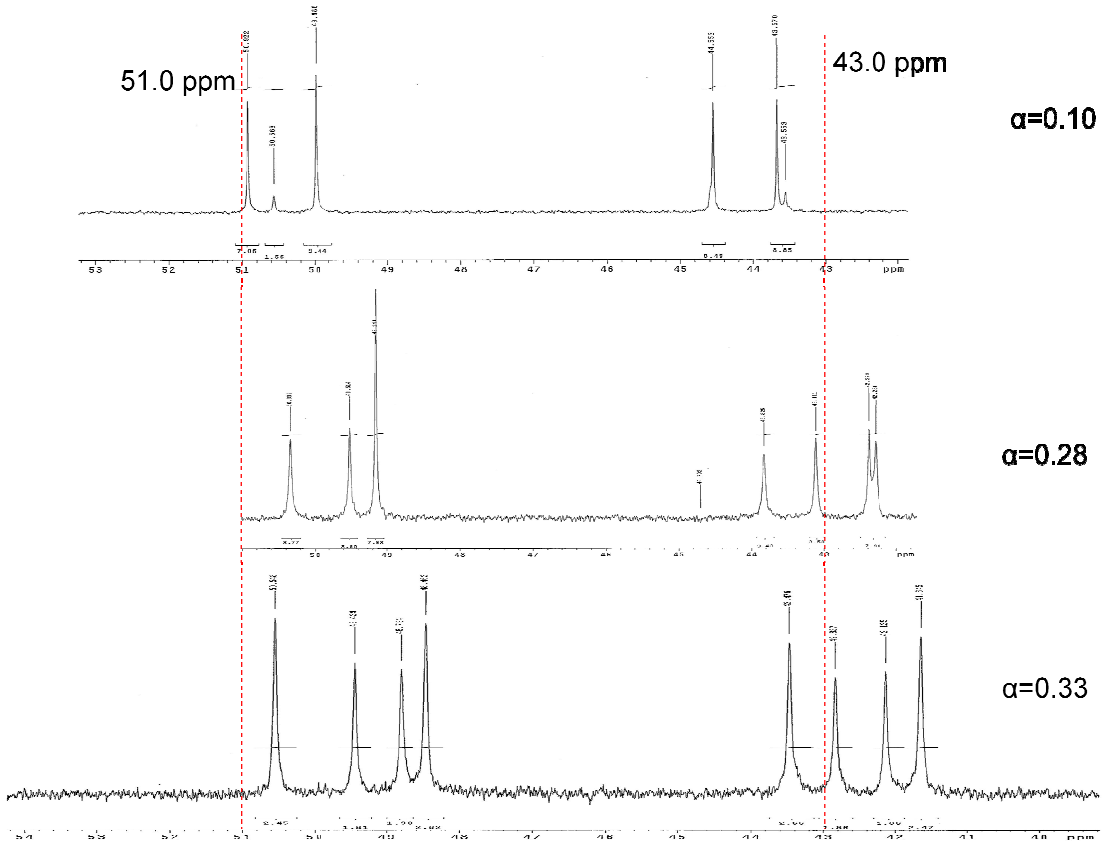

Figure 4: ^{13}C NMR Spectra from 40 to 53 ppm for 8 m 2MPZ, α = 0.10, 0.28 and 0.33 mol/mol alkalinity, T = 40 °C.

The same methodology in the previous report is followed in analyzing the NMR spectra for 2MPZ solution at two leaner loadings. Quantitative analysis based on ^{13}C NMR downfield and upfield is combined to determine the composition of loaded amine solution. The change in speciation along with CO_2 loading is shown in Figure 5. 2MPZ or 2MPZH+ decreases linearly with loading. At the same time, the unhindered amine increases rapidly with loading. There is no significant amount of hindered amine observed until the loading is above 0.25. As seen in Table 1, less than 3% of original 2MPZ is converted to dicarbamate in the loading range studied, while 50% of 2MPZ turns into unhindered carbamate at rich loading.

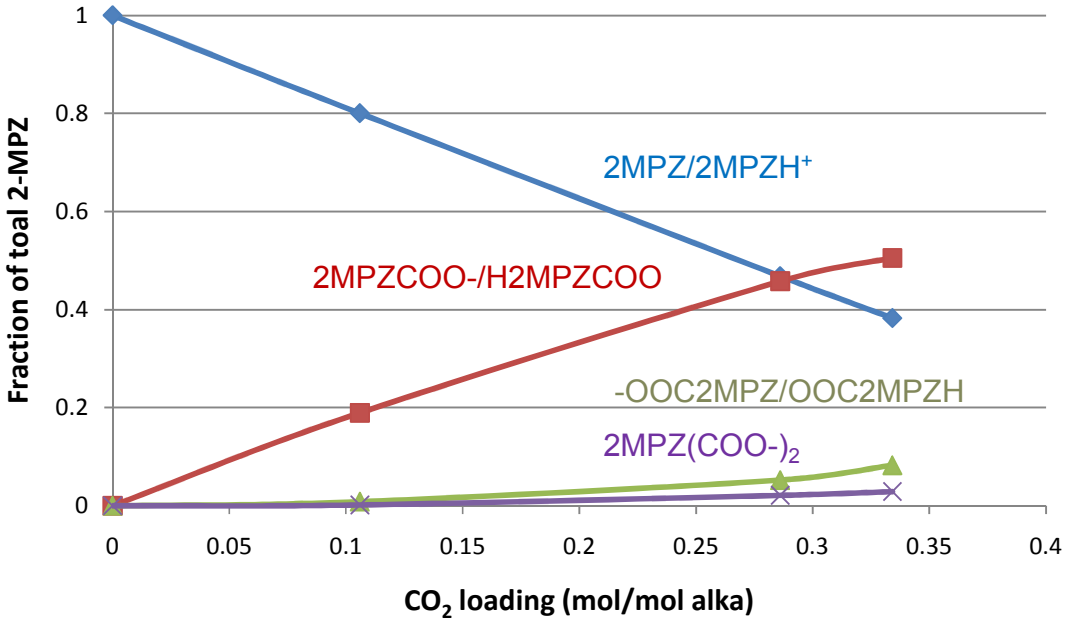

Figure 5: Effect of CO_2 loading on 2MPZ speciation.

Table 1: Speciation of 2MPZ at various loadings determined from NMR spectra

	Loading (mol/mol$_{alk}$)		
	0.11	0.29	0.33
Component	% of 2MPZ	% of 2MPZ	% of 2MPZ
2MPZ/2MPZH$^+$	80	47	38
2MPZ-COO$^-$/$^+$H2MPZ-COO$^-$	19	46	51
$^-$OOC-2MPZ/$^-$OOC-2MPZH$^+$	1	5	8
2MPZ(COO$^-$)$_2$	0	2	3

CO_2 solubility and capacity

CO_2 solubility data in the PZ/1MPZ/DMPZ blend are shown in Figure 6. The data were used for regression of the semi-empirical solubility models (Equation 1), which are drawn as lines in the plot.

$$\ln P^*_{CO_2} = a + \frac{b}{T} + c\,\alpha + \frac{d\,\alpha}{T} + e\,\alpha^2 \qquad \textbf{(1)}$$

The regressed values of the constants are shown in Table 2.

Table 2: Value of parameters for solubility model used for PZ/1MPZ/1,4-DMPZ

a	b	c	d	e
37.29	-11354.1	-16.27	11975.41	3.41

The capacity calculated for the blend is 0.88 mol CO_2/kg solvent. The heat of CO_2 absorption is obtained by applying Gibbs-Helmholtz Equation

$$\Delta H_{abs} = -R\frac{d(\ln P)}{d(1/T)} = -R(b + d\alpha)$$

The calculated heat of absorption for the blend is 67 kJ/mol CO_2.

As expected, the solubility curve for the blend at 40 °C falls between that for 8 m PZ and 8 m 1MPZ. By finding the lean and rich CO_2 loading corresponding to 0.5 and 5 kPa equilibrium CO_2 partial pressure, the cyclic CO_2 capacity of the blend is calculated, which is 0.88 mol CO_2/kg solvent and 10% larger than that of PZ. By applying the Gibbs-Helmholtz equation, the heat of CO_2 absorption was also obtained for the blend.

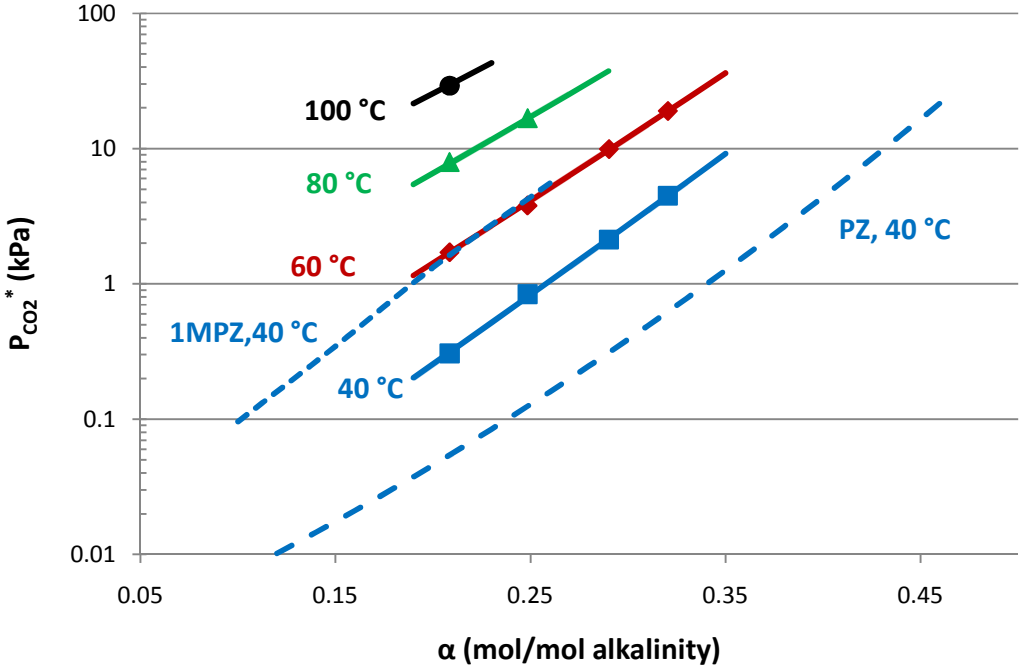

Figure 6: CO_2 solubility in 3.75 m PZ/3.75 m 1MPZ/0.5 m DMPZ

Absorption/Desorption rates in PZ/1MPZ/DMPZ

In Figure 7, absorption/desorption rates for PZ blend at 40, 60, 80, and 100 °C are compared with those of 7 m MEA at 40 °C and 8 m PZ at 40 °C and 60 °C. The blend has almost the same rates as PZ at both 40 and 60 °C. A change in temperature from 40 °C to 60 °C does not affect kg' value for either solvent. It has been shown in the past that 1MPZ has a similar rate to PZ at the same CO_2 partial pressure. The blend of 1MPZ, PZ, and DMPZ is expected to maintain the same rates as the amount of DMPZ is much smaller than the other two components.

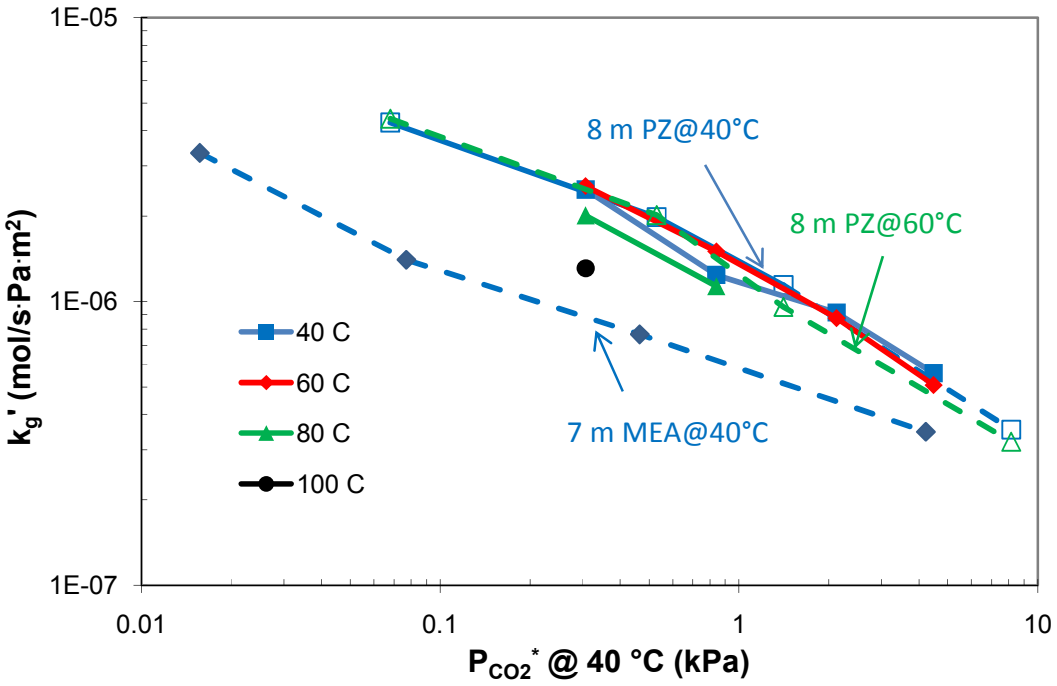

Figure 7: CO_2 mass transfer rate for 3.75 m PZ/3.75 m 1MPZ/0.5 m DMPZ

The solubility and rate data for the blend in the WWC is given in Table 3. The detailed experimental data are shown in Appendix.

Table 3: CO_2 solubility and k_g' for 3.75 m PZ/3.75 m 1MPZ/0.5 m 1,4-DMPZ

Temp (°C)	CO_2 Loading (mol/mol alka)	P_{CO2} (kPa)	kg' ($\times 10^7$mol/s·Pa·m^2)
40	0.21	0.3	24.8
40	0.25	0.8	12.4
40	0.29	2.1	9.2
40	0.32	4.5	5.6
60	0.21	1.7	25.5
60	0.25	3.8	15.0
60	0.29	9.9	8.7
60	0.32	19.0	5.1
80	0.21	8.0	20.1
80	0.25	16.8	11.3
100	0.21	29.2	13.1

Conclusions

The unhindered carbamate (4-carboxyl-2-methylpiperazine) accounts for 95 to 80% of the carbamate of 2-methylpiperazine as the CO_2 loading increases from 0.11 to 0.33 mol/mol$_{alka}$. At a loading of 0.33, the hindered carbamate is about 1/6 of the the unhindered carbamate and only 3% of the 2MPZ is present as dicarbamate.

In 3.75 m PZ/3.75 m 1-methylpiperazine/0.5 m 1,4-dimethylpiperazine the rate of CO_2 absorption at 40 °C is practically the same as 8 m PZ. The solution capacity (P_{CO2}^*= 0.5 to 5 kPa at 40 °C) is 0.88 mol CO_2/kg solution, compared to 0.79 for 8 m PZ. The heat of absorption at P_{CO2}^*= 1.5 kPa is 67 kJ/mol CO_2 compared to 70 for 8 m PZ.

The CO_2 solubility in 3.75 m PZ/3.75 m 1-methylpiperazine/0.5 m 1,4-dimethylpiperazine is given by:

$$\ln P_{CO_2}^* = 37.29 - \frac{11354.1}{T} - 16.27\alpha + 11975.41\frac{\alpha}{T} + 3.41\alpha^2$$

Future work

Speciation data from this study will be used for modeling work in Aspen Plus® and Fortran. Efforts will be focused on setting up a valid thermodynamic and kinetic model on PZ-2MPZ solvent to be able to predict its performance in the amine-scrubbing process.

Appendix: Detailed Wetted Wall Column data for 3.75 m PZ/3.75 m 1MPZ/0.5 m 1,4-DMPZ

CO_2 Loading	T	P_{tot}	Q_{liquid}	Q_{gas}	$Q_{gas,wet}$	$PP_{CO2,in,wet}$	$PP_{CO2,out,wet}$	P_{CO2}*	N_{CO2}	$(P_{CO2}-P_{CO2}^{*})_{LM}$	K_g	k_g	k_g'	Gas Res	Liq Res
mol/mol$_{alk}$	°C	psig	ml/s	L/min	L/min	Pa	Pa	Pa	mol/s·m^2	Pa	mol/s·Pa·m^2	mol/s·Pa·m^2	mol/s·Pa·m^2	%	%
0.209	40	20	4	5.0	5.2	4	112	307	-4.5E-04	-245	1.61E-06	4.57E-06	2.48E-06	35%	65%
0.209	40	20	4	5.0	5.2	58	134	307	-3.1E-04	-209	1.61E-06	4.57E-06	2.48E-06	35%	65%
0.209	40	20	4	5.0	5.2	108	164	307	-2.3E-04	-170	1.61E-06	4.57E-06	2.48E-06	35%	65%
0.209	40	20	4	5.0	5.2	347	330	307	7.2E-05	31	1.61E-06	4.57E-06	2.48E-06	35%	65%
0.209	40	20	4	5.0	5.2	447	403	307	1.8E-04	116	1.61E-06	4.57E-06	2.48E-06	35%	65%
0.209	40	20	4	5.0	5.2	497	440	307	2.4E-04	159	1.61E-06	4.57E-06	2.48E-06	35%	65%
0.209	60	20	4	5.0	5.5	15	569	1713	-2.4E-03	-1403	1.67E-06	4.83E-06	2.55E-06	35%	65%
0.209	60	20	4	5.0	5.5	618	957	1713	-1.5E-03	-915	1.67E-06	4.83E-06	2.55E-06	35%	65%
0.209	60	20	4	5.0	5.5	1208	1346	1713	-6.1E-04	-432	1.67E-06	4.83E-06	2.55E-06	35%	65%
0.209	60	20	4	5.0	5.5	1857	1809	1713	2.1E-04	119	1.67E-06	4.83E-06	2.55E-06	35%	65%
0.209	60	20	4	5.0	5.5	2478	2240	1713	1.0E-03	639	1.67E-06	4.83E-06	2.55E-06	35%	65%
0.209	60	20	4	5.0	5.5	3094	2666	1713	1.9E-03	1154	1.67E-06	4.83E-06	2.55E-06	35%	65%
0.209	80	40	4	5.0	5.7	0	2847	7966	-8.3E-03	-6438	1.24E-06	3.21E-06	2.01E-06	38%	62%
0.209	80	40	4	5.0	5.7	2967	4632	7966	-4.9E-03	-4110	1.24E-06	3.21E-06	2.01E-06	38%	62%
0.209	80	40	4	5.0	5.7	5868	6500	7966	-1.9E-03	-1763	1.24E-06	3.21E-06	2.01E-06	38%	62%
0.209	80	40	4	5.0	5.7	14275	12101	7966	6.4E-03	5145	1.24E-06	3.21E-06	2.01E-06	38%	62%
0.209	80	40	4	5.0	5.7	17044	13965	7966	9.0E-03	7432	1.24E-06	3.21E-06	2.01E-06	38%	62%
0.209	80	40	4	5.0	5.7	19780	15710	7966	1.2E-02	9636	1.24E-06	3.21E-06	2.01E-06	38%	62%
0.209	100	40	4	5.0	6.2	41	9301	29161	-3.0E-02	-24195	8.65E-07	2.54E-06	1.31E-06	34%	66%
0.209	100	40	4	5.0	6.2	9554	15400	29161	-1.9E-02	-16512	8.65E-07	2.54E-06	1.31E-06	34%	66%
0.209	100	40	4	5.0	6.2	17701	21092	29161	-1.1E-02	-9666	8.65E-07	2.54E-06	1.31E-06	34%	66%
0.209	100	40	4	5.0	6.2	33996	32641	29161	4.3E-03	4121	8.65E-07	2.54E-06	1.31E-06	34%	66%

0.249	40	20	4	5.0	5.2	53	220	840	-6.9E-04	-700	9.73E-07	4.57E-06	1.24E-06	21%	79%
0.249	40	20	4	5.0	5.2	280	391	840	-4.6E-04	-502	9.73E-07	4.57E-06	1.24E-06	21%	79%
0.249	40	20	4	5.0	5.2	598	656	840	-2.4E-04	-212	9.73E-07	4.57E-06	1.24E-06	21%	79%
0.249	40	20	4	5.0	5.2	1268	1171	840	4.1E-04	377	9.73E-07	4.57E-06	1.24E-06	21%	79%
0.249	40	20	4	5.0	5.2	1627	1464	840	6.8E-04	703	9.73E-07	4.57E-06	1.24E-06	21%	79%
0.249	40	20	4	5.0	5.2	1984	1749	840	9.8E-04	1022	9.73E-07	4.57E-06	1.24E-06	21%	79%
0.249	60	30	4	5.0	5.3	58	1006	3795	-3.2E-03	-3240	1.07E-06	3.69E-06	1.50E-06	29%	71%
0.249	60	30	4	5.0	5.3	1239	1997	3795	-2.5E-03	-2155	1.07E-06	3.69E-06	1.50E-06	29%	71%
0.249	60	30	4	5.0	5.3	2507	2881	3795	-1.3E-03	-1090	1.07E-06	3.69E-06	1.50E-06	29%	71%
0.249	60	30	4	5.0	5.3	6225	5571	3795	2.2E-03	2086	1.07E-06	3.69E-06	1.50E-06	29%	71%
0.249	60	30	4	5.0	5.3	7521	6493	3795	3.4E-03	3185	1.07E-06	3.69E-06	1.50E-06	29%	71%
0.249	60	30	4	5.0	5.3	8732	7377	3795	4.5E-03	4223	1.07E-06	3.69E-06	1.50E-06	29%	71%
0.249	80	40	4	5.0	5.7	33	4339	16816	-1.3E-02	-14524	8.37E-07	3.21E-06	1.13E-06	26%	74%
0.249	80	40	4	5.0	5.7	4912	7822	16816	-8.5E-03	-10381	8.37E-07	3.21E-06	1.13E-06	26%	74%
0.249	80	40	4	5.0	5.7	9692	11305	16816	-4.7E-03	-6283	8.37E-07	3.21E-06	1.13E-06	26%	74%
0.249	80	40	4	5.0	5.7	28121	25404	16816	8.0E-03	9884	8.37E-07	3.21E-06	1.13E-06	26%	74%
0.249	80	40	4	5.0	5.7	32505	28642	16816	1.1E-02	13666	8.37E-07	3.21E-06	1.13E-06	26%	74%
0.249	80	40	4	5.0	5.7	37054	31966	16816	1.5E-02	17571	8.37E-07	3.21E-06	1.13E-06	26%	74%
0.290	40	40	4	5.0	5.1	26	570	2121	-1.4E-03	-1809	6.94E-07	2.87E-06	9.15E-07	24%	76%
0.290	40	40	4	5.0	5.1	684	979	2121	-7.7E-04	-1284	6.94E-07	2.87E-06	9.15E-07	24%	76%
0.290	40	40	4	5.0	5.1	1338	1496	2121	-4.1E-04	-701	6.94E-07	2.87E-06	9.15E-07	24%	76%
0.290	40	40	4	5.0	5.1	4044	3583	2121	1.2E-03	1682	6.94E-07	2.87E-06	9.15E-07	24%	76%
0.290	40	40	4	5.0	5.1	4717	4128	2121	1.5E-03	2289	6.94E-07	2.87E-06	9.15E-07	24%	76%
0.290	40	40	4	5.0	5.1	5382	4627	2121	2.0E-03	2867	6.94E-07	2.87E-06	9.15E-07	24%	76%
0.290	60	40	4	5.0	5.3	36	2451	9926	-6.5E-03	-8626	6.76E-07	2.98E-06	8.74E-07	23%	77%
0.290	60	40	4	5.0	5.3	3250	4593	9926	-3.6E-03	-5980	6.76E-07	2.98E-06	8.74E-07	23%	77%
0.290	60	40	4	5.0	5.3	6499	7128	9926	-1.7E-03	-3102	6.76E-07	2.98E-06	8.74E-07	23%	77%

0.290	60	40	4	5.0	5.3	18855	16836	9926	5.5E-03	7876	6.76E-07	2.98E-06	8.74E-07	23%	77%
0.290	60	40	4	5.0	5.3	21855	19196	9926	7.2E-03	10543	6.76E-07	2.98E-06	8.74E-07	23%	77%
0.290	60	40	4	5.0	5.3	24676	21512	9926	8.6E-03	13105	6.76E-07	2.98E-06	8.74E-07	23%	77%
0.320	40	40	4	5.0	5.1	222	931	4480	-1.9E-03	-3893	4.68E-07	2.87E-06	5.59E-07	16%	84%
0.320	40	40	4	5.0	5.1	1922	2339	4480	-1.1E-03	-2343	4.68E-07	2.87E-06	5.59E-07	16%	84%
0.320	40	40	4	5.0	5.1	3918	4019	4480	-2.6E-04	-510	4.68E-07	2.87E-06	5.59E-07	16%	84%
0.320	40	40	4	5.0	5.1	9131	8328	4480	2.1E-03	4237	4.68E-07	2.87E-06	5.59E-07	16%	84%
0.320	40	40	4	5.0	5.1	11053	9959	4480	2.9E-03	6009	4.68E-07	2.87E-06	5.59E-07	16%	84%
0.320	40	40	4	5.0	5.1	13049	11683	4480	3.6E-03	7866	4.68E-07	2.87E-06	5.59E-07	16%	84%
0.320	60	30	4	5.0	5.3	173	2665	18984	-8.3E-03	-17535	4.46E-07	3.69E-06	5.08E-07	12%	88%
0.320	60	30	4	5.0	5.3	5302	6916	18984	-5.4E-03	-12858	4.46E-07	3.69E-06	5.08E-07	12%	88%
0.320	60	30	4	5.0	5.3	10317	11305	18984	-3.3E-03	-8163	4.46E-07	3.69E-06	5.08E-07	12%	88%
0.320	60	30	4	5.0	5.3	29510	28157	18984	4.5E-03	9834	4.46E-07	3.69E-06	5.08E-07	12%	88%
0.320	60	30	4	5.0	5.3	34581	32755	18984	6.1E-03	14665	4.46E-07	3.69E-06	5.08E-07	12%	88%
0.320	60	30	4	5.0	5.3	39135	36582	18984	8.6E-03	18846	4.46E-07	3.69E-06	5.08E-07	12%	88%

CO_2 Rates with Amino Acids

Quarterly Report for July 1 – September 30, 2010

by Le Li

Supported by the Luminant Carbon Management Program

Department of Chemical Engineering

The University of Texas at Austin

October 31, 2010

Abstract

Two amino sulfonic acid solvents with taurine and homotaurine were tested in the wetted wall column during this quarter. The solvents are 5 m TauK and a blend of 3 m TauK/5 m HomotauK. The absorption rate (k_g') and CO_2 solubility were measured for 5 m TauK at 0.2 CO_2 loading only, because the solvent begins to precipitate at higher loadings. 5 m TauK has a higher absorption rate and lower CO_2 solubility than 7 m MEA at this loading. The calculated heat of absorption for 5 m TauK at 0.2 loading is 84.3 kJ/mol. The blend of 3 m TauK/5 m HomotauK was chosen to maximize the total alkalinity of the solvent to 8 m. The k_g' and CO_2 solubility was measured for the blend at five CO_2 loadings across the lean and rich operating conditions. The absorption rate of the blend is higher than 7 m MEA at low loadings. The CO_2 solubility of the blend is higher than 5 m TauK and similar to 7 m MEA. The cyclic capacity for the blend is calculated to be approximately 0.2 mol CO_2/kg solvent, and the heat capacity is at a competitive range of 75–80 kJ/mol. The absorption rate, CO_2 capacity, and heat of absorption were calculated for all tested amino acid solvents at operating conditions specific to coal applications as well as natural gas. The absorption rates of the amino acid solvents are 3–5 X higher in the gas operation region than coal. The heat of absorption is also more attractive at the gas conditions. Amino acid solvents have low capacities in general, at approximately 0.2–0.35 mol CO_2/kg solvent, which is 50% of 7 m MEA. While amino acids are not attractive for coal power plant applications, they are competitive solvents for treating natural gas power plants.

Introduction

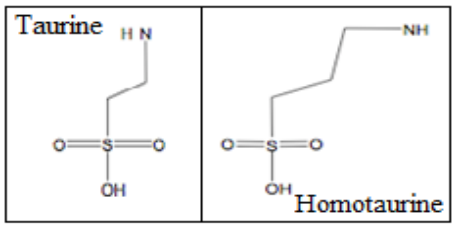

Figure 1: Chemical Structure of Taurine and Homotaurine

Two taurine-based amino acid solvents were screened using the wetted wall column this quarter. They are 5 m TauK and a blend of 3 m TauK/5 m HomotauK. The molecular structures of the two amino acids, taurine and homotaurine, are shown in Figure 1. Both amino acids contain

sulfonic acid groups, compared to carboxylic acid groups in previously screened amino acids (glycine and sarcosine). Sulfonic acid groups are attractive because the acid does not partake in amide formation reactions that occur during thermal degradation. However, it has been observed that the amino sulfonic acids are less soluble with CO_2 loading than amino carboxylic acids (Hook, 1997). A rough solubility screening exercise was conducted to determine the maximum amino acid solvent concentration without solid precipitation. TauK precipitates at 5 m concentration with 0.2 loading at room temperature (approx 25 °C), but is soluble when heated to 40 °C and above. It is expected that the solubility of the solution will decrease with further loading (Majchrowicz, 2009). Therefore, only one set of wetted wall column experiments was performed with 5 m TauK at a loading of 0.2 and temperatures at 40 °C, 60 °C, 80 °C, and 100 °C. Similar solid precipitation phenomena have been observed with other amino acids of interest (Majchrowicz, 2009), which limits the total alkalinity of these solvents at approximately 6 m or less. It is important to increase the alkalinity of amino acid solvents to compete against typical amine solvents such as 7 m MEA and 8 m PZ. Blending amino acid solvents at various concentration ratios was proposed to maximize the solubility limit of these solvents. A blend of 3 m TauK/5 m HomotauK with a total alkalinity of 8 m was soluble. The blend also maintains a potential thermal degradation advantage since both amino acids used are sulfonic acid.

Both amino acid solvents were neutralized using an equimolar amount of potassium hydroxide.

Experimental Methods

The wetted wall column apparatus was used to measure the absorption/desorption rates and the CO_2 solubility of the two amino acid solvents. The experimental method is identical to that used by Chen (2010).

Materials

Table 1: Materials Used for Taurine-Based Solvent Preparation

Chemical	Purity	Source
Taurine	99.00%	Alfa Aesar
Homotaurine	98.00%	AK Scientific
Potassium Hydroxide (solid)	87.00%	Fisher Chemical
Potassium Hydroxide (liquid)	45.5%	Fisher Chemical
DDI Water	100.00%	Millipore, Direct-Q

Table 2: Chemical Species in 5 m Potassium Taurate Initial Solution

Chemical Species	Mass (g)	Wt %
Taurine	931.02	32.2%
Potassium Hydroxide	417.36	14.4%
Water	1540.79	53.3%
TauK (salt)	1221.13	42.3%

Table 3: Chemical Species in 3 m (Potassium) Taurate/5 m Homotaurate Initial Solution

Chemical Species	Mass (g)	Wt %
Taurine	300.5	14.9%
Homotaurine	556.7	27.6%
Potassium Hydroxide	359.6	17.8%
Water	801.2	39.7%
TauK/HomotauK	1107.2	54.9%

The chemicals used to prepare the 5 m TauK and 3 m TauK/5 m HomotauK are listed in Table 1. Potassium hydroxide in the form of solid pellets was used to neutralize the 5 m TauK solution. For the blend, liquid potassium hydroxide (45.5 wt % in water) was used. Using the aqueous potassium hydroxide can potentially improve the accuracy of the mass measured, as the solid pellets tend to absorb atmospheric CO_2 and H_2O during the solution making process. Each CO_2 loading conditions of the solvents was obtained by bubbling gaseous CO_2 (99.99%, Matheson Tri-Gas) into the solvent.

Solubility Screening

Two solubility tests were performed to determine the maximum solvent concentration without solid precipitation. The first test was performed using potassium hydroxide to neutralize the amino acid solution. An equimolar amount of potassium hydroxide was added to a known amount of taurine; water was then added in small increments until all solids dissolved. The solution was constantly stirred, and sufficient time was allowed between each addition of water for the solvent to reach equilibrium. This test allows for the rough estimation of the maximum concentration of an amino acid with zero CO_2 loading. However, many amino acid solvents have high solubility without CO_2, but precipitate when loaded with CO_2 (6 m GlyK and TauK). Therefore, a second solubility test was performed using potassium carbonate (K_2CO_3). For every two moles of potassium (K+) added, one mole of CO_2 is also added to the mixture. Neutralizing a known amount of an amino acid using K_2CO_3 gives the mixture a CO_2 loading of 0.5 (mol CO_2/mol alk). The maximum solvent concentration with 0.5 loading can then be determined by adding small increments of water into the mixture until all solids dissolve.

Results and Discussions

Solid Solubility Observations

5 m TauK was soluble at room temperature with zero CO_2 loading, but the solvent precipitated after being loaded to 0.2 mol CO_2/mol alk. At 40 °C and higher, the loaded (0.2) 5 m TauK is soluble. The blend of 3 m TauK/5 m HomotauK was soluble at room temperature at a loading of 0.5 mol CO_2/mol alk. However, after the blend was left undisturbed (no stirring or movement) for approximately a week, solid crystals were found at the bottom of the container.

Absorption / Desorption Rates

The rate of CO_2 absorption of 5 m TauK was measured at 0.2 loading only. The measured liquid film mass transfer coefficient (k_g') at 40 °C, 60 °C, 80 °C, and 100 °C is compared against the 40 °C absorption rate of 7 m MEA, 8 m PZ, 3.55 m GlyK, and 6 m SarK (Figure 2). When

compared at the same equilibrium CO_2 partial pressure (P_{CO2}^*) measured at 40 °C, 5 m TauK has higher absorption rate than 7 m MEA and the other two amino acid solvents. The absorption rates for the solvent show scattered behavior as temperature varies. The tested CO_2 loading condition at 0.2 corresponds to an equilibrium CO_2 partial pressure of 41 Pa at 40 °C (Table 4), which is much lower than the optimal lean operation loading condition for coal flue gas applications (P_{CO2}^* = 500Pa) as well as natural gas applications (P_{CO2}^* = 100Pa). Rate measurements for 5 m TauK were not collected at the operating loading conditions since the solvent was expected to precipitate. Even though the measured loading condition is not a true representation of the solvent rate at its operation conditions, the result offers motivation to investigate TauK solvents at lower concentrations which could bypass the precipitation issue while maintaining attractive rate performance.

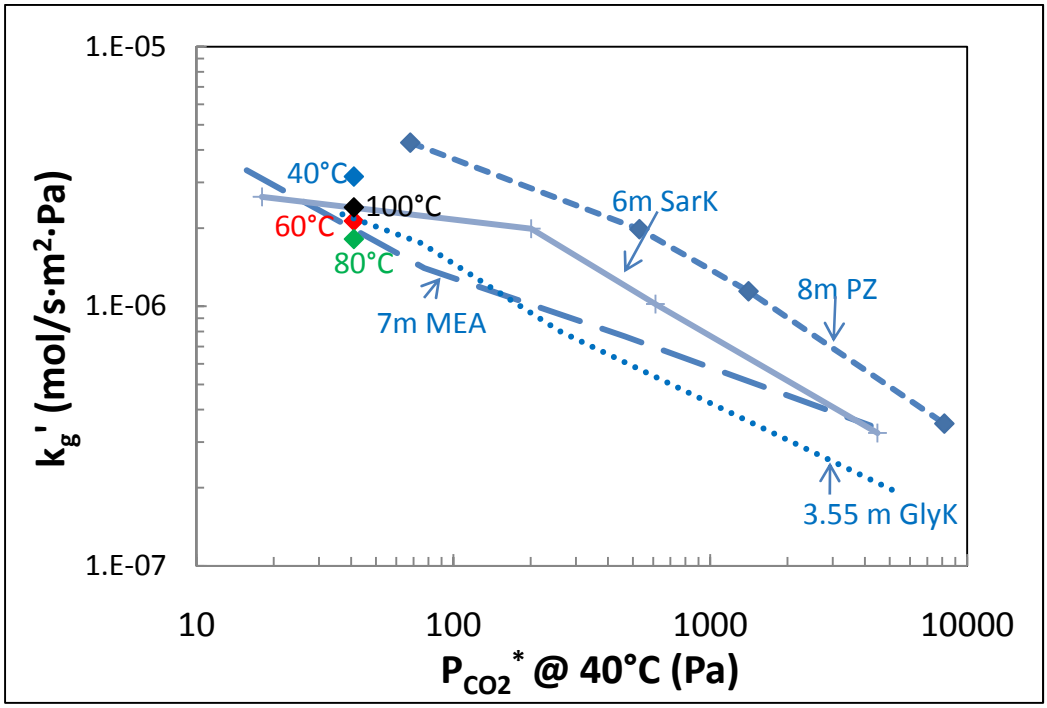

Figure 2: CO_2 Liquid Phase Mass Transfer Coefficient (k_g') for 5 m TauK

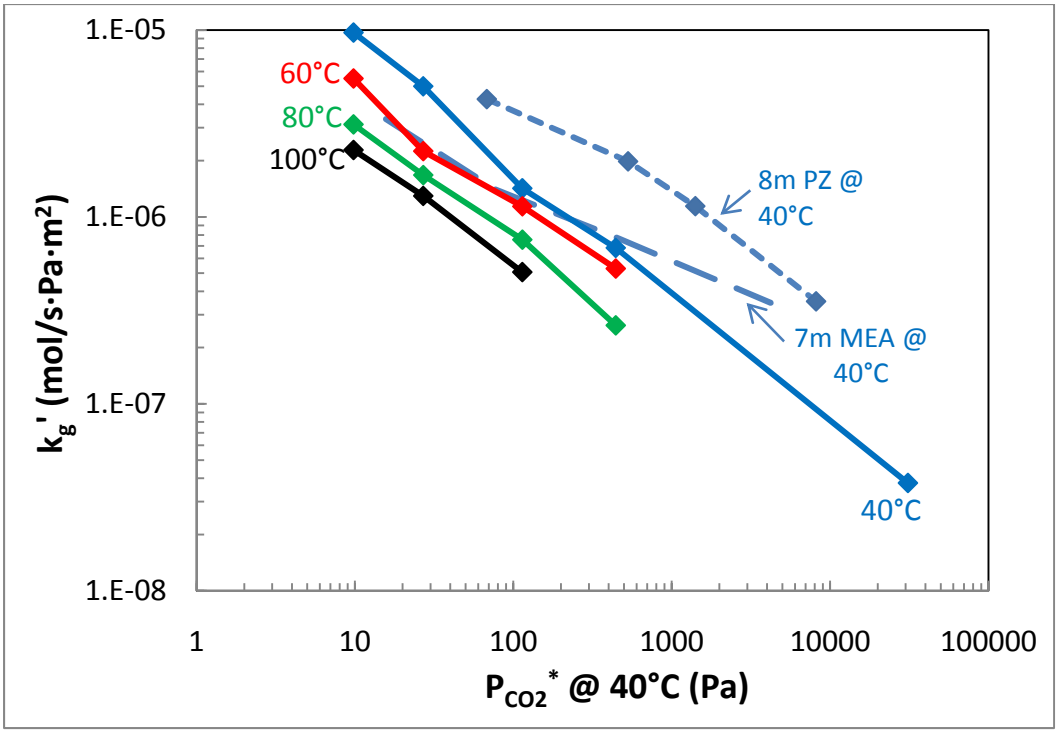

Figure 3: CO_2 Liquid Phase Mass Transfer Coefficient (k_g') for 3 m TauK/5 m HomotauK

The absorption rate for the blend of 3 m TauK/5 m HomotauK was measured at five loading conditions across the lean and rich loading range. The k_g' for the blend is plotted against the absorption rate of 7 m MEA at 40 °C and 8 m PZ at 40 °C (Figure 3). At 40 °C, the blend has much higher absorption rates than 7 m MEA at lean loading conditions, but its rate decreases significantly as solvent loading increases. The rate behavior of the blend demonstrated consistent temperature dependence, where the rate decreases with increasing temperature throughout the loading range tested.

CO_2 Solubility

The P_{CO2}* of 5 m TauK was measured at 0.2 loading and temperatures of at 40 °C, 60 °C, 80 °C, and 100 °C (Figure 4). When compared against 7 m MEA, 5 m TauK has much lower CO_2 solubility, with much higher P_{CO2}* measured at all four temperatures. The thermodynamic model cannot be generated for this solvent due to the lack of experimental data at other loading conditions.

$$\ln(P) = a + b/T + c \cdot \alpha + d \cdot \alpha / T + e \cdot \alpha^2 \quad (1)$$

The blend of 3 m TauK/5 m HomotauK was tested for its P_{CO2}* at five loadings and four temperatures (Figure 5). The CO_2 solubility of the blend is very similar to 7 m MEA at the four low loading conditions tested. The significant difference in CO_2 solubility between 5 m TauK and the blend can be explained by the presence of homotaurine. It can be predicted that the high CO_2 solubility of homotaurine dominates CO_2 solubility of the blend at the lower loading conditions. The CO_2 solubility of the blend decreases dramatically at a loading of 0.5, corresponding to a significant increase in P_{CO2}* (Figure 5). This trend can be explained by the consumption of free homotaurine by absorbed CO_2 which shifts the dominating absorption

species to taurine around 0.5 loading. The experimental data points are regressed together to generate a thermodynamic model for the blend using a semi-empirical VLE model (Equation 1). The resulting model, plotted as a solid line in Figure 5, fits the experimental data well at the low loadings but does not match the data at 0.5 loading. This is because the model used is relatively simple, correlating P_{CO2}* with CO_2 loading and temperature only and does not account for speciation in the solvent. Therefore, it does not predict the solubility for the blend well at rich loading conditions, where the speciation of the components in solution becomes important.

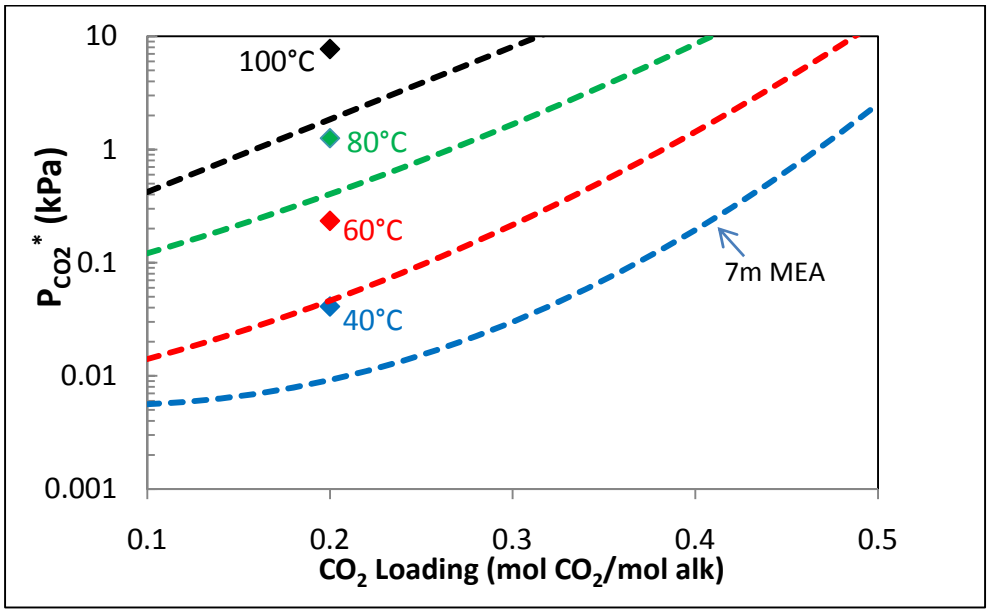

Figure 4: CO_2 Solubility Measured for 5 m TauK

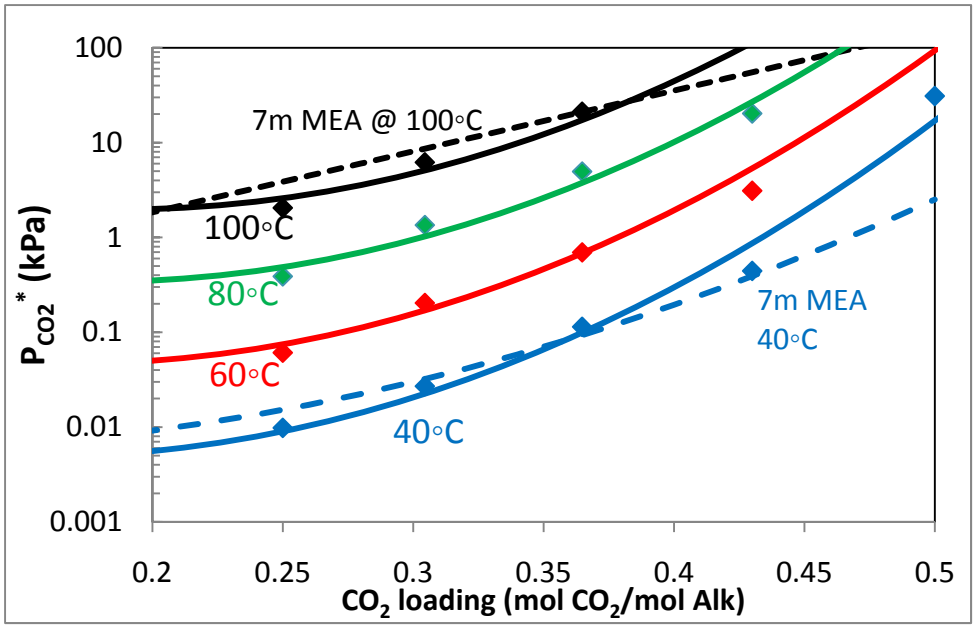

Figure 5: CO_2 Solubility Measured for 3 m TauK/5 m HomotauK

The absorption rate and CO_2 solubility measured for 5 m TauK are summarized in Table 4. The results for 3 m TauK/5 m HomotauK are shown in Table 5. The detailed wetted wall column data used to extrapolate the reported k_g' and P_{CO2}* values for these two solvents (as well as previously tested amino acid solvents) are included in the appendix of this report.

Table 4: CO_2 Solubility and k_g' Measured at Various Temperatures for 5 m Potassium Taurate

Loading	Temperature	k_g'	P_{CO2}*
(mol CO_2/mol alk)	(°C)	X 10^{-7} (mol/s·Pa·m^2)	(kPa)
0.2	40	31.60	0.041
0.2	60	21.32	0.234
0.2	80	18.16	1.259
0.2	100	24.05	7.73

Table 5: CO_2 Solubility and k_g' Measured at Various Loading and Temperatures for 3 m TauK/5 m HomotauK

Loading	Temperature	k_g'	P_{CO2}*
(mol CO_2/mol alk)	(°C)	X 10^{-7} (mol/s·Pa·m^2)	(kPa)
0.25	40	96.98	0.0098
0.3045	40	50.01	0.027
0.3648	40	14.22	0.114
0.43	40	6.83	0.443
0.5	40	0.38	30.982
0.25	60	55.01	0.061
0.3045	60	22.48	0.204
0.3648	60	11.39	0.696
0.43	60	5.29	3.112
0.25	80	31.29	0.389
0.3045	80	16.75	1.351
0.3648	80	7.56	4.958
0.43	80	2.63	20.299
0.25	100	22.81	2.051
0.3045	100	12.94	6.2
0.3648	100	5.06	21.232

Table 6: Measured Properties of Tested Amino Acid Solvents for CO_2 Absorption

Amine	CO_2 Capacity (mol CO_2/kg Solution)		k_g'$_{avg}$ (@40◦C) (X 10^{-7} mol CO_2/s Pa m^2)		Mid ΔH_{abs} (kJ/mol)	
					P_{CO2}^* = 1.5kPa	P_{CO2}^* = 0.5kPa
	Coal	Gas	Coal	Gas	Coal	Gas
GlyK (3.55 m)	0.25	0.25	3	10.2	64	69
GlyK (6 m)	0.35*	0.35	0.2*	3.2	64*	
SarK (6 m)	0.22	0.236	5	18.9	56.5	64
Tau/Htau (3/5 m)	0.195	0.23	2.2	10.3	74.5	80
Proline (8 m, Chen)	/	/	0.1*	3.6	/	/
MEA (7 m) (Dugas)	0.47	0.55	4.3	11.7	82	83

Key solvent parameters calculated using the measured rate and solubility data for all tested amino acid solvents are summarized in Table 6. Each solvent is analyzed at operating conditions specific to coal applications, as well as conditions for natural gas applications. The k_g'$_{avg}$ values reported are calculated using the following equation (Chen, 2010):

$$k_g{}'_{avg} = \frac{Flux_{CO_2,LM}}{(P_{CO_2,gas} - P^*_{CO_2})_{LM}} = \frac{(Flux_{CO_2,top} - Flux_{CO_2,bottom}) / \ln(Flux_{CO_2,top} / Flux_{CO_2,bottom})}{[(P_{CO_2,top} - P^*_{CO_2,lean}) - (P_{CO_2,bottom} - P^*_{CO_2,rich})] / \ln(\frac{(P_{CO_2,top} - P^*_{CO_2,lean})}{(P_{CO_2,bottom} - P^*_{CO_2,rich})})} \quad (2)$$

The value of k_g'$_{avg}$ is representative of the rate performance of the solvent across the entire absorber.

Heat of Absorption

The heat of absorption for each solvent is calculated by applying the following thermodynamic relationship to its semi-empirical VLE model (Equation 1):

$$\Delta H_{Abs} = -R\frac{d\ln P}{d(1/T)} = -R(b + d \cdot \alpha) \quad (3)$$

For each amino acid solvent, heat of absorption is calculated at the midpoint of the operating range for coal and natural gas applications separately (Table 6). The blend has a high heat of absorption, particularly at the natural gas conditions. The heat of absorption for 5 m Tau cannot be calculated using Equation 3 since a thermodynamic model is not available. However, a heat of absorption value can be calculated for the solvent at the CO_2 loading of 0.2 by performing a linear regression using the measured P_{CO2}* results and the respective temperatures (Figure 6). The resulting value for heat of absorption of 5 m TauK is 84.3 kJ at 0.2 CO_2 loading.

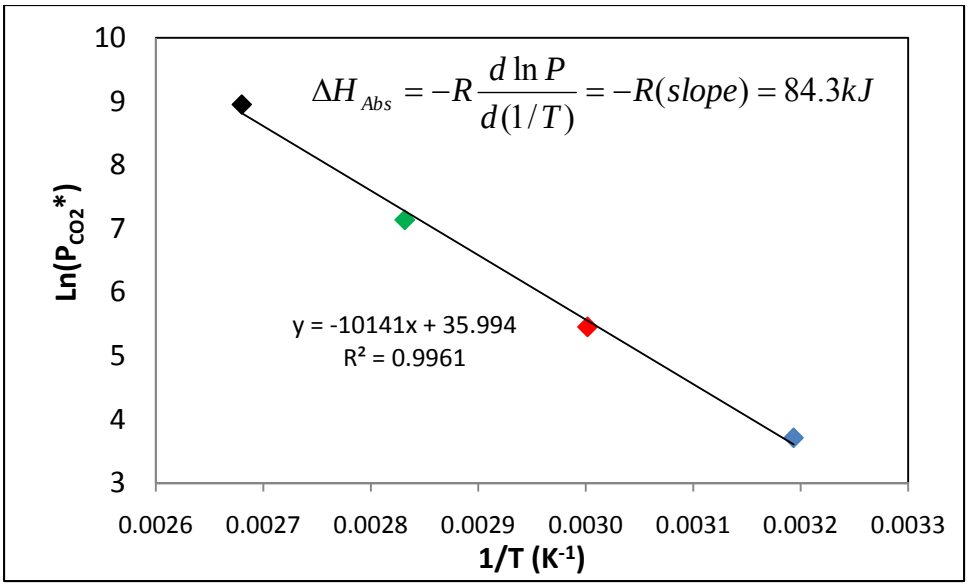

Figure 6: Heat of Absorption for 5 m TauK at 0.2 CO_2 loading

CO_2 Capacity

Capacity of a solvent refers to moles of CO_2 a solvent can carry per unit mass of the solvent and can be express as shown below:

$$Capacity = mol\ CO_2/kg\ solvent = \frac{(\alpha_{rich} - \alpha_{lean}) \cdot mol\ alkalinity}{kg\ solvent} \quad (4)$$

The values for the rich loading (α_{rich}) and lean loading (α_{lean}) in Equation 4 are obtained using the regressed thermodynamic model of the solvent at 40 °C for each solvent. For coal-fired power plants, the rich and lean loadings of a solvent correspond to equilibrium CO_2 partial pressures of 5 kPa and 0.5 kPa at 40 °C, respectively. Alternatively, solvent conditions of P_{CO2}* at 1 kPa (rich) and P_{CO2}* at 0.1 kPa (lean) were chosen for natural gas power plants. Mathematically, a larger delta loading results in a larger capacity. The mole of alkalinity term in the numerator indicates that more concentrated solvents will have higher capacities. Since the "kg solvent" term is in the denominator, solvents with a smaller molecular mass will have higher capacities. The solid solubility limit of many amino acid solvents restricts the concentration of most of the tested amino acid solvents at 6 m, which is lower than 7 m MEA and 8 m PZ. Also, since amino acid solvents require the addition of an equimolar amount of base to activate for CO_2 absorption (MW of potassium: 39 mol/kg), amino acid solvents will always have a higher mass than amine solvents at the same alkalinity. The combined effect of solubility limitations and high solvent mass gives amino acid solvents an intrinsic disadvantage in terms of CO_2 capacity. The calculated capacities for amino acid solvents range from 0.2 to 0.35 mol CO_2/kg solvent, which is approximately 50% of the 7 m MEA capacity (Table 6).

Natural Gas Applications

When compared at operating ranges specified for natural gas versus coal power plant flue gas conditions, all amino acid solvents demonstrated different levels of performance (Table 6). The low CO_2 content in the flue gas from natural gas power plants requires the absorption solvents to

be operated at lower loading range which is advantageous to amino acid solvents. The absorption rate ($k_g'_{avg}$) and heat of absorption are higher for all solvents in the natural gas operating range. The improvement in rate is particularly significant, with a calculated increase of 3–5 times for all amino acid solvents. When operating at a low loading, amino acid solvents are more likely to avoid potential solid precipitation issues. Though the capacity of amino acid solvents remains relatively constant as the operating range shifts from coal conditions to natural gas, solvent capacity is less important relative to rate performance when used to treat natural gas power plants. Since flue gas from a gas turbine is three times the volume of coal flue gas (compared at the same energy output), a much larger absorber is required. As the capital cost of a natural gas treating process becomes more important, optimizing the energy cost by using a solvent with higher capacity will have little effect on the economics of the process. It can be generalized for natural gas specific processes that it is more important to use a solvent that minimizes the absorber cost than a solvent with more efficient energy consumption.

Volatility and biodegradability are two advantages of amino acid solvents which reduce absorber costs, as the need for a water wash can be eliminated. The oxygen content of a natural gas plant is two to three times that of coal plants. As a result, the oxidative degradation performance, which is an additional strength for some amino acid solvents, becomes more important. Natural gas power plants, therefore, would be the appropriate application of an amino acid solvent-based CO_2 capture process.

Conclusions

The solid solubility limit for TauK solvents is much lower than for other amino acid solvents. TauK precipitates at a lower amino acid concentration and lower CO_2 loading conditions than GlyK, SarK, or HomotauK. The absorption rate for 5 m TauK is higher than 7 m MEA and GlyK and 6 m SarK at the loading of 0.2 mol CO_2/mol alk. At the 0.2 loading, the CO_2 solubility of 5 m TauK is lower than 7 m MEA, and the heat of absorption is 84.3 kJ/mol. To fully analyze the potential of taurine as a CO_2 absorption solvent, the total amino acid concentration in the solvent must be lowered. The blend of 3 m TauK/5 m HomotauK has competitive absorption rates at low loading conditions, but the rate decreases rapidly as loading increases. The blend has similar CO_2 solubility to 7 m MEA, which suggests homotaurine potentially has higher CO_2 solubility than taurine. The capacity of the blend is low at approximately 0.2 mol CO_2/kg solvent, but the heat of absorption is attractive at 80 kJ/mol (at natural gas application conditions). It can be concluded that amino acid solvents in general have low intrinsic CO_2 capacities. The capacities of tested amino acid solvents range from 0.2 to 0.35 mol CO_2/kg solvent, which is less than 50% of the capacity of 7 m MEA. Based on measured parameters, amino acid solvents are not competitive against conventional amine solvents at coal power plant flue gas conditions. However, due to the specific flue gas properties of natural gas power plants, amino acid solvents are attractive solvents for these applications.

Future Work

The screening work on amino acid-based solvents will continue during the next quarter. A series of alanine based amino acid solvents will be tested using the wetted wall column.

References

Chen X, Closmann F, Rochelle GT. “Accurate Screening of Amines by the Wetted Wall Column.” *Energy Proc*. 2010.

Hook RJ. “An Investigation of Some Sterically Hindered Amines as Potential Carbon Dioxide Scrubbing Compounds.” *Ind Eng Chem Res*. 1997;36:1779–1790.

Majchrowicz ME, Brilman DWF, Groeneveld MJ. “Precipitation regime for selected amino acid salts for CO_2 capture from flue gases.” *Energy Proc*. 2009;1:979–984.

Rochelle GT et al. "CO_2 Capture by Aqueous Absorption, Second Quarterly Progress Report 2010." Luminant Carbon Management Program. The University of Texas at Austin. 2010.

Appendix

Table A-1a: Detailed Wetted Wall Column Data for 3.55 m GlyK

GlyK	CO_2 ldg	P_{CO2}*	Temp	Pressure	Gas_{Dry}	Gas_{wet}	$P_{CO2in, dry}$	$P_{CO2in, wet}$	$P_{CO2out, dry}$	$P_{CO2out, wet}$	CO_2 flux	K_G	k_g	K_G/k_g	k_g'
m	mol CO_2/mol alk	Pa	C	psig	Std L/min	Std L/min	Pa	Pa	Pa	Pa	mol/s m^2	mol/s Pa m^2	mol/s Pa m^2		mol/s Pa m^2
3.55	0.35	37	40	20	5	5.16	0	0.00	14.5	14.05	-5.85E-09	1.51E-06	4.57E-06	0.33	2.26E-06
							10	9.69	17.8	17.25	-3.15E-09				
							20	19.38	23.1	22.39	-1.25E-09				
							60	58.15	51.7	50.10	3.35E-09				
							70	67.84	62.4	60.47	3.07E-09				
							80	77.53	67.2	65.13	5.17E-09				
3.55	0.35	180	60	20	5	5.45	0	0.00	50	45.83	-2.02E-08	1.18E-06	4.83E-06	0.25	1.57E-06
							50	45.83	81.5	74.71	-1.27E-08				
							100	91.67	120.5	110.46	-8.27E-09				
							250	229.17	238	218.17	4.84E-09				
							300	275.00	277	253.92	9.28E-09				
							350	320.83	313	286.92	1.49E-08				
3.55	0.35	1063	80	40	5	5.72	0	0.00	395	345.37	-1.01E-07	1.25E-06	3.21E-06	0.39	2.04E-06
							500	437.18	773	675.88	-6.99E-08				
							1000	874.36	1079	943.43	-2.02E-08				
							1500	1311.53	1420	1241.58	2.05E-08				
							2000	1748.71	1710	1495.15	7.43E-08				
							2500	2185.89	2050	1792.43	1.15E-07				
3.55	0.35	4435	100	40	5	6.84	0	0.00	1825	1334.58	-4.67E-07	1.28E-06	3.76E-06	0.34	1.93E-06
							2500	1828.19	3665	2680.12	-2.98E-07				
							5000	3656.37	5330	3897.69	-8.45E-08				
							10000	7312.75	8720	6376.72	3.28E-07				
							12500	9140.93	10460	7649.13	5.23E-07				
							15000	10969.12	12370	9045.87	6.74E-07				
3.55	0.4	75	40	20	5	5.16	0	0.00	25	24.23	-1.01E-08	1.27E-06	4.57E-06	0.28	1.75E-06
							25	24.23	35	33.92	-4.04E-09				
							50	48.46	55	53.30	-2.02E-09				
							150	145.37	129	125.02	8.48E-09				
							175	169.60	156	151.19	7.67E-09				
							200	193.83	164	158.94	1.45E-08				
3.55	0.4	462	60	40	5	5.28	0	0.00	161	152.49	-4.12E-08	9.44E-07	2.98E-06	0.32	1.38E-06
							150	142.07	244	231.10	-2.41E-08				
							300	284.14	332	314.45	-8.19E-09				
							600	568.28	579	548.39	5.38E-09				
							750	710.35	676	640.26	1.90E-08				
							850	805.07	741	701.83	2.79E-08				

Table A-1b: Detailed Wetted Wall Column Data for 3.55 m GlyK

GlyK	CO_2 ldg	P_{CO2} *	Temp	Pressure	Gas_{Dry}	Gas_{wet}	$P_{CO2in, dry}$	$P_{CO2in, wet}$	$P_{CO2out, dry}$	$P_{CO2out, wet}$	CO_2 flux	K_G	k_g	K_G/k_g	k_g'
m	mol CO_2/mol alk	Pa	C	psig	Std L/min	Std L/min	Pa	Pa	Pa	Pa	mol/s m^2	mol/s Pa m^2	mol/s Pa m^2		mol/s Pa m^2
3.55	0.4	2341	80	40	5	5.71	0	0.00	688	601.56	-1.76E-07	9.25E-07	3.21E-06	0.29	1.30E-06
							1000	874.36	1512	1322.03	-1.31E-07				
							2000	1748.71	2180	1906.09	-4.60E-08				
							4000	3497.42	3630	3173.91	9.46E-08				
							5000	4371.78	4345	3799.07	1.67E-07				
							6000	5246.13	5120	4476.70	2.25E-07				
3.55	0.4	9949	100	60	5	6.22	0	0.00	3350	2690.80	-6.28E-07	7.41E-07	2.54E-06	0.29	1.05E-06
							5000	4016.11	7050	5662.72	-3.84E-07				
							10000	8032.23	10720	8610.55	-1.35E-07				
							14000	11245.12	13360	10731.05	1.20E-07				
							19000	15261.23	17350	13935.91	3.09E-07				
							24000	19277.34	20800	16707.03	5.99E-07				
3.55	0.49	260	40	20	5	5.16	0	0.00	41	39.73	-1.66E-08	6.81E-07	4.57E-06	0.15	8.01E-07
							75	72.69	103	99.82	-1.13E-08				
							150	145.37	168	162.82	-7.27E-09				
							300	290.74	297	287.83	1.21E-09				
							375	363.43	357	345.98	7.27E-09				
							450	436.11	423	409.95	1.09E-08				
3.55	0.49	1641	60	40	5	5.28	0	0.00	353	334.34	-9.04E-08	6.69E-07	2.98E-06	0.22	8.62E-07
							500	473.57	785	743.50	-7.30E-08				
							1000	947.14	1185	1122.36	-4.74E-08				
							2000	1894.27	1932	1829.87	1.74E-08				
							2500	2367.84	2341	2217.24	4.07E-08				
							3000	2841.41	2710	2566.74	7.43E-08				
3.55	0.49	6735	80	40	5	5.72	0	0.00	1480	1294.05	-3.79E-07	6.21E-07	3.21E-06	0.19	7.70E-07
							3000	2623.07	3890	3401.24	-2.28E-07				
							6000	5246.13	6340	5543.41	-8.71E-08				
							10000	8743.55	9540	8341.35	1.18E-07				
							13000	11366.62	11980	10474.78	2.61E-07				
							16000	13989.68	14430	12616.95	4.02E-07				
3.55	0.49	23325	100	60	5	6.22	0	0.00	5660	4546.24	-1.06E-06	4.74E-07	2.54E-06	0.19	5.83E-07
							12000	9638.67	15080	12112.60	-5.77E-07				
							24000	19277.34	24650	19799.44	-1.22E-07				
							36000	28916.01	34380	27614.79	3.03E-07				
							48000	38554.68	44650	35863.89	6.28E-07				
							60000	48193.35	54520	43791.69	1.03E-06				

Table A-1c: Detailed Wetted Wall Column Data for 3.55 m GlyK

GlyK	CO_2 ldg	P_{CO2}*	Temp	Pressure	Gas_{Dry}	Gas_{wet}	$P_{CO2in, dry}$	$P_{CO2in, wet}$	$P_{CO2out, dry}$	$P_{CO2out, wet}$	CO_2 flux	K_G	k_g	K_G/k_g	k_g'
m	mol CO_2/mol alk	Pa	C	psig	Std L/min	Std L/min	Pa	Pa	Pa	Pa	mol/s m^2	mol/s Pa m^2	mol/s Pa m^2		mol/s Pa m^2
3.55	0.53	5361	40	20	5	5.16	0	0.00	248	240.35	-1.00E-07	1.84E-07	4.57E-06	0.04	1.92E-07
							1500	1453.71	1670	1618.46	-6.86E-08				
							3000	2907.42	3117	3020.81	-4.72E-08				
							7000	6783.98	6893	6680.29	4.32E-08				
							8500	8237.70	8390	8131.09	4.44E-08				
							10000	9691.41	9820	9516.96	7.27E-08				
3.55	0.53	20079	60	40	5	5.28	0	0.00	1380	1307.05	-3.53E-07	1.51E-07	2.98E-06	0.05	1.59E-07
							5000	4735.68	5730	5427.09	-1.87E-07				
							10000	9471.35	10480	9925.98	-1.23E-07				
							30000	28414.06	29500	27940.50	1.28E-07				
							35000	33149.74	34250	32439.39	1.92E-07				
							40000	37885.42	39050	36985.64	2.43E-07				
3.55	0.53	47888	80	60	5	5.51	0	0.00	4190	3804.50	-7.86E-07	1.46E-07	2.28E-06	0.06	1.56E-07
							20000	18159.90	21800	19794.29	-3.38E-07				
							40000	36319.80	40390	36673.92	-7.32E-08				
							60000	54479.71	59210	53762.39	1.48E-07				
							67500	61289.67	66800	60654.07	1.31E-07				
							75000	68099.63	73800	67010.04	2.25E-07				

Table A-2a: Detailed Wetted Wall Column Data for 6 m GlyK

GlyK	CO_2 ldg	P_{CO2}*	Temp	Pressure	Gas_{Dry}	Gas_{wet}	$P_{CO2in, dry}$	$P_{CO2in, wet}$	$P_{CO2out, dry}$	$P_{CO2out, wet}$	CO_2 flux	K_G	k_g	K_G/k_g	k_g'
m	mol CO_2/mol alk	Pa	C	psig	Std L/min	Std L/min	Pa	Pa	Pa	Pa	mol/s m^2	mol/s Pa m^2	mol/s Pa m^2		mol/s Pa m^2
6	0.35	18	40	20	5	5.16	0	0.00	7.15	6.93	-2.89E-09	2.10E-06	4.57E-06	0.46	3.88E-06
							5	4.85	9.45	9.16	-1.80E-09				
							10	9.69	14.75	14.29	-1.92E-09				
							30	29.07	25.7	24.91	1.74E-09				
							35	33.92	29.1	28.20	2.38E-09				
							40	38.77	30.6	29.66	3.79E-09				
6	0.35	95	60	20	5	5.45	0	0.00	27.9	25.57	-1.13E-08	1.48E-06	4.83E-06	0.31	2.14E-06
							30	27.50	54.8	50.23	-1.00E-08				
							60	55.00	72.1	66.09	-4.88E-09				
							120	110.00	112.2	102.85	3.15E-09				
							150	137.50	136	124.67	5.65E-09				
							180	165.00	160.1	146.76	8.03E-09				
6	0.35	536	80	40	5	5.72	0	0.00	177	154.76	-4.53E-08	1.14E-06	3.21E-06	0.35	1.76E-06
							200	174.87	353	308.65	-3.92E-08				
							400	349.74	476	416.19	-1.95E-08				
							800	699.48	735	642.65	1.66E-08				
							1000	874.36	877	766.81	3.15E-08				
							1200	1049.23	1007	880.48	4.94E-08				
6	0.35	2549	100	40	5	6.84	0	0.00	995	727.62	-2.55E-07	1.33E-06	3.76E-06	0.35	2.05E-06
							1000	731.27	1904	1392.35	-2.32E-07				
							2000	1462.55	2480	1813.56	-1.23E-07				
							4500	3290.74	4185	3060.38	8.07E-08				
							5500	4022.01	4820	3524.74	1.74E-07				
							6500	4753.29	5560	4065.89	2.41E-07				
6	0.4	100	40	20	5	5.16	0	0.00	24.9	24.13	-1.01E-08	9.77E-07	4.57E-06	0.21	1.24E-06
							25	24.23	37.8	36.63	-5.17E-09				
							50	48.46	60.2	58.34	-4.12E-09				
							150	145.37	139.8	135.49	4.12E-09				
							175	169.60	161.8	156.81	5.33E-09				
							200	193.83	178.6	173.09	8.64E-09				
6	0.4	620	60	40	5	5.28	0	0.00	129	122.18	-3.30E-08	7.16E-07	2.98E-06	0.24	9.42E-07
							200	189.43	323	305.92	-3.15E-08				
							400	378.85	472	447.05	-1.84E-08				
							800	757.71	772	731.19	7.17E-09				
							1000	947.14	916	867.58	2.15E-08				
							1200	1136.56	1065	1008.70	3.46E-08				

Table A-2b: Detailed Wetted Wall Column Data for 6 m GlyK

GlyK	CO_2 ldg	P_{CO2}*	Temp	Pressure	Gas_{Dry}	Gas_{wet}	$P_{CO2in,\ dry}$	$P_{CO2in,\ wet}$	$P_{CO2out,\ dry}$	$P_{CO2out,\ wet}$	CO_2 flux	K_G	k_g	K_G/k_g	k_g'
m	mol CO_2/mol alk	Pa	C	psig	Std L/min	Std L/min	Pa	Pa	Pa	Pa	mol/s m^2	mol/s Pa m^2	mol/s Pa m^2		mol/s Pa m^2
6	0.4	3243	80	40	5	5.72	0	0.00	728	636.53	-1.86E-07	6.93E-07	3.21E-06	0.22	8.84E-07
							1000	874.36	1619	1415.58	-1.59E-07				
							2000	1748.71	2386	2086.21	-9.89E-08				
							4000	3497.42	3930	3436.22	1.79E-08				
							5000	4371.78	4730	4135.70	6.91E-08				
							6000	5246.13	5504	4812.45	1.27E-07				
6	0.4	13529	100	60	5	6.22	0	0.00	3970	3188.79	-7.44E-07	6.32E-07	2.54E-06	0.25	8.40E-07
							5000	4016.11	7785	6253.09	-5.22E-07				
							10000	8032.23	11680	9381.64	-3.15E-07				
							20000	16064.45	19276	15482.92	1.36E-07				
							25000	20080.56	23040	18506.25	3.67E-07				
							30000	24096.68	26870	21582.59	5.86E-07				
6	0.45	225	40	20	5	5.16	0	0.00	21	20.35	-8.48E-09	5.12E-07	4.57E-06	0.11	5.77E-07
							75	72.69	97	94.01	-8.88E-09				
							150	145.37	163	157.97	-5.25E-09				
							350	339.20	338	327.57	4.84E-09				
							425	411.88	399	386.69	1.05E-08				
							500	484.57	469	454.53	1.25E-08				
6	0.45	1530	60	40	5	5.28	0	0.00	318	301.19	-8.14E-08	5.78E-07	2.98E-06	0.19	7.16E-07
							750	710.35	917	868.52	-4.28E-08				
							1500	1420.70	1529	1448.17	-7.43E-09				
							2500	2367.84	2300	2178.41	5.12E-08				
							3250	3078.19	2935	2779.84	8.07E-08				
							4000	3788.54	3558	3369.91	1.13E-07				
6	0.45	6619	80	40	5	5.72	0	0.00	1330	1162.89	-3.41E-07	5.79E-07	3.21E-06	0.18	7.06E-07
							3000	2623.07	3850	3366.27	-2.18E-07				
							6000	5246.13	6271	5483.08	-6.94E-08				
							10000	8743.55	9580	8376.32	1.08E-07				
							13000	11366.62	12045	10531.61	2.45E-07				
							16000	13989.68	14462	12644.93	3.94E-07				
6	0.45	23675	100	60	5	6.22	0	0.00	5385	4325.35	-1.01E-06	4.34E-07	2.54E-06	0.17	5.23E-07
							10000	8032.23	13050	10482.05	-5.71E-07				
							20000	16064.45	21430	17213.06	-2.68E-07				
							40000	32128.90	38020	30538.52	3.71E-07				
							50000	40161.13	46560	37398.04	6.44E-07				
							60000	48193.35	55020	44193.31	9.33E-07				

Table A-3a: Detailed Wetted Wall Column Data for 6 m SarK

SarK	CO_2 ldg	P_{CO2}*	Temp	Pressure	Gas_{Dry}	Gas_{wet}	$P_{CO2in,\ dry}$	$P_{CO2in,\ wet}$	$P_{CO2out,\ dry}$	$P_{CO2out,\ wet}$	CO_2 flux	K_G	k_g	K_G/k_g	k_g'
m	mol CO_2/mol alk	Pa	C	psig	Std L/min	Std L/min	Pa	Pa	Pa	Pa	mol/s m^2	mol/s Pa m^2	mol/s Pa m^2		mol/s Pa m^2
6	0.2	102	80	20	5	6.23	0	0.00	68.7	55.09	-2.77E-08	3.22E-06	5.45E-06	0.59	7.89E-06
							30	24.06	74.5	59.74	-1.79E-08				
							60	48.12	88	70.57	-1.13E-08				
							150	120.29	131.6	105.53	7.42E-09				
							180	144.35	154.3	123.74	1.04E-08				
							210	168.41	179	143.55	1.25E-08				
6	0.2	690	100	20	5	8.67	0	0.00	681	392.52	-2.75E-07	3.96E-06	7.26E-06	0.55	8.72E-06
							250	144.10	695	400.59	-1.80E-07				
							500	288.19	736	424.22	-9.52E-08				
							1500	864.58	1282	738.93	8.79E-08				
							1750	1008.68	1531	882.45	8.83E-08				
							2000	1152.78	1647	949.31	1.42E-07				
6	0.29	115	60	20	5	5.45	0	0.00	65	59.58	-2.62E-08	2.77E-06	4.83E-06	0.57	6.48E-06
							50	45.83	77	70.58	-1.09E-08				
							150	137.50	141	129.25	3.63E-09				
							175	160.42	166	152.17	3.63E-09				
6	0.29	1136	80	20	5	6.23	0	0.00	596	477.95	-2.40E-07	2.50E-06	5.45E-06	0.46	4.62E-06
							250	200.48	701	562.16	-1.82E-07				
							500	400.97	809	648.77	-1.25E-07				
							1500	1202.91	1461	1171.63	1.57E-08				
							1750	1403.39	1642	1316.78	4.36E-08				
							2000	1603.88	1767	1417.02	9.40E-08				
6	0.29	2266	100	40	5	6.84	0	0.00	1526	1115.93	-3.91E-07	2.16E-06	3.76E-06	0.58	5.09E-06
							750	548.46	1823	1333.11	-2.75E-07				
							1500	1096.91	2052	1500.58	-1.41E-07				
							4500	3290.74	3835	2804.44	1.70E-07				
							6000	4387.65	4846	3543.76	2.96E-07				
							12000	8775.30	7832	5727.34	1.07E-06				
6	0.35	19	40	20	5	5.16	0	0.00	15.5	15.02	-6.26E-09	1.67E-06	4.57E-06	0.37	2.64E-06
							40	38.77	29.3	28.40	4.32E-09				
							80	77.53	50.3	48.75	1.20E-08				
							120	116.30	86.7	84.02	1.34E-08				
							150	145.37	107.1	103.79	1.73E-08				
							180	174.45	131	126.96	1.98E-08				

Table A-3b: Detailed Wetted Wall Column Data for 6 m SarK

SarK	CO_2 ldg	P_{CO2}*	Temp	Pressure	Gas_{Dry}	Gas_{wet}	$P_{CO2in,\ dry}$	$P_{CO2in,\ wet}$	$P_{CO2out,\ dry}$	$P_{CO2out,\ wet}$	CO_2 flux	K_G	k_g	K_G/k_g	k_g'
m	mol CO_2/mol alk	Pa	C	psig	Std L/min	Std L/min	Pa	Pa	Pa	Pa	mol/s m^2	mol/s Pa m^2	mol/s Pa m^2		mol/s Pa m^2
6	0.35	164	60	20	5	5.45	0	0.00	76.5	70.12	-3.09E-08	2.16E-06	4.83E-06	0.45	3.91E-06
							50	45.83	93	85.25	-1.73E-08				
							100	91.67	130	119.17	-1.21E-08				
							200	183.33	192	176.00	3.23E-09				
							250	229.17	225	206.25	1.01E-08				
							300	275.00	253	231.92	1.90E-08				
6	0.35	2330	80	40	5	5.72	0	0.00	1058	925.07	-2.71E-07	1.36E-06	3.21E-06	0.42	2.36E-06
							2000	1748.71	2190	1914.84	-4.87E-08				
							4000	3497.42	3393	2966.69	1.55E-07				
							5000	4371.78	4193	3666.17	2.07E-07				
							6000	5246.13	4802	4198.65	3.07E-07				
6	0.35	3947	100	40	5	6.84	0	0.00	2031	1485.22	-5.20E-07	1.55E-06	3.76E-06	0.41	2.65E-06
							2000	1462.55	3075	2248.67	-2.75E-07				
							4000	2925.10	4460	3261.49	-1.18E-07				
							8000	5850.20	7180	5250.55	2.10E-07				
							10000	7312.75	8450	6179.27	3.97E-07				
							12000	8775.30	9510	6954.42	6.38E-07				
6	0.43	201	40	20	5	5.16	0	0.00	66.7	64.64	-2.69E-08	1.39E-06	4.57E-06	0.30	1.99E-06
							25	24.23	76.7	74.33	-2.09E-08				
							50	48.46	86.3	83.64	-1.47E-08				
							250	242.29	232	224.84	7.27E-09				
							275	266.51	255	247.13	8.07E-09				
							300	290.74	280	271.36	8.07E-09				
6	0.43	826	60	20	5	5.45	0	0.00	176	161.33	-7.10E-08	1.01E-06	4.83E-06	0.21	1.27E-06
							500	458.33	585	536.25	-3.43E-08				
							2000	1833.33	1797	1647.25	8.19E-08				
							2250	2062.50	1985	1819.58	1.07E-07				
							2500	2291.67	2146	1967.17	1.43E-07				
6	0.43	7096	80	40	5	5.72	0	0.00	2837	2480.55	-7.27E-07	1.12E-06	3.21E-06	0.35	1.72E-06
							4000	3497.42	4982	4356.04	-2.51E-07				
							10000	8743.55	9335	8162.11	1.70E-07				
							12000	10492.26	10770	9416.81	3.15E-07				
							14000	12240.97	12260	10719.60	4.46E-07				
6	0.43	16699	100	40	5	6.84	0	0.00	5730	4190.20	-1.47E-06	8.56E-07	3.76E-06	0.23	1.11E-06
							4000	2925.10	7680	5616.19	-9.43E-07				
							8000	5850.20	10720	7839.26	-6.97E-07				
							24000	17550.59	23510	17192.27	1.26E-07				
							28000	20475.69	27030	19766.35	2.48E-07				
							30000	21938.24	28660	20958.33	3.43E-07				

Table A-3c: Detailed Wetted Wall Column Data for 6 m SarK

SarK	CO_2 ldg	P_{CO2}*	Temp	Pressure	Gas_{Dry}	Gas_{wet}	$P_{CO2in, dry}$	$P_{CO2in, wet}$	$P_{CO2out, dry}$	$P_{CO2out, wet}$	CO_2 flux	K_G	k_g	K_G/k_g	k_g'
m	mol CO_2/mol alk	Pa	C	psig	Std L/min	Std L/min	Pa	Pa	Pa	Pa	mol/s m^2	mol/s Pa m^2	mol/s Pa m^2		mol/s Pa m^2
6	0.48	610	40	20	5	5.16	0	0.00	112	108.54	-4.52E-08	8.36E-07	4.57E-06	0.18	1.02E-06
							250	242.29	327	316.91	-3.11E-08				
							500	484.57	519	502.98	-7.67E-09				
							1500	1453.71	1343	1301.56	6.34E-08				
							1750	1696.00	1547	1499.26	8.19E-08				
							2000	1938.28	1751	1696.97	1.01E-07				
6	0.48	2430	60	20	5	5.45	0	0.00	422	386.83	-1.70E-07	7.41E-07	4.83E-06	0.15	8.75E-07
							1000	916.67	1228	1125.67	-9.19E-08				
							2000	1833.33	2116	1939.67	-4.68E-08				
							8000	7333.33	7165	6567.91	3.37E-07				
							9000	8249.99	8072	7399.33	3.74E-07				
							10000	9166.66	8820	8084.99	4.76E-07				
6	0.48	12260	80	40	5	5.72	0	0.00	4413	3858.53	-1.13E-06	8.04E-07	3.21E-06	0.25	1.07E-06
							4000	3497.42	5720	5001.31	-4.41E-07				
							8000	6994.84	8821	7712.69	-2.10E-07				
							22000	19235.82	20210	17670.72	4.58E-07				
							26000	22733.24	23180	20267.56	7.22E-07				
							30000	26230.66	26240	22943.08	9.63E-07				
6	0.48	31295	100	60	5	6.22	0	0.00	12180	9783.25	-2.28E-06	4.41E-07	2.54E-06	0.17	5.33E-07
							10000	8032.23	15090	12120.63	-9.54E-07				
							20000	16064.45	23080	18538.38	-5.77E-07				
							45000	36145.02	44250	35542.60	1.41E-07				
							50000	40161.13	47890	38466.33	3.95E-07				
6	0.51	4477	40	20	5	5.16	0	0.00	412	399.29	-1.66E-07	3.03E-07	4.57E-06	0.07	3.25E-07
							1000	969.14	1215	1177.51	-8.68E-08				
							2000	1938.28	2118	2052.64	-4.76E-08				
							6000	5814.84	5880	5698.55	4.84E-08				
							7000	6783.98	6855	6643.46	5.85E-08				
							8000	7753.13	7781	7540.88	8.84E-08				
6	0.51	17877	60	60	5	5.2	0	0.00	6995	6724.22	-1.31E-06	2.45E-07	2.16E-06	0.11	2.77E-07
							5000	4806.45	7030	6757.86	-3.80E-07				
							10000	9612.89	10680	10266.57	-1.27E-07				
							40000	38451.57	37040	35606.16	5.55E-07				
							45000	43258.02	41710	40095.38	6.17E-07				
							50000	48064.47	46800	44988.34	6.00E-07				

Table A-4a: Detailed Wetted Wall Column Data for 3 m TauK/5 m HomotauK

TauK/ HomotauK	CO_2 ldg	P_{CO2}*	Temp	Pressure	Gas_{Dry}	Gas_{wet}	$P_{CO2in, dry}$	$P_{CO2in, wet}$	$P_{CO2out, dry}$	$P_{CO2out, wet}$	CO_2 flux	K_G	k_g	K_G/k_g	k_g'
m	mol CO_2/mol alk	Pa	C	psig	Std L/min	Std L/min	Pa	Pa	Pa	Pa	mol/s m^2	mol/s Pa m^2	mol/s Pa m^2		mol/s Pa m^2
(3 / 5)	0.26	9.8	40	20	5	5.16	0.0	0.0	5.3	5.1	-2.12E-09	3.11E-06	4.57E-06	0.680	9.70E-06
							8.4	8.1	9.1	8.8	-2.90E-10				
							18.4	17.8	13.2	12.7	2.12E-09				
							34.9	33.8	23.2	22.5	4.73E-09				
							93.0	90.2	50.0	48.4	1.74E-08				
							125.8	121.9	64.3	62.4	2.48E-08				
(3 / 5)	0.26	61	60	20	5	5.45	0.0	0.0	31.8	29.2	-1.28E-08	2.57E-06	4.83E-06	0.532	5.50E-06
							32.5	29.8	46.4	42.5	-5.59E-09				
							61.5	56.3	63.6	58.3	-8.68E-10				
							87.8	80.5	75.1	68.8	5.11E-09				
							121.5	111.4	95.2	87.3	1.06E-08				
							182.7	167.5	133.5	122.3	1.99E-08				
(3 / 5)	0.26	389	80	40	5	5.72	0.0	0.0	206.6	180.7	-5.29E-08	1.59E-06	3.21E-06	0.494	3.13E-06
							195.7	171.1	280.9	245.6	-2.18E-08				
							367.6	321.4	383.4	335.3	-4.06E-09				
							578.8	506.0	530.1	463.5	1.25E-08				
							742.4	649.1	623.2	544.9	3.05E-08				
							911.3	796.8	716.0	626.0	5.00E-08				
(3 / 5)	0.26	2051	100	20	5	5.16	0.0	0.0	972.8	711.4	-2.96E-07	1.42E-06	3.76E-06	0.377	2.28E-06
							1048.2	766.5	1613.7	1180.1	-1.72E-07				
							2066.2	1510.9	2254.7	1648.8	-5.74E-08				
							4102.2	2999.8	3725.1	2724.1	1.15E-07				
							5384.1	3937.3	4516.9	3303.1	2.64E-07				
							6741.5	4929.9	5421.8	3964.8	4.02E-07				
(3 / 5)	0.3	27	40	20	5	5.16	0.0	0.0	12.9	12.5	-5.21E-09	2.39E-06	4.57E-06	0.522	5.00E-06
							14.8	14.4	21.5	20.9	-2.70E-09				
							35.9	34.8	30.9	29.9	2.03E-09				
							48.6	47.1	38.7	37.6	3.96E-09				
							59.6	57.7	45.2	43.8	5.79E-09				
							70.1	67.9	53.6	51.9	6.66E-09				
(3 / 5)	0.3	204	60	20	5	5.45	0.0	0.0	72.2	66.2	-2.91E-08	1.53E-06	4.83E-06	0.318	2.25E-06
							67.4	61.8	109.1	100.0	-1.68E-08				
							119.4	109.4	145.4	133.3	-1.05E-08				
							292.8	268.4	270.8	248.2	8.87E-09				
							345.1	316.4	310.2	284.4	1.41E-08				
							403.0	369.4	351.8	322.5	2.06E-08				

Table A-4b: Detailed Wetted Wall Column Data for 3 m TauK/5 m HomotauK

TauK/ HomotauK	CO_2 ldg	P_{CO2}*	Temp	Pressure	Gas_{Dry}	Gas_{wet}	$P_{CO2in, dry}$	$P_{CO2in, wet}$	$P_{CO2out, dry}$	$P_{CO2out, wet}$	CO_2 flux	K_G	k_g	K_G/k_g	k_g'
m	mol CO_2/mol alk	Pa	C	psig	Std L/min	Std L/min	Pa	Pa	Pa	Pa	mol/s m^2	mol/s Pa m^2	mol/s Pa m^2		mol/s Pa m^2
(3 / 5)	0.3	1351	80	40	5	5.72	0.0	0.0	512.8	448.3	-1.31E-07	1.10E-06	3.21E-06	0.343	1.68E-06
							678.7	593.4	953.9	834.1	-7.05E-08				
							1338.5	1170.3	1364.9	1193.4	-6.76E-09				
							3382.0	2957.1	2790.1	2439.5	1.52E-07				
							4064.5	3553.8	3280.2	2868.1	2.01E-07				
							4694.1	4104.3	3725.1	3257.1	2.48E-07				
(3 / 5)	0.3	6200	100	40	5	6.84	0.0	0.0	2111.4	1544.0	-5.41E-07	9.63E-07	3.76E-06	0.256	1.29E-06
							1998.3	1461.3	3544.2	2591.8	-3.96E-07				
							4034.3	2950.2	5052.3	3694.6	-2.61E-07				
							9350.6	6837.8	9048.9	6617.3	7.73E-08				
							11311.2	8271.6	10632.5	7775.3	1.74E-07				
							13196.4	9650.2	12140.7	8878.2	2.70E-07				
(3 / 5)	0.365	114	40	20	5	5.16	0.0	0.0	31.6	30.6	-1.27E-08	1.09E-06	4.57E-06	0.237	1.42E-06
							11.2	10.9	34.9	33.8	-9.56E-09				
							44.7	43.3	59.6	57.7	-5.99E-09				
							164.3	159.2	150.0	145.3	5.79E-09				
							226.0	219.1	201.6	195.4	9.85E-09				
							282.2	273.5	247.1	239.5	1.42E-08				
(3 / 5)	0.365	696	60	20	5	5.45	0.0	0.0	162.9	149.3	-6.57E-08	9.22E-07	4.83E-06	0.191	1.14E-06
							246.6	226.0	327.9	300.6	-3.28E-08				
							457.1	419.0	509.7	467.2	-2.12E-08				
							1272.7	1166.6	1162.7	1065.8	4.44E-08				
							1466.4	1344.2	1332.5	1221.4	5.40E-08				
							1653.0	1515.2	1497.5	1372.7	6.27E-08				
(3 / 5)	0.365	4958	80	40	5	5.72	0.0	0.0	1150.0	1005.5	-2.95E-07	6.12E-07	3.21E-06	0.190	7.56E-07
							1979.5	1730.7	2658.1	2324.1	-1.74E-07				
							4090.9	3576.9	4317.1	3774.7	-5.79E-08				
							13252.9	11587.8	11782.5	10302.1	3.77E-07				
							15175.8	13269.1	13366.0	11686.7	4.63E-07				
							17023.3	14884.4	14949.6	13071.3	5.31E-07				
(3 / 5)	0.365	21232	100	40	5	6.84	0.0	0.0	3921.2	2867.5	-1.00E-06	4.46E-07	3.76E-06	0.119	5.06E-07
							8634.2	6314.0	10934.1	7995.9	-5.89E-07				
							16665.1	12186.8	17683.1	12931.2	-2.61E-07				
							44603.7	32617.6	42756.3	31266.6	4.73E-07				
							51842.9	37911.4	49165.9	35953.8	6.86E-07				
							59383.7	43425.8	55839.5	40834.0	9.08E-07				

Table A-4c: Detailed Wetted Wall Column Data for 3 m TauK/5 m HomotauK

TauK/ HomotauK	CO_2 ldg	P_{CO2}*	Temp	Pressure	Gas_{Dry}	Gas_{wet}	$P_{CO2in,\ dry}$	$P_{CO2in,\ wet}$	$P_{CO2out,\ dry}$	$P_{CO2out,\ wet}$	CO_2 flux	K_G	k_g	K_G/k_g	k_g'
m	mol CO_2/mol alk	Pa	C	psig	Std L/min	Std L/min	Pa	Pa	Pa	Pa	mol/s m^2	mol/s Pa m^2	mol/s Pa m^2		mol/s Pa m^2
(3 / 5)	0.42	21232	40	20	5	5.16	0.0	0.0	71.8	69.5	-2.90E-08	5.94E-07	4.57E-06	0.130	6.83E-07
							138.7	134.4	181.8	176.2	-1.74E-08				
							275.1	266.6	287.0	278.2	-4.83E-09				
							487.9	472.9	478.4	463.6	3.86E-09				
							767.8	744.1	724.7	702.4	1.74E-08				
							911.3	883.2	858.7	832.2	2.12E-08				
(3 / 5)	0.42	3112	60	20	5	5.45	0.0	0.0	406.6	372.7	-1.64E-07	4.77E-07	4.83E-06	0.099	5.29E-07
							1078.7	988.8	1294.0	1186.1	-8.68E-08				
							2131.1	1953.5	2226.8	2041.2	-3.86E-08				
							4312.5	3953.1	4195.3	3845.6	4.73E-08				
							5264.4	4825.7	5025.2	4606.4	9.65E-08				
							6388.6	5856.2	6149.4	5636.9	9.65E-08				
(3 / 5)	0.42	20299	80	40	5	5.72	0.0	0.0	2299.9	2011.0	-5.89E-07	2.43E-07	3.21E-06	0.076	2.63E-07
							6070.3	5307.6	7390.0	6461.5	-3.38E-07				
							11235.8	9824.1	11763.6	10285.6	-1.35E-07				
							32161.5	28120.5	31218.9	27296.4	2.41E-07				
							42266.1	36955.6	40833.4	35702.9	3.67E-07				
							52295.3	45724.7	50146.2	43845.6	5.50E-07				
(3 / 5)	0.51	30982	40	20	5	5.16	0.0	0.0	358.8	347.7	-1.45E-07	3.74E-08	4.57E-06	0.008	3.77E-08
							1243.7	1205.4	1530.8	1483.5	-1.16E-07				
							6673.2	6467.3	6864.5	6652.7	-7.72E-08				
							13035.4	12633.2	13155.0	12749.1	-4.83E-08				
							19373.8	18775.9	19445.5	18845.4	-2.90E-08				
							41737.3	40449.3	41689.4	40402.9	1.93E-08				

Table A-5: Detailed Wetted Wall Column Data for 5 m TauK

TauK	CO_2 ldg	P_{CO2}*	Temp	Pressure	Gas_{Dry}	Gas_{wet}	$P_{CO2in,\ dry}$	$P_{CO2in,\ wet}$	$P_{CO2out,\ dry}$	$P_{CO2out,\ wet}$	CO_2 flux	K_G	k_g	K_G/k_g	k_g'
m	mol CO_2/mol alk	Pa	C	psig	Std L/min	Std L/min	Pa	Pa	Pa	Pa	mol/s m^2	mol/s Pa m^2	mol/s Pa m^2		mol/s Pa m^2
5	0.2	32	40	20	5	5.16	0.00	0.00	12.6	12.21	-5.09E-09	1.99E-06	4.57E-06	0.44	3.53E-06
							2.87	2.78	15.5	15.02	-5.10E-09				
							5.98	5.80	15.6	15.12	-3.88E-09				
							42.81	41.49	38.1	36.92	1.90E-09				
							72.71	70.47	58.2	56.40	5.86E-09				
							87.78	85.07	69.8	67.65	7.26E-09				
5	0.2	234	60	20	5	5.45	0.00	0.00	83	76.08	-3.35E-08	1.48E-06	4.83E-06	0.31	2.13E-06
							33.96	31.13	92	84.33	-2.34E-08				
							116.72	106.99	150	137.50	-1.34E-08				
							295.87	271.21	279	255.75	6.81E-09				
							375.99	344.66	344	315.33	1.29E-08				
							464.49	425.78	407	373.08	2.32E-08				
5	0.2	1259	80	40	5	5.72	0.00	0.00	492	430.18	-1.26E-07	1.16E-06	3.21E-06	0.36	1.82E-06
							490.15	428.57	819	716.10	-8.42E-08				
							904.89	791.20	1051	918.95	-3.74E-08				
							2752.39	2406.56	2330	2037.25	1.08E-07				
							6899.82	6032.89	5087	4447.85	4.64E-07				
							19869.97	17373.41	13853	12112.44	1.54E-06				
5	0.2	7730	100	40	5	6.84	0.00	0.00	4245	3104.26	-1.09E-06	1.47E-06	3.76E-06	0.39	2.40E-06
							11424.29	8354.29	10390	7597.94	2.65E-07				
							22019.09	16102.01	17930	13111.76	1.05E-06				
							27033.72	19769.07	21375	15631.00	1.45E-06				
							32123.75	23491.28	25145	18387.90	1.79E-06				

CO_2 Solubility at 100–160 °C in Aqueous Amines

Quarterly Report for July 1 – September 30, 2010

by Qing Xu

Supported by the Luminant Carbon Management Program

Department of Chemical Engineering

The University of Texas at Austin

October 31, 2010

Abstract

In this quarter the total pressure screening at 100–160 °C has been continued with a blend of piperazine (PZ)/1-methyl-piperazine (1MPZ)/1,4-dimethyl-piperazine (1,4-DMPZ). CO_2 partial pressure was derived from the total pressure data. At 100 °C, 0.320 loading, the CO_2 partial pressure is 271 kPa; at 160 °C, the CO_2 partial pressure is 1107 and 2727 kPa for 0.221 and 0.270 loading. Based on the data at 40–160 °C, an empirical model of CO_2 partial pressure was developed; the heat of absorption of CO_2 is given by the derivative of that expression. In the following equations P_{CO2} is in Pa, T is in K and α is the CO_2 loading.

$$\ln P_{CO2} = (34.4 \pm 0.2) + \frac{-10597 \pm 81}{T} + (7627 \pm 177) \cdot \frac{\alpha}{T}$$

At the mid-loading where P_{CO2} is 1.5 kPa at 40°C, the ΔH_{abs} is 70±1 kJ/mol CO_2 for the blend.

Temperature and pressure calibrations were conducted with the high temperature-pressure vapor liquid equilibrium apparatus. 7 m MEA was used as the solvent for a test run. Better temperature control was achieved with the oil bath, so vapor condensation was avoided. At 120 °C, the volatility of 6.2 m MEA is 167 and 108 Pa at 0.38 and 0.48 loading; at 140°C, the volatility of 6.3 m MEA is 332 Pa at 0.46 loading.

Introduction

With concentrated aqueous piperazine thermal degradation is negligible up to 150 ºC (Freeman et al., 2008). Better energy performance may be obtained by increasing stripper temperature without degradation of PZ (Rochelle et al., 2008). Multi-stage flashes instead of a simple stripper show a better performance by flashing at elevated temperature. Some other configurations for stripping at elevated temperature also give better energy performance than the simple stripper (Rochelle et al., 2010a).

For thermally resistant amines such as piperazine (PZ), 1-methyl-piperazine (1MPZ) , 2-methyl-piperazine (2MPZ), and Diglycolamine® (DGA®), the stripper temperature can be increased. With amines of relatively high thermal degradation rates, for instance, MEA, stripper temperature is limited but the thermal reclaimer operating temperature is up to 150 ºC. Measurements of CO_2 solubility at high temperature expand the temperature range to 160 °C to get the temperature dependence of CO_2 solubility and the heat of absorption. The data are also important for the design of the high temperature processes.

Freeman found that PZ/1MPZ/1,4-DMPZ ratio is stable around 3.75 m/3.75 m/0.5 at m 175 °C. All the amines in this blend have CO_2 absorption capacity. These make the blend a promising solvent for high temperature applications. The high temperature CO_2 solubility in the blend will be presented in this work.

Total Pressure Experiment

Apparatus

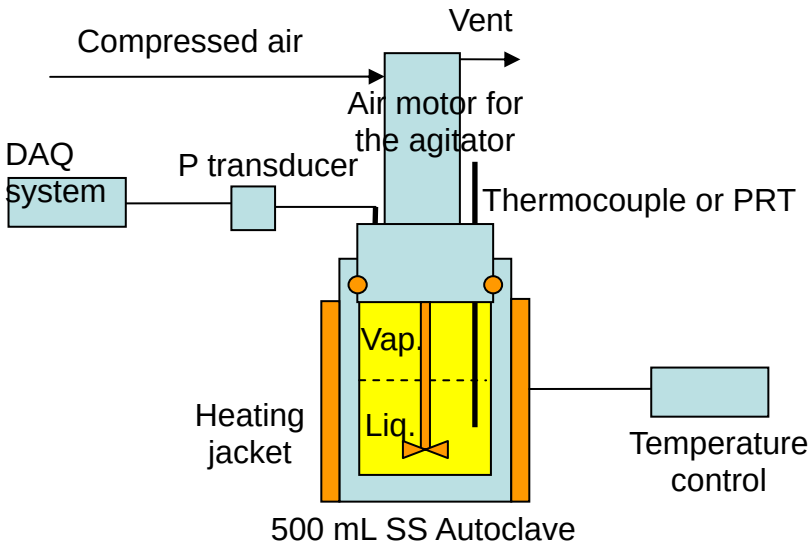

Figure 1: Total Pressure Measurement with an Autoclave

As shown in Figure 1, an autoclave (ZipperClave®, by Autoclave Engineers) was used as the equilibrium cell. Its designed operating range is up to 2000 psia and 232 ºC. The 500 mL pressure vessel is made of 316 SS stainless steel. Closure is effected by a resilient spring member inserted through a circumferential groove in the body and cover (Autoclave Engineers). A magnetic hollow shaft agitator (MAG075, MagneDrive II Series, by Autoclave Engineers) was used to get equilibrium without leaking to the atmosphere. It was driven by a compressed air motor (2AM-NCC-16, by Gast®). The agitator circulates both liquid and vapor phases.

Temperature was controlled by a Fuji Electric PXZ-4 temperature controller, with connection to a K-type thermocouple placed inside the thermal well of the autoclave.

A pressure transducer (Druck® PTX 611, 0-30 bar absolute) was connected to a signal converter and a data logger NI USB 6009; LabView® SignalExpress® software was used for data recording. The pressure reading system was calibrated by a dead weight pressure tester (S/N 19189/278, by Budenberg Volumetrics, Inc.).

Before each run, about 300 to 350 mL of the CO_2 loaded aqueous amine solution was prepared and added into the autoclave. To avoid the effects of O_2, N_2 was used to purge air out and then the cell was sealed. Initial pressure and temperature readings were recorded for later data correction. Then the cell was heated. Data recording of pressure started at around 100 ºC and the intervals of the data points were 10 ºC. Liquid samples were collected before and after each experiment and analyzed by TIC and acid titration. The agitation rate varied from 1200 RPM to 1800 RPM.

Analytical methods

Total Inorganic Carbon (TIC)

The concentration of CO_2 in solution was determined by TIC analysis. The liquid samples collected before and after each run were diluted by a factor of 100. About 10–15 μL diluted sample was injected into a CO_2 analyzer (Model 525, Horiba PIR 2000). Details can be found in Appendix B.2 of Hilliard's dissertation (2008).

Acid Titration

The total alkalinity of solution was determined by acid titration using a Metrohm-Peak 835 Titrando equipped with an automatic dispenser, Metrohm-Peak 801 stirrer, and 3M KCl pH probe. Details are available in Appendix A.3 of Hilliard (2008) and Appendix F of Sexton (2008).

Results Summary

In this period the total pressure in CO_2 loaded 3.75 m PZ/3.75 m 1MPZ/0.5 m 1,4-DMPZ was measured at 100–160 °C. CO_2 partial pressure was calculated by subtracting the partial pressure of N_2 and water from the total pressure. P_{water} was assumed following Raoult's Law and P_{amine} was ignored. The calculation example is in Appendix 4 in the section by Xu inRochelle et al. (2009).

The liquid composition has been corrected with measurements at 100–160 °C because the real CO_2 loading in the liquid phase is less than that measured at room temperature, and this difference becomes significant at high temperature and high loading.

Mychal Zipper, an undergraduate research assistant, assisted in the experiments.

Table 1: Total Pressure and CO_2 Partial Pressure in 3.75 m/3.75 m/0.5 m PZ/1MPZ/1,4-DMPZ

T (°C)	Loading in liq.	P_t (Pa)	P_{CO2} (Pa)	T (°C)	Loading in liq.	P_t (Pa)	P_{CO2} (Pa)
100	0.242	129416	40802	100	0.320	359890	270789
120	0.240	333650	160123	110	0.316	573143	447208
130	0.237	505666	269638	120	0.311	864708	690227
140	0.234	771260	455561	130	0.304	1256507	1019182
150	0.228	1142481	726722	140	0.294	1790054	1472620
160	0.221	1646585	1106796	150	0.284	2437098	2019052
				160	0.270	3269303	2726545

There are 40–100 °C CO_2 solubility data from WWC experiments by Chen (Rochelle et al., 2010c). An empirical model was developed by regressing the low temperature data and the new high temperature data.

$$\ln P_{CO2} = (34.4 \pm 0.2) + \frac{-10597 \pm 81}{T} + (7627 \pm 177) \cdot \frac{\alpha}{T} \qquad (1)$$

$R^2 = 0.9989$

According to the Gibbs-Helmholtz Equation, the heat of absorption can be derived from the empirical CO_2 partial pressure model.

$$\Delta H_{abs} = -R\frac{\partial \ln P_{CO_2}}{\partial(\frac{1}{T})} = -R(-10597 + 7627\alpha) \quad (J/mol\ CO_2) \tag{2}$$

Figure 2 gives the CO_2 partial pressure over the blend from 40 to 160 °C at various loadings. The model fairly predicts the data.

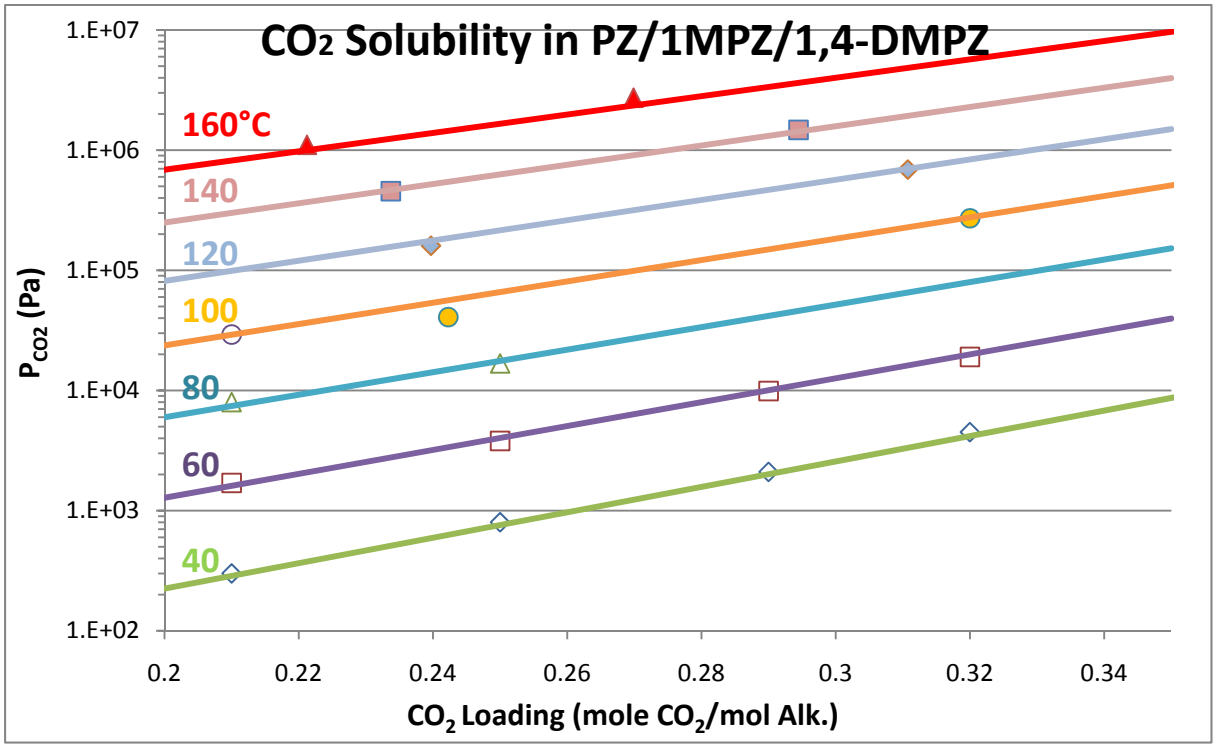

Figure 2: CO_2 Solubility in 3.75 m/3.75 m/0.5 m PZ/1MPZ/1,4-DMPZ

Comparison of heat of absorption

Table 2 compares the heat of absorption of CO_2 in PZ, MEA, 1MPZ, 2MPZ, 2MPZ/PZ blend, DGA®, and PZ/1MPZ/1,4-DMPZ blend. The other empirical models are from previous regression work (Rochelle et al., 2010a). The loadings are defined as moles of CO_2 per mole alkalinity. Therefore for MEA and DGA®, the loading $\alpha = \frac{CO_2(mol)}{MEA\ or\ DGA®(mol)}$; for PZ and PZ derivatives, $\alpha = \frac{CO_2(mol)}{amine\ (mol)\cdot 2}$.

MEA and DGA® have the highest ΔH_{abs}, while PZ and 2MPZ have similar lower ΔH_{abs}. 1MPZ and PZ/1MPZ/1,4-DMPZ are in the middle range.

Table 2: Comparison of the heat of absorption of CO_2

Solvent	ΔH_{abs} (J/mol CO_2)	ΔH_{abs} (kJ/mol CO_2)*	Mid-loading**
3.5-13 m MEA	$-R(-12155+1105\alpha+12800\alpha^2)$	71±4	0.486
0.9-12 m PZ	$-R(-11065+4702\alpha+11699\alpha^2)$	66±2	0.328
7.7-8 m 1MPZ	$-R(-10344+9741\alpha)$	69±3	0.207
6.7-8 m 2MPZ	$-R(-12554+14509\alpha)$	66±3	0.314
4/4 m PZ/2MPZ	$-R(-12998+14684\alpha)$	66±3	0.341
9.6-10 m DGA®	$-R(-7572-25209\alpha+50113\alpha^2)$	73±3	0.447
PZ/1MPZ/1,4-DMPZ	$-R(-10597+7627\alpha)$	70±1	0.278

* The heat of absorption of CO_2 at mid-loading.
** The loading where P_{CO2} is 1.5 kPa at 40 °C, calculated from the 40–160 °C empirical models.

High Temperature Pressure VLE

Apparatus

A new high temperature and pressure vapor-liquid equilibrium (HTPVLE) apparatus was developed in this quarter. A test run with MEA was conducted.

Figure 3 shows the apparatus. A 200 mL and a 600 mL stainless steel vessel (Parr Instrument Co.) were used as the equilibrium cells in series. Both of the vessels were submerged under the oil in a bath (EX-35, by Thermo Fisher Scientific) for temperature control. CO_2 feed pressure was controlled by a regulator. Vapor sample was collected from the top of the second cell, with a Parker H0 needle valve on the line for the flow rate control. This vapor sample was diluted by about 1.5 L/min of N_2. Both the N_2 stream and the diluted vapor were maintained at 180 °C. The diluted stream was then analyzed on-line by the FTIR (Gasmet, DX-4000) with Calcmet® software. Liquid samples were withdrawn from the second cell, cooled to room temperature, and analyzed.

Temperature of the second cell was measured by a K-type thermocouple and read by an HH506RA data logger from Omega®.

A pressure transducer (Druck® PTX 611, 0-30 bar absolute) was connected to a signal converter and data logger NI USB 6009. LabView® SignalExpress® software was used for data recording. The pressure reading system was calibrated by a dead weight pressure tester (S/N 19189/278, by Budenberg Volumetrics, Inc.).

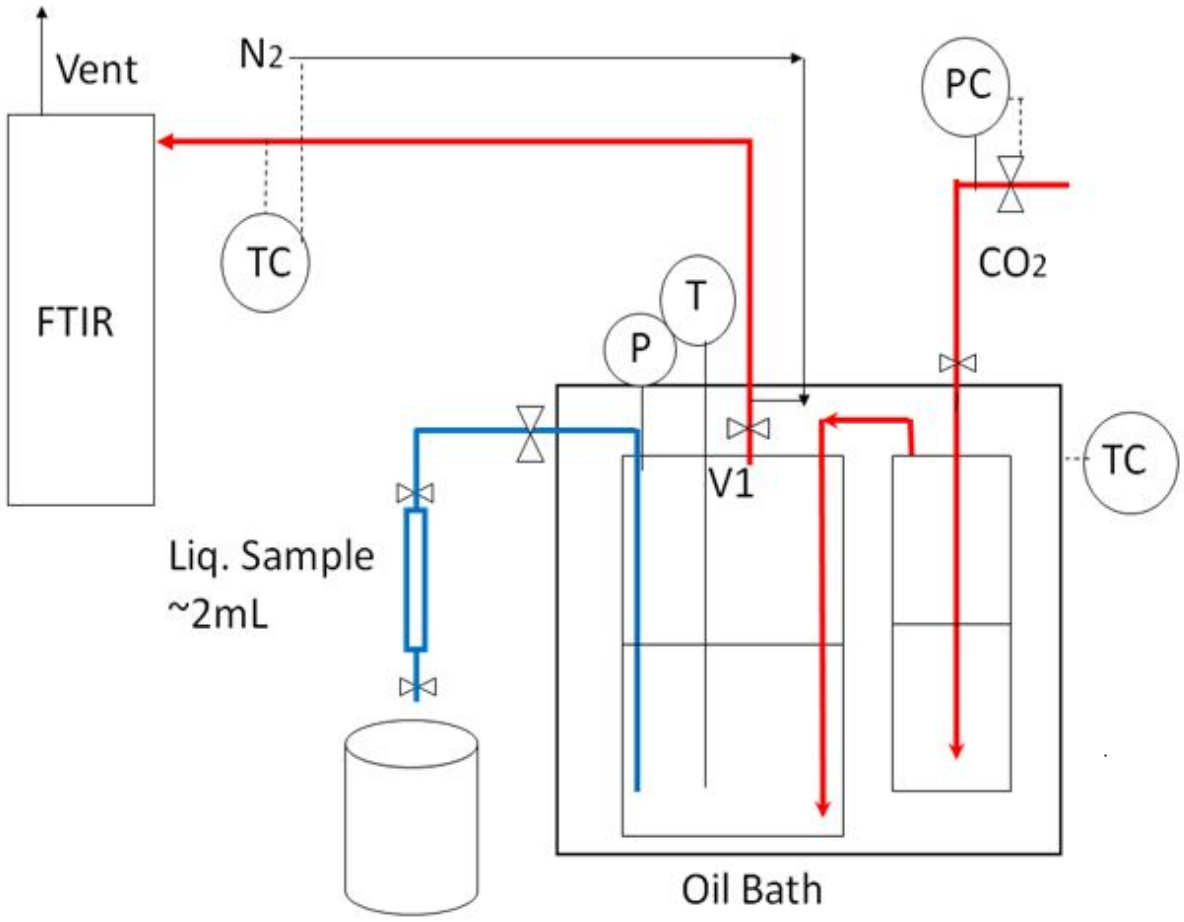

Figure 3: Scheme of the Single Vapor Pass VLE Apparatus with an Oil Bath
Red: vapor passing line; blue: liquid sampling line

Procedure

Aqueous amine was prepared and certain amount of CO_2 was loaded into the solution before each run. About 100 mL and 300 mL of the solution was filled into the 2 cells, respectively. To avoid oxidative degradation, CO_2 was used to purge air and then the cells were sealed and submerged under the oil.

After the temperature stabilized at the target value, the CO_2 feed valve was opened. The total pressure inside the equilibrium cells was controlled by the CO_2 feed pressure regulator. A vapor stream was continuously withdrawn from the vapor sampling line, diluted by 1.5 L/min N_2 and then analyzed by FTIR on line with Calcmet® software. The N_2, mixed gas and FTIR cell were held at 180 °C. The flow rate of the vapor sample was controlled by the needle valve at 50–300 mL/min at standard pressure. The needle valve opening was adjusted to get proper concentrations in the FTIR.

After the concentrations in the FTIR were stable, the liquid sampling valves were opened to let about 25–50 mL high pressure liquid flush through the line, and were closed to trap about 2 mL liquid in the sample bomb. Liquid samples were then cooled to room temperature and analyzed by TIC and titration, which can be found in the Analytical Methods in Total Pressure Experiment section in this report.

Results and Discussion

Calibrations

Before all the experiments, the pressure transducer was calibrated by a dead weight tester and the correlation equation of pressure and voltage was obtained.

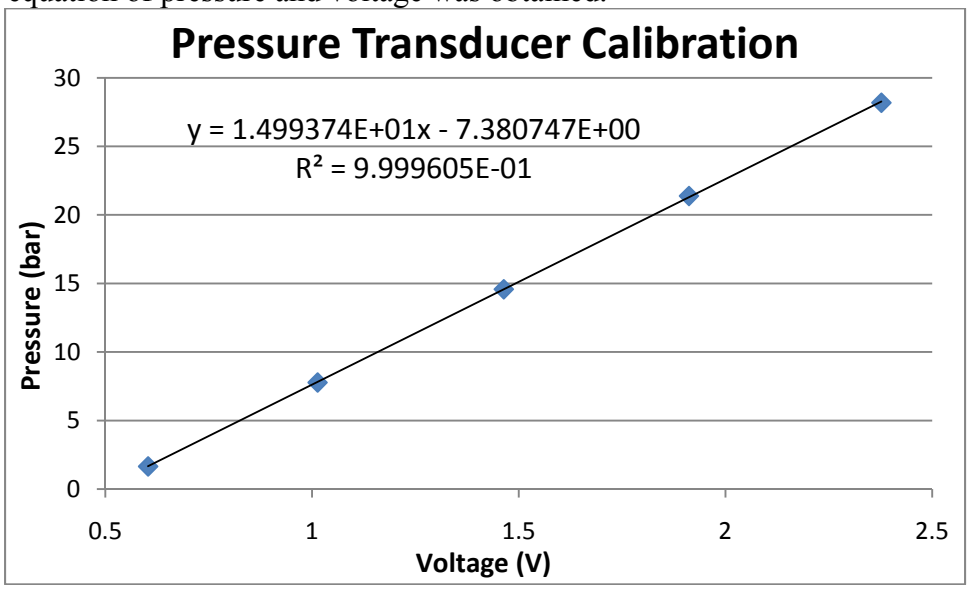

Figure 4: The Pressure Transducer Calibration

The temperature reader was not accurate, so a temperature calibration was conducted with a Fuji Electric PXZ-4 temperature controller. Multiple thermocouples were held at the same position in the oil bath and multiple points were read by the temperature reader and the Fuji Electric PXZ-4 temperature controller. Readings from the two were correlated in Figure 5, where the correlation equation was used in the following experiments.

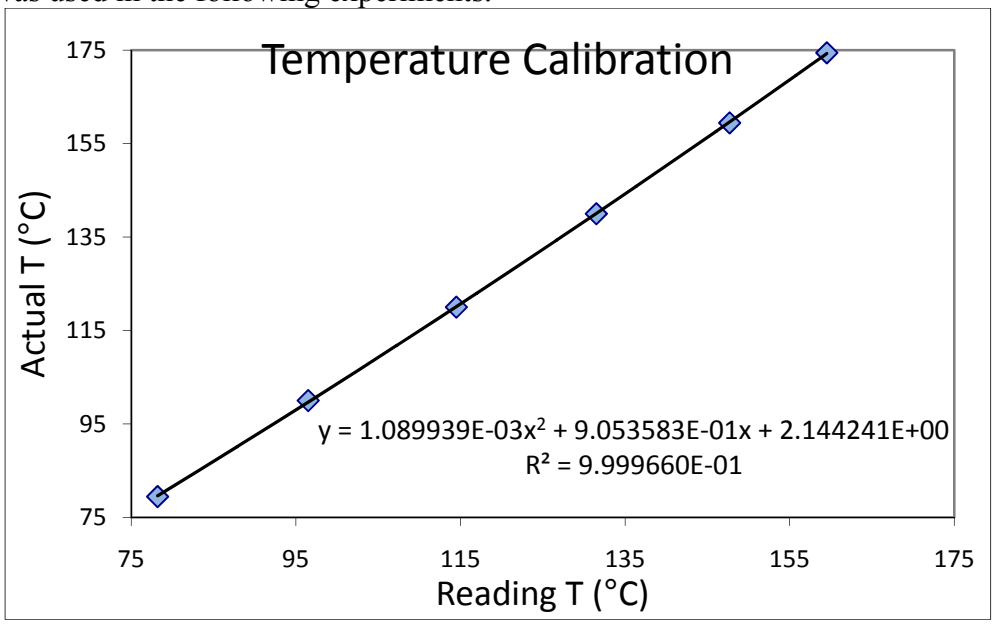

Figure 5: Temperature Calibration

Results of MEA-F1

Figure 6 gives the total pressure log during the MEA-F1 run. Three equilibrium stages can be found in the figure. At the end of each stage, a liquid sample was collected.

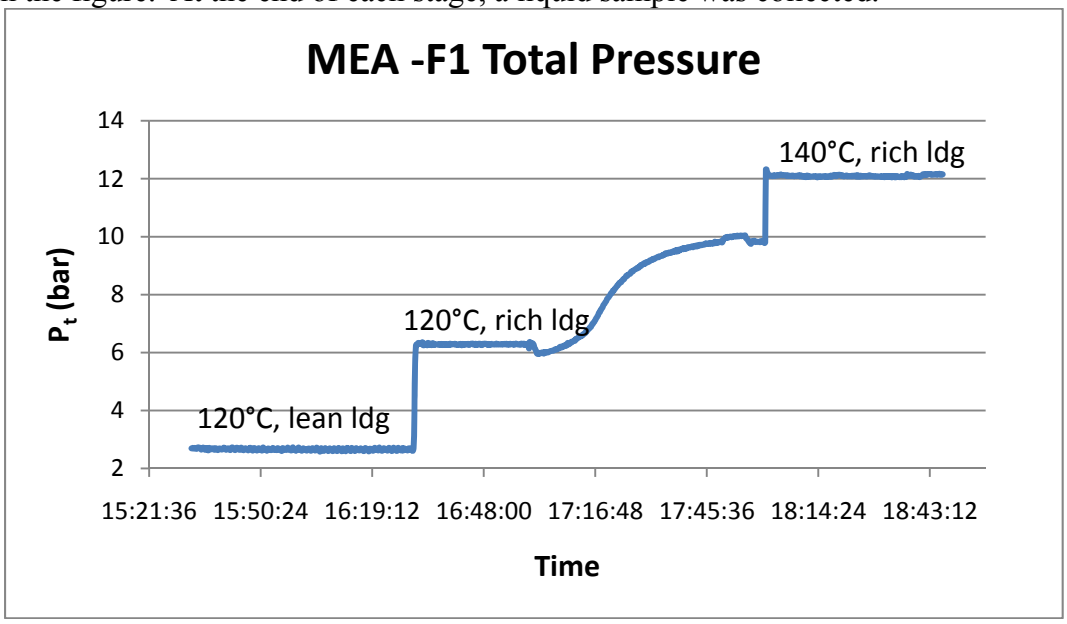

Figure 6: Total Pressure of the MEA-F1 Run

The vapor compositions in the diluted stream were analyzed by FT-IR and these were converted into concentrations in the vapor phase inside equilibrium cell:

$$y_i = \frac{y'_i}{y'_{H_2O} + y'_{amine} + y'_{CO_2}} \tag{3}$$

y_i - mole fraction of component i in vapor
y'_i - mole fraction of component i in diluted gas.
i is water, amine or CO_2.

The partial pressure of each component was calculated from concentrations and total pressure using equation (4):

$$P_i = P_t \cdot y_i \tag{4}$$

P_t - total pressure, Pa.
P_i - partial pressure of i, Pa.
i is water, amine or CO_2.

Table 3 gives a summary of the results.

Table 3: Summary of the MEA-F1 Run

Sample #	T(°C)	MEA (m)	Ldg	P_t (bar)	P_{MEA} (Pa)	P_{CO2} (Bar)	P_{H2O} (Bar)
A	120	6.23	0.38	2.65	167	0.86	1.80
B	120	6.21	0.48	6.29	108	4.50	1.79
C	138.5	6.27	0.46	12.09	332	8.86	3.23

Figure 7 gives the compositions of the liquid samples.

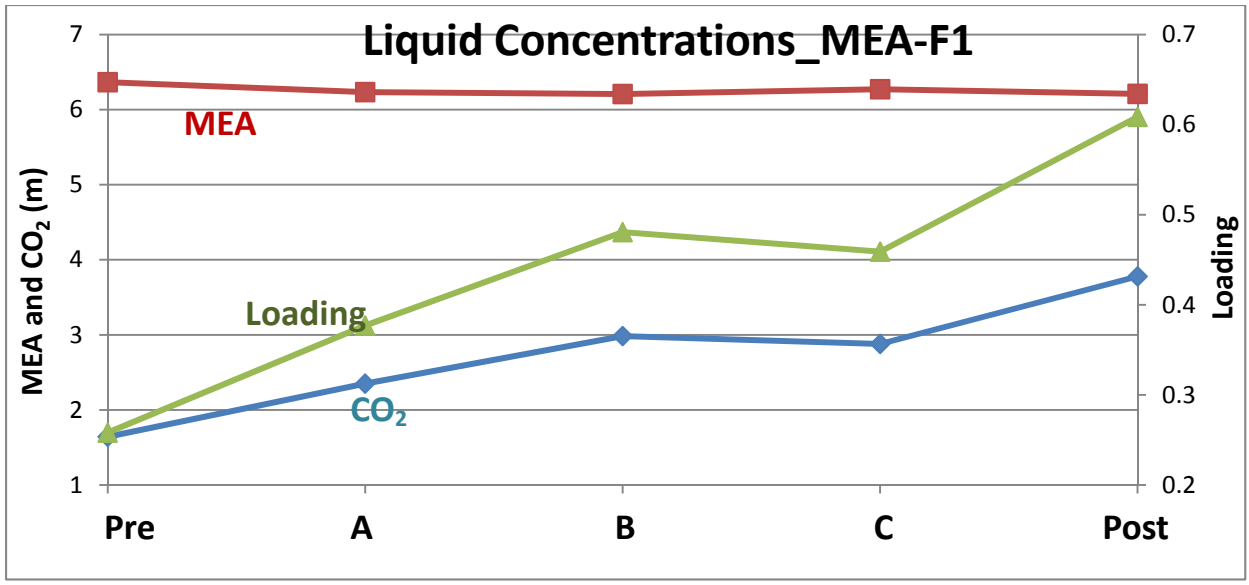

Figure 7: The Liquid Compositions of the MEA-F1 Run

Comparison with Previous Data

Figure 8 compares the total pressure of MEA-3, MEA-6, MEA-F1 and previous total pressure data. MEA-3 and MEA-6 were done in the first quarter 2010 (Rochelle et al., 2010b), with the autoclave as the equilibrium cell, using the same liquid sampling device as MEA-F1. MEA-3 has one outlier at low loading, mainly because it was the first point using the modified liquid sampling device. At higher CO_2 loading, the new total pressure data are generally higher than the previous ones, indicating flash might happen and cause a lower CO_2 loading in the collected liquid samples. However, the previous total pressure data is only for reference because its CO_2 loading was calculated, instead of measured. Improvements need to be made to further eliminate possible flash.

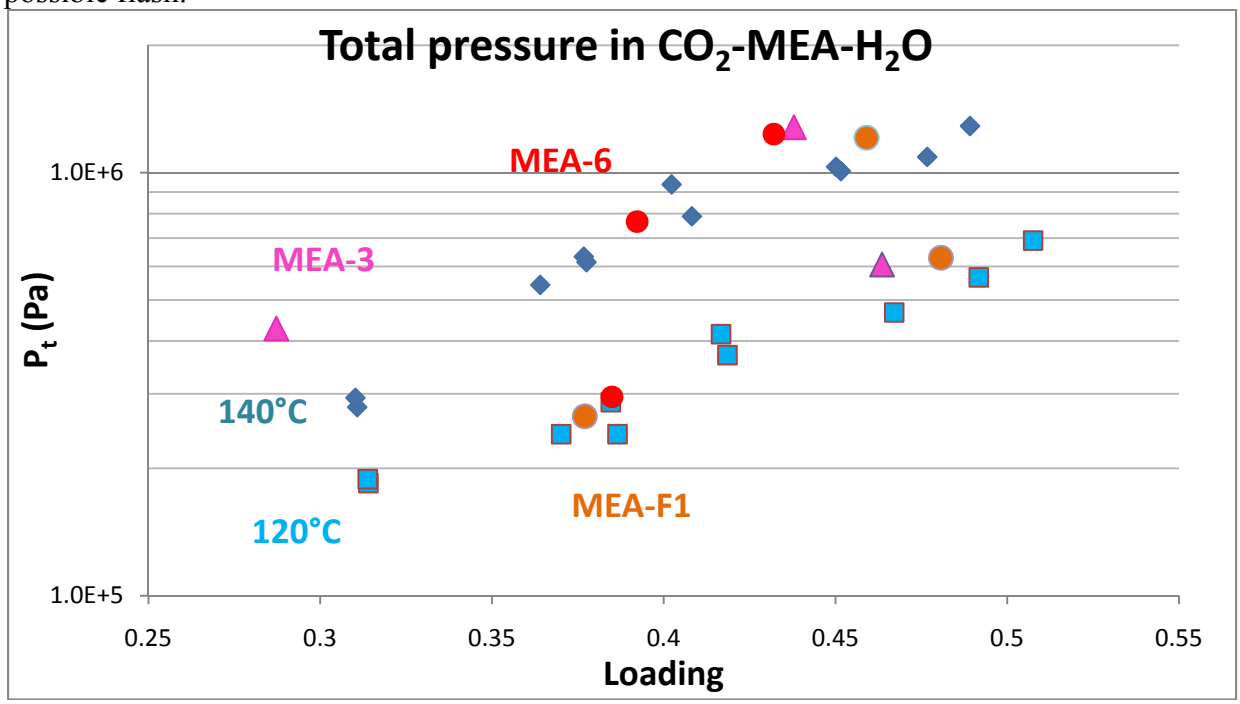

Figure 8: Comparison of Total Pressure over MEA-CO_2-H_2O at 120 and 140 °C

Figure 9 compares P_{MEA}/x_{MEA} in MEA-CO_2-H_2O. P_{MEA} was normalized by dividing by x_{MEA}. The new data from MEA-F1 fall into the right range. The orange oval covers the more reasonable experimental data. The 3 points from MEA-6 are significantly lower than the other high temperature data, probably due to condensation in the vapor sampling line in the earlier work.

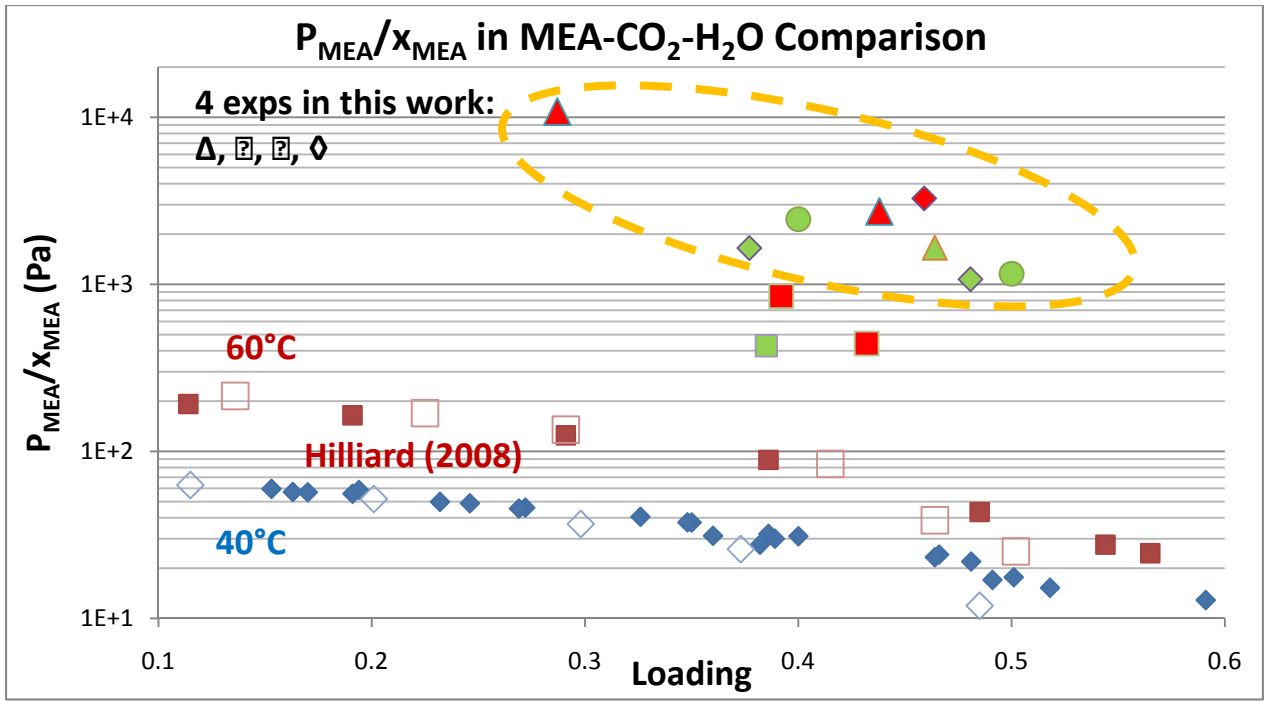

Figure 9: Comparison of P_{MEA}/x_{MEA} in MEA-CO_2-H_2O

Green: 120 °C; red: 140 °C; ○: MEA-2; Δ: MEA-3; □: MEA-6; ◊: MEA-F1.

To illustrate the temperature dependence, P_{MEA}/x_{MEA} is plotted against reciprocal temperature at lean and rich loadings in Figure 10.

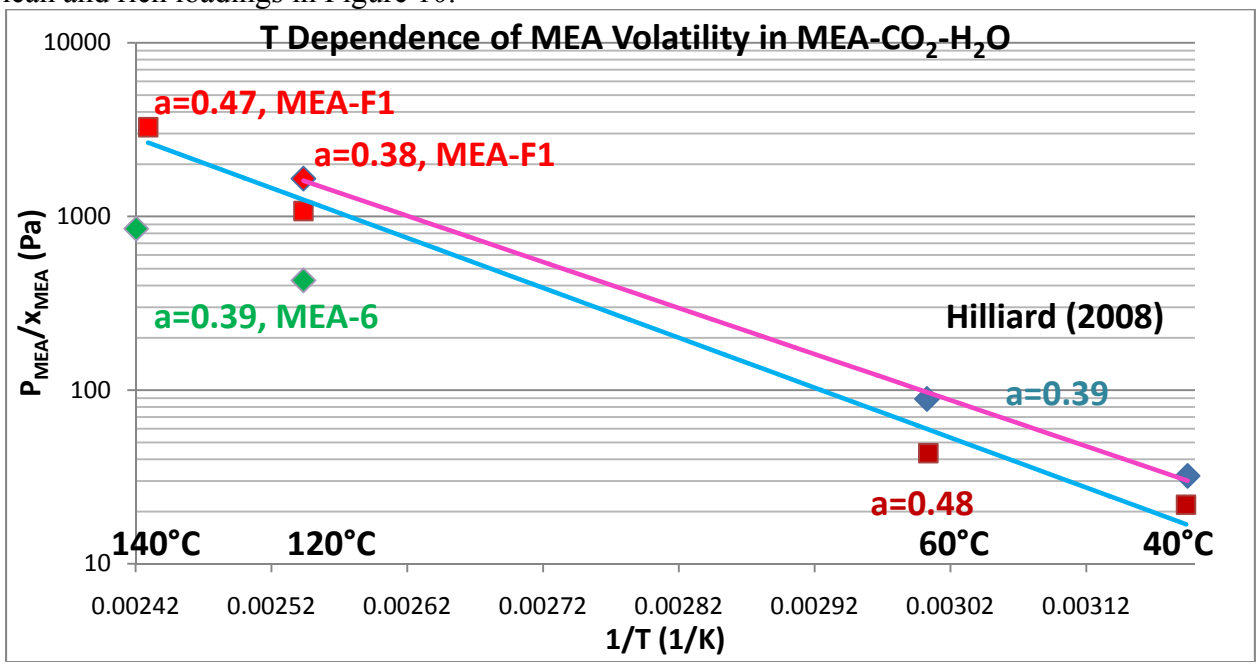

Figure 10: Temperature Dependence of MEA Volatility in MEA-CO_2-H_2O

Conclusions

In this quarter the total pressure was measured at 100–160 °C for CO_2 loaded 3.75 m PZ/3.75 m 1MPZ/0.5 m 1,4-DMPZ. CO_2 solubility data were generated from the total pressure and an empirical model was developed. At 160 °C, CO_2 partial pressure is 1107 and 2727 kPa for 0.221 and 0.270 loading in the blend.

The heat of absorption was derived from the P_{CO2} empirical model. Among the seven screened solvents, at the mid-loading which corresponds to 1.5 kPa P_{CO2} at 40 °C, the ΔH_{abs} are in the following sequence: DGA®>MEA>PZ/1MPZ/1,4-DMPZ>1MPZ>PZ≈2MPZ≈PZ/2MPZ. At the mid-loading, the ΔH_{abs} is 70 kJ/mol CO_2 for the PZ/1MPZ/1,4-DMPZ blend.

At 120 °C, the volatility of 6.2 m MEA is 167 and 108 Pa at 0.38 and 0.48 loading; at 140 °C, the volatility of 6.3 m MEA is 332 Pa at 0.46 loading.

Future Work

The following work is proposed for the next quarter.

1. Solve the problems by modifying the HTPVLE apparatus:

(a) Oil leaking when closing the needle valve: switch the needle valve and the on and off valve, add a filter to protect the FTIR line and change the sequence of closing the valves when shutting down the experiment.

(b) Possible flashing in the liquid sampling device: add water or ice cooling system to the sampling line.

2. Use the apparatus to measure the high temperature VLE for MEA and PZ with various loadings and amine concentrations.

3. Measure the total pressure for 7/2 MDEA/PZ blend and 11 m MEA at various loadings.

References

Autoclave Engineers®, Zipperclave® 500 & 1000 mL stirred reactor, http://www.autoclaveengineers.com/ae_pdfs/SR_500_1000_Zip.pdf

DIPPR, 1998-Provo, UT: BYU DIPPR, Thermophysical Properties Laboratory, 1998-V. 13.0.

Freeman SA, Dugas R, Van Wagener D, Nguyen T, Rochelle GT. "Carbon dioxide capture with concentrated, aqueous piperazine." *GHGT-9*. Washington D.C. 2008.

Hilliard MD. *A Predictive Thermodynamic Model for an Aqueous Blend of Potassium Carbonate, Piperazine, and Monoethanolamine for Carbon Dioxide Capture from Flue Gas.* The University of Texas at Austin. Ph.D. Dissertation. 2008.

Rochelle GT et al. "CO_2 Capture by Aqueous Absorption, Third Quarterly Progress Report 2008." Luminant Carbon Management Program. The University of Texas at Austin. 2008.

Rochelle GT et al. "CO_2 Capture by Aqueous Absorption, Second Quarterly Progress Report 2009." Luminant Carbon Management Program. The University of Texas at Austin. 2009.

Rochelle GT et al. "CO_2 Capture by Aqueous Absorption, Fourth Quarterly Progress Report 2009." Luminant Carbon Management Program. The University of Texas at Austin. 2010a.

Rochelle GT et al. "CO_2 Capture by Aqueous Absorption, First Quarterly Progress Report 2010." Luminant Carbon Management Program. The University of Texas at Austin. 2010b.

Rochelle GT et al. "CO_2 Capture by Aqueous Absorption, Third Quarterly Progress Report 2010." Luminant Carbon Management Program. The University of Texas at Austin. 2010c.

Sexton AJ. *Amine Oxidation in CO_2 Capture Processes*. The University of Texas at Austin. Ph.D. Dissertation. 2008.

Amine Volatility

Quarterly Report for July 1 – September 30, 2010

by Thu Nguyen

Supported by the Luminant Carbon Management Program

Department of Chemical Engineering

The University of Texas at Austin

October 31, 2010

Abstract

The volatilities of 10 amines in water were measured using the FTIR and expressed as amine Henry's constants. Regarding the intrinsic amine volatility in water, it was determined that: MDEA < DGA < PZ < 2MPZ < MAPA < EDA < MEA < 1,2 Diaminopropane < 1MPZ < AMP. Most importantly, it was found that the volatility of an amine in water does not necessarily track the pure amine boiling point. An empirical correlation was successfully developed to estimate the amine Henry's constant at 40 ˚C by accounting for molecular group contributions: ln $H_{amine,40\,^{o}C}$ = [4.19 (±0.09)] – [1.65(±0.17)](N) – [0.21(±0.07)](NH) – [1.55(±0.17)](R-O-R) + [0.7(±0.08)](Non Cyclic C-CH_3) + [2.63(±0.21)](Cyclic N-CH_3). Predictions of amine volatilities in water by UNIFAC-DMD theory (in Aspen Plus®) overestimated measured values, by up to an order of magnitude, for most of the amines studied except for MEA.

At conditions at the top of the absorber (~40 ˚C and nominal lean loading), the amine volatilities are: 7 m MEA: 2.7 Pa; 8 m PZ: 0.78 Pa; 7 m MDEA/2 m PZ blend: 0.49 Pa/0 Pa, respectively. The amine heats of solutions at their respective nominal lean loadings (~500 Pa P_{CO2}) were estimated to be: 7 m MEA: 10.2 kJ/mol; 8 m PZ: -37.1 kJ/mol; 7 m MDEA/2 m PZ: --1.5kJ/mol/-74.6 kJ/mol, respectively. PZ in the blend is even less volatile than 8 m PZ.

Introduction

The first part of this report discusses the experimental volatilities of 10 amines in unloaded amine-H_2O systems at 40 ˚C and atmospheric pressure. These results were used to develop an empirical correlation which relates the amine volatilities, expressed as Henry's constants to molecular group contributions. The predictions from this correlation are then compared to predictions obtained from the UNIFAC-Dortmund Modified model which also uses molecular group contributions. The main difference between the two approaches is that our correlation makes use of a much smaller subset of group parameters, which are used to predict the Henry's constant directly. UNIFAC, on the other hand, is a comprehensive model which contains an extensive set of molecular parameters used to predict species activity coefficients instead of Henry's constants. Nevertheless, with these activity coefficients, one can easily estimate the corresponding amine Henry's constants by incorporating the vapor pressures.

This report also presents the volatility of amines in loaded systems, in particular baseline 7 m MEA, 8 m PZ, and the blend of 7 m MDEA/2 m PZ from 40 ºC to 70 ºC. Amine volatility is analyzed by looking at the apparent amine activity coefficient behavior as a function of temperature, loading, and amine concentration effects.

Experimental Methods

Amine Volatility Measurements

Amine volatility was measured in a stirred reactor coupled with a hot gas FTIR analyzer (Fourier Transform Infrared Spectroscopy, Temet Gasmet Dx-4000) as shown in Figure 1.

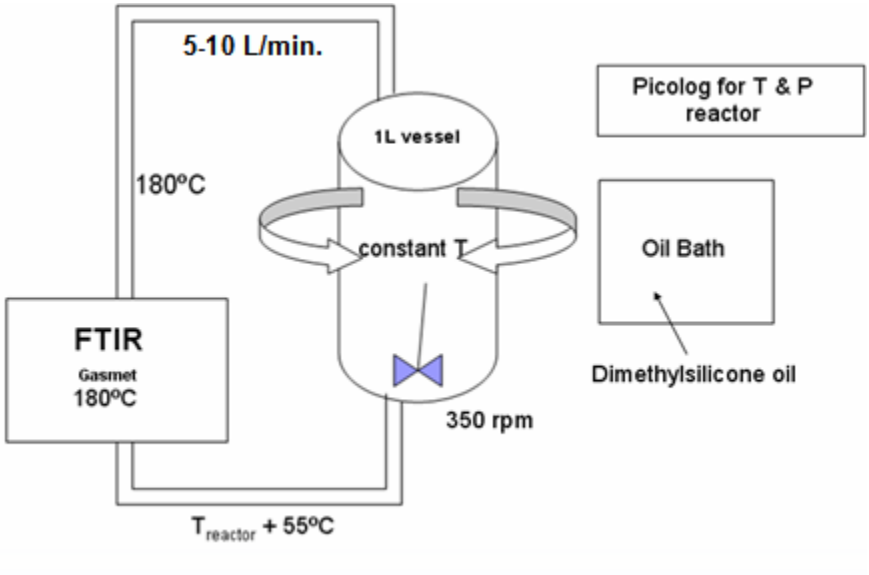

Figure 1: Amine Volatility Experimental Setup

The 1 L glass reactor was agitated at 350 rpm. Temperature in the reactor was controlled by circulating dimethylsilicone oil. The reactor was insulated with thick aluminum insulation material. Vapor from the headspace of the reactor, primarily 5–10 L/min., was circulated by a heated sample pump to the FTIR through a heated Teflon line. Both the line and analyzer were maintained at 180 ºC to prevent possible condensation or adsorption of amine. The FTIR measured amine, CO_2, and water concentration in the gas. After the gas passed through the FTIR, it was returned to the reactor through a heated line maintained ~55 ºC hotter than the reactor. It was determined that the 55 ºC difference was sufficient to ensure that the return gas does not upset the solution that is in equilibrium with the gas inside the reactor, and to prevent potential heat loss at the bottom of the reactor.

Amine Concentration

The amine concentration was determined by acid titration (Hilliard, 2008) with an automatic Titrando series titrator with an automatic equivalence point detection. A 300X diluted sample was titrated with 0.1 N H_2SO_4 to a pH of 2.4. The amount of acid needed to reach the equivalence point at a pH of 3.9 was used to calculate the total amine concentration.

Loading Verification

The loadings of solutions are verified by using the Total Inorganic Carbon (TIC) analysis. The samples are diluted in H_2O and subsequently dissolved in 30 wt % H_3PO_4 to release aqueous carbon-containing products. The CO_2 is carried by an N_2 stream to an infrared detector which analyzes and records the CO_2 composition in terms of voltage. The resulting voltage peaks are integrated and correlated to CO_2 concentrations using a 1000 ppm inorganic carbon standard made from a mixture of potassium carbonate and potassium bicarbonate (Ricca Chemical, Pequannock, NJ).

Theory

Amine Volatility in Unloaded Amine-H_2O System

Amine volatility in water is represented as the amine Henry's constant. This parameter carries physical significance, and can also be adequately correlated to molecular group contributions. Furthermore, the Henry's constant is believed to provide a better representation of amine volatility in water than the activity coefficient because it accounts for only amine-water interactions without the confounding effects of amine-amine interactions. The Henry's constant is computed as follows:

$$H_{amine,T} = P_{amine} / x_{amine} = \gamma_{amine}^{\infty} * P^{sat}_{amine} \quad (1)$$

where:

P_{amine} is the partial pressure of the amine in the gas
x_{amine} is the liquid phase mole fraction of the amine
γ_{amine}^{∞} is the amine activity coefficient at infinite dilution in water
P^{sat}_{amine} is the amine saturation pressure at a given temperature

Very dilute amine solutions were used, with concentrations between 0.3–2 m amine in water, as the volatilities at these low concentrations are comparable to what they would be at infinite dilution.

The amine heat of absorption is estimated per the Gibb's Helmholtz relation:

$$d(\ln H_{amine}) / d(1/T) = -\Delta H_{abs}/R \quad (2)$$

Amine Volatility in Loaded Amine-H_2O-CO_2 System

For a loaded amine-water-CO_2 system, the amine volatility is expressed as the amine apparent activity coefficient. From the Modified Raoult's Law this quantity is computed as follows:

$$\gamma_{amine} = P_{amine} / (x_{amine} * P°_{amine}) \quad (3)$$

where:

γ_{amine} is the apparent activity coefficient of the amine
P_{amine} is the partial pressure of the amine in the gas
x_{amine} is the liquid phase mole fraction of the amine
$P°_{amine}$ is the vapor pressure of the amine at a given temperature

This calculation yields an apparent activity coefficient, instead of a true coefficient, because the liquid phase mole fraction used assumes total amine unspeciated in the presence of total CO_2 instead of the free amine.

Data

Table 1: Henry's Constants of Amines (MEA data from Hilliard)

T (C)	P_{amine} (Pa)	P_{H2O} (Pa)	H_{amine} (Pa)		T (C)	P_{amine} (Pa)	P_{H2O} (Pa)	H_{amine} (Pa)
2.86 m MDEA					**0.204 m DGA®**			
40	0.59	6935	12.7		50	0.18	12257	33.4
50	0.81	11156	16.2		55	0.22	15645	40.8
55	0.91	14271	18.1		60	0.27	18435	50.1
60	1.24	18191	23.3		65	0.33	22322	61.2
65	1.70	22613	31.8		70	0.59	27404	110
70	2.40	29045	44.5					
1.95 m PZ					**3.5 m MEA**			

40	1.51	6797	43.4		40	4.19	6940	70.7
50	2.79	11195	80.3		46	5.88	8690	99.2
60	6.35	16892	183		49	7.29	9760	135
70	14.2	30786	409		56	11.2	13600	189
					60	13.2	17100	223
					65	18.2	19900	321
0.5 m MAPA					**0.48 m EDA**			
40	0.53	8977	59.3		40	0.56	7694	62.7
45	0.72	11622	80.9		45	0.87	9692	97.5
50	1.01	15830	113		50	1.26	12590	141
55	1.33	20038	149		55	1.87	15688	210
60	2.28	25749	255		60	2.74	18485	307
65	3.41	31661	382					
0.95 m 2MPZ					**0.3 m DAP**			
40	0.81	6758	48.2		40	0.61	6453	114
45	1.26	8674	75.0		45	1.14	8439	212
50	2.13	10850	127		50	1.54	10821	287
55	2.87	13685	171		55	2.11	13899	392
60	4.46	17798	265		60	3.02	17870	563
65	7.24	21681	431		65	4.01	22536	748
70	10.6	33589	630					
1.05 m 1MPZ					**0.29 m AMP**			
40	2.65	6871	143		40	1.55	7486	288
45	4.94	8822	266		45	2.23	9682	414
50	7.51	12333	405		50	3.55	12278	662
55	11.6	14637	628		55	4.99	15672	929
60	18.7	18631	1010		60	7.09	18367	1320
65	29.1	23671	1566		65	10.2	22360	1896
					70	15.1	27550	2806

Table 2: Volatility and CO_2 Solubility for 7 m MEA (Hilliard, 2008)

MEA (m)	T (C)	Loading	P_{MEA} (Pa)	P_{CO2} (Pa)	P_{H2O} (Pa)	γ_{MEA}
7.0	40	0	10.0	0	7500	0.54
7.0	60	0	27.1	0	18300	0.36
6.9	40	0.153	6.6	5.7	6600	0.37
7.0	40	0.17	6.4	7.2	6650	0.35
7.0	40	0.163	6.4	6.6	6690	0.36
6.9	40	0.194	6.5	9.9	6710	0.37
7.0	40	0.191	6.2	10.0	6610	0.35
6.9	40	0.272	5.1	22.4	6650	0.29
7.1	40	0.232	5.6	14.6	6630	0.31

7.1	40	0.246	5.5	19.1	6650	0.31
7.1	40	0.269	5.2	23.1	6630	0.29
7.1	40	0.36	3.6	96.6	6750	0.20
7.1	40	0.35	4.2	72.1	6750	0.24
7.1	40	0.386	3.6	120	6660	0.20
7.1	40	0.389	3.4	113	6590	0.19
7.1	40	0.4	3.5	128	6710	0.20
7.6	40	0.382	3.3	131	6720	0.18
7.0	40	0.466	2.7	574	6750	0.15
7.1	40	0.591	1.5	28300	6720	0.08
7.1	40	0.481	2.5	883	6730	0.14
7.2	40	0.464	2.7	750	6670	0.15
7.1	40	0.501	2.0	1870	6800	0.11
7.1	40	0.491	1.9	1100	6680	0.11
7.1	40	0.518	1.7	3030	6800	0.10
7.1	40	0.326	4.6	48.5	6600	0.26
7.0	40	0.348	4.2	66.2	6600	0.24
7.0	60	0.114	21.5	19.4	16600	0.29
7.1	60	0.191	18.6	58.9	16700	0.25
7.1	60	0.291	14.1	209	16600	0.19
7.0	60	0.386	10.0	763	16700	0.14
7.1	60	0.485	4.9	4860	16800	0.07
7.2	60	0.544	3.2	25800	16800	0.04
7.4	60	0.565	2.9	50200	18000	0.04

loading is defined as moles of CO_2/mole of alkalinity

Table 3: Volatility and CO_2 Solubility for 8 m PZ

PZ (m)	T (C)	Loading	P_{PZ} (Pa)	P_{CO2} (Pa)	P_{H2O} (Pa)	γ_{PZ}
7.88	50	0	17.3	0	9415	0.0685
7.88	55	0	23.6	0	11618	0.0713
7.88	60	0	37.0	0	14723	0.0861
7.88	65	0	58.0	0	18629	0.1049
7.88	70	0	75.7	0	23437	0.1071
8.17	40	0.260	1.28	115	5762	0.0093
8.17	45	0.260	2.25	172	7252	0.0122
8.17	50	0.260	3.59	349	9338	0.0147
8.17	55	0.260	5.89	513	11921	0.0184
8.17	60	0.260	8.33	707	14703	0.0200
8.17	65	0.260	11.12	1120	18677	0.0208
7.96	40	0.293	0.78	410	5889	0.0059
7.96	45	0.293	1.30	599	7486	0.0073

7.96	50	0.293	2.22	944	9583	0.0094
7.96	55	0.293	3.42	1331	12378	0.0110
7.96	60	0.293	5.58	1844	15572	0.0138
7.96	65	0.293	8.07	3031	19365	0.0155
7.96	70	0.293	11.94	4051	24556	0.0180
7.93	40	0.395	0.11	8187	5918	0.0008
7.93	45	0.395	0.16	11737	7595	0.0009
7.93	50	0.395	0.29	15979	9765	0.0013
7.93	55	0.395	0.56	20121	12428	0.0019
7.93	60	0.395	1.09	23968	15486	0.0028
7.93	65	0.395	1.95	28308	20319	0.0038

loading is moles of CO_2/mol of alkalinity

Table 4: Volatility and CO_2 Solubility for 7 m MDEA/2 m PZ

T (C)	Loading	P_{CO2} (Pa)	P_{MDEA} (Pa)	P_{PZ} (Pa)	P_{H2O} (Pa)	γ_{MDEA}	γ_{PZ}
40	0	0	0.66	0.64	6110	1.42	0.018
45	0	0	0.90	1.08	7612	1.23	0.023
50	0	0	1.34	1.75	10016	1.19	0.028
55	0	0	1.85	2.68	12620	1.08	0.033
60	0	0	2.66	3.86	15725	1.03	0.036
65	0	0	3.98	5.85	20032	1.05	0.042
70	0	0	5.79	9.10	25841	1.05	0.052
40	0.09	176	0.55	0.08	5878	1.21	0.002
45	0.09	246	0.85	0.22	7373	1.18	0.005
50	0.09	437	1.32	0.40	9565	1.18	0.006
55	0.09	613	1.84	0.69	12055	1.09	0.009
60	0.09	916	2.74	1.34	15144	1.08	0.013
65	0.09	1429	4.07	2.07	19528	1.09	0.015
70	0.09	2249	6.24	3.32	25207	1.15	0.019
40	0.13	532	0.49	0	5801	1.09	0
45	0.13	813	0.75	0.06	7302	1.06	0.001
50	0.13	1087	1.28	0.21	9702	1.16	0.003
55	0.13	1603	1.87	0.35	12403	1.11	0.004
60	0.13	2423	2.65	0.47	15503	1.05	0.004
65	0.13	3581	4.06	0.96	19704	1.09	0.007
40	0.2	2300	0.42	0	5499	0.94	0
45	0.2	3440	0.65	0	7299	0.92	0
50	0.2	5369	0.94	0	9399	0.86	0
55	0.2	7539	1.49	0.00	12099	0.90	0.000
60	0.2	10799	2.34	0.09	15698	0.94	0.001
65	0.2	13898	3.63	0.33	19898	0.99	0.002

70	0.2	18698	5.71	0.76	25497	1.07	0.004
40	0.28	7674	0.39	0	5695	0.88	0
45	0.28	9353	0.63	0	7294	0.91	0
50	0.28	15268	0.95	0	9492	0.88	0
55	0.28	21283	1.43	0	12290	0.87	0
60	0.28	28477	2.15	0	15588	0.87	0
65	0.28	31275	3.62	0.05	20384	1.00	0.000
70	0.28	37270	5.95	0.43	25979	1.13	0.003

loading is defined as moles of CO_2/(mol total alkalinity)

Results

Volatility of Amines in Binary Amine-H2O Systems

The volatilities of the amines are correlated with molecular groups and structural shapes. Amines having one or more polar groups, such as the amine, hydroxyl, and ether groups, tend to be less volatile due to favorable interactions with water. The presence of one or more methyl groups in a structure contributes to non-polarity or greater volatility as in the case of AMP. As a second order effect, the presence of an N-CH_3 contribution in a straight-chained amine, or a C-CH_3 contribution in a cyclic amine, correlates to lower volatility. Finally, to a lesser extent, the cyclic amines appear to be less volatile than straight-chained amines. Table 2 shows the 10 amines studied in order of increasing Henry's constants at 40 °C.

The amine Henry's constant at 40 °C is given as a function of the various polar and non-polar group contributions as shown in Equation (4).

$$\ln H_{amine,40\ ^oC} = [4.19\ (\pm 0.09)] - [1.65(\pm 0.17)](N) - [0.21(\pm 0.07)](NH) - [1.55(\pm 0.17)](R\text{-}O\text{-}R) + [0.7(\pm 0.08)](\text{Non Cyclic C-}CH_3) + [2.63(\pm 0.21)](\text{Cyclic N-}CH_3) \quad (4)$$

In Equation 4, (N) represents the number of tertiary nitrogen present, (NH) is the number of secondary nitrogen, (R-O-R) is the number of ether groups, (Non Cyclic C-CH_3) is the number of C-CH_3 grouping provided that the amine is non-cyclic, (Cyclic N-CH_3) is the number of N-CH_3 contribution provided that the amine is cyclic.

The UNIFAC-DMD method in Aspen Plus® was used to estimate the amine Henry's constants at 40 °C. Structural information for UNIFAC group contribution estimates was available for most amines with the exception of 1MPZ and 2MPZ. The vapor pressures of many amines had to be estimated in Aspen Plus® using the Mani method in conjunction with the amine normal boiling points. Table 5 shows the measured amine Henry's constants, predictions from Equation 4 and UNIFAC-DMD, and estimated amine heats of absorption.

Table 5: A Comparison of Measured Amine Henry's Constant at 40 ˚C to Values Estimated by Equation4 and by UNIFAC-DMD

Amine	Structure	B.P. (C)	H (Pa)	$H_{pred.}$ (Pa)	H_{UNIFAC} (Pa)	- ΔH_{amine} (kJ/mol)
MDEA	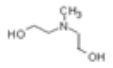	245	12.7	12.7	43.6	57
DGA	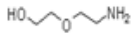	223	(13.9)	13.9	216	37
PZ		146	43.4	43.5	887	67
2-MPZ		155	48.2	43.5	221	77
MAPA	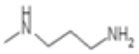	139	59.3	53.5	388	66
EDA		117	62.7	66	25.8	68
MEA		170	70.7	66	72.7	53
DAP		119	114	133	308	57
1-MPZ	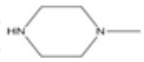	138	143	143	335	79
AMP	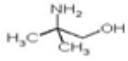	166	288	267	634	68

While many of the amine Henry's constants were overestimated by UNIFAC-DMD, the Henry's constant for MEA was accurately predicted within a small margin of error. This result is expected as the MEA-H_2O system is well-studied with adequate supporting data. The most important finding is that there is no correlation between the amine normal boiling points and their Henry's constants. This result is rather surprising as it indicates that one amine may be more volatile than another in its pure form but the opposite is true when the amine is in water.

Volatilities of Amines in Key Loaded Systems

Figure 2 shows MEA volatility for the baseline 7 m MEA-CO_2-H_2O system.

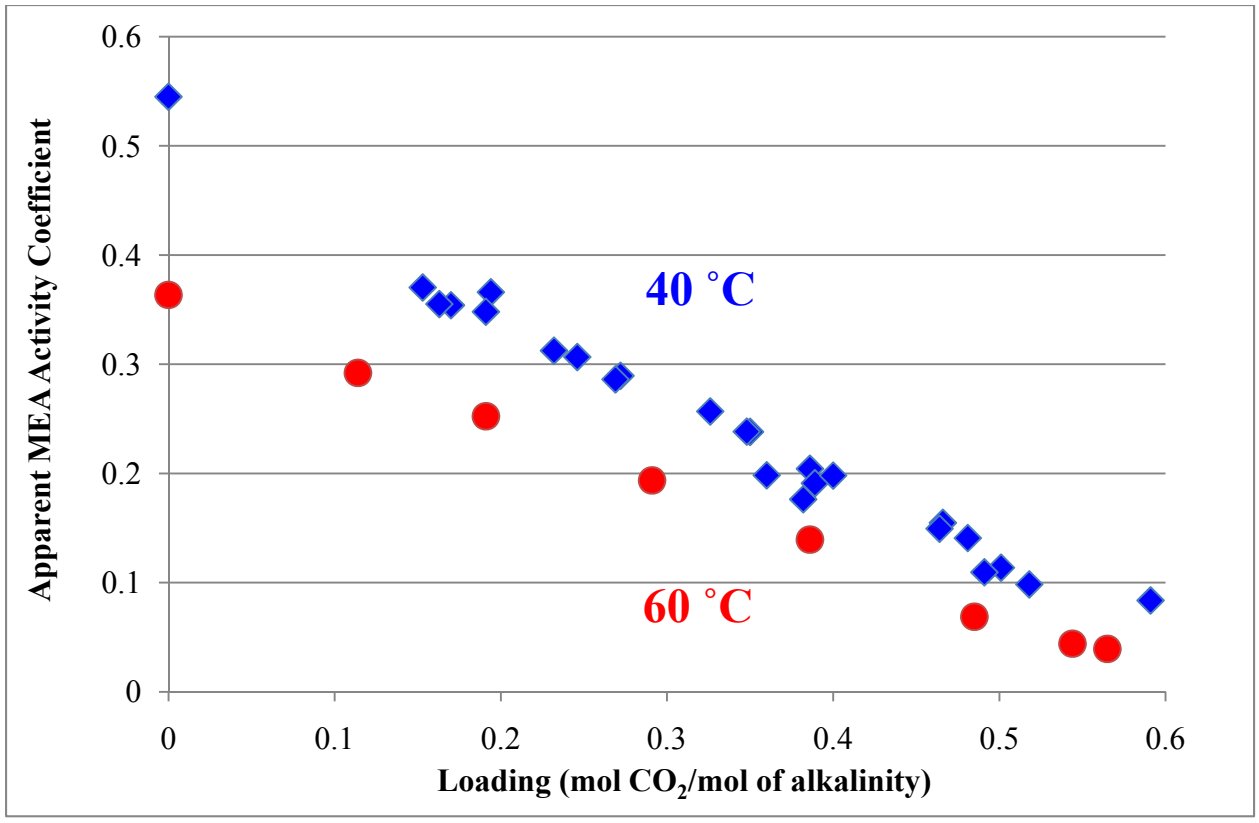

Figure 2: MEA Volatility for 7 m MEA-CO_2-H_2O

The apparent MEA activity coefficient is greater at 40 ˚C than it is at 60 ˚C which gives rise to an endothermic MEA heat of solution of 10.2 kJ/mol at a nominal lean loading of 0.4 mol CO_2/mol alkalinity. MEA volatility at the top of the absorber was measured at roughly 2.7 Pa.

Figure 3 illustrates the volatility of PZ in loaded 8 m PZ.

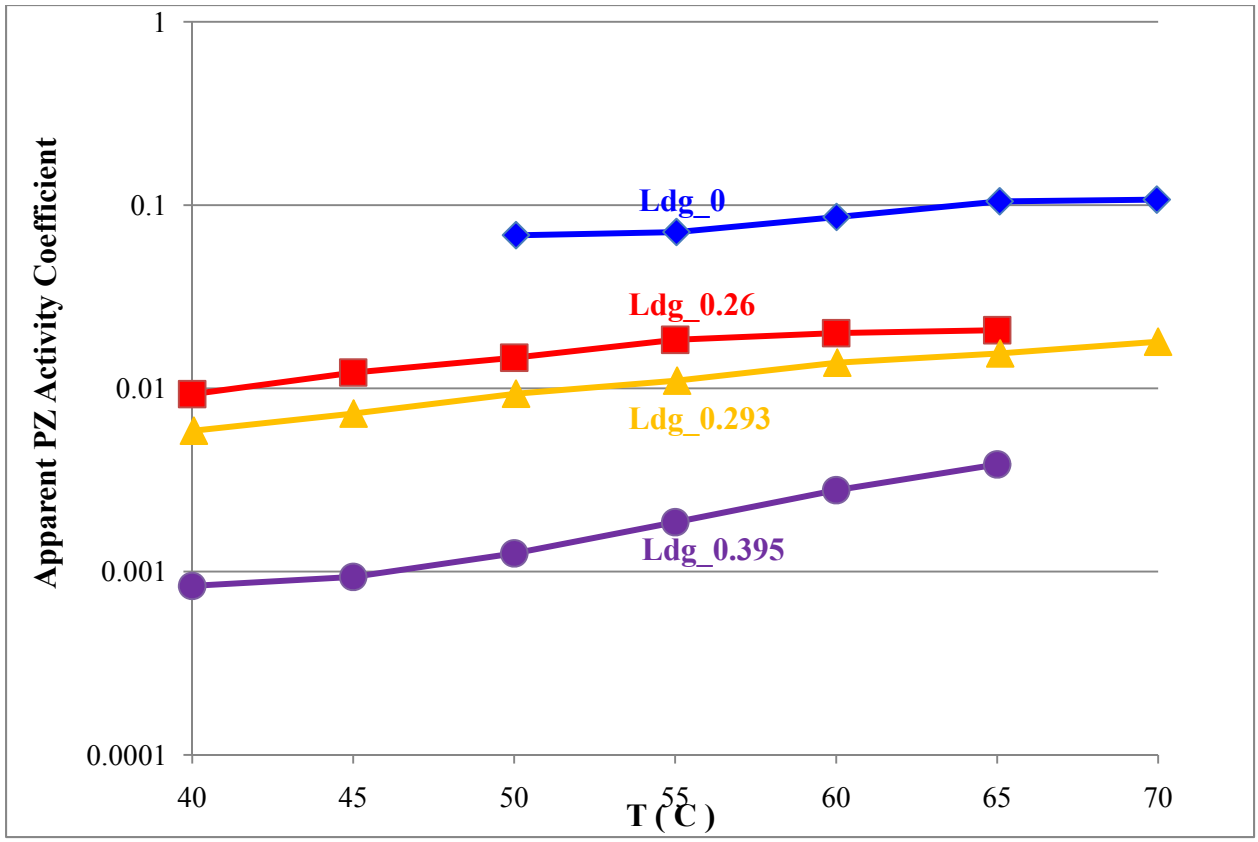

Figure 3: PZ Volatility for 8 m PZ-CO_2-H_2O

PZ heat of solution for this system at the nominal lean loading of 0.29 mol CO_2/mol alkalinity is approximately -37.1 kJ/mol. Given that the apparent activity coefficient of PZ is at least one order of magnitude smaller than that of MEA, one can conclude that the ratio of PZ-solvent interaction relative to pure PZ self-interaction is greater than the ratio of MEA-solvent interaction relative to pure MEA self-interaction. While PZ-solvent interaction is comparable to MEA-solvent interaction, PZ has a weaker self-interaction relative to MEA self-interaction because the latter can form a hydrogen bond with itself. Lastly, PZ volatility measured at conditions at the top of the absorber (40 ˚C, nominal lean loading) is ~0.78 Pa.

The volatility of MDEA in 7 m MDEA/2 m PZ is presented in Figure 4.

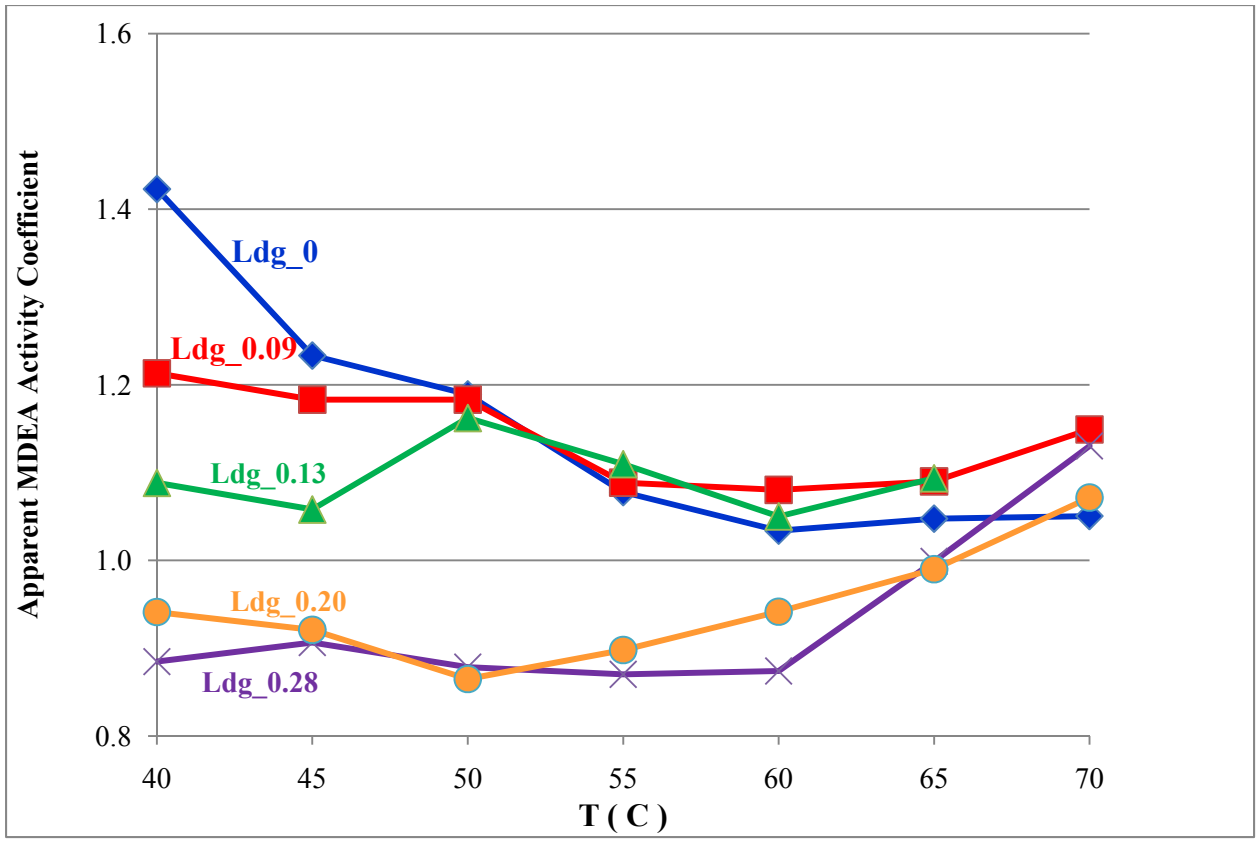

Figure 4: MDEA Volatility for 7 m MDEA/2 m PZ

MDEA heat of solution for this blend is approximately 1.5 kJ/mol at the nominal lean loading of 0.13 mol CO_2/mol total alkalinity. MDEA volatility at conditions at the top of the absorber is ~ 0.49 Pa.

PZ volatility in 7 m MDEA/2 m PZ is presented in Figure 5.

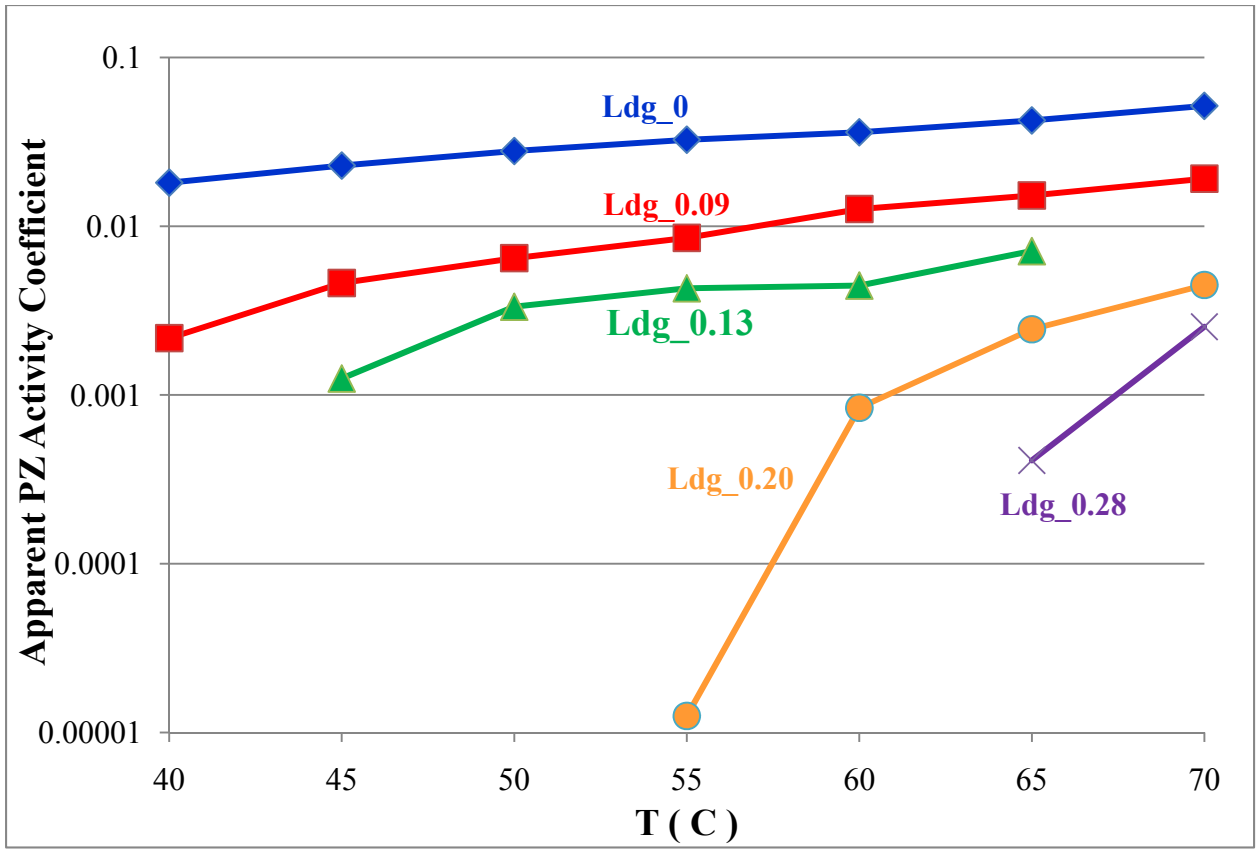

Figure 5: PZ Volatility for 7 m MDEA/2 m PZ

PZ heat of solution in the blend is approximately -74.6 kJ/mol at the nominal lean loading of ~0.13. Additionally, PZ heat of solution, graphically represented by the slope of the curves, increases dramatically with loading. At zero loading approaching the nominal lean loading, PZ heat of solution is dependent on free PZ concentration. In the regime of rich loadings which is 0.2 or greater, the free PZ concentration is completely depleted. At this point, the PZ heat of solution no longer depends on the free PZ concentration, but rather on the energetics of all the PZ product species present in solution. Finally, PZ volatility measured at conditions representing the top of the absorber is negligible.

Conclusions

1. The volatility of an amine in water does not necessarily track its pure boiling point.

2. In regard to intrinsic amine volatility in water, it was found that: MDEA < DGA < PZ < 2MPZ < MAPA < EDA < MEA < 1,2 Diaminopropane < 1MPZ < AMP.

3. UNIFAC-DMD theory overestimated the volatilities of most amines studied with the exception of MEA.

4. 8 m PZ is approximately 3.5 times less volatile than baseline 7 m MEA at conditions at the top of the absorber.

5. The blend of 7 m MDEA/2 m PZ is 5.5 times less volatile than 7 m MEA at conditions at the top of the absorber.

Future Work

The heat capacities of the 7 m MDEA/2 m PZ blend, and that of 5 m MDEA/5 m PZ, will be measured at 40–120 ˚C. NMR speciation will also be obtained for these blends at their nominal lean and rich loadings at 25 ˚C and 40 ˚C. The volatilities of amines in blends consisting of PZ and its derivatives will be investigated. Effort will also be made to continuously upgrade the Aspen Plus® thermodynamic model for MDEA/PZ.

References

Hilliard, M.D. *A Predictive Thermodynamic Model for an Aqueous Blend of Potassium Carbonate, Piperazine, and Monoethanolamine for Carbon Dioxide Capture from Flue Gas.* The University of Texas at Austin. Ph.D. Dissertation. 2008.

Modeling MDEA/PZ Thermodynamics, Hydraulics, and Kinetics

Quarterly Report for July 1 – September 30, 2010

by Peter Frailie

Supported by the Luminant Carbon Management Program

Department of Chemical Engineering

The University of Texas at Austin

October 31, 2010

Abstract

The goal of this study is to evaluate the performance of an absorber/stripper operation that utilizes MDEA/PZ. Before analyzing unit operations and process configurations, thermodynamic, hydraulic, and kinetic properties for the blended amine must be satisfactorily regressed in Aspen Plus®. The approach used in this study is first to construct separate MDEA and PZ models that can later be reconciled via cross parameters to model accurately the MDEA/PZ blended amine. This study is currently in the process of finalizing the MDEA/PZ model based on thermodynamic, hydraulic, and kinetic data. Separate MDEA and PZ models have been finished that accurately predict VLE, heat capacity, unloaded amine volatility, CO_2 activity coefficient, and CO_2 absorption rate over operationally significant temperature, amine concentration, and loading ranges. All available thermodynamic and hydraulic data for 7 m MDEA/2 m PZ and 5 m MDEA/5 m PZ have also been regressed. The goal for the next quarter is to improve MDEA/PZ CO_2 absorption rate predictions and begin modeling an absorption/stripping/compression process.

Introduction

The removal of CO_2 from process gases using alkanolamine absorption/stripping has been extensively studied for several solvents and solvent blends. An advantage of using blends is that the addition of certain solvents can enhance the overall performance of the CO_2 removal system. A disadvantage of using blends is that they are very complex compared to a single solvent, thus making them much more difficult to model.

This study will focus on a blended amine solvent containing piperazine (PZ) and methyldiethanolamine (MDEA). Previous studies have shown that this particular blend has the potential to combine the high capacity of MDEA with the attractive kinetics of PZ (Bishnoi, 2000). These studies have supplied a rudimentary Aspen Plus®-based model for an absorber with MDEA/PZ. The report also makes the recommendation that more kinetic and thermodynamic data must be acquired concerning the MDEA/PZ blend before the model can be significantly improved. Three researchers in the Rochelle lab have been acquiring these data, and the data are currently being incorporated into the model. One of the major goals of this study will be to improve the supplied Aspen Plus® absorber model with up-to-date thermodynamic and kinetic data. Another major goal of this study will be to make

improvements to the MDEA and PZ thermodynamic models, which should simplify the construction of the blended amine model.

Methods and Discussion

During the past quarter the MDEA/PZ thermodynamic and hydraulic models were finished, and significant progress was made in regressing the kinetics of 7 m MDEA/2 m PZ. What follows is a description of the sequential regression used to develop the models, as well as a brief discussion of each of the incorporated data sets.

MDEA/PZ Thermodynamic Model

MDEA/PZ/H_2O Regression

The first set of data incorporated into the MDEA/PZ thermodynamic model was unloaded amine volatility measured by Nguyen (2009). Figure 1 compares the experimental data (points) and the Aspen Plus® predictions (before and after regression) for low temperature volatility in unloaded 7 m MDEA/2 m PZ.

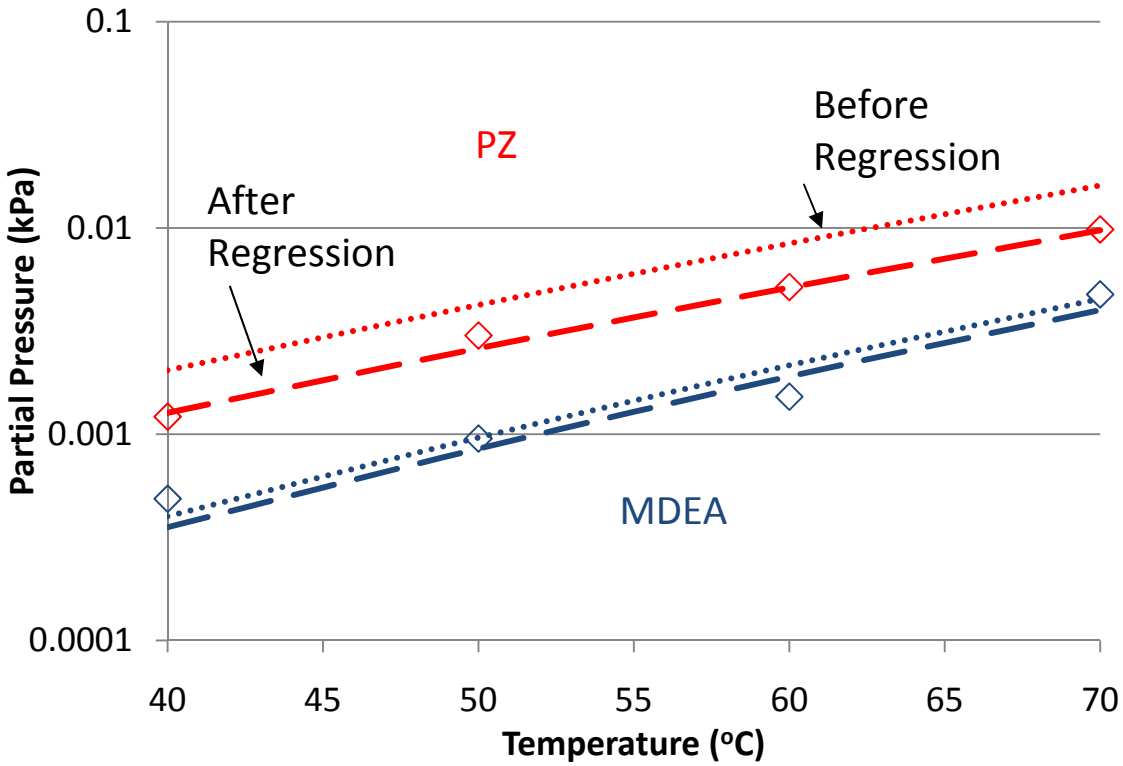

Figure 1: Amine volatility as a function of temperature for 7 m MDEA/2 m PZ unloaded solutions between 40 °C and 70 °C

Aspen Plus® predictions before and after the regression are shown to provide some perspective on the efficacy of the sequential regression method. MDEA and PZ volatility data were fit separately for earlier models. The only parameters that could be used to fit blend data were the cross parameters that consider the interactions between MDEA and PZ. Before regressing those parameters, the model slightly over predicts the volatilities of both amines. This result may be

attributed to favorable interactions between the amines, which are unaccounted for in the earlier models. MDEA would rather interact with PZ than water (and vice versa), so the addition of another amine to the solution should reduce the volatility of each amine. The parameters used to fit unloaded amine volatility are infinite dilution activity coefficients. Table 1 reports all of the parameters and their standard deviations.

Table 1: Parameters used to regress unloaded MDEA/PZ volatility

Parameter	Species	Std. Dev.
NRTL/1	MDEA/PZ	0.058
NRTL/1	PZ/MDEA	0.045

MDEA/PZ/H_2O/CO_2 Regression

Because the ΔG_{form}, ΔH_{form}, and $C_{P,aq}$ of all species present in MDEA/PZ/H_2O/CO_2 have already been regressed, the only remaining adjustable parameters were the cross parameters used in the calculation of activity coefficients. These parameters were used to fit 7 m MDEA/2 m PZ and 5 m MDEA/5 m PZ VLE data (Chen, 2010) between 40 °C and 100 °C. Figure 2 compares the experimental data and Aspen Plus® predictions for 7 m MDEA/2 m PZ.

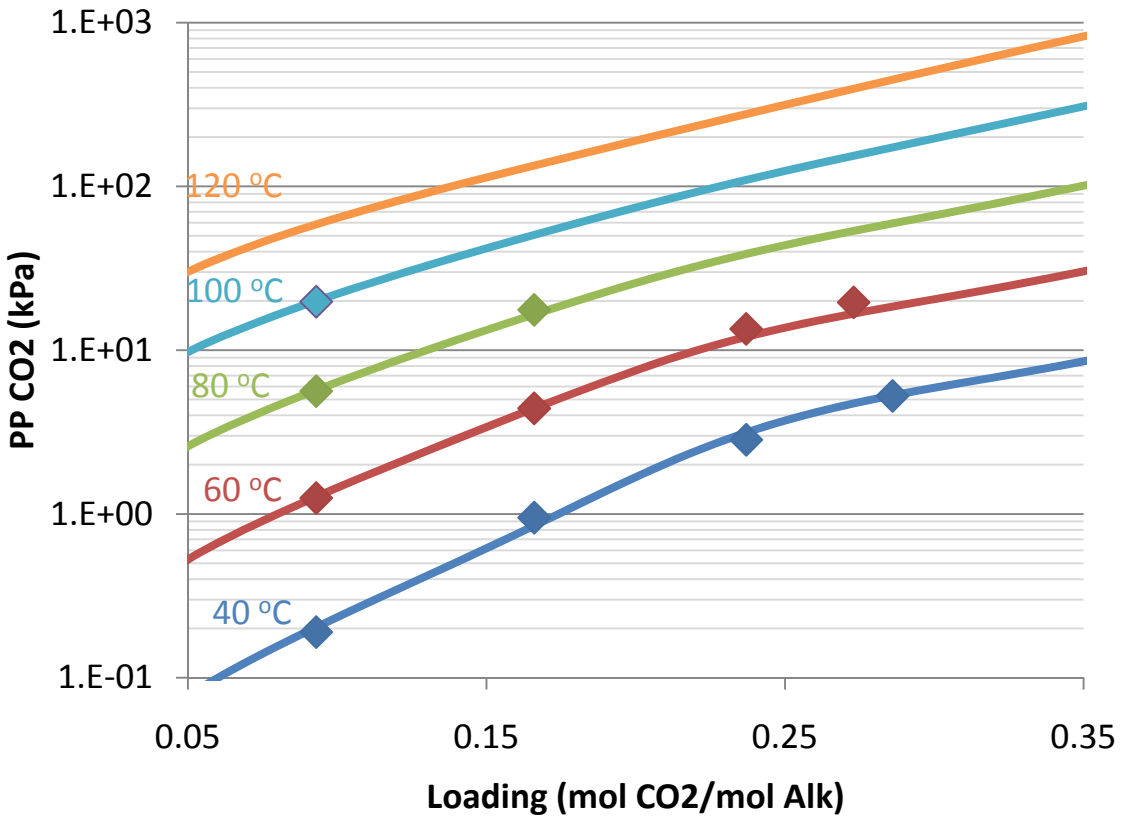

Figure 2: Aspen Plus® predictions (lines) and experimental data (points) for VLE of 7 m MDEA/2 m PZ between 40 °C and 100 °C

Figure 3 compares the experimental data and Aspen Plus® predictions for 5 m MDEA/5 m PZ between 40 °C and 100 °C.

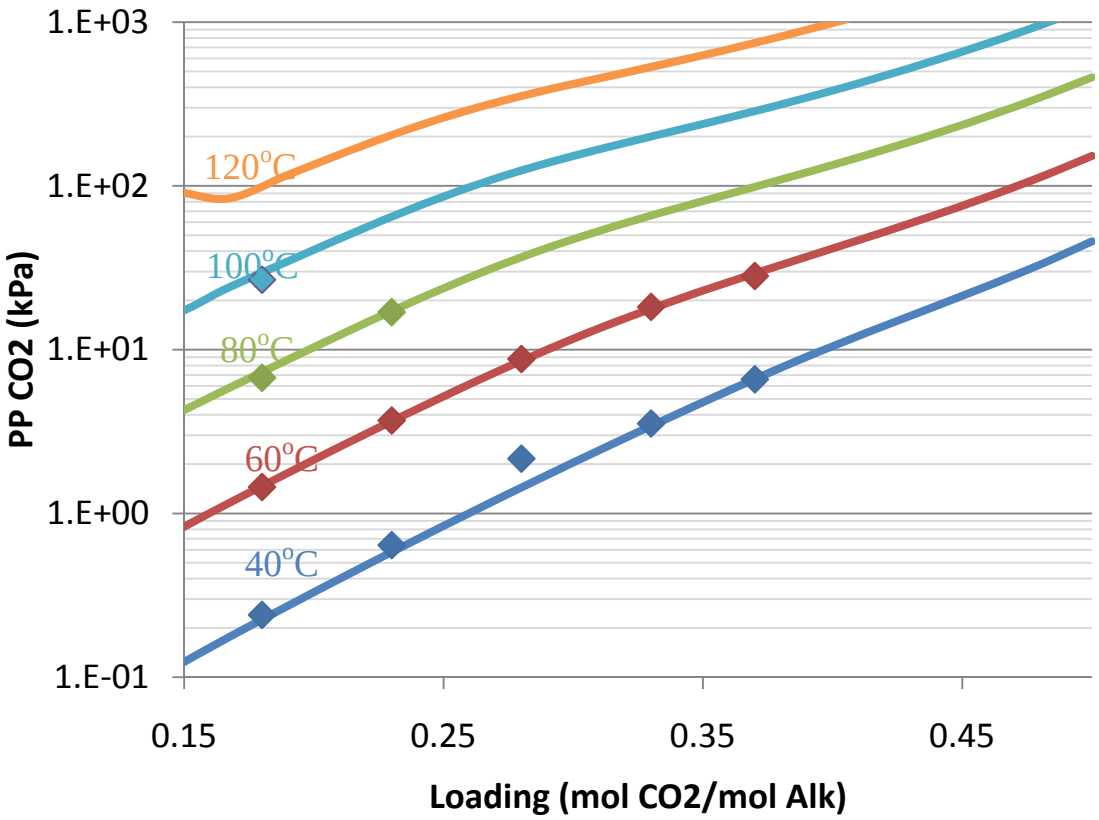

Figure 3: Experimental (points) and Aspen Plus® predictions (lines) for VLE of 5 m MDEA/5 m PZ between 40 °C and 100 °C

At this point the only experimental data available for MDEA/PZ/H_2O/CO_2 are the VLE data in Figures 2 and 3. Heat capacity data for both blends are currently being collected, and the results will be compared to model predictions as soon as possible.

Table 2 lists the five cross parameters that exhibited the greatest influence on model predictions.

Table 2: Parameters used to regress MDEA/PZ VLE

Parameter	Species	Std. Dev.
$\tau_{ca\text{-}m}$	$(MDEAH^+, PZCOO^-)$/MDEA	1.46
$\tau_{ca\text{-}m}$	$(MDEAH^+, PZ(COO)_2^{2-})$/MDEA	1.03
$\tau_{ca\text{-}m}$	(PZH^+, HCO_3^-)/MDEA	1.14
$\tau_{ca\text{-}m}$	$(PZH^+, HCO_3^-)/H^+PZCOO^-$	1.77
$\tau_{ca\text{-}m}$	$(MDEAH^+, PZ(COO)_2^{2-})$/PZ	0.41

The results in Table 2 suggest that the model shows a strong dependence on cross parameters where MDEA is the solvent. This may be attributed to the fact that throughout the operational loading, temperature, and amine concentration ranges, MDEA does not react as readily as PZ and, thus, is present in significant concentrations in both 7 m MDEA/2 m PZ and 5m MDEA/2 m PZ. It is interesting to note that there was very little dependence on cross parameters where H_2O is the solvent, even though it is always present in significant amounts.

MDEA/PZ Hydraulic Model

Viscosity, density, and diffusivity were incorporated into the model via FORTRAN subroutines.

Viscosity and Density

Equations 1 and 2 are used to calculate mixture viscosity and density, respectively, as functions of temperature, total amine and/or CO_2 concentration, and loading.

$$\mu_{Blend} = \left(A + B * wt_{Amine} + C * ldg + D * wt_{Amine} * ldg\right) \frac{\exp\left(\frac{E}{T}\right)}{\exp\left(\frac{E}{313.15K}\right)} \quad (1)$$

$$\rho_{Blend} = (A + B * T) \ln\left[C * x_{CO2} + D * x_{Amine} + E\left(\frac{x_{CO2}}{x_{Amine}}\right) + F\right] \quad (2)$$

The parameters in these expressions were regressed in Microsoft Excel using the data regression tool. The final values for these parameters can be found in Table 3.

Table 3: Regressed parameter values for viscosity and density subroutines

Parameter	Viscosity	Density
A	-0.007	1.30
B	0.025	-0.0007
C	-0.03	0.19
D	0.1	1.45
E	3526	0.53
F	N/A	2.4

Figures 4 and 5 compare the Aspen Plus® predictions and experimental data for MDEA/PZ viscosity and density, respectively. Viscosity is shown as a function of total amine weight fraction, and density is shown as a function of loading. The purpose of plotting data in these terms is to highlight the possibility of using online density and viscosity measurements to determine loading and amine concentration in the pilot plant.

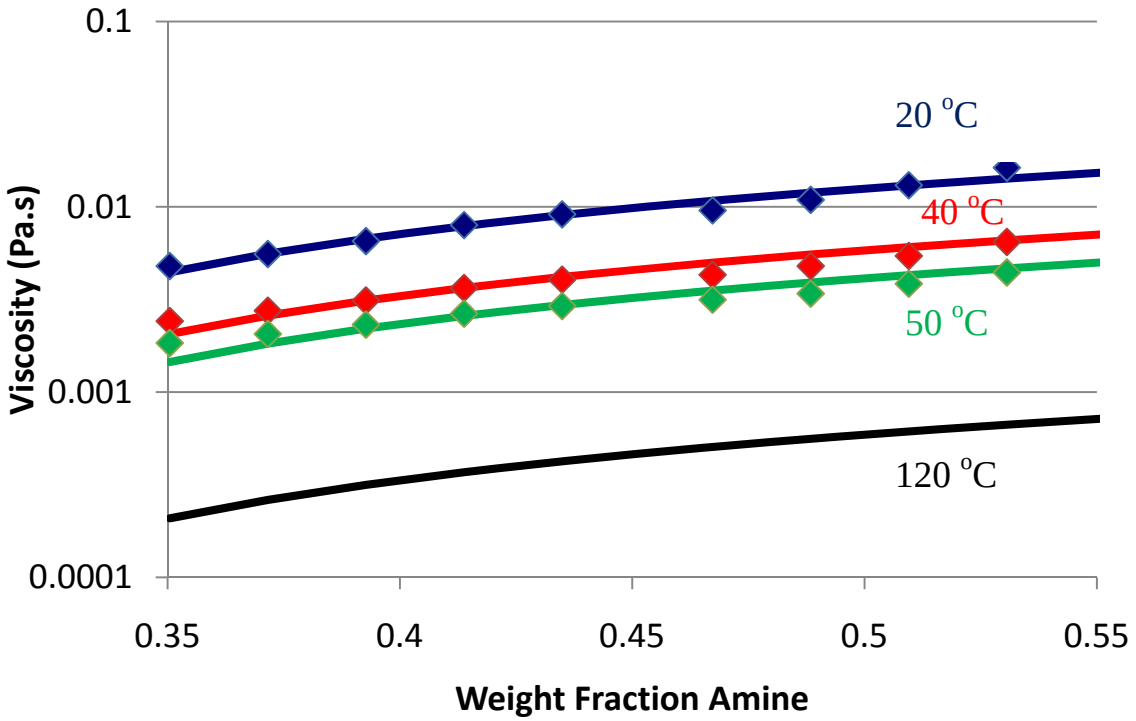

Figure 4: Experimental (points) and Aspen Plus® predictions (lines) for viscosity of unloaded MDEA/PZ between 20 °C and 120 °C

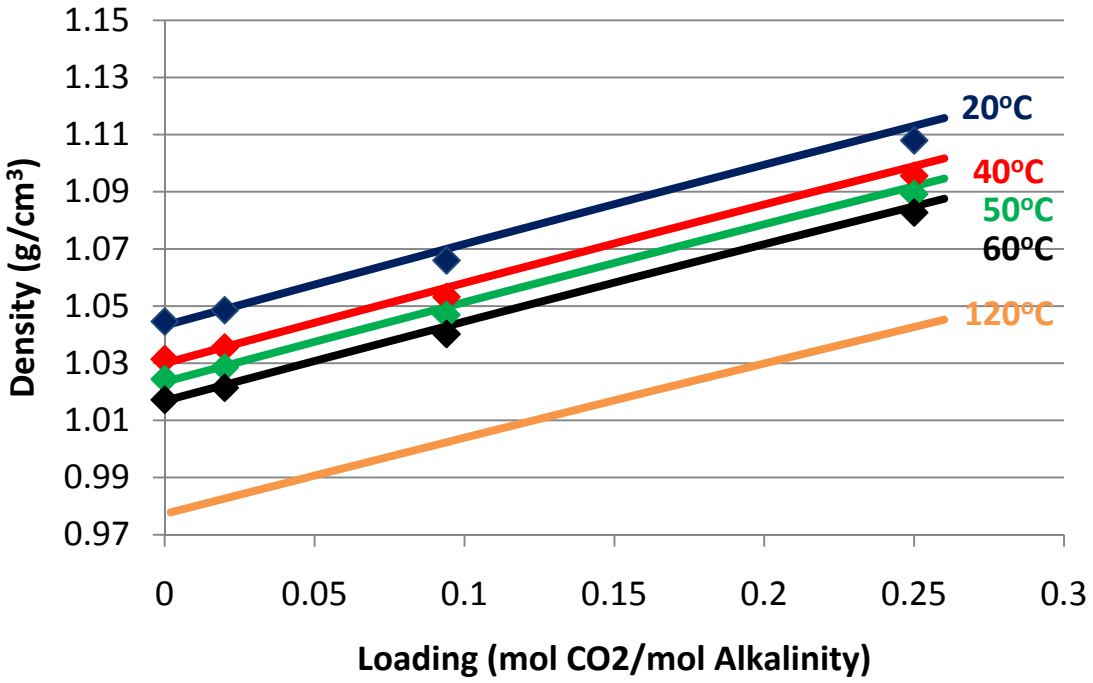

Figure 5: Experimental (points) and Aspen Plus® predictions (lines) for density of 7 m MDEA/2 m PZ between 20 °C and 120 °C

Diffusivity

In all previous Aspen Plus® models binary diffusivities have been left fixed at temperature-independent default values, suggesting that the absorption rate of CO_2 is limited by reaction rate rather than mass transfer. This assumption has been adequate for most cases, but for complex ionic solutions (i.e. PZ and MDEA/PZ) at elevated temperatures the absorption rate of CO_2 is more limited by mass transfer than reaction rates. The reactions are almost instantaneous, but key reactants, which must diffuse from the bulk to the reaction interface, are present in relatively low concentrations. Therefore, diffusion constants must be adjusted to allow for adequate mass transfer of key reactants from the bulk to the reaction interface.

Diffusion constants for molecules and ions were calculated by a user-supplied FORTRAN subroutine using Equations 3 and 4, respectively.

$$D_i = \left(\frac{RT}{z_i F^2}\right)\left(l_{1,i} + l_{2,i} * T\right)\sum_k x_k \tag{3}$$

$$D_i = k_i * T\left(\mu_{Blend}\right)^{-\alpha} \tag{4}$$

Equation 3 is the default equation for Aspen Plus® with default values of 5 and 0 for l_1 and l_2, respectively. These values were used in the user-supplied FORTRAN subroutine for all ionic species. Equation 4 is used by several sources in literature (Derks, 2008; Samanta, 2007; Dugas, 2009), and the regressed values of k and α for MDEA, PZ, and CO_2 are reported in Table 4.

Table 4: Regressed parameter values for diffusivity subroutines

Species	k_i	α
MDEA	2.921E-14	0.71
PZ	2.937E-14	0.73
CO_2	3.182E-14	0.66

MDEA/PZ Kinetic Model

Rate data were incorporated into the model by adjusting reaction rate constants in a wetted wall column (WWC) simulation in Aspen Plus® to match experimental values (Chen, 2010) for the flux of CO_2. Equations 5–12 are the equilibrium and forward kinetic reactions used to model MDEA/PZ.

$$PZCOO^- + PZH^+ \longleftrightarrow H^+PZCOO^- + PZ \tag{5}$$

$$MDEA + PZH^+ \longleftrightarrow MDEA^+ + PZ \tag{6}$$

$$MDEA + H_2O + CO_2 \longrightarrow MDEAH^+ + HCO_3^- \tag{7}$$

$$PZ + H_2O + CO_2 \longrightarrow PZH^+ + HCO_3^- \tag{8}$$

$$MDEA + PZ + CO_2 \longrightarrow MDEAH^+ + PZCOO^- \tag{9}$$

$$2PZ + CO_2 \longrightarrow PZH^+ + PZCOO^- \tag{10}$$

$$MDEA + PZCOO^- + CO_2 \longrightarrow MDEAH^+ + PZ(COO)_2^{2-} \tag{11}$$

$$PZ + PZCOO^- + CO_2 \longrightarrow PZH^+ + PZ(COO)_2^{2-} \tag{12}$$

All reverse rates were calculated using equilibrium constants based on regressed thermodynamic parameters. Because the WWC simulation only allows for one adjustable parameter, all forward

rates were either fixed or ratioed to another reaction using literature values. Equations 7 and 8 were fixed from experimental data (Ko, 2000), Equation 12 was ratioed to Equation 10 using relative CO_2 reaction rates (Cullinane, 2005), and every reaction involving MDEA as the proton acceptor (9, 11) was ratioed to its PZ counterpart via pKa values (Hetzer, 1968; Hamborg, 2007). Ultimately, the forward rate of Equation 10 was the only independently adjusted parameter.

These forward and reverse reaction rates were adjusted to match CO_2 absorption rate data from 40 ^oC–80 ^oC and 0.10–0.30 mol CO_2/mol alkalinity for 7 m MDEA/2 m PZ. The data regression tool in Microsoft Excel was used to match these rate constants by adjusting the k_0 and E_A terms in Equation 13 for every forward and reverse reaction.

$$k = k_0 \exp\left[\frac{-E_A}{R}\left(\frac{1}{T} - \frac{1}{T_{ref}}\right)\right] \tag{13}$$

Figure 6 compares the predicted and experimental fluxes of CO_2 from 40 ^oC–80 ^oC and 0.10–0.30 mol CO_2/mol alkalinity.

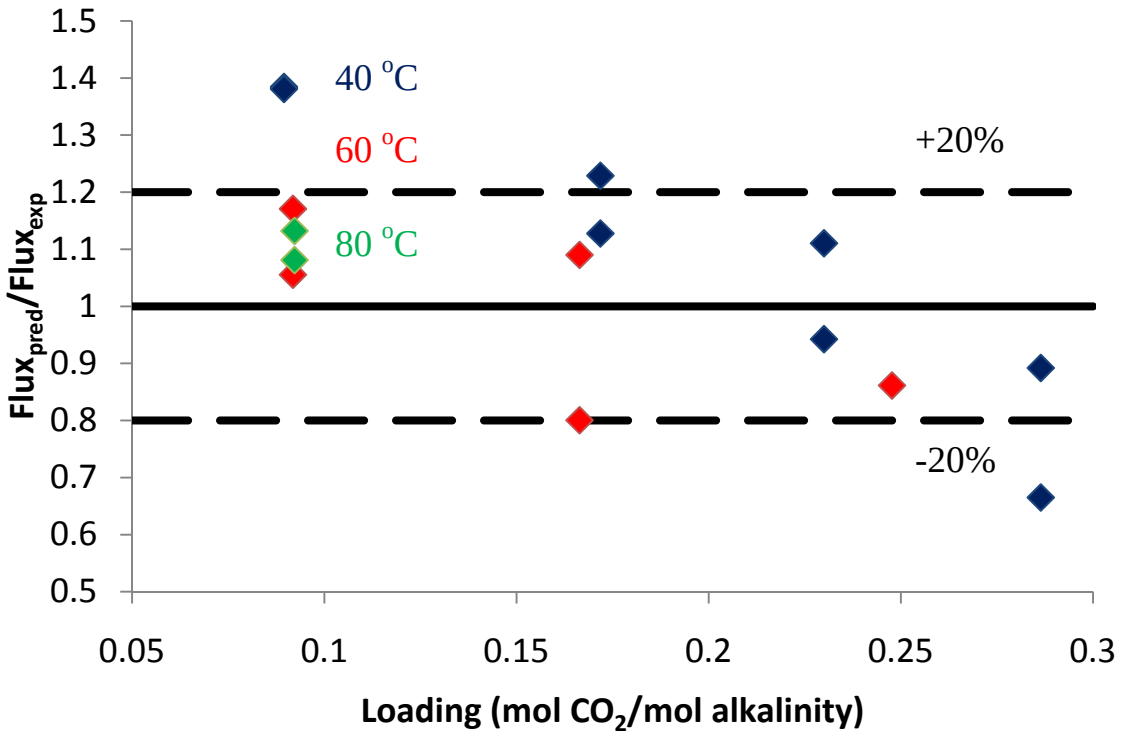

Figure 6: Residual plot of predicted and experimental CO_2 fluxes from 40 ^oC–80 ^oC and 0.10–0.30 mol CO_2/mol alkalinity

Two steps remain in the development of the kinetic model: (1) transformation of the reaction set so that it is more consistent with the kinetic model for PZ/H_2O/CO_2, and (2) incorporation of amine activity terms into Equation 13 to account for the effect of loading on the flux of CO_2. A PZ/H_2O/CO_2 kinetic model has already been developed (Plaza, 2010) with rate constant expressions for the production of $PZCOO^-$, $PZ(COO)_2^{2-}$, and HCO_3^- by PZ. Rather than adjust those parameters for this model, they will be fixed so that the resulting model will be able to fit MDEA, PZ, and MDEA/PZ absorption rates. However, the PZ/H_2O/CO_2 model uses different

kinetic reactions for the generation of $PZ(COO)_2^{2-}$ and HCO_3^-, necessitating that Equations 8 and 12 be converted to Equations 14 and 15, respectively.

$$PZCOO^- + H_2O + CO_2 \longrightarrow H^+PZCOO^- + HCO_3^- \quad (14)$$

$$2PZCOO^- + CO_2 \longrightarrow H^+PZCOO^- + PZ(COO)_2^{2-} \quad (15)$$

The incorporation of amine activity terms into Equation 13 to account for the effect of loading is a routine procedure that has already been successfully employed to fit MEA absorption rate data (Plaza, 2008).

Conclusions

The thermodynamics, hydraulics, and kinetics of 7 m MDEA/2 m PZ were incorporated into Aspen Plus®. The model adequately predicts VLE, density, viscosity, and diffusivity data over significant loading and temperature ranges (0.10–0.30 loading and 40 °C–120 °C). Regressed expressions for the density and viscosity of the blend could be used to perform online loading and amine weight fraction measurements in the pilot plant. Experimental data concerning absorption rate of CO_2 are still being incorporated. The flux of CO_2 appears to show a strong dependence on loading, suggesting that a loading effect must be incorporated into the rate expression.

Future Work

The kinetics of MDEA/PZ will be the top priority for the next quarter. This will include fitting rate data for 7 m MDEA/2 m PZ and 5 m MDEA/5 m PZ with the WWC simulation in Aspen Plus®. Once this is completed, an absorption/stripping/compression process will be designed and optimized.

References

Bishnoi S. *Carbon Dioxide Absorption and Solution Equilibrium in Piperazine Activated Methyldiethanolamine*. The University of Texas at Austin. Ph.D. Dissertation. 2000.

Chen X. Accurate screening of amines by the Wetted Wall Column. *GHGT-10*. Amsterdam, Netherlands. 2010.

Cullinane JT. *Thermodynamics and Kinetics of Aqueous Piperazine with Potassium Carbonate for Carbon Dioxide Absorption*. The University of Texas at Austin. Ph.D. Dissertation. 2005.

Derks PWJ, Hamborg ES, Hogendoorn JA, Niederer JPM, Versteeg GF. Densities, Viscosities, and Liquid Diffusivities in Aqueous Piperazine and Aqueous (Piperazine + N-Methyldiethanolamine) Solutions. *J Chem Eng Data*. 2008;53: 1179–1185.

Dugas RE. *Carbon Dioxide Absorption, Desorption, and Diffusion in Aqueous Piperazine and Monoethanolamine*. The University of Texas at Austin. Ph.D. Dissertation. 2009.

Hamborg ES, Niederer JPM, Versteeg GF. Dissociation Constants and Thermodynamic Properties of Amino Acids Used in CO_2 Absorption from (293 to 353) K. *J Chem Eng Data*. 2007;52:2491–2502.

Hetzer HB, Robinson RA, Bates RG. Dissociation Constants of Piperazinium Ion and Related Thermodynamic Quantities from 0 to 50°. *J Phys Chem.* 1968;72(6):2081–2086.

Ko article (I'll find it an insert the reference in the revised version of the report)

Nguyen, personal communication, July 20, 2009.

Plaza JM, Van Wagener DH, Rochelle GT. Modeling CO_2 capture with aqueous monoethanolamine. *GHGT-9*. Washington DC. 2008.

Samanta A, Roy S, Bandyopdhyay SS. Physical Solubility and Diffusivity of N_2O and CO_2 in Aqueous Solutions of Piperazine and (N-Methyldiethanolamine + Piperazine). *J Chem Eng Data*. 2007;52:1381–1385.

N-methyl-1,3-propanediamine (MAPA) for CO_2 capture

Quarterly Report for July 1 – September 30, 2010

by Solrun Johanne Vevelstad

Supported by the SOLVit project, NTNU

October 10, 2010

Abstract

Several thermal and oxidative degradation experiments were performed with 9 m N-methyl-1,3-propanediamine (MAPA). The samples were analyzed for degradation products using anion IC, cation IC, amino acid IC, IC-MS, LC-MS, GC-MS, and MS-MS. Alkalinity and total inorganic carbon were also measured. The thermal samples were analyzed for metals. Amine volatility of 9 m MAPA was measured using hot gas FTIR. Chen measured CO_2 solubility and liquid mass transfer coefficient in the wetted-wall column (8 m MAPA). Viscosity of 9 m MAPA was measured at different loadings at 40 °C.

The degradation experiments show that MAPA degrades faster than MEA. Under oxidative conditions, complete degradation was obtained after 5 days in the low gas flow apparatus, with stainless steel metals mixture. Inhibitor A was shown to reduce the amine loss to 35–37%. Most of the degradation products from thermal and oxidative experiments were not identified and quantified. However, it is believed that one of the main thermal degradation compounds is 1-methyltetrahydro-2(1H)-pyrimidone (*N*-methyl-*N*,*N*'-trimethyleneurea). In oxidation at low gas flow without Inh A, formate was produced at 2.4 mol /kg solution.

Apparent activity coefficient, partial pressure of MAPA, liquid mass transfer coefficient, and viscosity were compared with ethylenediamine (EDA). EDA loaded with CO_2 is less volatile than loaded MAPA. MAPA is more viscous than EDA. EDA had a higher CO_2 partial pressure than MAPA; however, the liquid mass transfer coefficient for MAPA was higher than EDA at lower CO_2 partial pressure.

Introduction

Absorption using chemical absorbents has been widely used in natural gas acid gas removal for over 60 years. The best absorbents are the ones with high net cyclic capacity, high reaction/absorption rates for CO_2, high chemical stability, low vapor pressure, and low corrosiveness. The most usual alkanolamines studied are monoethanolamine (MEA), diethanolamine (DEA), N-methyldiethanolamine (MDEA), 2-amino-2-methylpropanol (AMP), and blends of these. Alkanolamines have been and are still widely used as solvents for post-combustion CO_2 capture because the compounds have two functional groups which, in combination, give an increase of CO_2 solubility in water and absorption of CO_2 (Kohl, 1997). The work of Lepaumier using diamines as absorbents shows promising results (Lepaumier, 2009a; 2009b; 2009c) and the general pathway found for EDA degradation with CO_2 or air is given in Figures 1 and 2 (Lepaumier, 2009b; 2009c).

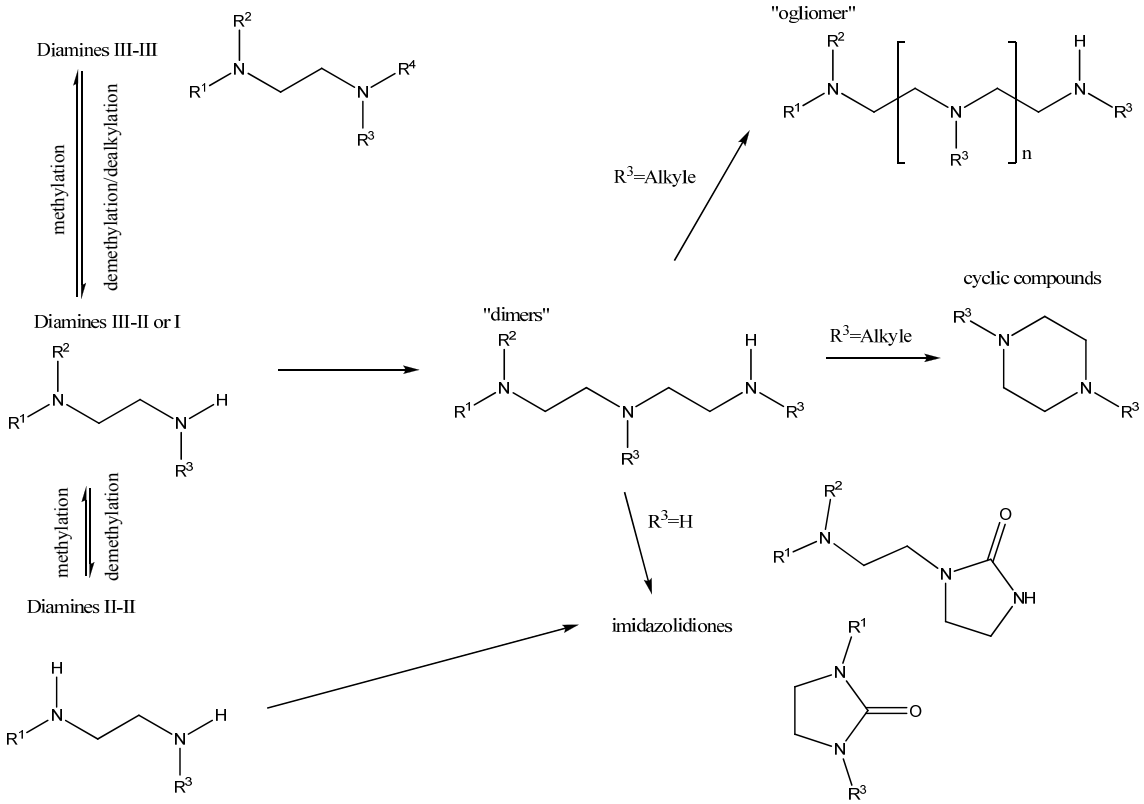

Figure 1: General pathway for ethylenediamine degradation with CO_2

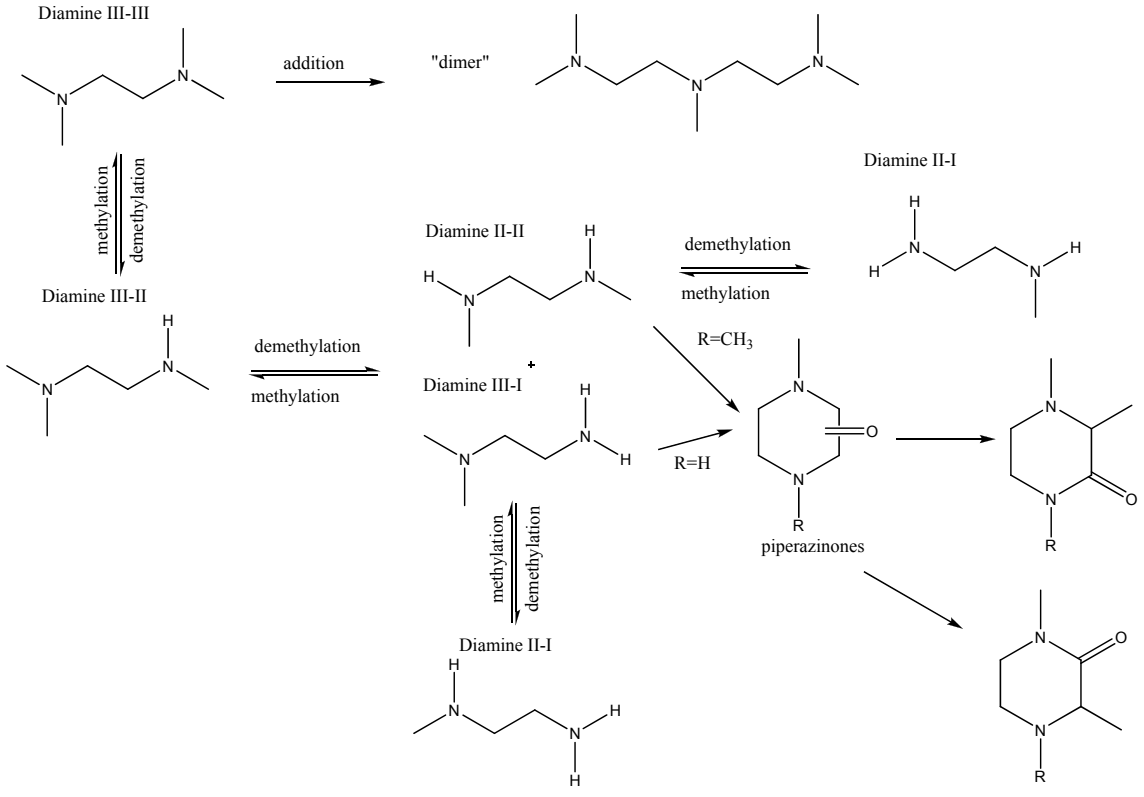

Figure 2: General pathway for ethylenediamine degradation with air

One of the main issues for amine-based processes is solvent degradation, which causes additional operating costs related to solvent loss, corrosion of the process equipment, fouling, foaming, and the potential risk the degradation products may pose to the environment (Kohl, 1997; Chakma, 1986; Strazier, 2003). There are several degradation routes depending on the process conditions; temperature, pressure, gas composition, amine concentration, pH of the amine solution, and the presence of metal ions (Rooney, 1998). These routes are called thermal degradation with or without CO_2 and oxidative degradation. Thermal degradation with CO_2 has been studied for a long time, but degradation in an oxidizing environment as in flue gases has been limited. Initial work was done in the 1950s and '60s by the US Navy, which wanted to clean CO_2-contaminated air in nuclear powered submarines (Rooney, 1998; Sexton, 2009). Increased insight into the mechanisms, through knowledge of the stoichiometry, kinetics, and chemical pathways associated with degradation, may result in elimination or strongly reduced degradation (Strazier, 2003; Supap et al., 2001).

There are few published results regarding N-methyl-1,3-propanediamine (MAPA). Lepaumier studied different ethylenediamines with different amine functions, but never the combination of a secondary and primary diamine like MAPA. One of the few published results for MAPA is the determination of the vapor-liquid equlibria of pure, ternary, and binary system of MAPA done by Kim (Kim et al., 2008). The vapor pressure for water and MAPA was determined and the results are given in Figure 3.

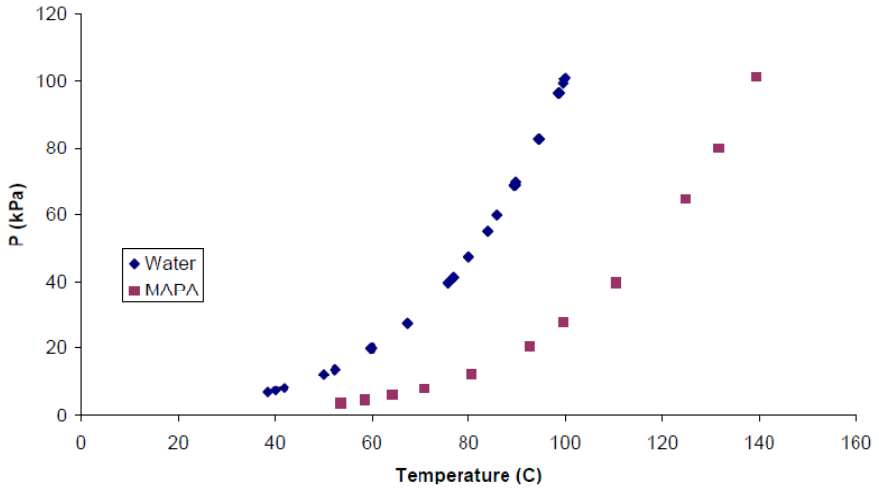

Figure 3: Vapor pressure for water and MAPA

The vapor-liquid equilibria (VLE) are fundamental properties which are essential for the design and operation of separation process (Kim et al., 2008). Nguyen and Chen have also studied MAPA and compared properties such as volatility, CO_2 solubility, and liquid mass transfer coefficient (k_g') for amines such as MEA and piperazine (PZ). The ammonia production rate for high gas flow oxidative degradation of MAPA (8 m) has been studied by Voice, and the results have been compared to MEA (7 m), see Figure 4 (Rochelle et al., 2010a).

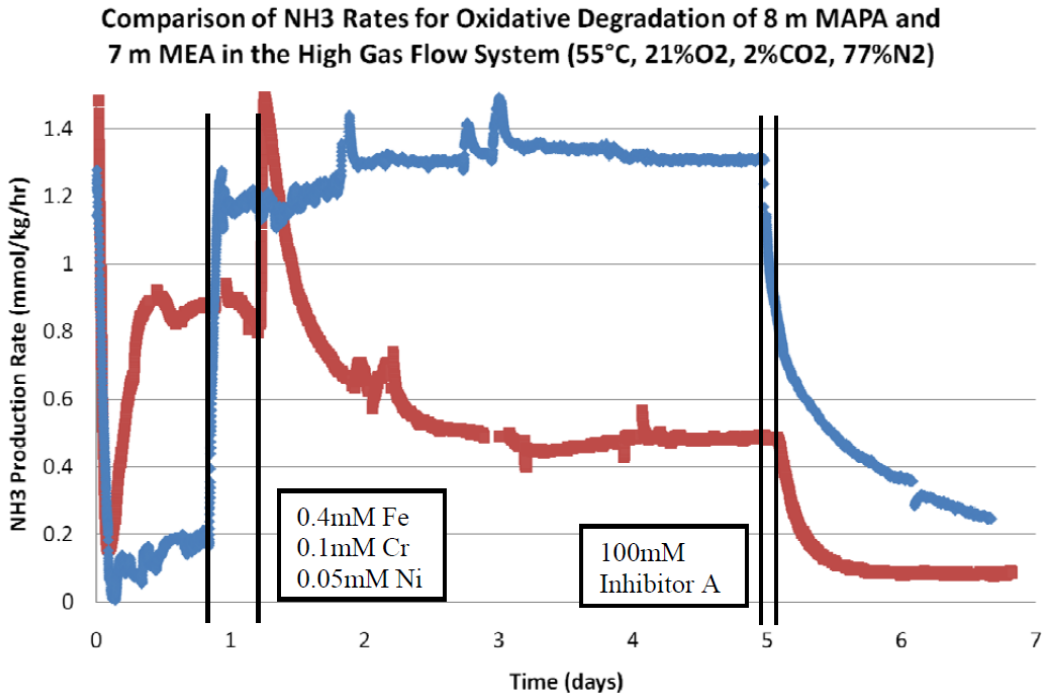

Figure 4: Ammonia production rate for 7 m MEA (blue) and 8 m MAPA (red) at different conditions in the high gas flow experiment (Rochelle et al., 2010a)

The figure shows that the ammonia production rate increased for MEA and decreased for MAPA after a metal mix was added, and that there was a reduction in ammonia production rate for both when Inhibitor A was added. The ammonia rates in the different experimental conditions (neat solution, with metals, and with Inh A) are given in Table 1. Comparisons with several other amines are given by Voice (Rochelle et al., 2010b).

Table 1: NH_3 production rates (mmol/kg/hr) of 7 m MEA and 8 m MAPA, High Gas Flow Experiment, 55 °C, 21% O_2, 2% CO_2 (Rochelle et al., 2010b)

Experimental Conditions	7 m MEA	8 m MAPA
Neat solution	0.15	0.87
0.4 mM Fe^{2+} 0.1 mM Cr^{3+} 0.05 mM Ni^{2+}	1.32	0.48
Inhibitor A	0.23*	0.08

* System did not reach steady state.

Voice also observed that MAPA did not produce significant concentrations of any of the anionic degradation products or corresponding amides. Formate was believed to be produced in small amounts. Total alkalinity and TIC Data for the same experiment are given in Table 2.

Table 2: MEA (7 m) and MAPA (8 m) High Gas Experiments – Total alkalinity and TIC Data - 55 °C, 21% O_2, 2% CO_2 (Rochelle et al., 2010b)

7 m MEA				8 m MAPA			
Time	Alkanility (mol/kg)	MEA (mol/kg)	TIC (mol/kg)	Time	Alkalinity (mol/kg)	MAPA (mol/kg)	TIC (mol/kg)
0.000		4.260	2.286	0.000	3.860	3.160	3.979

Experimental

The raw data for all of the experiments are given in Appendix A.

Thermal degradation

Thermal degradation experiments were performed using a set of 10 mL stainless reactors, as described by Davis (Davis et al., 2003). The reactors were filled with amine solution which was loaded with CO_2 gravimetrically by bubbling CO_2 through the solution until the desired concentration was reached. The reactors were placed in a forced convection oven at 135 °C for several weeks or months. Samples were collected over the time period, cooled, and placed in a refrigerator. All the samples were transferred to glass vials when the experiment was finished. The conditions for each thermal experiment are given in Table 3.

Table 3: Experimental conditions for the thermal experiments

Experiment	Concentration of MAPA (m)	Concentration of H_2SO_4 (m)	Loading (mole CO_2/mole total alkalinity)	Time (days)
Regular thermal experiment (1)	9	0	0.4	82
Neutralization of half of the MAPA with H_2SO_4 (2)	9	4.5	0.4	21
Neutralization of half of the MAPA with H_2SO_4 (3)	9	4.5	0	21

A small amount of the sample was removed and diluted in deionized water (18.2 Ω), 2% formic acid, or 2% HNO_3 depending on the analysis instrument. The overview of the analysis for the different experiments is given in Table 4 and the conditions for each method are given in the Analysis section.

Table 4: Overview of analysis of thermal degradation experiments

Experiment	1	2	3
Cation IC	X	X	X
Anion IC	X	X	X
Anion IC-amino acids	X	X	X

Cation IC-MS	X		
LC-MS	X		
GC-MS	X		
MS-MS	X		
ICP-metal	X	X	X
AA-metal	X		
TIC	X	In progress	In progress

Oxidative degradation

Low gas flow apparatus

The low gas flow apparatus used for the experiments is explained by Sexton (2008). The amine solution, *N*-methyl-1,3-propanediamine (MAPA) (9 m) was loaded gravimetrically with CO_2 to the desired concentration (α = 0.2 mol CO_2 per mole/total mole alkalinity). The solution was then added to the jacketed glass reactor which was maintained at 55 °C. A metal mixture (Fe (0.4 mM), Cr (0.1 mM), Ni (0.05 mM)) and/or Inh A (0 mM or 100 mM), was added to the solution, which was stirred at 1440 rpm for 14 or 21 days. A wet gas flow of 100 mL/min of 2% CO_2/98% O_2 was introduced at the top of the gas liquid interface. Water was added during the experiment to compensate for water loss due to evaporation. Samples were taken out during the experiment with increasing time intervals between samples.

The overview of the analysis for the different experiments is given in Table 5 and the conditions for each analysis method are given in the description of the methods.

Table 5: Analytical methods used with the oxidative degradation experiments

Experiment	LG1	LG2 (100 mM Inh A)
Cation IC	X	X
Anion IC	X	X
Anion IC-amino acids	X	X
Cation IC-MS	X	
LC-MS	X	X
GC-MS	X	
MS-MS	X	X
TIC	X	In progress
TOC	In progress	In progress
TN	In progress	In progress

High gas flow apparatus

The high gas flow apparatus and methods used are similar to the ones developed by Goff and Sexton (Goff, 2005; Sexton, 2008), but have been further developed by Voice (Rochelle et al., 2009). The loaded (α = 0.4 mole CO_2/mole total alkalinity) MAPA solution (9 m, 350 ml) was placed in an agitated 1 L jacketed glass reactor heated with dimethylsilicone oil to maintain a solution temperature of 55 °C. Air (98%) and carbon dioxide (2%) were introduced into the bottom of the reactor by two Brooks mass flow controllers at a rate of approximately 0.23 mol/min. Water was added to the reactor to maintain the water balance. The experiment was run at two different temperatures (55 and 70 °C) and a liquid sample was collected before and after the experiment. The gas phase was continuously monitored using an FTIR analyzer.

The total dry gas flow rate was calculated to be 5.049148 l/min from formulae given earlier by Voice (Rochelle et al., 2009). The ammonia production rate was evaluated at steady state (Rochelle et al., 2010b; Rochelle et al., 2009). The detailed equipment specification is given by Voice (Nguyen et al., 2010). The liquid samples were analyzed for anion, cation, and alkalinity.

Volatility (VLE)

The vapor-liquid equilibrium apparatus is explained by Nguyen (Rochelle et al., 2009; Nguyen et al., 2010). A MAPA solution (9 m, α = 0, 0.225 and 0.47 mol CO_2/mole total alkalinity, 500 ml) was placed in a 1 L agitated jacketed reactor, circulated by dimethylsilicone oil. The reactor was insulated using aluminium foil. A hot gas FTIR analyzer (Fourier Transform Infrared Spectroscopy technique) from Gasmet Inc. continuously analyzed the vapor from the headspace of the reactor. The experimental setup for the volatility measurements is given in Figure 5 and the detailed experimental setup is described by Nguyen (Rochelle et al., 2009; Nguyen et al., 2010).

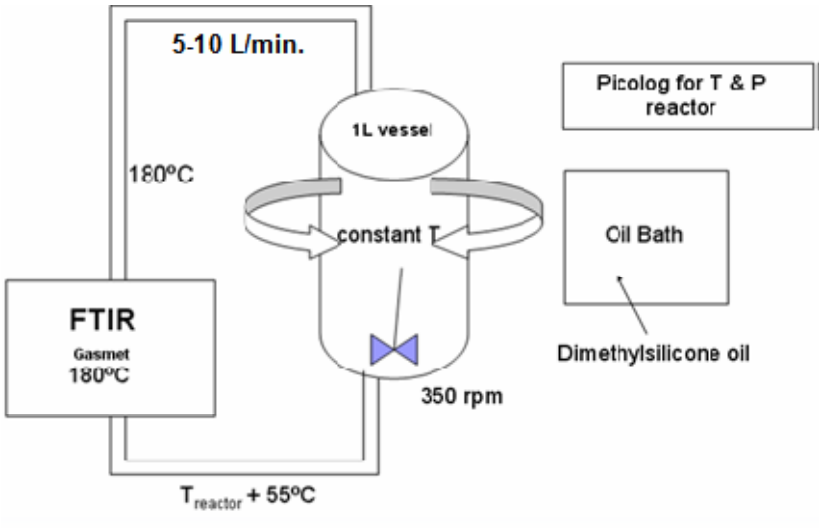

Figure 5: Amine Volatility Experimental Setup (Rochelle et al., 2009; Nguyen et al., 2010)

Amine concentration was found by acid titration and CO_2 concentration was found by TIC analysis as described below.

Rate measurement

The details on the wetted wall column and experimental procedure has been described in previous reports (Rochelle et al., 2009) and papers (Bishnoi, 2002), and will not be repeated here.

Viscosity

Viscosity of MAPA solution with α = 0.2, -0.5 mole CO_2/mole total alkalinity was measured using a Physica MCR 300 cone and plate rheometer (Anton Paar) as described by Freeman (2009).

Analysis

IC

Anion Chromatography: The samples were diluted in deionized water (18.2 Ω) and analyzed/quantified for formate, acetate, glycolate, oxalate, nitrate, nitrite, malonate, and sulfate on an ICS-3000 Dual RFIC Ion Chromatography System. The system is equipped with an IonPac AG15 guard column (4*50 mm) and AS15 analytical column (4*250 mm), ASRS suppressor (4 mm), carbonate removal device (CRD-200, 4 mm) which removes carbonate from the eluent, a continuously regenerated anion trap column (CR-ATC) which removes carbonate from the degraded sample, and a conductivity detector. The detailed equipment specifications are given in Sexton (2008). The eluent was 2 mM KOH for 17 minutes which was increased over 8 minutes to 45 mM and kept at 45 mM for 10 minutes.

The amide and total acid content was found by treating the samples with 5 N sodium hydroxide (1:2) or (1:5) for 48 hours and then the samples were further diluted in water before being analyzed on the anion system to determine additional released organic acids (Sexton, 2008; 2009).

For the analysis of amino acids, the final samples were diluted in water or in 2% formic acid and run on the ICS-3000 Dual RFIC Ion Chromatography System. The system is equipped with AminoPac PA10 columns in series and an electrochemical detector. The detailed specifications are given by Sexton (2008). The eluent was sodium hydroxide, deionized water, and sodium acetate.

Cation Chromatography: The samples were diluted in deionized water (18.2 Ω) and analyzed/quantified for amine (MAPA) on a Dionex ICS-2500 Ion Chromatography system. The system is equipped with IonPac CG17 Guard column (4*50 mm), IonPac CS17 analytical column (4*250 mm), a CSRS suppressor (4 mm), an LC25 chromatography oven, and a CD25 conductivity detector. The detailed specifications of the system are given in Sexton (2008). The eluent was 5 mM methanesulfonic acid for 7 minutes, 11 mM at 7 minutes, increased to 39 mM over 5 minutes, and then held at 39 mM for 3 minutes.

Cation-IC-MS: The final samples for the first thermal and the first low gas oxidative experiment were analyzed on a similar cation ion chromatography system as above which was connected to a Thermo Finnigan thermal TSQ MS with electrospray ionisation (ESI) (Rochelle, 2010a).

LC-MS/GC-MS

LC-MS: Some of the samples were analyzed on an LC system connected to a Thermo Finnigan thermal TSQ MS with electrospray ionisation (ESI). The system also contained a PDA (photo diode array) detector. Three different columns were tried: Shimadzu Premier C18, 5 µm, 150*4.6 mm; Phenomenex Luna 3u Silica (2) 100 A; and

AcclaimRPolarAdvantage II, C18, 5 µm, 4.6*250 mm with an eluent mixture of water with 0.1% formic acid and acetonitrile.

GC-MS: Columns and conditions used are described by Voice (Rochelle, 2010a).

Metals

The samples were diluted in water/2% HNO_3 and analyzed for iron, chromium, and nickel on two different atomic absorption spectrophotometry (AA) instruments. The Perkin Elmer 1100B flame atomic absorption spectrophotometer (AA) uses a lamp producing a specific wavelength of light for each of the metals as described by Freeman (Rochelle, 2010a). The samples for the first thermal experiments were also analyzed on an older flame atomic absorption instrument, which is described by Voice (Rochelle, 2010a).

TOC/TIC/TN

Total organic carbon (TOC), total inorganic carbon (TIC), and total nitrogen (TN) were found when the samples were analyzed on an Aurora 1030 Combustion TOC Analyzer.

Titration

The total alkalinity of the solution was determined by acid titration using a Metrohm-Peak 835 Titrando equipped with an automatic dispenser, Metrohm-Peak 801 stirrer, and 3M KCl pH probe. The degraded sample (200 µl) was weighed and diluted in water (60 ml). The beaker was placed on the stirrer and the titration was started. Complete details of the equipment and procedure are available in Appendix A.3 of Hilliard (2008) and Appendix F of Sexton (2008).

Chemical reagents and standards

The chemical reagents and standards used are given in Table 6.

Table 6: Chemical reagents and standards used in the experiments and analyses

Compound	CAS	M (g/mol)	Company	Product nr	Lot	Purity (%)
Sodium acetate	6131-90-4	136.08	EM Science	SX0255-1	-	99.5-100.5
Sodium nitrate	7631-99-4	84.99	Fisher Scientific	S343-500	-	A.C.S
Potassium formate	590-29-4	85	Alfa Aesar	A14551	I24U012	99
Sodium oxalate	62-76-0	134	JT Baker	3800-01	C05113	99.9
Glycolic acid	79-14-1	76.05	Fisher Scientific	06108-50	040893	
Sodium nitrite	7632-00-0	69	Fisher Scientific	S80187	AD-6094-29	>97
Sodium sulfate	7757-82-6	142.04	JT Baker	3891-01	C22097	99.6
Malonic acid	141-82-2	104.06	Sigma Aldrich	M1296-5G		99
Sodium hydroxide (5 N)			Fisher Scientific	SS256-500	091973	
MAPA	6291-84-5	88.15	Alfa Aesar	B23319	10136917	93
MAPA	6291-84-5	88.15	Alfa Aesar	B23319	10138449	93
H_2SO_4	7664-93-9		Acros	424525000	#B00J6894	95
$FeSO_4*7H_2O$	7782-63-0	278.01	Spectrum	F1060	HC131	99
$Cr_2SO_43*xH_2O$	--	--	Pfaltz and Bauer	C21794	123	
$NiSO_4*6H_2O$	10101-97-0	262.85	Alfa Aesar	36336	D09S034	98

Results/discussion

Thermal degradation with and without CO_2

Three thermal experiments were performed with MAPA (9 m): in two experiments, H_2SO_4 (4.5 m) was added to the amine solution previously loaded with CO_2 or not (α = 0/0.4 mole CO_2/mole total alkalinity). Amine loss (found from IC-cation) over time is given in Figure 6. Sample 2B (#26) from experiment 1 and sample 4A (#3) from experiment 2 were removed because of obvious leakage.

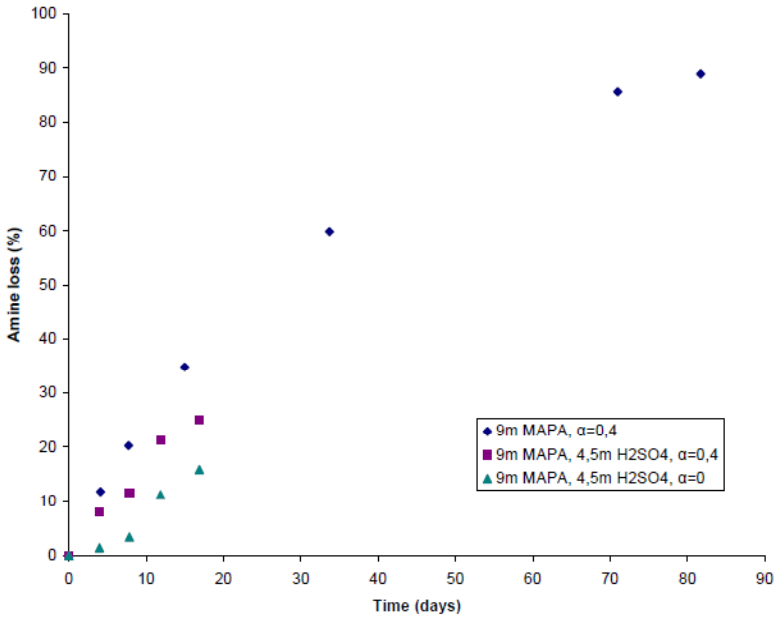

Figure 6: Amine loss for the three different thermal experiments

The amine loss from acid titration and IC-cation largely agrees for experiment 1, but for experiment 2 the loss in alkalinity is a little higher than the MAPA loss and for experiment 3 the alkalinity loss is less than the MAPA loss. As expected the amine loss increase is highest for the experiment with only MAPA (9 m, α = 0.4 mole of CO_2/mole total alkalinity) and lowest for the one in which half of the MAPA was neutralized with H_2SO_4 and no CO_2.

The amine loss for MAPA (9 m, α = 0.4 mole of CO_2/mole total alkalinity) and MEA (7 m, α = 0.4 mole of CO_2/mole total alkalinity) (MEA data from Davis (2009)), is given in Figure 7.

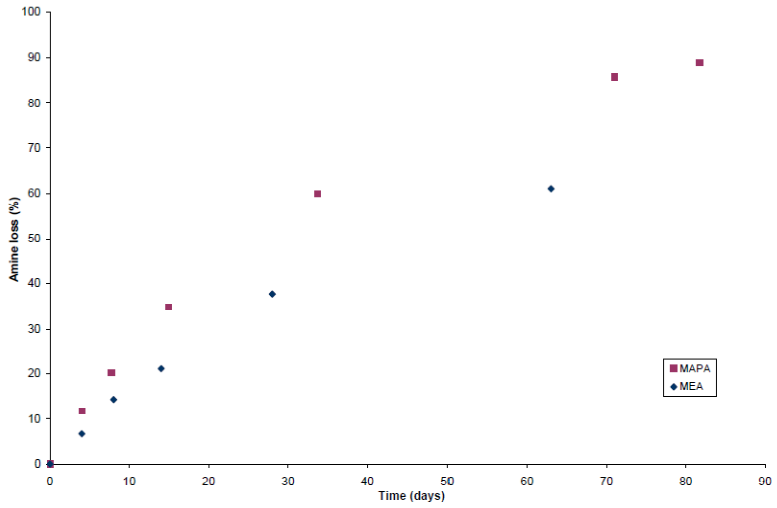

Figure 7: Comparison of MEA and MAPA degradation – MEA data from Davis (2009)

The results show that MAPA degrades faster than MEA and that the difference between them increases over time.

Metal analysis for the three thermal experiments is shown in Figure 8.

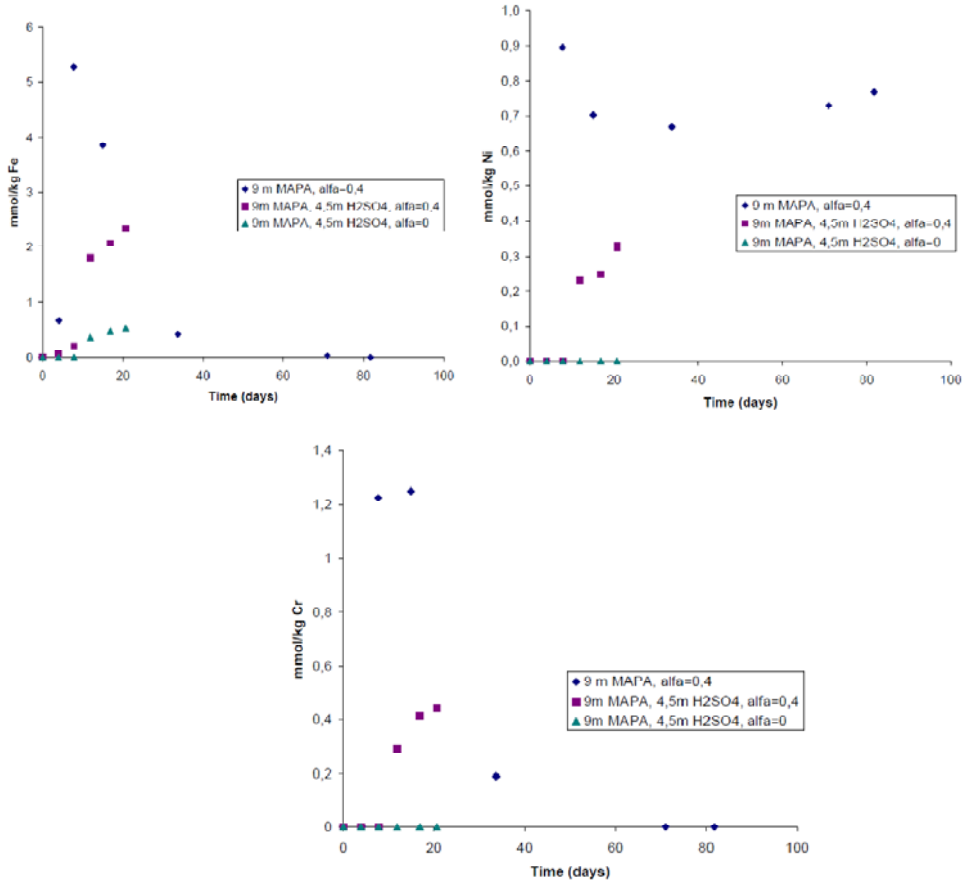

Figure 8: Iron (Fe), nickel (Ni), and chromium (Cr) in the three different thermal experiments

The results show that the metals increase over time and that the order of metal is Fe>Ni>Cr.

The concentration of anions (mmol/kg) in the different thermal experiments is given in Figure 9 and the IC-anion chromatogram for one of the samples from the first thermal experiment (with and without NaOH (1:2) treatment) is given in Figure 10.

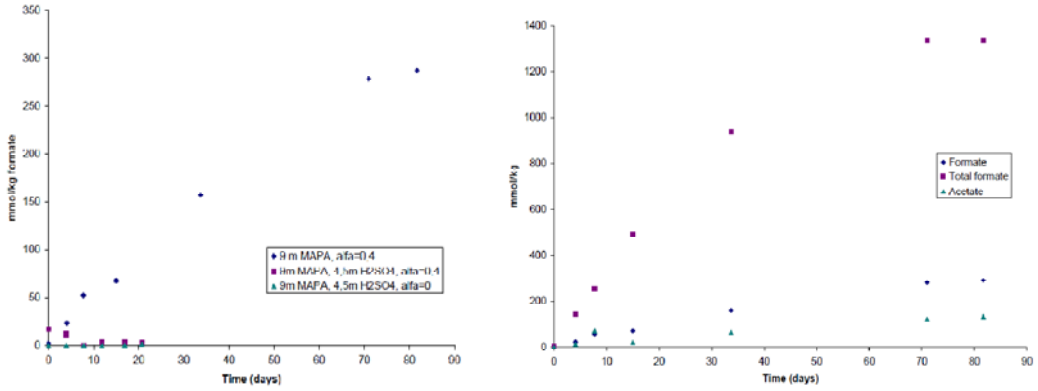

Figure 9: Formate in the three different experiments (to the left) and the anions in the first thermal experiment (to the right), where total formate is formate in the sample after NaOH treatment.

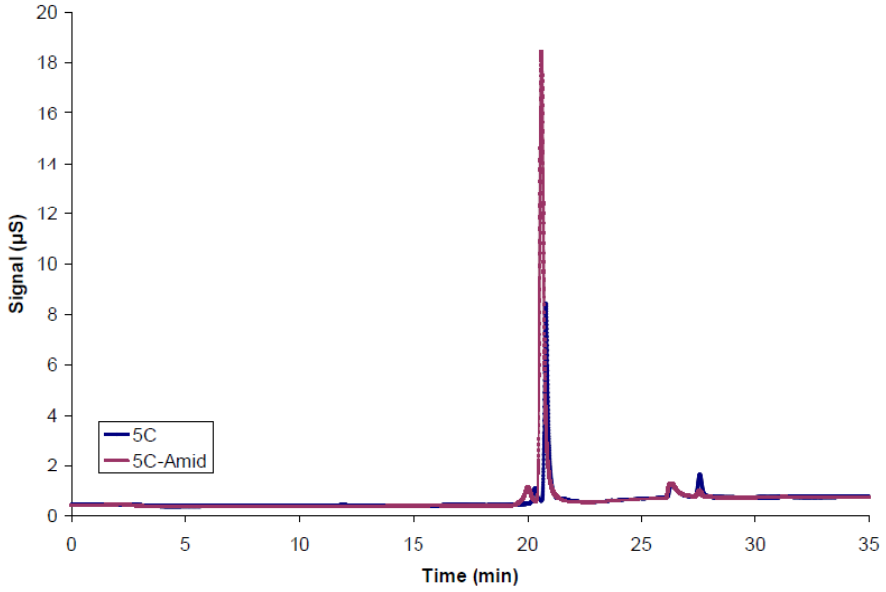

Figure 10: The anion chromatogram for a sample (5C, blue) and the same sample treated with NaOH (1:2) (pink) from the first thermal experiment.

The results show that a small amount of formate (300 mmol/kg) is formed during the first thermal experiment while the two other only have trace amounts of formate. However, treating the thermal samples with NaOH (1:2) for 48 hours and then diluting them with water gave almost 5 times more formate for the final sample. This means that degradation compounds (formamide or other degradation compounds) react with OH- to produce formate.

The total inorganic carbon and MAPA concentration (mol/kg) for the first thermal experiment is given in Figure 11.

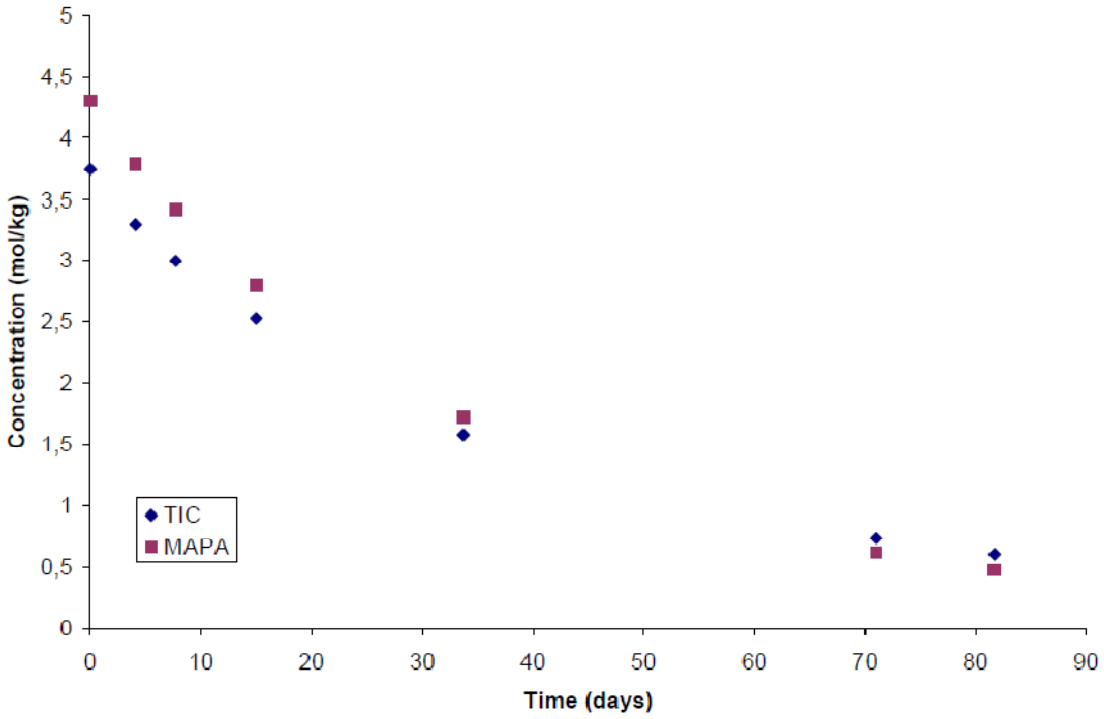

Figure 11: The total inorganic carbon and MAPA (mol/kg) for the first thermal experiment

The results show that the CO_2 amount decreases over time as the amine degrades.

The final sample for thermal experiment 1 was analyzed on MS-MS and GC-MS. The masses found and suggestion of structures are given in Table 7.

Table 7: MS results for thermal experiment 1

M+1	Suggested compound	Supported by	Likely
44.22	-	-	-
58.17	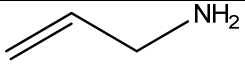	Possible Hoffman elimination	Yes
72.16	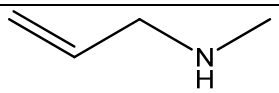	Possible Hoffman elimination	Yes
89.16	-	-	-
113.13	-	-	-

115.12	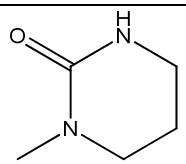	Supported by high resolution CI, molecular formula (C5H11N2O) and DBE (1.5)	Yes
129.13	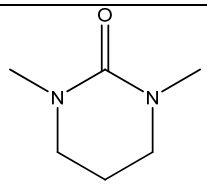	Supported by high resolution CI, molecular formula (C6H13N2O) and DBE (1.5)	Yes
137.09	-	-	-
155.11	-	-	-
167.06	-	-	-
190.15	-	-	-
227.10	-	-	-
251.11	-	Molecular formula: $C8H15N10^{+1}$, DBE: 6.5 or molecular formula: $C9H21N3O5^{+1}$, DBE: 1.0	-
255	-	Molecular formula ($C12H23N4O2^{+1}$), DBE (3.5)	-
265.12	-	-	-
283.03	-	-	-

None of the suggested structures are verified by standards.

Oxidative degradation

Low gas flow and high gas flow oxidative experiments were done with MAPA (9 m) with a metal mix of Fe (0.4 mM), Cr (0.1 mM) and Ni (0.05 mM), Inh A (0 mM or 100 mM) with a loading of 0.2 mole CO_2/mole total alkalinity for the low gas flow and $\alpha = 0.4$ for the high gas flow experiments..

Low gas

The amine loss found from titration and analysis for MAPA on the IC-cation seem to be in the same area. The amine loss found from IC-cation for the low gas experiment with and without Inh A is given in Figure 12.

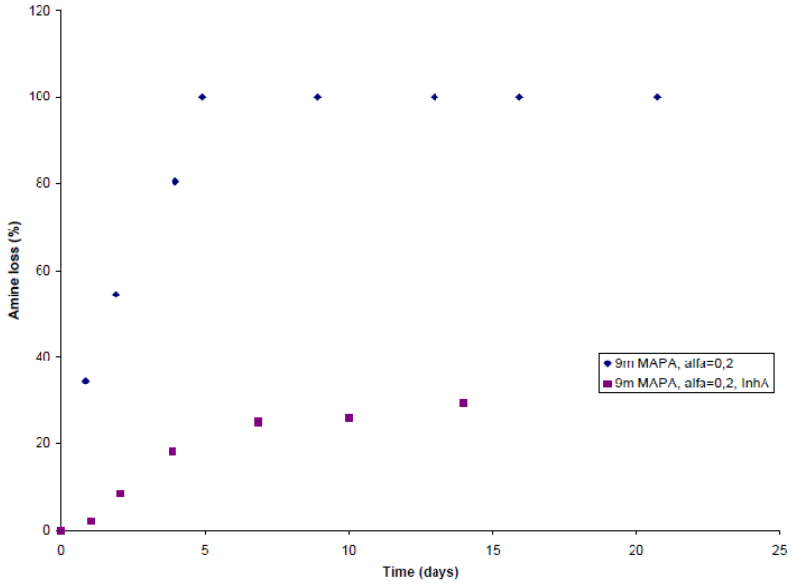

Figure 12: Comparison of amine loss (found from IC-cation) for the low gas experiment with and without Inhibitor A

The results show that low gas experiment with a metal mix without Inh A degrades completely in 5 days. Inh A slows down the degradation, giving an amine loss of 30–35%.

The total inorganic carbon (TIC) and the MAPA concentration (mol/kg) for the low gas experiment without Inh A are given in Figure 13.

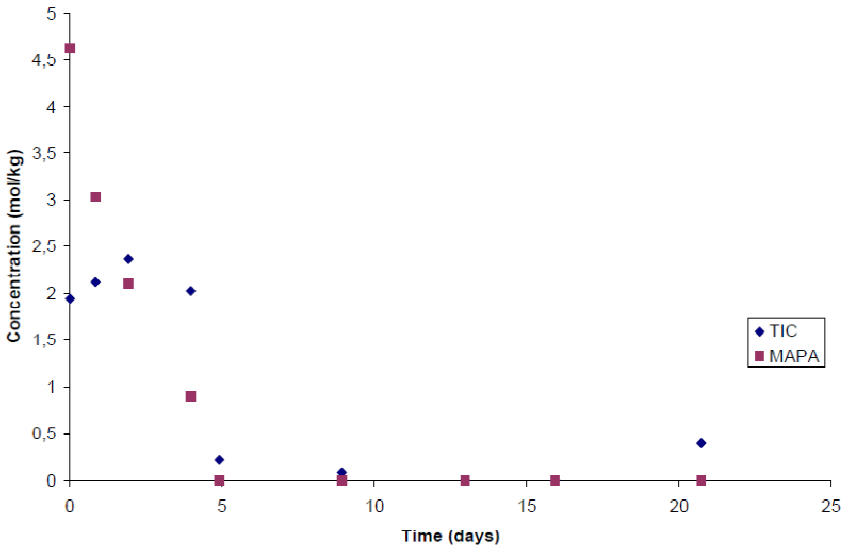

Figure 13: Total inorganic amount for the low gas experiment

The results show that CO_2 increases in the beginning and then follows the decrease in MAPA concentration.

The amount of anion for the low gas experiment without Inh A is given in Figure 14.

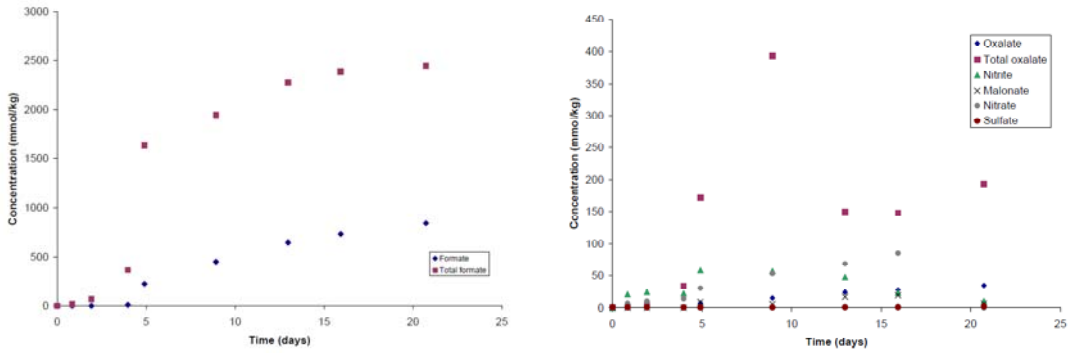

Figure 14: Anion concentration (mmol/kg) for the low gas experiment without Inh A

The total formate and oxalate stands for formate and oxalate detected on the anion-IC after 5N NaOH treatment for 48 hours. Homogenous samples for the amide treatment were obtained with the degradation sample: 5N NaOH (1:5). With less NaOH a precipitate formed in the sample after 24 hours. The precipitate was not identified. It is not known if the difference between total formate and formate is formamide or other degradation compounds that react with NaOH to form formic acid.

The concentration of anion for the low gas flow experiment with Inh A is given in Figure 15.

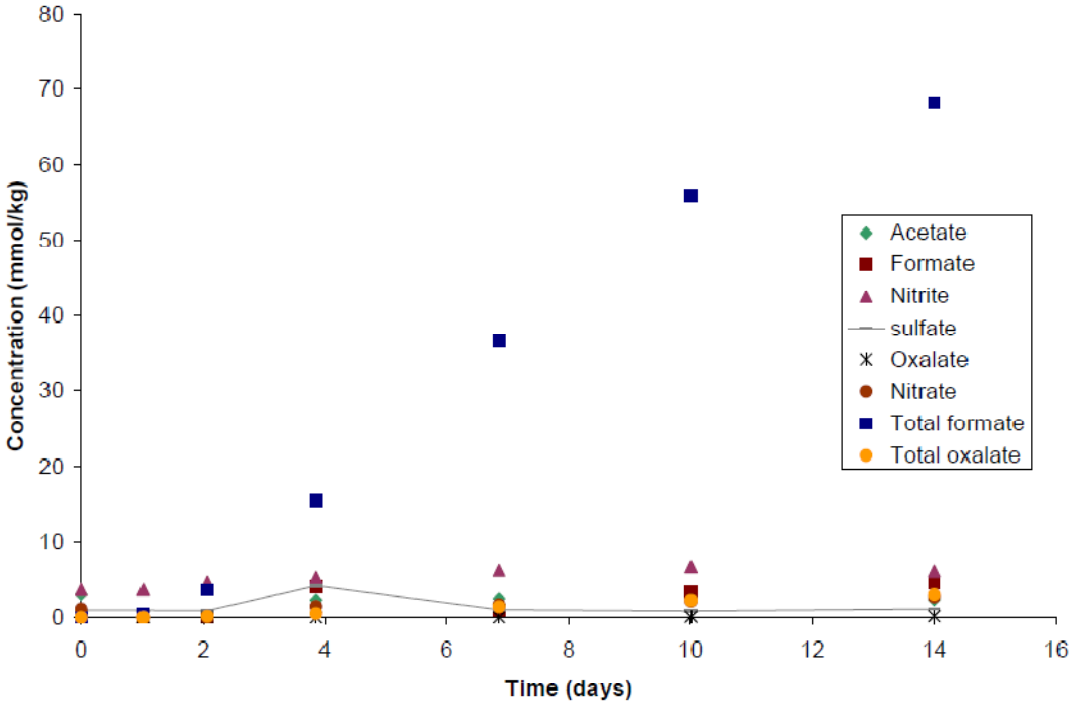

Figure 15: Anion content for oxidative low gas experiment with Inh A

The total formate is after treating the degradation samples with 5N NaOH (1:2) for 48 hours. No precipitation was discovered. The water balance is a little off for the sample taken after 4–5 days, however this did not seem to affect any of the results significantly.

After 14 days the oxidative degradation experiment without Inh A resulted in 2276 mmol/kg total formate and 647 mmol/kg formate, while the experiment with Inh A resulted in 68 mmol/kg total formate and 5 mmol/kg formate. The total formate amount for the

experiments is obtained by treating the samples with different amounts of NaOH. The experiment without Inh A gave almost 130 times more formate than the experiment with Inh A.

The IC-cation chromatogram for different samples from the oxidative experiment without Inh A is given in Figure 16.

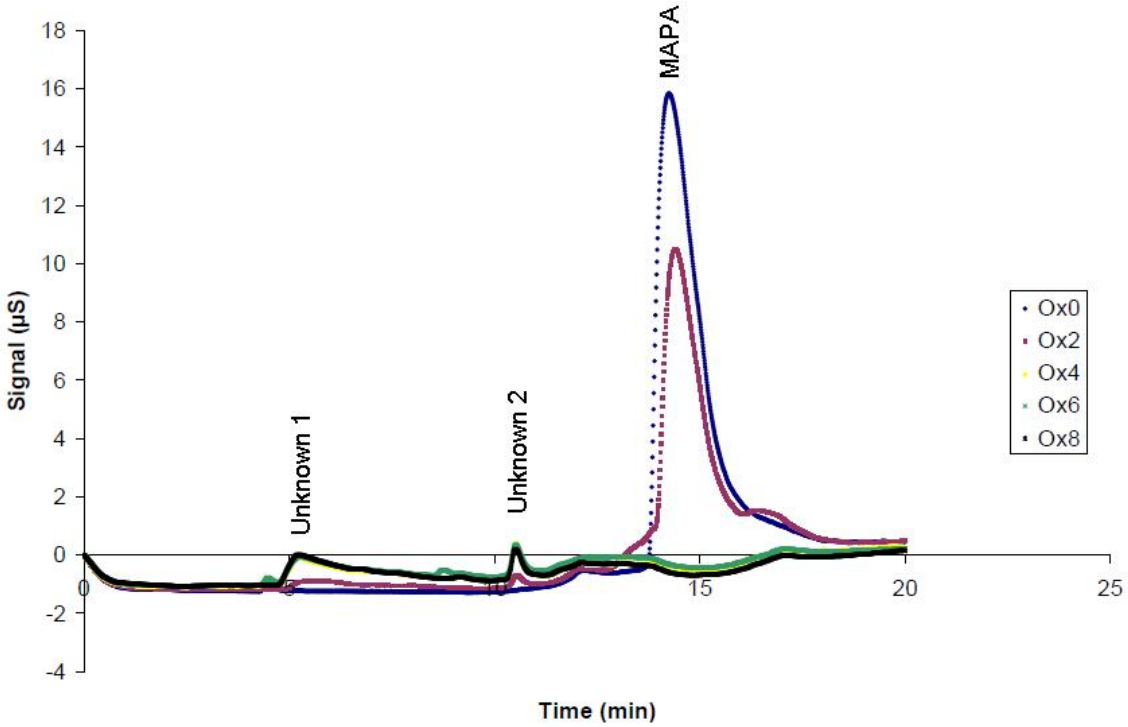

Figure 16: IC-cation (1000X) for several of the LG1 samples

The figure illustrates the disappearance of MAPA and the increase of two unknown peaks, which seem to reach a maximum after 5 days and then remain constant during the rest of the experiment. These two peaks are unidentified and are only responsible for small amounts of degradation compound. The unknown peak number 2 is only visible in the low gas flow experiment with Inh A as illustrated in Figure 17, which shows the IC-anion chromatogram for the final sample for the two low gas flow experiments.

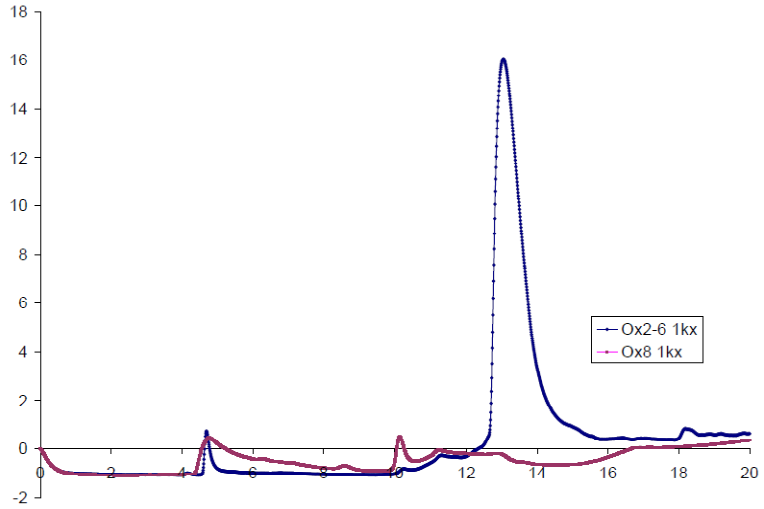

Figure 17: Chromatogram for the final sample of LG1 and LG2

The final sample for the low gas experiment without Inh A was analyzed on MS-MS and GC-MS. The masses found and possible structures are given in Table 8.

Table 8: MS results for LG oxidative experiment without Inhibitor A

M+1	Suggested compound	Supported by	Likely
42.20	-	-	-
44.19	-	-	-
58.15	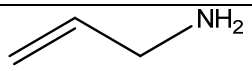	Possible Hoffman elimination or Cope elimination	Yes
72.13	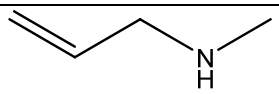	Possible Hoffman elimination	Yes
86.14	-	-	-
99.14	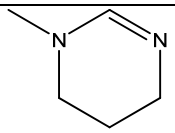	Supported by high resolution CI: molecular formula (C5H11N2) and DBE (1.5) correct. Likely formed from MAPA and formic acid.	But also three more formulae suggested
100.13		-	-
115.1	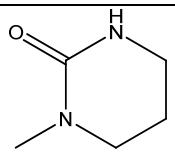	Supported by high resolution CI, molecular formula (C5H11N2O) and DBE (1.5) correct	But also two more formulae suggested
129.09	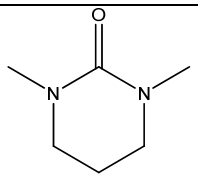	Supported by high resolution CI, molecular formula (C6H13N2O) and DBE (1.5) correct	But also two more formulae suggested

139.1		Formula: C6H7N2O2, DBE=4.5; C5H7N4O, DBE=4.5; CH9N5O3, DBE=0; C6H9N3O, DBE=4; C7H11N2O, DBE=3.5, C6H11N4, DBE=3.5; C8H15N2, DBE=2.5	
152.08	-	-	-
155.11	-	-	-
157.11	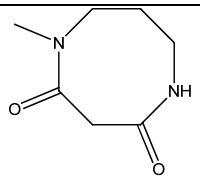	8 ring is not the most favorable ring	Maybe
199.08	-	-	-
209.08	-	-	-
228.1	-	-	-
241.11	-	-	-
253.14	-	-	
255.12	-	-	
281.13	-	-	-

None of the suggested structures were verified with standards.

The comparison between low gas flow experiments with MAPA and MEA (work done by Voice), with the same metal mixture as before and without Inh A is given in Figures 18–20.

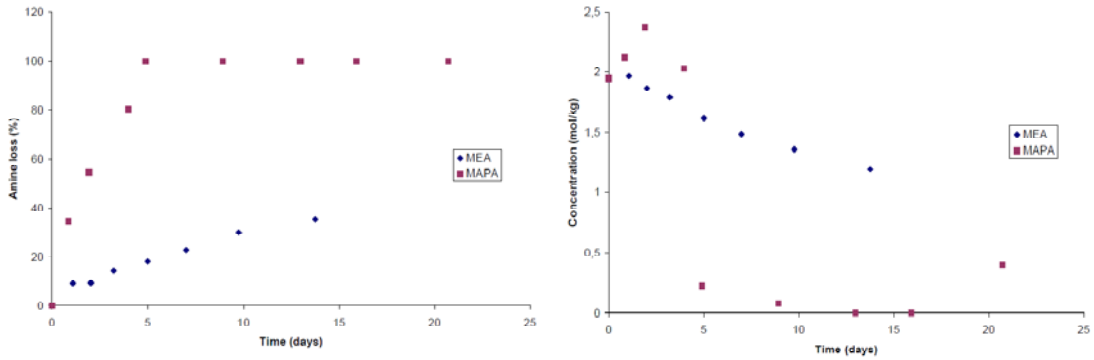

Figure 18: Amine loss (to the left) and TIC (to the right) for low gas experiment without Inh A for MEA and MAPA

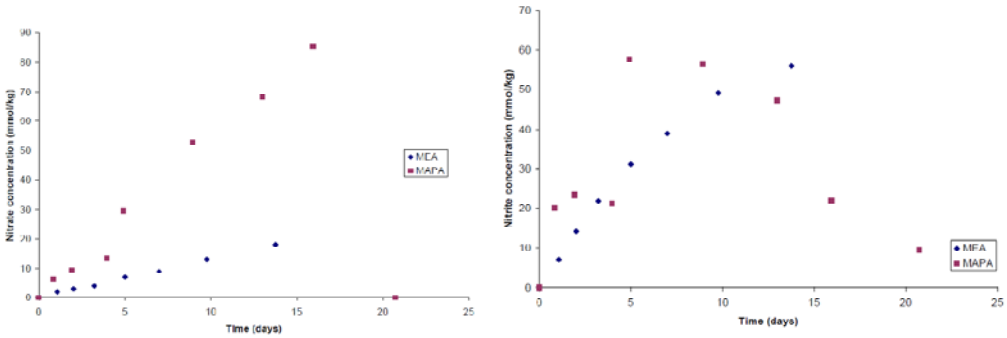

Figure 19: Nitrate (to the left) and nitrite (to the right) concentration for the LG experiment with MEA and MAPA

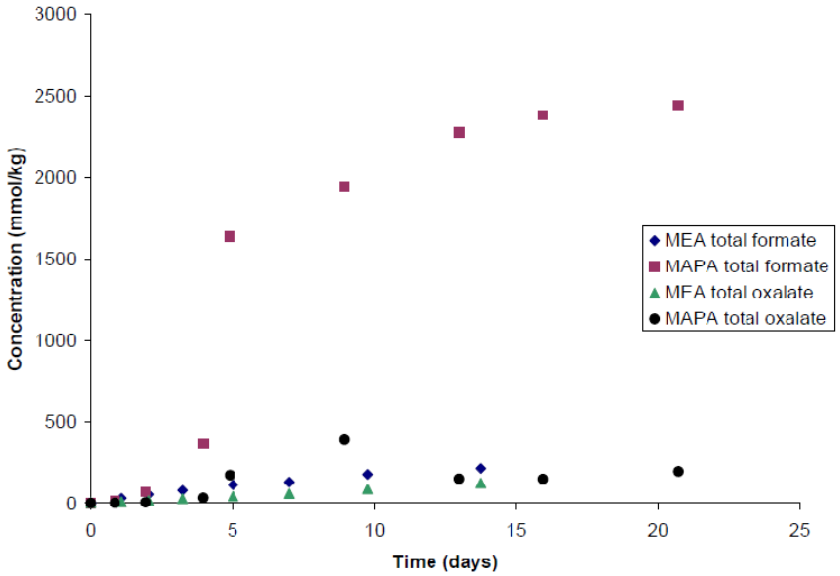

Figure 20: Total oxalate and formate for LG experiments with MEA and MAPA

The results show that MEA is much more stable than MAPA against oxidative degradation and that formate is the main anionic degradation compound.

High gas flow oxidative

Three high gas flow experiments were done in cooperation with Voice and the comparison of the ammonia production rate between MAPA and MEA (work done by Voice) at different temperatures is given in Figure 21.

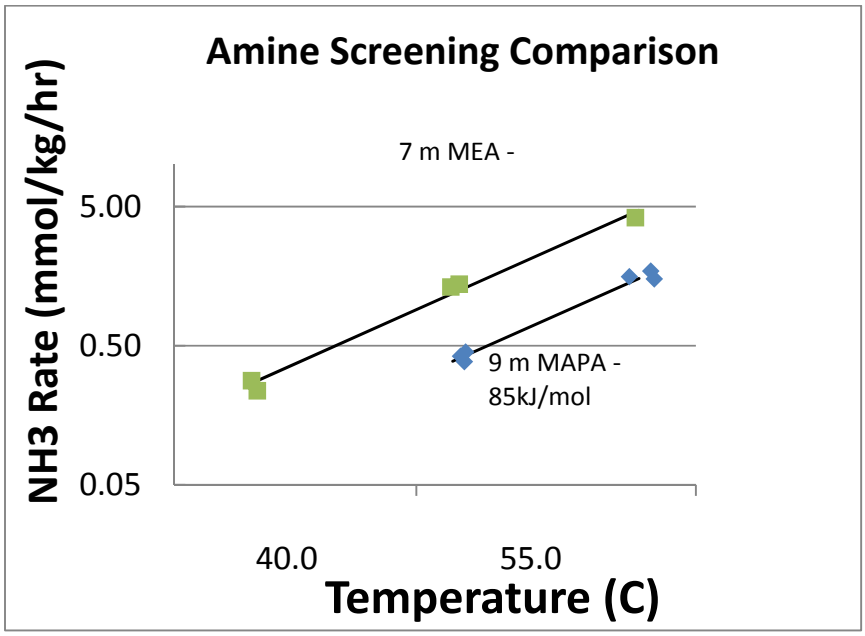

Figure 21: Comparison of ammonia evolution rate between MAPA and MEA at different temperatures.

* MEA (7 m) done by Voice, MAPA (9 m) work done together with Voice.

The results show that MAPA (9 m) has a lower NH_3 production rate than MEA (7 m) and it agrees with High Gas Flow experiment for MAPA (8 m) done by Voice (Rochelle et al., 2010a).

Anion analysis shows that there are only small amounts of formate and these amounts also exist in the initial samples. This is the same result that Voice discovered with MAPA (8 m) experiments. However there is an increase below 1 mmol/kg of nitrite and 45–50 mmol/kg nitrates for the two last experiments with MAPA.

Volatility

A MAPA (9 m) solution with loading (mole CO_2/mole total alkalinity); 0, 0.225 and 0.47 were investigated using an equilibrium experiment with the hot gas FTIR (the work was done in cooperation with Nguyen). The apparent activity coefficient and partial pressure of MAPA towards temperature are given in Figure 22.

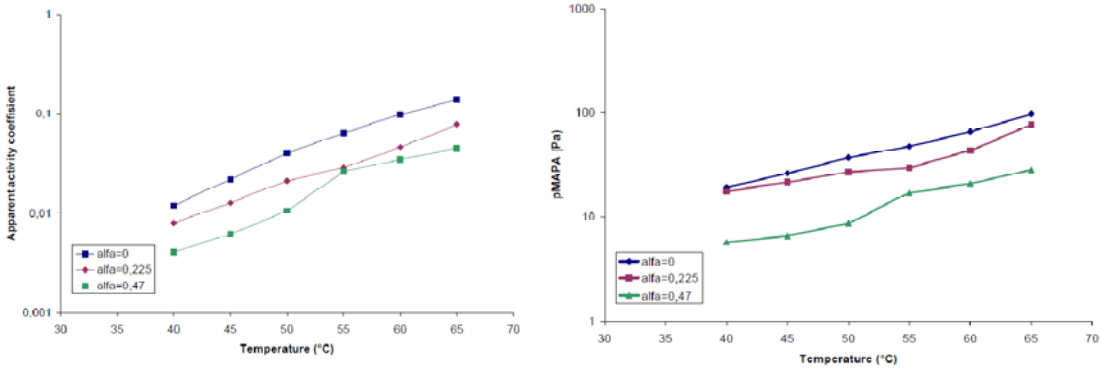

Figure 22: Apparent activity coefficient (left) and partial pressure of MAPA (right) against temperature.

* Work with Nguyen

The results show that the partial pressure of MAPA is reduced with loading, because more MAPA has reacted with CO_2 and there is therefore less free amine available in the solution. The activity coefficient is also much less than ideal for all the loadings, and gets more non-ideal with higher loading.

The volatility of MAPA (9 m) and EDA (~8 m) (from the work of Zhou (Rochelle et al., 2009)) at different loadings and temperature is compared in Figure 23.

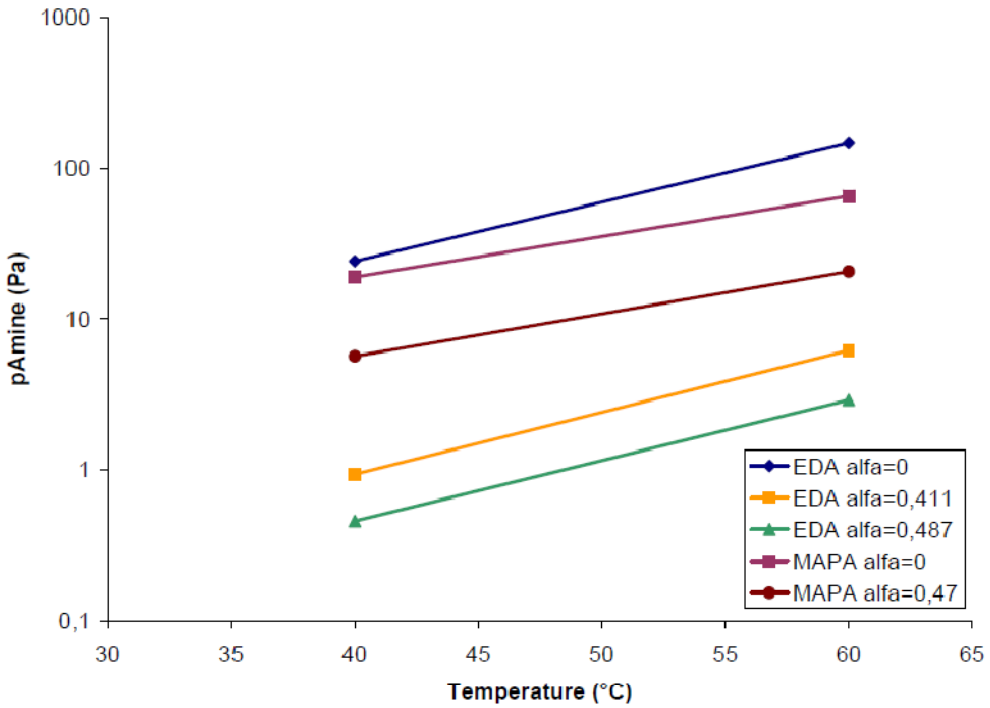

Figure 23: Volatility of MAPA (9 m) and EDA (~8 m) at different temperatures

The results show that EDA (8 m) is more volatile than MAPA (9 m). However the volatility of EDA is less than MAPA when CO_2 is added to the solution.

Rate measurements

The absorption rate between MAPA (8 m) and CO_2 was measured in the wetted wall column by Chen. The liquid film mass transfer coefficient (kg'), which is a function of both physical diffusion of reactants and products and reaction kinetics, was calculated from Equation 1,

$$\frac{1}{K_G} = \frac{1}{k_g} + \frac{1}{k_g'} \qquad (1)$$

where K_G is the overall mass transfer coefficient which is calculated from the flux and driving force and k_g is the gas mass transfer coefficient which is calculated from a correlation (Cullinane, 2002).

Absorption/desorption rates for MAPA (8 m) at 40, 60, 80, and 100 °C are given in Figure 24 and the comparison with EDA (12 m) (Rochelle et al., 2009) is given in Figure 25.

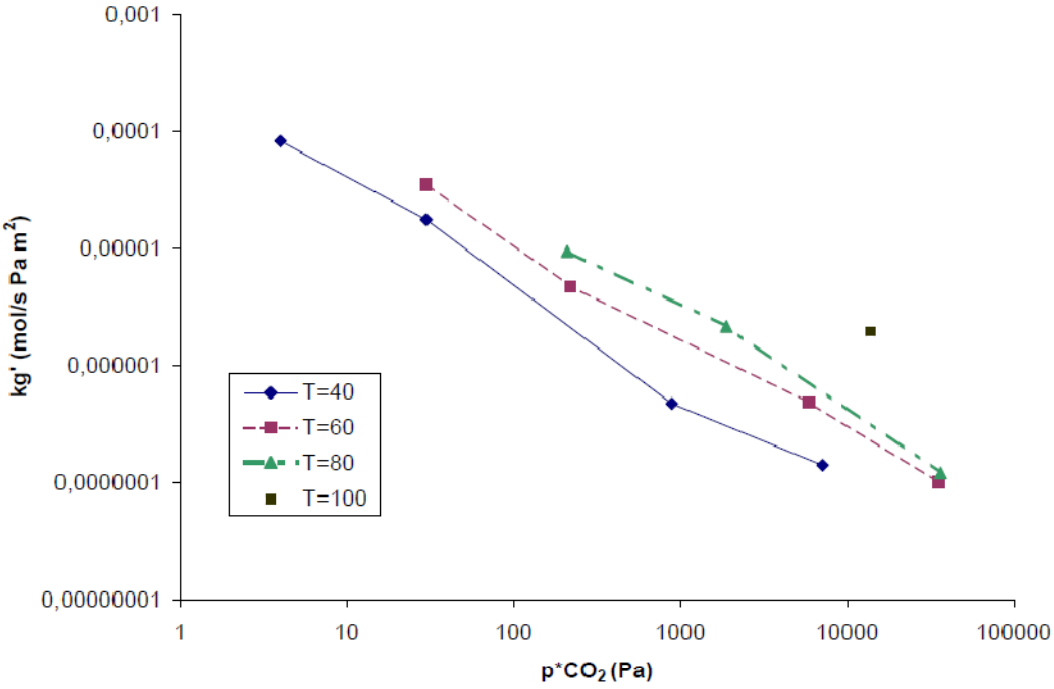

Figure 24: Liquid film mass transfer coefficient of MAPA (8 m)

*Work done by Chen.

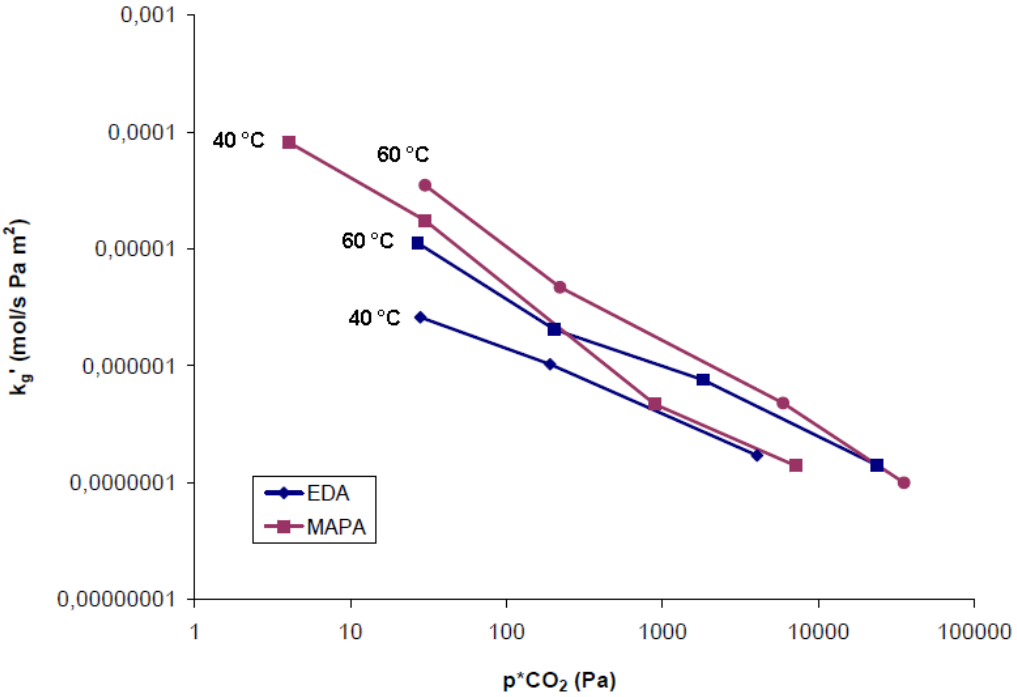

Figure 25: Liquid film mass transfer coefficient of EDA (12 m) and MAPA (8 m)

The result shows that the liquid mass transfer coefficient for MAPA (8m) decreases with increasing partial pressure of CO_2 and that the MAPA has a higher liquid mass transfer coefficient than EDA. However this difference is reduced at higher partial pressure of CO_2.

CO_2 solubility of EDA (12 m) and MAPA (8 m) are given in Figure 26.

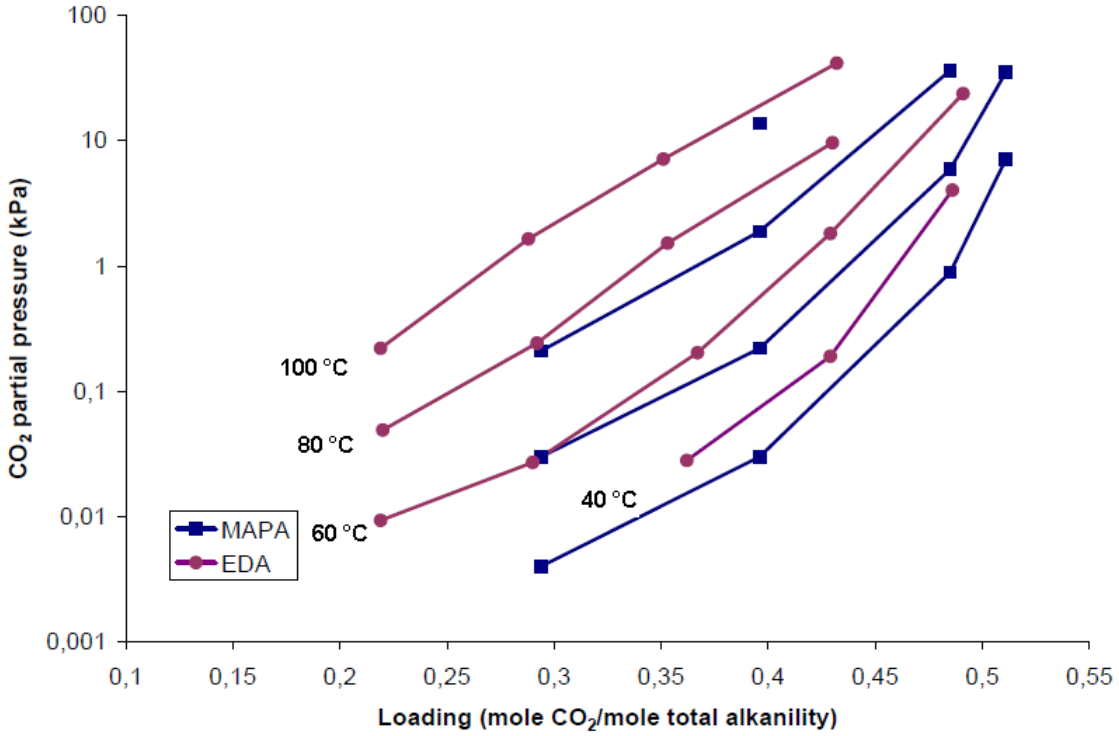

Figure 26: CO_2 solubility of EDA (12 m) and MAPA (8 m) at different loading and temperatures from 40–100 °C

The results show that EDA seem to have a slightly higher CO_2 partial pressure than MAPA, and it has earlier been shown by Zhou that EDA has lower CO_2 partial pressure than PZ (8 m).

Viscosity

The viscosity of MAPA (9 m) with 0.2–0.5 mole CO_2/mole total alkalinity was measured at 40 °C using a Physica MCR 300 cone and plate rheometer (Anton Paar). The viscosity versus loading is given in Figure 27.

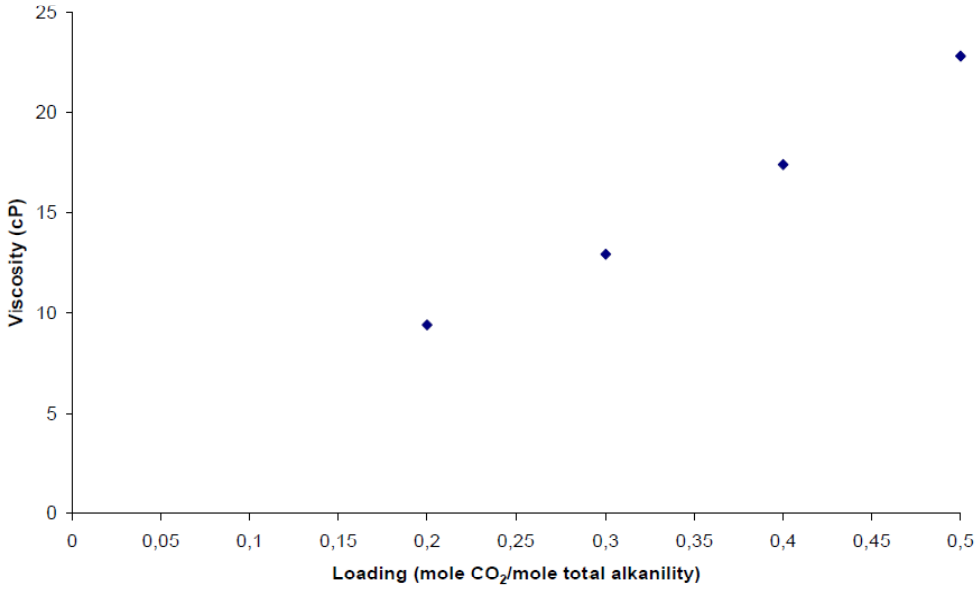

Figure 27: Viscosity measurements at 40°C at different loadings.

* Work with Chen

The results show that viscosity increases with the CO_2 loading.

The viscosity measurements were compared to Zhou's results for EDA (8 m, 12 m) (Rochelle et al., 2009) and are shown in Figure 28.

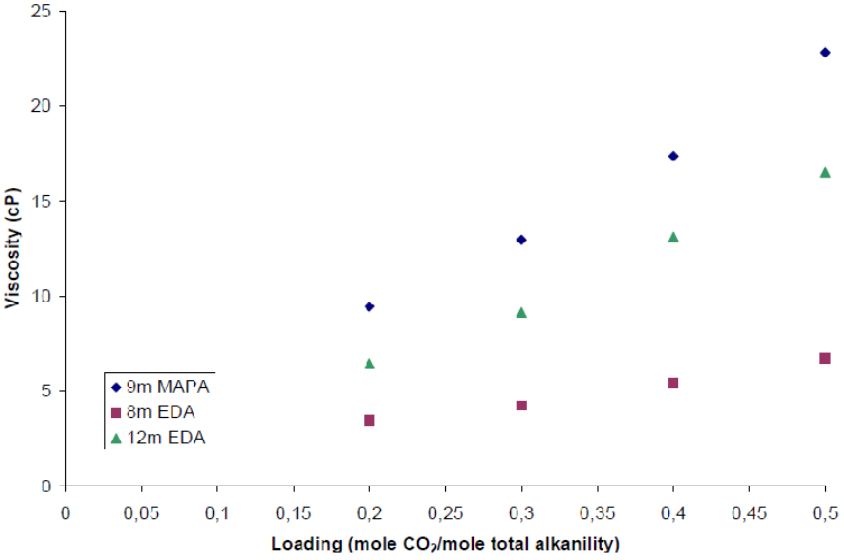

Figure 28: Viscosity measurement at 40 °C at different loadings for MAPA (9 m) and EDA (8 m and 12 m)*

* Zhou (Rochelle et al., 2009)

The results show that MAPA (9 m) is more viscous than EDA.

Conclusions

Degradation experiments show that MAPA degrades faster than MEA and that there was complete degradation of MAPA in the low gas flow oxidative experiment after 5 days. Inhibitor A was shown to reduce the oxidative degradation, however MAPA still degrades faster than MEA. Not all the degradation compounds from thermal and oxidative experiments are identified and quantified, however it is believed that one of the main thermal degradation compounds is 1-methyltetrahydro-2(1H)-pyrimidone (*N*-methyl-*N*,*N*'-trimethyleneurea). For the low gas flow oxidative degradation experiment without Inh A, 2.4 mol/kg total formate was found.

Apparent activity coefficient, partial pressure of MAPA, liquid mass transfer coefficient, and viscosity were compared with EDA and it was shown that EDA with CO_2 was less volatile than MAPA with CO_2 and that MAPA was more viscous than EDA. EDA had higher CO_2 partial pressure than MAPA; however the liquid mass transfer coefficient for MAPA was higher than EDA at lower CO_2 partial pressure.

Acknowledgements

The author acknowledges Dr. Gary Rochelle, Alex Voice, Bich-Thu Nguyen, Xi Chen, Stephanie Freeman, and the rest of Gary Rochelle's group for all the help and guidance during her stay.

Financial support from the SOLVit project, performed under the strategic Norwegian research program CLIMIT, is appreciated. The author acknowledges the partners in SOLVit: Aker Clean Carbon, Gassnova, EON, Scottish Power, Statkraft, and the Research Council of Norway for their support.

References

Bishnoi S, Rochelle GT. "Absorption of CO_2 in Aqueous Piperazine/Methyldiethanolamine." *AIChE J.* 2002;48(12):2788–2799.

Chakma A**,** Meisen A. "Corrosivity of Diethanolamine Solutions and their Degradation Products**.**" *Ind Eng Chem Res.* 1986;25:627–630.

Cullinane JT. *Thermodynamics and Kinetics of Aqueous Piperazine with Potassium Carbonate for CO_2 Absorption*, in *Chemical Engineering*. Ph.D. Dissertation. The University of Texas at Austin. 2002:164.

Davis J. *Thermal Degradation of Aqueous Amines used for Carbon Dioxide*. Ph.D. Dissertation. The University of Texas: Austin. 2009:307.

Davis J, Rochelle GT. "Thermal degradation of monoethanolamine at stripper conditions." Energy *Proc.* 2009;1(1):327–333.

Freeman SA, Dugas RE, Van Wagener DH, Nguyen T, Rochelle GT. "Carbon dioxide capture with concentrated, aqueous piperazine." *Energy Proc.* 2009;1(1):1489–1496.

Goff GS. *Oxidative Degradation of Aqueous Monoethanolamine in CO2 Capture Processes: Iron and Copper Catalysis, Inhibition, and O_2 Mass Transfer*, in *Chemical Engineering*. Ph.D. Dissertation. University of Texas at Austin. 2005:283.

Hilliard MD. *A Predictive Thermodynamic Model for an Aqueous Blend of PotassiumCarbonate, Piperazine, and Monoethanolamine for Carbon Dioxide Capture from Flue Gas*, in *Chemical Engineering*. Ph.D. Dissertation. University of Texas: Austin. 2008:1083.

Kim I, Svendsen HF**,** Børresen E. "Ebulliometric Determination of Vapor-Liquid Equilibria for Pure Water, Monoethanolamine, *N*-Methyldiethanolamine, 3-(Methylamino)-propylamine, and Their Binary and Ternary Solution." *J Chem Eng Data.* 2008;53:2521–2531.

Kohl AL, Nielsen RB. *Gas purification*. Houston, TX; Gulf Professional Publishing. 1997.

Lepaumier H, Carrette PL, Picq D. "Degradation study of new solvents for CO_2 capture in post-combustion." *Energy Proc.* 2009a;1(1):893–900.

Lepaumier H, Picq D, Carette PL. "New Amines for CO_2 Capture. II. Oxidative Degradation Mechanisms." *Ind Eng Chem Res.* 2009b;48:9068–9075.

Lepaumier H, Picq D, Carette PL. "New Amines for CO_2 Capture. I. Mechanisms of Amine Degradation in the Presence of CO_2." *Ind Eng Chem Res.* 2009c;48:9061–9067.

Nguyen T, Hilliard MD, Rochelle GT. "Amine volatility in CO_2 capture." *Int J Greenhouse Gas Control.* 2010;4:707–715.

Rochelle GT et al. "CO_2 capture by aqueous absorption summary of 1st quarterly progress reports 2010." The University of Texas at Austin. 2010a.

Rochelle GT et al. "CO_2 Capture by Aqueous Absorption Summary of 2nd Quarterly Progress reports 2010." The University of Texas at Austin. 2010b:334.

Rochelle GT et al. "CO_2 capture by aqueous absorption summary of 2nd quarterly progress reports 2009. " The University of Texas at Austin. 2009b:299.

Rochelle GT et al. "CO_2 capture by aqueous absorption summary of 3rd quarterly progress reports 2008." The University of Texas at Austin. 2008:179.

Rooney PC, Bacon TR, DuPart MS. "Oxygen's role in alkanolamine degradation." *Hydroc Proc.* 1998;7(7):109–113.

Sexton A, Rochelle GT. "Catalysts and inhibitors for oxidative degradation of monoethanolamime." *Int J Greenhouse Gas Control.* 2009;3:704–711.

Sexton AJ. *Amine oxidation in CO_2 capture processes*. Ph.D. Dissertation. The University of Texas at Austin. 2008:262.

Sexton AJ, Rochelle GT. "Catalysts and inhibitors for MEA oxidation." *Energy Proc.* 2009;1:1179–1189.

Strazisar BR, Anderson RR, White CM. "Degradation Pathways for Monoethanolamine in a CO_2 Capture Facility." *Energy & Fuels.* 2003;17:1034–1039.

Supap T, Idem R, Veawab A, Aroonwilas A, Tontiwachwuthikul P, Chakma A, Kybett BD. "Kinetics of the Oxidative Degradation of Aqueous Monoethanolamine in a Flue Gas Treating Unit." *Ind Eng Chem Res.* 2001;40:3445–3450.

Appendix A: Raw data

A.1. Thermal degradation with and without CO_2

Table A.1: Thermal degradation of 9 m MAPA at 135 °C with 0,4 mole CO_2/mole total alkalinity

Cylinders	Time (days)	MAPA Conc. (mol/kg)	Total Formate (mmol/kg)	Nitrite (mmol/kg)	Alkalinity (mol base/kg solution)	TIC (mol/kg)	Fe (mmol/kg)	Cr (mmol/kg)	Ni (mmol/kg)	Comment
Initial	0.00	4.297	2.291	3.232	4.106	3.749	-0.153	-0.155	-0.103	
1A #95	4.08	3.783	120.736	3.126	3.717	3.343	0.198	-0.037	-0.006	
1B #18A	4.08	3.796	119.469	3.074	3.747	3.244	1.123	-0.007	-0.014	
2A #52	7.72	3.425	199.913	3.117	3.450	2.998	5.283	1.225	0.896	
2B #26	7.72	3.741	93.314	3.360	3.733	3.387	0.096	-0.130	-0.015	leakage
3A #96	14.97	2.777	371.763	2.690	2.925	2.466	3.809	1.244	0.663	
3B #17C	14.97	2.822	477.794	3.171	2.945	2.587	3.891	1.257	0.741	
4A #99	33.69	1.702	783.003	1.705	2.030	1.561	0.473	0.051	0.653	
4B #3	33.69	1.796	743.639	3.180	2.043	1.680	0.561	0.493	0.874	
4C #98	33.69	1.675	813.411	1.708	1.991	1.499	0.230	0.027	0.480	
5A #17B	70.98	0.607	1023.121	3.241	1.200	0.737	-0.010	-0.110	0.505	
5B #17A	70.98	0.666	1014.961	3.021	1.168	0.750	0.161	-0.121	1.006	
5C #5	70.98	0.575	1124.395	3.234	1.146	0.716	-0.066	-0.124	0.677	
6A #8A	81.70	0.478	1048.309	3.273	1.076	0.581	-0.072	-0.130	0.831	
6B #16	81.70	0.464	1006.745	3.227	1.046	0.632	-0.067	-0.136	0.796	
6C #93	81.70	0.488	1081.711	3.262	1.053	0.592	-0.057	-0.136	0.679	

Table A.2: Thermal degradation of 9 m MAPA, 4.5 m H_2SO_4 at 135 °C with 0.4 mole CO_2/mole total alkalinity

Cylinders	Time (days)	MAPA Conc. (mol/kg)	Total Formate (mmol/kg)	Acetate (mmol/kg)	Fe (mmol/kg)	Cr (mmol/kg)	Ni (mmol/kg)	Comment
Inital 1	0.00	3.296	16.484	7.654	-0.178	-0.173	-0.122	
#96-2	3.96	3.033	11.769	4.514	0.058	-0.095	-0.105	
#8A-3	7.82	2.917	0.000	2.314	0.207	-0.138	-0.055	
#3-4A	11.84	2.357	1.962	2.458	0.084	-0.118	-0.088	leakage
#93-4B	11.84	2.595	4.034	15.709	1.799	0.291	0.231	
#196-5A	16.87	2.622	5.658	2.853	2.485	0.540	0.316	
#18A-5B	16.87	2.324	1.281	3.472	1.655	0.290	0.176	
#52-6A	20.69	2.490	3.926	2.502	1.662	0.344	0.236	
#16-6B	20.69	2.479	2.656	4.537	2.999	0.543	0.418	

Table A.3: Thermal degradation of 9 m MAPA, 4.5 m H_2SO_4 at 135 °C with 0 mole CO_2/mole total alkalinity

Cylinders	Time (days)	MAPA Conc. (mol/kg)	Total Formate (mmol/kg)	Acetate (mmol/kg)	Fe (mmol/kg)	Cr (mmol/kg)	Ni (mmol/kg)
Initial I	0.00	3.420	0.000	2.487	-0.172	-0.167	-0.117
#17B II	3.96	3.370	0.000	0.000	-0.147	-0.171	-0.094
#99 III	7.82	3.302	0.000	0.000	-0.143	-0.169	-0.099
#95 IVA	11.84	3.108	0.000	0.000	-0.128	-0.165	-0.106
#17A IVB	11.84	2.963	0.000	0.000	0.866	-0.157	-0.048
#17C VA	16.87	2.879	0.488	0.000	0.209	-0.163	-0.102
#98 VB	16.87	2.876	0.051	0.000	0.739	-0.124	-0.089
#5 VIA	20.69	3.055	0.918	0.000	0.757	-0.156	-0.059
#DI VIB	20.69	2.897	1.848	0.000	0.304	-0.163	-0.108

A.2. Oxidative degradation

Table A.4: Low gas oxidative degradation of 9 m MAPA at 55 °C, 0.4 mM Fe, 0.1 mM Cr, 0.05mM Ni with 0.2 mole CO_2/mole total alkalinity

Time (days)	0	0.84	1.92	3.97	4.9	8.92	12.98	15.93	20.73
MAPA Conc. (mol/kg)	4.625	3.033	2.103	0.906	0.000	0.000	0.000	0.000	0.000
Total Formate (mmol/kg)	0.000	14.651	69.630	366.381	1635.506	1943.676	2276.205	2385.947	2445.477
Formate (mmol/kg)	0.000	0.000	0.108	9.825	222.682	447.827	647.201	733.992	845.282
Total Oxalate (mmol/kg)	0.000	1.319	5.249	32.732	171.355	393.776	149.020	147.522	193.476
Oxalate (mmol/kg)	0.000	0.000	0.000	0.601	6.715	14.282	23.102	26.894	33.940
Nitrate (mmol/kg)	0.000	6.290	9.436	13.348	29.610	52.783	68.193	85.083	0.000
Nitrite (mmol/kg)	0.000	20.069	23.529	21.342	57.732	56.554	47.262	22.117	9.526
Malonate (mmol/kg)	0.000	0.000	0.000	0.000	8.219	5.140	16.084	18.357	5.885
Sulphate (mmol/kg)	0.907	0.855	0.734	0.572	0.531	0.704	0.843	0.927	2.118
Alkalinity (mol base/kg solution)	4.442	3.677	3.134	2.271	0.395	0.000	0.000	0.000	0.000
TIC (mol/kg)	1.947	2.120	2.367	2.028	0.221	0.084	0.000	0.000	0.394

Table A.5: Low gas oxidative degradation of 9 m MAPA at 55 °C, 0.4 mM Fe, 0.1 mM Cr, 0.05 mM Ni, 100mM Inh A w/ 0.2 mole CO_2/mole total alkalinity

Time (days)	0	1.01	2.06	3.85	6.86	10.01	14
MAPA Conc. (mol/kg)	4.493	4.391	4.107	3.678	3.362	3.323	3.173
Total Formate (mmol/kg)	0.000	0.407	3.662	15.481	36.569	55.991	68.285
Formate (mmol/kg)	0.000	0.000	0.000	4.132	0.982	3.382	4.551
Total Oxalate (mmol/kg)	0.000	0.000	0.160	0.513	1.424	2.249	3.044
Oxalate (mmol/kg)	0.145	0.073	0.065	0.000	0.000	0.091	0.170

Acetate (mmol/kg)	3.073	0.000	0.000	2.309	2.486	2.742	2.346
Nitrate (mmol/kg)	1.118	0.000	0.000	1.446	1.691	2.179	2.712
Nitrite (mmol/kg)	3.713	3.719	4.678	5.307	6.223	6.681	6.118
Sulphate (mmol/kg)	0.978	0.946	0.901	4.222	1.019	0.853	1.121
Alkalinity (mol base/kg solution)	4.364	4.259	4.088	3.876	3.660	3.645	3.618

Table A.6: High gas oxidative degradation of 9 m MAPA

Experiment	Temperature (°C)	NH_3 rate
1	55.6	0.42
1	69.2	1.57
2	55.9	0.38
2	71	1.72
3	56	0.45
3	71.3	1.51

Table A.7: Alkalinity, MAPA, and anionic concentration for High Gas Flow Experiment

Experiment	Sample	Alkalinity (mol base/kg solution)	MAPA (mol/kg)	Formate (mmol/kg)	Nitrate (mmol/kg)	Nitrite (mmol/kg)	Sulfate (mmol/kg)
1	Initial	4.113	4.296	3.062	0.000	3.155	0.390
	End	3.772	3.766	2.865	0.000	3.978	1.014
2	Initial	4.140	4.260	2.985	0.000	3.314	0.973
	End	3.993	4.192	2.941	45.708	3.589	0.891
3	Initial	3.959	4.258	3.290	0.000	3.198	0.472
	End	3.945	3.135	2.980	40.961	3.338	1.142

Table A.8: Amine loss for MAPA High Gas Flow Experiment.

Experiment	Amine loss (%) IC	Amine loss titration
1	12.340	15.509
2	1.598	7.019
3	26.365	0.722

A.3. Volatility measurements

Table A.9: Vapor-liquid equilibrium and volatility data for MAPA solution from FTIR

Experiment	T (°C)	Loading (mol CO_2/2mol MAPA)	P_{CO2}(kPa)	P_{MAPA} (kPa)
	40		0	0.0189
	45		0	0.0261
	50		0	0.0368
	55		0	0.0474
	60		0	0.0651
1	65	0	0	0.0972
	40		-	0.0176
	45		-	0.0213
	50		-	0.0268
	55		-	0.0295
	60		-	0.0431
2	65	0.225	-	0.0763
	40		24.93	0.00567
3	45	0.47	29.54	0.00653

	50		34.73	0.00854
	55		37.52	0.0171
	60		40.33	0.0206
	65		43.24	0.0282

A.4. Wetted wall column

Table A.10: Vapor-Liquid Equilibrium and Rate Data from wetted wall column for 8 m MAPA.

Temp (°C)	CO_2 Loading (mol/mol alka)	P_{CO2}* (kPa)	k_g' ($\times 10^7$mol/s·Pa·m^2)
	0.294	0.004	817
	0.396	0.03	175
40	0.485	0.89	4.7
	0.511	7.12	1.4
	0.294	0.03	350
	0.396	0.22	47
60	0.485	5.92	4.8
	0.511	35.3	1
	0.294	0.21	93.5
80	0.396	1.89	21.4
	0.485	36.4	1.2
100	0.396	13.75	19.4

A.5. Viscosity

Table A.11: Viscosity of 9 m MAPA at 40 °C

CO_2 loading (mole CO_2/mole total alkalinity)	Viscosity (cP)
0.2	9.42
0.3	12.96
0.4	17.37
0.5	22.8

Modeling Stripper Performance for CO_2 Capture by Amines

Quarterly Report for July 1 – September 30, 2010

by David Van Wagener

Supported by the Luminant Carbon Management Program

Department of Chemical Engineering

The University of Texas at Austin

October 31, 2010

Summary

Five stripper flowsheets with varying levels of complexity were simulated in Aspen Plus® using 9 m MEA and 8 m PZ. The configurations included a 1-stage flash, 2-stage flash, simple stripper, adiabatic lean flash, and interheated column. Many specifications were implemented to allow adequate comparison between the configurations. These constants included constant rich loading, isothermal stripping at 120 °C or 150 °C, a 5 °C temperature approach on all cross exchangers, equimolar vapor production on each stage, 5 m of packing, a final CO_2 pressure of 150 bar, and rich and lean pump outlet pressures which matched the destination vessel pressure and added 50 kPa for pressure drop and additional pressure for the elevation gain of the packing. Although the absorber was not modeled, the rich loadings used for the two solvents accounted for the faster CO_2 reaction rate of PZ in the absorber. A compressor correlation similar to that used in previous work was utilized to avoid convergence issues of the MCOMP block in stripper simulations. The goal of the simulations was to obtain energy consumption estimates in the stripper when running CO_2 capture with concentrated PZ. A rough estimate had previously been calculated with a first generation Aspen Plus® model. The new rigorous model in Aspen Plus® has just been completed, and these are its first results in the stripper.

The simulations demonstrated that increased configuration complexity improved the efficiency of the stripper by 5–8%, depending on the solvent, operating temperature, and rich loading. The most improvement over the simple stripper was observed with the interheated column. The improvements were attributed to better reversibility of the more complex flowsheets. Furthermore, 8 m PZ consistently had a lower energy requirement than 9 m MEA. Configurations with packed columns exhibited improvements in energy consumption of 9–11%. The base case configuration and solvent was a simple stripper with 9 m MEA, and its energy requirement was 36.1 kJ/mol CO_2. Using the simple stripper with 8 m PZ at its maximum temperature of 150 °C showed an energy requirement of 33.1 kJ/mol CO_2, and improvement of 3.0 kJ/mol CO_2. The most energy efficient configuration, an interheated column, provided an energy requirement of 34.2 kJ/mol CO_2 and 30.9 kJ/mol CO_2 for 9 m MEA and 8 m PZ, respectively. These numbers demonstrate a 14% improvement of the interheated column with 8 m PZ at 150 °C over the base case.

Introduction

Work in previous quarters addressed the effect of increasing process complexity in the stripper on its energy efficiency. 9 m monoethanolamine (MEA) had been selected as the solvent for the analysis since a robust solvent model was available for Aspen Plus® (Hilliard, 2008). Additionally, the solvent was a concentrated form of the industry standard, 7 m MEA. The higher concentration had been previously used in a pilot plant campaign and verified to be a workable solvent for CO_2 capture (Plaza, 2010). The complexity analysis demonstrated a clear improvement in the efficiency of the stripper with higher complexity configurations. The quantitative definition of complexity was somewhat arbitrary, so the different types of complexity that were added resulted in an inexact improvement trend. However, the most important improvement was found to be interheating in the middle of a stripping column. This improvement alone resulted in the best performance.

MEA has been thoroughly analyzed, so the relative performance of piperazine (PZ) will be investigated. Concentrated PZ has shown promise as a competitive amine solvent for CO_2 capture. In comparison with 7 m MEA, it has twice the effective reaction rate (k_g'), slower oxidative degradation, higher resistance to thermal degradation, twice the CO_2 capacity, and slightly improved amine volatility. One of the only apparent negative qualities of PZ is its lower heat of absorption, which has been previously shown to reduce the stripper efficiency (Oyenekan, 2007). However, PZ can be run up to 150 °C in the stripper, whereas MEA could only be safely run at maximum of 120 °C to avoid substantial thermal degradation. It was uncertain whether the ability to run at high temperature would more than offset the low heat of absorption, but initial estimates suggest that the ability to run 30 °C higher would make PZ a more competitive solvent. The average heat of absorption of concentrated PZ is only approximately 65 kJ/mol CO_2, compared to MEA whose average heat of absorption is approximately 80 kJ/mol CO_2.

A model for concentrated PZ in Aspen Plus® has been finalized by Frailie (2010). Like previous models by Hilliard, it accurately predicts VLE and heat capacity of the solvent, but it also addresses previous imperfections in the amine volatility and heat of absorption predictions. The model is robust for process simulations, and it will be used for stripper simulations in concurrence with absorber simulations by Plaza.

Methods and Results

A rigorous thermodynamic model was difficult to develop due to the large number of species present in the H_2O-PZ-CO_2 system, including a non-volatile zwitterion. A model for PZ has been developed (Frailie, 2010), and its structure is based on the AG, AH, Cp, and τ specification method of in the electrolyte non-random two-liquid (e-NRTL) activity coefficient model used by Hilliard (2008). In the Aspen Plus® regression of this model, a large database of thermodynamic properties was used, including CO_2 solubility, amine vapor pressure, enthalpy of absorption, heat capacity, and NMR speciation.

The specifications for the stripper configurations were similar to previous quarters. The simulations used Aspen Plus®, and their scope included the stripping vessels, rich and lean pumps, cross exchanger, and multi-stage, intercooled compressor. Several variables were held constant across all simulations to permit adequate comparison between solvents and configurations. The simulations were run with a constant rich CO_2 loading, and lean loading was

varied and optimized. A 5 °C cold side approach was specified on the main cross exchanger, and the reboiler(s) also had a 5 °C approach. In configurations with multiple pressure stages, equal vapor production on a molar basis was maintained. By stipulating equal steps across the pressure stages, the most reversible operation was preserved to improve efficiency. Also in an effort to enhance reversibility, the analysis used a constant maximum temperature in the regenerator, which resulted in variable pressures at different lean loadings. Finally, the outlet pressures of the pumps were specified to consistently account for frictional and gravitational losses in the pipes. These approximations considered 50 kPa of pressure drop in the crossexchanger, and an appropriate amount of head to reach the elevation gain in configurations with packed columns.

Configurations with packed columns used a height of 5 m, which was enough packing to maintain a rich end pinch for all runs. Since all runs were pinched, they could be compared on a common level. IMTP#40 random packing was used with the Onda correlations for mass transfer coefficient and interfacial area and with the Chilton and Colburn correlation for heat transfer coefficient. Both of these correlations are standard options in Aspen Plus®. The reactions within the column were specified as equilibrium, assuming that the chemical reaction during desorption was fast enough that the mass transfer was the limiting step. The diameter of the column was always specified to have a maximum fractional capacity of 0.8. Configurations with flash tanks were modeled with thermal and chemical equilibrium. Also as in previous work, a correlation for the multi-stage compressor was used:

$$W_{comp}\left(\frac{\text{kJ}}{\text{gmol CO2}}\right) = \begin{cases} 4.572\ ln\left(150/P_{in}\right) - 4.096, & P_{in} \leq 4.56\ \text{bar} \\ 4.023\ ln\left(150/P_{in}\right) - 2.181, & P_{in} > 4.56\ bar \end{cases} \quad (1)$$

where P_{in} is the compressor feed vapor coming from the highest pressure stage in bar.

Five configurations were explored with concentrated PZ previously utilized with 9 m MEA as well. The configurations included a 1-stage flash, 2-stage flash, simple stripper, adiabatic lean flash, and interheated column (Rochelle, 2010).

Results

Equivalent work was used to compare the performance between the different configurations and solvents. Equivalent work (kJ/gmol CO_2), calculated as in equation 5 below, uses the total heat duty (Q_i, in kJ/gmol CO_2), temperature of heat source (T_i), pump work, and compressor work to calculate a total work requirement on an electricity basis. The pumps and compressors would be run with electricity directly drawn from the power plant, and the reboiler(s) uses steam that could otherwise generate electricity in the plant turbines. The net work of the lean pump was ignored if the stripper pressure was higher than the outlet pressure required to pump the solvent back to the top of the absorber. The equation used the 5 K driving force for the reboiler(s). The sink temperature (T_{sink}) was assumed to be 313K. Pump efficiency was 72%, and compressor work was calculated using equation 4.

$$W_{eq} = \sum_{i=1}^{n_{reboilers}} 0.75 Q_i \left(\frac{T_i + 5K - T_{sink}}{T_i + 5K}\right) + W_{pumps} + W_{comps} \quad (2)$$

PZ results

PZ demonstrates fast kinetics in the absorber, and a rich loading of 0.40, corresponding to 5 kPa P^*_{CO2} at 40 °C, could be expected. PZ demonstrates a higher resistance to thermal degradation

than MEA, and its ceiling temperature is 150 °C (Freeman, 2010). It was also desired to observe the performance of PZ in a process designed for MEA with reboiler temperature(s) of 120 °C. For these reasons, PZ was evaluated using 120 °C and 150 °C. The work requirement for each configuration at the two operating temperatures is detailed in Table 1.

The lean loading was optimized for each configuration. However, the optimal lean loading demonstrated understripping in many cases, where the P^*_{CO2} at 40 °C of the solution with the optimal lean loading was greater than 10% of the rich equilibrium partial pressure. Some cases, particularly those with high complexity and/or high operating temperature, yielded a saturated optimum lean loading which was equal to the 90% removal spec. The only case that had an optimum lean loading that was overstripped was the interheated column at 150 °C. The equivalent work reported for each configuration in Table 4 was for the saturated lean loading except for the interheated column at 150 °C, which had an optimum lean loading of 0.28. Cases demonstrating overstripping in the optimum lean loading would be ideal for the absorber to achieve the desired performance and rich loading. The improvement in the equivalent work between 120 °C and 150 °C was marginal, only 1–3% for the cases with optimized lean loadings, but the tabulated values with lean loadings at saturation or lower demonstrated a 2–8% improvement. Additionally, the reduced capital cost of the multi-stage compressor would favor operating at the elevated temperature of 150 °C. The effect of complexity on the equivalent work was still noticeable, with a %5 and 6% maximum improvement over the simple stripper base case for 120 °C and 150 °C, respectively.

Table 1: Energy Requirement with 8 m PZ. 0.4 Rich Ldg, 0.31 Lean Ldg (* = 0.28 Lean Ldg)

Configuration	**Equivalent Work**	
	kJ/mol CO_2	
T (°C)	*150*	*120*
1SF	36.1	39.2
SS	33.1	33.7
ALF	32.3	32.9
2SF	34.1	35.7
IHC	30.9*	31.8

Absorber performance approximation

In order to appropriately compare the performance of the stripper using 9 m MEA and 8 m PZ, rich and lean loadings that represent similar performance in the absorber were needed. PZ has approximately twice the reaction rate with CO_2 of MEA, so it could realistically achieve a higher rich loading in the absorber. The overall reaction rate constant k_g' combined the kinetic and mass transfer effects and can be used to calculate CO_2 flux with the gas side driving force between the bulk gas and interface concentrations:

$$\boldsymbol{N_{CO_2} = k'_g\left(P_{CO_2} - P^i_{CO_2}\right)} \quad (3)$$

Data for k_g' in MEA and PZ were tabulated by Dugas (2009) as a function of P^*_{CO2} at 40 °C, which was directly indicative of the loading of the solution. The rate constant was also measured with varying temperature and solvent concentration, both of which had little effect (between 40 °C and 60 °C). These data were correlated to give k_g' as a function of P^*_{CO2} at 40 °C for MEA using 40 °C and 60 °C data for 7 m, 9 m, 11 m, and 13 m MEA. A similar correlation was derived for PZ using 40 °C and 60 °C data for 2 m PZ, 5 m PZ, and 8 m PZ. The final correlation for each is shown below:

$$\boldsymbol{MEA}: \quad \boldsymbol{ln\, k'_g = -0.40 \cdot ln\, P^*_{CO_2,40°C} - 14.35} \tag{4}$$

$$\boldsymbol{PZ}: \quad \boldsymbol{ln\, k'_g = -0.41 \cdot ln\, P^*_{CO_2,40°C} - 13.44} \tag{5}$$

Next, corresponding rich and lean loading sets for MEA and PZ were calculated which balanced the log mean fluxes, thereby indicating roughly equivalent absorber performance for the two solvents while using identical packing heights. A log mean flux across the absorber was assumed to be adequate for this calculation because k_g' essentially varies logarithmically with the loading, so integrating the mass transfer across the height of the column should give a similar result. Loading was defined in this work as the ratio of CO_2 moles per mole of alkalinity. This definition accounted for the presence of two amine groups on the PZ molecule. The lean loading was specified to match 10% of the rich equilibrium partial pressure since 90% removal in the absorber is expected.

Prior work (Oyenekan, 2007) used a common rich and lean loading set for MEA corresponding to 5 kPa/0.5 kPa of P^*_{CO2} at 40 °C. Table 2 shows that these loadings for MEA correspond to loadings for PZ that provide 8.4 kPa/0.84 kPa P^*_{CO2} at 40 °C. It is expected that a more realistic loading set for PZ is 5 kPa/0.5 kPa, so this pair and the corresponding set for MEA will be used for the simulations. These estimates assume an isothermal absorber at 40 °C. For each rich loading, saturated 90% removal was represented by an optimized lean loading equal the respective lean loading in Table 2. For example, rich and lean loadings of 0.5 and 0.45 for MEA represent a 90% reduction in equilibrium CO_2 partial pressure from 5.0 kPa to 0.5 kPa.

Table 2: Rich and Lean Loadings for MEA and PZ to Match Log Mean Flux in Absorber

MEA rich		MEA lean		PZ rich		PZ lean	
P^*_{CO2} (kPa)	ldg	P^*_{CO2} (kPa)	ldg	P^*_{CO2} (kPa)	ldg	P^*_{CO2} (kPa)	ldg
5.0	0.50	0.50	0.45	8.4	0.42	0.84	0.33
1.5	0.48	0.15	0.40	5.0	0.40	0.50	0.31

MEA results

In the previous quarter, 9 m MEA was evaluated with a constant rich loading of 0.5. In this work the 5 configurations were reevaluated to adequately compare the relative performance of MEA and concentrated PZ. Simulations were run with two different rich loadings as suggested in Table 2 above: 0.50 mol CO_2/mol MEA corresponding to 5 kPa P^*_{CO2} at 40 °C, and 0.48 corresponding to 1.5 kPa P^*_{CO2} at 40 °C. High temperature yields the best performance in the stripper due to greater CO_2 pressure, but the maximum temperature considered for MEA was 120 °C due to elevated thermal degradation rates at higher temperatures (Davis, 2009). Temperatures lower than 120 °C were not of interest in this study, so only the reboiler

temperature of 120 °C was used for MEA. The work requirement and optimum lean loading for each configuration at the two rich loadings is detailed in Table 3.

Table 3: Work Requirement for configurations using 9 m MEA. Heating to 120 °C and Lean Loading adjusted to minimize equivalent work.

Configuration	Equivalent Work	Lean Loading	Equivalent Work	Lean Loading
	kJ/mol CO_2	*mol CO_2/mol alk*	*kJ/mol CO_2*	*mol CO_2/mol alk*
	0.5 rich ldg		*0.48 rich ldg*	
1SF	34.9	0.41	37.2	0.39
SS	34.0	0.39	36.1	0.36
ALF	33.6	0.39	35.4	0.36
2SF	33.5	0.39	35.5	0.38
IHC	32.5	0.37	34.2	0.35

The lean loading was optimized for each configuration to minimize equivalent work. Every case demonstrated an overstripped optimum lean loading, where the P^*_{CO2} at 40 °C was less than 10% of the rich equilibrium partial pressure. This result would be fortunate news for the design of the absorber because the lower lean loading would provide a greater driving force for absorption and reduce the size of the column. The best case scenario with a 0.5 rich loading improved the optimum performance of each configuration by 5% to 9%, with the greatest influence on the 2-stage flash. The performance typically improved with increased complexity. All configurations except the 1-stage flash showed improvement over the simple stripper base case. The best performance for both rich loadings was with the interheated column, demonstrating a 7.8% and 4.6% improvement over the simple stripper using rich loadings of 0.48 and 0.50, respectively.

Comparison of MEA and PZ Performance

The use of 8 m PZ with a rich loading of 0.4 in place of 9 m MEA with a rich loading of 0.48 yielded a 3–11% improvement depending on the configuration. When changing only the solvent, the simple stripper showed the greatest improvement (11%), followed by the interheated column (10%), and the adiabatic lean flash had the third-best improvement (9%). The 1- and 2-stage flash configurations did not benefit much by using 8 m PZ, demonstrating only a 4% and 3% improvement, respectively. Table 4 summarizes the results of important solvent/configuration combinations. The total equivalent work was separated into its three components as used by Equation 5: heating work, pump work, and compression work.

Various mechanisms within the stripper dictated the improvement of each combination. Changes in compression and pump work were straightforward. Compression work decreased with any increase in the pressure of the vessel(s), and pump work increased with any increase in the pressure of the vessel(s). However, pump work also decreased with reduced lean loading due to increased capacity and decreased solvent circulation rate. Several mechanisms directed changes in the heating work. First, increased reboiler temperature raised the heating work since

the steam used would be of higher quality. Next, improved solvent capacity decreased the heat duty since less solvent would need to be heated to balance the temperature approach across the cross exchanger. Finally, the difference in the heat of desorption of CO_2 of the solvents would affect the amount of heat duty dedicated to desorption. The improvements of each combination in Table 4 can be explained using these mechanisms. 8 m PZ consistently performed better than 9 m MEA, mostly because it could be operated at 150 °C. At the higher temperature, the vessel pressures were significantly higher in the PZ cases, drastically reducing the compression work.

A comparison that demonstrated another major difference between the two solvents was the difference between the simple stripper and the 2-stage flash. The flash configuration was capable of reducing the work requirement with MEA, but the performance worsened when transitioning from the simple stripper to the 2-stage flash with PZ. Comparing the changes in work components for this modification with each solvent, it was apparent that PZ was not able to effectively use the 2-stage flash because it did not experience as significant a drop in compression work as compared to MEA. Coupled with a slightly greater effect on both heat work and pump work, the 2-stage flash did not prove to be a better option with PZ. The Gibbs-Helmholtz relation suggests that the low heat of desorption of PZ yields a low CO_2 partial pressure in the stripper compared to an equal change in temperature with MEA. The partial pressure of water is roughly the same for the two solvents at equally high temperature, so the selectivity for CO_2 is lower for PZ than for MEA. Heat of desorption has previously been linked to improved performance for this reason (Oyenekan, 2007). Configurations using PZ need to effectively utilize the latent heat contained in the stripping steam which otherwise escapes with the CO_2, eventually becoming wasted heat as the steam is knocked out in the condenser preceding the multi-stage compressor.

Table 4: Noteworthy Solvent/Configuration Combinations

System	W_{eq}	Lean Ldg	Pressure	Q_{total}	Q work	Pumps	Comp
	kJ/mol CO_2	*mol/mol*	*bar*	*kJ/mol CO_2*			
MEA - SS - 0.5 rldg	34.0	0.39	5.1	131	21.1	1.5	11.5
MEA - SS - 0.48 rldg	36.1	0.36	3.9	137	21.9	1.6	12.6
MEA - 2SF - 0.48 rldg	35.5	0.38	7.1 / 4.4	145	23.1	1.5	10.8
PZ - SS - 150 °C	33.1	0.31	9.3	112	22.6	1.5	9.0
PZ - 2SF - 150 °C	34.1	0.31	13.4 / 9.4	120	24.2	1.8	8.1
PZ - IHC - 150 °C	30.9	0.28	7.6	100	20.1	1.0	9.8

Table 4 clarifies the source of improvement with the interheated column. First, since the heat contained in the lean stream was more effectively recycled to the column, the reboiler duty decreased, so the heating work also decreased. Next, the column pressure was lower with the lower lean loading, so the rich pump pressure change decreased by 15%. The lower optimum lean loading caused the solvent rate to decrease by 25%, so the overall decrease in rich pump work was 33%. The compression work increased by 9% due to the lower column pressure, but the other savings resulted in a much more efficient configuration.

Table 5: Rich/Lean Loadings Accounting for Varying Reaction Rates

Solvent	Rich		Lean	
	P^*_{CO2} (kPa)	ldg	P^*_{CO2} (kPa)	ldg
MEA	1.5	0.479	0.09	0.360
PZ	4.5	0.394	0.45	0.308

Finally, the difference in optimum lean loadings between MEA and PZ needed to be addressed. The process optimized to overstripped lean loadings for MEA, but the optimum lean loadings with PZ only typically represented a saturated 90% removal. The absorber approximation determined that rich loadings of 0.48 and 0.4 for MEA and PZ, respectively, would provide an accurate comparison of the solvents when paired with the respective lean loadings corresponding to 90% removal. The magnitude of k_g' increases with decreasing loading. Since MEA optimized with lower lean loading, the log mean CO_2 flux in the absorber would be greater, so the rich and lean loadings for PZ also needed to be lower to similarly increase its log mean flux in the absorber. Table 5 summarizes the final set of rich and lean loadings for 9 m MEA and 8 m PZ. The optimized runs in Table 3 demonstrated optimum lean loadings from 0.35 to 0.37, so a representative value of 0.36 was selected. The new calculated loadings for PZ were not significantly different from the originally selected values. Consequently, the simple stripper at 150 °C had an energy requirement of 33.57 kJ/mol CO_2, only 0.4 kJ/mol CO_2 (1.4%) greater than the requirement with a rich loading of 0.4. Approximately the same change could be expected for the other configurations.

Conclusions

- With both MEA and PZ, greater complexity in the stripper usually resulted in better energy efficiency due to a closer approach to a reversible process. The improvement over the simple stripper depended on the solvent, rich loading, and reboiler temperature, but the interheated column consistently required 4.8-7.8% less equivalent work.
- 8 m PZ consistently had a lower energy requirement than 9 m MEA when using a rich loading that accounted for the faster reaction rate of PZ in the absorber. The simple stripper and complex configurations with packed columns demonstrated substantial improvement of 9–11% better energy performance with PZ. The multi-stage flash configurations were 3–4% better with PZ.
- Increasing the stripping temperature of 8 m PZ from 120 °C to 150 °C reduced the work requirement by 1–3%.

Future Work

The results of the pilot plant campaign from November 2008, which used concentrated PZ, will be used to validate the Aspen Plus® thermodynamic model. The pilot plant campaign currently in progress utilizing high pressure stripping with the 2-stage flash configuration and the concentrated PZ solvent will be analyzed and simulated with the Aspen Plus® model.

References

Davis JD, Rochelle GT. "Thermal degradation of monoethanolamine at stripper conditions." *GHGT-9*. Washington, DC. 2009.

Dugas RE, Rochelle GT. "Absorption and desorption rates of carbon dioxide with monoethanolamine and piperazine." *GHGT-9*. Washington, DC 2009.

Frailie PT, Plaza JM, Van Wagener DH, Rochelle GT. "Modeling piperazine thermodynamics." *GHGT-10*. Amsterdam. 2010.

Freeman SA, Dugas RE, Van Wagener DH, Nguyen T, Rochelle GT. "Carbon dioxide capture with concentrated, aqueous piperazine." *IJGGC.* 2010;4(2):119–24.

Hilliard MD. *A Predictive Thermodynamic Model for an Aqueous Blend of Potassium Carbonate, Piperazine, and Monoethanolamine for Carbon Dioxide Capture from Flue Gas*. Ph.D. Dissertation. The University Of Texas at Austin. 2008.

Oyenekan BA, Rochelle GT. "Alternative Stripper Configurations for CO_2 Capture by Aqueous Amines." *AIChE J*. 2007;53(12):3144–54.

Rochelle GT et al. "CO_2 Capture by Aqueous Absorption, Second Quarterly Progress Report 2010." Luminant Carbon Management Program. The University of Texas at Austin. 2010.

Modeling CO_2 Absorption Using Aqueous Amines

Quarterly Report for July 1 – September 30, 2010

by Jorge M. Plaza

Supported by the Luminant Carbon Management Program

Department of Chemical Engineering

The University of Texas at Austin

October 31, 2010

Abstract

Data from the November 2008 pilot plant campaign were analyzed using the 5deMayoV1 model. 14 data points were studied. The only variable parameter was the interfacial area. It was reduced 2% from the value generated using Tsai et al. (2008). Two data points were discarded due to noticeable variations in the final reconciled data. Results show that it is possible to obtain 90% removal using 6.1 m of Mellapak 2X packing and concentrated PZ. The model is capable of simulating absorber operation. Loadings and removal fraction were matched (less than 0.03 difference). Temperature profiles were adequately traced and the temperature bulge location was closely approximated.

The validated model was used to test intercooling with 8 m PZ. Absorber performance was evaluated with respect to changes in L/G and lean loading. As in previous work, intercooling was most effective in the critical L/G region. For the studied system, the critical L/G is approximately 4 and intercooling is capable of increasing absorber removal by as much as 12%.

The critical L/G equation gave a close approximation to the critical L/G. It predicted 4.2 (mol/mol) for 90% and 4.4 (mol/mol) for 80% removal.

November 2008 campaign reconciliation

A pilot plant campaign was conducted for 5 m, 8 m, and 9 m PZ at the J.J. Pickle Research Campus of The University of Texas at Austin. The absorber column has a diameter of 0.427 m and was packed with 6.1 m of Mellapak 2X. Gas rate was kept constant at 350 ACFM. Table 1 shows the conditions for the runs of the November 2008 campaign.

Gas and liquid compositions were specified using individual component streams in the simulation as shown in Figure 1. Inlet temperature and pressure conditions were entered in the simulation using heat exchangers. Table 2 shows the specified standard deviations for model reconciliation as well as the range of variation in the reconciled data.

Table 1: November 2008 pilot plant campaign conditions

Run	PZ (m)	Liquid		Loading (mol CO_2/mol alkalinity)		Gas				Removal (%)
		T (^oC)	Flow (gpm)	Lean	Rich	P (kPa)	T (^oC)	y_{CO2}	y_{H2O}	
1	7.5	40.3	15	0.285	0.340	101.7	15.39	0.1194	0.0129	85.9
2	7.9	40.0	15	0.308	0.370	101.2	11.50	0.1206	0.0110	66.6
3	9.2	39.6	15	0.254	0.330	103.2	0.03	0.1204	0.0038	88.0
4	8.2	38.9	15	0.386	0.400	102.7	19.78	0.1184	0.0036	30.67
5	7.8	40.5	12	0.284	0.360	102.5	7.61	0.1206	0.0059	68.2
6	8.2	39.9	18	0.302	0.360	102.9	-5.11	0.1197	0.0025	77.1
7	8.1	40.0	15	0.305	0.360	102.2	21.89	0.1189	0.0052	73.7
8	7.9	39.8	12	0.298	0.370	101.7	14.44	0.1199	0.0118	61.2
9	7.8	40.6	18	0.267	0.340	101.7	21.44	0.1216	0.0120	92.3
10	7.7	40.6	15	0.331	0.380	101.6	22.61	0.1196	0.0113	48.7
11	4.8	40.7	18	0.316	0.380	103.3	13.56	0.1191	0.0033	60.7
12	4.9	39.5	18	0.274	0.360	103.3	5.72	0.1206	0.0023	88.6
13	4.9	40.6	15	0.257	0.360	103.8	-5.22	0.1194	0.0028	78.3
14	4.6	39.5	12	0.262	0.380	103.7	7.39	0.1189	0.0033	66.8

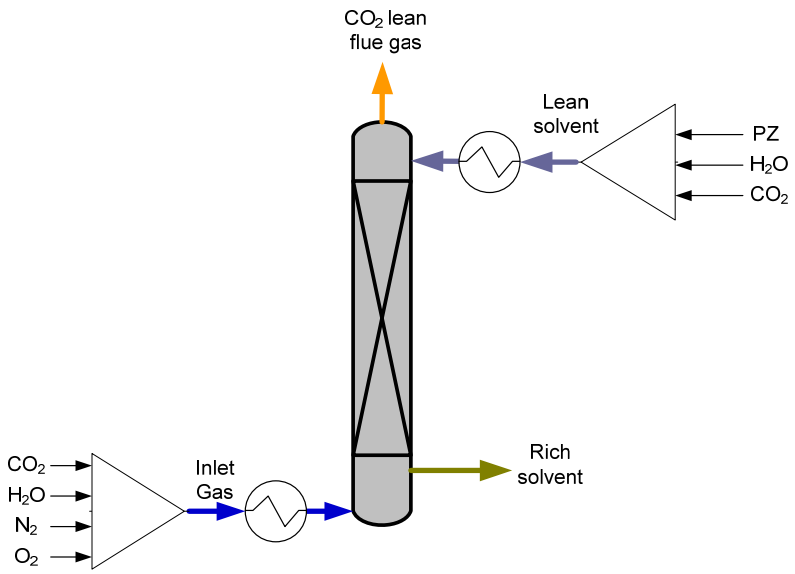

Figure 1: Aspen Plus® pilot plant process flow diagram for data reconciliation

Table 2: Pilot Plant reconciliation input standard deviations and reconciled variation

Variable	Specified standard deviation	Reconciled variation range	Variable	Specified standard deviation	Reconciled variation range
Area Factor	±1.0	Not applicable	T (^oC)**		
Inlet liquid flow (kg/s)			Inlet Gas	±3	0.2 to 9.5
PZ	5%	-4.0% to 2.6%	Inlet Solvent	±3	-6.6 to -3.1
CO_2	5%	-2.9% to 3.9	Outlet Gas	±3	-0.19 to 2.6
H_2O	5%	-2.6% to 3.2%	Z/Z_{Total}		
Lean ldg (mol CO_2/mol alkalinity)	*	-0.01 to 0.03	0.14	±3	3.0 to 10.7
Rich ldg (mol CO_2/mol alkalinity)	±0.03	0.0004 to 0.03	0.34	±3	2.3 to 15.6
Gas mol flow (kmol/s)			0.50	±3	0.3 to 5.8
CO_2	5%	-0.2% to 8.9%	0.64	±3	-2.4 to 6.4
H_2O	5%	0.0% to 0.2%	0.72	±3	-5.9 to 2.0
N_2	5%	-3.5% to 0.04%	0.84	±3	-17.8 to -1.2
O_2	5%	-0.9% to 0.01%	0.90	±3	-19.3 to -0.5
y_{out}	5%	-0.0005 to 0.0006	1.06***	±3	-2.5 to 0.02
Removal fraction	5%	0.008 to 0.02	1.08***	±3	-3.8 to -1.3

* Lean loading was not specified directly. It was entered as individual streams of PZ, CO_2, and water.

** Z/Z_{Total} = 1 is the bottom of the column.

*** Z/Z_{Total} greater than 1 refers to thermocouples located below the packing bed.

Data for runs 4 and 8 were not included in the final reconciliation. Initial inclusion of run 4 data generated an adjustment of the interfacial area of around 60%. For run 8, the CO_2 removal fraction was adjusted initially more than 10%, which was off the trend for the rest of the data. Removal of these data points generated a better fit and solved initial convergence issues.

Figures 2 through 13 show the mass transfer and reconciled temperature profiles for the pilot plant runs in the November 2008 campaign along with the registered temperatures during the run.

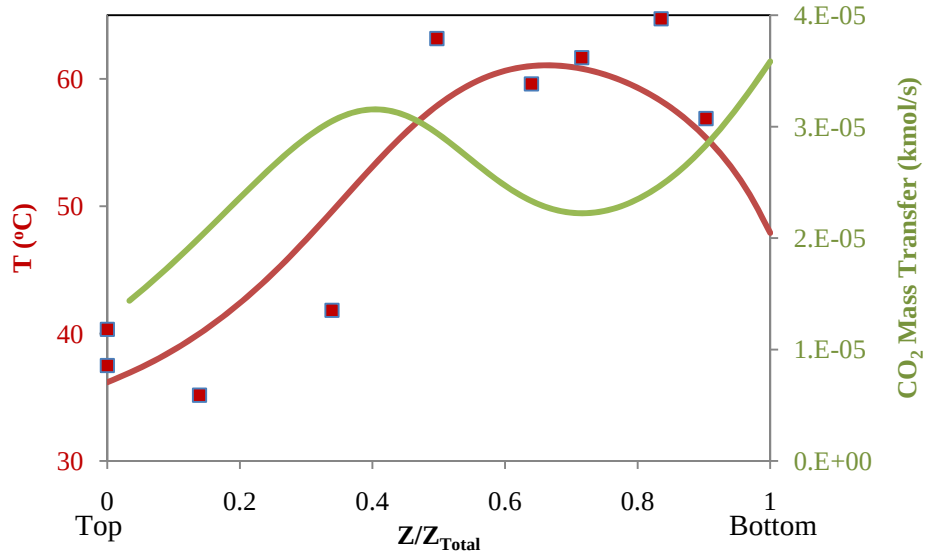

Figure 2: Liquid temperature and mass transfer profiles for Run 1

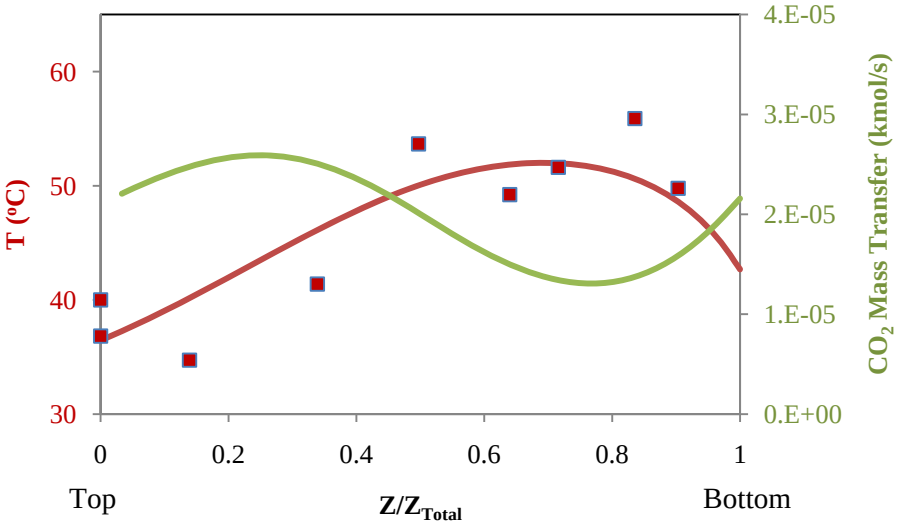

Figure 3: Liquid temperature and mass transfer profiles for Run 2

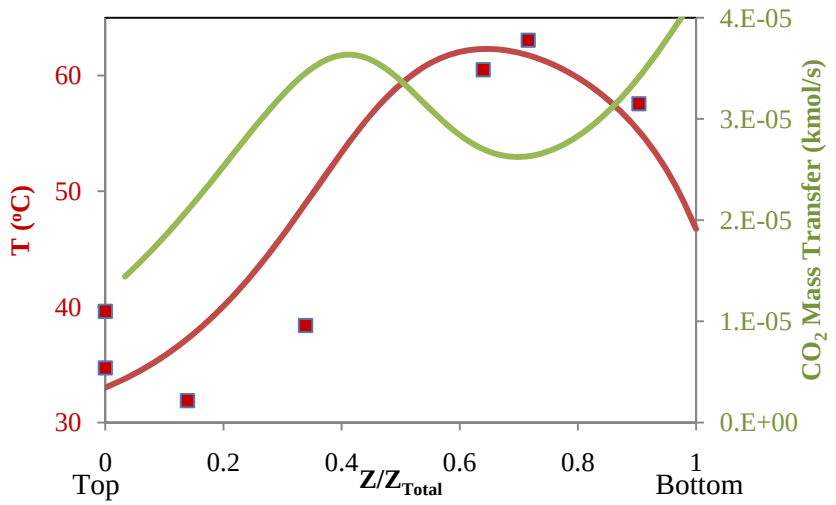

Figure 4: Liquid temperature and mass transfer profiles for Run 3

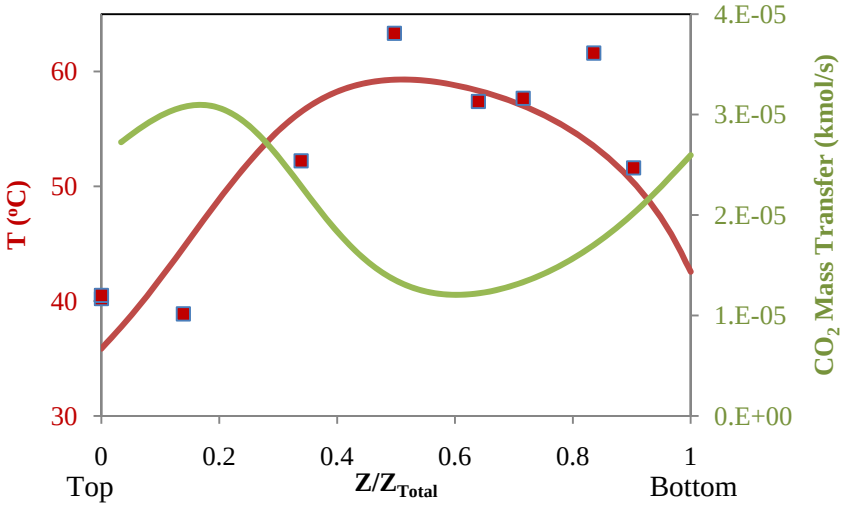

Figure 5: Liquid temperature and mass transfer profiles for Run 5

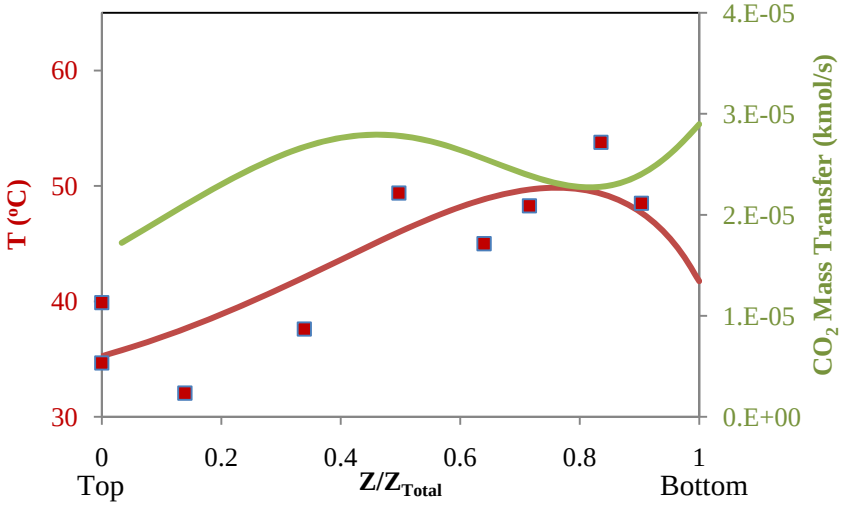

Figure 6: Liquid temperature and mass transfer profiles for Run 6

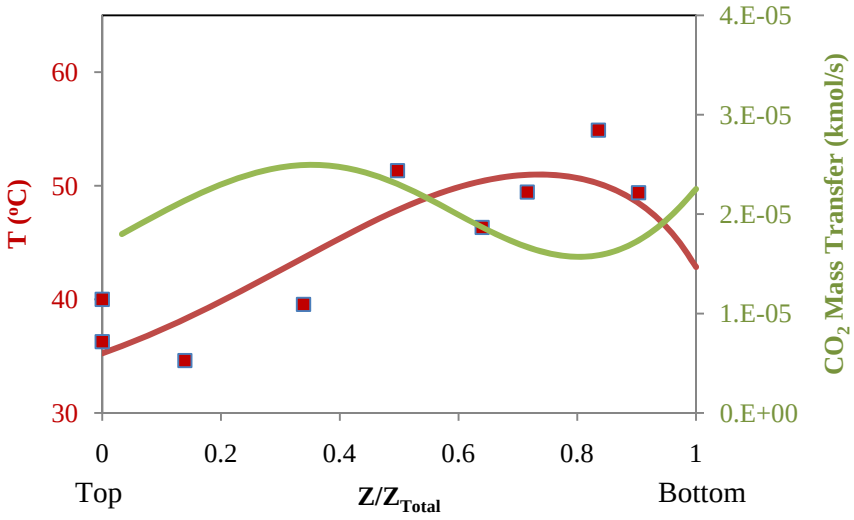

Figure 7: Liquid temperature and mass transfer profiles for Run 7

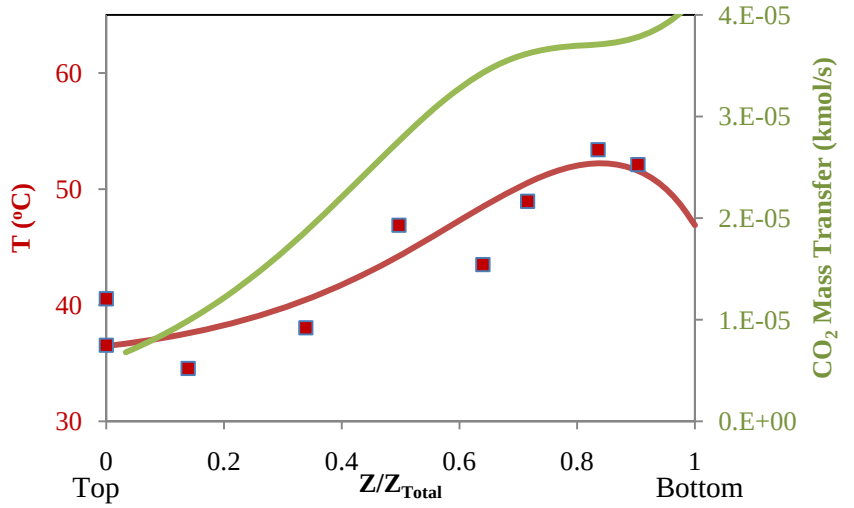

Figure 8: Liquid temperature and mass transfer profiles for Run 9

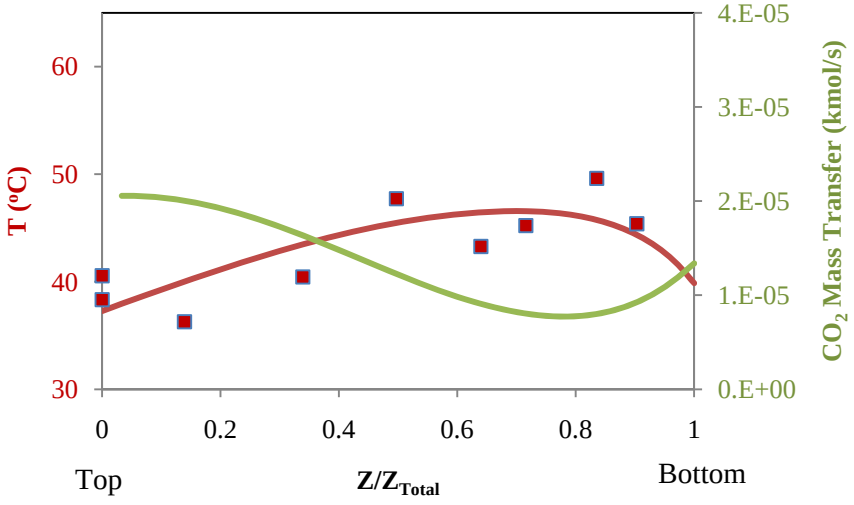

Figure 9: Liquid temperature and mass transfer profiles for Run 10

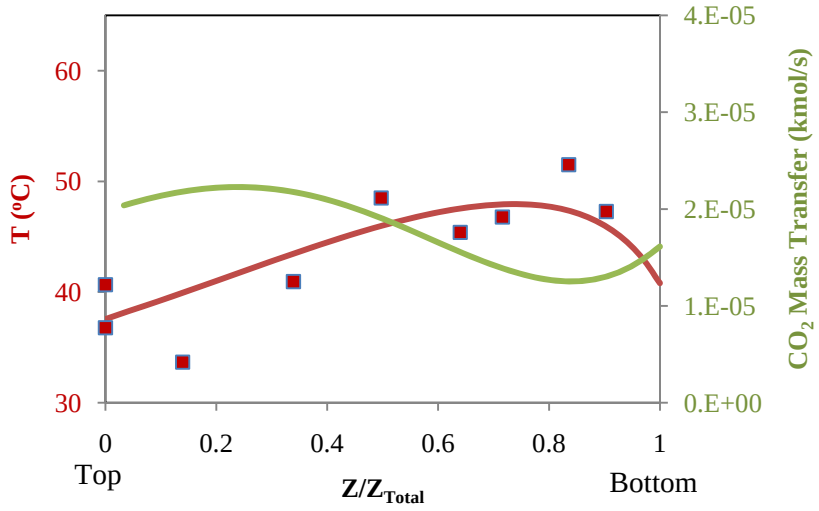

Figure 10: Liquid temperature and mass transfer profiles for Run 11

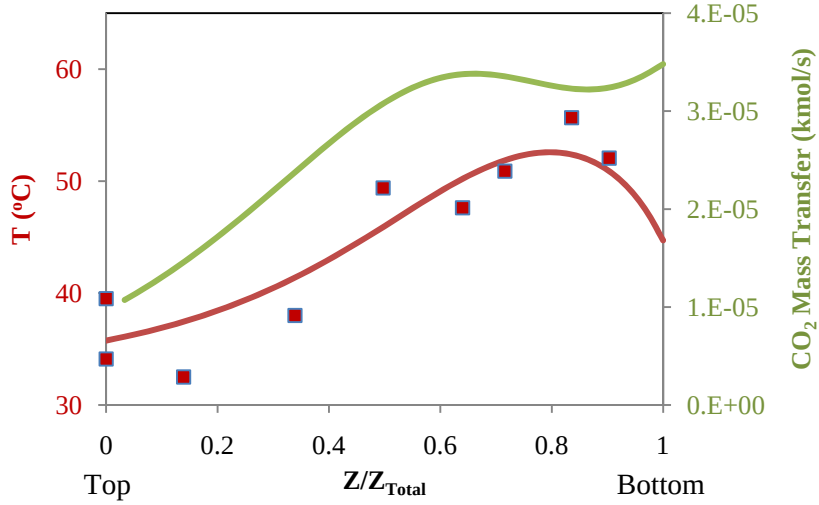

Figure 11: Liquid temperature and mass transfer profiles for Run 12

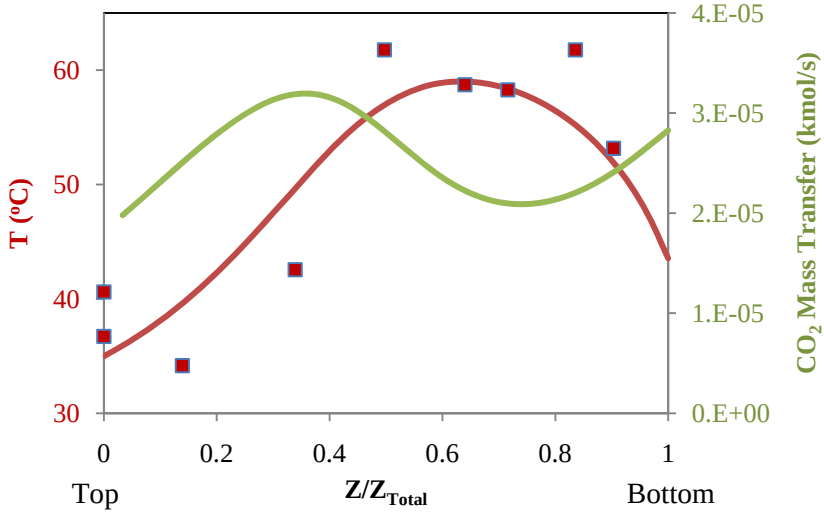

Figure 12: Liquid temperature and mass transfer profiles for Run 13

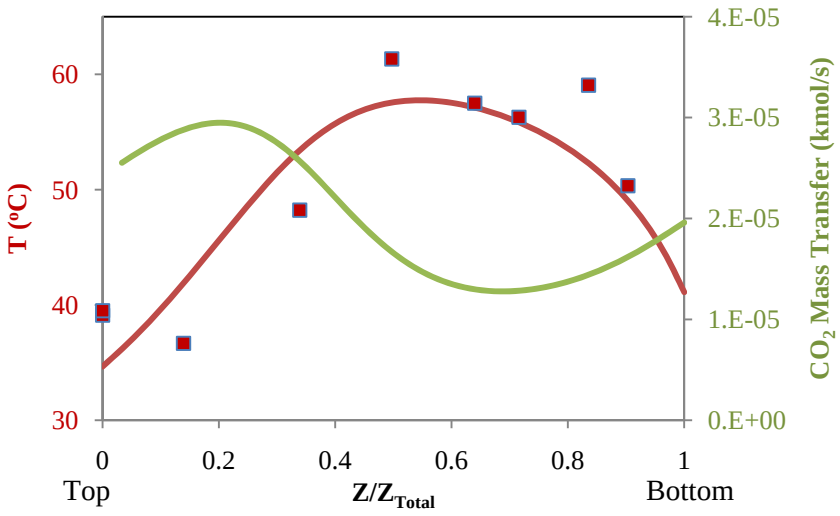

Figure 13: Liquid temperature and mass transfer profiles for Run 14

Temperature profiles were adequately matched by the model as well as loadings, flow rates, and removals, as shown by the range of deviations in Table 2.

Absorber intercooling with 8 m PZ

The validated PZ model was used to study the effects of intercooling on CO_2 removal performance and rich loading using 8 m PZ. Figure 14 shows the base conditions used. Lean loading was varied at different L/G ratios. Intercooling was set to reach 40 ^{o}C liquid temperature at half packing height.

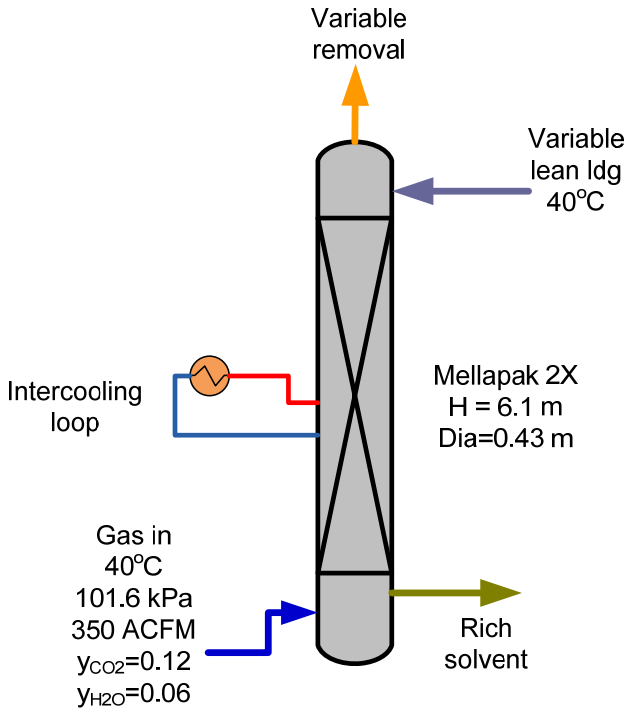

Figure 14: Base conditions for intercooling cases for 8 m PZ

Figure 15 shows the effect of intercooling on absorber performance. At constant removal (dashed lines) at low L/G (around 3) and high L/G (>5) the increase in rich loading using intercooling is negligible. However, at an L/G around 4 the discontinuity in the constant removal curve is minimized by using intercooling, allowing for a considerable increase in rich loading. This discontinuity has been previously observed by Plaza et al. (2009) for the K/PZ solvent and referred to as the critical L/G region. Similarly at constant lean loading the increase in removal can be as high as 10% for the critical L/G region.

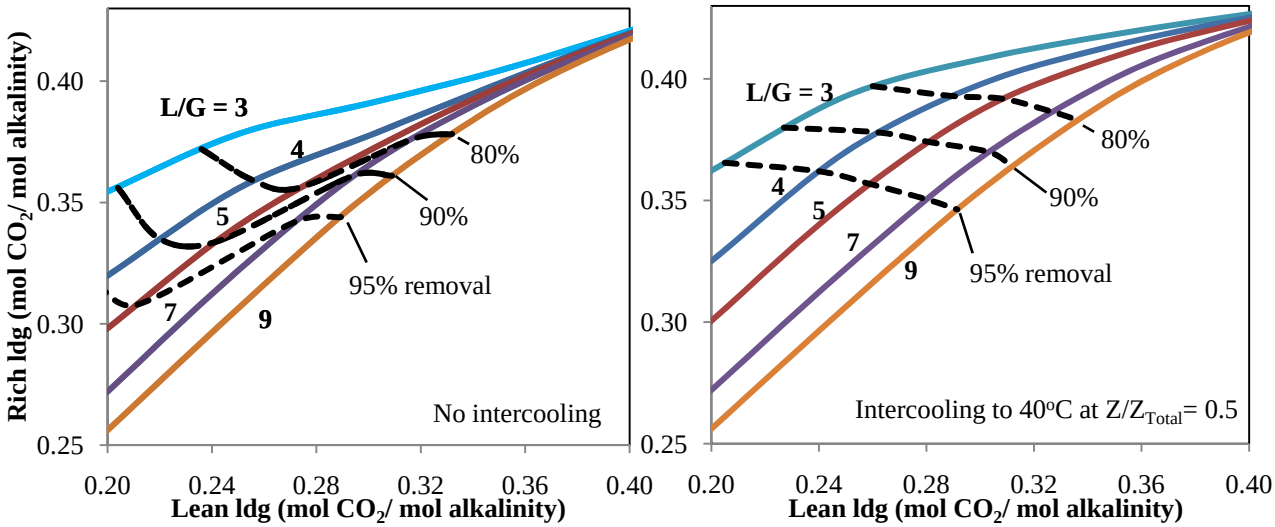

Figure 15: Effect of solvent lean loading on rich loading for 6.1 m Mellapak 2X. Diameter 0.427 m, 8 m PZ. y_{CO2} = 0.12. Inlet gas and liquid T = 40 °C.

The resulting temperature and CO_2 mass transfer profiles (Figure 16) in the critical L/G region (i.e., 3.8 mol/mol) show a mass transfer pinch coinciding with the temperature bulge near the middle of the column, similar to the cases in Plaza et al. (2009). Intercooling to 40 °C (Figure 17) breaks the pinch, allowing the absorber to reach 89% removal with a rich loading of 0.38.

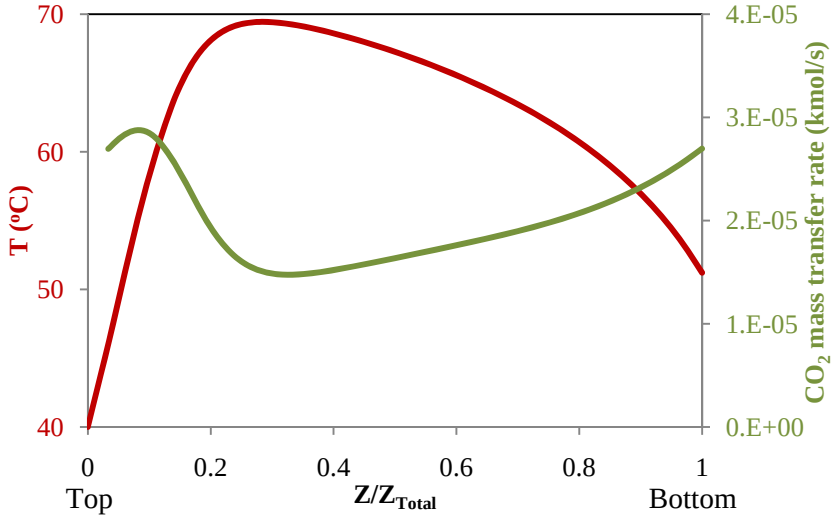

Figure 16: Liquid temperature and CO_2 mass transfer profiles for L/G = 3.8 mol/mol, 8 m PZ. Lean loading = 0.26. Rich loading = 0.36. 76.8% CO_2 removal.

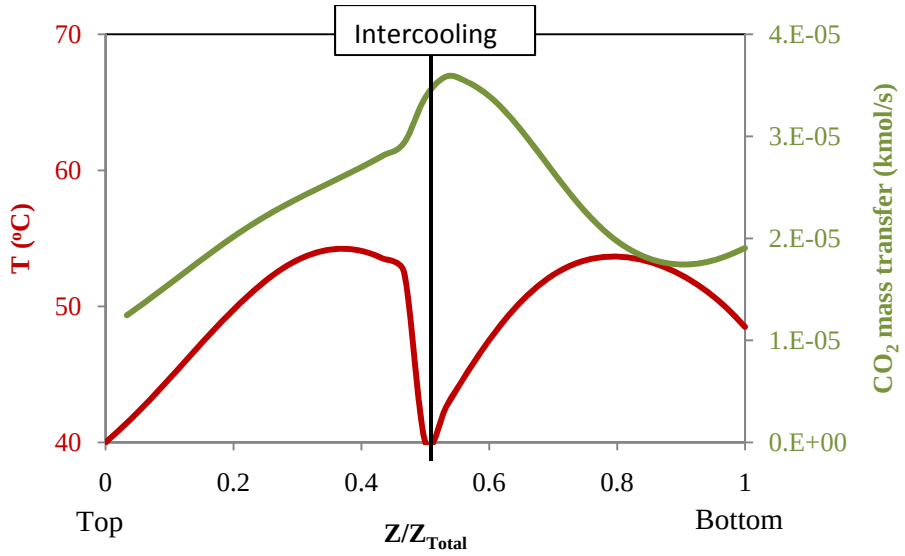

Figure 17: Liquid temperature and CO_2 mass transfer profiles for L/G = 3.8 mol/mol, 8 m PZ. Lean loading = 0.26. Rich loading = 0.38. Intercooling placed at Z/Z_{Total} = 0.5 and set to 40 °C. 89.2% CO_2 removal.

Plaza proposed an equation to estimate the critical L/G. It used the heat of absorption of the solvent and heat capacity values for gas and liquid.

$$\left(\frac{L}{G_i}\right)_c = \left(1 + (1-R)Y_{in}^{CO_2} + Y_{out}^{H_2O}\right)\left(\frac{Cp_{out}^G}{Cp_{in}^L}\right) + \frac{\left(Y_b^{CO_2} - (1-R)Y_{in}^{CO_2}\right)h_{abs}\big|_{T_b} + \left(Y_{out}^{H_2O} - Y_b^{H_2O}\right)h_{vap}\big|_{T_b}}{Cp_{in}^L(T_{in}^L - T_b)} \quad (1)$$

where: $(L/G)_c^i$ is the critical ratio of liquid to inert gas species;

Y^{H2O}, Y^{CO2} are the fractions of water and carbon dioxide respectively to inert species in the gas stream (n^{CO2}/G^i, n^{H2O}/G_i).

R is the specified removal.

Using a heat of absorption (h_{abs}) of 15.5 kcal/mol for 8 m PZ the critical L/G for 90% CO_2 removal is 4.2 mol/mol. This value is close to the location of the discontinuity at 90% constant removal observed in Figure 15. Similarly for 80% constant removal the critical L/G is closely predicted at 4.4 mol/mol.

Conclusions

- Pilot plant results show that it is possible to obtain 90% removal using 6.1 m of Mellapak 2X packing and 8 m PZ (Table 1).

- Reconciled pilot plant results demonstrate model capability of simulating absorber operation. Loadings and removal fraction were matched (less than 0.03 difference) (Table 2). Temperature profiles were adequately determined and the temperature bulge location was closely approximated (Figures 2–13). The interfacial area factor used was equal to 0.98 showing and adequate prediction of the effective area using Tsai et al. (2008) .

- When the absorber operates close to the critical L/G, intercooling is capable of generating an increase in CO_2 removal as high as 12%. Intercooling eliminates the mass transfer pinch and lowers overall absorber temperature leading to higher removal and richer rich loadings (Figures 16 & 17)

- The critical L/G region for this system is near 4 mol/mol for 90% removal. It can be determined by following the location of the discontinuity in the constant removal curve (Figure 15)

- The observed critical L/G (Figure 15) was closely predicted using the equation in Plaza et al. (2009).

Future Work

A pilot plant campaign is underway to test absorber intercooling with MEA and PZ. Both MEA and PZ models using intercooling will be validated using the generated pilot plant data.

Results for K/PZ, MEA, and PZ will be used to improve the proposed equation (Plaza et al., 2009) to predict the critical L/G.

Possible MEA and PZ absorber process modifications will be studied. (i.e., various contactors, hybrid contactors, height-diameter relations). A framework for an exergy and economic analysis will be developed to evaluate the resulting configurations.

References

Plaza JM, Chen E, Rochelle GT. "Absorber Intercooling in CO_2 Absorption by Piperazine Promoted Potassium Carbonate." *AIChE J.* 2009;56(4):905–914.

Tsai R, Seibert F, Eldridge B, Rochelle GT. "Influence of Viscosity and Surface Tension on the Effective Mass Transfer Area of Structured Packing." *Energy Proc.* 2008;1:1197–1204.

Electric Grid-Level Implications of Flexible CO_2 Capture Operation

Quarterly Report for July 1 – September 30, 2010

by Stuart Cohen

Supported by the EPA STAR Fellowship Program and the

Luminant Carbon Management Program

Department of Chemical Engineering

The University of Texas at Austin

October 31, 2010

Summary

Flexible post-combustion absorption/stripping that vents carbon dioxide (CO_2) or stores rich solvent at partial or zero load is investigated for its ability to improve profits by operating in response to volatile electricity prices. A versatile mixed-integer linear programming optimization model is created to maximize annual profits at a coal-fired facility with CO_2 capture. The model includes constraints on minimum/maximum load, ramp limits, startup behavior, and minimum up and down time for the base plant, absorption, and stripping equipment.

The first comprehensive analysis using the model was reported in the GHGT-10 paper "Optimal operation of flexible post-combustion CO_2 capture in response to volatile electricity prices." This analysis considered a nominal 500 MW coal-fired facility in the Electric Reliability Council of Texas (ERCOT) grid using an amine scrubbing unit with 7 m monoethanolamine (MEA). The analysis concluded the following:

- CO_2 venting improves profits over inflexible capture by up to 10% but is uneconomical at high CO_2 prices.
- Solvent storage improves profits over inflexible capture from 29% at \$30/tCO_2 to 9% at \$100/tCO_2.
- CO_2 emissions reductions are significant with flexible capture above any CO_2 price required to justify operating CO_2 capture (~\$30/tCO_2).
- Profit improvements with flexibility are achieved for any reasonable capture system response time.
- For the current case study, the most valuable solvent storage system is only large enough to exploit 15–30 minutes of high prices each day.

Future work will investigate the tradeoff between model accuracy and computation time when more accurate constraints are added. Sensitivity to several power, CO_2 capture, and electricity system parameters will be studied, especially in the context of solvent storage system design.

Introduction to Flexible CO_2 Capture

Flexible operation of a post-combustion amine absorption and stripping system entails varying the liquid and vapor flow rates in the stripping and/or absorption systems in order to choose the most economical CO_2 capture operating point for current electricity market conditions. During partial- or zero-load CO_2 capture, some or all of the steam being used for solvent regeneration would be redirected back to the power cycle to increase electrical output. The resulting decrease in CO_2 flow out of the stripper also reduces energy requirements for CO_2 compression. Solvent flow to the absorber and stripper and flue gas flow to the absorber could also be modulated for efficient system operation.

Flexible CO_2 capture could allow the plant operator to increase power output when electricity prices are high if additional electricity sales offset any increase in CO_2 emissions costs under a CO_2 regulatory framework (Ziaii et al., 2008). In addition, operating CO_2 capture at zero load during annual peak electricity demand can eliminate the need to spend billions of dollars to replace generation capacity lost when CO_2 capture operates at full load (Cohen et al., 2010a).

There are two general concepts for flexible CO_2 capture using amine absorption/stripping. One concept reduces the energy requirements of solvent stripping and CO_2 compression while allowing CO_2 removal rates to fall. Figure 1 displays one such configuration, where the steam and rich solvent flow rates to the stripper are reduced equally and simultaneously during partial- or zero-load operation (Ziaii et al., 2008). At partial load, rich solvent that is not sent to the stripper is recycled to the absorber, so CO_2 removal rates in the absorber will decrease as solvent becomes saturated with CO_2. Zero load could involve recirculating all solvent through the absorber, or the CO_2 capture system could be bypassed completely. This design has negligible capital cost, but its primary disadvantage is increased CO_2 emissions and any associated costs.

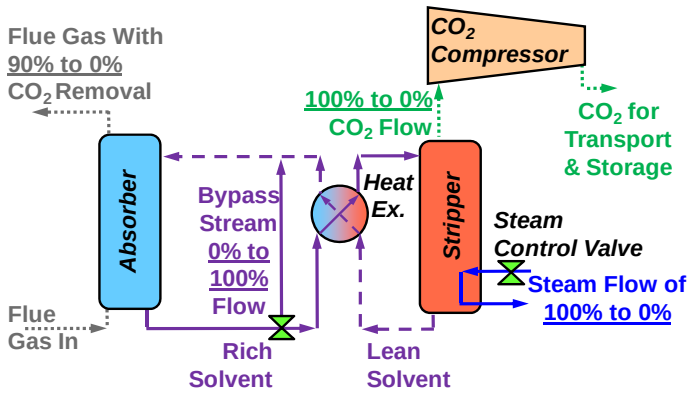

Figure 1: Simultaneously reducing steam and rich solvent flow to the stripper allows increased output but at the expense of additional CO_2 emissions.

Another flexible CO_2 capture concept uses large solvent storage tanks to maintain high CO_2 removal when stripping and compression systems operate at partial or zero load (Figure 2) (Chalmers and Gibbins, 2007; Rochelle et al., 2009). When electricity prices are high, the plant might operate in net "storage mode" with stripping and compression at partial or zero load while absorber load remains high by receiving lean solvent from one storage reservoir and depositing rich solvent into another. Net "regeneration mode" is then utilized when electricity prices are low; stripping and compression systems return to a higher load to treat the current process stream

and the stored rich solvent. To treat both current stream and stored solvent, stripping and compression systems must be larger and require more total energy than a CO_2 capture system without solvent storage. Maintaining high CO_2 removal keeps operating costs down while storing rich solvent, but any operating profit improvement must be weighed against the capital cost of solvent inventory, storage tanks, and larger stripping and compression equipment. Maintenance requirements require the ability to bypass the CO_2 capture system, so a facility with solvent storage system would likely maintain the option to vent additional CO_2 when necessary or desired.

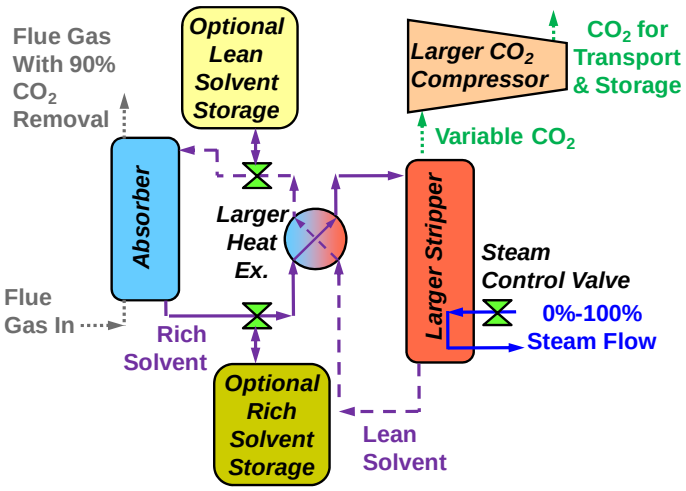

Figure 2: Including solvent storage incurs significant capital costs but allows continued high CO_2 removal at partial and zero load.

GHGT-10: Flexible Capture in Response to Volatile Electricity Prices

My paper for the GHGT-10 conference proceedings, "Optimal operation of flexible post-combustion CO_2 capture in response to volatile electricity prices," describes the general methodology and results from an optimization model that maximizes annual profits for a nominal 500 MW coal-fired facility by varying its base plant and CO_2 capture load in response to volatile electricity prices (Cohen, 2010b). Profits and CO_2 emissions for the facility are compared with and without CO_2 capture and with inflexible and flexible CO_2 capture systems of the types shown in Figures 1 and 2. The effects of electricity price foreknowledge, CO_2 price, CO_2 capture system response time, and the size of a solvent storage system are all investigated. The paper is attached to this report.

Versatile Model Formulation to Analyze Price-Responsive Capture

The primary purpose of this quarterly report is to present a model formulation that can be used as a versatile modeling framework for analyzing a power plant that operates post-combustion CO_2 capture in response to volatile electricity prices. The formulation has been updated from that used in my GHGT-10 analysis. By substituting site-specific input parameters into the equations below, one can use this model to find profit maximizing operation for a wide variety of facilities. Though completed analyses only consider post-combustion CO_2 capture using 7 m monoethanolamine (MEA) at a coal-fired facility, the model can easily be used for gas-fired facilities or any chemical solvent.

Decision Variables

The formulation is considered a mixed-integer program because there are both continuous and integer decision variables. The primary continuous decision variables are positive variables that specify gross output from the base plant, fractional load on the absorber and stripper, and quantity of CO_2 currently stored in rich solvent (for solvent storage cases). The primary integer decision variables are binary variables to indicate the commitment of the base plant, absorber, and stripper; 1 indicates the system is on, 0 indicates the system is off. There are also binary variables to indicate the presence of a startup during a given time interval, and these variables are constrained using the commitment variables. An analogous binary shutdown variable can also be defined if desired. All variables exist for each time period *t*.

$x_t =$ base plant gross output (MW), $u_t^p =$ base plant unit commitment (1=on, 0=off)

$on_t^p =$ base plant startup indicator (1=yes, 0=no)

$y_t^s =$ stripper load (fraction of max steam flow), $u_t^s =$ stripper unit commitment

$on_t^s =$ stripper startup indicator

$y_t^a =$ absorber load (fraction of max qty of CO_2 removed), $u_t^a =$ absorber unit commitment

$on_t^a =$ absorber startup indicator

Input Electricity Prices

The model reads an electricity price (P_t^{elec} in \$/MWh) in each time interval *t* of *T* hours in length. To approximate the effect of a CO_2 price on electricity prices in the Electric Reliability Council of Texas (ERCOT) grid, electricity prices are increased uniformly by the product of the assumed CO_2 price (P^{CO_2} in \$/tCO_2) and the average CO_2 emissions rate of all ERCOT natural gas-fired facilities (C^{NGavg} in tCO_2/MWh).

Objective

The objective, along with all constraint equations, is a linear function of the decision variables, which greatly improves model solvability and decreases computation time. The objective is to maximize profits across all time intervals, so the objective function can be written mathematically as the sum of revenues from selling the plant's net electrical output $x_{net,t}$ less all the costs associated with plant operation.

$$\text{Profit} = \sum_{\forall t} \begin{pmatrix} P_t^{elec} x_{net,t} T \\ -Cost_{startup,t} \\ -Cost_{fuel,t} - Cost_{baseO\&M,t} - Cost_{CO_2,t} \\ -Cost_{solv,t} - Cost_{caustic,t} - Cost_{waste,t} \\ -Cost_{capwater,t} - Cost_{trans/store,t} \end{pmatrix} \quad (1)$$

The equations for startup, fuel, CO_2, and base plant operation and maintenance (O&M) costs are shown below. A single value for base plant startup cost is used because variable startup costs depending on downtime are not considered important for understanding CO_2 capture operation. Currently, the model uses one value for the startup cost of the absorption or stripping/compression components of the CO_2 capture system, but different costs could easily be

incorporated. Base plant heat rate is assumed to be an average value and is kept constant across the base plant operating range. A detailed operating curve would improve accuracy, but a constant heat rate is used to maintain linearity of the model, which is important to ensure solvability and limit computational effort.

$$Cost_{startup,t} = SU^{p} on_t^{p} + SU^{c}(on_t^{a} + on_t^{s}) \quad (2)$$

$SU^{p} =$ base plant startup cost ($/startup)

$SU^{c} =$ capture component startup cost ($/startup)

$$Cost_{fuel,t} = P^{fuel} H^{B} x_t T \quad (3)$$

$P^{coal} =$ fuel price ($/MMBTU), $H^{B} =$ base plant heat rate (MMBTU/MWh)

$$Cost_{baseO\&M,t} = OM^{p} x_t T \quad (4)$$

$OM^{p} =$ non-fuel/CO_2 base plant O&M cost ($/MWh)

$$Cost_{CO_2,t} = P^{CO_2} C_{emit,t} T \quad (5)$$

$C_{emit,t} =$ net CO_2 emissions rate (tCO_2/MWh)

The remaining costs are associated with solvent makeup ($Cost_{solv}$), caustic used in thermal solvent reclaiming ($Cost_{caustic}$), reclaimer waste disposal ($Cost_{waste}$), additional water use for CO_2 capture/compression ($Cost_{capwater}$), and CO_2 transport and storage ($Cost_{trans/store}$). As with base plant heat rate, all performance parameters are assumed the same for all operating points in order to maintain model linearity. Initially, the 1/2 factor in the water cost equation implies that half of the water used for CO_2 capture can be attributed components related to CO_2 absorption (flue gas cooler, lean amine cooler) and half can be attributed to CO_2 stripping and compression (compressor intercooling). This assumption is not highly accurate, but it has a negligible effect on model results because water costs are generally a very small fraction of the total.

$$Cost_{solv,t} = \left(P^{solv} C^B R\bar{x}(D - D^t) y_t^s + P^{solv} C^B R\bar{x} D^t \right) T \quad (6)$$

P^{solv} = solvent price (\$/kg), R = fractional CO_2 removal,

$\bar{x}$ = maximum gross output capacity (MW),

C^B = base plant CO2 emissions rate (tCO_2/MWh),

D = total solvent degradation rate (kg/tCO_2),

D^t = subset of solvent degradation from thermal effects (kg/tCO_2)

$$Cost_{caustic,t} = P^{caustic} C^B R\bar{x} D^{caustic} y_t^s T \quad (7)$$

$P^{caustic}$ = caustic price (\$/kg), $D^{caustic}$ = caustic consumption (kg/tCO_2)

$$Cost_{waste,t} = \frac{P^{waste} C^B R\bar{x} \left[D^t + (D^{NaOH} + D - D^t) y_t^s \right] T}{1 - w^R} \quad (8)$$

P^{waste} = waste disposal price (\$/kg), w^R = fraction of water in reclaimer

$$Cost_{capwater,t} = P^{water} w\bar{x} \frac{1}{2} (y_t^s + y_t^a) T \quad (9)$$

P^{water} = water price (\$/m^3),

w = water used for capture per MW of gross plant size (m^3/MW),

$$Cost_{trans/store,t} = P^{trans/store} C^B R\bar{x} y_t^s T \quad (10)$$

$P^{trans/store}$ = transport/storage price (\$/tCO_2)

Base Plant Constraints

The constraints governing behavior of the base plant, independent of the CO_2 capture system, are listed below along with definitions of any parameters not already listed. The constraint on output range requires inclusion of unit commitment variables to assure correct switching between 0 MW and $\underline{x}$ during startup or shutdown. The startup test is required to include startup costs in the objective, and a similar constraint could be used to constrain *off* variables if one wished to specify shutdown costs separately. The ramp limit constraints allow for the transition between 0 MW and $\underline{x}$ during startup or shutdown and enforce the ramp limit whenever there are two successive intervals when the plant is on.

The minimum up time constraints are separated into three parts. The equation active in $1 \le t \le U^0$ forces the plant to remain on for a specified number of intervals after the initial time period, which is meant to enforce the minimum up time constraint if one assumes that a startup occurred before the time period of interest. The equation active in $U^0 < t < N - UT + 2$ enforces the minimum up time constraint throughout most time periods, and the equation active in

$N - UT + 2 \le t \le N$ assures the plant remains on for the remainder of the study period if a startup occurs when the remaining time intervals are less than the minimum up time. The minimum down time constraints are defined analogously to the minimum up time constraints.

Output Range

$$\underline{x} u_t^{\,p} \le x_t \le \overline{x} u_t^{\,p} \tag{11}$$

Startup test

$$on_t^{\,p} \ge u_t^{\,p} - u_{t-1}^{\,p} \tag{12}$$

Ramp Limits

$$-R^{p,down} u_{t-1}^{\,p} - (1 - u_t^{\,p})\underline{x} \le x_t - x_{t-1} \le R^{p,up} u_{t-1}^{\,p} + (1 - u_{t-1}^{\,p})\underline{x} \tag{13}$$

Minimum Up Time

$$\forall t \,|\, 1 \le t \le U^0, u_t^{\,p} = 1 \tag{14a}$$

$$\forall t \,|\, U^0 < t < N - UT + 2, \sum_{t'=t}^{t+UT-1} u_{t'}^{\,p} \ge UT(u_t^{\,p} - u_{t-1}^{\,p}) \tag{14b}$$

$$\forall t \,|\, N - UT + 2 \le t \le N, \sum_{t'=t}^{N} u_{t'} \ge (N - t + 1)(u_t^{\,p} - u_{t-1}^{\,p}) \tag{14c}$$

Minimum Down Time

$$\forall t \,|\, 1 \le t \le D^0, u_t^{\,p} = 0 \tag{15a}$$

$$\forall t \,|\, D^0 < t < N - DT + 2, \sum_{t'=t}^{t+DT-1} (1 - u_{t'}^{\,p}) \ge DT(u_{t-1}^{\,p} - u_t^{\,p}) \tag{15b}$$

$$\forall t \,|\, N - DT + 2 \le t \le N, \sum_{t'=t}^{N} (1 - u_{t'}) \ge (N - t + 1)(u_{t-1}^{\,p} - u_t^{\,p}) \tag{15c}$$

$\underline{x} =$ minimum gross output (MW)

$R^{p,up} =$ base plant ramp up limit (MW/interval)

$R^{p,down} =$ base plant ramp down limit (MW/interval)

$N =$ total number of time intervals

$U^0 =$ number of intervals plant must be on after first time interval

$UT =$ minimum number of intervals on after startup

$D^0 =$ number of intervals plant must be off after first time interval

$DT =$ minimum number of intervals off after shutdown

Constraints Related to CO_2 Capture Integration

The net electrical output used in the objective function is calculated by subtracting the energy required for CO_2 absorption and CO_2 stripping/compression. Energy for pumps and blowers can be included in the E^a and E^s parameters. Net CO_2 emitted is the difference between total CO_2 produced and CO_2 absorbed and must be calculated to determine CO_2 emissions costs.

The absorber load is the ratio of the current quantity of CO_2 removed to the total quantity removed with the base plant and absorber at full load, so a flexible CO_2 capture configuration must not allow absorber load to exceed base plant fractional load. Inflexible CO_2 capture implies that all flue gas being produced must be treated with the CO_2 capture system, so absorber load must equal base plant fractional load. Without a solvent storage system, absorber load must always equal stripper load, which is defined as the ratio of the current stripping steam flow to the steam required to treat all rich solvent when the absorber and base plant operate at full load. This formulation assumes stripper and compressor loads are equal, but a more complex formulation could decouple stripper and compressor load (or load on any component) by defining additional variables and constraints governing component relationships.

Net Output Calculation

$$x_{net,t} = x_t - x_{capture,t} = x_t - E^s C^B R\bar{x} y_t^{\,s} - E^a C^B R\bar{x} y_t^{\,a} \tag{16}$$

Net CO_2 Emitted Calculation

$$CO_{2,emit} = CO_{2,produced} - CO_{2,captured} = \left(C^B x_t - C^B \bar{x} R y_t^{\,a}\right) T \tag{17}$$

Maximum Absorber Load with Flexible Capture

$$y_t^{\,a} \le x_t \big/ \bar{x} \tag{18}$$

Absorber Load with Inflexible Capture

$$y_t^{\,a} = x_t \big/ \bar{x} \tag{19}$$

Absorber/Stripper Load Equality with Inflexible/Venting-only Flexible Capture

$$y_t^{\,a} = y_t^{\,s} \tag{20}$$

$E^s =$ energy required for CO_2 stripping/compression equipment (MWh/tCO_2)

$E^a =$ energy required for CO_2 absorption equipment (MWh/tCO_2)

Additional CO_2 Capture Constraints

The model also includes constraints on ramp limit, minimum value, and minimum up and down time for the absorption and stripping systems. The equations associated with these constraints are of the same form as the analogous base plant constraints and can be written by substituting $y_t^{\,a}$ or $y_t^{\,s}$ for x_t, $u_t^{\,a}$ or $u_t^{\,s}$ for $u_t^{\,p}$ and appropriate parameters for minimum load, ramp limits, minimum up/down time, and initial up/down time.

Additional Constraints with Solvent Storage

Absorber and stripper load are decoupled with solvent storage, so additional constraints must specify the maximum stripper load constrained by available low pressure (LP) steam or equipment size. Available LP steam depends on the current base plant load, the quantity of steam required for full-load stripping, and the minimum load on the LP turbine. The equipment size constraint shown here is formulated assuming the solvent storage system undergoes a full empty/fill cycle each day, but future work will investigate alternative design approaches.

The stored CO_2 level is tracked by a CO_2 flow balance, and the maximum quantity of CO_2 that can be stored in the rich solvent is specified by the storage tank size, design operating conditions, and solvent properties. The model must also specify an initial quantity of CO_2 stored and has the option of further requiring the quantity of stored CO_2 to return to a specified value at regular time intervals. A periodic stored CO_2 set point is one way to simulate imperfect future knowledge of electricity prices.

Maximum stripper load

$$y_t^s \le \frac{1-Y_{\min}^{Turb}}{F^{Steam}} \frac{x_t}{\overline{x}} \text{ (steam availability)} \tag{21}$$

$$y_t^s \le \frac{24}{24-H_{\max}} \text{ (equipment size)} \tag{22}$$

$$H_{\max} = \frac{SW\rho}{C^B \overline{x} R \Delta L} \frac{M_{CO_2}}{M_{Solv}} \tag{23}$$

Stored CO_2 Level

$$CO_{2,stored,t} = CO_{2,stored,t-1} + CO_{2,absorbed,t} - CO_{2,stripped,t} = CO_{2,stored,t-1} + tC^B \overline{x} R\left(y_t^a - y_t^s\right) \tag{24}$$

$$CO_{2,stored,\max} = \frac{1}{\Delta L} \frac{M_{CO_2}}{M_{Solv}} W\rho S \tag{25}$$

$Y_{\min}^{Turb}$ = minimum flow fraction on LP turbine, W = weight fraction of solvent in solution

ΔL = delta loading (kmol solvent/kmol CO_2), ρ = solution density (kgsoln/m^3soln)

M = molecular weight (kg/kmol), S = storage tank size (m^3)

F^{Steam} = fraction of LP stream extracted for capture with all systems at full load

$H_{\max}$ = maximum time with stripper off and absorber at full load (hours)

Tradeoffs When Adding Constraints

The version of the model used for the GHGT-10 analysis did not include any minimum up and down time constraints, startup costs for the CO_2 capture components, or separate unit commitment variables for CO_2 capture components. As the model is complicated by adding decision variables, constraints, and terms to the objective, the tradeoff between model accuracy and computation time becomes important. While there are theoretical relationships between problem size and computation time for continuous linear optimization formulations, adding integer variables necessitates solution algorithms that use heuristic searches to find feasible solutions that approach optimality. Therefore, adding constraints and variables can lead to large and unpredictable increases in computation time.

The tradeoff between model accuracy and computation time is investigated by assuming a default set of input parameters and comparing computation time and annual profits with and without a specific constraint. For a given constraint, the model is run with several values of the parameters associated with the constraint in order to gauge sensitivity to the constraint.

Results for constraints associated with minimum up and down time of the base plant are shown in Figure 3, with annual profits plotted for a range of specified minimum up/down time. Minimum up time is set equal to minimum down time for these studies. The points on the curves indicate the best feasible solution found within the allotted computation time, and the caps on the vertical bars indicate the best possible solution remaining when certain integer variables are allowed to take non-integer values. The gap between the best feasible and best possible solution indicates how close the solution has come to optimality. Studies with minimum up and down time set to 6 hours or less typically converge in 30 minutes or less, but higher minimum up and down times typically required the model to run for its entire allotted computation time of three or sometimes six hours. Without the constraint, convergence is achieved in 8 minutes or less except for the solvent storage case. Profits dropped by 4–9% without CO_2 at high minimum up/down times because a plant without CO_2 capture has incentive to turn power systems on and off more often when CO_2 price is \$50/tCO_2. All other configurations had profit reductions of 2% or less. If the plant under consideration is expected to operate for the majority of the year (a base load facility), the computational expense of including the base plant minimum up and down time constraint is not justified.

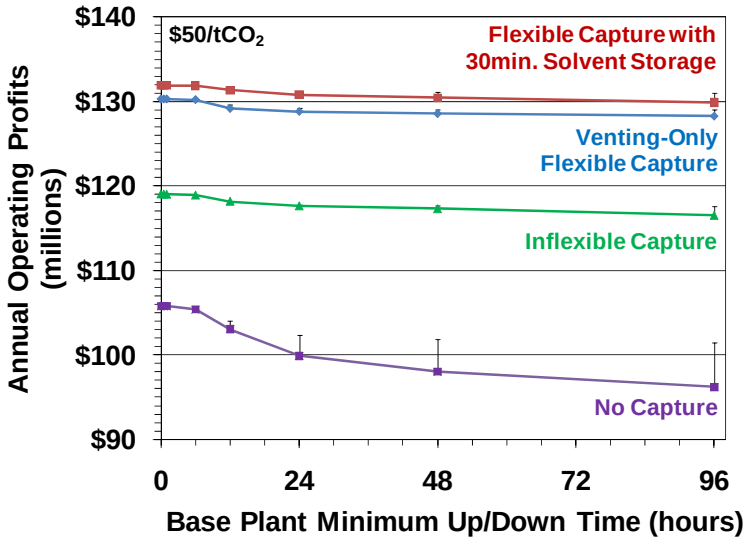

Figure 3: Base plant minimum up/down time does not have significant effect on profits for base load facilities.

Constraints associated with minimum up and down time of the absorber and stripper, absorber/stripper startup costs, and costs for changing absorber/stripper load will also be studied in this manner.

Conclusions

The following conclusions are drawn from this report and Cohen (2010b).

- A versatile optimization model has been created to study profit-maximizing flexible CO_2 capture in response to volatile electricity prices. Both CO_2 venting and solvent storage are modeled.

- CO_2 venting improves profits over inflexible capture by up to 10% but is uneconomical at high CO_2 prices.
- Solvent storage improves profits over inflexible capture from 29% at \$30/tCO_2 to 9% at \$100/tCO_2.
- CO_2 emissions reductions are significant with flexible capture above any CO_2 price required to justify operating CO_2 capture (~\$30/tCO_2).
- Profit improvements with flexibility are achieved for any reasonable capture system response time.
- For the current case study, the most valuable solvent storage system is only large enough to exploit 15–30 minutes of high prices each day.

Future Work

After finishing sensitivity studies on several model constraints and deciding which are necessary for future analyses, several sensitivity analyses will be performed on plant, capture, and electricity market parameters. Parameters of interest include base plant size, base plant ramp rate, CO_2 capture energy performance, and fuel prices; cross-sensitivity to CO_2 price will also be investigated.

The solvent storage configuration will be investigated in detail by comparing different solvents and design operating points to test tradeoffs between solvent price, solvent capacity, and energy performance. Sensitivity to the capital cost of stripping and compression equipment will be explored, as well as the degree to which equipment is oversized for treating stored rich solvent.

Once finished with these studies, the next major modeling initiative is to incorporate the representation of the flexible CO_2 capture system in a least-cost electricity dispatch model with multiple facilities of different power plant types. This modeling framework will be useful to investigate the ability of flexible CO_2 capture systems to provide reserve capacity and operate in response to intermittent renewable energy sources.

References

Chalmers H, Gibbins J. “Initial evaluation of the impact of post-combustion capture of carbon dioxide on supercritical pulverised coal power plant part load performance.” *Fuel.* 2007;86:2109–2123.

Cohen SM, Rochelle GT, Webber ME. “Optimal operation of flexible post-combustion CO2 capture in response to volatile electricity prices.” *10th International Conference on Greenhouse Gas Technologies*. Amsterdam, The Netherlands, 2010a.

Cohen SM, Rochelle GT, Webber ME. “Turning CO_2 Capture On & Off in Response to Electric Grid Demand: A Baseline Analysis of Emissions and Economics.” *ASME Journal of Energy Resources Technology*. 2010b;132.

Rochelle GT, et al. “CO_2 Capture by Aqueous Absorption, Second Quarterly Progress Report 2009.” Luminant Carbon Management Program, The University of Texas at Austin. 2009.

Ziaii S, Cohen SM, Rochelle GT, Webber ME. “Dynamic operation of amine scrubbing in response to electricity demand and pricing.” 9*th International Conference on Greenhouse Gas Technologies*. Washington, DC, 2008.

Measurement of Packing Effective Area and Mass Transfer Coefficients

Quarterly Report for July 1 – September 30, 2010

by Chao Wang

Supported by the Luminant Carbon Management Program,

and the Carbon Management Program, Process Science and Technology Center

Department of Chemical Engineering

The University of Texas at Austin

October 31, 2010

Abstract

Packing is widely used in distillation, stripping, and scrubbing processes because of its relatively low pressure drop, good mass transfer efficiency, and ease of installation. Packing is being investigated for the post-combustion carbon capture process for these reasons. Research continues to focus on development of high performance packing, especially on minimizing pressure drop, maximizing mass transfer efficiency, and minimizing costs. The design of packed absorbers for carbon dioxide capture will require the reliable measurement and accurate prediction of the effective area a_e, gas and liquid film mass transfer coefficient k_G and k_L. My research is focused on the measurement of these important fundamental parameters for packings and construction of a mechanistic design model.

In this quarterly report, end effects for associated mass transfer measurement were considered. End effects account for about 20% of k_G measurement when using a short packed bed of approximately 42 inches. The area and k_L measurements utilize a ten-foot packed bed and, as a result, the end effects appear to be negligible.

In this quarter, a new packing, 1-inch plastic Pall ring, was studied. This plastic packing has the advantages of low cost, light weight construction, and resistance to breakage.

The Pall ring is an economic and versatile industrial standard packing with well-known performance characteristics. Pressure drop, liquid hold-up, and mass transfer effective area were measured this quarter. Gas and liquid phase film mass transfer coefficients will be measured in November 2010. Next quarter, the performance characteristics of the Raschig Super Ring #0.7 will be examined, and in January 2011, the performance characteristics of 1-inch metal Pall rings will be studied.

End effect measurement

For consistent mass transfer measurements, the effective area a_e, and liquid side film mass transfer coefficient k_L were operated with ten feet of packing. However, for the gas side mass transfer coefficient k_G measurement, packing height had to be reduced because of the fast reaction and the range limit of SO_2 analyzer. The inlet SO_2 concentration is controlled under 100 ppm. The maximum relative range is approximately 130 ppm. The lower limit is approximately 0.1 ppm. The reaction between SO_2 and NaOH is fast and the outlet concentration can go down

to ppb levels if ten feet of packing is used. Therefore, a packed height of less than 44 inches is necessary for the k_G measurement when using one SO_2 analyzer.

End effects can be divided into two parts: end effect coming from the bottom and end effect coming from the top and wall. The end effect associated with the bottom sump appears to dominate.

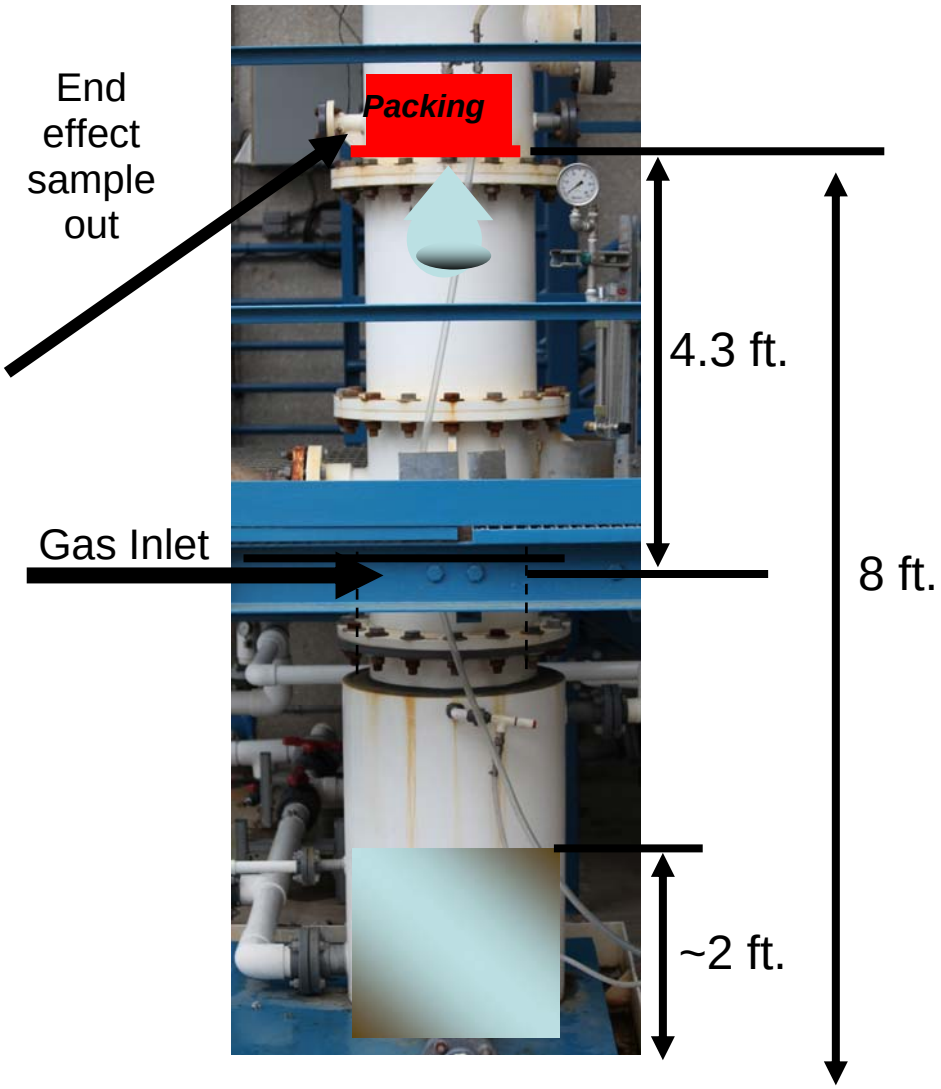

Figure 1: Measurement of bottom end effects

Figure 1 shows the bottom structure of the column. There can be as much as an 8 feet long gap between the bottom of the packing and the liquid level. Two sample lines were used to measure the mass transfer at the bottom: one is gas inlet and the other comes directly from the below the packing. Four runs have been performed and the results are shown in Table 1.

Table 1: Results of bottom end effects measurement

Run	SO_2 inlet, ppm	SO_2 end effect out, ppm	NTU bottom end effect
1	102.5	25.1	1.41
2	100.0	20.3	1.60
3	99.5	27.0	1.30
4	99.0	30.6	1.17

Another possible end effect contribution comes from the top of the packing and the walls. To account for the sump mass transfer and the top and wall mass transfer, the packed height was varied. As shown in Figure 2, when these data are extrapolated to zero packed height, the number of transfer units varies between 1.3 and 2.2 which is very similar to the values measured in the sump alone.

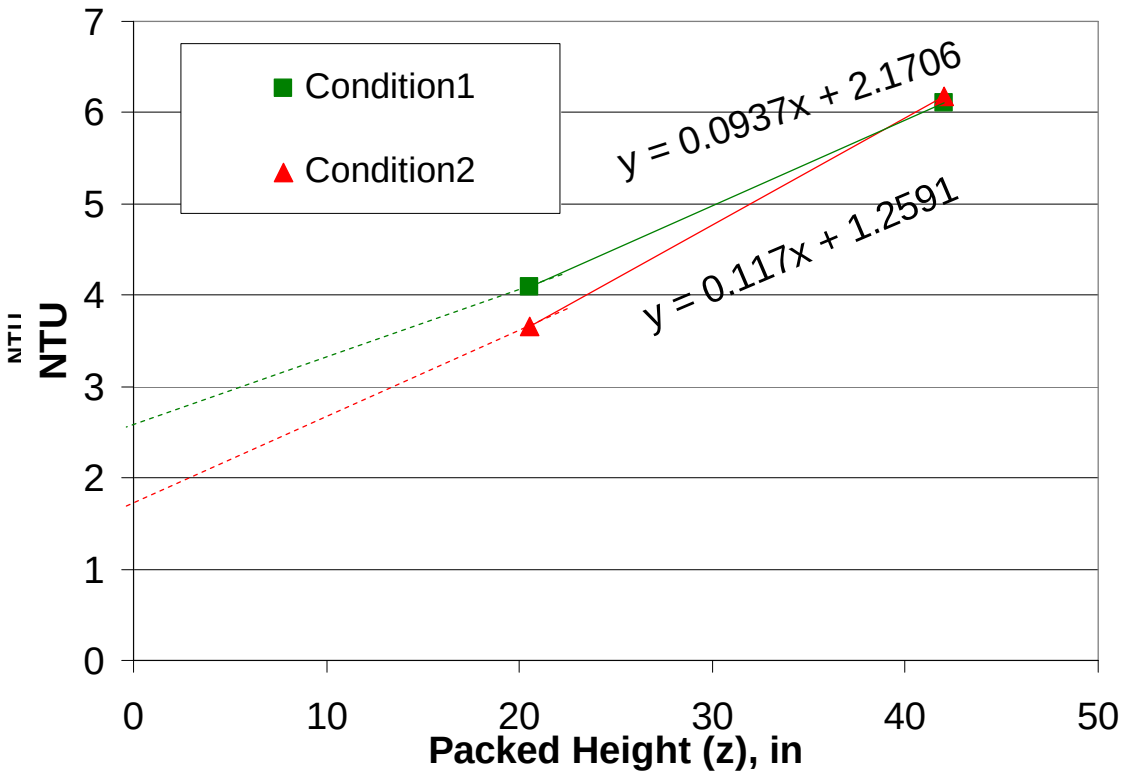

Figure 2: End Effect Measurement

.

The total end effects add up to about 1.48 NTU. This end effect NTU has been subtracted from overall NTUs in the k_G measurement.

In the k_G measurement, the average overall NTU for RSP 250 is 6.563, for Flexipak 1.6 Y HC is 6.30, for Mellapak 2X is 5.968, for RSR # 0.5 is 6.092. Thus, the end effect NTU accounts for 24% of the total NTU.

One Inch Plastic Pall Ring

Pall ring packing is an industry standard packing with well-known performance characteristics. It has higher capacity and lower pressure than ceramic packing. It has low sensitivity to liquid and vapor distribution. The ring and spoke construction provides high mechanical strength, which allows use in deep beds. The plastic Pall ring studied in this work was provided by Raschig-Jaeger and constructed of polypropylene.

The physical properties for the 1-inch plastic Pall ring are shown in Table 2. (Data are from Raschig-Jaeger).

Table 2: physical properties for 1-inch plastic pall ring

Pall Rings	Nominal Size	Bulk Density	Surface Area	Pieces Per ft^3	Free Space
	Inches	(lb/ft^3)	(ft^2/ft^3)	Approx	%
1" PPR	1"	5.5	64	1400	92%

Pressured drop results for the 1-inch plastic Pall ring are shown in Figure 3. The relationship between pressure drop and F-factor for this packing is quite similar to other packings we have measured. Pressure drop increases steadily with F-factor till flooding point when pressure drop increases rapidly.

Figure 4 shows the comparative pressure drop of different packings. The liquid flow rate chosen is 10 gpm/ft^2. From this figure we can see that at the same condition, pressure drop: 1" plastic Pall ring > RSR # 0.5 > Flexipac 1.6 Y HC >= RSP 250 > Mellapak 2X. At the same conditions, the pressure drop of the 1" plastic Pall ring is approximately 1.3 times that of RSR #0.5, 3.1 times that of Flexipac 1.6 Y HC, 3.5 times that of RSP 250, and 11.4 times that of Mellapak 2X. This is expected since the small random packing will have a larger pressure drop than structured packing. Mellapak 2X has a 60-degree corrugation angle, which will allow gas to flow much more smoothly.

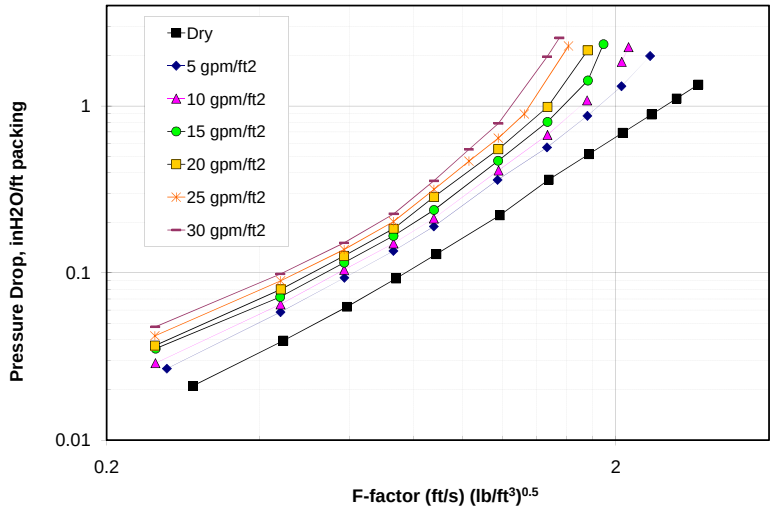

Figure 3: Pressure drop measurement for 1” plastic Pall ring

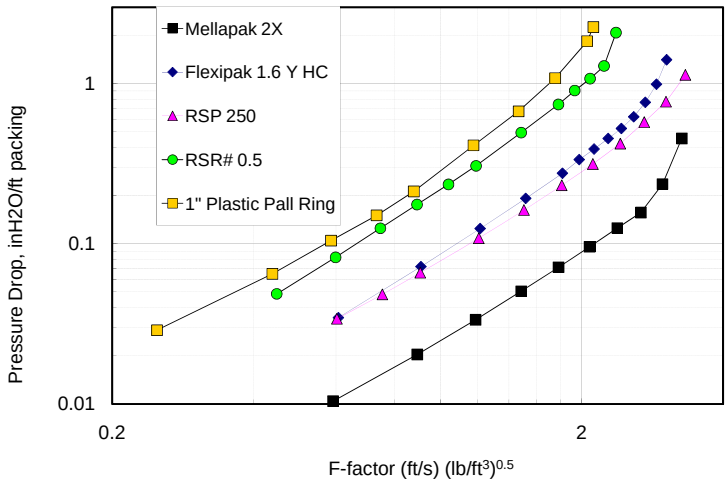

Figure 4: Pressure drop comparison among packings

Figure 5 shows the effective mass transfer area for 1" plastic Pall rings. As with other packings, the effective area shows some dependence on liquid flow rate but little dependence on gas flow rate. However, the fractional area for this packing is relatively small compared with metal packings. This is because the hydrophobicity of plastic hinders the contact between liquid and packing which will make the packing not totally wetted.

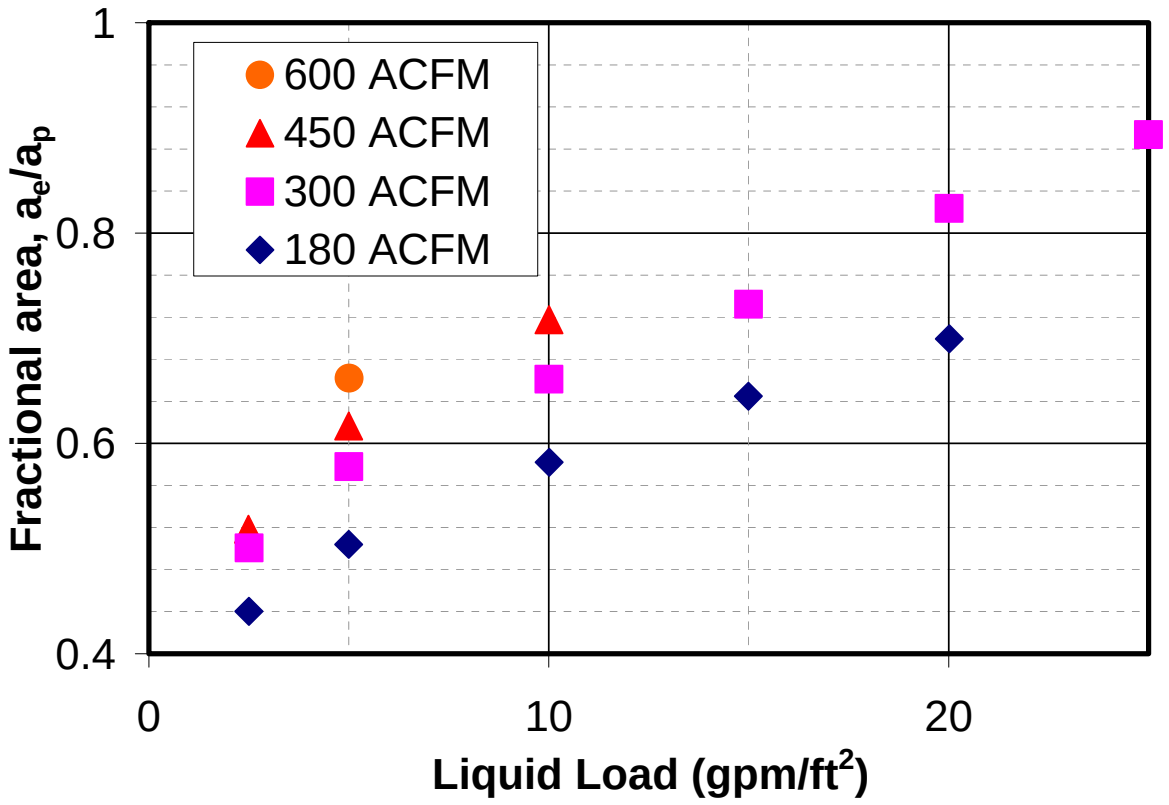

Figure 5: Effective mass transfer area measurement for 1" plastic Pall ring

Figure 6 shows the comparison of fractional area among different packings. The fractional area of plastic Pall ring is much smaller than other metal packings at the same conditions. However, the exponent of effective area on liquid flow rate for this packing is larger than others. This is because the increased liquid flow rate will offset the effect of hydrophobicity of the packing material.

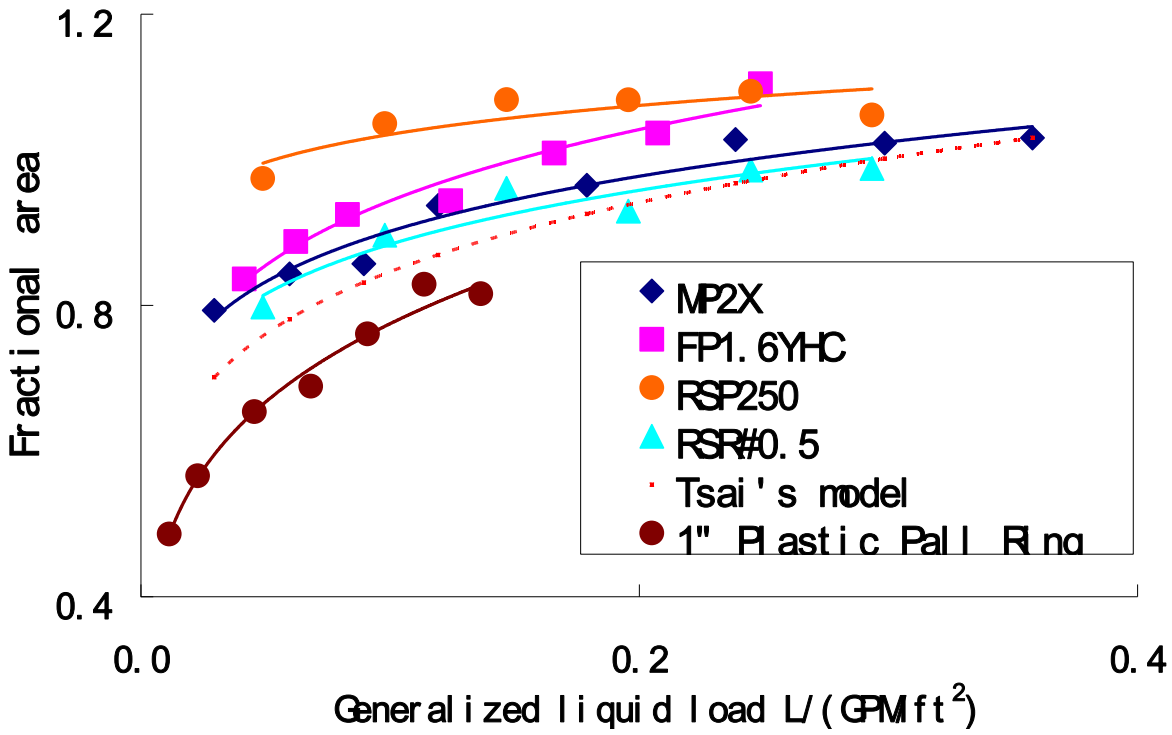

Figure 6: Fraction area comparison among different packing

Conclusions

In the measurement of k_g with four feet of packing, the end effects account for about 24% of the total NTU. Therefore it is necessary to correct for the end effects in k_G measurement.

The pressure drop of one-inch plastic Pall rings is approximately 1.3 times that of RSR # 0.5, 3.1 times that of Flexipac 1.6 Y HC, 3.5 times that of RSP 250, and 11.4 times that of Mellapak 2X, at the same conditions. This is expected since random packing will usually have a larger pressure drop than structured packing. Mellapak 2X has a 60-degree corrugation angle, which will allow gas flow much more smoothly.

The effective fractional mass transfer area of one-inch plastic Pall rings is smaller than metal packings. This is because the hydrophobicity of plastic hinders the contact between liquid and packing which will make the packing not totally wetted. However, the exponent of effective area on liquid flow rate for this packing is larger than others, which means the effective area of this packing increases much faster with liquid flow rate. This is because the increased liquid flow rate will offset the effect of hydrophobicity of the packing material.

Future Work

Next quarter we will complete the measurement of gas and liquid phase mass transfer coefficient for 1” plastic Pall ring.

The next packing to be measured will be 1-inch metal Pall ring. The results will be analyzed and compared with 1-inch plastic Pall ring.

References

Billet R, Schultes M. “Predicting Mass Transfer in packed columns.” *Chem Eng Technol.* 1993;16:1–9.

Bravo JL, Rocha JA, Fair JR. “Mass transfer in gauze packings.” *Hydroc Proc.* 1985;64:91–95.

Rocha JA, Bravo JL, Fair, JR. “Distillation Columns Containing Structured Packings: A Comprehensive Model for Their Performance.2. Mass-Transfer Model.” *Ind Eng Chem Res.* 1996;35:1660–1667.

Wagner I, Stichlmair J, Fair JR. “Mass Transfer in Beds of Modern, High-Efficiency Random Packings.” *Ind Eng Chem Res.* 1997;36:227–237.

Perry M. “Consistent Measurements of Packing Hydraulics.” Austin, Texas/Process Science and Technology Center – Spring Meeting. April 13, 2010.

RASCHIG-JAEGER TECHNOLOGIES. “Plastic Jaeger Rings & Saddles.” Ludwigshafen, Germany

Pilot Plant Testing of Advanced Process Concepts using Concentrated Piperazine

Quarterly Report for July 1 – September 31, 2010

by Eric Chen

Supported by the Luminant Carbon Management Program,

the Industrial Associates Program for CO_2 Capture by Aqueous Absorption,

the CO_2 Capture Pilot Plant Project of the Process Science and Technology Center,

NRGEnergy, and the U.S. Department of Energy

Department of Chemical Engineering

The University of Texas at Austin

October 22, 2010

Summary

Pilot plant testing of 8 m piperazine in a two-stage heated flash with absorber intercooling is planned for fall 2010. In this reporting period, mechanical fabrication of the two-stage flash pilot skid was completed. Process and utility piping and instrumentation tie-ins of the skid into the pilot plant were also completed. A gross leak check of the skid and tie-in piping and configuration of the primary skid instrumentation with the DeltaV control system was completed. Troubleshooting of the skid using water is currently underway. A small absorber intercooling skid was fabricated and retrofitted onto the pilot absorber at the UT Pickle Research Campus. Absorber intercooling tests were completed for 9 molal MEA (35 wt %) and 8 molal piperazine (42 wt %).

Absorber intercooling tests using the simple stripper configuration were completed for 9 m MEA and 8 m piperazine. The packing in the absorber and stripper was Sulzer Mellapak 2X and Raschig-Jaeger RSP 250 (new version), respectively. The test matrix for the 12 MEA runs was structured such that for a given gas and liquid rate and lean loading, the absorber was first operated with the intercooler off and then on. The conditions for MEA testing varied over the following ranges:

lean loading = 0.2 to 0.36 mol CO_2/mol MEA
gas rate = 350 to 500 cfm
L/G ratio (mass basis) = 2 to 6
absorber intercooling to 40 °C
stripper temperature = 115 °C
stripper pressure = 1.5 to 2.2 bar.

A total of 13 runs were completed for piperazine. The test matrix for piperazine was structured to achieve 90% CO_2 removal for a given lean loading and gas rate. The liquid rate was adjusted to maintain 90% CO_2 removal. The addition test conditions were:

lean loading = 0.22 to 0.30 mol CO_2/mol total alkalinity
gas rate = 350 to 750 cfm
L/G ratio (mass basis) = 2.6 to 5.8
absorber intercooling to 40 °C
CO_2 removal = 90%
stripper temperature = 120 °C
stripper pressure = 2.1 to 2.7 bar.

Three runs at 350 cfm and variable L/G were completed without absorber intercooling for comparison.

At a gas rate of 350 cfm, L/G ~ 3.6, 90% CO_2 removal, and absorber intercooling to 40 °C, the specific heat duty for piperazine (1171 Btu/lb CO_2) was 20% less than MEA (1435 Btu/lb CO_2). The piperazine runs demonstrated a 6.5% reduction of specific heat duty with absorber intercooling for a given L/G ratio (gas rate = 350 cfm, L/G range = 2.5 to 4.5, and 90% CO_2 removal). The MEA runs showed that at low (2.1) and high (5.8) L/G, absorber intercooling did not have any effect on specific heat duty.

A HAZOP was conducted for the skid to identify potential hazards and worst-case scenarios with the operators and technical staff at SRP. No major design or safety flaws were found. Additional interlocks will be built into the control system setup to address some of the minor safety concerns.

Two MicroMotion 7829 online viscometers and the associated flow chambers were donated by Emerson Process Management and installed on the skid. The viscometers measure viscosity, density, and temperature and will be used to determine online amine concentration and CO_2 loading through the viscosity and density measurements, respectively. There are currently some issues with getting the inputs from the viscometers into the DeltaV that are currently being resolved.

Troubleshooting of the two-stage flash skid using water is currently underway and has already identified a few issues. The steam control valves were specified to fail-close but upon installation they were found to be fail-open and will need to be rectified for safety concerns. The liquid level control valve on the low pressure vessel was found to be sized too small, resulting in an upper flow limit of 18 gpm. A by-pass around the low pressure liquid control valve will be installed to fix the problem. Finally, it was determined that the electronics of variable speed drive (VSD) on the high pressure pump was not working properly. The pump drive will need to be sent back to the manufacture for repair or replacement.

The preliminary stages of skid troubleshooting have also shown that startup of the skid will require pressurizing the two gas-liquid separator tanks because there are no pumps downstream of each tank to pump the solvent back to the main pilot unit. However, the liquid flow issue disappears once the solvent has been heated and pressure begins to build. Aside from these issues, control of the gas pressures, liquid levels, and flash temperatures seem to work well with the water tests. A heat loss test for the skid will need to be completed before the piperazine campaign with two-stage flash begins.

The schedule for startup of the two-stage flash campaign will be contingent on the replacement of the pump VSD. The lead time is currently unknown. At this time, start-up is tentatively scheduled for late November or early December.

MDEA/PZ Degradation in Cycled Solvents

Quarterly Report for July 1 – September 30, 2010

by Fred Closmann

Supported by the Luminant Carbon Management Program

and the

Carbon Management Project, Process Science and Technology Center

Department of Chemical Engineering

The University of Texas at Austin

October 15, 2010

Abstract

When 7 m MDEA amended with 200 mM formate was cycled from 55 to 120 °C, DEA production was suppressed (0.2 mM/hr) when compared to a similar experiment without formate amendments (2.6 mM/hr), whereas bicine production (0.9 mM/hr) was 3X the rate measured without formate amendment.

When 7 m MDEA/2 m PZ (α = 0.14 mols CO_2/mol alkalinity) was cycled from 55 to 120 °C for 570 hours, first order loss rates of MDEA and PZ were 12 and 20%/wk, respectively. The major degradation products observed in the experiment were diethanolamine (DEA), 1-methyl piperazine (MPZ), 1,4-dimethyl piperazine (DMPZ), aminoethyl piperazine (AEP), N-formyl piperazine (FPZ), bicine, and formate. We accounted for approximately 69% of lost carbon and 69% of lost nitrogen. Ethylenediamine (EDA) was not observed in the degraded blend. DEA comprised 40 and 35%, respectively, of the total carbon and nitrogen loss of the parent amines. Bicine production experienced no lag time, but formed at approximately one-third the rate observed in cycled 7 m MDEA (0.14 vs. 0.34 mM/hr). We accounted for approximately 57% of PZ ring loss by accounting for PZ-derivative degradation products. The ratio of moles of MDEA lost to moles of PZ lost after approximately 350 hours of solvent cycling was 2:1. The ratio of moles of alkalinity from MDEA loss to moles alkalinity from PZ loss was 1:1. The loss rate of nitrogen from MDEA and PZ was 2.3 mM/hr each for a total loss rate of 4.6 mM/hr; compared to 6.2 mM/hr measured in cycled 7 m MDEA (C-6) and 2.4 mM/hr measured in cycled 8 m PZ (C-16). Total alkalinity loss rates for the three solvents from greatest to least were measured as: 7 m MDEA/2 m PZ > 7 m MDEA > 8 m PZ. Based on a comparison of the loss rate of PZ in the blend (20%/wk) and the loss rate of PZ in cycled 8 m PZ at the same conditions (5%/wk), the blend experienced a preferential loss of PZ on a percentage basis.

When we cycled 7 m MDEA/2 m PZ from 55 to 90 °C and 120 °C, formate production lagged amide formation for approximately 50 hours of cycling, but a peak in the ratio occurred at approximately 390 hours, with a leveling off at a slightly lower ratio (~0.82). Amide formation occurred to a greater extent at the beginning of the degradation process until formate production reached an equilibrium condition with amides in the solvent. In terms of formate production at

the lower thermal temperature of 90 °C, from greatest to least formate production, the solvents can be ranked as follows: 7 m MDEA/2 m PZ > 7 m MDEA > 8 m PZ.

Introduction

During the 3rd quarter 2010, we completed one degradation experiment (C-20) with 7 m MDEA and two experiments with 7 m MDEA/2 m PZ (C-21 and C-22) in the Integrated Solvent Degradation Apparatus (ISDA). The experiments with the blend were the first with this solvent in the ISDA. Prior to these experiments and at the beginning of the quarter, experiment C-19 was attempted with 8 m PZ cycled from 55 to 130 °C, but the experiment was aborted due to pressure limits with the system. Thermal experiments 15, 16, and 17 were also started in this quarter. Thermal 15 and 17 are near completion, while several thermal cylinders for Thermal 16 remain in the ovens to ensure data over an extended length of time at all temperatures. Data for all three thermal experiments will be available in the fourth quarter 2010.

Experiment C-20 was conducted in the ISDA with 7 m MDEA at a loading of 0.1 mols CO_2/mol alkalinity, and spiked with 200 mM formate immediately after loading the charge of solvent into the system. The experiment was conducted to determine the effect of formate on the production of other degradation products including the amino acid bicine (bis(hydroxyethyl)glycine) and DEA. The experiment was designed to test for a competition for dissolved oxygen among formate, bicine, and DEA in the system as degradation of MDEA proceeded; if a competition did exist, an initially high concentration of formate would suppress the production of other products until the formate was oxidized to a concentration in equilibrium with other products.

Experiment C-21 was the first cycling experiment with 7 m MDEA/2 m PZ (α = 0.14 mols CO_2/mole alkalinity); the blend was cycled from 55 to 120 °C for almost 600 hours. As with all previous experiments, the CO_2 loading in this solvent approximately matches the CO_2 solubility condition at 55 °C for the 2 kPa CO_2 gas provided to the oxidative reactor headspace; the CO_2 solubility at 55 °C was checked against the latest Aspen Plus® model developed by Frailie (2010) for the blend to determine the appropriate loading. An additional experiment (C-22) was conducted with the same solvent cycled from 55 to 90 °C. Results from C-22 are only partially available and discussed in this report. However, a full discussion of the results of C-21 is presented in this report. The solvent in all ISDA experiments included the stainless steel metals mix (0.4 mM Fe, 0.1 mM Cr, and 0.05 mM Ni), with metals added as dissolved metal sulfate salts. The experimental setup for all experiments discussed in this quarterly report included an oxidative reactor headspace gas of 98% O_2/2% CO_2 at a flow rate of 100 ml/min.

Cycling (ISDA) Experiments Discussion

Table 1 provides a summary of the degradation rates measured for each of the ISDA experiments. Comprehensive data tables for experiments C-20 through C-22 are included at the end of this quarterly report as Tables A-1 through A-6.

Experiment C-20

Experiment C-20 was conducted to test the effect of initially spiking 7 m MDEA (α = 0.1 mols CO_2/mol alk) with 200 mM formate and cycling the solvent from 55 to 120 °C. The results can be compared to those for the comparable experiment without formate spiking (C-6), which are presented with all previous 7 m MDEA cycling experiments in Table 1. Figure 1 presents the concentration of MDEA and its major degradation products over the course of the experiment.

The initial concentration of formate as measured by cation chromatography was approximately 176 mM. Note the initial loss of approximately 200 mM of MDEA at time zero (Sample No. C-20-0b), which is the sample collected immediately after spiking the solvent charge with ~200 mM formate as formic acid; the formic acid neutralized ~200 mM alkalinity associated with the MDEA, resulting in loss of MDEA as measured by cation chromatography.

Table 1: Cycling results for 7 m MDEA (α = 0.1 mols CO_2/mol alkalinity)

Cycling Experiment Results (7 m MDEA)											
Expt	Solvent	T_{th} (°C)	Stir Rate (rpm)	Purge Gas	Other Conditions	Alk Loss (mM/hr)	MDEA Loss (mM/hr)	PZ Loss (mM/hr)	DEA Prod Rate (mM/hr)	Formate Prod (mM/hr)	Formate w/ Hydrolysis (mM/hr)
C-8	7 m MDEA	120	1440	N_2/CO_2	SS metals; bubble vessel	1.7	1.9	NA	0	0.013	0.001
C-9	7 m MDEA	120	0	N_2/CO_2	SS metals; bubble vessel	3	4.1	NA	0	0.024	0.002
C-13	7 m MDEA	120	1440	Air/CO_2	SS metals; bubble vessel	0.76	0.24	NA	0.37	0.084	0.08
C-14	7 m MDEA	90	1440	Air/CO_2	SS metals; bubble vessel	0.76	0.22	NA	0.08	0.044	0.058
C-18	7 m MDEA	120	1440	O_2/CO_2	SS metals; mod bubble vessel with N2 purge	0.74	0	NA	0.39	0.047	0.044
C-4	7 m MDEA	120	520	O_2/CO_2	SS metals	2.8	3.4	NA	NM	0.17	0.15
C-5	7 m MDEA	120	1000	O_2/CO_2	SS metals; bubble removal	4.3	8.5	NA	NM	0.37	0.57
C-1	7 m MDEA	120	1440	O_2/CO_2		5.2	8.8	NA	NM	0.59	0.98
C-2	7 m MDEA	55	1440	O_2/CO_2		1.4	~0.0	NA	NM	0.0052	~0
C-15	7 m MDEA	90	1440	O_2/CO_2	SS metals; BR, Inh A	1.82	2.37	NA	~0	0.15	0.23
C-7*	7 m MDEA	120	1440	O_2/CO_2	SS metals; BR, Inh A	5.4	5	NA	1.8	0.22	0.29
C-3	7 m MDEA	55	1440	O_2/CO_2	SS metals	1.5	0.9	NA	0	0.0018	0.01
C-11	7 m MDEA	80	1440	O_2/CO_2	SS metals; bubble vessel	1.3	0.91	NA	0	0.034	0.057
C-12	7 m MDEA	90	1440	O_2/CO_2	SS metals; bubble vessel	2.5	2.87	NA	1.55	0.12	0.15
C-10	7 m MDEA	100	1440	O_2/CO_2	SS metals; bubble vessel	3	4.1	NA	1.64	0.18	0.31
C-6	7 m MDEA	120	1440	O_2/CO_2	SS metals; bubble vessel	5.3	4.6	NA	2.56	0.31	0.34
C-20	7 m MDEA	120	1440	O_2/CO_2	SS metals; bubble vessel	1.3	4.2	NA	0.18	Spiked	Spiked

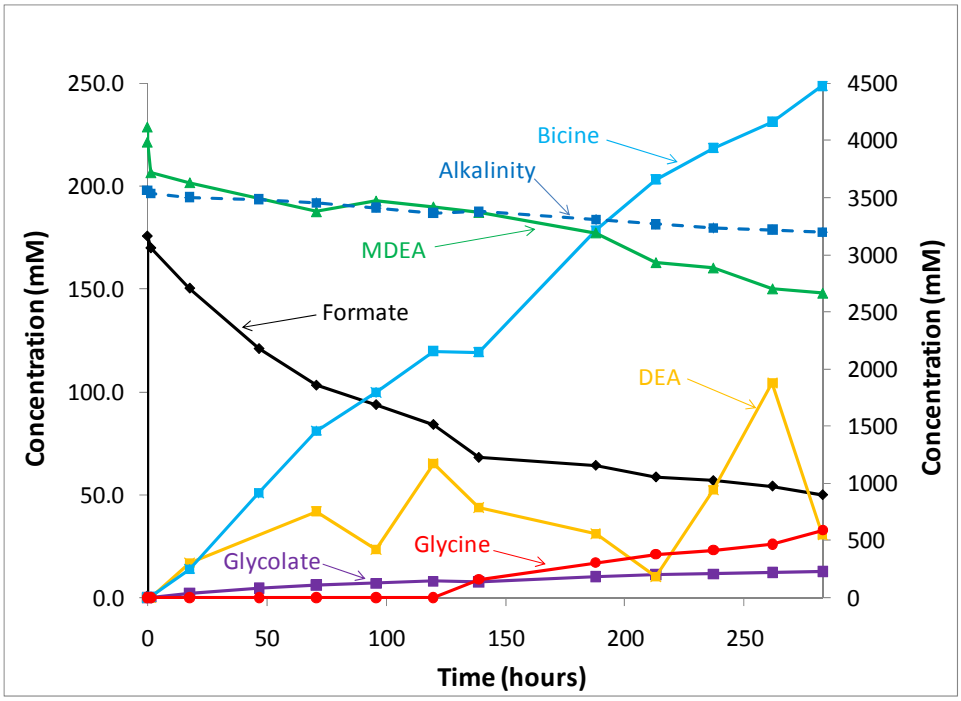

Figure 1: Degradation Products in 7 m MDEA (α = 0.1); Amended with 200 mM formate

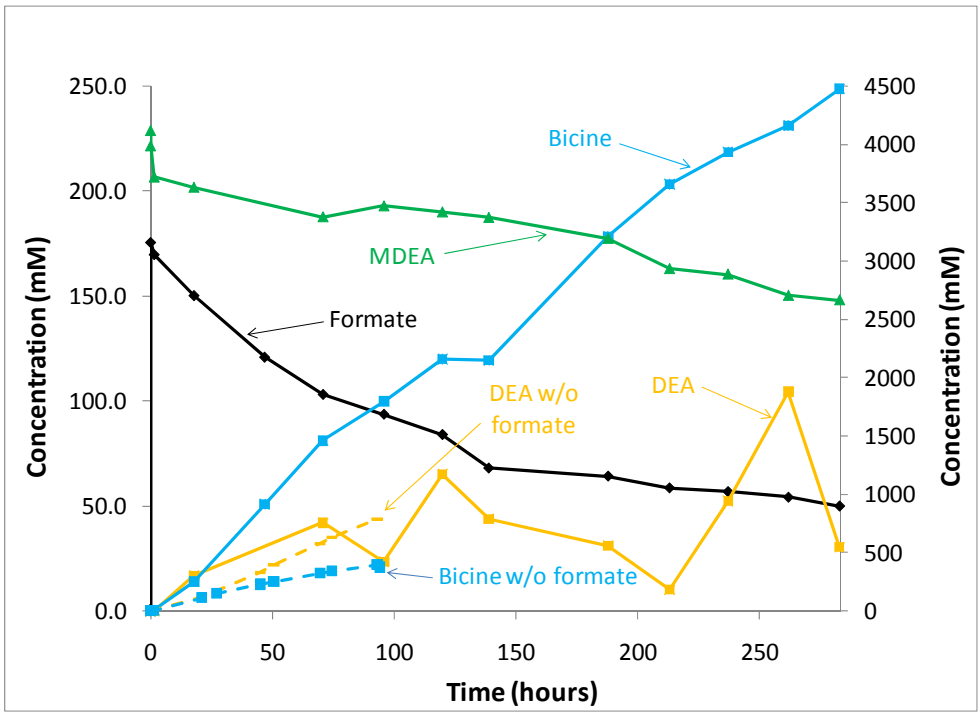

Figure 2: Comparison of Degradation Products in Cycled 7 m MDEA (α = 0.1) in formate amended (200 mM) and unamended solvent

The MDEA loss rate was measured as 4.2 compared to 4.6 mM/hr measured in C-6 conducted at comparable conditions. However, the alkalinity loss rate was measured as 1.3 mM/hr compared to 5.3 mM/hr in C-6, indicating that, despite having nearly comparable MDEA loss rate as in C-6, the alkalinity loss was one quarter the loss measured without the formate spike in C-6.

Figure 2 compares the basic degradation product concentrations in experiments C-6 and C-20. The DEA production rate was estimated at 0.2 mM/hr compared to the rate of 2.6 mM/hr measured in C-6, indicating that the production of DEA was suppressed in the experiment spiked with formate. Bicine production in C-20 was ~0.9 mM/hr compared to 0.3 mM/hr in C-6, indicating that spiking with formate increased bicine production 3X. Finally, the rate of production of formate in experiment C-6 indicates that the equilibrium concentration would have been comparable to the concentration observed after 280+ hours in experiment C-20 (~50 mM) where formate was spiked at an initial concentration of 175–200 mM.

One possible explanation for the suppression of DEA production in the presence of formate at 175 mM is that methyl group abstraction (loss) from the MDEA would typically result in the production of formate, but with excess formate in solution from the outset, the forward reaction (DEA formation through methyl group loss from MDEA) is slowed in order to reach equilibrium. The increased production of bicine in the presence of the formate spike is more difficult to explain. Bedell (2010) ran experiments with degraded triethanolamine (TEA) to observe the production of bicine but found none. Thus, an initial production of TEA from MDEA is likely not the explanation. One possible explanation is that formate causes simple arm-switching between MDEA (and DEA after its production) through an S_N2 substitution mechanism to occur at a greater rate than in the absence of excess formate. Bicine could be produced from a switch of the methyl group with a hydroxyethyl group from another molecule of MDEA or DEA.

Experiment C-21

In experiment C-21, 7 m MDEA/2 m PZ at an initial loading of 0.14 mols CO_2/mol alkalinity was cycled from 55 to 120 °C for 570 hours. The purge gas in the headspace of the oxidative reactor was 98% O_2/2% CO_2. The concentrations of MDEA, PZ, and degradation products are presented in **Error! Reference source not found.**. Note that the first order loss rate of MDEA and PZ was 12 and 20%/wk, respectively. Figure presents the cation IC chromatograph for the endpoint sample in C-21. The major degradation products observed in the experiment were DEA, MPZ, DMPZ, AEP, FPZ, bicine, and formate. Table 2 presents a carbon and nitrogen balance on the solvents; we accounted for approximately 69% of lost carbon and 69% of lost nitrogen (total of MDEA and PZ loss) with the positively identified compounds listed in Table 2. EDA was not observed in the degraded blend, whereas EDA is the major degradation product in cycled 8 m PZ.

As in all previous degradation experiments performed with the ISDA, we hydrolyzed samples with 50 wt % NaOH to reverse the formation of amides in solution, and measured heat stable salts (carboxylate ions) including formate and glycolate afterwards. We present these data as "total" formate, which represents the concentration of both formate and amides formed in solution. The difference between total formate and formate concentration is formyl amide concentration. Using cation IC, we identified and quantified FPZ in unhydrolyzed samples. For all carbon and nitrogen balance calculations, we assumed that amides formed were all FPZ, although the possibility exists that amides of other compounds including DEA were formed. Unlike cycled 7 m MDEA, the total formate concentration was more than double the formate concentration, indicating that the amount of FPZ measured in the blend was at least as much as formate.

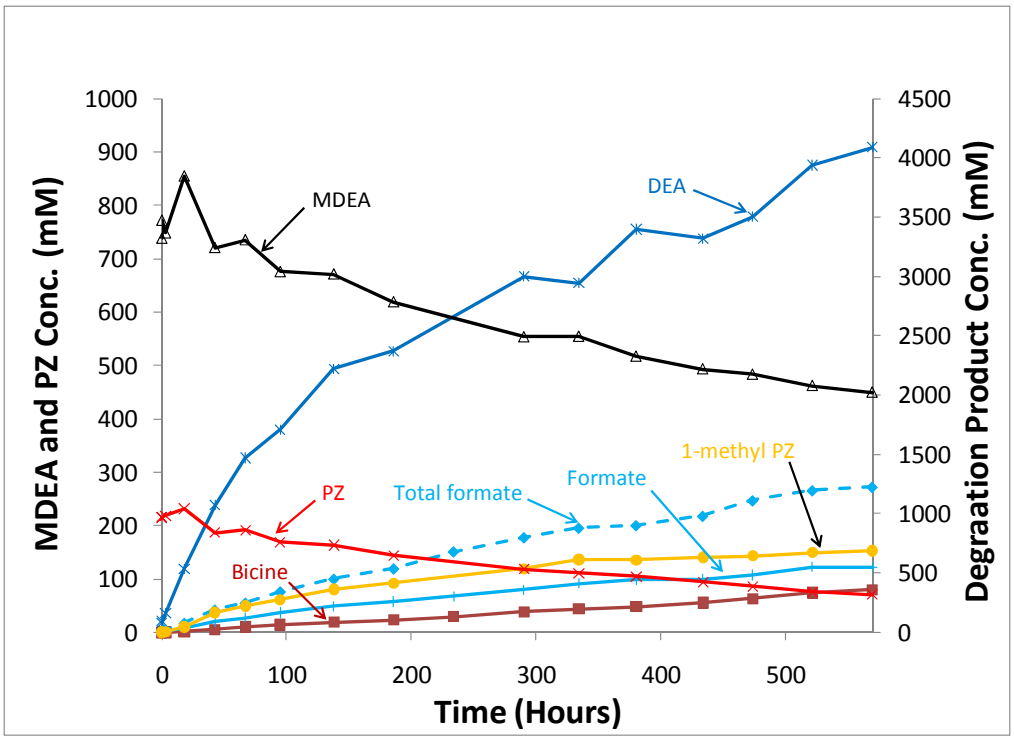

Figure 3: Degradation Products in 7 m MDEA/2 m PZ Cycled from 55 to 120 °C

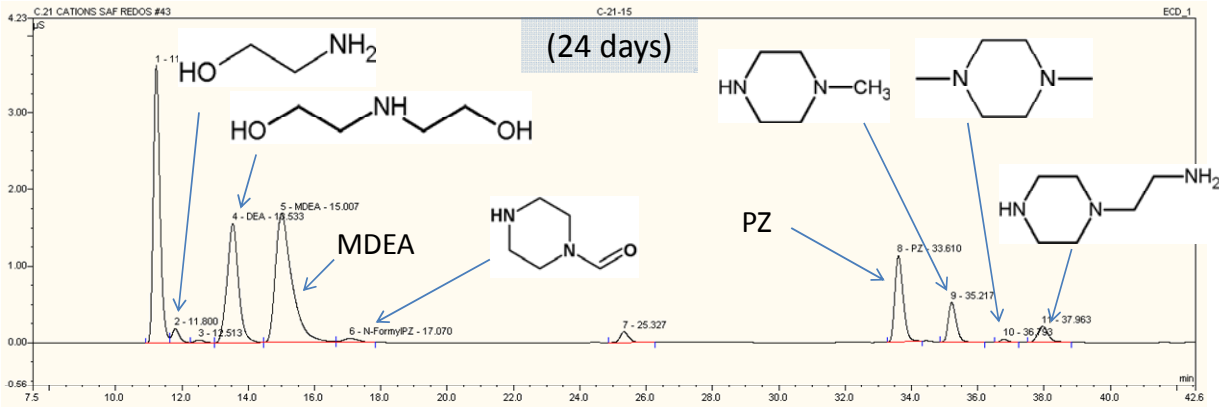

Figure 4: IC/MS Chromatogram - 7 m MDEA/2 m PZ cycled for 570 hrs from 55 to 120 °C

The carbon and nitrogen associated with DEA comprised 40 and 35%, respectively, of the total carbon and nitrogen loss of the parent amines in the solvent (MDEA and PZ). MPZ comprised 8.4 and 11.8%, respectively, of the carbon and nitrogen loss, making it the next major degradation product in the solvent. DMPZ concentrations comprised approximately one tenth of the carbon and nitrogen loss that MPZ represented, indicating that a second methyl group arm-switching step only occurs with one tenth of the MPZ formed as the solvent degrades. MPZ formed immediately as the solvent was cycled, reaching ~60 mM after only 100 hours of cycling, whereas, at this point in the cycling experiment, no DMPZ had formed. Likewise, no AEP had formed at this point in the experiment, indicating that the formation of both DMPZ and

AEP lagged the formation of MPZ by ~100 hours. It is likely that other products including MPZ and MEA act as intermediates in the formation of DMPZ and AEP before these products can form.

Table 2: Carbon and Nitrogen Balance – Cycled 7 m MDEA/2 m PZ

Compound	Quant Method	% of C-Loss	% of N-Loss
Diethanolamine	Cation IC	40	35
Ethylenediamine	Cation IC	0	0
1-methyl PZ	Cation IC	8.4	11.8
Dimethyl PZ	Cation IC	0.9	1
Aminoethyl PZ	Cation IC	3.5	6.2
Formate	Anion IC	1.3	0
Amides (as formate)	Anion IC	8.3	11.6
Oxalate	Anion IC	0.3	0
Acetate	Anion IC	0.9	0
Bicine	AAA - HPLC	5.3	3.1
Other Amino Acids	AAA - HPLC	~5	~3
	Total % =	69 (~74)	69 (~72)

The amino acid bicine, and to a much lesser extent glycine, were measured in the cycled blend. Bicine production experienced no lag time, but formed at approximately one-third the rate observed in cycled 7 m MDEA (0.14 compared to 0.34 mM/hr). Bicine was a major degradation product of MDEA, but was not observed when the 98% oxygen was replaced with 98% nitrogen in the headspace gas, indicating that bicine production requires dissolved oxygen. With this fact in mind, it is likely that the reduced bicine production rate was due to a competition for the dissolved oxygen in the solvent blend in C-21. DEA production was also increased and dependent on dissolved oxygen in 7 m MDEA, and this degradation process is likely competing with the process to create bicine for the oxygen as the blend degrades.

We compared the amount of carbon associated with DEA and bicine to that lost as MDEA only (excluding PZ carbon loss) and estimated it to be ~64%. The other positively identified products represent PZ derivatives, or carboxylate ions (heat stable salts) in the degraded solvent. The unaccounted for portion of the MDEA likely consists of amine degradation products similar in structure to monoethanolamine (MEA) and MDEA; we identified small amounts of MEA, methylaminoethanol (MAE) and dimethylaminoethanol (DMAE) in the final sample of cycled 7 m MDEA/2 m PZ. However, these compounds represent no more than 1% of carbon loss from MDEA.

We compared the amount of carbon associated with the PZ derivatives (MPZ, DMPZ, AEP, and FPZ) to that lost as PZ loss, and estimated this amount to be ~51%. In terms of conservation of PZ rings, we recovered approximately 57% of PZ ring loss by accounting for these same four compounds. The unaccounted for PZ ring loss is likely associated with some ring opening/destruction, creating ethylamino groups and other fragments in the degraded solvent.

Figure presents the amino acid chromatograph for the end sample from C-21. The amino acid analyses indicate that bicine and glycine form in degraded 7 m MDEA/2 m PZ, and at least one and possibly two other amino acids form at appreciable concentrations in the solvent with retention times between those of glycine and bicine. Assuming the peaks represent a single amino acid, and the response factor for this compound is approximately the same as for bicine, the concentration of this unidentified amino acid is approximately the same as reported for bicine given the peak area. Therefore, we can close the carbon and nitrogen balance for the degraded solvent another 5 to 10%, as listed in Table 2. With this additional carbon and nitrogen accounted for, the total recovered carbon and nitrogen are 74 and 72%, respectively.

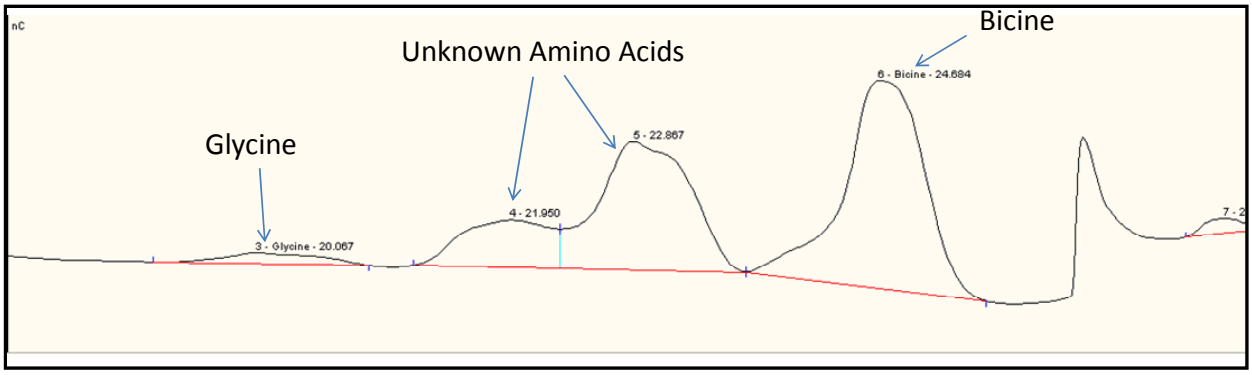

Figure 5: Amino Acid Chromatogram - Cycled 7 m MDEA/2 m PZ

Figure is a gas chromatography/mass spectrometry (GC/MS) chromatogram for the final sample collected in experiment C-21 (cycled for 570 hours). This sample was separated using a Stabilwax polar column and analyzed using a mass spectrometer (MS) in triple quad mode to fragment compounds and perform library matches of each. We have assigned compound identification to major compounds separated in the sample. Of significance, we identified methylaminoethanol (MAE), dimethylaminoethanol (DMAE), and two other amino acids in the sample. Both MAE and DMAE have been identified in cycled MDEA. However, based on the cation IC and amino acid chromatograms, none of these amines or amino acids comprise a significant portion of carbon or nitrogen.

Figure presents the ratio of mole of MDEA lost to moles of PZ lost. After approximately 350 hours of solvent cycling, the ratio was 2:1. With two moles of alkalinity per mole of PZ, this ratio of 2:1 represents a 1:1 ratio of moles of alkalinity from MDEA to moles alkalinity from PZ. The loss rate of nitrogen from MDEA and PZ was 2.3 mM/hr each for a total nitrogen loss rate of 4.6 mM/hr. This rate is in contrast to the total nitrogen loss rate of 6.2 mM/hr from cycled 7 m MDEA (C-6) and 2.4 mM/hr from cycled 8 m PZ (C-16). Total alkalinity loss rates for the three solvents from greatest to least were measured as: 7 m MDEA/2 m PZ > 7 m MDEA > 8 m PZ. If we compare the loss rate of PZ in the blend (20%/wk) to the loss rate of PZ in experiment C-16 (5%/wk) which entailed cycling 8 m PZ at the same conditions, the blend experienced a preferential loss of PZ.

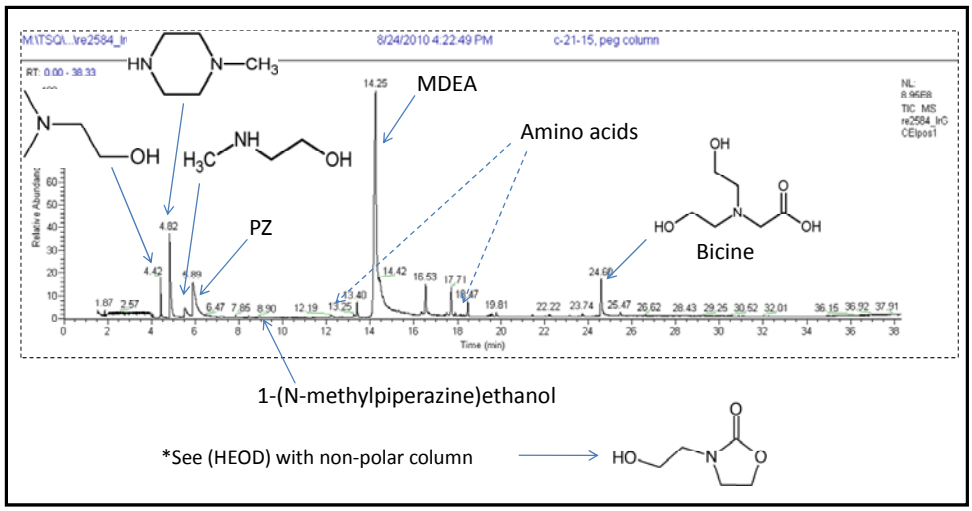

Figure 6: GC/MS Chromatogram - Cycled 7 m MDEA/2 m PZ

Explanations for the 1:1 ratio of alkalinity loss as MDEA and as PZ in the blend do not come from the typical mechanisms (Polderman, 1956) that explain the formation of DEA, DEA-carbamate, and 3-(2-hydroxyethyl)-2-oxazolidone (HEOD) in the degraded solvent. Further, from Figure it is evident that MDEA loss lags PZ loss in the blend, indicating that the PZ is being degraded preferentially (up to four-to-one rate) for the first 250 hours of the experiment. PZ is actively participating in a reaction that is converting the PZ to PZ derivatives from the beginning of the experiment (Figure 8). MPZ is formed immediately, with a slight lag in the formation of DMPZ, and a nearly 300 hour lag in formation of AEP. As discussed above, the MPZ is formed first, followed by the extraction of an additional methyl group from MDEA by the MPZ to produce DMPZ. This process only happens to approximately 10% of the MPZ by the end of the experiment.

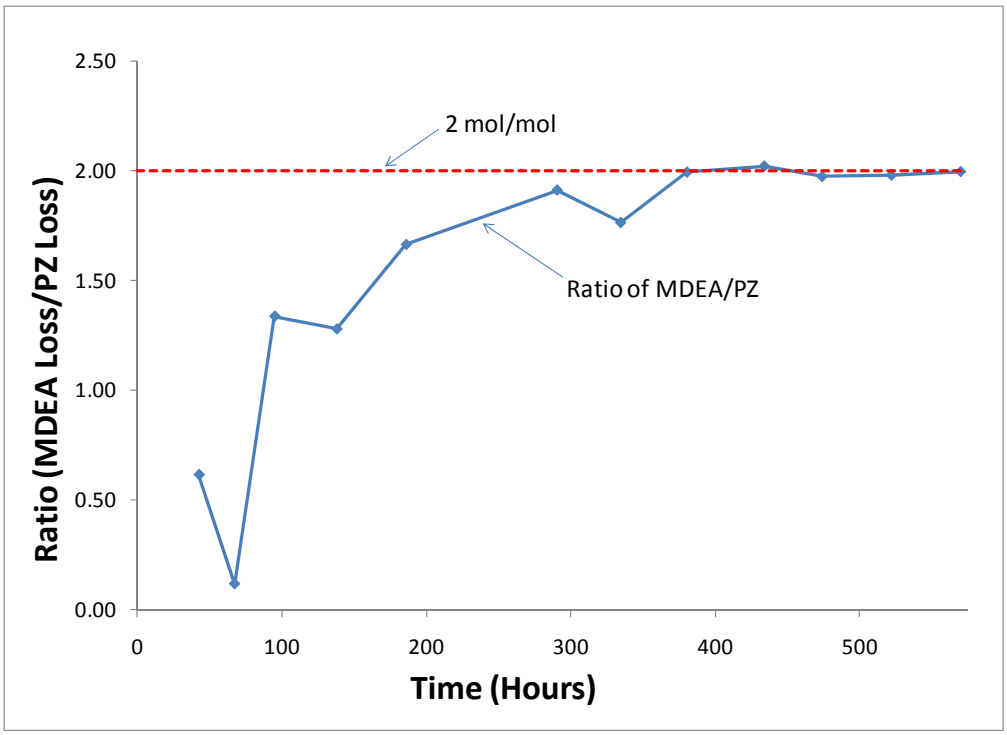

Figure 7: Ratio of MDEA Loss/PZ Loss - 7 m MDEA/2 m PZ from 55 to 120 °C

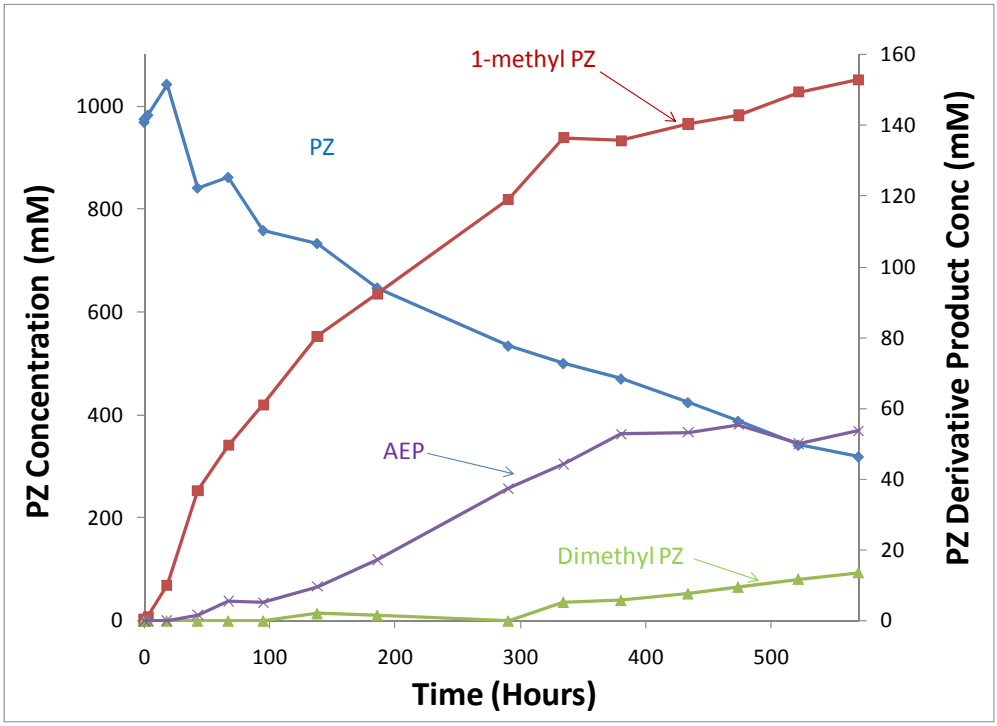

Figure 8: PZ Derivatives in Cycled 7 m MDEA/2 m PZ

Experiment C-22

Experiment C-22 was performed with 7 m MDEA/2 m PZ (α = 0.14 mols CO_2/mol alkalinity) cycled from 55 to 90 °C for almost 600 hours. The cation data associated with that experiment are incomplete at this time, but will be available within the next two weeks. However, the anion IC and amino acid data are now available and discussed in this quarterly report.

The formate production rate was ~0.41 mM/hr, compared to the rate measured in the blend when cycled to 120 °C of 0.5 mM/hr. The rate of 0.41 mM/hr can also be compared to the separate rates measured in 7 m MDEA and 8 m PZ of 0.12 and 0.01 mM/hr, respectively. The ratio of formate to amide produced with time is plotted for both C-21 and C-22 in Figure 9. In both cases, formate production lags amide formation for approximately 50 hours of cycling, but a peak in the ratio occurs at approximately 390 hours, with a relative leveling off at a slightly lower ratio (~0.82–0.85). Thus, amide formation occurs to a greater extent at the beginning of the degradation process until formate production reaches an equilibrium condition with amides in the solvent. In terms of formate production at the lower thermal temperature of 90 °C, from greatest to least formate production, the solvents can be ranked as follows: 7 m MDEA/2 m PZ > 7 m MDEA > 8 m PZ.

At 425 hours into this cycling experiment, the solvent sample was collected in triplicate, with all three samples handled in an identical manner, including dilution and injection in the cation and anion IC instruments. Using the data collected from these samples, we calculated the average and standard deviation of all major degradation product concentrations. The MDEA, formate, and bicine averages were 1857.6. ± 10.6 mM, 80.6 ± 1.6, and 80.0 ± 0.9 mM, respectively, indicating that all three methods (anion IC, cation IC, and amino acids-HPLC) provide a high level of reproducibility.

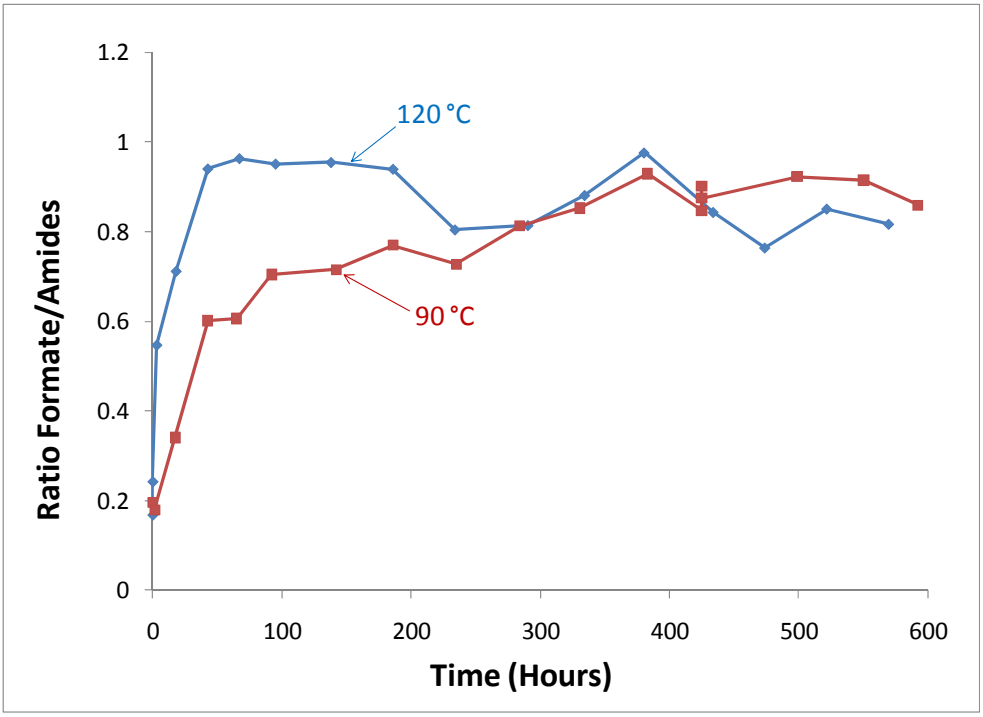

Figure 9: Ratio Formate/Amides in cycled 7 m MDEA/2 m PZ

Experiment C-23

Experiment C-23 was started at the end of the third quarter, and results will be available in the next quarterly report. C-23 entails cycling 7 m MDEA/2 m PZ at an initial loading of 0.14 mols CO_2/mol alkalinity from 55 to 100 °C in the ISDA. We will use the data generated in C-23 to develop a kinetic model similar to the model developed for 7 m MDEA (Rochelle et al., 2010).

Thermal Experiments

In the third quarter we initiated Thermal 15, 16, and 17. We completed the removal from the oven of all sample cylinders for Thermal 15 and 17, while sample cylinders will continue to be removed from the oven for Thermal 16 through November 2010 to ensure a complete set of degradation kinetics data.

Thermal No. 15

In Thermal 15, we thermally degraded 7 m MDEA combined with 1 m quaternary amine (tetramethyl ammonium chloride) at loadings of 0 and 0.2 mols CO_2/mol alkalinity in order to determine the effect of a more concentrated quaternary amine on the degradation of MDEA. In a previous thermal degradation experiment (Thermal 14) with MDEA and the quaternary amine, we determined that the quaternary amine caused arm-switching and the formation of MEA, DEA, N,N'-dimethyl ethanamine (DMEA), and hydroxyethyl piperazine (HEP). The sample cylinders in Thermal 14 were charged with solvent and the endcaps sealed under a nitrogen blanket. We did not detect the presence of bicine or DEA in that experiment, further supporting the conclusion that these compounds are formed through an oxidative process. In Thermal 15, we hope to determine the role of loading and quaternary amine concentration on the formation of products which are the result of arm-switching.

All sample cylinders for Thermal No. 15 have been removed from the ovens and are currently being analyzed. Data for this experiment will be available in the fourth quarter 2010.

Thermal No. 16

Thermal 16 is a repeat of Thermal 7 experiment conducted in 2008 in which we thermally degraded 7 m MDEA/2 m PZ at 120, 135, and 150 °C at two different loadings. Cylinders for Thermal 16 have been placed in ovens at 120, 135, and 150 °C and at loadings of 0, 0.1, and 0.25 mols CO_2/mol alkalinity. A subset of the sample cylinders was charged with solvent and the endcaps sealed under a nitrogen gas blanket to minimize the role of oxygen in the thermal degradation process.

In the process of completing Thermal No. 7, we encountered several issues including the failure of several Swagelok thermal sample cylinders due to over-pressurization or improper seal of the endcaps. Therefore we are repeating this important study to confirm several key observations made based on the data from the previous study. Those observations include an equimolar loss of MDEA and PZ over the course of the experiment until complete loss of the PZ was experienced. This observation is similar to that made in this quarterly report for C-21 where we observed an equimolar loss of alkalinity groups (N) from the MDEA and PZ, with the actual molar ratio of the parent compound loss 2:1 (MDEA:PZ). In the oxygen-free environment of the sample cylinders, the ratio may be closer to 1:1. Data from Thermal No. 16 will be available in the fourth quarter 2010.

Removal of all Thermal No. 16 sample cylinders from ovens will occur in November, and data from this experiment will be available in the fourth quarter 2010.

Thermal No. 17

In Thermal No. 17, we created a 7 m MDEA/2 m PZ solvent with no CO_2 loading. This solvent was then amended with 0.1 mols acid/mol alkalinity using toluene sulfonic acid (TSA). TSA has a molecular weight of 190.2 gm/gmol, and is considered monoprotic. This experiment was performed to test for the thermal degradation of the solvent when 10% of the alkalinity was neutralized, but in the absence of CO_2 to eliminate carbamate polymerization steps due to primary and secondary amine formation as the solvent degrades.

All sample cylinders for Thermal No. 17 have been removed from the ovens and are currently being analyzed. Data for this experiment will be available in the fourth quarter 2010.

Conclusions When 7 m MDEA was amended with 200 mM formate to test for a competition for dissolved oxygen among formate, bicine, and DEA, MDEA loss rate was comparable to that measured without formate amendment (4.2 mM/hr), but the alkalinity loss rate was one quarter (1.3 compared to 5.3 mM/hr). DEA production was suppressed (0.2 compared to 2.6 mM/hr), while bicine production (~0.9 mM/hr) increased 3X. The presence of formate at 175 mM may have caused the forward reaction (DEA formation through methyl group loss from MDEA) to slow in order to reach equilibrium.

When 7 m MDEA/2 m PZ (α = 0.14 mols CO_2/mol alkalinity) was cycled from 55 to 120 °C for 570 hours, the first order loss rates of MDEA and PZ were 12 and 20%/wk, respectively. The major degradation products observed were DEA, MPZ, DMPZ, AEP, FPZ, bicine, and formate, with 69% of lost carbon and nitrogen accounted for. FPZ concentration was at least as much as formate. This is in contrast to observations from 7 m MDEA where amide(s) concentration was less than formate.

The carbon and nitrogen associated with DEA comprised 40 and 35%, respectively, of the total carbon and nitrogen loss of the parent amines (MDEA and PZ). The carbon associated with the PZ derivatives (MPZ, DMPZ, AEP, and FPZ) comprised ~51% of PZ loss. These same four compounds make up 57% of PZ ring loss. The unaccounted for PZ ring loss may be associated with ring opening/destruction, creating ethylamino groups and other fragments in the degraded solvent. Bicine production experienced no lag time in the blend, but formed at approximately one-third the rate observed in cycled 7 m MDEA (0.14 compared to 0.34 mM/hr). Previous cycling experiments with 7 m MDEA established that bicine production requires dissolved oxygen.

The ratio of moles of MDEA lost to moles of PZ lost after 350 hours of cycling was 2:1, which is a 1:1 ratio of moles of alkalinity lost from MDEA to moles alkalinity lost from PZ. The loss rate of nitrogen from MDEA and PZ in the blend was 2.3 mM/hr each, for a total nitrogen loss rate of 4.6 mM/hr. The total nitrogen loss rate from 7 m MDEA and 8 m PZ were 6.2 mM/hr and 2.4 mM/hr, respectively. Total alkalinity loss rates for the three solvents from greatest to least were measured as: 7 m MDEA/2 m PZ > 7 m MDEA > 8 m PZ. The loss rate of PZ of 20%/wk in the blend indicates the blend experienced a preferential PZ loss.

When 7 m MDEA/2 m PZ (α = 0.14 mols CO2/mol alkalinity) was cycled from 55 to 90 °C, the formate production rate was ~0.41 mM/hr, which was greater than the rates measured in 7 m MDEA (0.12 mM/hr) and 8 m PZ (0.01 mM/hr). Formate production lagged amide formation

for approximately 50 hours of cycling at thermal reactor temperatures of 90 and 120 °C, but the ratio leveled off at ~0.82.

Future Work

Work planned for the 4th Quarter 2010 will include the completion of C-23 which is currently underway. C-23 involves the cycling of 7 m MDEA/2 m PZ from 55 to 100 °C with the 98% O_2/2% CO_2 headspace purge gas.

The ISDA will then be retrofitted with a thermal reactor that is approximately 1/10 the volume of the current reactor. This change is being conducted to test the effect on degradation reaction kinetics of reducing the residence time of solvent at the higher temperature; it is currently believed that any dissolved oxygen that travels with the solvent into the thermal reactor is completely consumed at the higher experimental temperatures (> 110 °C), resulting in an oxygen-depleted condition at these conditions. With a reduced thermal reactor size, we believe we will be able to measure reaction kinetics by allowing excess oxygen to exist in the solvent through the entire cycle.

We will complete cycling experiments with 7 m MDEA/2 m PZ at different temperatures to establish reaction rates and build an oxidative degradation model for this solvent as was completed for 7 m MDEA. Finally, we will cycle DEA to test for the production of bicine. Cycling of DEA will enable us to determine whether bicine is formed as a direct result of the degradation of MDEA to DEA, or through some other mechanism.

Finally, we will complete the data collection and analysis of samples from Thermals 15, 16, and 17 using IC, IC-MS, and GC-MS methods.

References

Bedell S, Dow, Personal communication with F. Closmann, January 2010.

Polderman LD, Steele AB. “Why Diethanolamine Breaks Down in Gas-Treating Service.” *Oil and Gas J*. July 30, 1956:206–214.

Rochelle GT et al. "CO_2 Capture by Aqueous Absorption, Second Quarterly Progress Report 2010." Luminant Carbon Management Program. The University of Texas at Austin. 2010.

Table A-1

Cycling Experiment C-20

Solvent: 7 m MDEA, Ldg = 0.1 moles CO_2/mole alkalinity, 200 mM Formate

Amendments: 0.4 mM Fe/0.1 mM Cr/0.05 mM Ni; 98 % O_2/2 % CO_2

Conditions: 55 °C/120 °C

Conducted: June/July 2010

		Amine Concentration					Heat Stable Salts Concentrations				Amino Acids	
Sample No.	Degradation Time (hr)	MDEA (Tit) (m)	MDEA (Cations) (mM)	α_{act} (moles CO_2/mole alk)	Corrected (m)	DEA (mM)	Formate (mM)	Glycolate (mM)	Oxalate (mM)	Sulfate (mM)	Bicine (mM)	Glycine (mM)
C-20-0a	0	6.87	4118.5	0.096	6.87	0.0	0.77	0.00	0.00	0.76	0.00	0.00
C-20-0b	0	5.89	3986.7	0.101	5.91	0.0	175.63	0.00	0.00	0.83	0.00	0.00
C-20-1	1.5	5.81	3718.7	0.098	5.83	0.0	169.86	0.28	0.00	0.94	0.39	0.00
C-20-2	17.8	5.72	3631.6	0.081	5.73	16.9	150.32	2.27	0.11	0.94	13.93	0.00
C-20-3	46.8	5.67	3517.7	0.073	5.68	146.6	120.94	4.66	0.67	0.88	50.79	0.00
C-20-4	70.8	5.58	3377.6	0.072	5.59	42.0	103.16	6.16	1.07	0.97	81.10	0.00
C-20-5	95.8	5.47	3471.9	0.052	5.48	23.4	93.69	7.05	1.04	0.61	99.84	0.00
C-20-6	119.8	5.34	3419.9	0.046	5.36	65.2	84.04	7.96	1.61	0.81	119.86	0.00
C-20-7	138.8	5.37	3372.0	0.044	5.38	43.9	68.05	7.63	1.62	0.91	119.33	8.93
C-20-8	187.8	5.18	3193.0	0.050	5.20	31.1	64.21	10.24	2.38	0.86	178.45	16.98
C-20-9	213	5.08	2932.6	0.050	5.10	10.1	58.58	11.16	3.01	0.88	203.33	21.08
C-20-10	237	5.00	2885.7	0.045	5.01	52.3	56.79	11.62	3.31	0.89	218.63	23.05
C-20-11	261.8	4.97	2703.3	0.025	4.98	104.4	54.15	12.23	3.64	0.86	231.28	25.93
C-20-12	282.8	4.91	2665.2	0.049	4.92	30.4	49.91	12.76	3.52	0.68	248.67	32.69

Table A-2

Cycling Experiment C-20 (Hydrolyzed Samples)

Solvent: 7 m MDEA, Ldg = 0.1 moles CO_2/mole alkalinity, 200 mM Formate

Amendments: 0.4 mM Fe/0.1 mM Cr/0.05 mM Ni; 98 % O_2/2 % CO_2

Conditions: 55 °C/120 °C

Conducted: June/July 2010

		Amine Concentration					Heat Stable Salts Concentrations				Amino Acids	
Sample No.	Degradation Time (hr)	MDEA (Tit) (m)	MDEA (Cations) (mM)	α_{act} (moles CO_2/mole alk)	Corrected (m)	DEA (mM)	Formate (mM)	Glycolate (mM)	Oxalate (mM)	Sulfate (mM)	Bicine (mM)	Glycine (mM)
C-20-0a+NaOH	0	6.87	3898.9	0.096	6.87	0.0	2.1	0.0	0.0	1.5	0.0	0.0
C-20-0b+NaOH	0	5.89	3558.2	0.101	5.91	0.0	175.5	0.0	0.0	1.4	0.0	0.0
C-20-1+NaOH	1.5	5.81	3604.5	0.098	5.83	61.9	174.7	0.5	0.0	0.9	0.0	0.0
C-20-2+NaOH	17.8	5.72	3464.2	0.081	5.73	46.3	168.1	2.9	0.2	0.9	12.0	0.0
C-20-3+NaOH	46.8	5.67	3670.9	0.073	5.68	22.5	142.7	5.1	0.9	1.3	46.4	0.0
C-20-4+NaOH	70.8	5.58	2908.3	0.072	5.59	46.1	126.7	6.6	1.4	1.3	74.5	0.0
C-20-5+NaOH	95.8	5.47	3339.2	0.052	5.48	31.3	118.5	7.5	1.6	1.8	94.7	4.9
C-20-6+NaOH	119.8	5.34	3849.1	0.046	5.36	23.5	125.3	9.6	1.8	1.5	128.0	7.9
C-20-7+NaOH	138.8	5.37	3205.2	0.044	5.38	80.4	104.5	10.1	1.9	0.9	124.0	7.4
C-20-8+NaOH	187.8	5.18	2953.0	0.050	5.20	91.4	89.0	10.6	2.9	1.3	163.4	11.6
C-20-9+NaOH	213	5.08	2799.1	0.050	5.10	35.7	82.6	11.3	3.5	1.2	180.5	12.8
C-20-10+NaOH	237	5.00	2548.1	0.045	5.01	83.7	78.9	11.9	3.7	1.5	192.3	14.1
C-20-11+NaOH	261.8	4.97	2415.3	0.025	4.98	30.1	75.0	12.4	4.2	1.1	206.3	15.9
C-20-12+NaOH	282.8	4.91	2553.7	0.049	4.92	53.1	71.1	12.8	4.1	1.4	225.3	19.8

Table A-3

Cycling Experiment C-21

Solvent: 7 m MDEA/2 m PZ, Ldg = 0.14 moles CO_2/mole alkalinity

Amendments: 0.4 mM Fe/0.1 mM Cr/0.05 mM Ni; 98 % O_2/2 % CO_2

Conditions: 55 °C/120 °C

Conducted: August 2010

							Heat Stable Salts Concentrations					Amino Acids	
Sample No.	Degradation Time (hr)	MDEA (Cations) (mM)	PZ (Cations) (mM)	α_{act} (moles CO_2/mole alk)	DEA (mM)	EDA (mM)	Formate (mM)	Glycolate (mM)	Oxalate (mM)	Acetate (mM)	Sulfate (mM)	Bicine (mM)	Glycine (mM)
C-21-0a	0	3321	968	0.138	18	0.0	0.3	0.0	0.0	0.2	1.0	0.0	0.0
C-21-0b	0	3473	974	0.137	21	0.0	0.6	0.0	0.0	0.1	1.1	0.0	0.0
C-21-1	3	3366	982	0.136	35	0.0	1.5	0.0	0.0	0.1	1.2	0.0	0.0
C-21-2	18	3846	1042	0.135	119	0.0	7.2	0.4	0.1	1.5	1.1	1.4	0.0
C-21-3	42.5	3242	841	0.137	238	0.0	20.5	0.5	0.7	4.2	1.3	5.0	0.0
C-21-4	67	3308	861	0.134	327	0.0	27.1	0.8	2.2	5.4	1.7	9.8	0.2
C-21-5	95	3040	758	0.129	380	0.0	37.3	0.8	2.3	7.9	1.3	14.0	0.4
C-21-6	138	3020	733	0.118	494	0.0	49.0	1.0	3.3	10.4	1.4	19.0	0.4
C-21-7	186	2785	647	0.108	527	0.0	57.9	1.5	3.2	13.0	1.1	23.2	0.7
C-21-8	234	3894	614	0.11	651	0.0	67.5	1.4	5.3	15.6	1.4	29.7	0.8
C-21-9	290.5	2490	534	0.107	667	0.0	79.9	1.4	6.7	20.4	1.4	38.4	1.1
C-21-10	334.5	2494	500	0.103	655	0.0	91.8	1.7	7.1	26.5	0.9	44.0	1.2
C-21-11	380.5	2327	470	0.091	755	0.0	99.1	2.0	9.0	27.0	1.3	47.7	1.4
C-21-12	434	2220	424	0.09	738	0.0	99.7	1.8	9.9	30.4	1.3	55.7	1.8
C-21-13	474	2174	388	0.096	779	0.0	107.0	1.9	11.7	33.0	1.2	63.3	2.3
C-21-14	522	2079	342	0.1	875	0.0	122.3	2.0	13.4	37.5	1.2	74.1	2.5
C-21-15	570	2023	319	0.09	909	0.0	122.5	2.2	15.6	41.3	1.4	79.9	2.8

Table A-4

Cycling Experiment C-21 (Hydrolyzed Samples)

Solvent: 7 m MDEA/2 m PZ, Ldg = 0.14 moles CO_2/mole alkalinity

Amendments: 0.4 mM Fe/0.1 mM Cr/0.05 mM Ni; 98 % O_2/2 % CO_2

Conditions: 55 °C/120 °C

Conducted: August 2010

							Heat Stable Salts Concentrations					Amides	Amino Acids	
Sample No.	Degradation Time (hr)	MDEA (Cations) (mM)	PZ (Cations) (mM)	α_{act} (moles CO_2/mole alk)	DEA (mM)	EDA (mM)	Formate (mM)	Glycolate (mM)	Oxalate (mM)	Acetate (mM)	Sulfate (mM)	NFPZ (mM)	Bicine (mM)	Glycine (mM)
C-21-0a	0	3523	1041	0.138	19	0.0	2.1	0.0	0.0	0.0	1.4	1.8	0.0	0.0
C-21-0b	0	3518	1034	0.137	34	0.0	3.0	0.0	0.7	0.0	1.6	2.4	0.0	0.0
C-21-1	3	3458	1028	0.136	56	0.0	4.2	1.2	0.1	0.4	1.3	2.7	0.0	0.0
C-21-2	18	3415	960	0.135	100	0.0	17.4	1.3	0.5	3.5	1.6	10.2	1.8	0.0
C-21-3	42.5	3614	937	0.137	256	0.0	42.4	0.0	1.2	7.0	1.4	21.8	7.6	0.0
C-21-4	67	3442	844	0.134	330	0.0	55.3	0.0	3.0	7.3	2.2	28.2	10.8	0.0
C-21-5	95	3175	798	0.129	427	0.0	76.5	2.0	3.8	9.4	2.2	39.2	15.2	0.5
C-21-6	138	3042	759	0.118	526	0.0	100.3	0.0	4.7	11.6	1.8	51.3	20.8	0.6
C-21-7	186	2890	702	0.108	577	0.0	119.6	3.2	6.3	14.6	2.0	61.7	26.1	0.7
C-21-8	234	2856	678	0.11	656	0.0	151.5	4.2	7.9	19.8	2.0	84.0	24.4	1.0
C-21-9	290.5	2747	602	0.107	770	0.0	178.0	3.0	9.4	21.6	2.1	98.2	41.0	1.1
C-21-10	334.5	2685	550	0.103	801	0.0	196.0	3.2	10.7	24.8	1.7	104.2	45.8	1.5
C-21-11	380.5	2628	515	0.091	831	0.0	200.6	4.0	12.3	25.8	1.9	101.5	51.7	1.4
C-21-12	434	2532	477	0.09	886	0.0	218.1	3.5	14.4	29.9	2.1	118.4	60.5	1.8
C-21-13	474	2458	453	0.096	928	0.0	247.2	4.9	16.4	33.6	2.2	140.2	67.6	2.4
C-21-14	522	2341	410	0.1	1014	0.0	266.1	3.6	20.3	37.3	2.2	143.8	77.4	2.8
C-21-15	570	2241	366	0.09	1013	0.0	272.5	3.5	18.2	37.9	2.2	150.0	NA	NA

Table A-5

Cycling Experiment C-22

Solvent: 7 m MDEA/2 m PZ, Ldg = 0.14 moles CO_2/mole alkalinity

Amendments: 0.4 mM Fe/0.1 mM Cr/0.05 mM Ni; 98 % O_2/2 % CO_2

Conditions: 55 °C/90 °C

Conducted: Aug/Sept 2010

							Heat Stable Salts Concentrations					Amino Acids	
Sample No.	Degradation Time (hr)	MDEA (Cations) (mM)	PZ (Cations) (mM)	α_{act} (moles CO_2/mole alk)	DEA (mM)	EDA (mM)	Formate (mM)	Glycolate (mM)	Oxalate (mM)	Acetate (mM)	Sulfate (mM)	Bicine (mM)	Glycine (mM)
C-22-0	0	NA	NA	NA	NA	NA	0.5	0.0	0.0	0.0	2.3	0.0	0.0
C-22-1	1.5	NA	NA	NA	NA	NA	0.6	0.0	0.0	0.0	1.8	0.0	0.0
C-22-2	17.5	NA	NA	NA	NA	NA	1.7	0.0	0.0	0.0	1.4	0.0	0.0
C-22-3	42.5	NA	NA	NA	NA	NA	3.7	0.0	0.0	0.0	1.6	0.0	0.0
C-22-4	65	NA	NA	NA	NA	NA	6.0	0.0	0.0	0.0	0.9	1.1	0.0
C-22-5	92	NA	NA	NA	NA	NA	8.2	0.0	0.0	0.0	1.6	3.1	0.0
C-22-6	142	NA	NA	NA	NA	NA	13.7	0.0	0.0	0.0	1.1	11.5	0.0
C-22-7	186	NA	NA	NA	NA	NA	26.6	0.0	1.5	0.0	1.8	24.8	0.0
C-22-8	235	NA	NA	NA	NA	NA	38.2	0.0	1.5	0.0	1.0	37.8	0.0
C-22-9	284	NA	NA	NA	NA	NA	54.2	0.0	2.5	0.0	1.0	50.2	0.0
C-22-10	330.5	NA	NA	NA	NA	NA	61.0	0.0	3.7	0.0	1.1	57.3	0.0
C-22-11	383	NA	NA	NA	NA	NA	75.4	0.0	5.1	0.0	1.3	71.5	0.0
C-22-12a	425	NA	NA	NA	NA	NA	79.3	0.0	6.5	0.0	1.4	79.1	0.0
C-22-12b	425	NA	NA	NA	NA	NA	80.0	0.0	6.0	0.0	1.3	79.8	0.0
C-22-12c	425	NA	NA	NA	NA	NA	82.4	0.0	5.9	0.0	1.2	81.0	0.0
C-22-13	499	NA	NA	NA	NA	NA	95.0	0.0	8.0	0.0	1.3	94.8	0.0
C-22-14	550.5	NA	NA	NA	NA	NA	102.7	0.0	9.5	0.0	1.5	110.5	0.0
C-22-15	592.5	NA	NA	NA	NA	NA	105.4	0.0	10.9	0.0	1.3	117.8	0.0

Table A-6

Cycling Experiment C-22 (Hydrolyzed Samples)

Solvent: 7 m MDEA/2 m PZ, Ldg = 0.14 moles CO_2/mole alkalinity

Amendments: 0.4 mM Fe/0.1 mM Cr/0.05 mM Ni; 98 % O_2/2 % CO_2

Conditions: 55 °C/90 °C

Conducted: Aug/Sept 2010

							Heat Stable Salts Concentrations					Amides	Amino Acids	
Sample No.	Degradation Time (hr)	MDEA (Cations) (mM)	PZ (Cations) (mM)	α_{act} (moles CO_2/mole alk)	DEA (mM)	EDA (mM)	Formate (mM)	Glycolate (mM)	Oxalate (mM)	Acetate (mM)	Sulfate (mM)	NFPZ (mM)	Bicine (mM)	Glycine (mM)
C-22-0	0	NA	NA	NA	NA	NA	3.0	0.0	0.0	0.0	2.2	2.5	0.0	0.0
C-22-1	1.5	NA	NA	NA	NA	NA	3.6	0.0	0.0	0.0	2.1	3.1	0.0	0.0
C-22-2	17.5	NA	NA	NA	NA	NA	6.6	0.0	0.0	0.0	1.7	4.9	0.0	0.0
C-22-3	42.5	NA	NA	NA	NA	NA	9.9	0.0	0.0	0.0	1.3	6.2	0.0	0.0
C-22-4	65	NA	NA	NA	NA	NA	15.9	0.0	0.0	0.0	5.7	9.9	2.7	0.0
C-22-5	92	NA	NA	NA	NA	NA	19.9	0.0	0.0	7.3	3.4	11.7	4.3	0.0
C-22-6	142	NA	NA	NA	NA	NA	32.9	0.0	0.0	0.0	1.7	19.2	9.0	0.0
C-22-7	186	NA	NA	NA	NA	NA	61.1	0.0	2.4	0.0	2.3	34.5	17.9	0.0
C-22-8	235	NA	NA	NA	NA	NA	90.8	0.0	4.0	0.0	1.8	52.6	34.3	0.0
C-22-9	284	NA	NA	NA	NA	NA	120.9	0.0	6.7	0.0	2.3	66.7	48.2	0.0
C-22-10	330.5	NA	NA	NA	NA	NA	132.4	0.0	7.0	0.0	1.6	71.5	50.4	0.0
C-22-11	383	NA	NA	NA	NA	NA	156.6	0.0	10.3	0.0	2.2	81.2	66.1	0.0
C-22-12a	425	NA	NA	NA	NA	NA	172.9	0.0	11.6	0.0	2.6	93.6	76.5	0.0
C-22-12b	425	NA	NA	NA	NA	NA	168.8	0.0	10.6	0.0	2.0	88.8	76.5	0.0
C-22-12c	425	NA	NA	NA	NA	NA	176.6	0.0	11.6	0.0	2.0	94.2	77.2	0.0
C-22-13	499	NA	NA	NA	NA	NA	198.0	0.0	14.2	0.0	2.2	103.0	91.0	0.0
C-22-14	550.5	NA	NA	NA	NA	NA	214.9	0.0	16.8	0.0	2.3	112.3	108.5	0.0
C-22-15	592.5	NA	NA	NA	NA	NA	228.2	0.0	15.1	0.0	2.6	122.8	103.8	0.0

Thermal Degradation and Oxidation of Concentrated Piperazine (PZ)

Quarterly Report for July 1 – September 30, 2010

by Stephanie A. Freeman

Supported by the Luminant Carbon Management Program

Department of Chemical Engineering

The University of Texas at Austin

October 31, 2010

Abstract

The concentration of piperazine (PZ) does not have a strong effect on the thermal degradation rate of 8 m PZ, indicating the rate is first order in amine loss. The concentration of formate and formyl amides increases directly with increased PZ and CO_2 concentration. The equilibrium between formate and formyl amides does not have a consistent trend between 4, 8, and 12 m PZ.

The concentration of ethylenediamine produced is consistent between degraded 4, 8, and 12 m PZ within the error limits of the cation IC, indicating that it is either not a direct function of PZ or CO_2 concentration, or likely an intermediate that also suffers from degradation itself.

In 12 m PZ, the formyl amides quantified through alkaline amide reversal track with N-formyl PZ measured directly with cation IC for the first six weeks of degradation at 175 °C. The N-formyl PZ then reaches an equilibrium concentration and the total formyl amides continue to increase.

Morpholine (Mor) is highly resistant to thermal degradation. A solution of 8 m Mor lost only 17% of the initial amine after 15 weeks of degradation at 175 °C, less than a comparable 8 m PZ experiment. Mor and piperidine are the only amines screened so far that are more resistant to thermal degradation than concentrated PZ. Hexamethylenediamine (HMDA) degrades readily at 175 °C losing 80% of the initial amine within 15 weeks.

A solution of 8 m PZ loaded with 0.3 mole $^{13}CO_2$ per mole alkalinity was degraded at 175 °C to show that formate is produced from CO_2 directly. ^{13}C NMR results of background samples and degraded PZ solutions confirmed the hypothesis that the carbon in formate is the same carbon as in the CO_2 molecule.

The addition of 500 mM formate to 8 m PZ did not strongly affect the oxidation of PZ or the generation of degradation products. In this experiment, formate quickly established equilibrium with formyl amides. Formate is not an oxidation inhibitor, and total formate was conserved, disproving the hypothesis that formate is being oxidized to CO_2.

The addition of 500 mM formaldehyde to 8 m PZ created stable, dense, white foam that persisted throughout the oxidation experiment. The foam likely decreased oxygen mass transfer rates, reducing the production of degradation products.

Oxidation of 8 m PZ with a rich loading of 0.42 mole CO_2 per mole alkalinity proceeded slower than a lean loading experiment (0.26 mole CO_2 per mole alkalinity). The result of the rich loading experiment was confounded by the increased CO_2 concentration, but reduced oxygen concentration.

The foaminess coefficient for oxidized 8 m PZ solutions does not accurately represent degradation. The measurement is not able to be repeated with any accuracy and is also a strong function of the amount of time between the end of an experiment and the foaminess test.

Introduction

Concentrated aqueous piperazine (PZ) is being investigated as a possible alternative to 30 wt % (or 7 m) MEA in absorber/stripper systems to remove CO_2 from coal-fired power plant flue gas (Freeman et al., 2010). PZ solutions are resistant to oxidation and thermal degradation, as previously shown at 5 and 8 m PZ (see previous quarterly reports). The kinetics of CO_2 absorption are faster in concentrated PZ (Cullinane and Rochelle, 2006; Dugas, 2009). The capacity of concentrated PZ is greater than that of MEA, while the heat of absorption and volatilities are both lower than MEA (Freeman et al., 2010; Nguyen and Rochelle, 2010)

This quarter was focused on continuing thermal degradation and oxidation experiments. Two experiments (TE32 and TE33) that concluded last quarter but were not analyzed in time to make the previous quarterly report are discussed here. Two experiments on PZ structural analogs (TE35 and TE36) concluded this quarter. One thermal degradation experiment was used in conjunction with NMR analysis to examine the production of formate in oxygen-poor thermal degradation (TE42). Two experiments (TE10 and TE11) continued through the quarter with periodic sampling. Sixteen new thermal experiments (TE43 through TE58) were started this quarter and will finish in the fourth quarter of 2010 and first quarter of 2011. Three new experiments in the newly redesigned oxidation reactor were completed and the results are reported here (OE20, OE21, and OE22). Mass spectrometry continued on experimental samples in an effort to identify new degradation products.

Analytical Methods

Total Inorganic Carbon Analysis (TIC)

Quantification of CO_2 loading was performed using a total inorganic carbon analyzer. In this method, a sample is acidified with 30 wt % H_3PO_4 to release the CO_2 present in solution (Hilliard, 2008). The CO_2 is carried in the nitrogen carrier gas stream to the detector. PicoLog software was used to record the peaks produced from each sample. A calibration curve was prepared at the end of each analysis using a TIC standard mixture of K_2CO_3 and $KHCO_3$. The TIC method quantifies the CO_2, CO_3^{-2}, and HCO_3^- present in solution. These species are in equilibrium in the series of reactions shown below in Equation 1.

$$CO_3^{2-} + 2H^+ \leftrightarrow HCO_3^- + H^+ \leftrightarrow H_2CO_3 \leftrightarrow CO_2 + H_2O \quad (1)$$

Acidification of the sample shifts the equilibrium toward CO_2 which bubbles out of solution and is detected in the analyzer.

Acid pH Titration

Titration with 0.2 N H_2SO_4 was used to determine the concentration of amines in experimental samples. The automated Titrando apparatus (Metrohm AG, Herisau, Switzerland) was used for

this method. A known mass of sample was diluted with water and the autotitration method was then used. The Titrando titrates the sample with acid while monitoring the pH. The equivalence points are recorded. The equivalence point around a pH of 3.9 corresponds to basic amine species in solution (Hilliard, 2008). The test is not sensitive to the type of amine, so if PZ has degraded to ethylenediamine (EDA), the titration test will detect the sum of contributions from the species.

Anion IC

The anion IC was used to determine the concentration of glycolate, acetate, formate, chloride, nitrite, sulfate, oxalate, and nitrate in experimental samples. A Dionex ICS-3000 instrument with AS15 IonPac column, 4-mm Anionic Self-Regenerating Suppressor (ASRS), carbonate removal device (CRD), and carbonate removal from eluent generation was used as previously described by Sexton using a linear KOH eluent concentration (Sexton, 2008). No major modifications have been made to the method in this quarter.

Cation IC

The cation IC was used to determine the concentration of PZ and ethylenediamine (EDA) in experimental samples. A Dionex ICS-2500 instrument with CS17 IonPac column with 4-mm Cationic Self-Regenerating Suppressor (CSRS) was used as previously described by Sexton with a linear increase of methanesulfonic acid (MSA) concentration in the eluent (Sexton, 2008). No major modifications have been made to the method in this quarter.

NaOH Treatment for Amides

An analytical test for the formation of amides was developed by Sexton and has been included in the results shown here. Experimental samples were treated with 5 N NaOH (in equal gravimetric amounts) and allowed to sit overnight. The anion IC analytical method was then used to quantify increases in the concentrations of analytes as compared to the original samples (Sexton, 2008). In most cases, the main increases were in the production of formate and oxalate following NaOH treatment.

The addition of strong base reverses the amide formation reaction that has occurred during the experiment. As an example, the formation of N-formylPZ (FPZ) is shown in Equation 2 below:

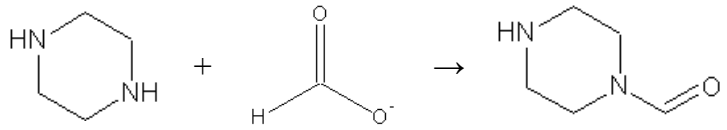

(2)

(PZ) (Formate) (N-formylPZ)

The addition of NaOH hydrolyzes the bond between the amine group and the carbon of the formyl group to reverse the reaction. In this way, the free formate created from reversing this reaction can be used to identify the formate bound as N-formylPZ. The same process can be used to identify the oxalate amine of PZ.

Nuclear Magnetic Resonance (NMR)

Nuclear magnetic resonance (NMR) spectroscopy is a technique used to obtain information on the molecular structure of species in solution. During an NMR analysis, the sample of interest is subjected to a magnetic field and electromagnetic pulses and the result is a spectrum of peaks

that are associated with individual atoms in the molecule. All atoms that are uniquely positioned within a molecule produce a separate response. Each individual atom can be assessed for the atoms to which it is directly connected and to which those atoms are connected. If multiple atoms have the same relative position, they are all represented by one response on the NMR spectrum.

The unique responses on the spectrum are represented as shifts in the peaks from a reference standard, usually dioxane. Specific functional groups have common areas of the spectrum to which their peaks usually shift. It is possible, therefore, to use tables of standard peak shifts to identify the type of functional group associated with an unknown peak. For example, the C=O in a carboxylic acid or carboxylate ion has a traditional shift in the region of 10 to 13 ppm on a ^{1}H NMR spectrum. The details of NMR analysis have been described previously in detail (Hilliard, 2008). Both ^{1}H and ^{13}C NMR measurements are performed at the University of Texas at Austin Department of Chemistry (Wallin and Storey, 2010).

Samples for NMR analysis were prepared according to previous work and the recommendations of the staff of the NMR Laboratory (Hilliard, 2008; Wallin and Storey, 2010). A solution was made with 10 wt % D_2O and 1 wt % dioxane with the balance being the sample of interest. The solution was then used to fill a 5.0 mm OD x 7 in NMR tube with 2–3 mL of solution (Item No. 507-PP-7, wall thickness of 0.38 mm, Wilmad Glass, Vineland, NJ). When working with sensitive samples containing ^{13}C labeled CO_2, the end of the tube was sealed by Mike Ronalter of the Chemistry glass shop (Ronalter, 2009).

Samples were then submitted to the NMR laboratory for analysis. Both ^{1}H and ^{13}C analyses were preformed for all samples along with correlation spectroscopy (COSY). This correlation helps during data analysis to identify which specific atoms are responsible for each peak on both spectrums.

Results and Discussion

Thermal Degradation

Two thermal degradation experiments exploring the effect of concentration on PZ degradation concluded last quarter (TE32 and TE33) and the results are presented here. Two experiments on structural analogs of PZ, morpholine (Mor) and hexamethylenediamine (HMDA), were concluded this quarter and the results are presented. Finally, a short thermal degradation experiment using ^{13}C-labelled CO_2 to analyze the production of formate was concluded. The thermal degradation results as well as the analysis of the NMR results are discussed.

Thermal Degradation of 4 m PZ (TE32)

A thermal degradation experiment was performed on 4 m PZ in an effort to understand the effect of amine concentration in thermal degradation of PZ. With that aim, 4 m PZ with 0.3 mole CO_2 per mole alkalinity was degraded at 175 °C for 15 weeks. Sampling was performed periodically with multiple thermal cylinders being sampled at one point for an estimation of error.

The concentrations of PZ, CO_2, and degradation products are shown in Figure 1 below. Trace concentrations of glycolyl amides and oxalyl amides were quantified but are not included in Figure 1. No glycolate, oxalate, nitrite, or nitrate was detected.

As seen with previous PZ thermal degradation experiments, the primary degradation products were formate and formyl amides. In this experiment, acetate and EDA were minor products, but

present in significant concentrations. The CO_2 loss tracked almost directly with the loss of amine although slightly slower than equimolar.

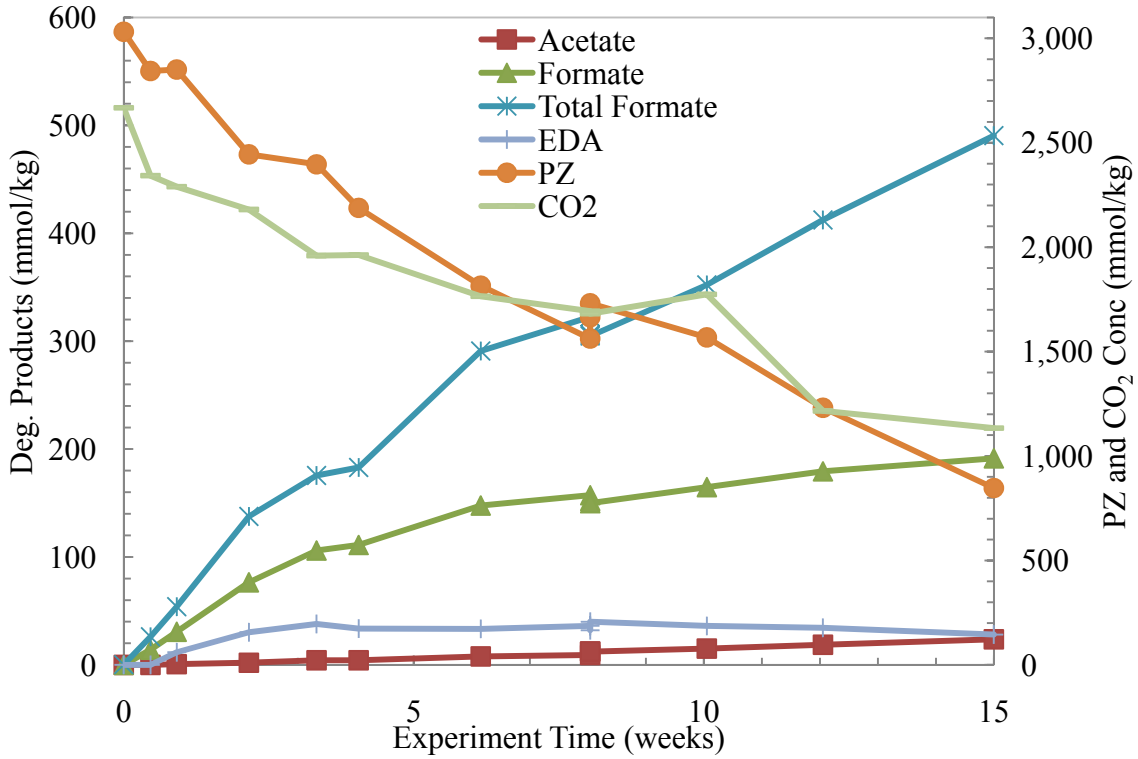

Figure 1: Concentration profiles for 4 m PZ with 0.3 mole CO_2 per mole alkalinity degraded at 175 °C

Thermal Degradation of 12 m PZ (TE33)

To complement the experiment discussed above, a high concentration PZ experiment was performed in an effort to understand the effect of PZ concentration on thermal degradation. A solution of 12 m PZ with 0.3 moles CO_2 per mole alkalinity was degraded at 175 °C for 15 weeks.

The concentrations of PZ, CO_2, and the degradation products are shown in Figure 2. This experiment was one of the first analyzed on the cation IC system in Civil Engineering, so the results for the quantified cation species are thought to be of very high quality. N-formyl PZ (FPZ) was quantified directly and both FPZ and formyl amides as determined from alkaline amide reversal are plotted on the figure. The concentrations track closely until about 6 weeks of degradation where FPZ begins to reach a plateau. After this point, the formyl amides continue to increase, indicating an additional type of amide is being generated after this point on top of the usually favored FPZ. No glycolate, glycolyl amides, nitrite, or nitrate was detected in this experiment. Small concentrations of acetyl and oxalyl amides were quantified but not shown in the figure. As with previous PZ thermal degradation experiments, formate and formyl amides are the dominant degradation products while EDA and acetate are minor products.

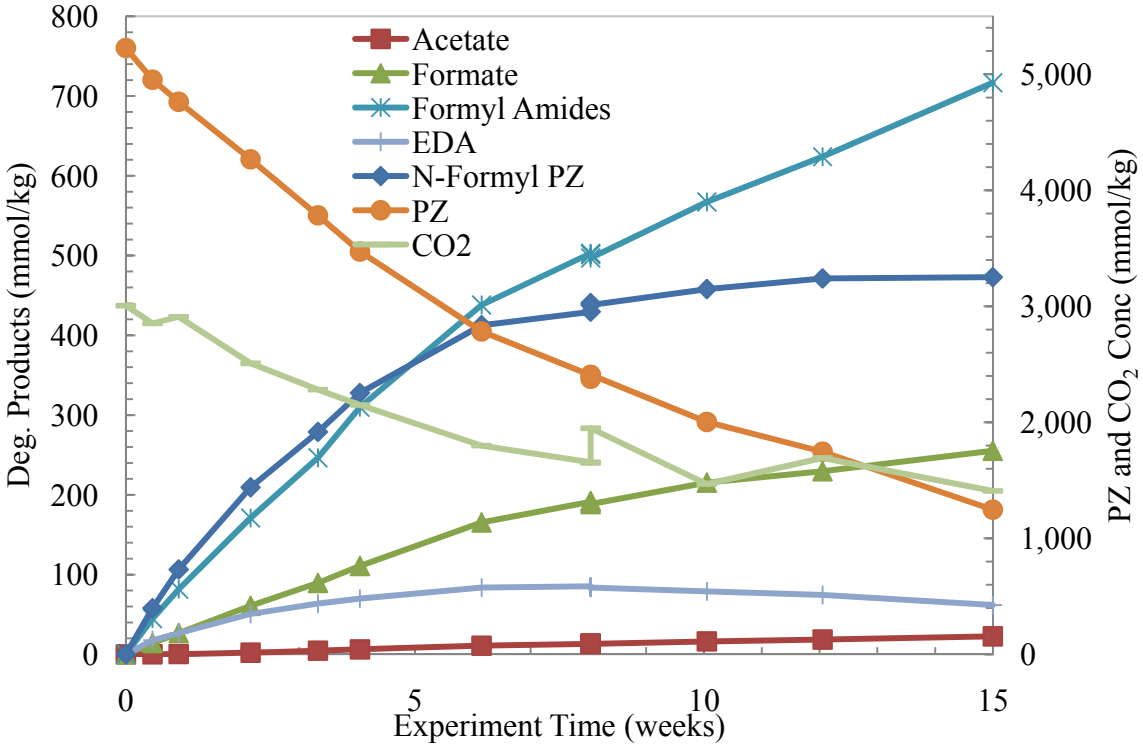

Figure 2: Concentration profiles for 12 m PZ with 0.3 mole CO_2 per mole alkalinity degraded at 175 °C

Effect of PZ Concentration on Thermal Degradation

With the conclusion of TE32 and TE33, the effect of PZ concentration on thermal degradation can be evaluated from 4 to 12 m PZ. The 8 m PZ experiment that will be compared is TE12 whose results were described previously (Rochelle, 2009; Rochelle, 2010a). The fractional loss of PZ is compared for the three experiments in Figure 3. The generation of total formate and the ratio of formate to formyl amides produced in each experiment are compared in Figures 4 and 5, respectively. Finally, the production of EDA is compared in Figure 6.

The increase of PZ concentration from 4 to 12 m does not appear to have a strong impact on the loss rate of PZ (Figure 3). This indicates that PZ thermal degradation is first order in PZ concentration. If the system were perfectly first order in PZ, the lines would all line right on top of each other. A slight increase in rate can be seen as PZ concentration increases from 4 to 12 indicating that the system demonstrates a small effect of concentration.

On the other hand, the generation of total formate is a function of PZ concentration, or alternatively CO_2 concentration (Figure 4). In each system, the CO_2 loading, not CO_2 concentration, was kept constant at 0.3 mole CO_2 per mole alkalinity. Therefore, the CO_2 concentration was highest in the 12 m PZ solution where the most formate was generated. As discussed later in this report, the generation of formate is closely linked with CO_2 concentration, so this is likely the cause rather than the difference in PZ concentration.

The ratio of formate produced to formyl amides produced is examined in Figure 5. There does not appear to be a trend among the three concentrations of PZ or CO_2. All three experiments end with ratios less than 1.0, indicating more formyl amides are always present after degradation has

occurred. The data for 12 m PZ degradation are consistent and point to about 2.8 times the concentration of formyl amides as formate in solution throughout the experiment.

The generation of EDA appears to have quite different behavior to that of formate and formyl amide products between the PZ concentrations. As shown in Figure 6, the final concentrations of EDA in all three experiments are quite similar. The EDA quantification is known to have more error due to dilution issues with PZ so the scatter is expected in each data set. After 15 weeks of degradation, all three experiments contain about 40 mmol/kg of EDA. Previous reports have hypothesized that the generation of EDA is associated with the presence or concentration of H^+PZ rather than any other species in solution (Rochelle, 2010b).

Thermal Degradation of 8 m Morpholine (TE35)

Morpholine (Mor) is a monoamine with an oxygen in the 4-position in a six-membered ring. This is a structural analog with PZ along with piperidine (PD). The thermal degradation rate of these three molecules, shown in Figure 7, will demonstrate the effect of changing heteroatoms. The data from these three experiments are compared and analyzed in my GHGT-10 paper (appended to this quarterly report) (Freeman and Rochelle, 2010).

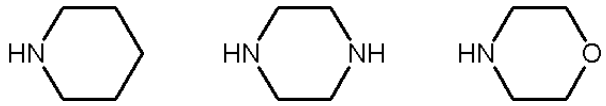

PD PZ Mor

Figure 7: Amine studied to examine the effect of changing heteroatoms

The concentrations of Mor, CO_2, formate, and formyl amides are shown in Figure 8 below. As with most amines, formate and formyl amides were the most abundant degradation products identified. No glycolate, glycolyl amides, nitrite, nitrate, or EDA was detected. Trace concentrations of acetate, acetyl amides, oxalate, and oxalyl amides were detected but omitted from Figure 8. Unfortunately, the CO_2, formate, and formyl amide data are very scattered and appear unreliable. These data will be reevaluated in the next quarter.

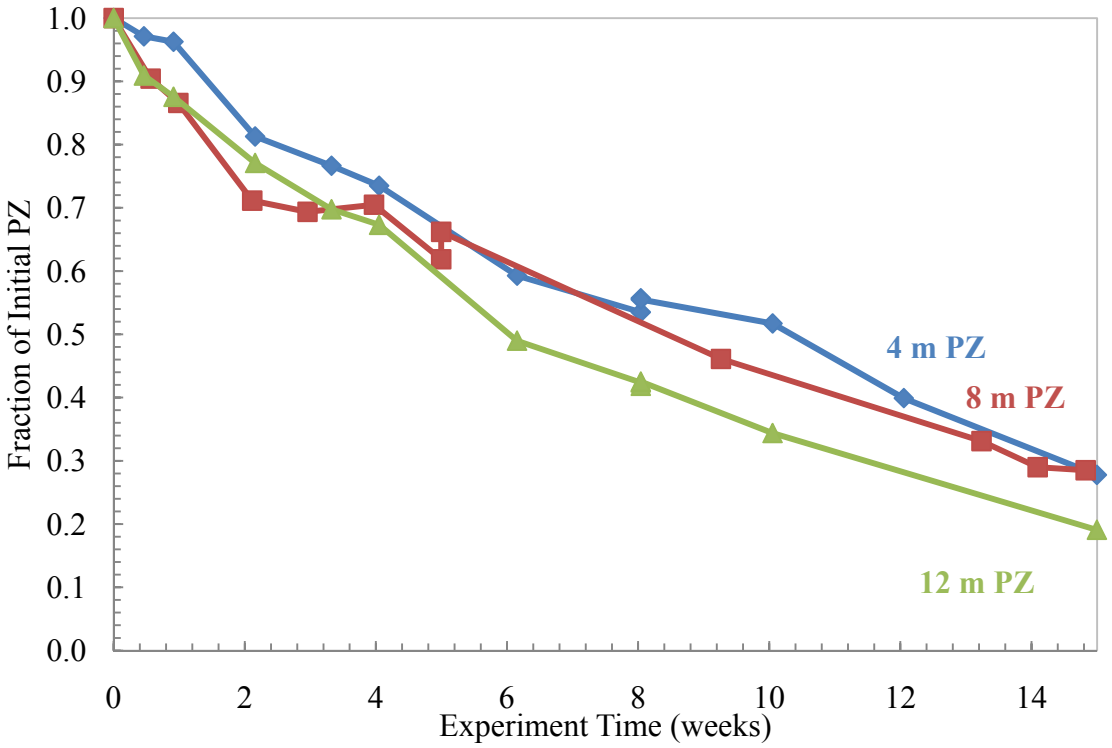

Figure 3: Comparison of PZ loss for 4, 8, and 12 m PZ with 0.3 mole CO_2 per mole alkalinity degraded at 175 °C

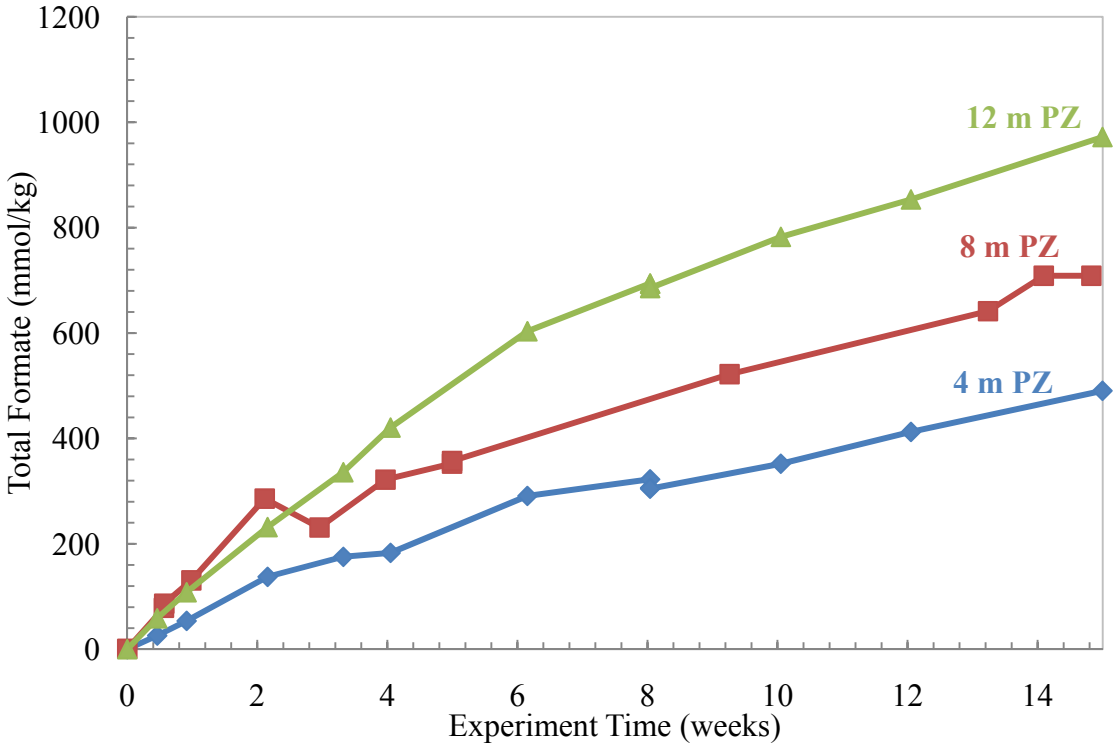

Figure 4: Comparison of total formate production for 4, 8, and 12 m PZ with 0.3 mole CO_2 per mole alkalinity degraded at 175 °C

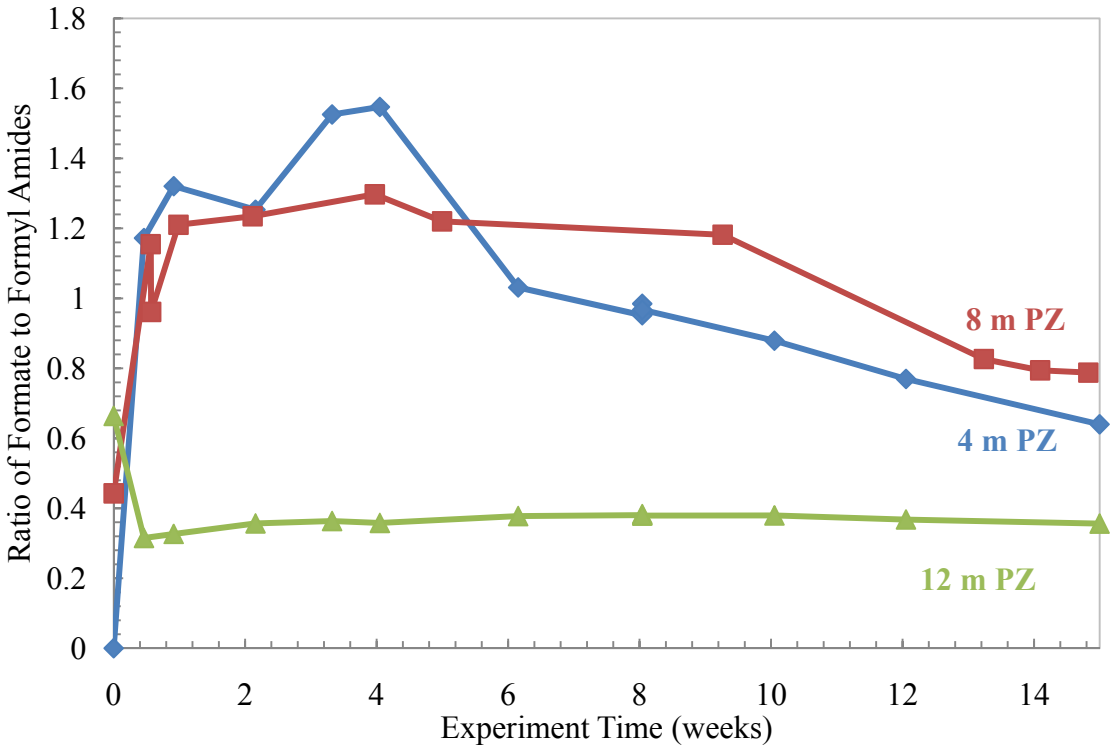

Figure 5: Comparison of the ratio of formate to formyl amides produced for 4, 8, and 12 m PZ with 0.3 mole CO_2 per mole alkalinity degraded at 175 °C

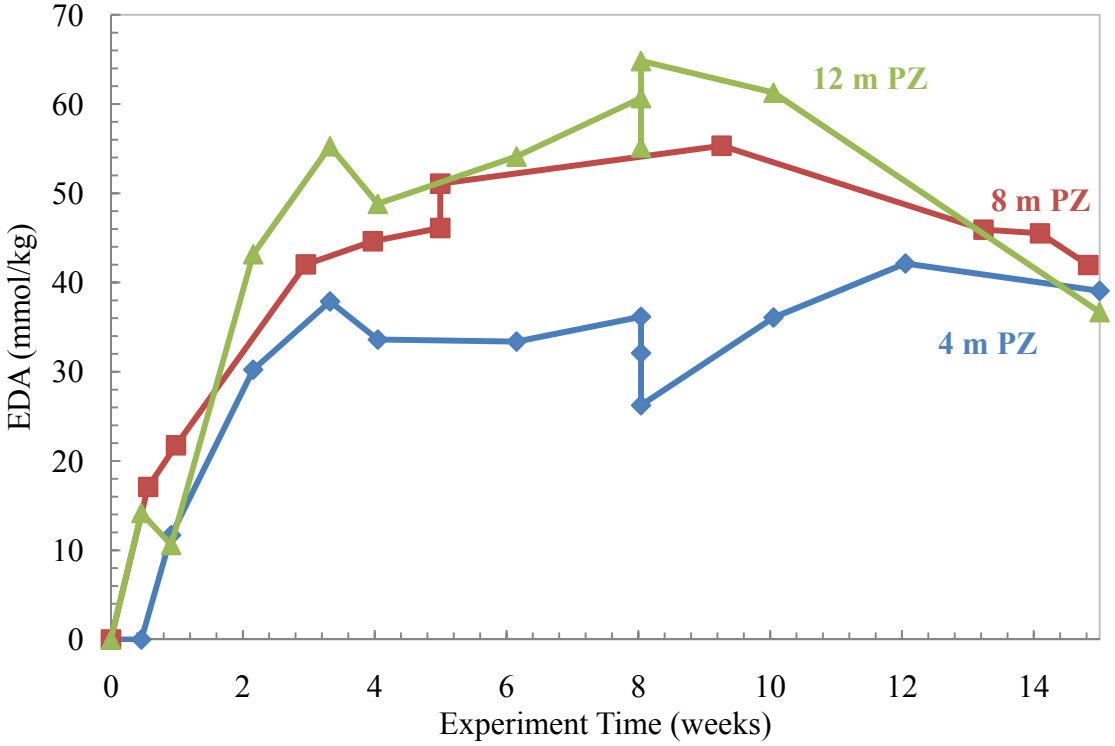

Figure 6: Comparison of EDA generation for 4, 8, and 12 m PZ with 0.3 mole CO_2 per mole alkalinity degraded at 175 °C

Overall the degradation characteristics of Mor are very favorable. Only 17% of the initial amine was lost over the course of 15 weeks which is less than 8 m PZ. Mor is therefore one of the most resistant amines to thermal degradation that has been screened in our laboratory. An analysis of the resistance of Mor to thermal degradation can be found in my GHGT-10 paper (Freeman and Rochelle, 2010). Requantifying the degradation products should shed more light on the stability of Mor as well.

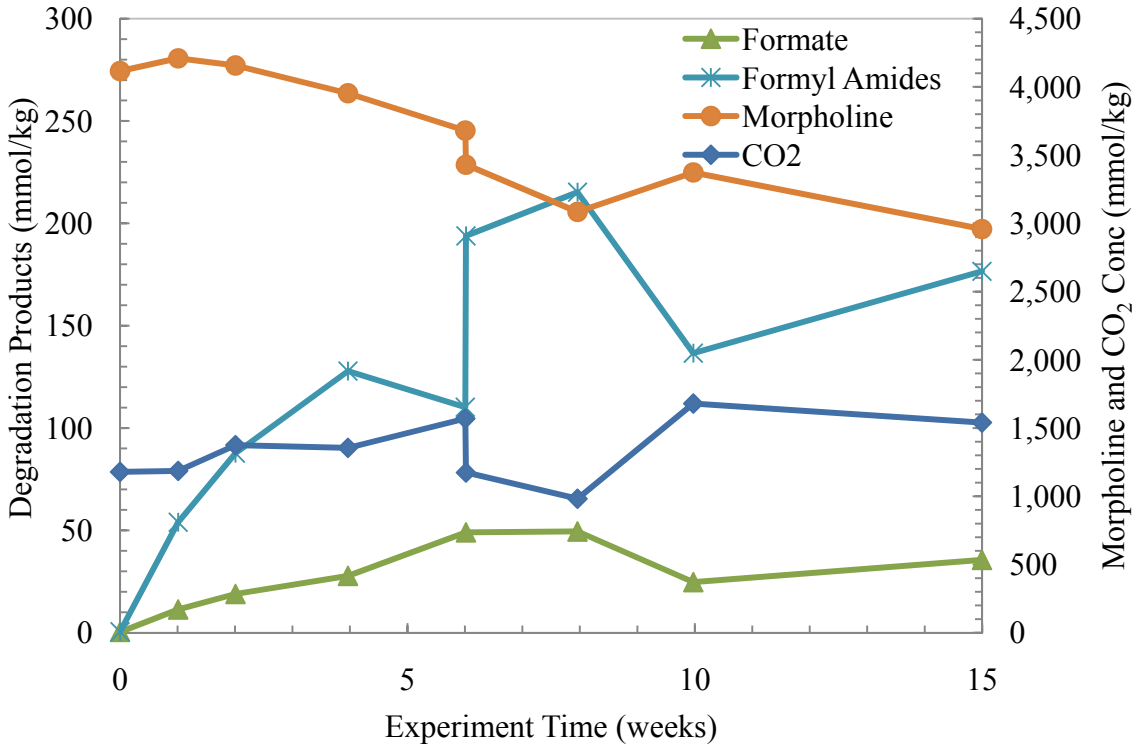

Figure 8: Concentration profiles for 8 m Mor with 0.3 mole CO_2 per mole alkalinity degraded at 175 °C

Thermal Degradation of 8 m Hexamethylenediamine (TE36)

Hexamethylenediamine is a diamine with six methylenes separating the amines. It is a structural analog of PZ and was studied to aid the comparison of the length of the chain between diamines. This comparison involves EDA data from Zhou compared with PZ and HMDA degradation data (Zhou et al., 2010). The structures are compared in Figure 9. As explored by Davis, the length of the chain between amino groups can affect the stability of intermediates and degradation products depending (Davis, 2009).

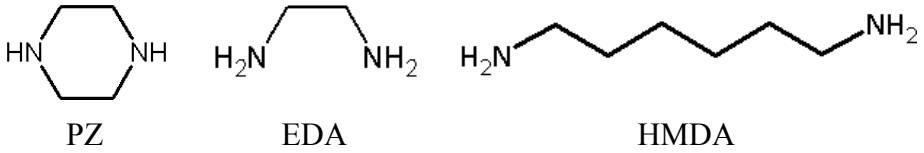

Figure 9: Amine studied to examine the effect of chain length between amino groups

The concentrations of HMDA, CO_2, formate, and total formate are compared in Figure 10 below. The initial sample vial broke and the recovered solution may not be reliable as suggested by the result in Figure 10. Both the HMDA and CO_2 concentrations are about half of what they should

have been based on the trends for the samples after t = 0. Formate and formyl amides were the most abundant degradation products. The final sample had an erroneous measurement for total formate so that point is omitted on the formyl amide curve. No glycolate, glycolyl amides, acetate, acetyl amides, or EDA were detected. Small concentrations of oxalate, oxalyl amides, nitrite, and nitrate were quantified but omitted from Figure 10.

HMDA is not stable to thermal degradation, losing about 80% of the initial amine after 15 weeks at 175 °C. Because of the broken vial, an estimate of 2500 mmol/kg was used for the HMDA concentration at the start of the experiment. The loss also appears to be higher than first order as plotting the amine concentration as a logarithm does not linearize the data. HMDA is not likely to be an amine of interest for CO_2 capture applications.

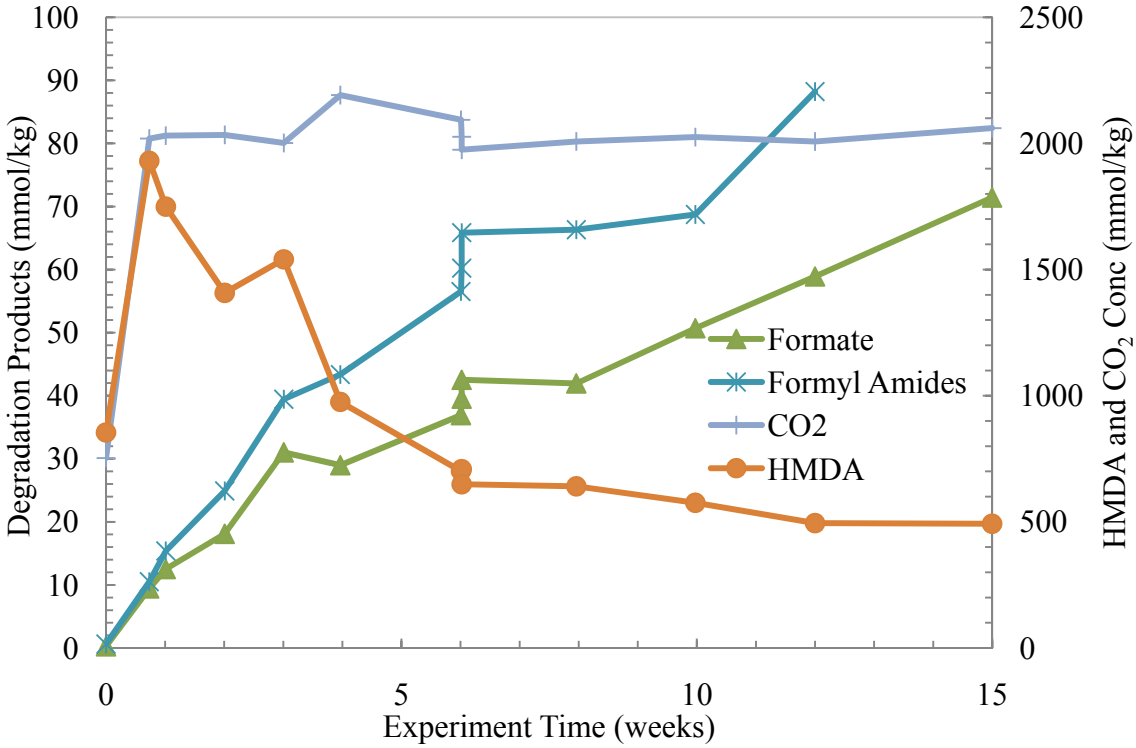

Figure 10: Concentration profiles for 8 m HMDA with 0.3 mole CO_2 per mole alkalinity degraded at 175 °C

Thermal Degradation of 8 m PZ with ^{13}C-labelled CO_2 (TE42)

In order to understand the generation of formate in oxygen-poor thermal degradation of concentrated PZ, an experiment was devised using ^{13}C-labelled CO_2 and NMR techniques. A solution of 8 m PZ was loaded with 0.3 mole CO_2 per mole alkalinity with ^{13}C-labelled CO_2. This solution was then placed in two thermal cylinders and degraded for up to six weeks. The degraded solutions were analyzed using ^{1}H and ^{13}C NMR in order to determine if the lost CO_2 ends up as formate. For the degradation portion of the experiment, a set of cylinders using standard 8 m PZ with 0.3 mole CO_2 per mole alkalinity of natural CO_2 was used as a reference. The ^{13}C-CO_2 samples were TE42A while the standard CO_2 samples were TE42B. Both sets of cylinders were degraded under the same conditions and analyzed in parallel to ensure that the data from TE42A were as reliable as possible.

The results of the degradation portion of the experiment are shown in Figures 11 and 12 for TE42A and TE42B, respectively. In each figure, the concentration of PZ, acetate, formate, EDA, and formate as predicted from the NMR are shown. The details of the prediction from NMR are described in detail in the next section. The NMR prediction is consistently lower than the anion IC results for formate. After 6 weeks of degradation, however, the NMR prediction is within 15% and 26% for TE42A and TE42B, respectively.

To ensure that the thermal degradation observed in TE42A and TE42B are representative of previous 8 m PZ results, the loss of PZ is compared among all the thermal degradation experiments done to date on 8 m PZ with 0.3 mole CO_2 per mole alkalinity at 175 °C in Figure 13. The experiments that have been performed at these conditions are TE4, TE12, TE18, TE42A, and TE42B. The loss of PZ in TE42A and TE42 is consistent with the other three experiments.

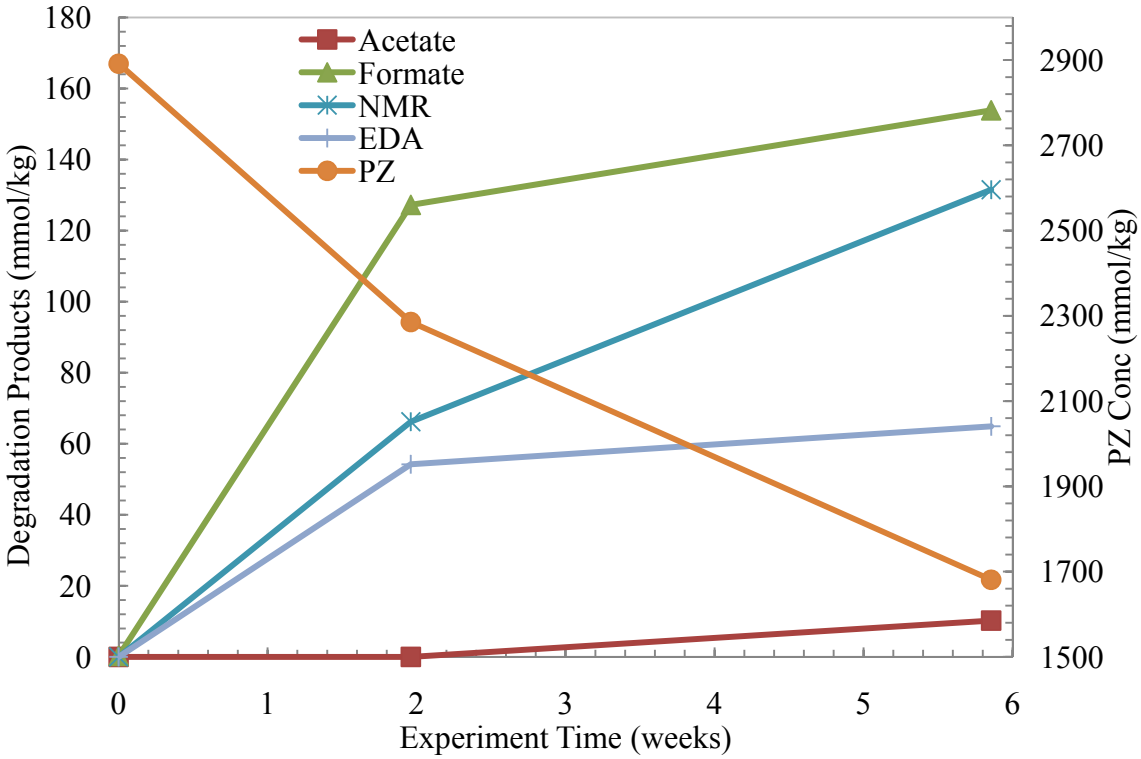

Figure 11: Concentration profiles for 8 m PZ with 0.3 mole ^{13}C-CO_2 per mole alkalinity degraded at 175 °C (TE42A)

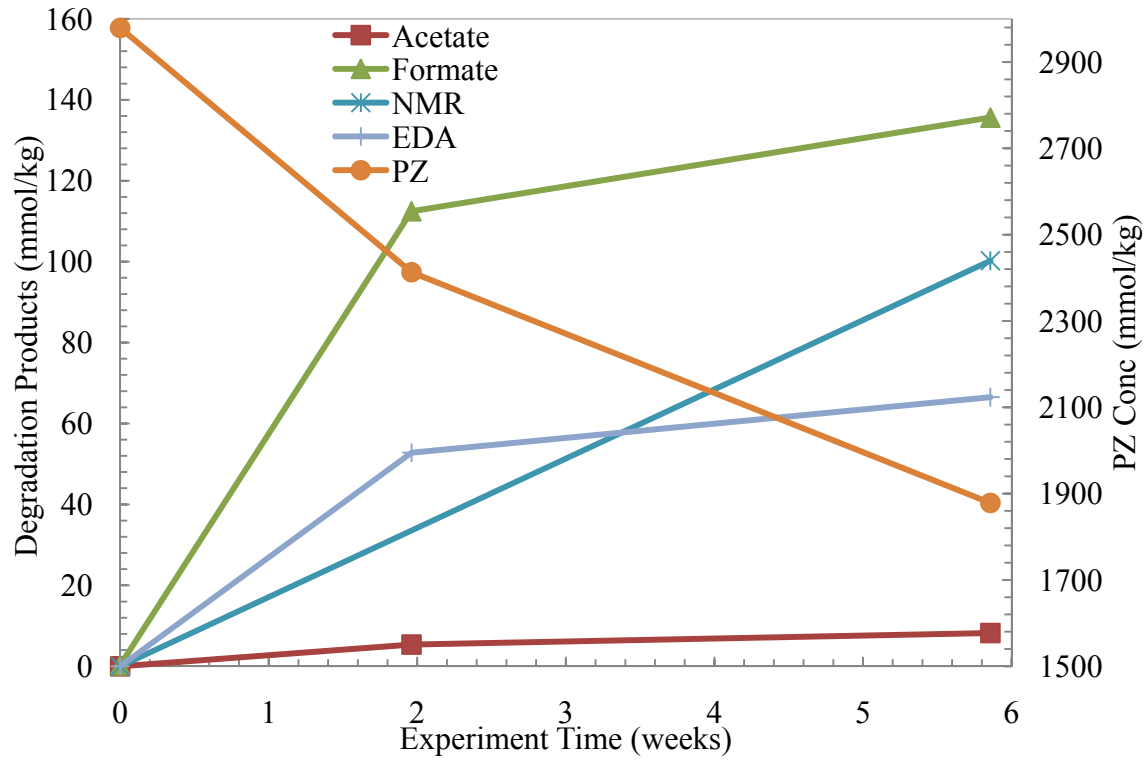

Figure 12: Concentration profiles for 8 m PZ with 0.3 mole CO_2 per mole alkalinity degraded at 175 °C (TE42B)

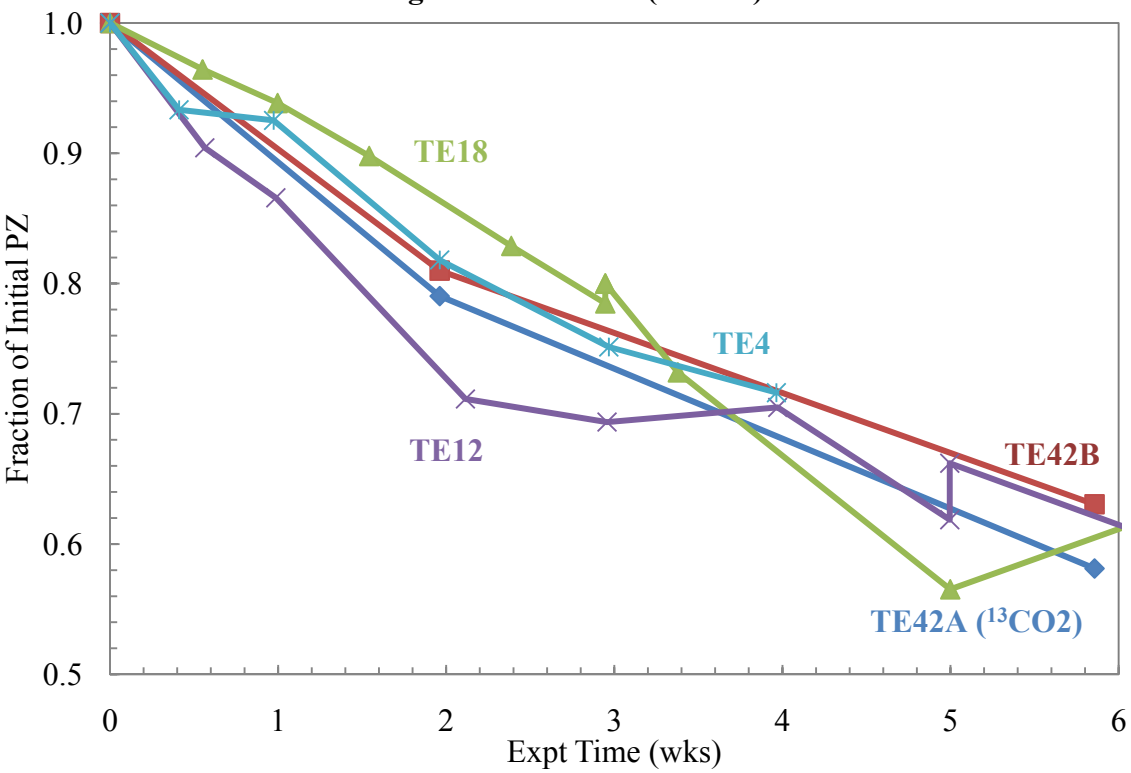

Figure 13: Comparison of PZ thermal degradation for 8 m PZ at 175 °C

NMR Results of ^{13}C-labelled CO_2 Degradation Study

After the two experiments were thermally degraded at 175 °C, the samples were analyzed using ^{1}H and ^{13}C NMR. The goal of the NMR work was to confirm the hypothesis that formate is generated during degradation from CO_2, not carbons of the PZ backbone. The NMR results would show if formate contained ^{13}C from ^{13}C-labelled CO_2, therefore indicating a mechanism for formate generation in an oxygen-poor environment. All NMR analysis was conducted at the NMR Laboratory at the University of Texas at Austin (Wallin and Storey, 2010).

To prepare for the NMR, background samples were analyzed to determine where formate generally appears in NMR spectra. First, the Spectral Database for Organic Compounds (SDBS) has a ^{13}C reference spectrum for formic acid (AIST, 2010). This spectrum was analyzed in the presence of $CDCl_3$ and shows the formic acid peak at 166.22 ppm (Figure 14). The peak expected for sodium formate in D_2O would be at 171.67 ppm (Gottlieb et al., 1997). The difference between these two chemical shifts is due to the pH of the solution in which formate was detected. This demonstrates the range of shift for formate ions in aqueous solution.

The region where formate is seen is the downfield range of the ^{13}C spectrum where carbons that are part of a carbonyl (C = O) generally appear. In loaded PZ samples, the carbons that are part of carbamate carbonyls and carbonate/bicarbonate carbonyls will also appear here. In degraded solutions, it is expected that carbons that are part of aldehyde carbonyls, ketone carbonyls, and amide carbonyls would appear in the same downfield area of the spectrum.

In order to anticipate what may be seen in degraded PZ solutions, two aliquots of loaded 8 m PZ were spiked with 38 and 305 mM formic acid and analyzed with NMR. The resulting downfield ^{13}C NMR spectra are shown in Figures 15 and 16 below. In these two samples, the formate peak appears as a chemical shift of 170.191 and 170.296 ppm, respectively. Both spectra also show peaks for the carbonyl in $PZCOO^-$ (162.334 and 162.375 ppm, respectively) and the carbonyl in CO_3^-/HCO_3^- (162.796 and 162.838 ppm, respectively) in the same downfield view. The sample with 38 mM also registered a peak for the $PZ(COO^-)_2$ at 163.135 ppm and it is not clear why that did not show up in the 305 mM sample. In our loaded PZ solutions, the chemical shift of the carbon in formate is not quite as great as that of sodium formate, but should be around 170 ppm. This test also demonstrates that the formate peak does not overlap with any of the carbamate or carbonate peaks expected in CO_2-loaded PZ.

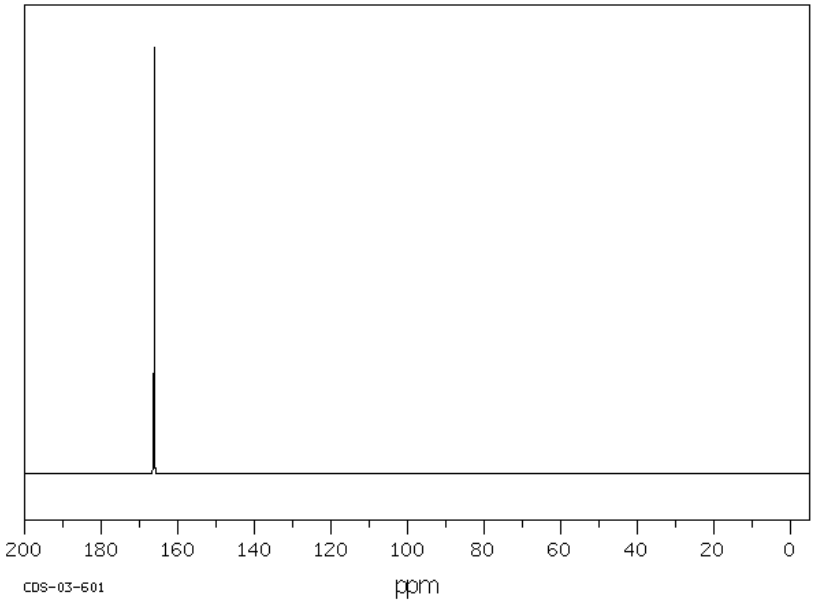

Figure 14: Reference ^{13}C spectrum for formic acid showing a major peak at 166.22 ppm (AIST, 2010)

In these experiments, the ^{13}C-labelled CO_2 is used to amplify the NMR signal. ^{13}C NMR, as the name indicates, only detects ^{13}C isotopes of carbon. In standard samples, the signal is generated from the naturally occurring ^{13}C that is present in every chemical, roughly 1% of all carbon. The effect of loading a PZ solution with $^{13}CO_2$ is seen when panels A and B of Figure 17 are compared. Panel A is a ^{13}C NMR spectrum of a standard loaded PZ solution. Panel B is a ^{13}C NMR spectrum of PZ loaded with ^{13}C-labelled CO_2. What is important to note is the relative size of the group of peaks upfield (~40 ppm) and downfield (~160 ppm). The upfield carbons are the carbons on the PZ backbone while the downfield carbons are carbonyl carbons representing $PZCOO^-$, $PZ(COO^-)_2$, and CO_3^-/HCO_3^-. Although the ordinate scales are different, the upfield carbons are approximately the same size in both panels representing the naturally occurring ^{13}C in PZ backbone carbons. The difference is the downfield carbons which demonstrate the ^{13}C present in the $^{13}CO_2$.

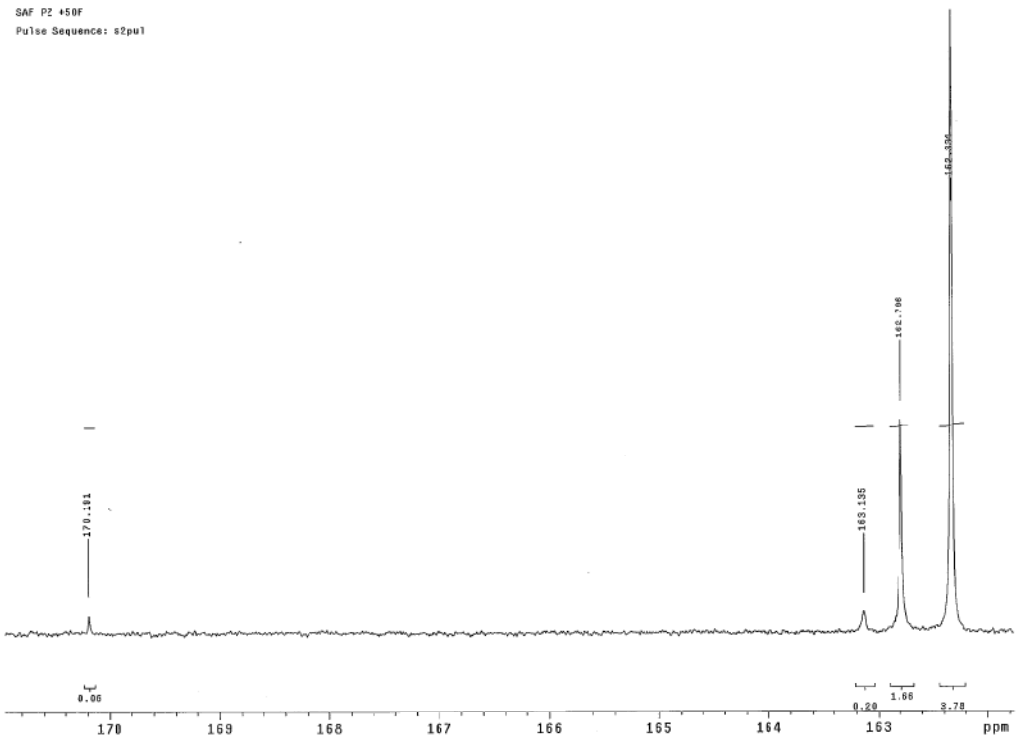

Figure 15: Downfield ^{13}C NMR spectrum for 8 m PZ with 0.3 mol CO_2 per mole alkalinity spiked with 38 mM formate

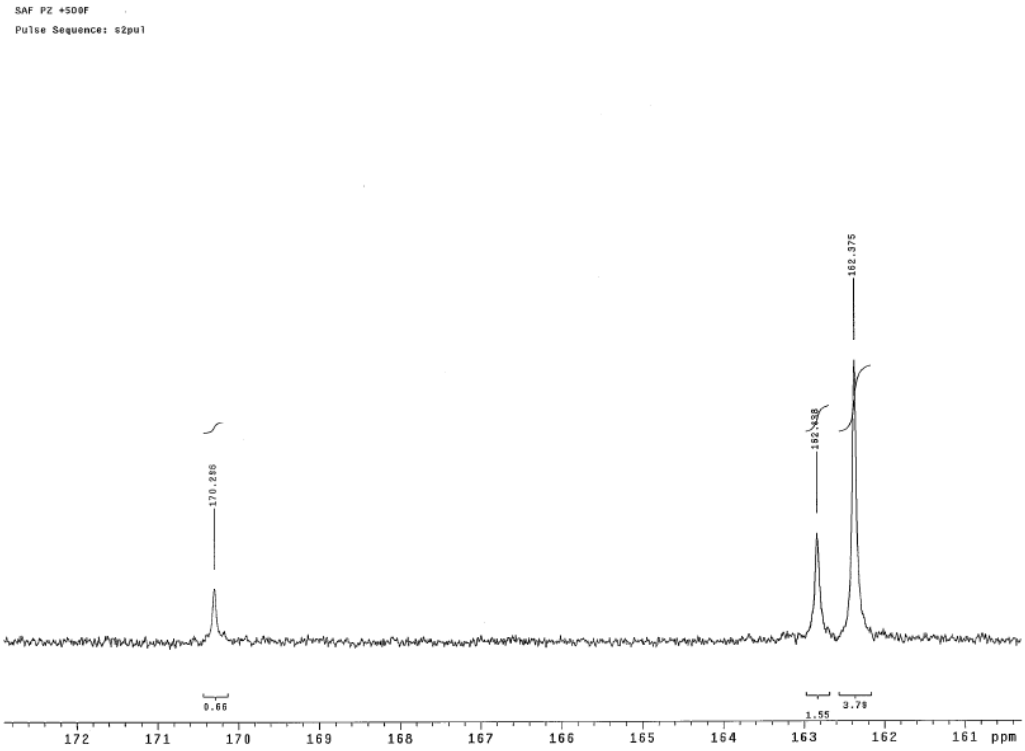

Figure 16: Downfield ^{13}C NMR spectrum for 8 m PZ with 0.3 mol CO_2 per mole alkalinity spiked with 305 mM formate

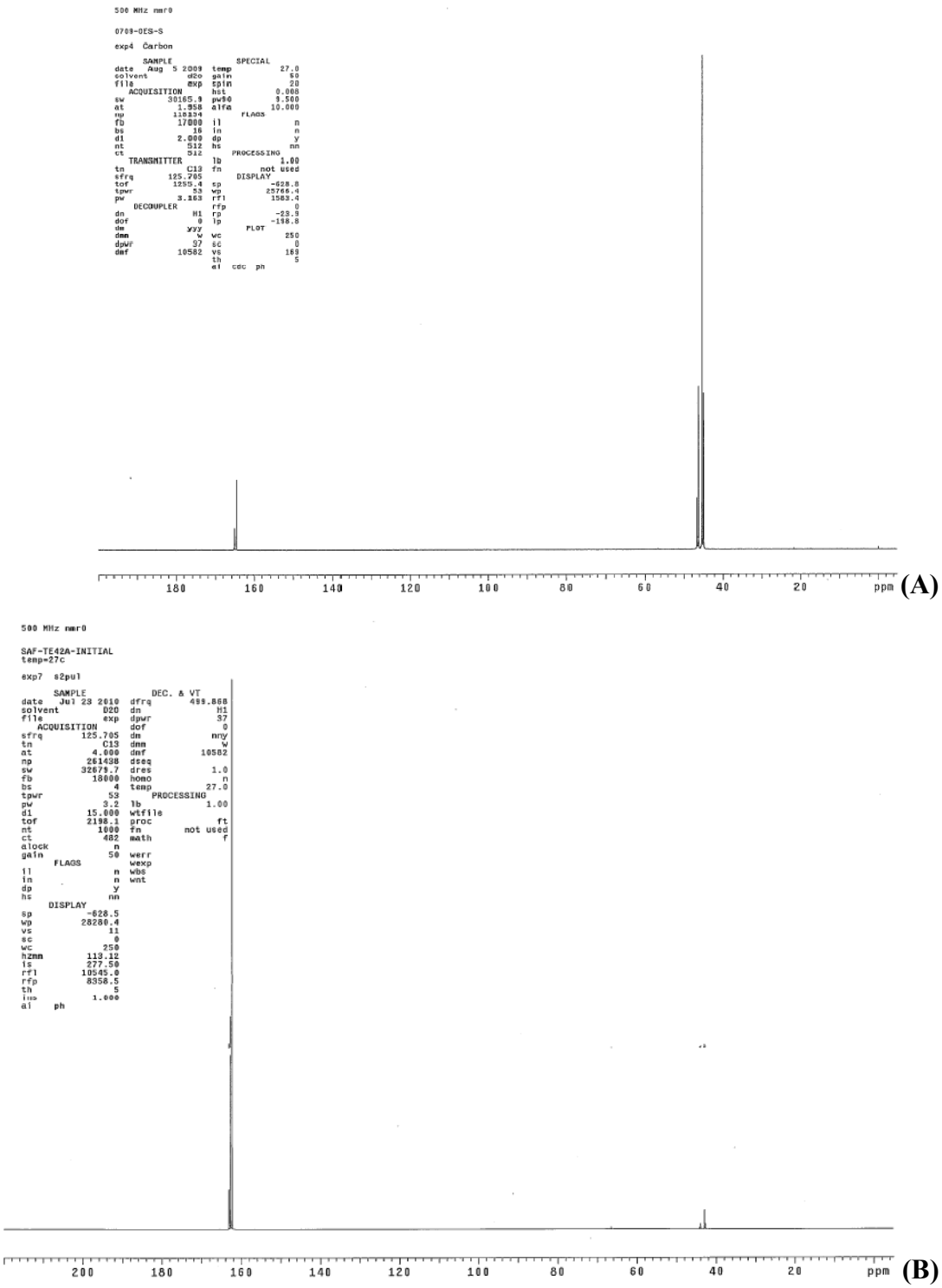

Figure 17: Comparison of ^{13}C NMR spectrums for 8 m PZ loaded with (A) natural or (B) ^{13}C-labelled CO_2 (aligned on horizontal ppm scale)

Samples were taken in TE42A and TE42B after 2 and 6 weeks of degradation and submitted for ^{13}C NMR analysis. As expected, the ^{13}C NMR spectra were very complex due severe PZ degradation achieved at 175 °C. Examples of the downfield ^{13}C NMR spectrum for TE42A and TE42B after 6 weeks of degradation are shown in Figures 18 and 19. The peaks at

approximately 170.1 ppm in both figures correspond to formate based on the background spectra analyzed in Figures 15 and 16 above.

From these spectra, the concentration of formate can be estimated using a reference standard. In all NMR samples analyzed, 1 wt % dioxane is added as an internal reference. The peak areas associated with dioxane (~3.5 ppm in 1H and 66.5 ppm in ^{13}C) can then be used to estimate the concentration of other species in solution. The calculation starts by determining the concentration of dioxane, $C_{Dioxane}$, in the submitted sample in units of moles dioxane per kg of total solution (Equation 3).

$$C_{Dioxane} = \frac{\text{g Dioxane}}{\text{g total}} \times \frac{\text{mol Dioxane}}{88.11\ \text{g Dioxane}} \times \frac{1000\ \text{g total}}{1\ \text{kg total}} \quad (3)$$

Then, a response factor, $RF_{Dioxane}$, can be calculated using that concentration of dioxane, the number of carbons in dioxane, and the area from the ^{13}C NMR spectrum, $Area_{Dioxane}$ (Equation 4).

$$RF_{Dioxane} = \frac{\text{mole Dioxane}}{\text{kg soln}} \times \frac{4\ \text{Carbons}}{\text{mole Dioxane}} \times \frac{1}{\text{Area}_{Dioxane}} \quad (4)$$

Finally, the concentration of the species of interest can be calculated using RFDioxane, the area of the peak, and the number of carbons of the species. When calculating concentrations for species that are assumed to contain only ^{13}C, the ratio of ^{13}C to ^{12}C must be applied since the reference chemical, dioxane, contains only naturally occurring ^{13}C. The concentration of formate, $C_{Formate}$, which is assumed to contain only ^{13}C, was calculated using Equation 5.

$$C_{Formate} = RF_{Dioxane} \times \text{Area}_{Formate} \times \frac{\text{mole Formate}}{1\ \text{Carbon}} \times \frac{0.0107\ \text{mole}\ ^{13}C}{0.9893\ \text{mole}\ ^{12}C} \quad (5)$$

Using Equations 3–5, the concentration of formate was calculated from the NMR spectrum for all the degraded PZ samples. These concentrations were compared with the concentration of formate obtained through anion IC analysis of the same samples. The formate concentration, not the total formate or formyl amide concentration was used because any amides would appear as separate peaks in the downfield region of the ^{13}C NMR. The peak at 170.1 ppm corresponds to the formate ion itself. A comparison of the results of anion IC (2nd Column) and NMR assuming all ^{13}C (3rd column) is shown in Table 1 below. The final column is the estimation of the formate concentration if the carbon is not assumed to be ^{13}C. This is essentially the same calculation except the ratio of ^{13}C to ^{12}C is omitted from Equation 5. In this way, the assumption is that the formate would only have a naturally occurring concentration of ^{13}C, matching the dioxane reference. It is clear from comparing the last two columns of Table 1 that the assumption that formate contains only ^{13}C is valid. The formate estimated from assuming only naturally occurring ^{13}C is up to 80X larger than the anion IC estimate. This comparison confirms the hypothesis that formate is generated from CO_2, not the carbons on the PZ backbone.

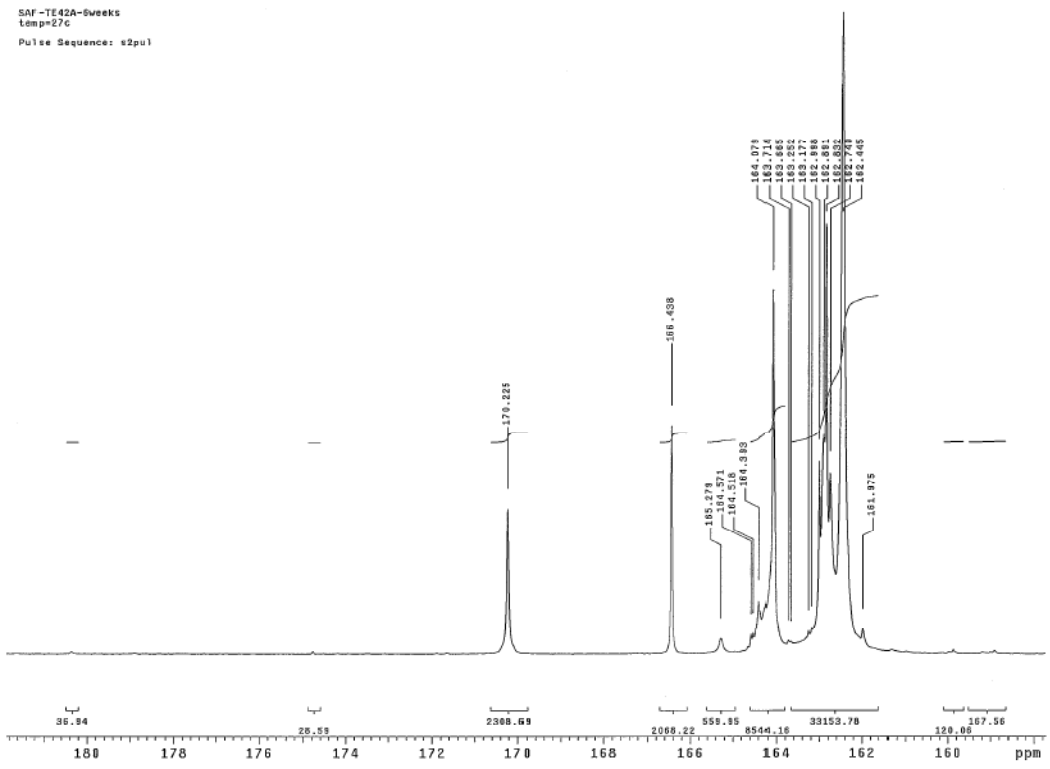

Figure 18: Downfield ^{13}C NMR spectrum for $^{13}CO_2$ loaded 8 m PZ after 6 weeks at 175 °C

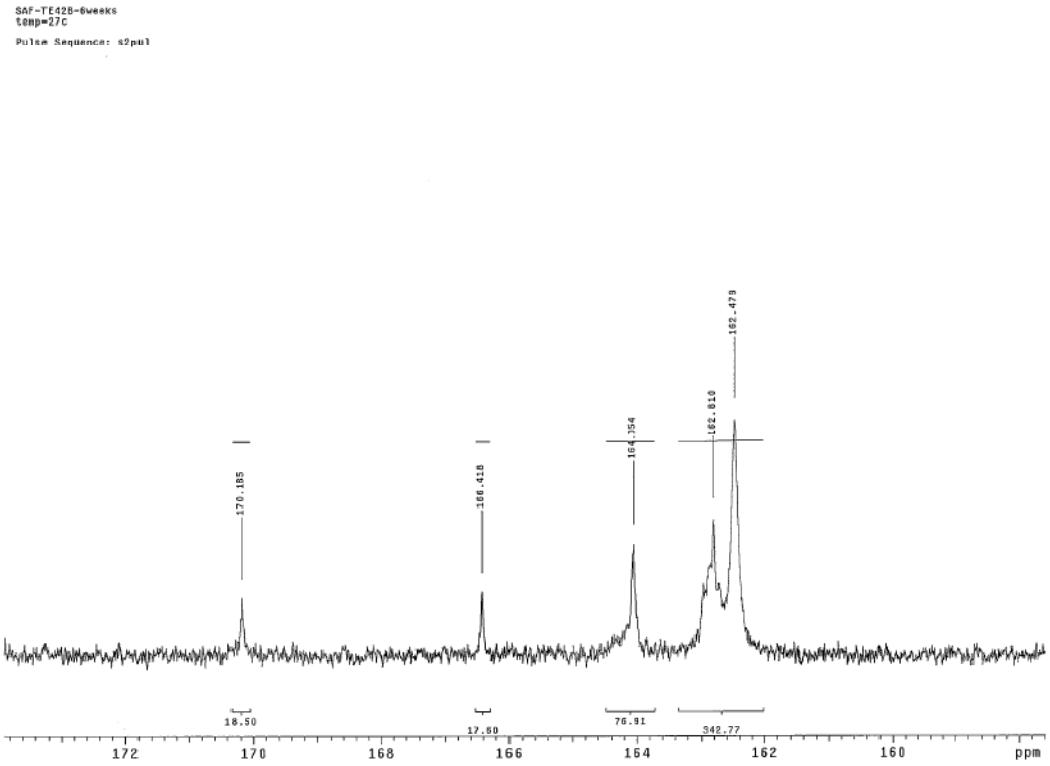

Figure 19: Downfield ^{13}C NMR spectrum for natural CO_2 loaded 8 m PZ after 6 weeks at 175 °C

Overall, the NMR analysis underestimated the formate concentration compared to the anion IC results. The NMR estimate is within 15% of the anion IC results for the final sample after 6 weeks of degradation. Given the nature of the NMR estimate, it is expected that the formate concentration contains more error when calculated this way compared to the direct measurement through anion IC.

Table 1: Comparison of formate quantified in degraded $^{13}CO_2$ loaded PZ (TE42A)

Deg. Time	Formate Concentration		
	Anion IC	NMR – ^{13}C	NMR – ^{12}C
wks	mmol/kg	mmol/kg	mmol/kg
0	0.27	0	0
2	127.2	66.2	6120
6	153.9	131.5	12,160

The NMR results show conclusively that the formate generated in degraded PZ solutions is from the CO_2 molecule. The carbon formate contains the CO_2 carbon and is not generated through break-up of the PZ molecule itself. The mechanism for this CO_2-reduction is not clear at this time.

This result is important since CO_2 is the only significant source of oxygen besides water in oxygen-poor thermal degradation. In addition, formate and formyl amides are found as a dominant degradation product in a variety of amines that have been screened for thermal degradation. This is primarily true in systems that do not undergo carbamate polymerization since that process uses the carbon of the CO_2 molecule to cyclicize alkanolamines to create oxazolidinones. The types of amines that produce significant formate concentrations include: cyclic diamines (PZ, 1-MethylPZ, 2-MethylPZ), cyclic amines (PD, Mor, Pyrrolidine, Hexamethyleneimine, HomoPZ), straight chain amines (EDA, HMDA), and some alkanolamines (MDEA). All of the screening experiments performed on the amines listed are loaded solutions. The presence of CO_2 is common in every experiment while the structures of the amine are very different including primary, secondary, and tertiary amines, linear and cyclic amines, and mono- or diamines.

Oxidative Degradation

Three new oxidation experiments were performed this quarter that examined the effect of formate, formaldehyde, and CO_2 loading on PZ oxidation. All three were performed in the Teflon Oxidation Reactor (TOR) as the Original Oxidation Reactor (OOR) is no longer being used for PZ oxidation studies. A second TOR was constructed this quarter as well, but has not been used for an experiment yet.

OE20 – Stainless Steel Metals and Formate at 70 °C with Low CO_2 Loading

An oxidation experiment was performed in the presence of 0.4 mM Fe^{2+}, 0.1 mM Cr^{3+}, 0.05 mM Ni^{2+}, and 500 mmol/kg formate at 70 °C with 2kPa CO_2 in the Teflon Oxidation Reactor (TOR). This experiment used the standard PZ oxidation conditions with the addition of 500 mM of formate. It was hypothesized that formate itself acts as an oxidation inhibitor for PZ. Based on previous oxidation results, we were curious if formate is being oxidized all the way to CO_2 which would not be seen in our typical analysis. If CO_2 was being generated as a degradation

product, the loading would not necessarily change because of the agitation and constant influx of CO_2 in the headspace of the reactor. It was hoped that this route for formate could explain why some PZ loss is seen while very little formate and formyl amides are recovered as degradation products. There were three predicted outcomes of this experiment:

1) Formate may just convert to formyl amides and the total formate (500 mmol/kg) be conserved. In this case, the experiment would just test the equilibrium between formate and formyl amides at 70 °C.
2) Formate would be oxidized to CO_2 and the total formate concentration would decrease as CO_2 is generated and lost to the headspace of the reactor.
3) Formate would act as an oxidation inhibitor and would also be conserved. Some formyl amides would be generated as well and the overall PZ loss rate would be less than a comparable experiment without the formate spike.

The concentrations of PZ, CO_2, formate, and formyl amides are shown below in Figure 20. Trace concentrations of acetate, acetyl amides, oxalate, oxalyl amides, nitrite, and nitrate were detected but are not shown in the figure. No EDA, glycolate, or glycolyl amides were detected. Over the course of 350 hours, approximately 8.8% of the initial PZ was lost.

During OE20, the overall concentration of formate was essentially conserved (purple line in Figure 20). The formate added to the solution at the beginning of the experiment quickly reacted with PZ in solution to form N-formyl PZ even in the initial reactor sample. The overall concentration remained very near 500 mmol/kg of total formate. The PZ loss was actually slightly increased over a comparable experiment without formate, although the error in the cation may be larger than the difference observed. This comparison is shown in Figure 21 below.

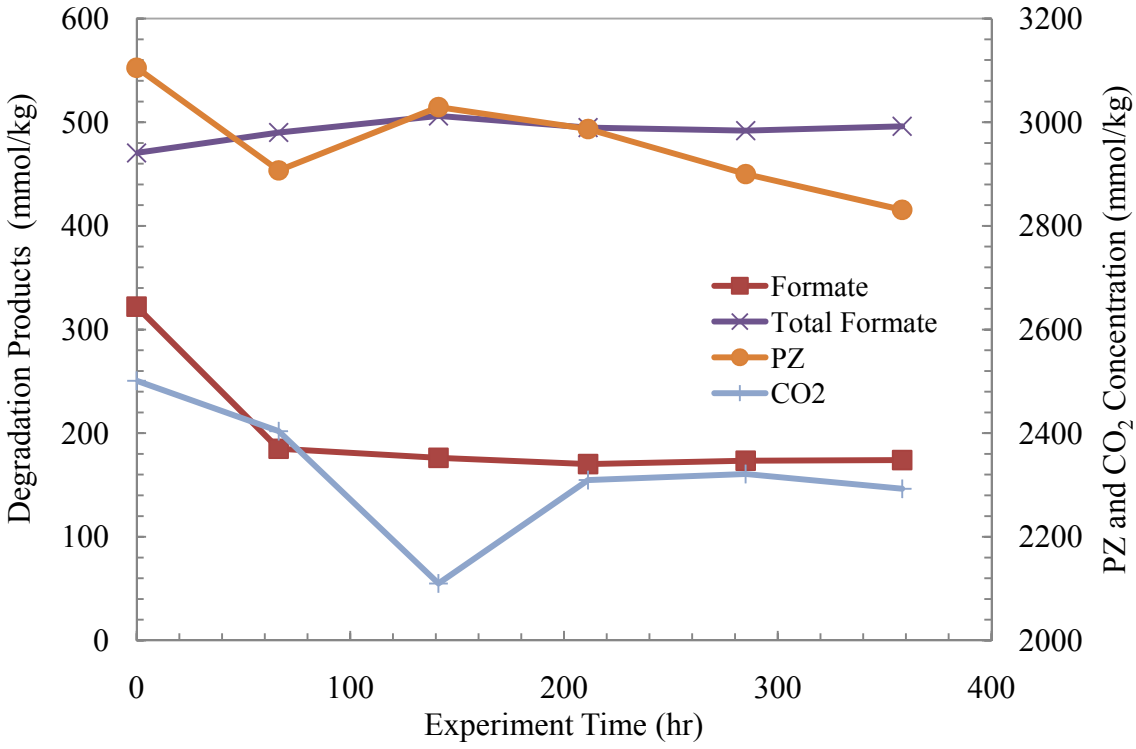

Figure 20: Concentration curves for OE20 (8 m PZ, 70 °C, 100 mL/min 98% O_2, α = 0.3 mol CO_2 per mol alkalinity, 0.4 mM Fe^{2+}, 0.1 mM Cr^{3+}, 0.05 mM Ni^{2+}, 500 mmol/kg

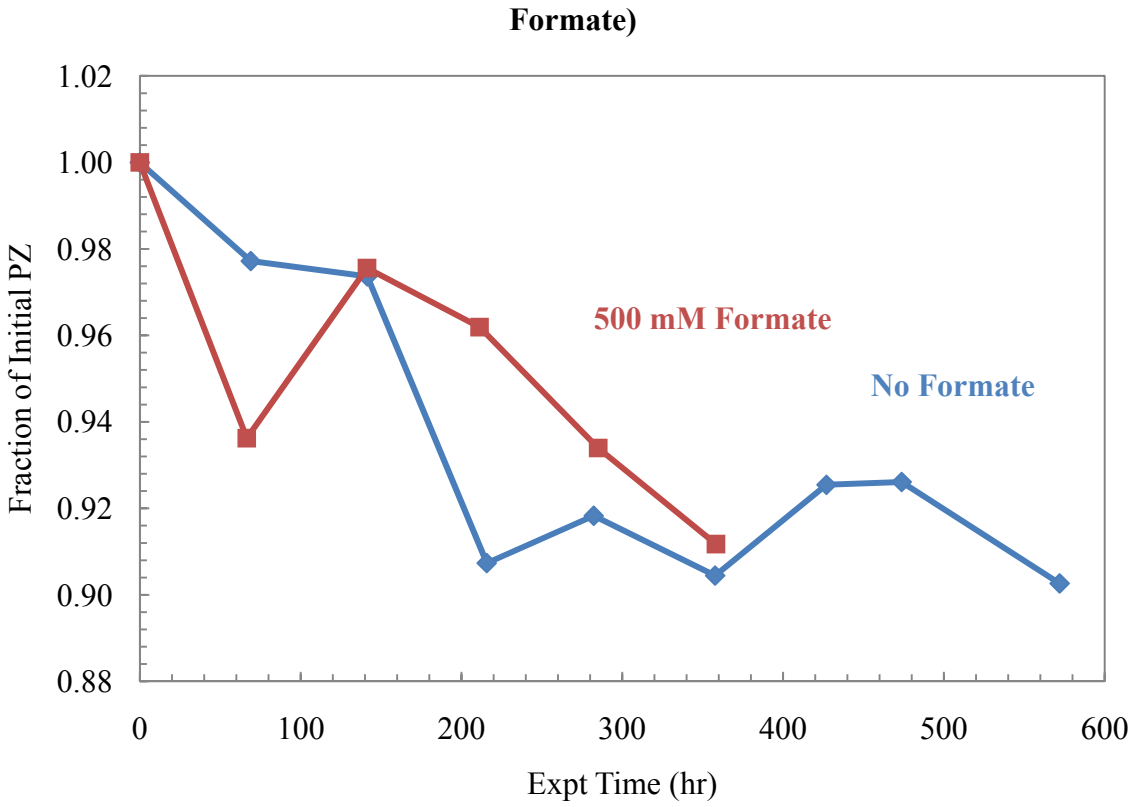

Figure 21: Effect of formate addition on PZ loss. Both experiments: 8 m PZ, 70 °C, 100 mL/min 98% O_2, α = 0.3 mol CO_2 per mol alkalinity, 0.4 mM Fe^{2+}, 0.1 mM Cr^{3+}, 0.05 mM Ni^{2+}

OE21 – Stainless Steel Metals and Formaldehyde at 70 °C with Low CO_2 Loading

As a complementary experiment to OE20, an oxidation experiment was performed in the presence of 0.4 mM Fe^{2+}, 0.1 mM Cr^{3+}, 0.05 mM Ni^{2+}, and 500 mmol/kg formaldehyde at 70 °C with 2kPa of CO_2 in the Teflon Oxidation Reactor (TOR). Formaldehyde was chosen as a spike in an attempt to accelerate oxidation of PZ. This species is suspected to be an important intermediate in the oxidation of PZ and it was hypothesized that the addition of this high concentration would catalyze the PZ degradation so that the oxidation could be quantified more easily compared to previous experiments where very little PZ is oxidized in the experimental time.

Unfortunately, the concentration was much too high and 500 mM generated an operational issue. When it was added, it reacted immediate to form very stable, dense, white foam on the surface of the reactor. This foam persisted even after stirring the reactor and the decision was made to continue the experiment to see how the formaldehyde and the foam would affect the results. The experiment was shorter than normal though, only 5 days.

The concentrations of PZ, CO_2, formate, formyl amides, acetyl amides, oxalyl amides, and N-formyl PZ (FPZ) are shown in Figure 22 below. No glycolate, acetate, nitrite, or nitrate was found in appreciable quantities. FPZ was quantified directly through cation IC and is shown in Figure 22 as well. The concentration of FPZ tracks in good agreement with that of formyl amides quantified via amide reversal indicating that FPZ is likely the only formyl amide of

appreciable quantity. Two samples were taken at the beginning of the experiment, one before (t = 0A) and one after (t = 0B) the addition of formaldehyde. The decrease in PZ between sample 0A and 0B indicates that PZ is being taken up in the dense white foam that was created from the addition of formaldehyde as only the liquid below the foam was sampled for 0B.

Through the course of the 5-day experiment, 7.8% or 2.3% of the initial PZ was lost if either sample 0A or 0B, respectively, was regarded as the initial sample. FPZ was the only amide produced, which is expected with such a large addition of formaldehyde. When compared to a baseline oxidation experiment under similar conditions, the production of formate and formyl amides was actually lower even with the large addition of formaldehyde. The production of formate and total formate in a baseline experiment (OE19) and this experiment with formaldehyde addition (OE21) is compared in Figure 23. Initially, the rates are somewhat similar for the two experiments but those for OE21 slow down and end up producing less formate and total formate overall. This was not expected since formaldehyde has been assumed to be a very reactive intermediate in the oxidation process, and was expected to rapidly oxidize to formate under the oxygen-rich conditions of the reactor.

The presence of the foam complicates the experiment since the concentration of formaldehyde in solution is not actually 500 mM. The exact composition of the foam is not known, but it is probable that it is a polymer of formaldehyde and PZ so the concentration of formaldehyde could be significantly lower than the 500 mM added. The fact that less formate was produced than a comparable solution is still unexpected even with a lower formaldehyde concentration than thought. It was anticipated that any spike of formaldehyde would increase the concentration of formate and formyl amides. The presence of the foam probably limited the amount of oxygen that was successfully absorbed into solution. Even with agitation, the foam was present and probably interfered with the mass transfer of oxygen into solution.

OE22 – Stainless Steel Metals

Since the TOR experiments have been done at 70 °C, the CO_2 flow has not been adjusted. The condition of 2% CO_2 (2kPa) has been maintained which has changed the CO_2 loading of these experiments compared to a condition of 2% CO_2 at 55 °C. A summary of the conditions of all of the experiments performed in the new TOR reactor is shown in Table 2 below. The first two experiments, OE17 and OE18, matched the conditions of all the previous experiments on the OOR. At 55 °C, 2 kPa of CO_2 corresponds roughly to a lean loading for PZ at 0.32 mole CO_2 per mole alkalinity. However, when the temperature was increased to 70 °C and the P_{CO2} was kept at 2 kPa, the corresponding expected loading was low at 0.26 mole CO_2 per mole alkalinity.

With these conditions in mind, an experiment was performed with a rich CO_2 loading for PZ. OE22 was performed with a P_{CO2} of 61 kPa, which corresponds to a rich loading of 0.42 mole CO_2 per mol alkalinity based on CO_2 solubility data previously gathered (Dugas, 2009). The experiment was only spiked with the standard concentrations of stainless steel metals (0.4 mM Fe^{2+}, 0.1 mM Cr^{3+}, 0.05 mM Ni^{2+}) to isolate the effect of changing loading. The only caveat to this experiment is that changing the P_{CO2} inherently changes the P_{O2}. Therefore, with the limitation of atmospheric pressure, the oxygen concentration must be lowered to achieve the rich loading. Future experiments will be done with this oxygen concentration to isolate the effect of oxygen and CO_2 concentrations separately.

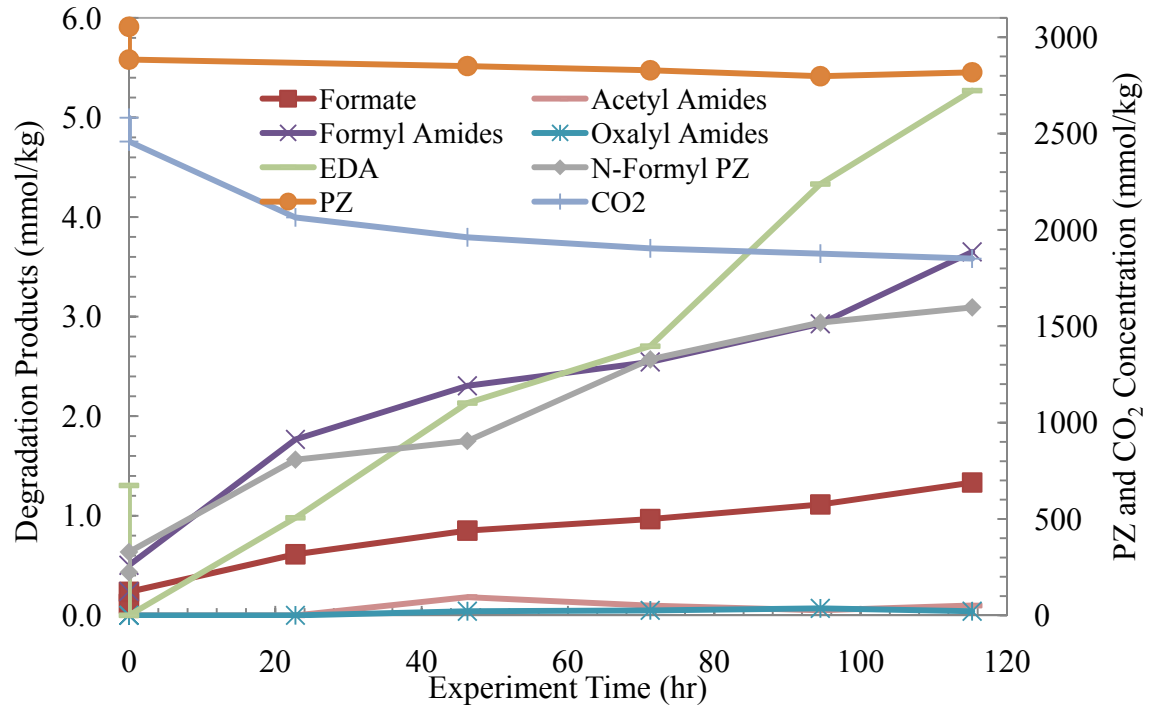

Figure 22: Concentration curves for OE21 (8 m PZ, 70 °C, 100 mL/min 98% O_2, α = 0.3 mol CO_2 per mol alkalinity, 0.4 mM Fe^{2+}, 0.1 mM Cr^{3+}, 0.05 mM Ni^{2+}, 500 mmol/kg formaldehyde)

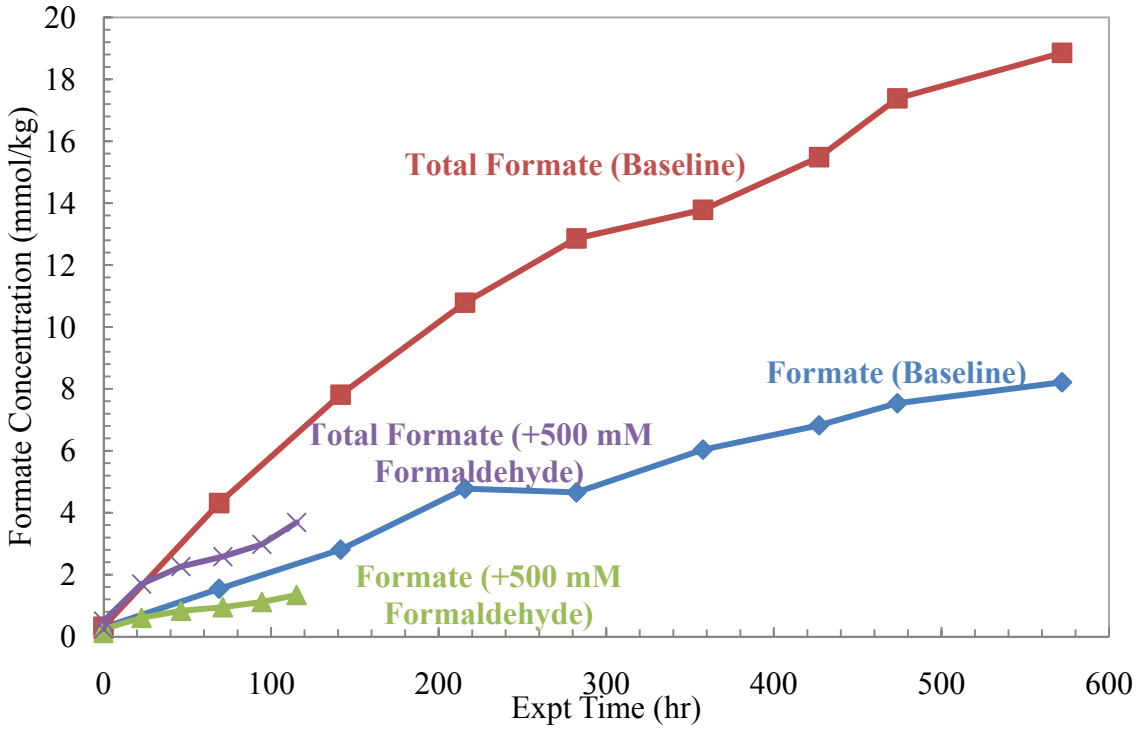

Figure 23: Effect of formaldehyde addition on formate and formyl amide production. Both experiments: 8 m PZ, 70 °C, 100 mL/min 98% O_2, α = 0.3 mol CO_2 per mol alkalinity, 0.4 mM Fe^{2+}, 0.1 mM Cr^{3+}, 0.05 mM Ni^{2+}

Table 2: Operational conditions for TOR experiments

Expt	Temp °C	P_{CO2} kPa	CO_2 Loading[1] mol/mol alk	P_{O2} kPa	Additives[2,3]
OE17	55	2	0.32	98	SS
OE18	55	2	0.32	98	SS
OE19	70	2	0.26	98	SS
OE20	70	2	0.26	98	SS, Formate
OE21	70	2	0.26	98	SS, Formaldehyde
OE22	70	61	0.42	39	SS

[1] Predicted from CO_2 solubility
[2] SS = Stainless steel metals (0.4 mM Fe^{2+}, 0.1 mM Cr^{3+}, 0.05 mM Ni^{2+})
[3] Spikes of formate and formaldehyde were each 500 mM

The concentrations of PZ, CO_2, formate, formyl amides, and EDA are shown below in Figure 24. No glycolate, glycolyl amides, acetate, acetyl amides, oxalate or oxalyl amides were detected using anion IC. Trace concentrations of nitrite and nitrate were detected but are omitted from Figure 24 due to their small concentration. Over the course of 600 hours, 10.2% of the original PZ was lost according to cation IC data. EDA was the dominant degradation product with formate and formyl amides also being present. Overall, all the degradation product concentrations were low relative to highly oxidized PZ solutions. The effect of changing both P_{CO2} and P_{O2} are shown in Figure 25 below. The solid curves are the baseline low loading experiment (OE19) while the dashed curves are the rich loading/low O_2 experiment (OE22). OE22 produced significantly less formate and formyl amides compared to OE19, but the PZ loss based on cation IC data was consistently lower. Unfortunately, the combined effect of increasing CO_2 concentration and lowering O_2 concentration cannot be separated in this experiment. Based on previous results for MEA, it is expected that increasing CO_2 concentration will decrease the oxidation rate while lowering the O_2 concentration will have the opposite effect. Since the oxidation rate is lower in OE22 than in OE19 based on the generation of common degradation products, the effect of changing CO_2 concentration appears to be dominating the results.

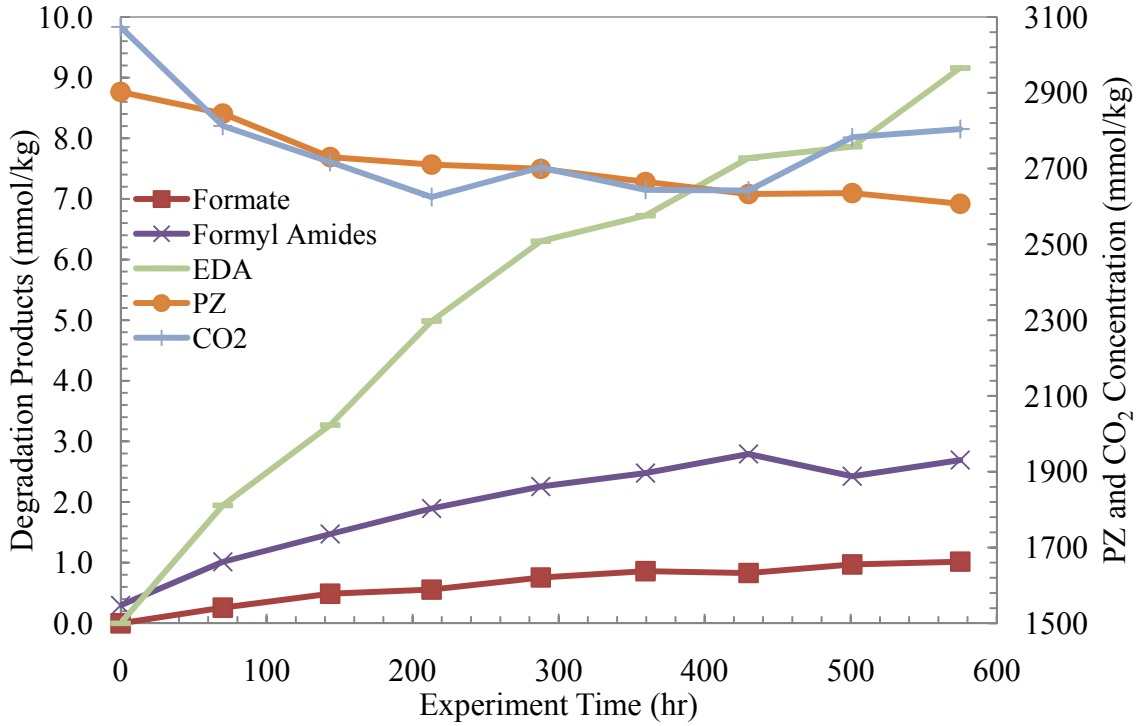

Figure 24: Concentration curves for OE22 (8 m PZ, 70 °C, 100 mL/min 60% O_2, α = 0.42 mol CO_2 per mol alkalinity, 0.4 mM Fe^{2+}, 0.1 mM Cr^{3+}, 0.05 mM Ni^{2+})

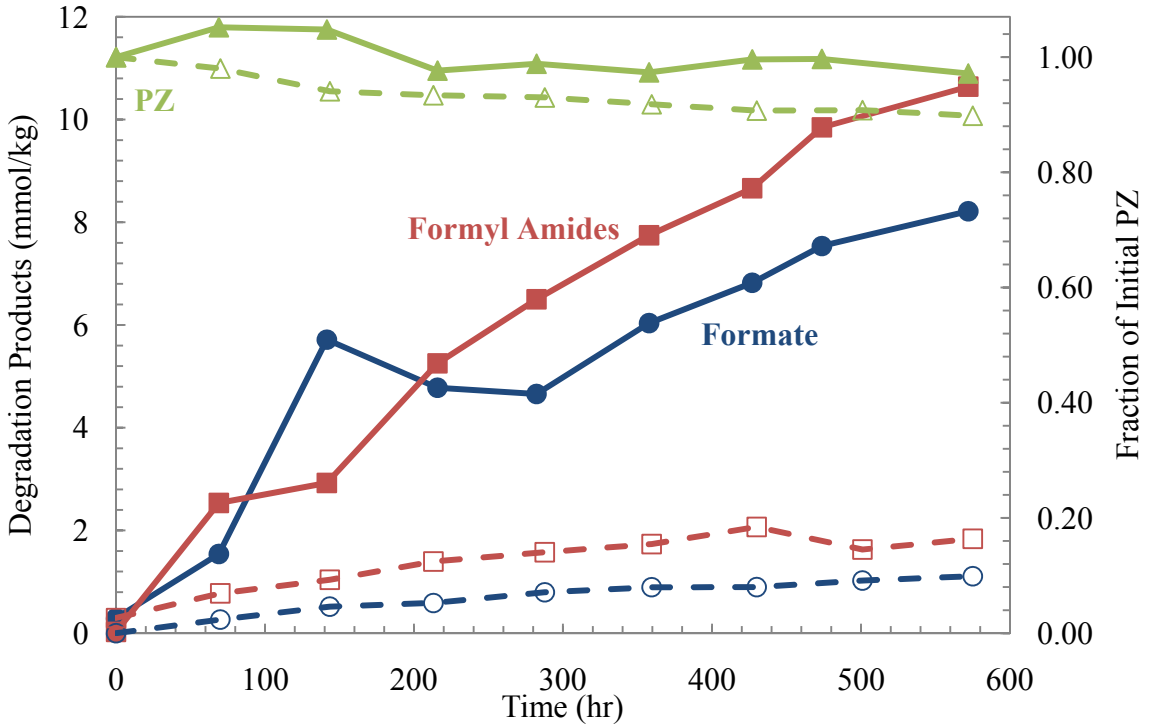

Figure 25: Comparison of PZ (green), formate (blue), and formyl amides (red) for α = 0.26 (solid) and α = 0.42 (dashed). Both experiments: 8 m PZ, 70 °C, 100 mL/min total gas, 0.4 mM Fe^{2+}, 0.1 mM Cr^{3+}, 0.05 mM Ni^{2+}.

Analysis of PZ Foaming Results to Date

The foaminess coefficient of solutions has been measured on every PZ oxidation experiment to date, except for a few cases where the solution was not available for testing. These results have been used in some cases to make the argument for PZ oxidation where the analysis of products was not conclusive. Unfortunately, the results have been contradictory and all of the foaming results were reanalyzed this quarter to determine the reliability of the measurements for oxidized PZ solutions.

The details of the foaming tests performed on oxidized PZ solutions are summarized in Table 3 below. A neat solution of 8 m PZ was analyzed by Chen and is included as the first entry in the table (Chen et al., 2010). All experiments were performed on 8 m PZ except for OE1 and OE2 which were 10 m PZ. The type of reactor was changed from the OOR to the TOR starting with OE17. Experiments OE1, OE2, and OE3 were not tested because the solutions were discarded before the apparatus was built. The foam stability of OE4 was not measured by Chen. OE14 was not tested for foaming because the reactor broke at the end of the experiment and there was no final solution to test. OE21 was not tested because the addition of 500 mM formaldehyde to the reactor created very stable white foam that persists in the final solution. The total formate at the end of the experiment is included in the table as an indication of the overall level of degradation.

The inconsistencies noticed in the foaming data can be demonstrated when looking at the four experiments that were degraded only in the presence of Fe^{2+}: OE5, OE5B, OE13, and OE17. These experiments are highlighted in bold in Table 3. The foaminess coefficients for these four experiments are 85, 300, 8, and 17 $\times$ 10^{-3} m^2-s, respectively, while the foam stability is >600, >600, 8, and 19 seconds, respectively. The experiments have differences such as reactor type and degradation time, but the range in the data is striking and suggests that all the foaming data should be reanalyzed. The high foaminess coefficient found for OE5B has been used as a rationale for the hypothesis that PZ is oxidizing while degradation products cannot be found in solution. This assumption is very weak in light of the other foaming results for oxidation, with 1.0 mM Fe^{2+} yielding similar concentrations of total formate (OE5, OE13, and OE17).

The oxidation of PZ has always been problematic because of a lack of detectable degradation products. Only formate, total formate, and occasionally EDA are present in appreciable concentrations after oxidation. It has been hypothesized separately that either the total formate concentration or foaminess of a solution should represent the overall PZ oxidation rate in lieu of accurately quantifying PZ loss during the experiment. The foaminess coefficient is plotted against the total formate concentration at the end of the experiment in Figure 26 below. The experiments with the same additives have been indicated using different colored data points. The experiments with 1.0 mM Fe^{2+} have red squares while those with 0.4 mM Fe^{2+}, 0.1 mM Cr^{3+}, and 0.05 mM Ni^{2+} are indicated with green triangles. The inconsistency of the data can easily be seen in this way.

Unfortunately, there is not a dependable relationship between the two variables and this inconsistency indicates that both cannot represent PZ oxidation as a whole. The three experiments with the highest concentrations of total formate (OE4, OE8, and OE19) have foaminess coefficients ranging from 88 to 300 $\times 10^{-3}$ m^2-s. However, what does not seem to make sense is that two of the experiments with the highest foaminess coefficients (OE5B and OE7) have very low total formate concentrations at 2.4 and 0.6 mmol/kg, respectively. The four

experiments with 1.0 mM Fe^{2+} (red squares) have a wide range of foaminess coefficients with consistent levels of total formate at the end of the experiment.

Table 3: Summary of foaming tests performed on oxidized PZ

Expt	Expt Additives[1]	Rxtr Temp	Deg Time	Total Formate	Before Foaming[3]	Foaminess Coefficient[3]	Foam Stability[3]
	mM	°C	hr	mmol/kg	day	10^{-3} m^2-s	sec
Neat	-	-	-			86	NT
OE1	0.2 Fe, 1.6 Cr, 0.2 Ni	55	606	7.3	NT	NT	NT
OE2	4 Cu	55	495	184.7	NT	NT	NT
OE3	0.1 Fe, 0.1 V	55	381	10.5	NT	NT	NT
OE4	1 Fe, 5 Cu, 100 A	55	742	20.5	195	300	NT
OE5	**1 Fe**	**55**	**70**	**2.4**	**1**	**85**	**>600**
OE5B	**1 Fe**	**55**	**163**	**2.1**	**0**	**300**	**>600**
OE6	1 Fe, 100A	55	70	1.3	1	92	>600
OE6B	1 Fe, 100A	55	163	1.4	0	68	>600
OE7	30 B	55	164	0.6	1	380	>600
OE8	30 EDTA	55	168	18.4	1	88	>600
OE9	-	55	336	2.5	283	3	10
OE10	-	55	336	4.7	207	20	40
OE11	-	55	314	2.4	198	11	37
OE12	-	55	296	1.8	225	18	19
OE13	**1 Fe**	**55**	**523**	**3.7**	**112**	**8**	**8**
OE14	1 Fe, 100A	55	381	3.6	NT	NT	NT
OE15	0.4 Fe, 0.1 Cr, 0.05 Ni	55	427	4.8	82	10	22
OE16	0.4 Fe, 0.1 Cr, 0.05 Ni, 10 A	55	427	1.3	82	16	25
OE17	**1 Fe**	**55**	**424**	**3.4**	**156**	**17**	**19**
OE18	0.4 Fe, 0.1 Cr, 0.05 Ni	55	576	4.3	49	117	45
OE19	0.4 Fe, 0.1 Cr, 0.05 Ni	70	572	18.9	11	195	35
OE20	0.4 Fe, 0.1 Cr, 0.05 Ni, 500 Formate	70	358	NA[2]	1	110	140
OE21	0.4 Fe, 0.1 Cr, 0.05 Ni, 500 Formaldehyde	70	115	3.7	NT	NT	NT
OE22	0.4 Fe, 0.1 Cr, 0.05 Ni	70	575	3.0	32	26.25	85

1 Abbreviations: Fe is Fe^{2+}, Cr is Cr^{3+}, Ni is Ni^{2+}, Cu is Cu^{2+}, V is V^{5+}, A is Inhibitor A, B is Inhibitor B.
2 NA = Not applicable since formate was an additive
3 NT = not tested

The stability of oxidized PZ solutions after an experiment has concluded was a primary concern considering the conflicting foaminess data. To analyze this, the number of days between the end of the oxidation experiment and the foaminess test was calculated for all the foaming tests performed. The number of days between the experiment end and the test are plotted against the foaminess coefficient in Figure 27 below.

With the exception of the data from OE4 (195 days, 300 $\times 10^{-3}$ m^2-s), there appears to be a slight correlation between the number of days and the overall foaminess coefficient. No measurements

past 60 days resulted in foaminess coefficients of more than 25 × 10^{-3} m^2-s except OE4. This suggests that the contaminants or degradation products in solution that cause foaming during the foaming tests continue to react while on the shelf and can greatly affect test results. If this is the case, there is a lot of additional error that has been introduced into the data since the protocol has not been consistent in the time between the experiment end and when foaming is performed. Plotting the number of days between the experiment end and the test as a function of the foam stability also produces a very clear correlation (Figure 28). High foam stability values cannot be achieved with longer wait times. It is important to note that the foam stability was not measured for OE4.

The measurement of foaminess coefficient is not a consistent measurement. It appears to be widely variable and any conclusions taken from foaminess data should be considered qualitative at best. Since the degradation products that are responsible for foaming have not been determined, it is not known which variables in these experiments most affect the measured foaminess coefficient. At this point, the time between the experiment end and the measurement appears to have the most impact on the results.

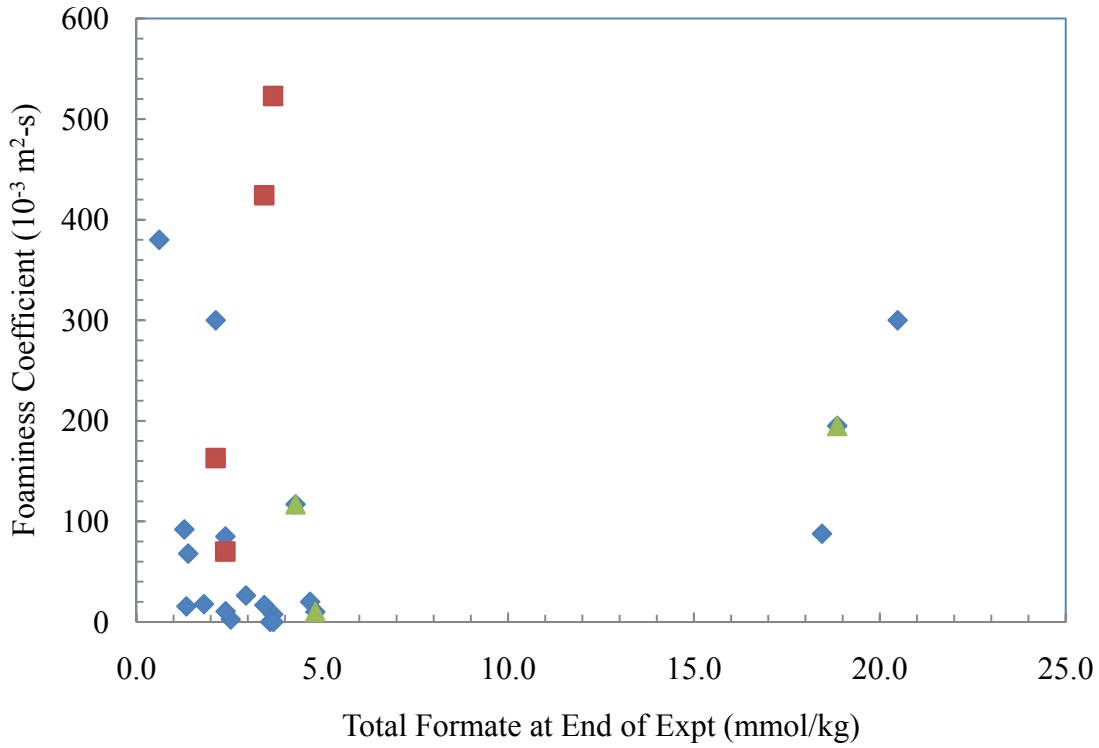

Figure 26: Relationship between the foaminess coefficient and total formate production

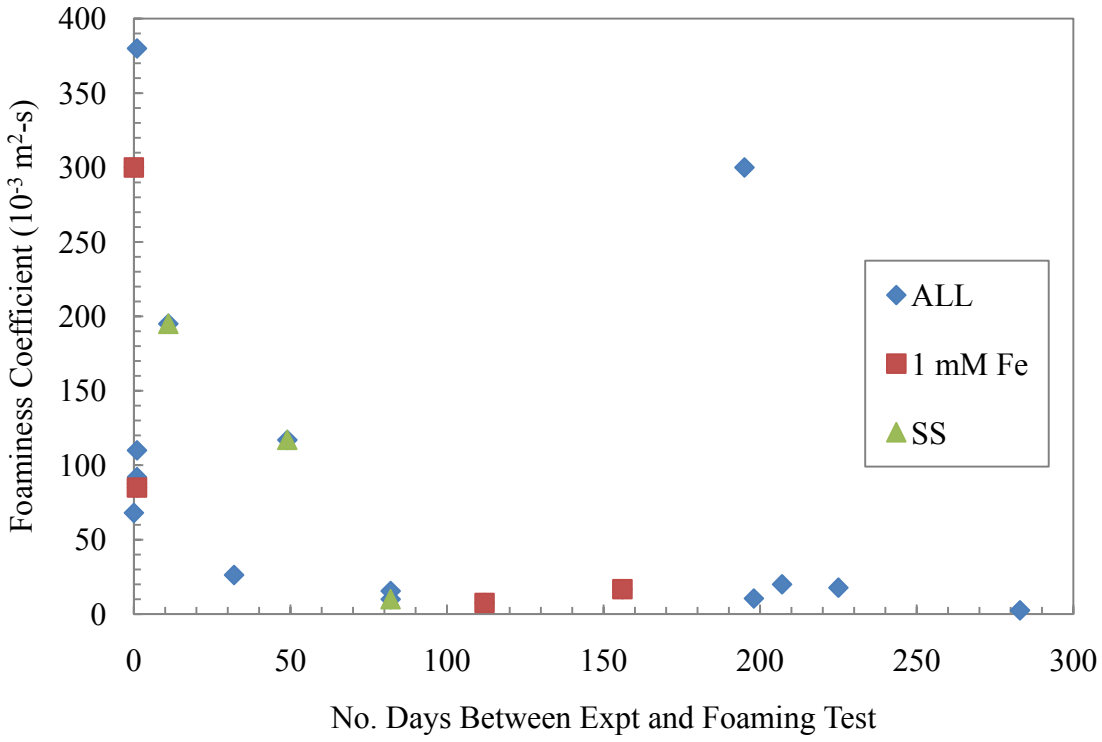

Figure 27: Relationship of foaminess coefficient and the delay in measurement

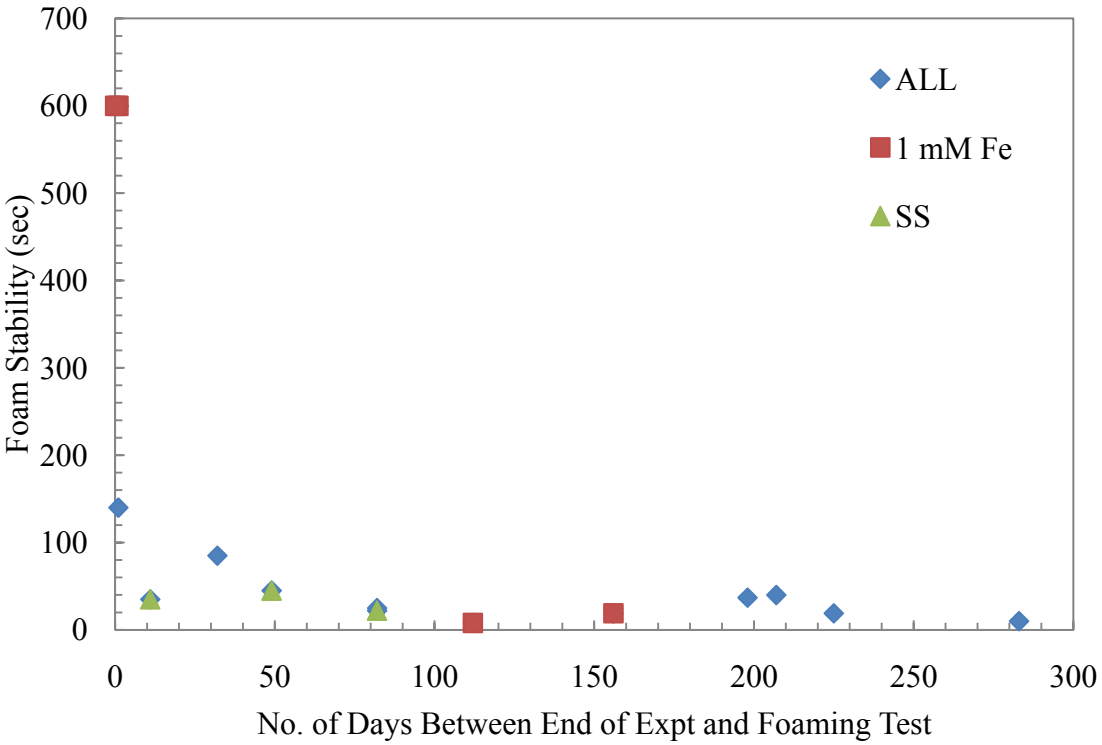

Figure 28: Relationship of foam stability and the delay in measurement

Conclusions

The concentration of PZ does not have a strong effect on the thermal degradation rate of 8 m PZ. This indicates that the thermal degradation of a concentrated PZ system is first order in PZ. There is, however, a slight but observable effect of concentration that is nearly within the error limits of the cation IC analysis. In 12 m PZ, the formyl amides quantified through alkaline amide reversal track with N-formyl PZ (FPZ) measured directly with cation IC for the first six weeks of degradation. The FPZ then reaches an equilibrium concentration and the total formyl amides continue to increase. The production of formate and formyl amides increases directly with increased PZ and CO_2 concentration. The equilibrium between formate and formyl amides does not have a consistent trend between 4, 8, and 12 m PZ. The concentration of EDA produced is consistent between degraded 4, 8, and 12 m PZ within the error limits of the cation IC, indicating that it is either not a direct function of PZ or CO_2 concentration or, perhaps more likely, is degrading itself and is essentially demonstrating its equilibrium concentration.

Morpholine (Mor) is highly resistant to thermal degradation. A solution of 8 m Mor lost only 17% of the initial amine after 15 weeks of degradation at 175 °C, less than a comparable 8 m PZ experiment. Mor and piperidine (PD) are the only amines screened so far that are more resistant to thermal degradation than concentrated PZ. Hexamethylenediamine (HMDA) degrades quickly at 175 °C, losing 80% of the initial amine within 15 weeks.

A solution of 8 m PZ loaded with 0.3 mole $^{13}CO_2$ per mole alkalinity was degraded at 175 °C to show that formate is produced directly from CO_2. ^{13}C NMR results of background samples and degraded PZ solutions confirmed the hypothesis that the carbon in formate is the same carbon as in the CO_2 molecule. This was hypothesized since CO_2 is the only significant source of oxygen besides water in oxygen-poor thermal degradation. This result is also consistent with the fact that formate and formyl amides are consistently the dominant degradation product in a variety of amine systems that do not undergo carbamate polymerization such as cyclic diamines (PZ, 1-MPZ, 2-MPZ), cyclic amines (PD, Mor), and alkanolamines (MDEA). Among all these amine systems, CO_2 is the common thread.

The addition of 500 mM formate to 8 m PZ did not strongly affect the oxidation of PZ or generation of degradation products. In this experiment, formate quickly established equilibrium with formyl amides and oxidation of PZ proceeded as it would in the absence of such a spike. Formate is not an oxidation inhibitor, and total formate was conserved, disproving the hypothesis that formate is being oxidized to CO_2. The addition of 500 mM formaldehyde to 8 m PZ created stable, dense, white foam that persisted through the oxidation experiment. The presence of the foam likely decreased the mass transfer rate of oxygen into solution. Lower concentrations of formate and formyl amides were produced in this oxidation experiment due to the decreased concentration of oxygen. Oxidation of 8 m PZ with a rich loading of 0.42 mole CO_2 per mole alkalinity proceeded more slowly than for a lean loading experiment. The result of the rich loading experiment was confounded by the increased CO_2 concentration, but reduced oxygen concentration.

The foaminess coefficient is not a consistent measurement and it is difficult to obtain repeatable results. The amount of time between the end of an experiment and the foaminess test appears to impact results, which is an unforeseen problem in the assay. The foaminess coefficient also does not accurately represent the overall degradation of an oxidized PZ solution.

Future Work

Investigation into the thermal degradation of PZ continues as 23 thermal experiments are currently underway. Analysis of these samples as the experiments conclude will be the focus of the thermal degradation work for this project. Understanding the mechanism that produces formate from CO_2 in oxygen-poor high temperature conditions will be a focus of the upcoming quarter.

Oxidation of PZ will also be a focus for the next quarter. Experiments will be done to amplify oxidation in an attempt to identify and measure more oxidation products. An experiment at high temperature (70 °C) with copper will be performed in order to get a highly oxidized solution to analyze with our newest analytical techniques. Also, some bench experiments will be performed using ^{13}C formaldehyde to determine the effect of formaldehyde in the oxidation of PZ.

References

AIST (2010). Spectral Database for Organic Compounds (SDBS), National Institute of Advanced Industrial Science and Technology (AIST).

Chen X, Freeman SA, Rochelle GT. "Foaming Behavior of Amine Solutions Used for CO_2 Capture with Different Additives." *IJGGC*. 2010; Submitted.

Cullinane JT, Rochelle GT. "Kinetics of carbon dioxide absorption into aqueous potassium carbonate and piperazine." *IECR*. 2006;45(8):2531–2545.

Davis JD. *Thermal Degradation of Aqueous Amines Used for Carbon Dioxide Capture*. The University of Texas at Austin. Ph.D. Dissertation. 2009:278.

Dugas RE. *Carbon Dioxide Absorption, Desorption, and Diffusion in Aqueous Piperazine and Monoethanolamine*. The University of Texas at Austin. Ph.D. Dissertation. 2009:253.

Freeman SA, Dugas RE, VanWagener DH, Nguyen T, Rochelle GT. "Carbon dioxide capture with concentrated, aqueous piperazine." *IJGGC*. 2010;4(2):119–124.

Freeman SA, Rochelle GT. "Thermal Degradation of Piperazine and its Structural Analogs." *Energy Proc*. 2010.

Gottlieb HE, Kotlyar V, Nudelman A. "NMR Chemical Shifts of Common Laboratory Solvents as Trace Impurities." *J Org Chem*. 1997;62:7512–7515.

Hilliard MD. *A Predictive Thermodynamic Model for an Aqueous Blend of Potassium Carbonate, Piperazine, and Monoethanolamine for Carbon Dioxide Capture from Flue Gas*. The University of Texas at Austin. Ph.D. Dissertation. 2008:1083.

Nguyen T, Hilliard MD, Rochelle GT. "Amine volatility in CO_2 capture." *IJGGC*. 2010;4(5):707–715.

Rochelle GT, et al. "CO_2 Capture by Aqueous Absorption, Third Quarterly Progress Report 2009." Luminant Carbon Management Program. University of Texas at Austin: 2009.

Rochelle GT, et al. "CO_2 Capture by Aqueous Absorption, Fourth Quarterly Progress Report 2009." Luminant Carbon Management Program. University of Texas at Austin: 2010a.

Rochelle GT, et al. "CO_2 Capture by Aqueous Absorption, Second Quarterly Progress Report 2010." Luminant Carbon Management Program. University of Texas at Austin: 2010b.

Ronalter M (2009). UT Chemistry Department Glass Shop. S. A. Freeman. Austin, TX, The University of Texas at Austin.

Sexton AJ. *Amine Oxidation in CO_2 Capture Processes*. The University of Texas at Austin. Ph.D. Dissertation. 2008:262.

Wallin J, Storey S. NMR Measurements (taken at) The University of Texas at Austin. 2010.

Zhou S, Chen X, Nguyen T, Voice AK, Rochelle GT. "Aqueous Ethylenediamine for CO_2 Capture." *ChemSusChem*. 2010;3(8):913–918.

Oxidative Degradation of Amino Acid Salts

Quarterly Report for July 1 – September 30, 2010

by Alexander K. Voice

Supported by the Luminant Carbon Management Program

Department of Chemical Engineering

The University of Texas at Austin

October 31, 2010

Abstract

Amino acids are shown to degrade oxidatively at rates comparable to other amines used in CO_2 capture. Ammonia (NH_3) production from a variety of amine and neutralized amino acid solutions was measured under moderate conditions representative of those in an absorber for CO_2 capture.

6 m potassium glycinate (GLY) degraded the most rapidly, showing a steady state rate of 6.25 mmol/kg/hr of NH_3 in the presence of 0.4 mM Fe^{2+}, 0.1 mM Cr^{3+}, and 0.05 mM Ni^{2+} at 80 °C. Under the same conditions, 7 m monoethanolamine (MEA) produced ammonia at a rate of 3.44 mmol/kg/hr. The rates for 5 m potassium taurinate (TAU), 3 m potassium taurinate/5 m potassium homotaurinate (HTAU), and sarcosine (SAR) were 0.62, 0.43, and 0.12 mmol/kg/hr, respectively.

The effect of metal salts and Inhibitor A was also assessed for these amino acids. Metals increased the ammonia production rate of GLY, TAU, TAU/HTAU, and MEA. No significant effect was observed for SAR. Inhibitor A decreased the NH_3 production rate for MEA, TAU, TAU/HTAU, but actually increased the rate for GLY.

Previous Work on Oxidation of Amino Acids

Oxidation of amino acids has been well studied over the last century. Previous research on this topic gives insight to the mechanism, products, and relative oxidation rates for amino acids in a carbon capture system. These findings can be compared to those for oxidation of MEA and other amines.

Mechanism of Amino Acid Oxidation with Metals

The proposed mechanism for oxidation of amino acids by molecular oxygen in the presence of a metal catalyst (Stadtman, 1993; Berlett, 1990) is very similar to the mechanism proposed for oxidation of MEA under the same conditions (Dennis, 1967; Denisov, 1996; Kovtun, 1973; Kovtun 1974; Stumm, 1961; Petrayev 1984). Oxidation begins with production of hydroxide radical via the Fenton reaction. This radical reacts with the amino acid by abstraction of a hydrogen from the alpha carbon to form an amino acid radical. This radical reacts with oxygen to form the peroxy radical, which in turn reacts with a superoxide radical to form oxygen and the amino acid peroxide. The peroxide decomposes to form the imino acid and hydrogen peroxide. The imino acid then hydrolyzes to form the primary products.

$$H_2O_2 + Fe(II) \rightarrow Fe(III) + OH^- + OH\bullet \quad (1)$$

$$NH_2CHR\text{-}CO_2H + OH\bullet \rightarrow NH_2C\bullet R\text{-}CO_2H + H_2O \quad (2)$$

$$NH_2C\bullet R\text{-}CO_2H + O_2 \rightarrow NH_2COO\bullet R\text{-}CO_2H \quad (3)$$

$$NH_2COO\bullet R\text{-}CO_2H + HOO\bullet \rightarrow NH_2COOH\text{-}R\text{-}CO_2H + O_2 \quad (4)$$

$$NHCR\text{-}CO_2H \rightarrow NHC\text{-}R\text{-}CO_2H + H_2O_2 \quad (5)$$

Oxidation is expected to occur in a coordination complex with the metal catalyst. Initially, the metal may be complexed with three bicarbonate molecules. The amino acid will dislodge one of these groups and attach to the metal catalyst by the nitrogen and carboxylic acid groups. Hydrogen peroxide reacts with this complex to oxidize the metal catalyst and produce the hydroxide radical. The radical then abstracts a hydrogen atom from the alpha carbon of the amino acid to form an imino acid. The imino acid decomposes and is replaced by another amino acid while the metal is reduced to its original state. Thus, oxidation occurs within the metal catalyst complex. With catalysis by dissolved iron, iron is cycled between the ferric and ferrous oxidation states, while free radicals generated remain within the complex and react directly with the amino acid (i.e. they do not diffuse into the bulk solution).

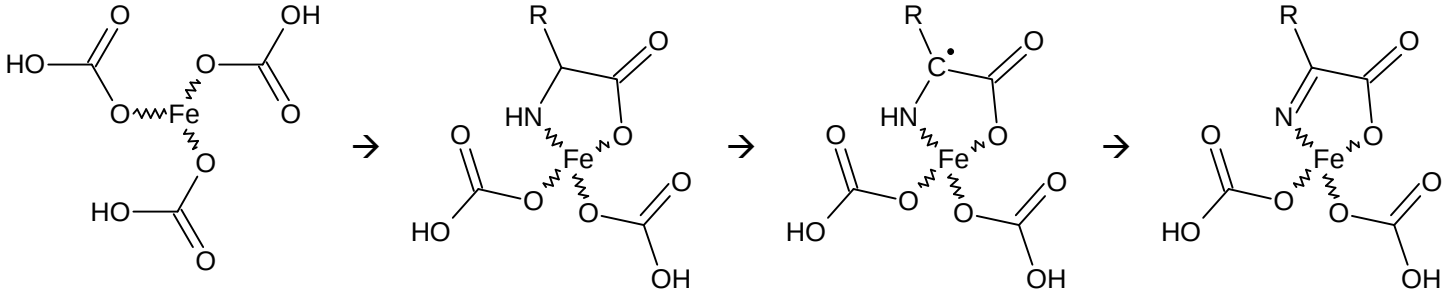

Figure 1: Iron-coordinated bicarbonate-dependent oxidation of amino acids by proton abstraction

Expected Products of Amino Acid Oxidation

In most cases, the primary products are ammonia and either an aldehyde and carbon dioxide, or an α-ketoacid and CO_2. Secondary products may be formed as the aldehyde may oxidize further to a carboxylic acid, and the α-ketoacid can decompose to a carboxylic acid and carbon dioxide (Greenstein, 1961).

Primary oxidation products:

$$NH_2CH\text{-}R\text{-}CO_2^- \rightarrow RCOCO_2^- + NH_3 + H_2O \quad (6)$$

$$NH_2CH\text{-}R\text{-}CO_2H \rightarrow RCHO + NH_3 + CO_2 + H_2O \quad (7)$$

Secondary oxidation products:

$$RCOCO2^- + H_2O_2 \rightarrow RCO_2^- + CO_2 + H_2O \quad (8)$$

$$RCHO + H_2O_2 \rightarrow RCO_2^- + H^+ + H_2O \quad (9)$$

Oxidative degradation of alpha amino acids has been carried out for many common amino acids. For a variety of oxidants, the products formed are ammonia, carbon dioxide, and an aldehyde. The products formed are both general (ammonia and carbon dioxide) and specific (the aldehyde). Therefore, oxidation of amino acids can be used to determine which amino acids are present, as well as the total amount of amino acid in solution (Greenstein, 1961).

$$NH_2CH\text{-}R\text{-}CO_2H \rightarrow NH_3 + CO_2 + RCHO \quad (10)$$

NH_3 stoichiometry was determined by oxidation of the amino acid with ninhydrin at low pH. The low pH prevents the formation of the colored ninhydrin product that comes from reaction with the alpha amino group (traditionally used to quantify the amount of free primary amine in a solution), and favors ammonia production instead. Carbon dioxide evolved from the solution was also quantified. These experiments have shown that most amino acids form stoichiometric quantities of ammonia when oxidized. One notable exception to this was proline, which produced a stoichiometric quantity of carbon dioxide, but no ammonia. Another exception was alanine: α-alanine produced stoichiometric quantities of ammonia and carbon dioxide, but β-alanine did not produce any ammonia or carbon dioxide (Greenstein, 1961).

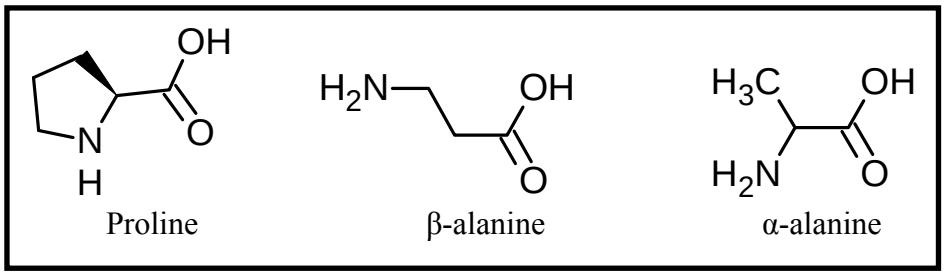

Figure 2: Structures of some amino acids

Some screening work has been carried out to determine which amino acids oxidize readily. Herbst conducted oxidation of amino acids with boiling aqueous silver oxide (Herbst, 1934). Although the experimental conditions do not represent the conditions of an amine scrubbing system, the results are instructive with regard to the relative stability of amino acids and the nature of products formed (Table 1).

Table 1: Selected Results of Amino Acid Oxidation by Boiling Silver Oxide

Amino Acid	Relative Ease of Oxidation	Structure	Unique Products[1]
Sarcosine	Very rapid	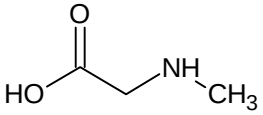	Methylamine
Dimethyl glycine	Very rapid	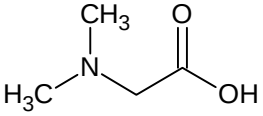	Dimethylamine

Glycine	Rapid	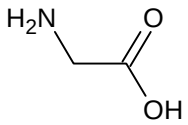	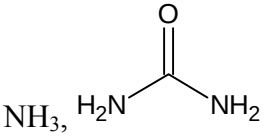 (trace)
Alanine	Rapid	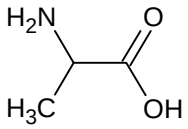	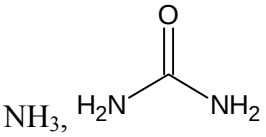 (trace) 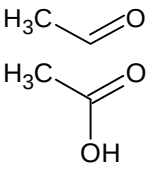
Proline	Rapid	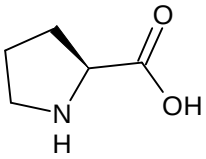	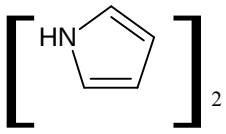
Glycyl alanine	Slow	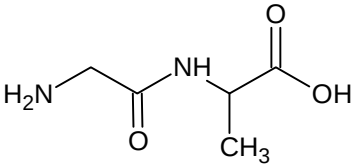	--
Betaine	Not oxidized	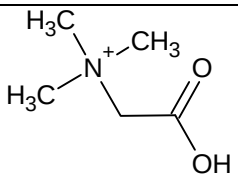	--
Dimethyl dantoin	Not oxidized	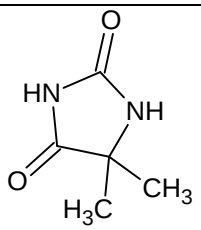	--

[1]All amino acids that oxidized formed CO_2
[2]Proline yielded a "volatile base with pyrrole odor"

Herbst made several observations based on these results. First, the amino group must be attached to the α carbon for oxidation to occur. Second, methylation of the α-carbon or amino group does not inhibit oxidation; in fact, methylation of the amino group increases the reduction potential of the amino acid. Third, complete methylation of the amino group (as with betaine) inhibits oxidation by silver oxide. This is likely because the imine cannot be formed following hydrogen abstraction (Figure 1).

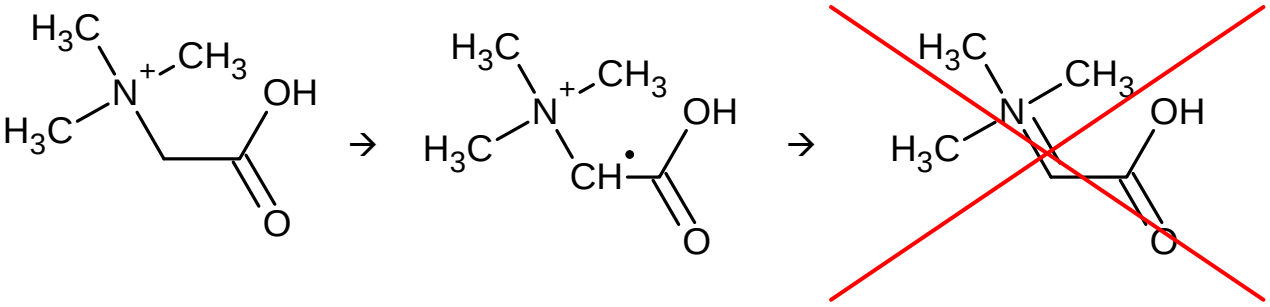

Figure 3: Oxidation Intermediates of Betaine

Fourth, it was observed that acylation of the nitrogen protected the amino acid from oxidation. This observation is consistent with the metal complex mechanism proposed by Stadtman, in that acylation would reduce the ability of the nitrogen to complex a metal catalyst as a result of the contribution of a minor resonance structure (Figure 3). Finally, incorporation of the carboxyl group into a peptide prevented oxidation, demonstrating that the free carboxyl group promotes oxidation. This is also consistent with the metal complex mechanism, as the carboxyl group occupies one of the coordination sites (Figure 2).

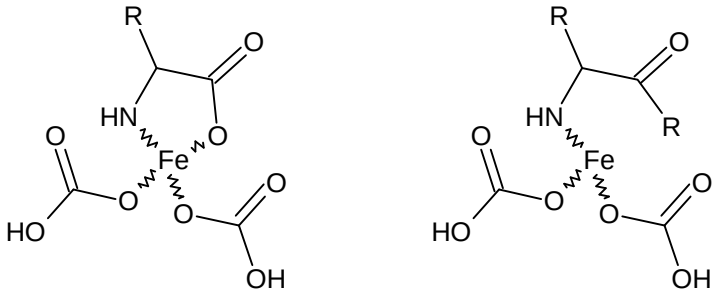

Figure 4: Polypeptide bonds remove the free carboxyl group and prevent formation of the amino acid-metal complex

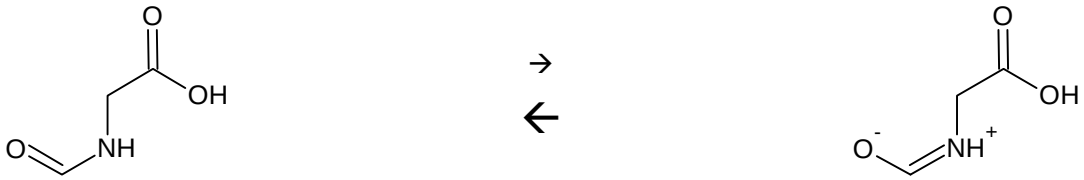

Figure 5: Acylation reduces formation of the amino acid-metal complex due to the contribution of a minor resonance structure

The metal catalyzed oxidation of proteins is also described by Stadtman. The result is useful because oxidation of proteins is presumed to occur by Fenton-type chemistry. The proposed mechanism is very similar to that of the oxidation of free amino acids, in that free radicals are generated within a metal complex and react with the alpha hydrogen of an amino acid in the residue. The key difference is that the metal may be coordinated by multiple sites in the residue, rather than by the free amino acid and bicarbonate. Stadtman lists the products (from multiple

sources) of oxidation of some amino acids in proteins, using iron or copper, oxygen, and an electron donor (Figure 4).

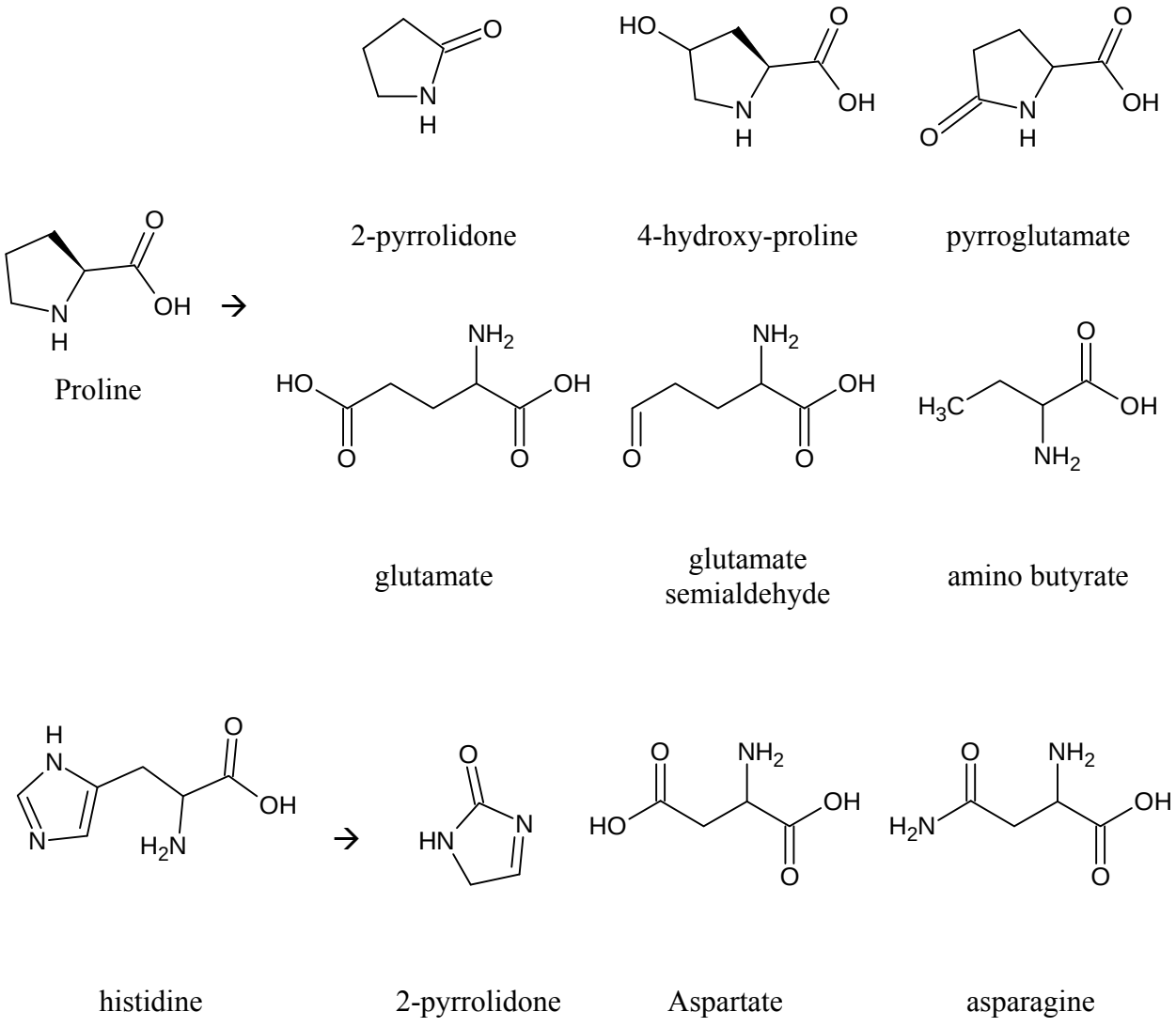

Figure 6: Oxidation Products of Proline and Histidine in Protein Residues

Previous Oxidative Degradation Screening Experiments with Molecular Oxygen

Kindrick studied the oxidation of amine solutions for use in a submarine atmosphere purification system (Kindrick, 1953). The conditions of the experiment were to contact 100 mL 2.5 M amino acid (potassium salt) solution with 50 kPa oxygen and 50 kPa carbon dioxide at a gas rate of 100 mL/min and at 80 °C for one week. The solutions were analyzed for total alkalinity, total primary amine concentration, total nitrogen, and total ammonia evolved. Two amino acids were tested in this study as their potassium salts. These were dimethylglycine and alanine.

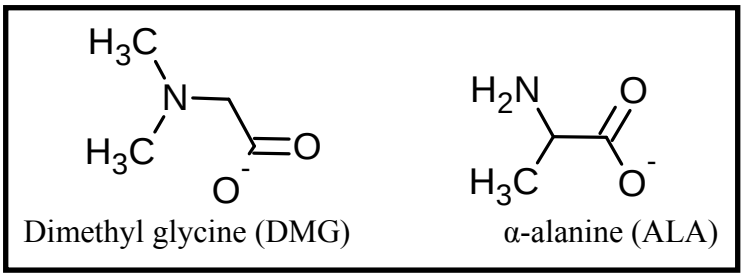

Figure 7: Structures of amino acids studied by Kindrick

Both amino acids showed significant resistance to oxidative degradation compared with MEA. In the case of DMG, this is expected as all tertiary amines studied by Kindrick (and others) showed resistance to oxidative degradation In the case of alanine, the resistance may be due to steric hindrance around the alpha carbon, preventing abstraction of the alpha hydrogen. The results for these amino acids are compared with MEA and MDEA in Table 2.

Table 2: Oxidation of Amines and Amino Acids at 80 °C with 50 kPa O_2 and 50 kPa CO_2

Amine	Alk. Loss (%)	Prim. Am. Loss (%)	Total N Loss (%)	NH_3 Prod. (mM)
MEA	45.7	43.5	11.2	60
DMG	6.07	--	5.33	20
ALA	-2.40	-2.47	-2.01	30
MDEA	1.63	--	0.79	10

Sexton studied oxidative degradation of potassium glycinate (GLY) (Sexton, 2008). In this experiment, 350 mL 2 m GLY was contacted with 98 kPa oxygen and 2 kPa CO_2at a rate of 100 mL/min at 55 °C for 11 days in the presence of 1 mM Fe^{2+}. Samples from the liquid phase were taken over the course of the experiment. The final analysis showed no loss of glycine over the 11 days. Only a small amount (6 mM) of formate was detected in the final solution.

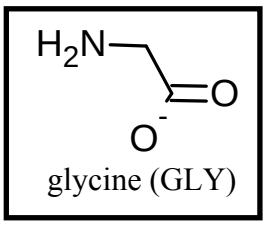

Figure 8: Structure of glycine

Epp also studied the oxidation of potassium glycinate and compared the results with MEA. The conditions of the experiment were 135 mL 50 wt % amine in contact with 90 mL oxygen in a batch system. Oxygen consumption and ammonia production were about three times higher for MEA than for GLY. MEA produced about 1 mol formaldehyde for every 5 mols NH_3, whereas GLY did not produce any formaldehyde. Amine loss was not determined (Epp, 2010).

$$xMEA + 1\ O_2 \rightarrow 1\ NH_3 + 0.2\ COH \quad (11)$$

$$xGLY + 1\ O_2 \rightarrow 1\ NH_3 \quad (12)$$

Experimental Methods

Amines and amino acids were degraded oxidatively in the high gas flow (HGF) apparatus, which has been used in previous degradation experiments. The HGF apparatus is a semi-batch glass jacketed reactor, containing a batch liquid phase and continuously sparged gas phase. Gas exiting the reactor was continuously analyzed by a hot gas fourier transform infrared analyzer (FTIR). Samples were taken at the start and finish of the experiment; these samples have not yet been analyzed.

Degradation Apparatus

In this work, three amino acid potassium salts and one amino acid blend have been studied for oxidative stability by contacting with oxygen and detection of gas phase degradation products (currently ammonia and methylamine). Two experimental setups have been used (Table 3). In both, 350 mL amino acid solution were contacted with 98 kPa air and 2 kPa carbon dioxide by sparging through the bottom of the reactor.

Table 3: Comparison of Two Types of Degradation Experimental Conditions

Variable	Design 1	Design 2
Temperature	55 °C	80 °C
Agitation	1440 RPM	None
Gas Rate	5 SLPM	7.5 SLPM
Solution volume	350 mL	350 mL
Catalyst	1 mM Fe	0.4 mM Fe^{2+}
		0.1 mM Cr^{2+}
		0.05 mM Ni^{2+}
Condenser	No	Yes
Pre-Saturator	No	Yes

The amino acids studied in this work are shown below. Each was neutralized with an equimolar quantity of potassium hydroxide and loaded with pure CO_2 to a loading of 0.2–0.4. After the start of the experiment, the amine typically took 1–2 hrs to come into equilibrium with the reaction gas, which contained 2 kPa CO_2.

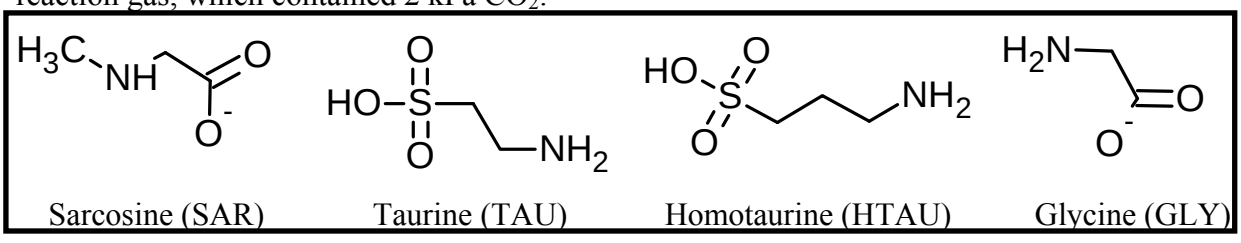

Figure 9: Structures of amino acids studied in this work

For each experiment, the neat solution was oxidized until the rate became relatively stable (usually after 1–6 hours). After this, a mixture of 0.4 mM Fe, 0.1 mM Cr, and 0.05 mM Ni was added to the reactor and the solution was degraded for a further 6–12 hours. Finally, 100 mM Inhibitor A was added to the reactor and the solution was degraded for 1–6 hours. A step change was typically observed on addition of metals or inhibitor to the solution.

Analytical Methods

Gas exiting the reactor was analyzed by a hot gas FTIR. This instrument analyzes the IR absorbance spectrum from 850 to 4000 cm^{-1} and uses an eigenvector analysis to quantify up to 60 compounds and minimize the residual area. A summary of the measuring ranges for several gas phase compounds is given in Table 4

Table 4: Summary of Analysis Regions used for sample spectrum analysis by FTIR in degradation experiments

Compound	Range 1 (cm^{-1})	Range 2	Range 3
Water	3157–3477		
CO_2	910–1003	3425–3616	2165–2251
MEA	2416–3150		
NH_3	915–988	2423–2560	
CH_3NH_2	2655–3191		

Results

Results are presented for the amino acids studied. The steady state rate of ammonia or methylamine production in the presence of metals indicates that:

$$6\text{ m GLY} > 7\text{ m MEA} >> 5\text{ m TAU} \approx (3\text{ m TAU} + 5\text{ m HTAU}) > 6\text{ m SAR}$$

The relative resistance of taurine and homotaurine to oxidation, as compared with glycine, may be due to the relative binding strength of the sulfate functional group with iron relative to the strength of the carboxyl group with iron. The extra carbon atom may also reduce the stability of the iron coordinated with both the nitrogen and sulfate group, which is most likely the reactive species.

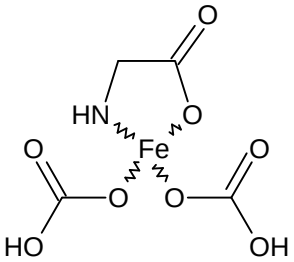

Glycine

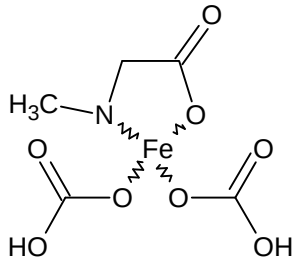

Sarcosine

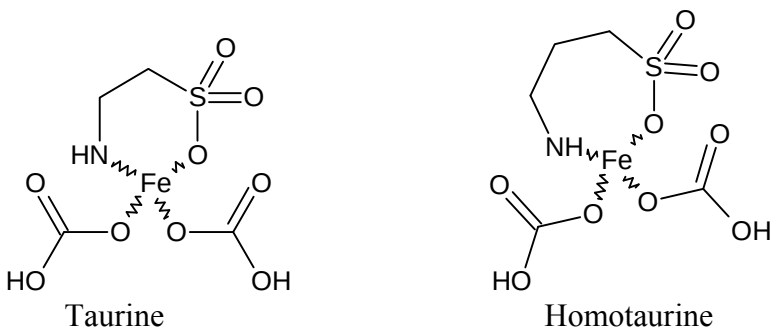

Figure 10: Iron-coordinated complex of various amino acids with bicarbonate

In the case of sarcosine, the methyl group may create a steric hindrance that disfavors formation of the metal complex.

A sample plot of the raw data from degradation of 6 m K^+ glycinate is shown below (Figure 5). The ammonia rate flattens out after approximately one hour. Addition of metals causes a step change in the ammonia rate, followed by a slow increase over the course of several days. Addition of Inhibitor A increases the ammonia production rate.

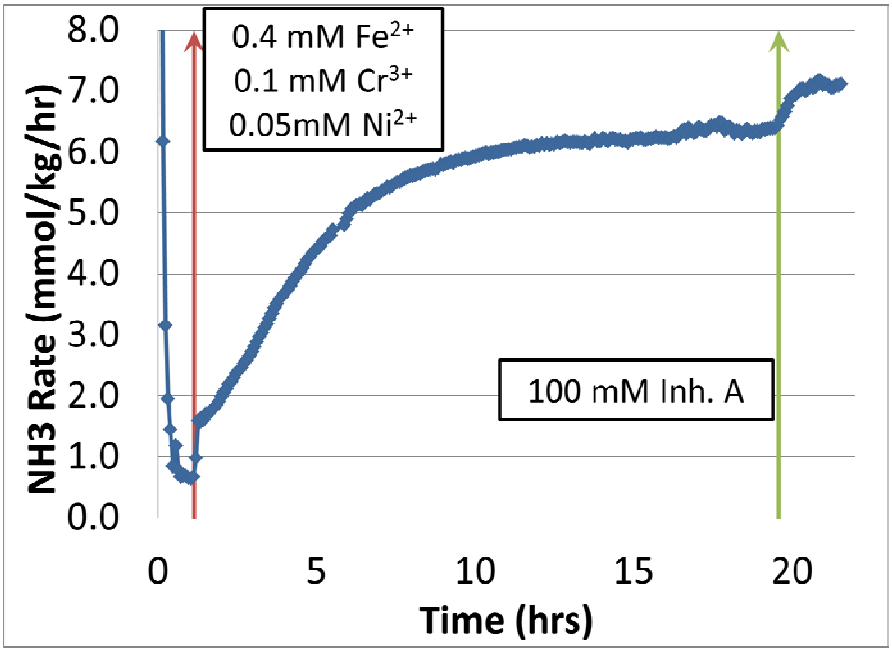

Figure 11: Oxidation of 6 m Glycine with Oxygen in the HGF Apparatus. Conditions: 80 °C, 7.5 LPM, 98 kPa air/2 kPa CO_2, no agitation, condenser+saturator

Addition of Metals

The effect of metals on the rate of ammonia or methylamine production from amino acid solutions is shown below (Figure 6). In each case, the red line represents addition of 0.4 mM Fe^{2+}, 0.1 mM Cr^{3+}, and 0.05 mM Ni^{2+} as the sulfate salt in sulfuric acid to the reactor. In the case of glycine and taurine, addition of the metals results in an immediate increase in the NH_3, followed by a sustained, higher steady-state rate. For the taurine/homotaurine blend, a burst of

NH_3 is observed, but no significant change in the steady-state rate occurs. For sarcosine, the metals do not have a significant effect on ammonia production.

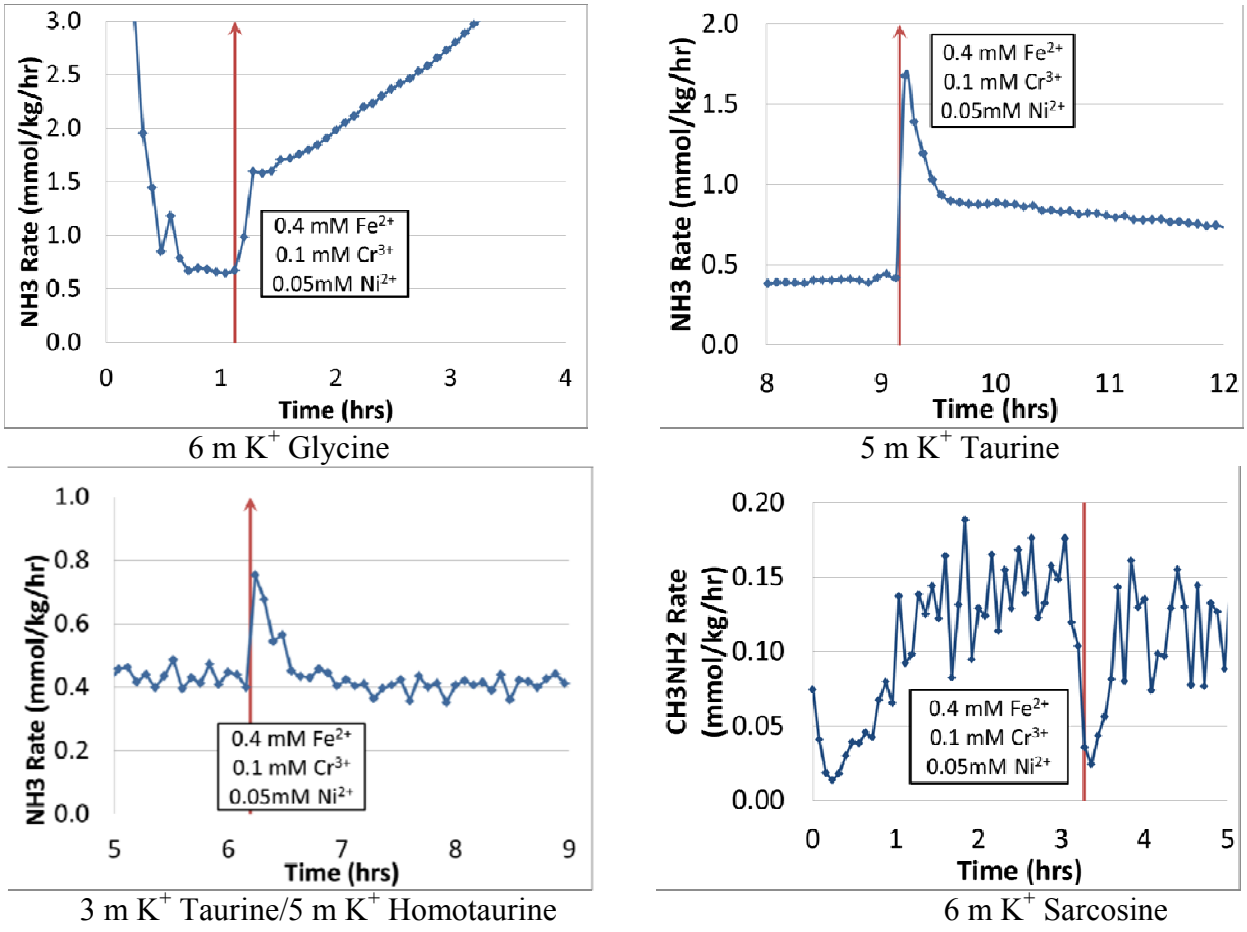

Figure 12: Effect of Metals on NH_3 or CH_3NH_2 rate from amino acid solutions in the presence of metal in the HGF. Conditions: 80 °C, 7.5 LPM, 98k Pa air/2 kPa CO_2, no agitation, condenser+saturator, 0.4 mM Fe, 0.1 mM Cr, 0.1 mM Ni.

Analysis of the sample spectrum for oxidative degradation of SAR demonstrates that methylamine, and not ammonia, is produced. In Figure 7, the contribution of ammonia (in red) to the total absorption spectrum is plotted with the residual spectrum (noise, in black). The spectrum falls well within the background noise of the measurement. In Figure 8, the residual spectrum is shown for the sample when only water, carbon dioxide, and ammonia are being analyzed. A significant peak is observed around 3000 cm^{-1}. When methylamine is included in the analysis, the peak in the residual disappears (Figure 9). Figure 10 shows that methylamine has a high (10:1) signal to noise ratio, indicating that it is present in a statistically significant quantity.

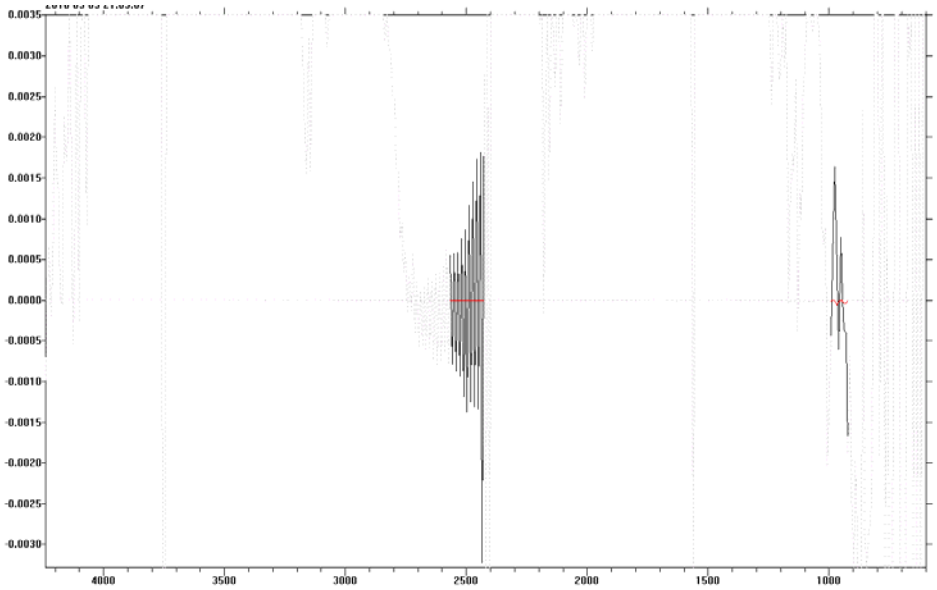

Figure 13: Residual (black) and ammonia spectrum (red)

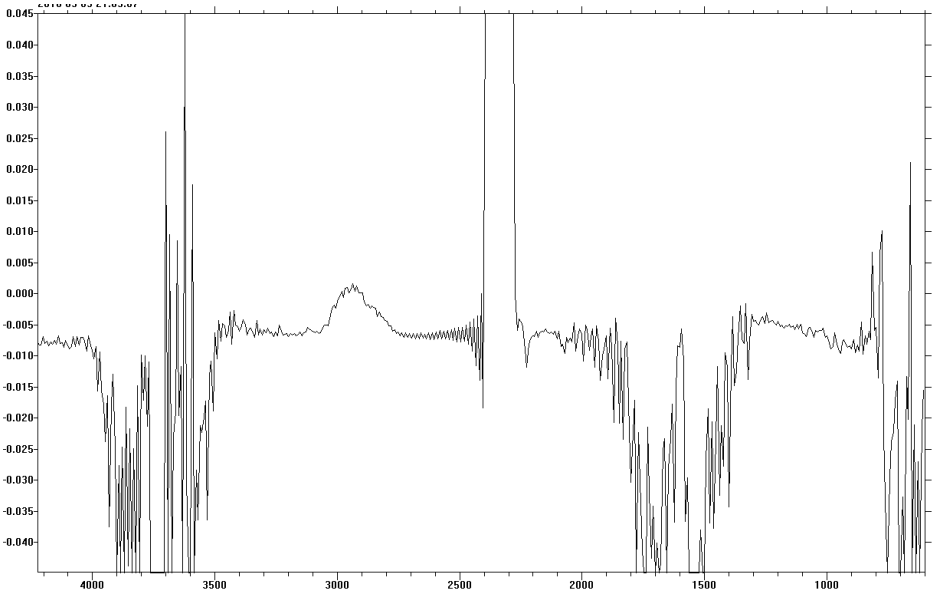

Figure 14: Spectrum residual w/o methylamine

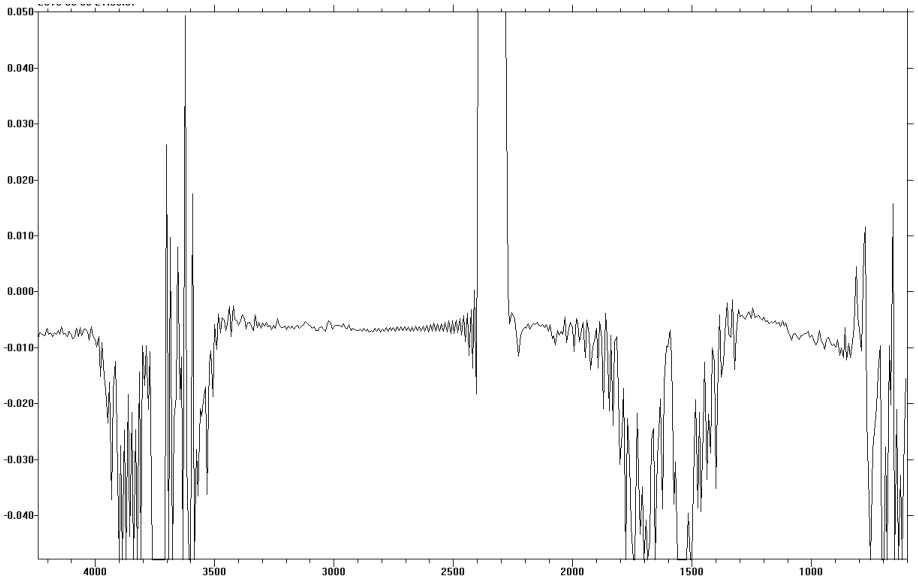

Figure 15: Residual spectrum with methylamine

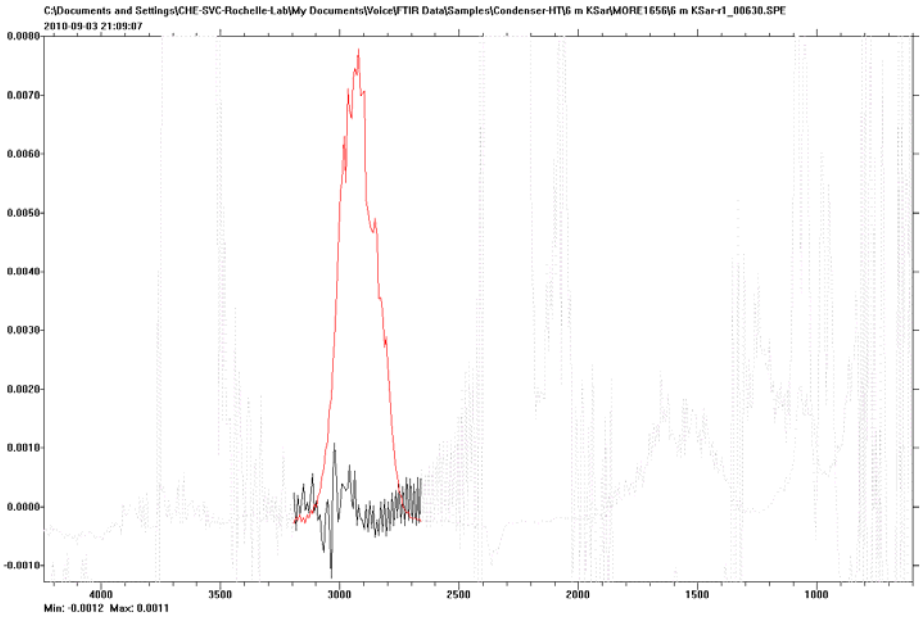

Figure 16: Methylamine spectrum (red) and residual (black)

Figures 7–10 show the statistical significance of the presence of NH_3 and CH_3NH_2 in oxidative degradation of SAR analyzed by hot gas FTIR. Conditions: 80 °C, 7.5 LPM, 98 kPa air/2 kPa CO_2, no agitation, condenser+saturator, 0.4 mM Fe, 0.1 mM Cr, 0.1 mM Ni.

Addition of Inhibitor A

The effect of Inhibitor A is shown in the plots below (Figure 11). In each case, the green line indicates addition of 100 mM of Inh A. For taurine, this resulted in a significant decrease in the steady-state ammonia rate. For the taurine/homotaurine blend, an immediate decrease was

observed, but the steady-state rate was not significantly altered. In the case of glycine, the steady-state rate was actually increased by addition of Inh A.

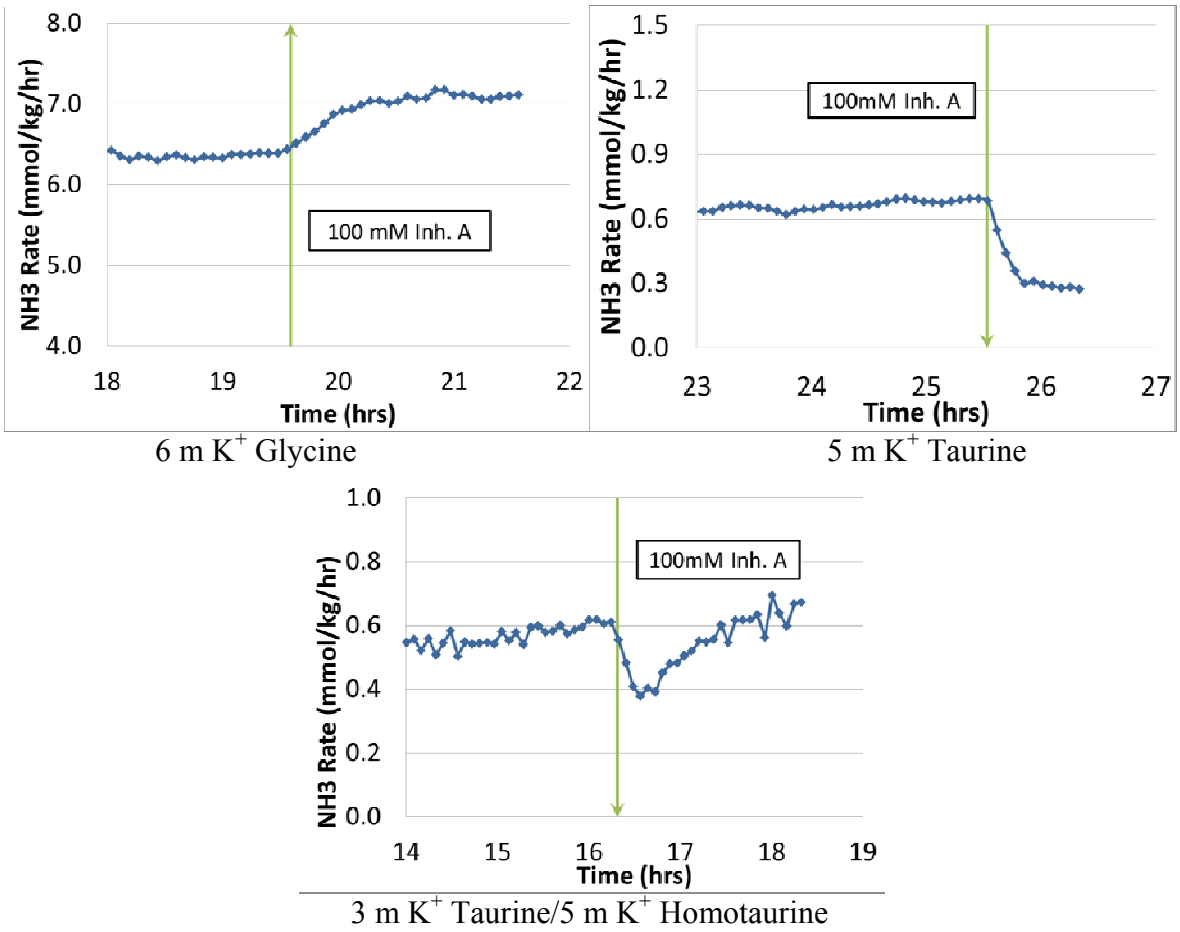

6 m K^+ Glycine

5 m K^+ Taurine

3 m K^+ Taurine/5 m K^+ Homotaurine

Figure 17: Effect of Inh A on NH_3 rate from amino acid solutions in the presence of metal in the HGF. Conditions: 80 °C, 7.5 LPM, 98 kPa air/2 kPa CO_2, no agitation, condenser+saturator, 0.4 mM Fe, 0.1 mM Cr, 0.1 mM Ni.

Overview of Results

The total amount of ammonia or methylamine evolved from the solution as a function of time over the course of the experiment is shown in Figure 12. Changes in the slope of the curve occur when metals or Inh A were added to the reactor.

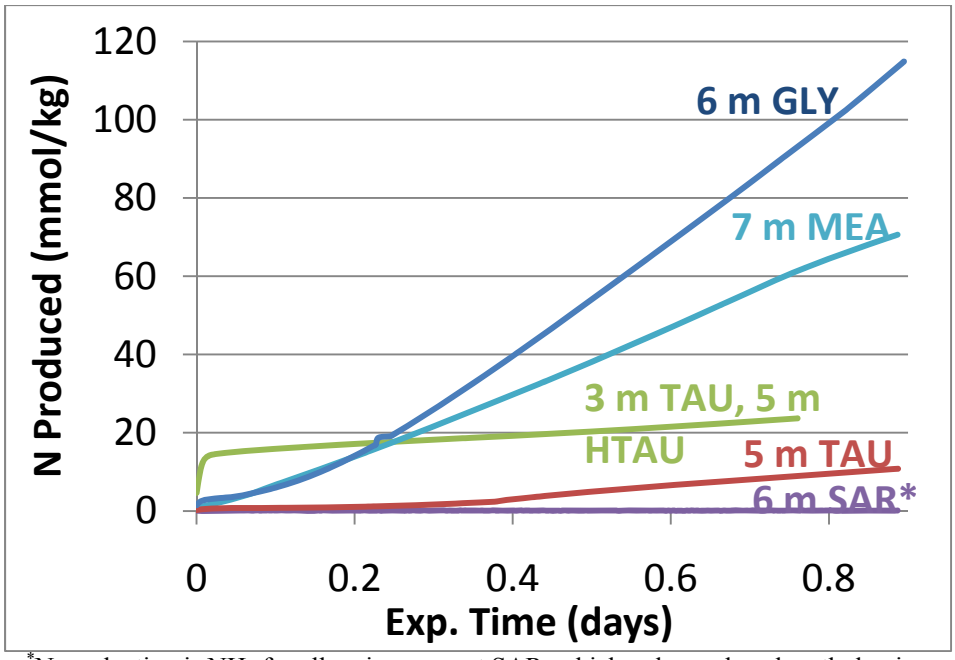

*N production is NH_3 for all amines except SAR, which only produced methylamine

Figure 18: Cumulative nitrogen production for various amino acids in the high gas flow apparatus. Conditions: 80 °C, 7.5 LPM, 98 kPa air/2 kPa CO_2, no agitation, condenser+saturator, 0.4 mM Fe, 0.1 mM Cr, 0.1 mM Ni.

The rate of NH_3 or CH_3NH_2 for each amino acid studied is reported in Table 5. The rates for amino acids are compared with the rates for MEA, which readily oxidizes, and piperazine (PZ), which is resistant to oxidation. The rates for each are reported as the average rate in the presence of the metal catalyst and before addition of any inhibitors. In all experiments where NH_3 was produced, a "burst" was observed on addition of the metals, which lasted 30–60 minutes before flattening out. Glycine showed unsteady-state behavior at both experimental conditions, although the ammonia rate eventually reached steady-state at the higher temperature condition. The cumulative degradation product produced is also reported (Table 6).

Table 5: Rate of ammonia and methylamine production from amine solutions using two experimental designs

Amine	Average Rate at 55 °C with 1 mM Fe – Design 1 (mmol/kg/hr)	Amine	Average Rate at 80 °C with metals – Design 2 (mmol/kg/hr)
7 m MEA	1.55	7 m MEA	3.44 (NH_3)
3.6 m K^+glycinate	0.16	6 m K^+GLY	6.25 (NH_3)
1.9 m K^+taurine	0.02	6 m K^+TAU	0.62 (NH_3)
8 m PZ	0.00	8 m PZ	0.00 (NH_3)
		3 m TAU/5M HTAU	0.43 (NH_3)
		6 m SAR	0.05 (CH_3NH_2)

Table 6: Cumulative ammonia and methylamine production in oxidative degradation screening. Experimental conditions (Design 1): 80 °C, 7.5 SLPM, 98 kPa air, 2 kPa CO_2, 0.4 mM Fe, 0.1 mM Cr, 0.05 mM Ni.

Amine	Total Product Evolved (mmol/kg)
7 m MEA	77 (NH_3)
6 m K^+GLY	115 (NH_3)
6 m K^+TAU	14 (NH_3)
3 m TAU/5M HTAU	24 (NH_3)
6 m SAR	3 (CH_3NH_2)

The effect of metals and Inh A on the NH_3 rate was assessed by sequential addition of metal sulfate salts and Inh A to the neat solution. Metals increased the NH_3 rate for all amines, which produced NH_3. Inh A was effective with all amine solutions except glycine (Table 7).

Table 7: Summary of the effect of metals and Inh A on the NH_3 or methylamine rate from amino acid solutions. Conditions: 80 °C, 7.5 LPM, 98 kPa air/2 kPa CO_2, no agitation, condenser+saturator, 0.4 mM Fe, 0.1 mM Cr, 0.1 mM Ni.

Amine	Effect of Fe/Cr/Ni	Effect of 100 mM Inh A
MEA	Increase	Decrease
GLY	Increase	Increase
TAU	Increase	Decrease
HTAU/TAU	Increase	Decrease
SAR (methylamine)	No effect	No effect

Conclusions

The results of this and other work indicate that amino acids will degrade oxidatively under the conditions present in an industrial amine scrubbing system. The reaction involves Fenton-type free radical production, followed by oxidation of the amine in a metal-coordinated complex. It is not clear that amino acids offer significant benefits of oxidative stability compared with standard amines.

- The order of degradation, based on the production of volatile degradation products, was 6 m GLY > 7 m MEA >> 5 m TAU ≈ (3 m TAU + 5 m HTAU) > 6 m SAR
- Inhibitor A reduced the ammonia rate for TAU, HTAU, and MEA. For GLY, the ammonia rate increased with inhibitor A.
- Amino acids, which complex well with iron, are predicted to be susceptible to oxidative degradation.

References

Berlett BS, Chock PB, Yim MB, Stadtman ER. "Manganese(II) catalyzes the bicarbonate dependent oxidation of amino acids by hydrogen peroxide and the amino acid-facilitated dismutation of hydrogen peroxide." *Proc Natl Acad Sci USA.* 1990;87:389–393.

Denisov ET. "Cyclic mechanisms of chain termination in the oxidation of organic compounds." *Russ Chem Rev.* 1996;65(6):505–520.

Dennis WH Jr, Hull DH, Rosenblatt H. "Oxidation of Amines. IV. Oxidative Fragmentation." *J Org Chem.* 1967;32(12):3783–3787.

Epp B, Fahlenkamp H, Vogt M. "Degradation of solutions of monoethanolamine, Diglycolamine®, and potassium glycinate in view of tail-end CO_2 capture." Submitted to *Int J Greenh Gas Con.* 2010.

Herbst RM, Clarke HT. "Oxidation of Amino Acids by Silver Oxide." *J Biol Chem.* 1934;104:769–788.

Kindrick RC, Atwood K, Arnold MR. "The Relative Resistance to Oxidation of Commercially Available Amines." Girdler Report No. T2.15-1-30;1950.

Kovtun GA, Aleksandrov AL. "Oxidation of Aliphatic Amines by Molecular Oxygen in the Liquid Phase-Commnunication 1-Kinetic principles of the uninhibited and inhibited oxidation of primary and secondary amines." *Izv Akad Nauk SSSR, Sev Khim* 1973;10:2208–2011.

Kovtun GA, Aleksandrov AL. "Oxidation of Aliphatic Amines by Molecular Oxygen-Communication 4-Regeneration of Inhibitors in Tertiary Amines Undergoing Oxidation." *Izv Akad Nauk SSSR, Sev Khim* 1974;1274-1279.

Petryaev EP, Pavlov AV, Shadyro OI. "Homolytic Deamination of Amino Alcohols." *Zh Org Khim* 1984;20:29–34.

Rooney PC, DuPart MS, Bacon TR. "Oxygen's Role in Alkanolamine Degradation." *Hydroc Proc.* Int. Ed. 1998;77(7):109–113.

Sexton AJ. *Amine Oxidation in CO_2 Capture Processes*. The University of Texas at Austin. Ph.D. Dissertation. 2008.

Stadtman ER. "Oxidation of free amino acids and amino acid residues in proteins by radiolysis and by metal-catalyzed reactions." *Annu Rev Biochem.* 1993;62:797–821.

Stumm W, Lee GF. "Oxygenation of Ferrous Iron." *Ind Eng Chem.* 1961;53:143–146.

Nitrosamine Formation in CO_2 Capture by Piperazine

Quarterly Report for July 1 – September 30, 2010

by Mandana Ashouripashaki

Supported by the Luminant Carbon Management Program

Department of Chemical Engineering

The University of Texas at Austin

October 31, 2010

Abstract

Secondary amines may react with nitrite to produce carcinogenic products called nitrosamines. Nitrosation reactions have been known for over 150 years but their carcinogenic properties were first discovered in 1956 and since then there has been an explosion of interest in their chemistry and particularly in methods of destroying them. Piperazine (PZ) is an amine of interest in our study and nitrosation products of PZ are N-nitrosopiperazine and N-N, dinitrosopiperazine (DNPZ).

A method for detecting and measuring dinitrosopiperazine (DNPZ) has been developed. A calibration curve with a sensitivity analysis of 6e-5 mmol/kg by liquid chromatography followed by mass spectrometry (LC-MS) has been established.

After considering methods to find out the probability of DNPZ presence, the kinetics of reaction between loaded PZ and nitrite are under investigation. Primary results show a first order reaction in nitrite in loaded PZ. However the amount of DNPZ produced is very small. Additional experiments will address the possible catalytic effects of formaldehyde and other degradation products on PZ nitrosation.

Introduction

Nitrosamine production occurs when secondary amines such as piperazine (PZ) undergo a nitrosation reaction in the presence of nitrite ions. The nitrosation reaction behind this formation has been known for over 150 years, but the carcinogenic properties of its products were first discovered in 1956 (Magee and Barnes).

PZ demonstrates that it is an effective promoter for carbon dioxide removal from gas streams. The rate constant is an order of magnitude higher than a primary amine (Bishnoi, 2000), but the reaction between PZ and nitrite may cause nitrosopiperazine formation.

The purpose of this research is to develop the analytical methods for detecting, measuring, and also monitoring nitrosamines, especially dinitrosopiperazine, in CO_2 capture using PZ. Kinetic studies of piperazine nitrosation are being performed. Experiments were conducted in order to find the effect of temperature, nitrite concentration, and amine concentration on nitrosation.

For the first objective standard pure dinitrosopiperazine solution was required to calibrate the instrument, and this was not available for purchase so it was synthesized using the USP 24 2000 method. This method uses PZ citrate (2C6H8O7, 3C4H10N2) and sodium nitrite ($NaNO_2$) in the presence of hydrochloric acid (HCl).

The investigation started with direct injection of a solution of dinitrosopiperazine in methanol as suggested by Attalla et al. (2010), but further experiments led us to change the solvent to a mixture of water and methanol to achieve better detection of DNPZ. Methanol must be used because DNPZ is not soluble in water. DNPZ is first dissolved in methanol then diluted by water and injected into the MS. A solution of 80% methanol and 20% water produces peaks that detect DNPZ, and a calibration curve for measuring DNPZ using LC-MS has been established.

After developing a method for detecting and measuring DNPZ, a kinetic study of 8 m loaded piperazine ($\alpha = 0.3$) was started. First, experiments were done with a rich concentration of nitrite ion (sodium nitrite) at varying temperature. The results showed a first degree reaction rate in nitrite. Next, rather than varying temperature, nitrite concentration and amine concentration were examined as reaction reagents.

Theory of nitrosation reaction

The most regularly used reagent for nitrosation is nitrous acid, generated in aqueous acid solution from a nitrite salt, typically sodium nitrite. Nitrous acid exists in aqueous solution in equilibrium with dinitrogen trioxide $\boldsymbol{N_2O_3}$, Equation 1, an effective nitrosating species which can be observed as nitrosonium nitrite (Equation 2).

$$2HNO_2 \rightleftarrows N_2O_3 + H_2O \quad (1)$$

$$N_2O_3 + Amine \rightarrow {}^{+}Amine - NO + NO_2^- \quad (2)$$

The rate equation, Equation 3, has been established for a range of amines.

$$Rate = k[HNO_2]^2[A] \quad (3)$$

This is the rate equation expected for rate limiting attack by an equilibrium concentration of N_2O_3 on amine, and the third order rate constant k in Equation 3 is given by $k_2 k_{\mathbf{N_2O_3}}$, where k_2 is the second order rate constant for N_2O_3 attack and $k_{\mathbf{N_2O_3}}$ is the equilibrium constant for N_2O_3 formation.

In a CO_2 capture plant using PZ, the pH of the system is high, so the acidic condition which promotes formation of N_2O_3 as a most important nitrosation reagent is not available but there are sources of nitrite ions in different sections of the plant. Normally a nitrite ion has no capacity for effecting nitrosation. However, in the presence of some carbonyl group containing catalysts, nitrosation can be achieved in neutral and basic solution.

Catalysts include formaldehyde, chloral, benzaldehyde derivatives, and pyridox. Reaction 4 is particularly effective for the conversion of secondary amines to nitrosamines.

$$\begin{aligned} R_2NH + R'CHO &\overset{OH^-}{\longleftrightarrow} R_2N^+ = CHR' + H_2O \\ R_2N^+ = CHR' + NO_2^- &\rightarrow R_2N - CHR'ONO \\ R_2N - CHR'ONO &\rightarrow R_2NNO + R'CHO \end{aligned} \quad (4)$$

Product formation was efficient with the formation of an iminium ion intermediate, which reacts with nitrite ions giving a dialkilamino nitrite ester which breaks down rapidly and intramolecularly to give nitrosamine and regenerate the catalyst. This pathway has been suggested for the reaction of secondary amines with solid sodium nitrite in halogenated solvents (Roller et al., 1980).

Experimental Methods

The fundamental procedure for making standard DNPZ for calibrating the measuring system follows USP 24 for nitrosation reaction of piperazine citrate.

Direct injection of dinitrosopiperazine (DNPZ) to Mass Spectrometry

Mass spectrometry (MS) is an analytical technique for determination of the elemental composition of a sample or molecule. The instrument consists of three main sections:

1. Ion source which converts gas phase sample molecules into ions;
2. Mass analyzer that sorts the ions by their masses by applying electromagnetic fields;
3. Detector, which measures the value of an indicator quantity and provides data for calculating the abundances of each ion present.

Here is an short explanation of the keywords that appear later in this report;

Direct Injection: Using the syringe pump that can be connected directly to the ion source to provide a steady state introduction of sample or tuning and calibrating solution.

Fragmentation: Breaking molecules to specific ions. Fragmentation pattern has led to mass spectra being used as "fingerprints" for identifying compounds.

According to the suggested method (Atalla et al., 2010) for detecting dinitrosopiperazine, samples of 0.00007–0.7 mmol of DNPZ per ml of methanol have been injected directly to see if MS can detect it. The mass spectrum diagram is shown in Figure 1.

When there was not any evidence of DNPZ in mass spectrum of above injections, water was added to the solution and in this case DNPZ could be detected by MS. To obtain more accurate results, the fragmentation method was run with results shown in Figures 2–5. For quantifying DNPZ, an LC-MS system was used; the method of measurement was developed by employing a reverse phase column. A solution of 80% methanol and 20% water was used as dilution solution for gaining optimum results for detecting DNPZ; the calibration curve is shown in Figure 6.

Kinetics of piperazine nitrosation

The experiments started with 8 m loaded PZ and 50 mmolal $NaNO_2$ at 21 °C, 60 °C, and 75 °C, then reaction continued for 5 days. Results show that at 75 °C, nitrite concentration decreases faster than at the other two temperatures (Figure 7). Further experiments have been conducted at 60 ^{o}C with 5, 20, and 50 mmolal $NaNO_2$. Finally, the effect of PZ concentration on nitrosation reaction is under investigation.

Results

Direct injection of Dinitrosopiperazine to Mass Spectrometry (MS)

Samples of 0.00007–0.7 mmol of DNPZ per ml of methanol have been injected to MS directly to see if MS can detect it. The mass spectrum diagram is shown in Figure 1.

Mass spectrometry shows the mass per charge of molecules and their relative abundance. For DNPZ we are looking for m/z = 145 because the molecular weight of DNPZ is 144 and by protonating with one hydrogen atom, the mass of ion will be 145.

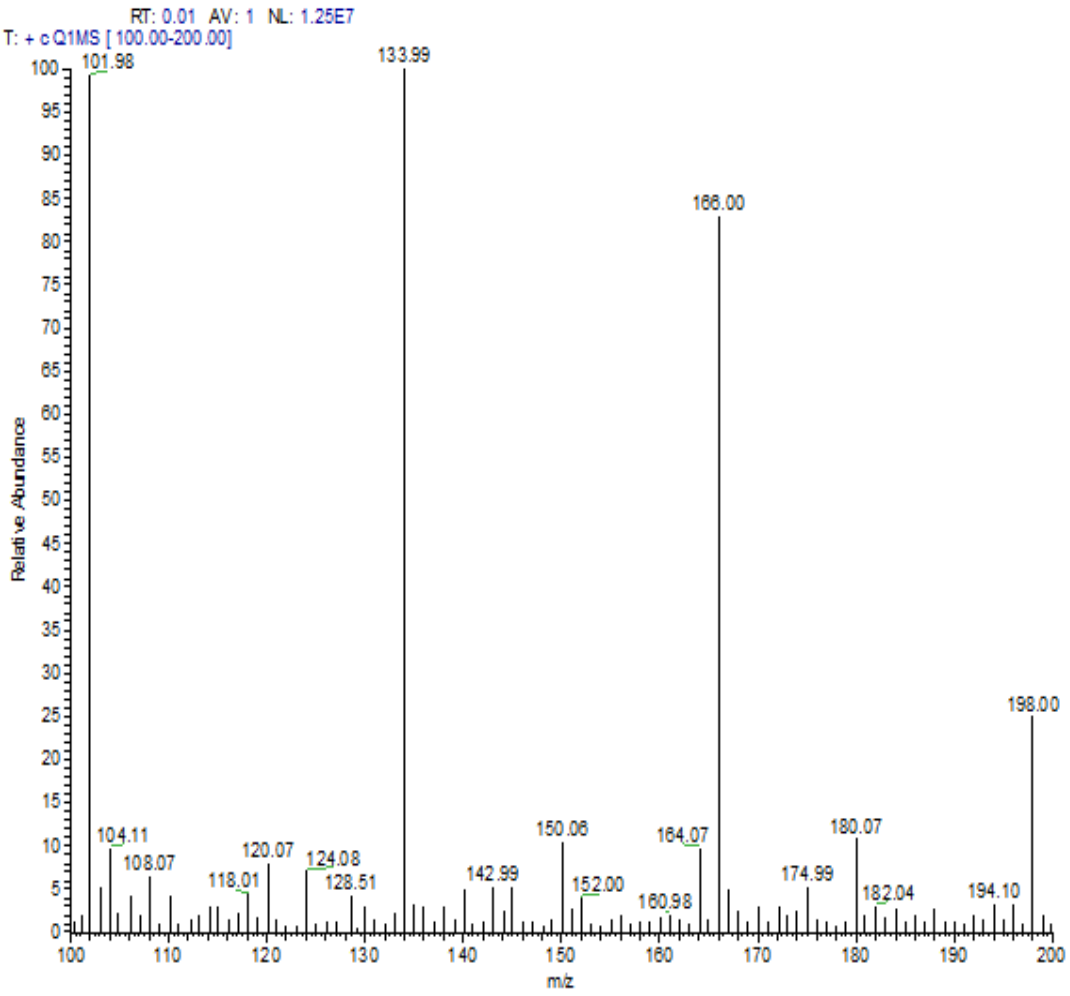

Figure 1: Mass spectrum of a sample of dinitrosopiperazine and methanol. (Relative abundance and m/z)

Figure 1 shows the typical mass spectrum of samples that have been injected into the MS. All sample results were very similar and in this report just one is described. There is no evidence of m/z = 145.

By adding water to the solutions (80% methanol and 20% water) and then injecting new samples to the MS, surprisingly mass spectrometry showed a peak at m/z of 145 which is DNPZ (Figure 2).

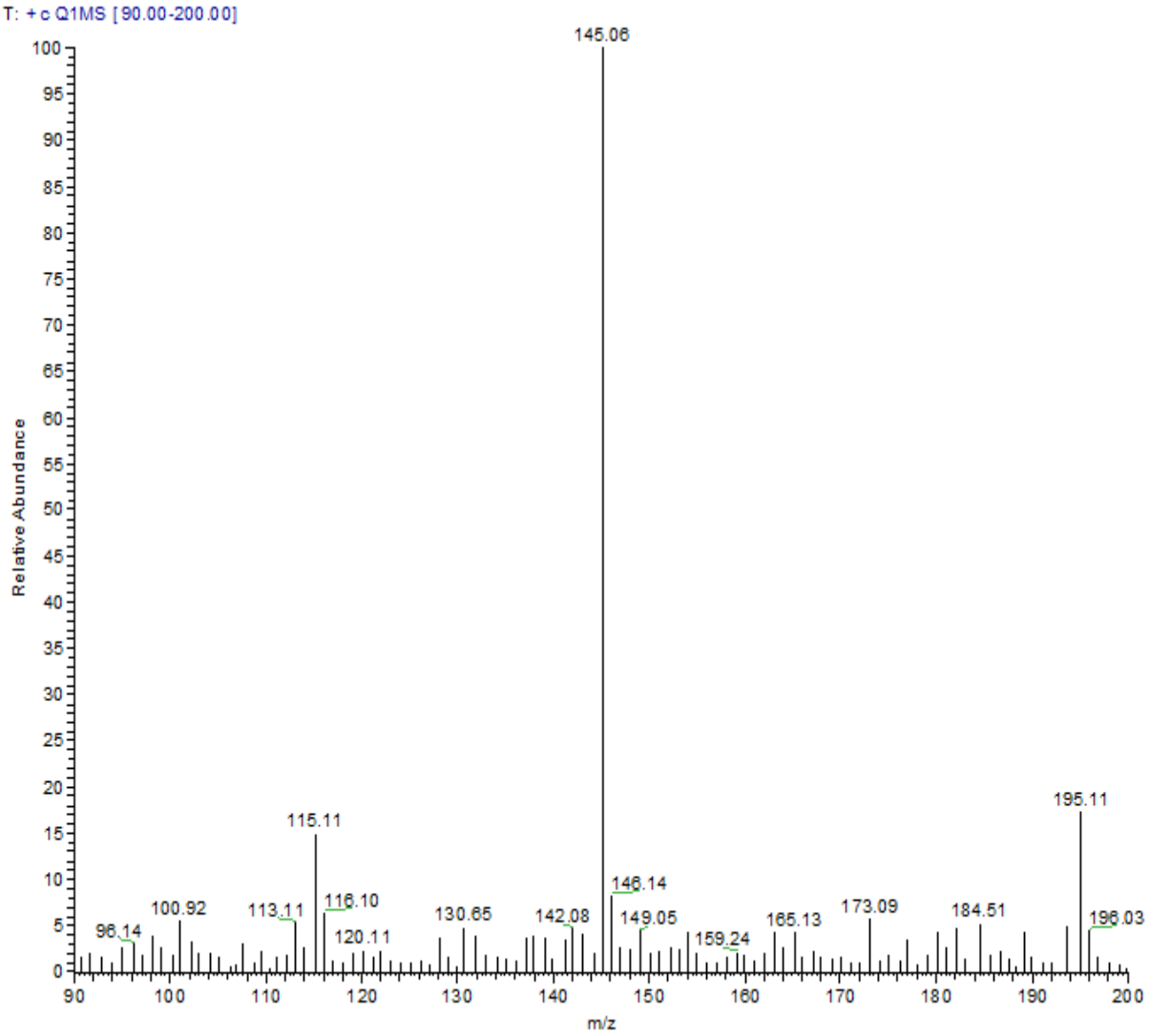

Figure 2: Mass spectrum of a sample of dinitrosopiperazine in methanol and water. (Relative abundance and m/z)

Rather than a big peak of DNPZ, there is a small amount of mononitrosopiperazine in the injected sample as shown in Figure 2. m/z of 116.1 represents the molecular weight of mononitrosopiperazine which is 115.

When there is very small amount of a molecule in a sample or where more than one molecule with the same molecular weight may exist, the fragmentation method has been used to confirm the presence of a specific molecule. By using fragmentation, an extremely small quantity of a component is recognizable.

Figures 3, 4, and 5 show the fragmentation steps of DNPZ to 2 ions with m/z of 85.1 and 56.15.

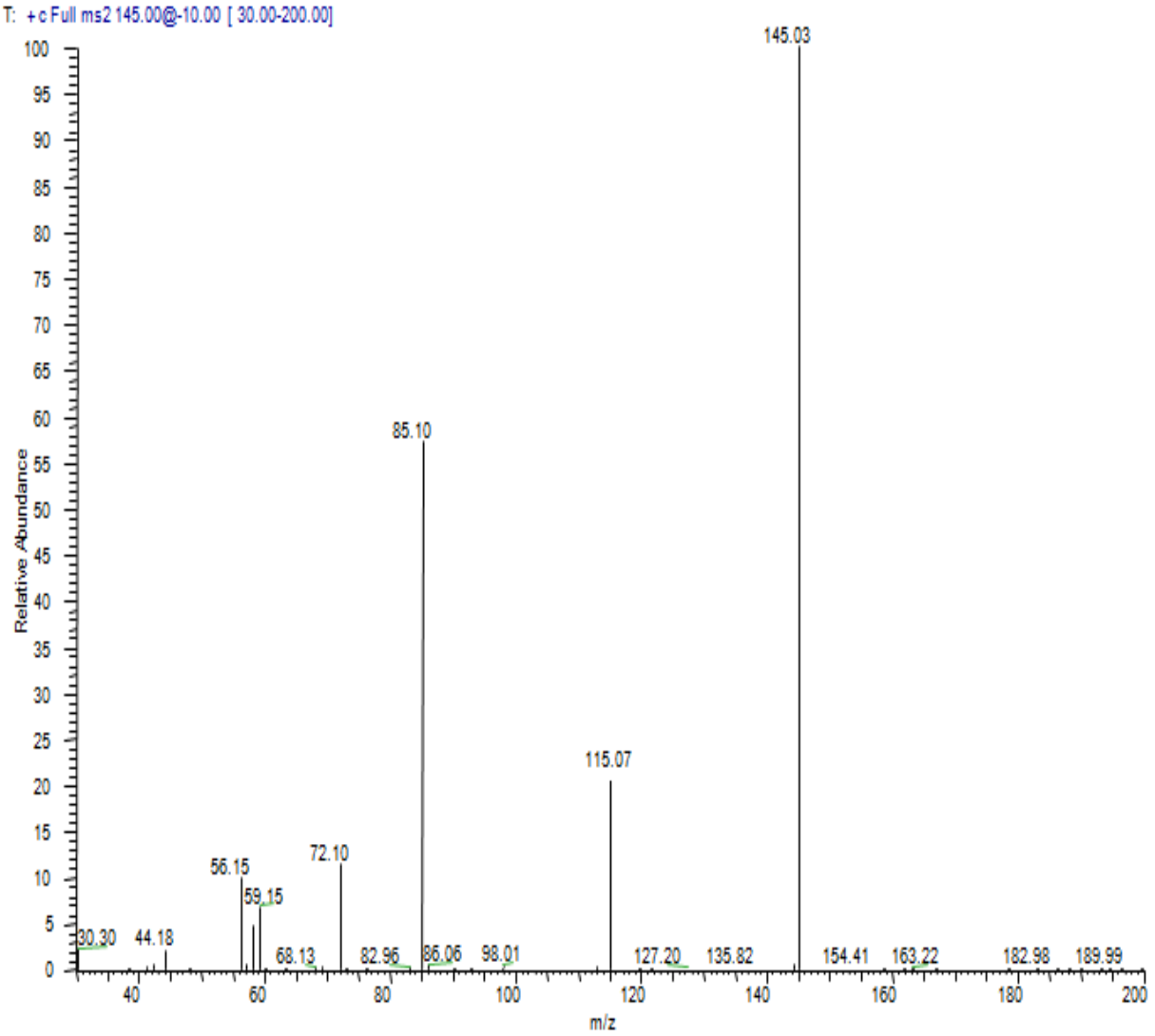

Figure 3: Mass spectrum of fragmentation of a sample of dinitrosopiperazine in methanol and water by collision energy of 10. (Relative abundance and m/z)

Figure 3 shows that collision energy of 10 does not fragment DNPZ very well and just one ion with m/z of 85.1 appears. By increasing collision energy to 20, DNPZ fragments and rather than decreasing in its relative abundance of ions, with m/z of 85.1 and 56.15 it showed up very well (Figure 4).

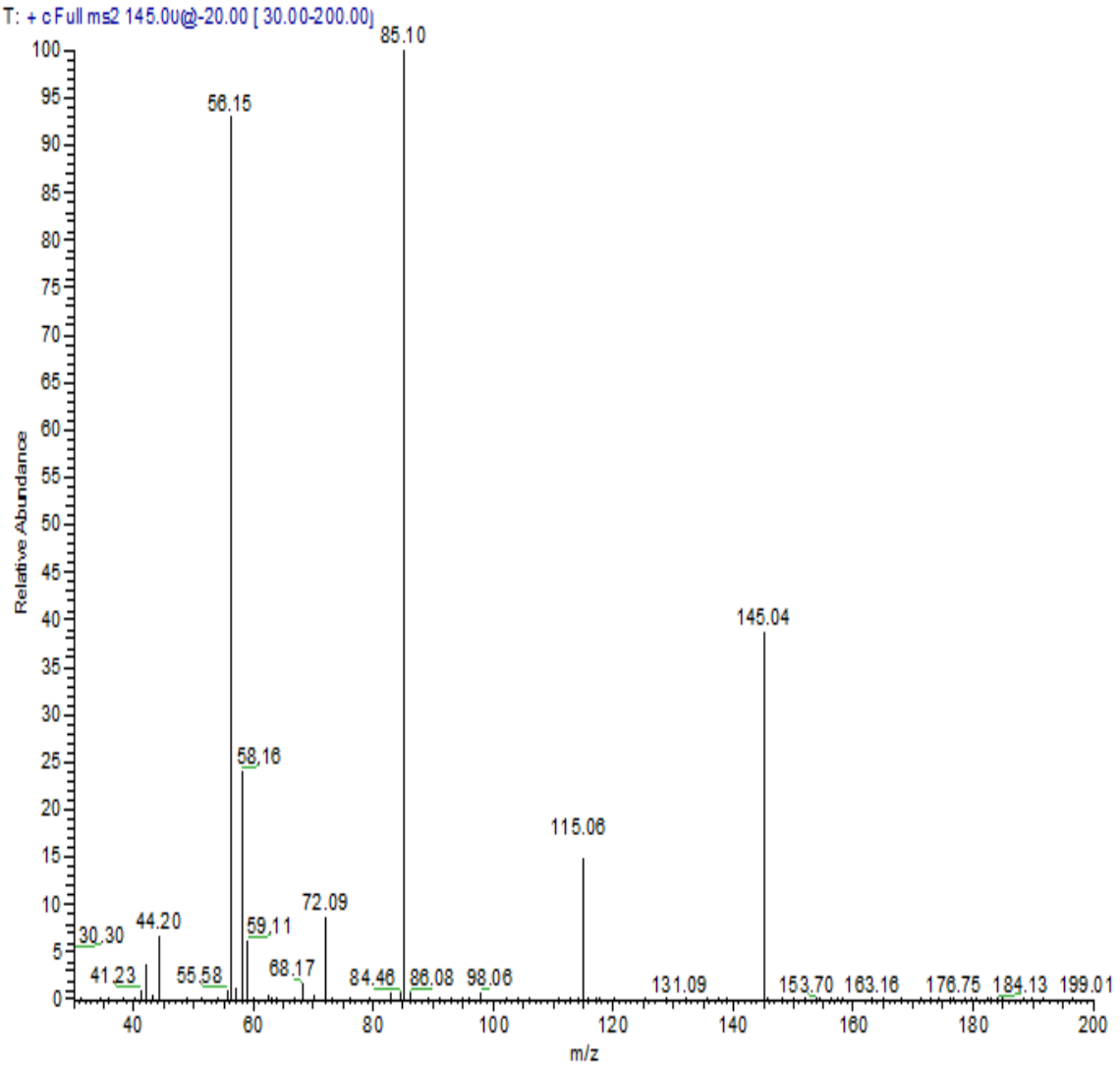

Figure 4: Mass spectrum of fragmentation of a sample of dinitrosopiperazine in methanol and water by collision energy of 20. (Relative abundance ands of m/z)

Collision energy of 20 fragments almost 40% of the DNPZ, so the collision energy has been increased one more step to 30. Figure 7 shows that with collision energy of 30 almost all DNPZ is fragmented to ions with m/z of 85.1 and 58.15.

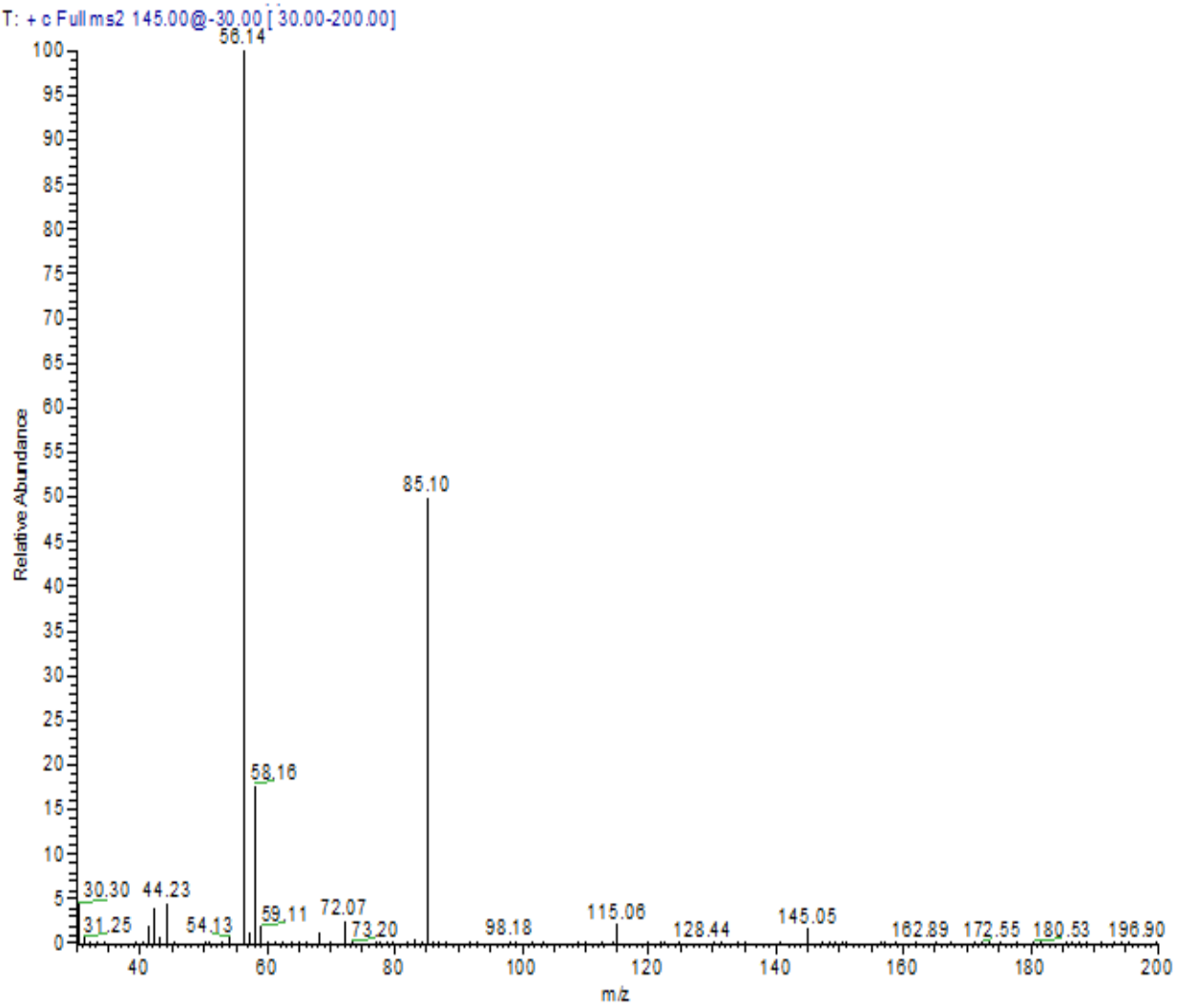

Figure 5: Mass spectrum of fragmentation of a sample of dinitrosopiperazine in methanol and water by collision energy of 30. (Relative abundance and of m/z)

Quantifying Dinitrosopiperazine by Liquid chromatography and Mass Spectrometry (LC-MS)

After detection of DNPZ by MS, for quantifying the concentration of DNPZ in different solutions, a LC-MS system was used. Different concentrations of standard DNPZ in 80% methanol and 20% water have been applied to LC-MS using a reverse phase column. The areas under the peaks in chromatograms are related to the concentration of each standard, so a calibration curve has been established with a sensitivity of $5x10^{-5}$ (Figure 6).

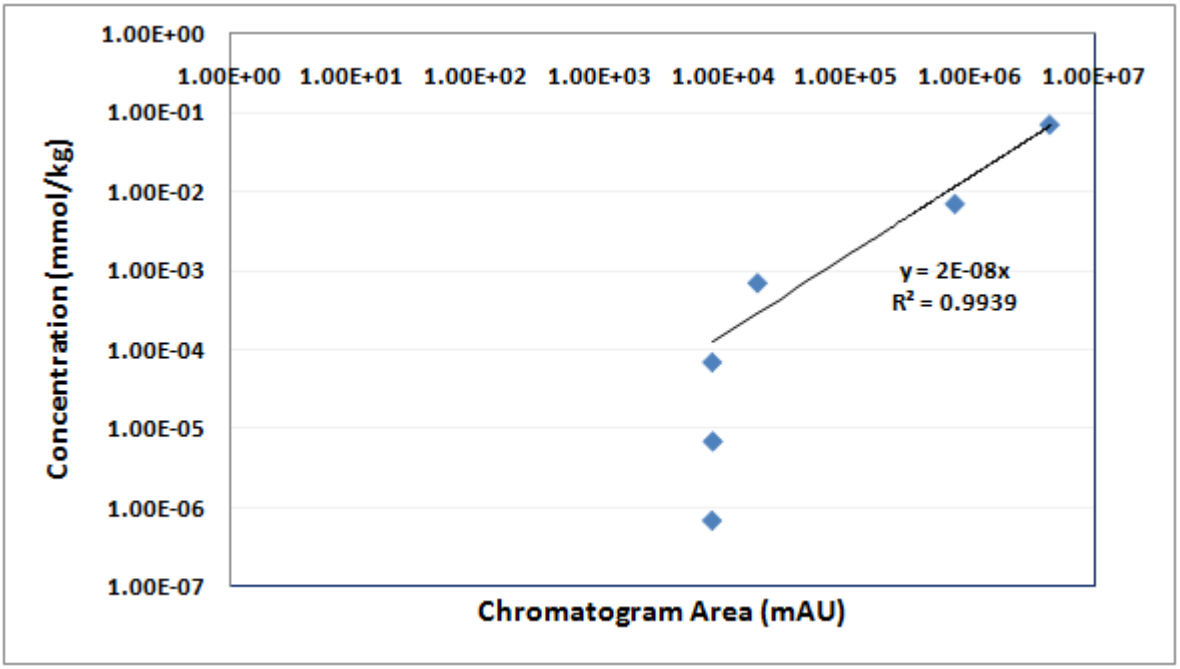

Figure 6: Calibration curve for standard DNPZ, with a detection limit of $9x10^{-5}$ mmol/kg

Figure 6 shows the chromatogram area related to the different concentrations of DNPZ, and respective calibration curve which is linear. This will be used when a sample with unknown concentration of DNPZ is injected into the LC-MS.

Kinetic study of piperazine nitrosation reaction between 8 m loaded piperazine and 50 mmolal $NaNO_2$ has been performed at 21, 60, and 75 °C. The results are given in Figure 7. The reaction rate is slow at 21 °C, but increases at higher temperatures.

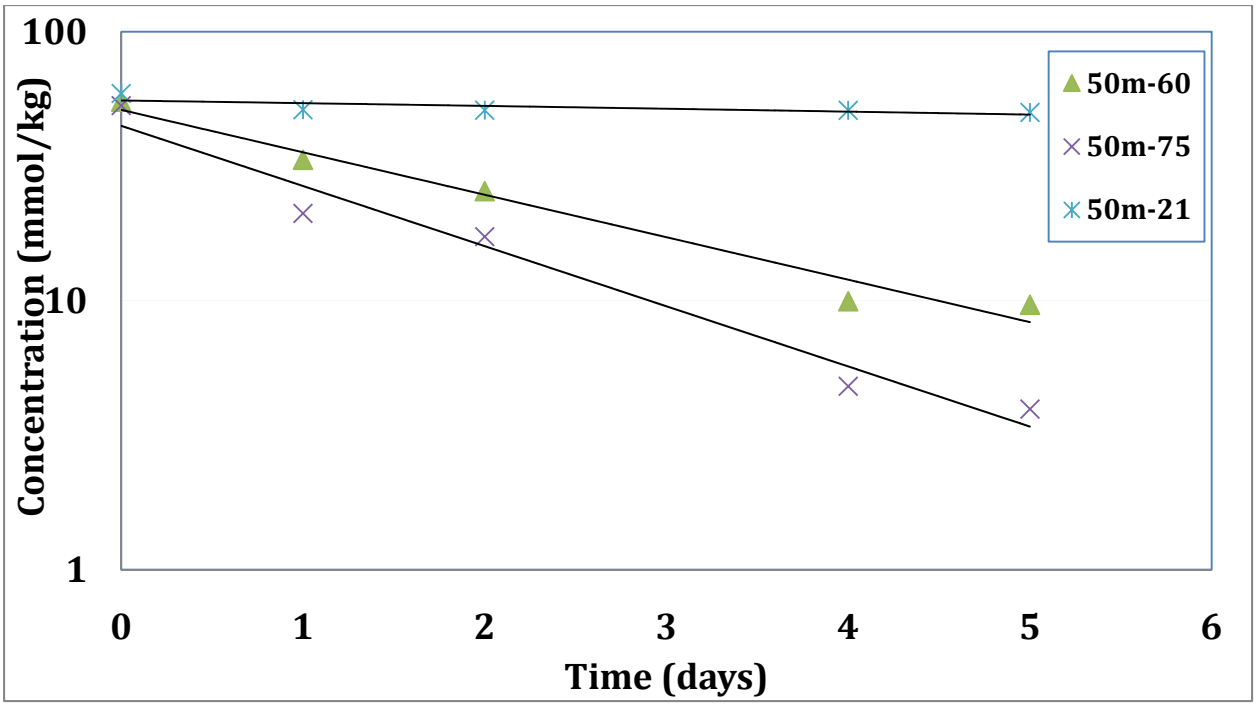

Figure 7: Nitrite concentration changes in different temperature at 5 days reaction time

Figure 7 shows that all three reactions followed a linear path on a log/linear plot so the slope of each line is the first order reaction rate constant at each temperature (K_r), which has been defined as follows:

$$K_r = K_o\, e^{(-E/RT)}$$

The reaction activation energy is obtained from the slope of ln(Kr) versus reciprocal temperature as in Figure 8.

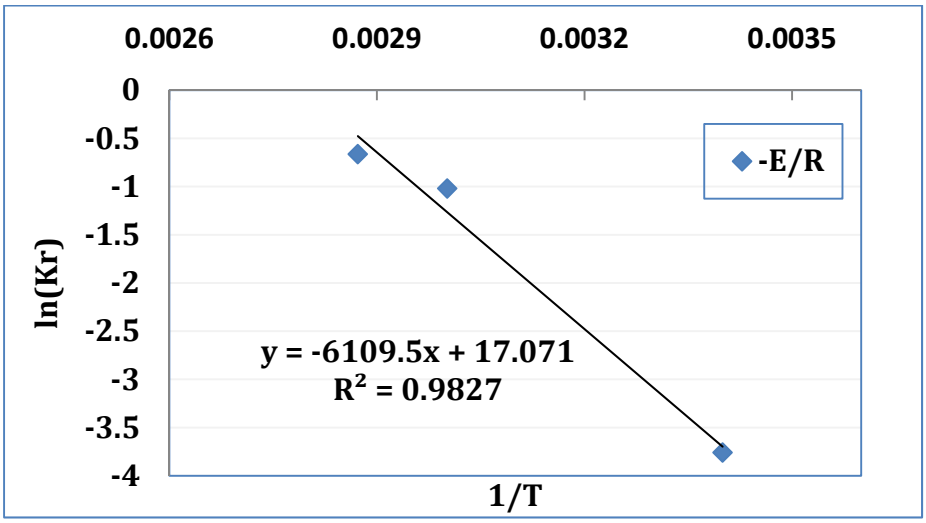

Figure 8: Natural log of reaction rate constant in terms of 1/T to calculate the activation energy of reaction

$$K_r = K_o\, e^{(-E/RT)}$$

$$Ln(K_r) = ln(K_o) + (-E/RT)$$

T(K)	1/T	Kr	Ln(Kr)	Kr (Calculated)
294.15	0.00339963	0.0233	-3.7593	0.0247
333.15	0.00300165	0.3605	-1.02026	0.281
348.15	0.00287233	0.515	-0.66359	0.621

R=8.314 J/K.mole
E/R= 6109.5, K_o =25932304
E_a=51 KJ/mole

Figure 9 gives the effect of varying initial nitrite from 3 to 50 mmolal at 60 ^oC.

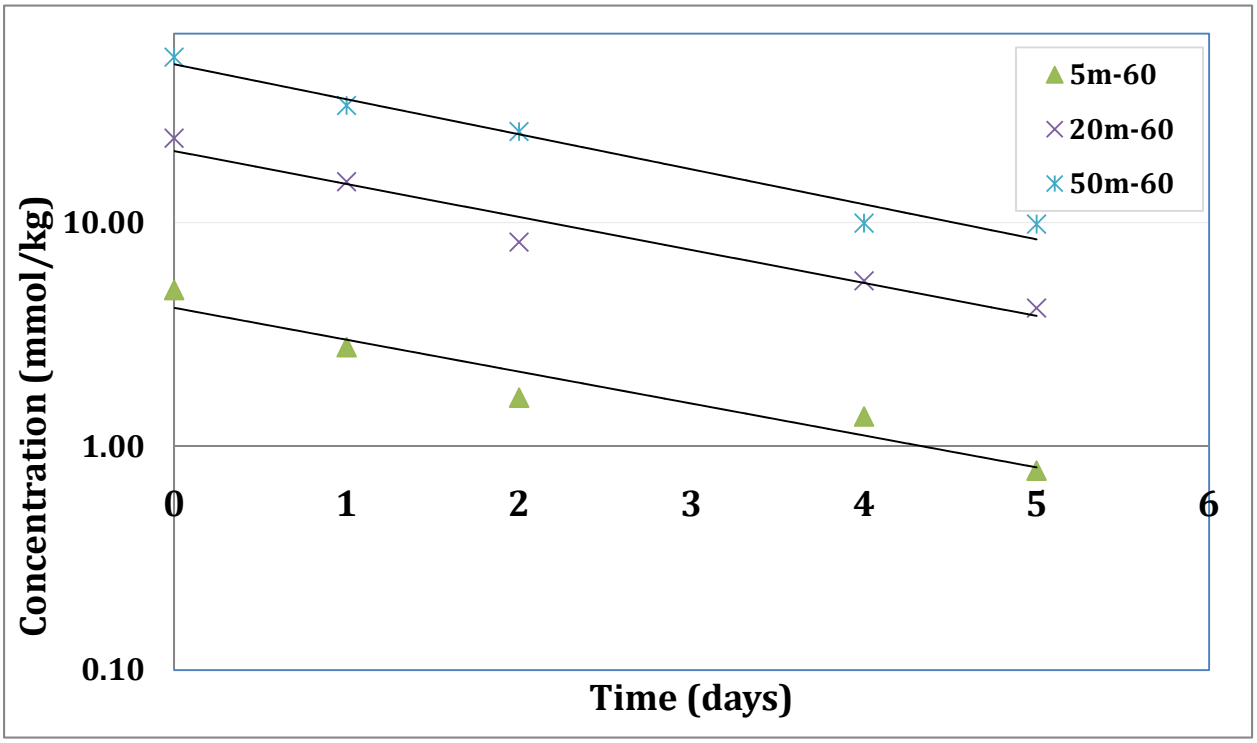

Figure 9: Nitrite concentration change in the reaction with constant temperature and different initial nitrite concentration, (5mmolal, 20 mmolal, and 50 mmolal)

Average DNPZ production in the above-mentioned experiments was $4x10^{-4}$ mmol/kg while the reactions used a rich concentration of nitrite, therefore the nitrosation of loaded PZ under the experimental conditions does not lead to the production of DNPZ only. Further investigations will be done to find out the exact reaction mechanism.

Conclusions

Mass spectrometry detects dinitrosopiperazine (DNPZ) and, at a collision energy of 30, fragments DNPZ to peaks at 56 and 85.

Dinitrosopiperazine can be measured by LC-MS using a reverse phase column, with a detection limit of 9e-5 mmol/kg.

The reaction of nitrite with 8 m loaded piperazine is first order in nitrite with a rate constant of 0.36 hr^{-1} at 60 ^{o}C. The activation energy is 50 kJ/mol.

Less than 4 e-4 mmol/kg dinitrosopiperazine is produced from the reaction of 50 mM nitrite with 8 m loaded piperazine at 60 ^{o}C.

Future Work

During the next quarter investigation of the reaction mechanism for nitrosation reaction of loaded piperazine from analysis of amine and nitrate and nitrite ions will be continued. This research will focus on CO_2 capture conditions in the liquid phase of the absorber and stripper to see the effect of degradation products on nitrosation reactions.

References

Attalla M, Azzi M. "Environmental impact of Atmospheric Emissions from Amine-based Post-Combustion CO_2 Capture." Presented in *NILU, 2010.*

Keefer LK, Roller PP. "N-Nitrosation by Nitrite Ion in Neutral and Basic Medium." *Science*, 1973;181:1245–1247.

Kunisaki N, Hayashi M. "Formation of N-Nitrosamines from Secondary Amines and Nitrite by Resting Cells of Escherichia coli B."*Appl Environ Microbiol*, 1978;37(2):279–282.

Lijinsky W, Keefer L, Loo J. "The preparation and properties of some nitrosamino acids." *Tetrahedron*, 1970;26:5137.

Mirvish S. "Formation of N-nitroso compounds chemistry kinetics and in-vivo occurrence." *Toxical Appl Pharmacol*, 1975;3(1):325.

Mirvish S, Wallcave L, Eagen M. "Ascorbate-Nitrite Reaction: Possible Means of Blocking the Formation of Carcinogenic N-Nitroso Compounds." *Science*, 1972;177(4043):65–68.

Osterdahl BG, Bellander B. "Determination of n-mononitrosopiperazine and n,n′-dinitrosopiperazine in human urine, gastric juice and blood." *J. Chromatogr*. 1983;278:71.

Roller PP, Keefer LK, Slavin BW. "N-Nitroso compounds: Analysis, Formation and Occurance." IRAC Publication 31, Lyon, 1980;119.

United States Pharmacopeia XXIV. National Formulary 19, Rockville, USP Convention, Washangton; 2000; 1341 & 2235.

Thermal Reclaiming of Aqueous Amines

Quarterly Report for July 1 – September 30, 2010

by Steven Fulk

Supported by the Luminant Carbon Management Program

Department of Chemical Engineering

The University of Texas at Austin

October 10, 2010

Abstract

In this quarter, liquid-liquid separation was investigated as a method for recycling oxidation and corrosion inhibitors in an absorption/stripping system, and a thermal reclaimer apparatus was built and tested to simulate thermal reclaiming of aqueous amine solutions.

Liquid-liquid equilibrium experiments were performed on 8 m piperazine (PZ) solutions containing Inhibitor A concentrations of 0.2–8 m between 40–70 °C. Phase separation was not observed for any of the test solutions; however, when solutions were cooled to ambient temperature (22 °C), solutions completely crystallized.

An isobaric thermal reclaiming apparatus was built and tested. A 7 m monoethanolamine (MEA) solution was heated to 120 °C and the vapor composition from the reclaimer was sampled by a hot gas FTIR. The water vaporization rate matched temperature increases; however, oil contamination in the heated line prevented accurate measurement of MEA in the vapor phase.

Goals for next quarter include performing two experiments. First, high temperature and high amine concentration vapor-liquid equilibrium experiments will be performed for a PZ system. Second, phase separations of aqueous PZ with contaminants such as potassium sulfate will be observed using differential scanning calorimetry.

Introduction

Alkanolamines have been used to treat acid gases since 1930 (GPSA, 2004). Since then, the need to develop new solvents to increase system capacity and optimize to meet economic and environmental concerns has become increasingly important. Although new and better solvents have been and are continually being developed to meet some of these demands, issues regarding process contaminants are becoming increasingly problematic. As carbon capture matures and applications shift from simulated to real flue gas, issues related to pollutants will become more problematic, especially for coal-fired power plants. System contaminants pose a number of problems such as increased solvent make-up costs, reduced system capacity due to amine degradation, waste disposal costs, equipment corrosion, and environmental concerns related to greenhouse gas and nitrosamine emissions.

Many methods for removing contaminants, or reclaiming, have been developed. Reclaiming methods include filtration and adsorption, thermal reclaiming, ion exchange, electrodialysis, foam fractionation, and sulfate crystallization. Each system operates on a different separation principle, and thus each process will have inherent advantages and disadvantages.

Thermal reclaiming separates components from process streams based on volatility. In flue gas treatment, a small slip-stream from the bottom of the stripper column is sent to a kettle reboiler where the temperature is increased, causing volatile components to exit at the top and solids and non-volatiles to accumulate in the bottom of the still. Unlike other reclaiming techniques, thermal reclaiming can remove nearly any type of process contaminant as long as it is less volatile than the amine. Since the separation is somewhat non-selective, bound amine in the form of heat stable salts and amides will be lost. In addition, user additives such as corrosion or oxidation inhibitors as well as antifoaming agents are likely to be removed due to their non-volatile nature.

The loss of corrosion and oxidation inhibitors through thermal reclaiming can lead to significant make-up costs. In this quarter, liquid-liquid separation was investigated as a way to selectively remove and recycle oxidation inhibitors in an absorption/stripping system. In addition, a thermal reclaimer apparatus was constructed and tested to gain understanding of the thermal reclaiming process as well as to create real thermally reclaimed solutions.

Experimental Methods

Liquid-Liquid Equilibrium Apparatus

The liquid-liquid equilibrium apparatus used this quarter consists of a 100 mL jacketed beaker, a Lauda E-100 Ecoline Staredition circulating water bath, a Corning model PC-220 Laboratory Stirrer/Hot Plate, and a Revolutionary Science Poly Probath™ non-circulating water bath. A diagram of the apparatus can be seen in Figure 1 below.

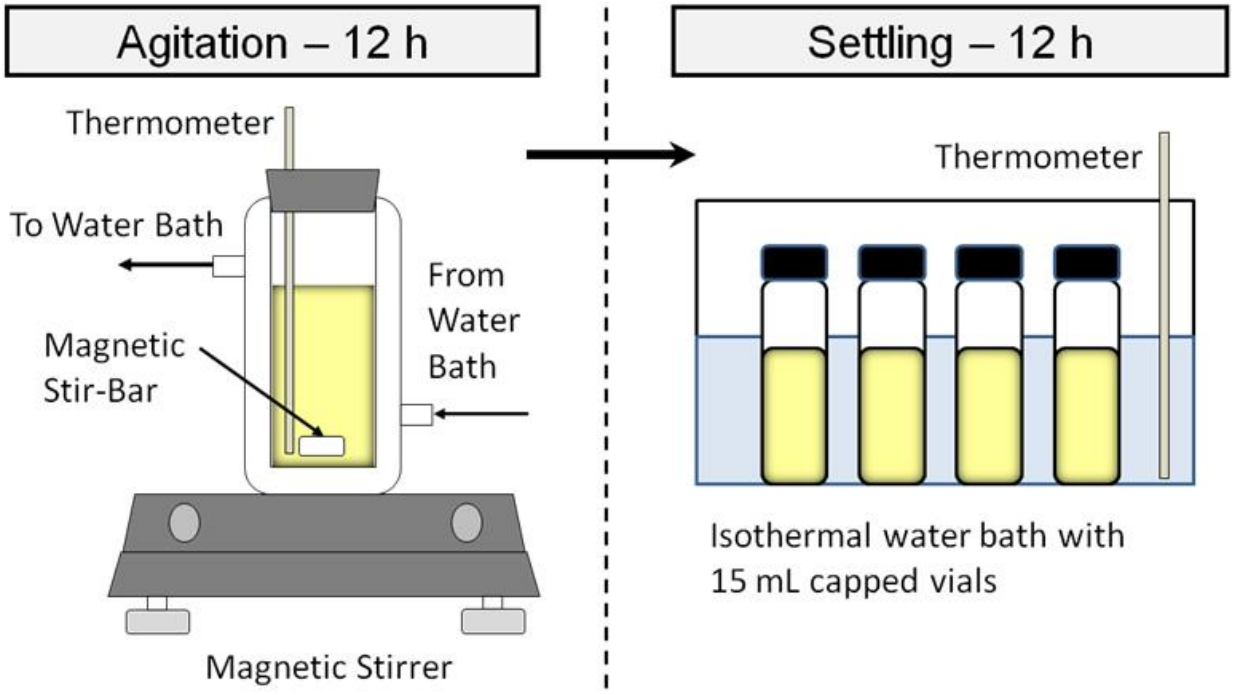

Figure 1: Liquid-liquid equilibrium: agitation apparatus (left), settling apparatus (right).

Procedures

Liquid-liquid equilibrium experiments began by filling the jacketed beaker with 50–75 mL of amine solution containing Inhibitor A. A magnetic stir-bar was placed in the solution and the beaker was sealed with a rubber stopper with an inserted thermometer. The sealed beaker was then placed on a magnetic stirrer and the circulating water bath was connected to the inlet and outlet connections of the beaker jacket. Stirring and jacket circulation was then initiated. The solution temperature and phase behavior was monitored for a period of twelve hours. Once the agitation period was complete, stirring and jacket circulation were stopped and the resulting solution was transferred by automatic pipette to 15 mL glass vials. The vials were capped and placed in a preheated, non-circulating water bath maintained at the same temperature as the agitation apparatus. Water bath temperature was monitored using a glass thermometer. After twelve hours of settling, the vials were removed from the water bath and phases were sampled by automatic pipette. The resulting solutions and samples were then placed on the lab bench to cool to ambient conditions.

Samples were analyzed using total alkalinity (acid titration), total inorganic carbon analysis (TIC), and cation chromatography to determine amine and additive concentrations and carbon dioxide loading. The specific analytical procedures are discussed in the Analytical Methods section of this report.

Thermal Reclaimer Apparatus

In this quarter, a bench-scale thermal reclaimer was built and tested. The reclaimer body consists of two stainless steel pressure vessels. The vessels are connected by a vapor line that takes vapor from the smaller vessel (Parr model 4750) and sparges the liquid in the larger vessel (Parr model 4760). The larger vessel head has 6 connections; a Druck® PTX-611 (0-45 psia)

pressure transducer, a liquid sampling line, a low-noise K-type thermocouple with miniature connector (model GKMQ-SS-125-U-12 by Omega®), a vapor sampling line, a vapor vent line, and a Fike Corporation P ST FS rupture disk pressure relief. The signal from the pressure transducer is sent to a current-to-voltage transmitter before it is sent to a NI USB 6009 data logger using LabView® SignalExpress software to read the pressure of the reclaimer. The pressure inside the reclaimer is kept constant by a Norgren® R44-221-RNEA (0-50 psig) pressure regulator located upstream of the reclaimer on the nitrogen sweep line. The reclaimer assembly is submerged in a Thermo Scientific® Digital One oil bath to regulate the reclaimer temperature.

Sample vapor from the reclaimer is mixed with nitrogen flowing at approximately 2–5 L/min in a heated line (180 °C) before entering a Gasmet™ DX-4000 FTIR gas analyzer with Calcmet® data collection software. For reclaiming runs near atmospheric pressure, a GasmetTM Portable Sampling System is used to pump the sample vapor from the reclaimer to the gas analyzer. A schematic of the thermal reclaiming apparatus can be seen in Figure 2 below.

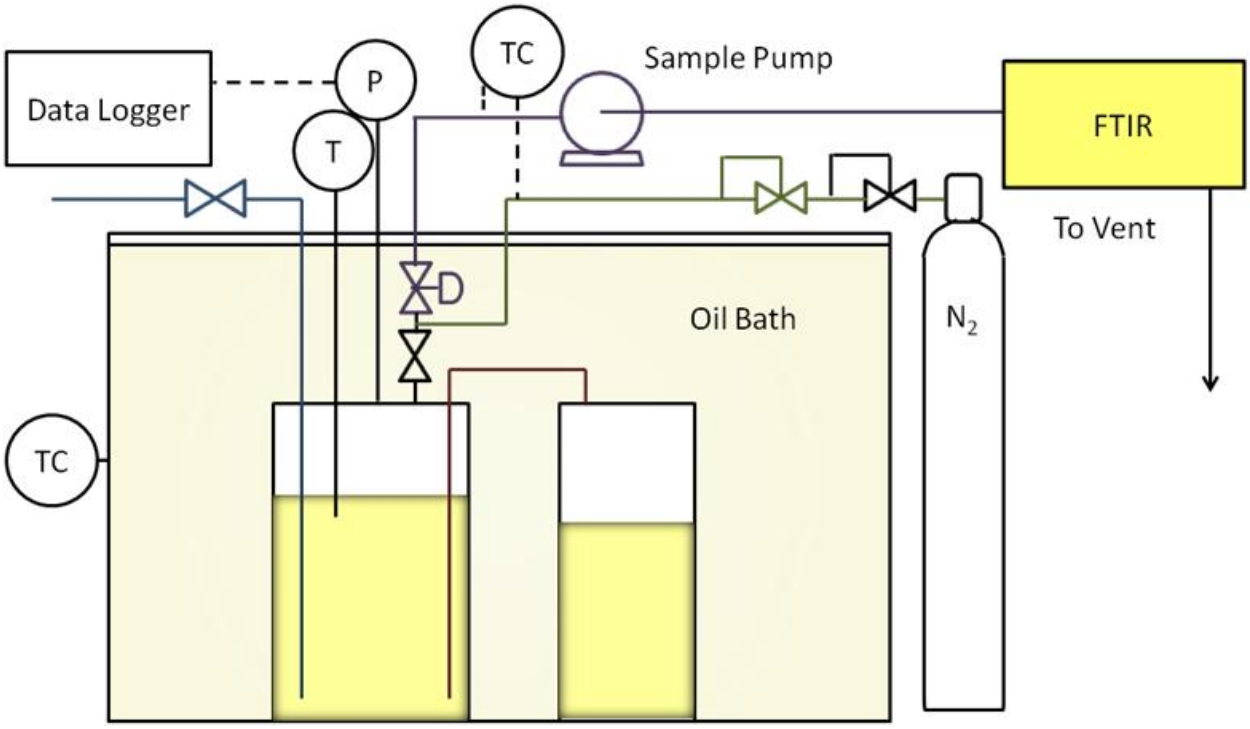

Figure 2: Bench-scale, isobaric thermal reclaiming apparatus.

Procedures

Thermal reclaiming experiments began by filling each pressure vessel about half-full with amine solution (350 mL) and sealing the heads before submerging them in the oil bath. The oil bath set-point temperature was 75 °C and the vessel began to heat. Nitrogen at a rate of approximately 2–5 L/min was flowed through a heated line to the vapor sampling line and finally to the FTIR while the sample lines heated to purge the gas analyzer so a background spectrum could be taken. Once a background spectrum was taken, the FTIR was set to sample the gas every minute. The block valve for the vapor sampling line was opened and vapor sampling began. Pressure and temperature measurements were made every subsequent minute.

As the solution in the reclaimer concentrated, the vapor rate decreased. Once the vapor rate had reached a steady value (evaporation rate) for about 10 minutes, the oil bath temperature was raised to the next set point.

Analytical Methods

Dilutions

Many of the analytical methods and sampling techniques performed this quarter required dilutions to achieve the desired concentration ranges or to prevent crystallization of the sampled material. Dilutions are performed gravimetrically by weighing a sample in a beaker, taring the balance, and weighing an amount of water added to the sample. The solution is then stirred and transferred to the appropriate vial. As a means of quantifying dilution, this report will use the term "dilution factor" which is calculated as follows:

$$\text{Dilution Factor} = \frac{\text{Mass of Sample} + \text{Mass of Added Water}}{\text{Mass of Sample}} \quad (1)$$

For this work, a dilution factor will be reported by an "x" following the value of the dilution factor. For example, a solution that is 100x diluted contains one part of the original sample for every 100 parts of the diluted solution by mass.

Total Alkalinity (Acid Titration)

The total alkalinity of solutions was determined by titration with 0.2 N H_2SO_4 using a Metrohm-Peak 835 Titrando with an auto-dispenser. In this method, a sample of known mass is diluted by water in a tall-profile titration beaker. The diluted solution is then titrated with acid and the pH of the solution is recorded. Once titration is complete, the volume of acid used to reach the equivalence point, nominally a pH of 3.9, is used to calculate the total alkalinity of the solution. Acidic titration is not selective for any particular specie and therefore reports the total alkalinity of the solution regardless of the mix of components displaying alkaline behavior. Typical sample masses and dilution factors for acid titration are 0.2 g and 300x, respectively.

For a more detailed description of the Total Alkalinity procedure, please see Appendix A.3 of Hilliard (2008).

Total Inorganic Carbon Analysis (TIC)

The Total Inorganic Carbon analysis was used to quantify CO_2 loading in samples. Generally, a sample of known mass is injected into a port containing 30 wt % H_3PO_4 where the sample is acidified and CO_2 is given off according to the following equilibrium equations:

$$HCO_3^- + H_2O \leftrightarrow H_3O^+ + CO_3^{2-} \quad (2)$$

$$CO_2 + 2H_2O \leftrightarrow H_3O^+ + HCO_3^- \quad (3)$$

The CO_2 is then carried by a nitrogen stream to a Horiba PIR 2000 CO_2 analyzer where voltage response versus time data is sent to a computer for tabulation. A plot of voltage versus time for a given experimental run reveals a series of peaks corresponding to sample injections. The area of a given injection peak provides a means of calculating the amount of CO_2 contained in a sample when compared to injections of a carbon standard. The carbon standard used for this analysis technique was a buffered $K_2CO_3/KHCO_3$ 1000 ppm by mass standard.

Injection volume depends on the concentration of CO_2 in the sample; consequently, the dilution factor of the sample plays a role in fine-tuning injection volumes to fall in the appropriate voltage range of the CO_2 analyzer. Once the solutions were diluted properly, the injection volumes were adjusted to achieve a voltage response of approximately 0.5 V. The injection volume of samples ranged from 25–45 μL. After all of the samples were injected in triplicate, five different volumes of the 1000 ppm by mass carbon standard were injected with a voltage response range encompassing all of the sample responses to create a calibration curve. The calibration curve was then used to calculate the moles of CO_2 contained in a sample. CO_2 concentration information given by TIC used in conjunction with amine concentration information from cation chromatography allows calculation of loading (moles CO_2/mol alkalinity) of the samples.

For a more detailed description of the TIC procedure, see Appendix B.2–B.7 of Hilliard (2008).

Cation Chromatography

Cation chromatography was performed this quarter using a Dionex ICS-2500 IC with an auto-sampler and a gradient pump providing a linear eluent concentration profile using methanesulfonic acid to quantify the amount of PZ in sample solutions. A detailed description of the cation chromatograph and procedures is described in Section 3.2 of the dissertation by Sexton (2008).

Results

Liquid-Liquid Equilibrium Apparatus

The results of 10 liquid-liquid equilibrium experiments are shown in Table 1 below.

Table 1: Phase results for mixtures of aqueous PZ, CO_2, and Inhibitor A at experiment and ambient temperatures.

PZ (mol/kg H_2O)	Inh. A (mol/kg H_2O)	Loading (mol CO_2/mol alk.)	T_{exp} (°C)	Phase(s)	Ambient Phase(s)
8	0.2	0	40	Solid	Solid
8	1	0	40	Liquid	Solid
8	2	0	40	Liquid	Solid
8	2	0	60	Liquid	Solid-Liquid*
8	2	0	70	Liquid	Liquid
8	4	0	40	Liquid	Solid Top-Liquid Bottom
8	6	0	40	Liquid	Liquid
8	8	0	50	Liquid	Solid Bottom-Liquid Top
8	2.3	0.3	40	Liquid	Solid Bottom-Liquid Top
1	8	0	50	Liquid	Liquid

* Half of the samples were solid, half were liquid at ambient conditions.

Table 1 shows that no liquid-liquid separation occurred for 8 m PZ with a range of 0.2-–8.0 m Inhibitor A over the measured temperature range of 40–70 °C. Previous work done by Cullinane

(2005) indicated that a PZ/K_2CO_3 system exhibited liquid-liquid separation for concentrations of PZ between 3.57 and 4.67 m, and K^+ concentrations between 0.22 and 1.79 m at 40 °C. Therefore, it is apparent that the speciation effects of loaded solutions have a greater effect on the activity coefficients in solution than A alone. Future liquid-liquid separation experiments should include CO_2 loading to determine if A will increase or decrease the two-phase liquid envelop region.

Solutions at ambient conditions tended to completely solidify regardless of the PZ to H_2O ratio. For an 8 m PZ solution, the solid phase is the hexahydrate of PZ. As the solution crystallizes, solution will be taken up as PZ·$6H_2O$ according to the following solubility product relation (Hilliard, 2008):

$$PZ{\cdot}6H_2O \leftrightarrow PZ + 6H_2O \tag{4}$$

$$K_{SP} = x_{PZ}\gamma_{PZ}(x_{H2O}\gamma_{H2O})^6 \tag{5}$$

As the concentration of Inhibitor A increases in solution, the changes in the mole fractions of water and PZ become larger for each mole of PZ·$6H_2O$ removed. A faster decrease in the mole fraction of water and PZ causes the equilibrium quotient to decrease at a faster rate. If the equilibrium quotient is larger than the solubility product, then precipitation occurs. Figure 3 shows the effect of A on the solubility of PZ·$6H_2O$ neglecting any effect of A on activity coefficients.

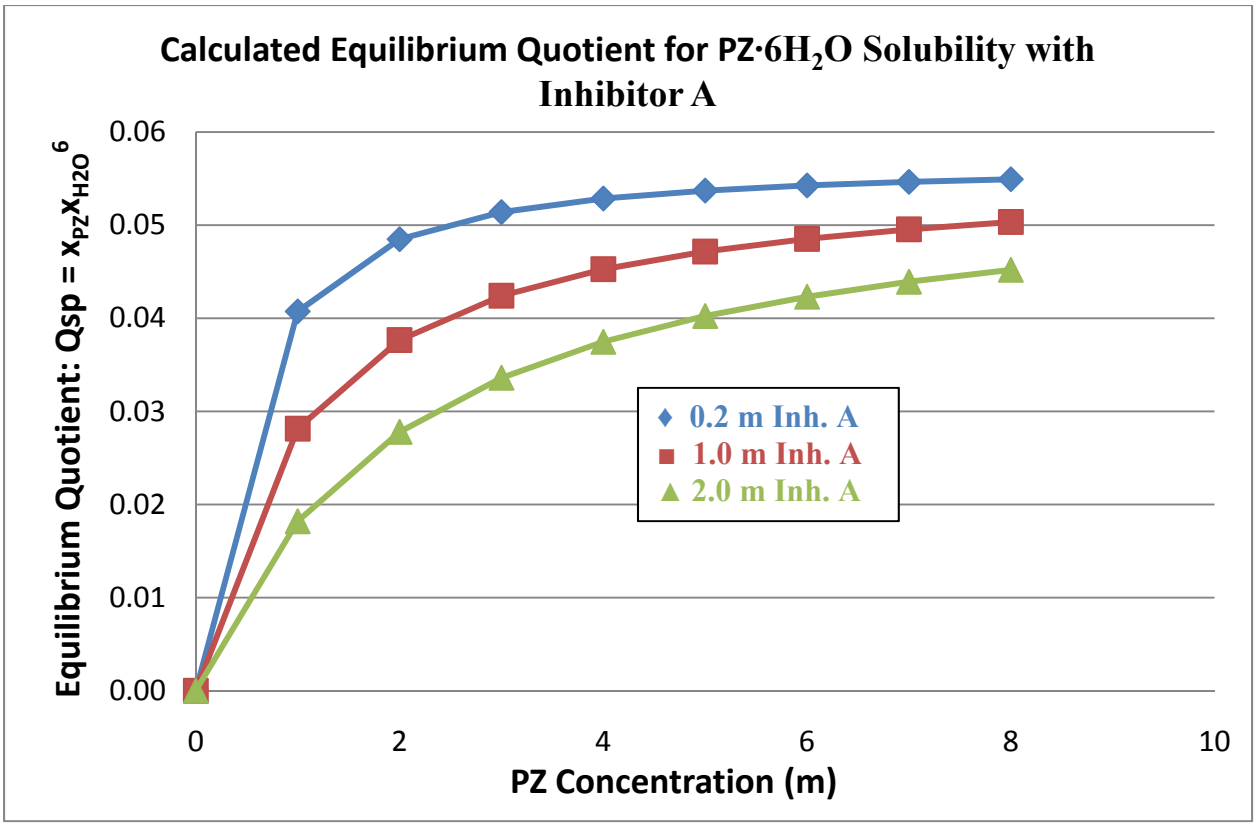

Figure 3: Calculated equilibrium quotient for PZ·$6H_2O$ solubility for varying Inhibitor A concentrations.

Furthermore, as PZ and water are removed from solution, the mole fraction of A increases. As the mole fraction of A increases, the effect on the activity coefficients of water and PZ becomes greater, making a phase separation more likely.

Thermal Reclaimer Apparatus

Pressure readings were calibrated using a dead weight pressure tester. The calibration curve for the 0–45 psia pressure transducer is shown in Figure 4 below.

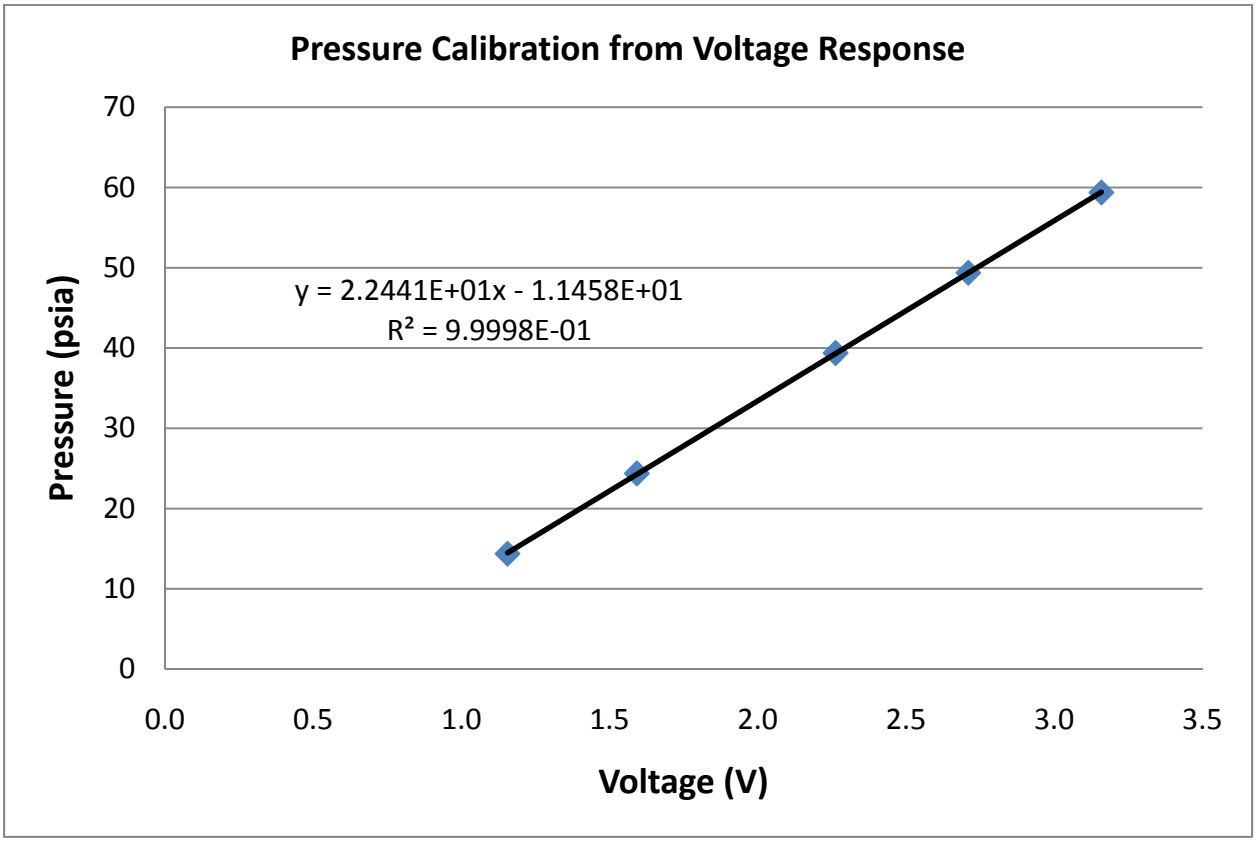

Figure 4: Pressure transducer calibration curve.

Figure 5 shows oil bath temperature, cell temperature, and cell pressure for a reclaiming run for 7 m MEA. The reclaimer remained isobaric as the cell and bath temperature increased. Figures 6 and 7 show the vaporization rate of water and the concentration of MEA, respectively.

Figure 6 shows distinct vaporization and evaporation regimes. As vaporization occurs, the less volatile components become more concentrated; consequently, the boiling point of the solution increases. Once the vaporization rate becomes negligible, evaporation becomes the dominant form of mass transfer. Increasing the temperature of the oil bath starts vaporization inside the cell until the boiling point of the solution increases beyond the cell temperature.

The concentration of MEA increased as the temperature in the cell increased. Oil leakage into the FTIR line interfered with the MEA measurements during experimentation as indicated by the residual error curve in Figure 7.

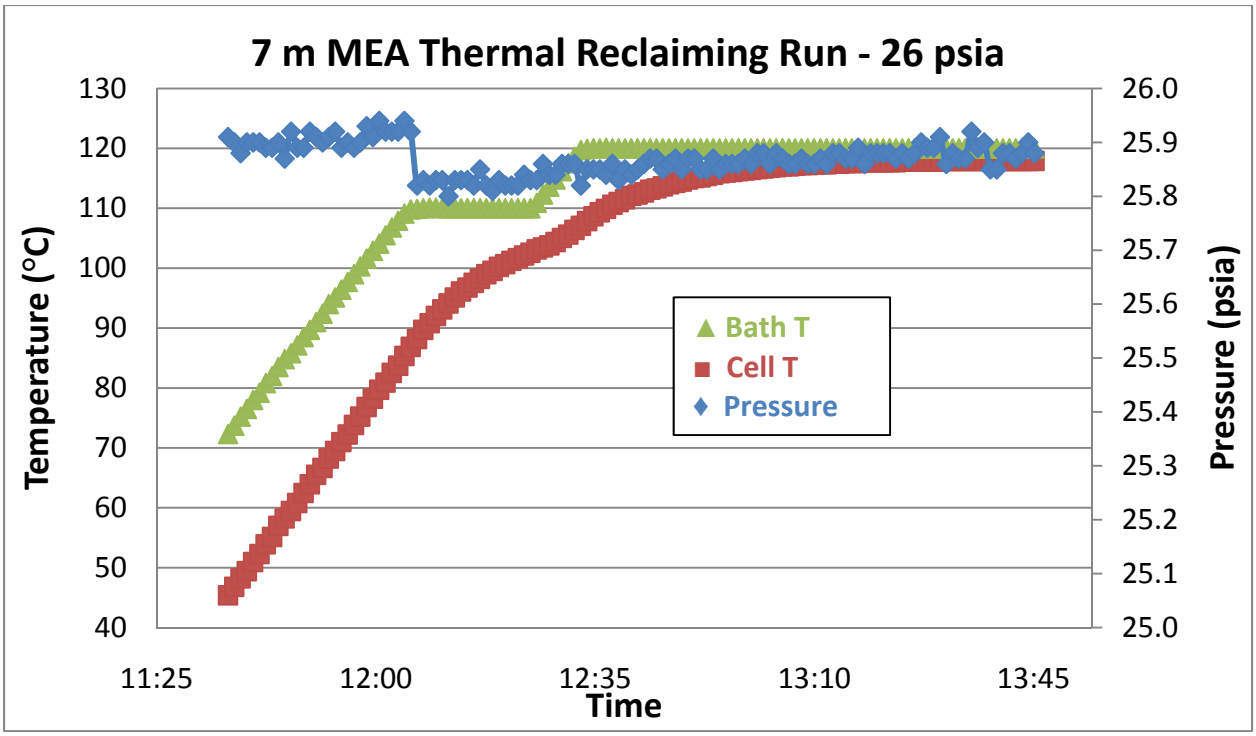

Figure 5: Pressure and temperature measurements for the thermal reclaimer apparatus vaporizing a 7 m MEA solution.

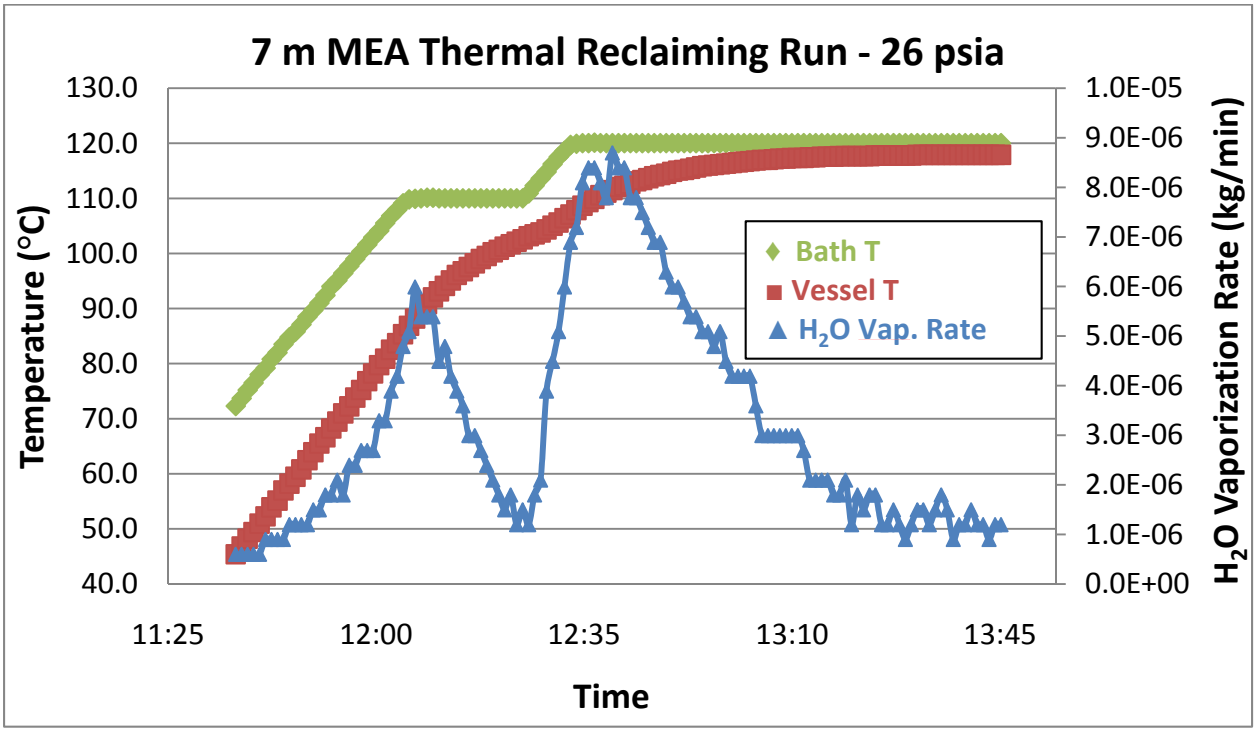

Figure 6: Water vaporization rate for the thermal reclaimer apparatus vaporizing a 7 m MEA solution.

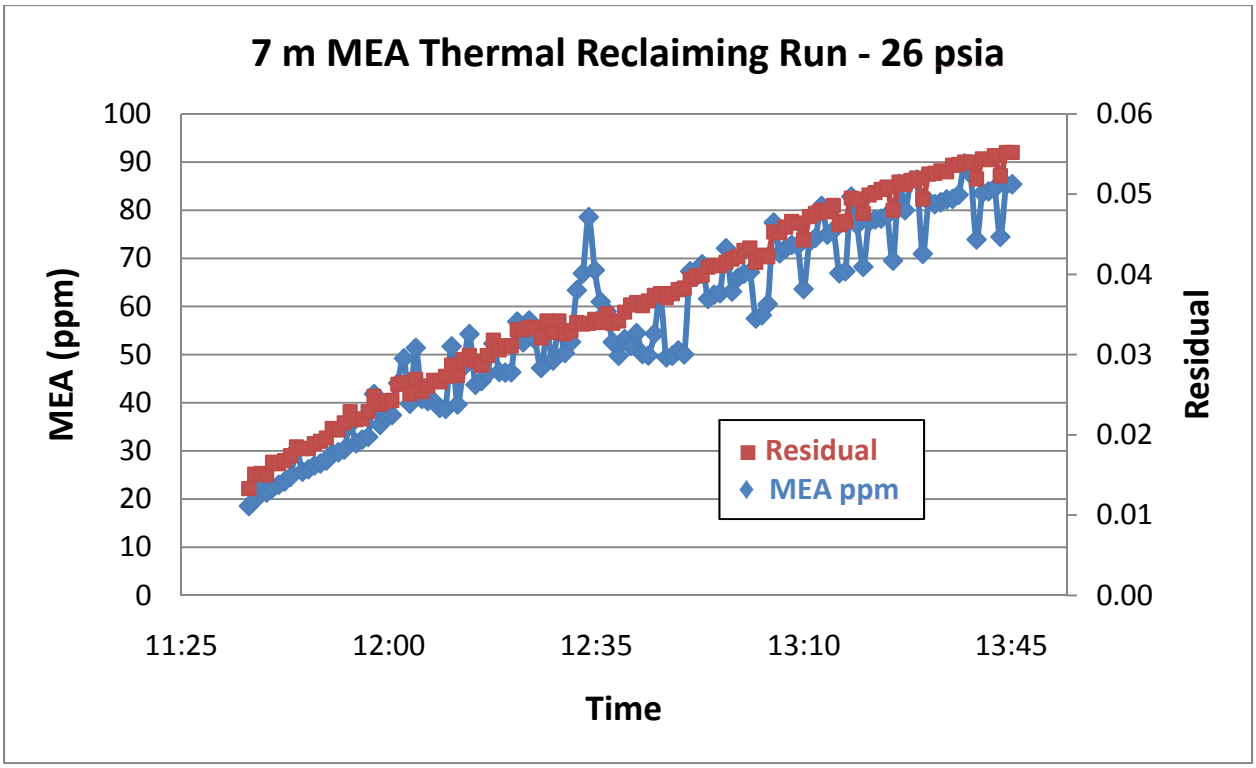

Figure 7: MEA concentration and residual measurement error for a thermal reclaiming run on a 7 m MEA solution.

Figures 5–7 demonstrate that the constructed thermal reclaimer operates isobarically and the vaporization rate of solution follows predicted behavior.

Future Work

High Temperature VLE

Correct modeling of chemical processes requires thermodynamic data over a range of process conditions. Current models developed for amine scrubbing systems include thermodynamic data for absorber and stripper operating conditions. Reclaimer design requires thermodynamic data at higher temperatures and concentrations than in the absorber or stripper.

In the next quarter, the thermal reclaimer apparatus presented in this work will be modified to measure vapor-liquid equilibrium for high temperatures and concentrations likely to be found in reclaimers. Process contaminants like sulfate and formate will be added to determine their effects on equilibrium.

Phase Characterization

In this quarter it was determined that solutions of PZ, water, and Inhibitor A are miscible between 40–70 °C. Solidification of samples made phase characterization difficult to measure; therefore, in the next quarter differential scanning calorimetry will be used to determine phase transition temperatures for PZ, water, CO_2, and other additive systems. Additives will include Inhibitor A and contaminants such as sulfate and formate.

References

Cummings AL, Smith GD, Nelsen DK. "Advances in Amine Reclaiming – Why There's No Excuse to Operate a Dirty Amine System." *Laurance Reid Gas Conditioning Conference.* 2007.

Freeman SA, Dugas R, Van Wagener DH, Nguyen T, Rochelle GT. "Carbon Dioxide Capture with Concentrated Aqueous Piperazine." *IJGGC*. 2009;4(2).

Hilliard MD. *A Predictive Thermodynamic Model for an Aqueous Blend of Potassium Carbonate, Piperazine, and Monoethanolamine for Carbon Dioxide Capture from Flue Gas.* The University of Texas at Austin. Ph.D. Dissertation. 2008.

Kohl A, Nielsen R. *Gas Purification.* 5th ed. Houston, TX: Gulf Publishing Company; 1997.

NGPSA. *Engineering Data Book.* Tulsa, OK; Natural Gas Processors Suppliers Association (NGPSA). 2004.

Rochelle GT et al. "CO_2 Capture by Aqueous Absorption, Third Quarterly Progress Report 2009." Luminant Carbon Management Program. The University of Texas at Austin. 2009.

Rochelle GT et al. "CO_2 Capture by Aqueous Absorption, First Quarterly Progress Report 2010." Luminant Carbon Management Program. The University of Texas at Austin. 2010.

Sandler SI. *Chemical, Biochemical, and Engineering Thermodynamics*. 4th ed. Hoboken, NJ: John Wiley & Sons, Inc.; 2006.

Sexton A. *Amine Oxidation in CO_2 Capture Processes*. The University of Texas at Austin. Ph.D. Dissertation. 2008.

Solvent Reclaiming by Solids Precipitation

Quarterly Report for July 1 – September 30, 2010

by Humera Abdul Rafique

Supported by the Luminant Carbon Management Program

Department of Chemical Engineering

The University of Texas at Austin

October 31, 2010

Abstract

The solubility of potassium sulfate (K_2SO_4) in piperazine (PZ) solution increases with increasing loading because of a greater concentration of carbamate and protonated amine in the system. The solubility decreases with a decrease in temperature. The solubility of K_2SO_4 is lower in PZ than in MEA when determined using the solid solubility experimental procedure, i.e., the solubility decreases in organic solutions with greater organic concentrations.

It has been determined that the solubility window for CO_2 in PZ solutions is between 0.3 and 0.46 mol CO_2/mol alkalinity (Freeman, 2008). In order to determine the loading limit of the PZ solutions, experiments are being carried out to determine the solubility of hydrated protonated piperazine carbamate by initially preparing the crystals and using the solid solubility method to determine the solubility.

A qualitative analysis to determine the solubility envelope of CO_2 loaded 3.9 m PZ/3.9 m 1MPZ/0.2 m 1,4 DMPZ and 3.75 m PZ/3.75 m 1MPZ/0.5 m 1,4 DMPZ blended solutions at varying temperatures was performed. A maximum CO_2 loading of 0.41 and 0.39 was obtained for the two blends, respectively, at room temperature without any solid precipitation. At zero loading, both the blends are solids (piperazine hexahydrate, PZ.6H_2O) up to 33 °C compared to PZ, which melts at 43 °C at zero loading.

Introduction

This quarter, further analyses were completed of the previous experiments on potassium sulfate solid solubility in 2 m, 5 m, and 12 m PZ at 0.4 CO_2 loading. The experiments were performed to determine the solubility of K_2SO_4 in aqueous PZ.

Figure 1 shows the solvent reclaiming system as modeled by Xu (2008) for an MEA absorption/stripping amine reclaiming system. A slip stream of the hot lean feed from the stripper is flashed though a three-stage flash system. Here CO_2 and H_2O are evaporated until the pressure in the system falls to 0.1 atmosphere.

Water is condensed in the precooler and intercoolers of the compressor. KOH is then fed to crystallize the sulfate present in the system. The K_2SO_4 solids are removed in the separator and the amine is returned to the absorption/stripping process (Xu, 2008). It is expected that a PZ absorption/stripping system will require a similar reclaiming system. The number of flash stages

needed for a PZ system will be determined when enough data are collected using solid solubility experiments.

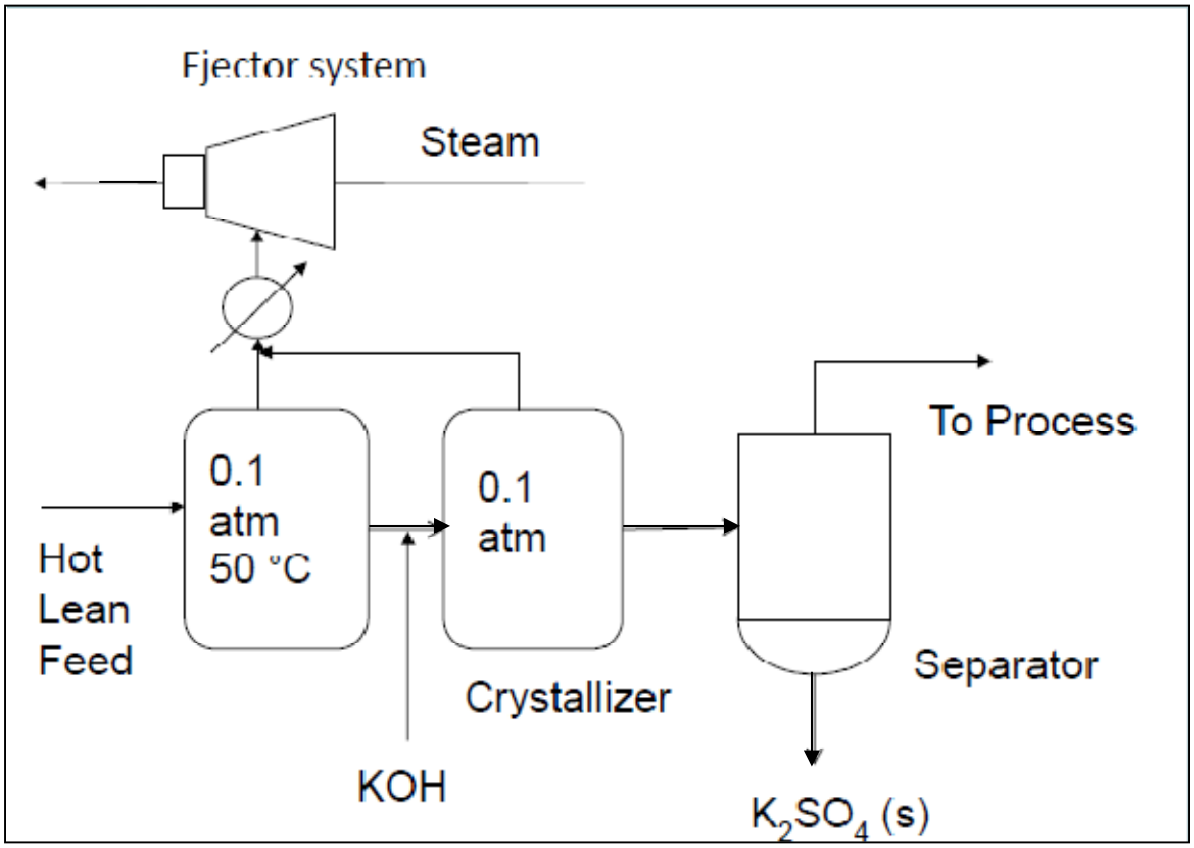

Figure 1: Solvent reclaiming system as predicted by Xu (2008) for MEA reclaiming

This quarter additional experiments were performed on the solubility of piperazine and piperazine blends (3.9 m PZ/3.9 m 1MPZ/0.2 m 1,4 DMPZ and 3.75 m PZ/3.75 m 1MPZ/0.5 m 1,4 DMPZ) containing solids in piperazine solutions. Determining the solubility window of PZ is partly a continuation of Freeman's work on classifying PZ solutions of various concentrations as either soluble or insoluble, depending on whether crystallization occurred after the PZ solution was loaded with CO_2.

Since PZ has been shown to be a useful amine for CO_2 removal by absorption/stripping, experiments are being carried out to understand better the solubility window that exists for PZ solutions as a function of concentration and CO_2 loading (Rochelle et al., 2008).

Experimental Methods

The experiments carried out last quarter to calculate the solubility of K_2SO_4 were as follows:
Experiments 1 and 2: Solid Solubility of K_2SO_4 in 8 m PZ with a CO_2 loading of 0.3.
Experiment 3: Solid Solubility of K_2SO_4 in 8 m PZ with a CO_2 loading of 0.4.
Experiment 4: Solid Solubility of K_2SO_4 in 2 m PZ with a CO_2 loading of 0.4
Experiment 5: Solid Solubility of K_2SO_4 in 5 m PZ with a CO_2 loading of 0.4
Experiment 6: Solid Solubility of K_2SO_4 in 12 m PZ with a CO_2 loading of 0.4

The temperature of the solution varied between room temperature and 80 °C. Solution was sampled using a filtered syringe and diluted in DDI water to prevent K_2SO_4 crystallization. Experimental samples were analyzed for K^+, SO_4^{-2}, CO_2, and PZ concentrations in the cation chromatograph, anion chromatograph, and TIC.

Analytical Methods

The concentration of K^+ and PZ in the samples was analyzed using a cation chromatograph. CO_2 concentration in solution was determined using a Total Inorganic Carbon (TIC) Analyzer, and the SO_4^{-2} concentration was analyzed using an anion chromatograph.

Cation Chromatography: The cation IC was used to determine the concentration of K^+ and PZ in experimental samples. A Dionex ICS-2500 with a CS17 IonPac column with 4-mm Cationic Self-Regenerating Suppressor (CSRS) was used as previously described by Sexton (2008) with a linear increase of methanesulfonic acid (MSA) concentration in the eluent.

Anion Chromatography: The anion IC was used to determine the concentration of SO_4^{-2} in the experimental samples. A Dionex ICS-3000 instrument with AS15 IonPac column, 4-mm Anionic Self-Regenerating Suppressor (ASRS), carbonate removal device (CRD), and carbonate removal from eluent generation was used as described by Sexton (2008).

Total Inorganic Carbon Analyzer: Quantification of CO_2 loading was performed using a total inorganic carbon analyzer. In this method, a sample is acidified with 30 wt % H_3PO_4 to release the CO_2 present in solution (Hilliard, 2008). The CO_2 is carried in the nitrogen carrier gas stream to the detector. PicoLog software was used to record the peaks produced from each sample. A calibration curve was prepared at the end of each analysis using a TIC standard mixture of K_2CO_3 and $KHCO_3$. The TIC method quantifies the CO_2, CO_3, and HCO_3 present in solution. These species are in equilibrium in the series of reactions shown below:

$$CO_3^{-2} + 2H^+ \leftrightarrow HCO^{-3} + H^+ \leftrightarrow H_2CO_3 \leftrightarrow CO_2 + H_2O \qquad (1)$$

Acidification of the sample shifts the equilibrium toward CO_2 which bubbles out of solution and is detected in the analyzer (Rochelle et al., 2010). The TIC analysis helps identify whether loss of CO_2 was prevalent at higher temperatures of the experiment.

Results and Discussion

K_2SO_4 solid solubility experiments: The results from the analytical methods employed above were tabulated in Tables 1 through 5 below.

Table 1: Solid Solubility of K_2SO_4 in 8 m PZ with CO_2 loading = 0.3

T (°C)	K^+ (mmol/kgsol)	PZ (mmol/kgsol)	SO_4^{-2} (mmol/kgsol)	CO_2 (mmol/kgsol)
21	74	2151	33	32
30	111	1869	47	29
40	171	2485	68	36
50	198	2465	87	39
60	191	2301	104	36
70	192	2185	122	34
80	246	2728	133	39

Table 2: Solid Solubility of K_2SO_4 in 8 m PZ with CO_2 loading = 0.3 (experiment 2)

T (°C)	K^+ (mmol/kgsol)	PZ (mmol/kgsol)	SO_4^{-2} (mmol/kgsol)	CO_2 (mmol/kgsol)
21	38	2116	27	31
30	94	2311	37	46
40	134	2565	57	35
50	164	3034	85	38
60	177	2938	90	38
70	108	1384	46	22
80	232	3525	115	45

Table 3: Solid Solubility of K_2SO_4 in 8 m PZ with CO_2 loading = 0.4

T (°C)	K^+ (mmol/kgsol)	PZ (mmol/kgsol)	SO_4^{-2} (mmol/kgsol)	CO_2 (mmol/kgsol)
30	133	2867	57	40
40	181	2939	81	39
50	250	3801	119	47
60	233	3121	132	39
70	290	3543	137	44
80	242	2881	117	37

Table 4: Solid Solubility of K_2SO_4 in 2 m PZ with CO_2 loading = 0.4

T (°C)	K^+ (mmol/kgsol)	PZ (mmol/kgsol)	SO_4^{-2} (mmol/kgsol)	CO_2 (mmol/kgsol)
23.0	779	1930	356	1172
31.0	854	1889	389	2177
40.0	943	1856	430	2114
50.0	1008	1828	467	1126
60.0	1100	1910	516	1114
70.0	1122	1785	519	1076
80.0	1182	1901	560	1016
70.0	1104	1917	520	1044
60.0	985	1843	456	1027

Table 5: Solid Solubility of K_2SO_4 in 5 m PZ with CO_2 loading = 0.4

T (°C)	K^+ (mmol/kgsol)	PZ (mmol/kgsol)	SO_4^{-2} (mmol/kgsol)	CO_2 (mmol/kgsol)
22.5	358	3030	150	2358
32.0	412	3098	175	2319
40.0	447	3016	194	2297
50.0	362	2259	165	2268
60.0	556	3198	256	2211
68.5	606	3293	279	2307
80.0	624	2924	256	2200
69.5	525	3183	238	2310
60.0	463	3272	208	2270

Experiment 6 is still under evaluation.

The study has been started with K_2SO_4 for two main reasons: first, K_2SO_4 can be used as a commercial fertilizer in industry, giving the precipitate a useful means of disposal. Secondly, experimental data obtained can be compared with the work of Xu (2008) to determine whether the results from the solid solubility method employed were comparable to published data.

This graph shows the effects of amine organic nature and concentration on K_2SO_4 solubility. The y-axis shows the SO_4^{-2} in mmol/kgmolsol against the inverse of temperature. The graph also shows the temperature in degrees Celsius. The solid points on the graph are the experimental data obtained from the solid solubility experiments for 8 m PZ at 0.3 loading and 8 m PZ at 0.4 loading. The outlined points are by Xu (2008). We can see that the sulfate solubility data obtained by Xu are close to those obtained by the solid solubility experiments, validating the experimental methods.

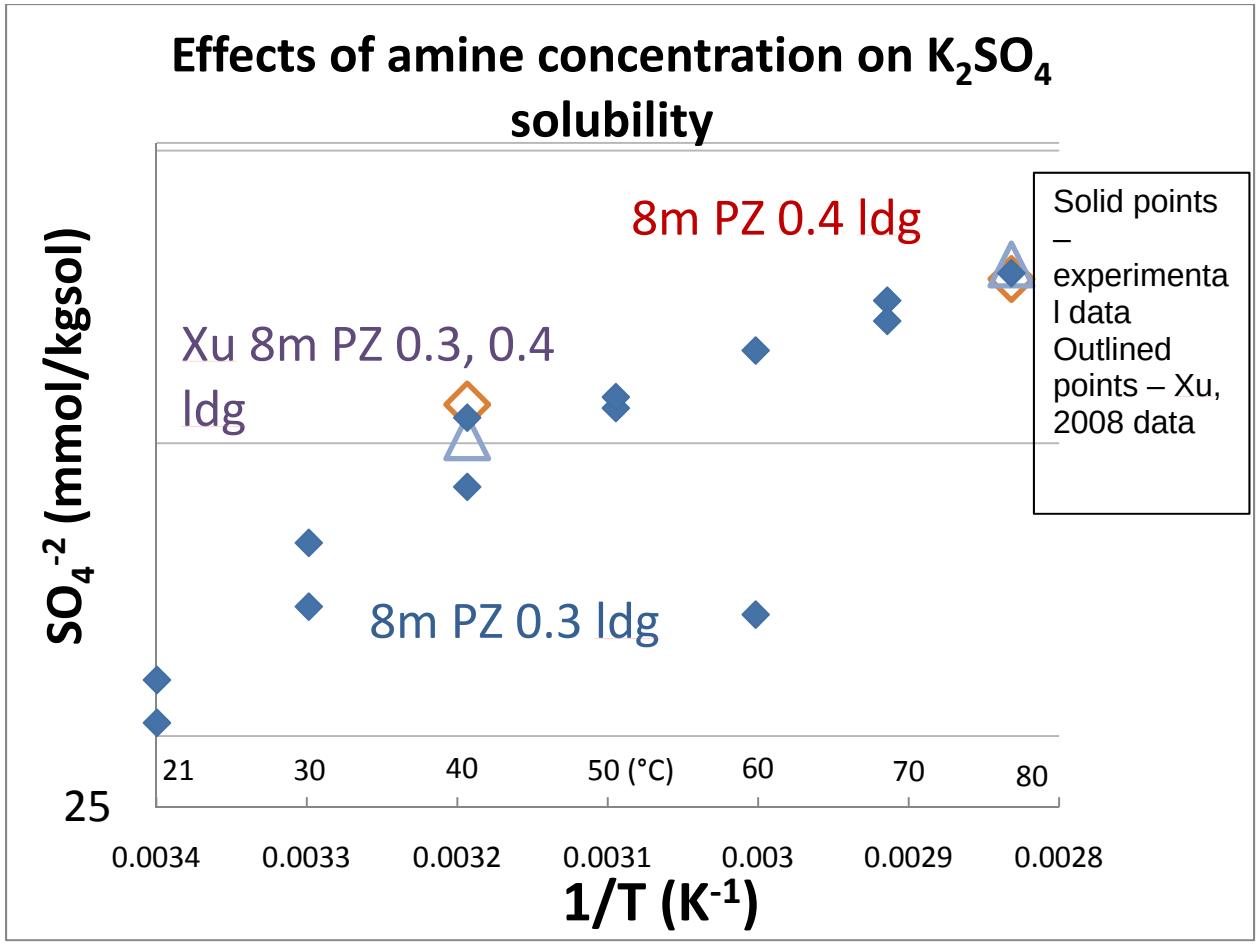

Figure 2: Solid Solubility Experiment Validation

Figure 2 shows the effects of amine organic nature and concentration on K_2SO_4 solubility. The solid points on the graph are the experimental data points obtained from the solid solubility experiments for 8 m PZ at 0.3 loading and 8 m PZ at 0.4 loading. The outlined points are by Xu

(2008). The concentrations of potassium in 8 m PZ with 0.3 CO_2 loading at 40 °C and 80 °C were within 2–5% of the results obtained by Xu. However, the concentration of potassium in 8 m PZ with 0.4 CO_2 loading at 40 °C and 80 °C was within 11–13%.

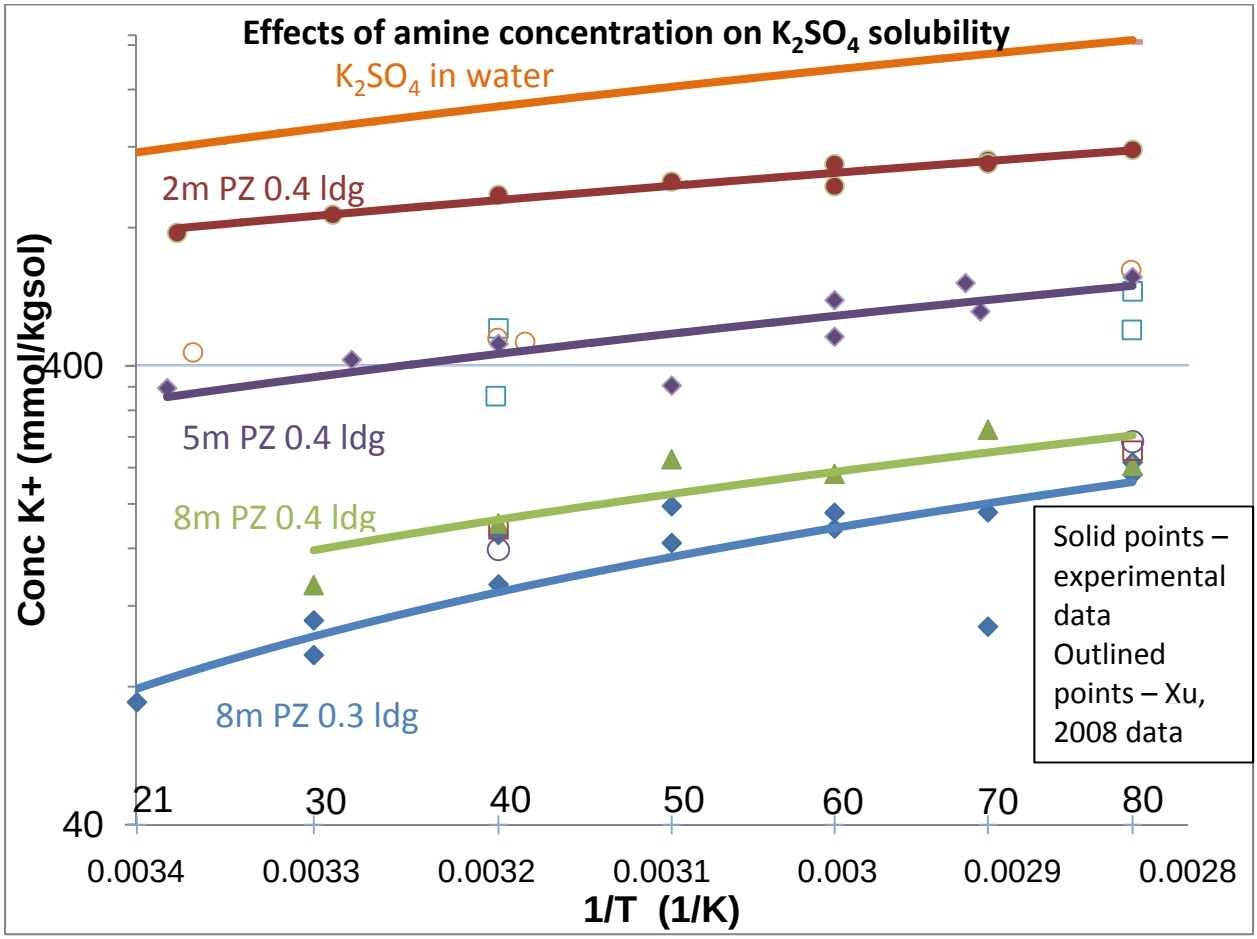

Figure 3: Concentration of Potassium in PZ saturated to K_2SO_4

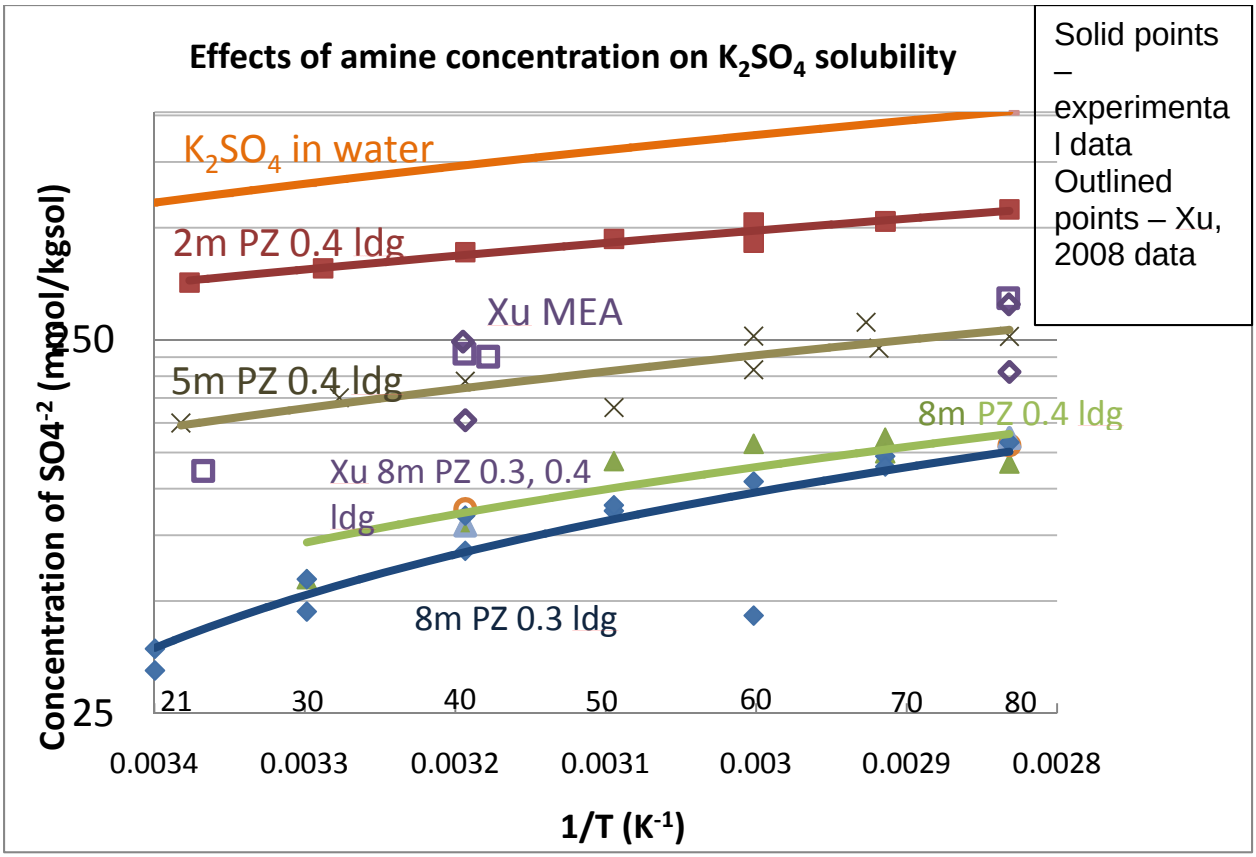

Figure 4: Concentration of Sulfate in PZ solutions

The concentration of K^+ (Figure 3) and SO_4^{-2} (Figure 4) measured by the cation chromatograph and anion chromatograph respectively, was plotted against the inverse of temperature for all three experiments. The solubility of K_2SO_4 in water (Söhnel, 1985) for varying temperatures was plotted in the same figure to compare the solubility of salt in the two different media. Plotted on the same curves were the K_2SO_4 solubility results for 7 m and 11 m MEA at 0.3 and 0.4 loading obtained from Xu (2008).

Figures 3 and 4 both show that the solubility of K_2SO_4 in solution increases with increasing loading because of a greater concentration of carbamate and protonated amine in the system. The solubility of the sulfate also increases with the temperature of the solution. The solubility of K_2SO_4, however, is lower in PZ than in MEA. This is because the ring-structured PZ is more organic in nature than MEA. A solvent reclaiming process ideally requires a large difference in solubility at different loadings. Xu (2008) correlated her experimental results for K_2SO_4 solubility in MEA with an empirical equation shown in Figure 5. The results obtained for 8 m PZ from experiments 1, 2, and 3 were fitted to this empirical equation and plotted in Figure 5.

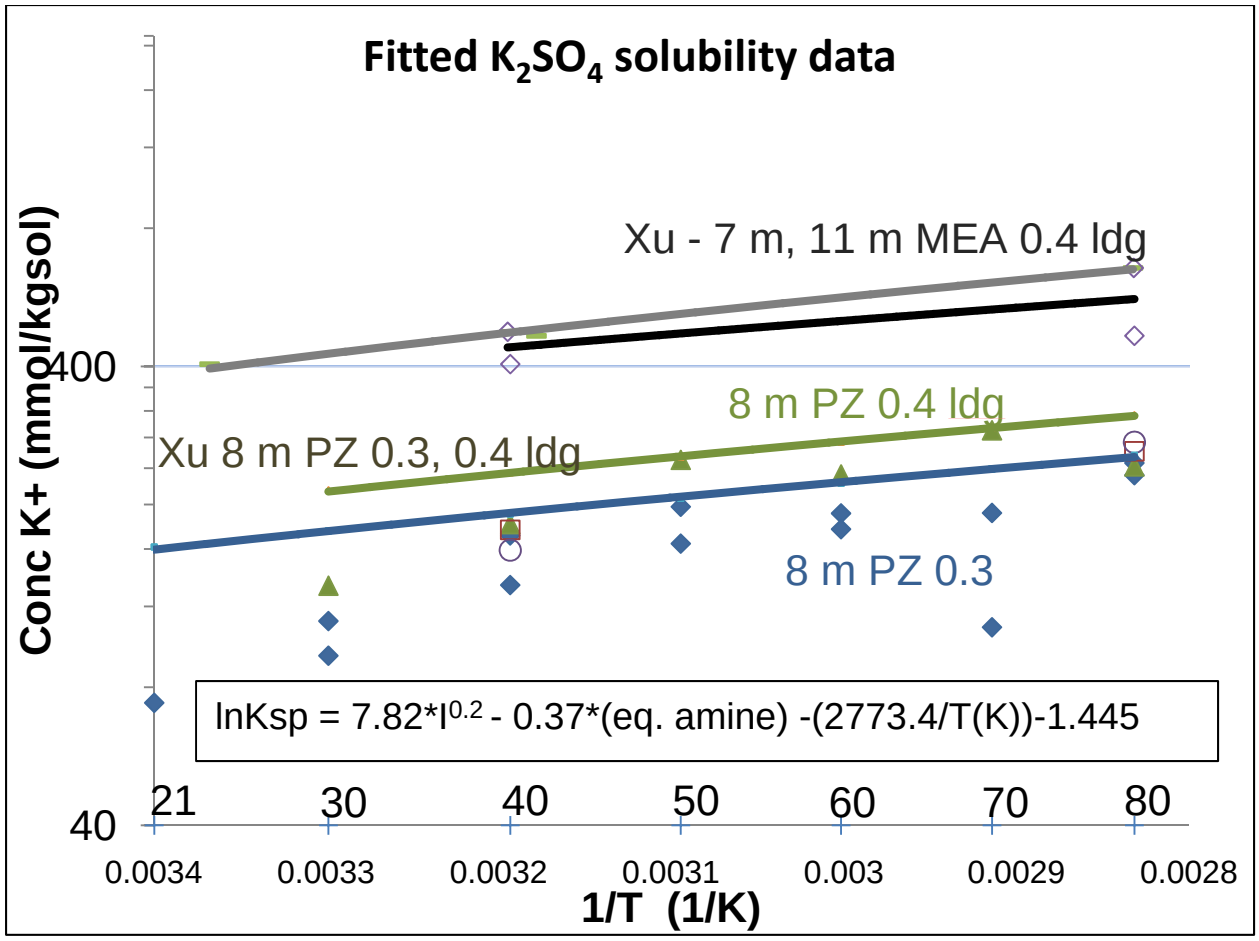

Figure 5: Fitted K_2SO_4 solubility data

Figure 5 shows that the empirical equation obtained by Xu (2008) for varying MEA concentrations does not relate very well to PZ solutions. As more solubility data are collected for PZ solutions, an empirical equation will be formed using the solid solubility method.

The concentration of CO_2 in solution at the various sampling temperatures was also analyzed using the TIC method. The raw data obtained were translated into mmol/kgsol and plotted against the inverse of temperature in Figure 6 below.

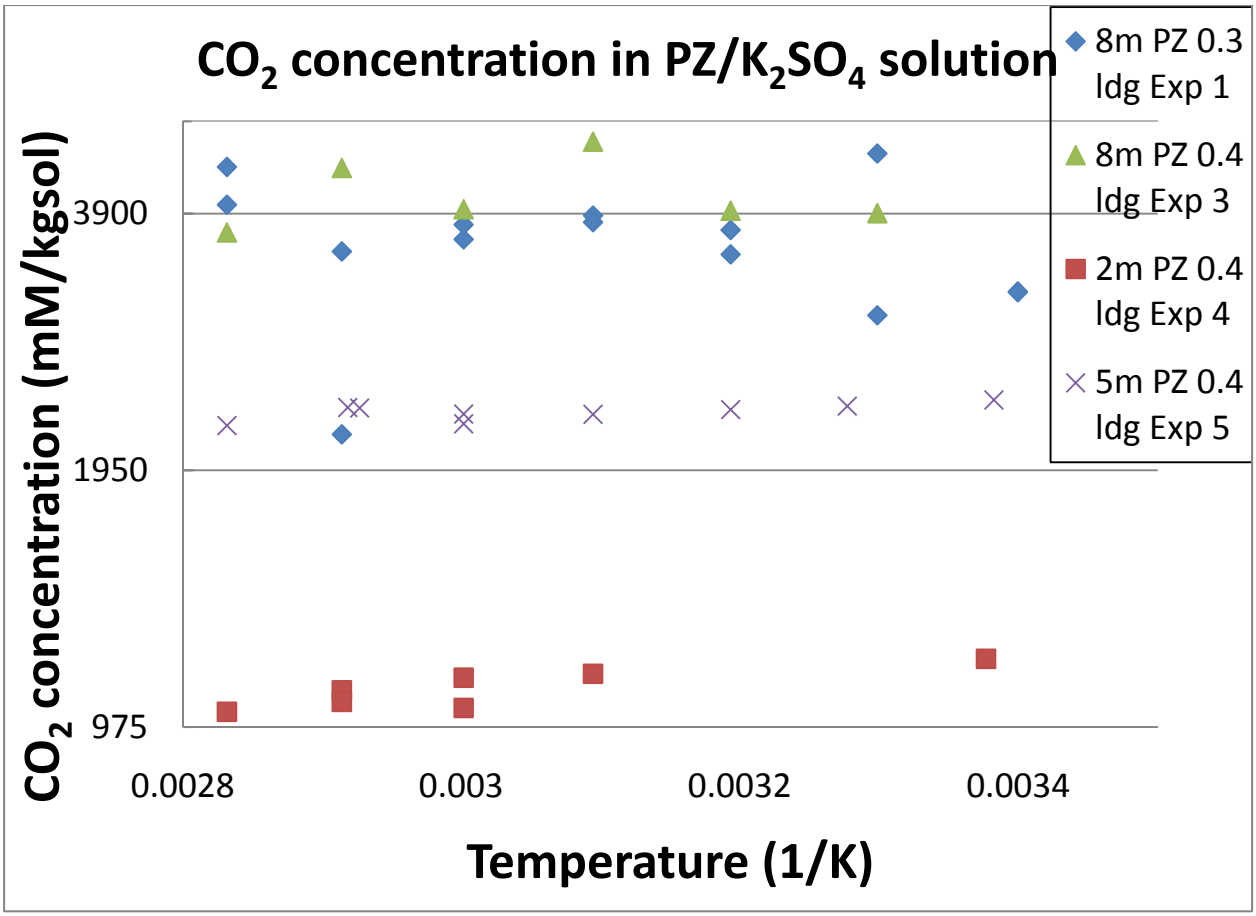

Figure 6: Concentration of CO_2 in K_2SO_4 solution

The reason for analyzing for CO_2 in PZ solutions is to determine if CO_2 was lost during the solid solubility experimental procedure. From Figure 6, a general observation can be made that at higher temperatures, some loss of CO_2 in solution does occur at higher piperazine concentrations. For future experiments, a change in experimental procedures is being investigated to reduce heat loss in the solid solubility system.

PZ solubility: Another set of experiments that has been started this quarter is in continuation of Hilliard's work (2008) and Freeman's CO_2 solubility in PZ measurement (Freeman, 2009). Freeman studied the solubility window for CO_2 in PZ solutions. The analysis for 8 m PZ and 10 m PZ is shown in Figure 7 below.

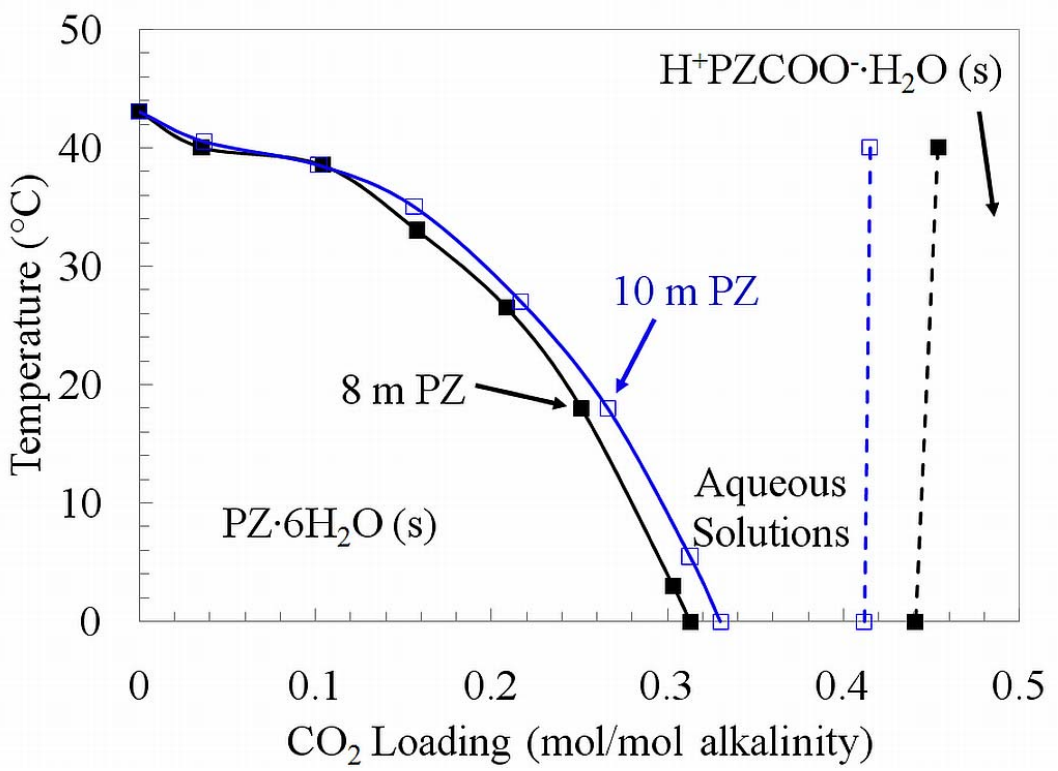

Figure 7: Solid-Liquid Transition Temperatures for Aqueous PZ

For 8 m PZ, a CO_2 loading of approximately 0.25 mole CO_2 per mole of alkalinity is required to maintain a liquid solution without precipitation at room temperature (20 °C) (Freeman, 2009). The points on the dotted lines show the CO_2 loading at which hydrated protonated PZ carbamate (H+PZCOO-.H_2O) is soluble in the PZ solution. It is predicted that beyond the 0.46 loading points H+PZCOO-.H_2O is precipitated. The trend of this solubility is predicted by the dotted lines. The actual trend for temperatures from 0 °C to beyond 50 °C is being determined from solid solubility experiments similar to those performed to determine the solubility of K_2SO_4 in PZ solutions. The crystals are first produced by loading the PZ solutions to above 0.46. If the precipitate is not formed during loading, the solution is stirred after loading until solids are seen. The solids are then airdried and solid solubility experiments performed to determine the amount of precipitate expected at a given loading.

PZ/1MPZ/1,4 DMPZ solubility: Solubility measurements for CO_2 loaded 3.9 m PZ/3.9 m 1MPZ/0.2 m 1,4 DMPZ and 3.75 m PZ/3.75 m 1MPZ/0.5 m 1,4 DMPZ solutions were taken to predict the solubility envelope of these blends. The solubility of the blends at varying loadings and temperatures is shown in Figure 8 for the 3.9 m PZ/3.9 m 1MPZ/0.2 m 1,4 DMPZ blend and Figure 9 for the 3.75 m PZ/3.75 m 1MPZ/0.5 m 1,4 DMPZ blend. While making solutions, it was observed that there was no precipitation when mixing only 1MPZ in water or only 1,4 DMPZ in water.

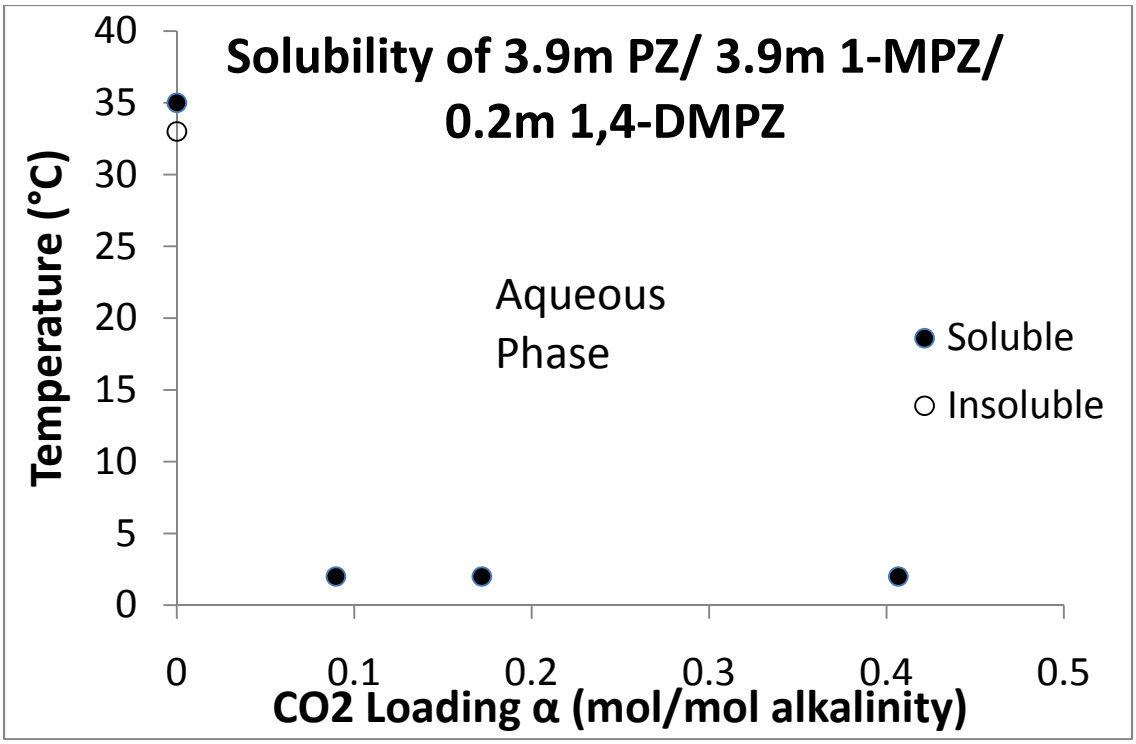

Figure 8: 3.9 m PZ/3.9 m 1MPZ/0.2 m 1,4 DMPZ solubility

A maximum CO_2 loading of 0.41 and 0.39 was obtained for the 3.9 m PZ/3.9 m 1MPZ/0.2 m 1,4 DMPZ blend and the 3.75 m PZ/3.75 m 1MPZ/0.5 m 1,4 DMPZ blend, respectively, at room temperature without any solid precipitation. Intermediary loaded solutions were prepared by appropriately mixing the rich loaded and zero loaded solutions and observing at temperatures between 0 °C and the melting point of the solution. It is expected that the loading can be increased by loading the solution in a chiller at lower temperatures and observing any precipitation of protonated piperazine carbamate ($H^+PZCOO^-.H_2O$) that may form (as with loaded PZ solutions shown in Figure 7).

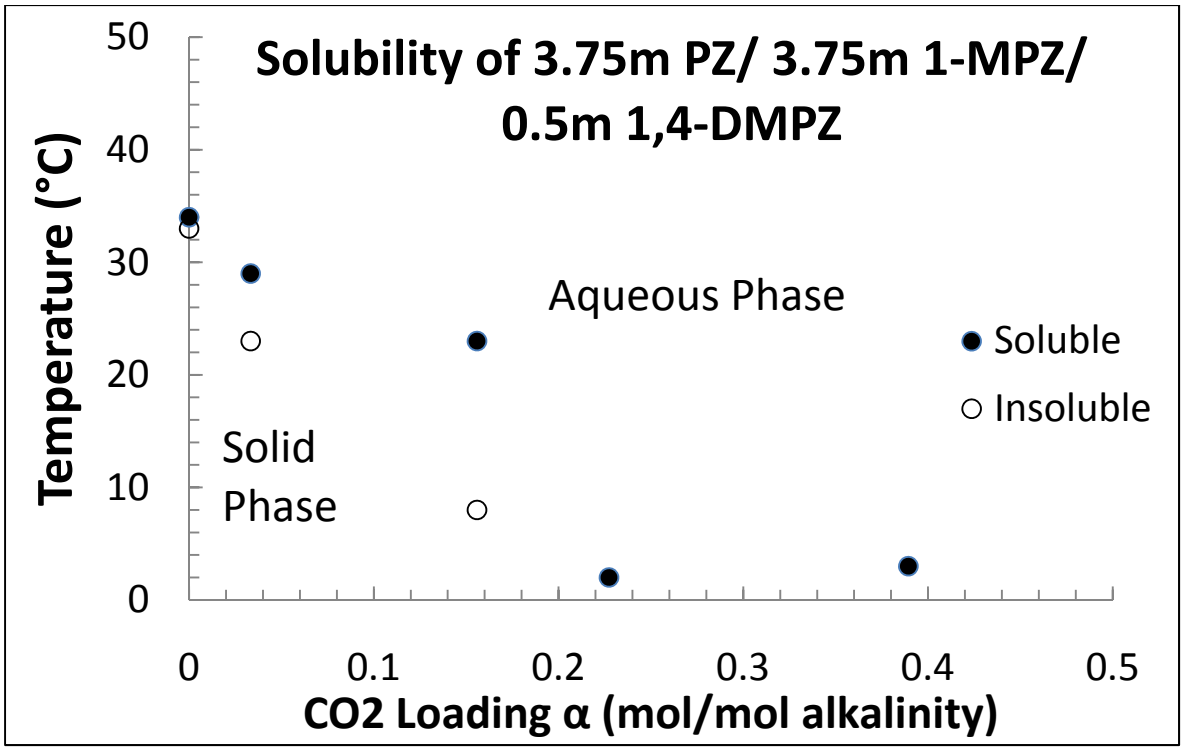

Figure 9: 3.75 m PZ/3.75 m 1MPZ/0.5 m 1,4 DMPZ solubility

In comparing the solubility window of the blends with PZ, it is predicted that the addition of a tertiary amine (1MPZ) will hinder the ability to produce solid $H^+PZCOO^-.H_2O$. As shown in Figure 7, in PZ solutions, $H^+PZCOO^-.H_2O$ is formed at loadings of 0.43 and higher for 8 m PZ. Currently, the blends have been loaded up to 0.41 and 0.39 for 3.9 m PZ/3.9 m 1MPZ/0.2 m 1,4 DMPZ and the 3.75 m PZ/3.75 m 1MPZ/0.5 m 1,4 DMPZ blends, respectively, without any solid precipitation at temperatures as low as 2 °C.

Piperazine hexahydrate ($PZ.6H_2O$), also a solid, is formed in PZ-loaded solutions of 0.22 and lower at 25 °C for 8 m PZ. Because of a lower concentration of PZ in the blends, the $PZ.6H_2O$ precipitates at lower temperatures (at approximately 33 °C for both blends), expanding the solubility envelope for both the blends.

Conclusion

The solubility of K_2SO_4 in aqueous PZ was measured using at varying temperatures, solvent concentrations, and CO_2 loadings. K_2SO_4 solubility increases with CO_2 loading because at higher CO_2 loading, the solvent is more ionic since it contains greater concentrations of carbamate and protonated amines. As a result, K_2SO_4 crystals are more soluble in the solution. In addition, K_2SO_4 solubility decreases as the organic nature and concentration of the solvent increases. K_2SO_4 is less soluble in PZ, which has a ring structure, than in MEA because PZ is more organic and less polar than MEA. Furthermore, the solubility of K_2SO_4 increases with temperature.

The concentration of K^+ in 8 m PZ at a CO_2 loading of 0.3 at 40 °C and 80 °C was within 2–5% of the results obtained by Xu. Furthermore, the concentration of K^+ in 8 m PZ at a CO_2 loading of 0.3at 40 °C and 80 °C was within 11–13%, validating the solid solubility experimental method The solubility envelope of CO_2 loaded 3.9 m PZ/3.9 m 1MPZ/0.2 m 1,4 DMPZ and 3.75 m PZ/3.75 m 1MPZ/0.5 m 1,4 DMPZ blended solutions at varying temperatures was determined. A maximum CO_2 loading of 0.41 and 0.39 was determined for the two blends, respectively, at room temperature without any solid precipitation. At zero loading, both blends are solids (piperazine hexahydrate, $PZ.6H_2O$) up to 33 °C compared to PZ, which melts at 43 °C at zero loading.

Future Work

Solid solubility experiments of K_2SO_4 in 12 m and 20 m PZ are being performed to determine an empirical equation for the solubility of K_2SO_4 in PZ using regression of data. In a similar manner, Xu (2008) determined the empirical equation for the solubility of K_2SO_4 in MEA. Aspen Plus® modeling for a PZ reclaiming system, as well as an economic analysis for the proposed reclaiming system, is currently being carried out.

For the PZ solubility experiments, 8 m PZ and 9 m PZ have been loaded to approximately 0.48 loading and crystals of hydrated protonated piperazine carbamate have been observed in the solution. The solution is being analyzed to determine the actual concentration and loading of the solutions. The crystals produced are being dried and analyzed by X-ray diffraction. They are also being prepared in bulk to determine the solubility of the carbamate in PZ solution.

For the PZ blend solutions, solid solubility experiments are being carried out to determine the solubility window and analyze any precipitation that occurs at CO_2 loadings higher than 0.4 by loading at temperatures lower than room temperature.

References

Freeman SA, Dugas R, Van Wagener DH, Nguyen T, Rochelle GT. "Carbon dioxide capture with concentrated, aqueous piperazine". *Int J Greenh Gas Cont.* 2010; 4(5):756–761 .

Hilliard MD. *A Predictive Thermodynamic Model for an Aqueous Blend of Potassium Carbonate, Piperazine, and Monoethanolamine for Carbon Dioxide Capture from Flue Gas.* The University of Texas at Austin. Ph.D. Dissertation. 2008.

Rochelle GT et al. "CO_2 Capture by Aqueous Absorption, Second Quarterly Progress Report 2008". Luminant Carbon Management Program. The University of Texas at Austin. 2008.

Rochelle GT et al. "CO_2 Capture by Aqueous Absorption, Fourth Quarterly Progress Report 2009". Luminant Carbon Management Program. The University of Texas at Austin. 2010.

Sexton A. *Amine Oxidation in CO_2 Capture Processes*. The University of Texas at Austin. Ph.D. Dissertation. 2008.

Söhnel O, Novotny P. *Densities of aqueous solutions of inorganic substances*. Elsevier, Amsterdam. 1985.

Xu Q. *Solvent Reclaiming by Crystallization of Potassium Sulfate*. The University of Texas at Austin. M.S. Thesis. 2008.

Available online at www.sciencedirect.com

ScienceDirect

Energy Procedia 00 (2010) 000–000

Energy Procedia

www.elsevier.com/locate/XXX

GHGT-10

Degradation of aqueous methyldiethanolamine by temperature and oxygen cycling

Fred Closmann and Gary T. Rochelle*

Luminant Carbon Management Program, Department of Chemical Engineering, The University of Texas at Austin, 1 University Station C0400, Austin, Texas, 78712, USA

Elsevier use only: Received date here; revised date here; accepted date here

Abstract

The primary degradation products identified in aqueous 7 molal (m) methyldiethanolamine (MDEA) loaded to 0.1 mol CO_2/mol alkalinity and degraded in the Integrated Solvent Degradation Apparatus (ISDA) were diethanolamine (DEA), bicine and formate. DEA and bicine represented 43 and 9 % of the carbon loss, respectively, after the solvent was cycled for 167 hours. An MDEA loss of 8.8 mM/hr and a formate production of 0.6 mM/hr were measured when 7 m MDEA cycled from 55 to 120 °C in the ISDA in its initial design, which allowed bubble entrainment. When bubble entrainment was minimized through coalescence and removal, the MDEA loss and formate production were cut in half (4.6 mM/hr and 0.31 mM/hr). When dissolved oxygen was stripped from cycled MDEA with N_2 gas at 2 L/min, the MDEA loss was negligible, and the formate production was reduced to 0.05 mM/hr. Designers of CO_2 scrubbing systems for post-combustion capture should minimize dissolved and entrained oxygen carryover into the stripper. Stripping of entrained and dissolved oxygen before the stripper is recommended to avoid high temperature oxidation.

An oxygen solubility limit exists at a thermal reactor temperature of 120 °C which can be expressed as an apparent upper limit of dissolved O_2 available to degrade ~1.3 mM MDEA/pass. The oxidative degradation model compensates for the complete consumption of dissolved oxygen in the thermal reactor at higher temperatures (>100 °C). The model assumes that all oxidative degradation is occurring in the thermal reactor under plug-flow reactor (PFR) behavior, and compensates for complete oxygen consumption with a stoichiometric factor (S). The regressed values of S, E_a, and k_o for formate were 0.1, 107 kJ/mol, and 2.4 1/hr, respectively. The predicted rates of formate production approximately match the measured rates over the entire measured temperature range of 55 to 120 °C. Oxidation Inhibitor A is ineffective over the temperature range of 90 to 120 °C in cycled solvents.

methyldiethanolamine; piperazine; oxidative degradation, solvent cycling; diethanolamine

1. Introduction

Alkanolamine solvents including aqueous MDEA have been used for decades for acid gas treating where feed gas composition is typically 75 % C1-C5 alkanes, 13 - 15 % CO_2, and no O_2 [1]. Under these conditions, solvent degradation is dominated by thermal and CO_2-catalyzed chemical processes. Alkanolamine solvent scrubbing will likely be the technology of choice for CO_2 capture from coal-fired power plants. Flue gas streams would typically be composed of 5 to 7.5 % O_2, in addition to CO_2, SO_2, N_2, and other impurities. The presence of O_2 at these concentrations presents challenges because many alkanolamines such as monoethanolamine (MEA) are susceptible to oxidative degradation. The problem of oxidative degradation of solvents in post-combustion service was addressed by Chakravarti [2] in the development of an approach to strip O_2 from rich amine streams.

We are interested in 7 m MDEA and MDEA blends (7 m MDEA/2 m PZ) because of the history of commercial use of MDEA, and the existence of patents for MDEA promoted with PZ [3]. 7 m MDEA/2 m PZ exhibits a liquid-side mass transfer coefficient (k_g') of 4.5e07 mol/s*Pa*m^2 which is equivalent to the performance of 8 m PZ, and better than 7 m MEA (k_g'~3.1e07 mol/s*Pa*m^2) at comparable rich CO_2 partial pressures [4]. The cyclic capacity of the blend is approximately 0.75 mol CO_2/(kg amine + water) at rich and lean CO_2 partial pressures of 7 kPa and 0.7 kPa, respectively, making this solvent competitive with 7

* Corresponding author. Tel.: +1-512-471-7230; fax: +1-512-471-7060.
E-mail address: gtr@che.utexas.edu.

m MEA and 8 m PZ. Versions of this solvent are already in commercial use for acid gas treatment, and its performance benefits make it attractive as an alternative to MEA for CO_2 capture.

Recent degradation studies have used batch reactors to accelerate oxidative degradation [5], and sealed stainless steel cylinders [6] and microcalorimeters [7] for the rapid screening of solvents for thermal degradation. Those degradation methods generally isolate oxidative or thermal degradation behavior. We degraded solvents in the Integrated Solvent Degradation Apparatus (ISDA), which alternately exposes solvents to oxidative and thermal degradation conditions in a single system. The ISDA simulates conditions observed in an absorber/stripper configuration designed for CO_2 capture. Because these conditions are integrated into a single experimental apparatus, secondary effects have been observed. The ISDA also allows us to evaluate the effect on degradation rates of carryover of dissolved and entrained oxygen into the cross-exchanger and stripper where temperatures can exceed 120 °C.

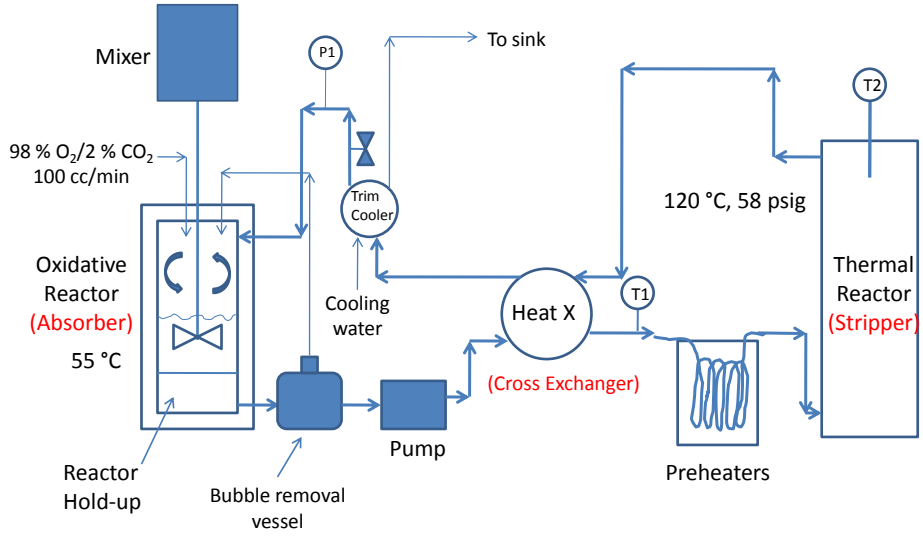

Figure 1 The Integrated Solvent Degradation Apparatus (ISDA)

2. Experimental Methods

The oxidative reactor in the ISDA (Figure 1) is a 750-ml flow-through jacketed glass vessel with an actively stirred top section of 400-ml nominal volume, and a 330-ml bottom section which simulates the sump in an absorber. The top section, which is exposed to a selected gas composition, is agitated at 1,440 rpm to maximize oxygen mass transfer. A 100 cc/min purge gas is introduced to the top section, which typically consists of 98% O_2/2% CO_2. The composition of this gas is varied to study oxidative effects on cycled solvent. Temperature control of the oxidative reactor at 55 °C is achieved by passing water through the jacket-side of the oxidative reactor. The system operates at a nominal liquid flow rate of 200 ml/min, which provides a residence time of 3.5-4.0 minutes in the oxidative reactor.

CO_2-loaded amine is continuously pumped from the bottom section of the oxidative reactor, through a bubble removal vessel, through a positive displacement pump, and into the shell side of a counter-currently operated single-pass tube-in-tube cross-exchanger where it takes on heat from amine exiting the thermal reactor. The amine is then passed through two pre-heaters consisting of stainless steel coiled tubing immersed in oil baths, and enters the internal section of a thermal reactor, which is a 1.2-L stainless steel tube-in-tube heat exchanger. Dimethyl silicone oil is passed through the jacket side of the thermal reactor to heat the amine. The hot amine exits the thermal reactor and passes back through the tube side of the cross-exchanger where it heats the cold amine passing on the shell side. The amine is then passed through a trim cooler (heat exchanger) where it is cooled before passing through a back-pressure valve (¼-inch metering valve) and returning to the oxidative reactor above the liquid surface at atmospheric pressure. All tubing is ¼-inch outer diameter. Materials of construction include 316 stainless steel for tubing, compression fittings, cross-exchanger, and thermal reactor, and glass for the oxidative reactor.

Degraded solvents are analyzed using cation chromatography for amines and degradation products exhibiting amine functionality (alkalinity), anion chromatography for heat stable salts (anions), liquid chromatography with electrochemical detection for amino acids, HPLC coupled to mass spectrometry (MS) and gas chromatography (GC) coupled to MS for identification of polar and non-polar degradation products. Alkalinity is measured using acid titration.

3. Results and Discussion

Figure 2 illustrates degradation product concentrations when 7 m MDEA was cycled from 55 °C in the oxidative reactor to 120 °C in the thermal reactor with a purge gas of 98 % air/2 % CO_2. The primary products identified and quantified in the degraded solvent included diethanolamine (DEA), bicine (bis-hydroxyethylglycine), formate, and formamide, all typical of cycled MDEA. The longer term trends demonstrated by this data indicate a possible competition between MDEA and its products for oxygen in the solvent. Using final concentrations of these products measured with ion chromatography, we

accounted for >55 % of the carbon loss (as MDEA). The carbon associated with DEA comprised >40 % of the carbon in MDEA loss. Table 1 lists MDEA and alkalinity loss and degradation product formation in relevant experiments conducted in the ISDA.

3.1. Temperature Effects/Oxidative Model

The concentration of formate measured in 7 m MDEA when cycled from 55 °C to a series of thermal reactor temperatures (55 to 120 °C) in separate experiments generally increased proportionally with the temperature maintained in the thermal reactor (Figure 3). The rates of formate production listed in Table 1 range from 0.004 mM/hr at 55 °C to 0.31 mM/hr at 120 °C. Very little formate was produced until the thermal reactor was set at 90 °C. However, the change in formate production from a thermal reactor temperature of 100 to 120 °C indicates that, at temperatures above 100 °C, the dissolved oxygen in the solvent may be completely consumed, creating an upper limit to the formate production rate (0.31 mM/hr).

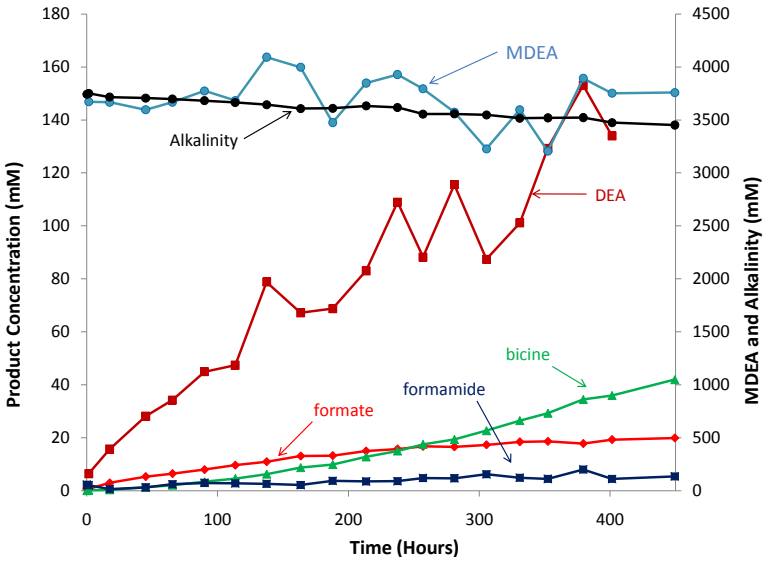

Figure 2 Degradation products in cycled 7 m MDEA

An oxidative degradation model based on degradation product formation in 7 m MDEA was developed to allow prediction of rates of oxidative degradation that can be expected in the heat exchanger and piping entering the top of the steam stripper. These are the most likely locations for oxygen to be present at higher temperatures in a practical absorber/stripper. A simple rate law relationship using the Arrhenius equation over-predicts oxidation rates at temperatures above 100 °C due to complete consumption of dissolved oxygen in ISDA in the thermal reactor.

The basis for the model is that solvent degradation in the ISDA behaves according to isothermal PFR behavior, and that all oxidative degradation occurs in the thermal reactor at the higher experimental temperatures. Rates of degradation product formation over the temperature range 55 to 80 °C are relatively low when compared to 90 °C and above, indicating that oxidative degradation processes are negligible in solvent while passing through the absorber (oxidative reactor in the ISDA). The factor (S) (Equation 1) relates the amount of degradation product formed to the amount of oxygen consumed per pass of solvent through the system. Henry's Law was used to relate dissolved oxygen in the solvent to that in the gas phase in contact with the solvent in the oxidative reactor. The PFR oxidative model (Equation 2) corrects for the depletion of dissolved oxygen at the higher temperatures.

Using degradation product formation rates measured over the thermal reactor temperature range of 55 to 120 °C, we regressed values of activation energy (E_a), rate constant (k_o), and S for formate, bicine and DEA. As a starting point, we chose the measured values of k_o at 90 °C for all components based on the knowledge that dissolved oxygen was not completely consumed at this temperature in the ISDA. We estimated k_o, E_a and S for the three components as listed in Table 2. The model currently provides values of each parameter within an expected range for DEA and formate, but does not provide expected values for bicine. Further, k_o for bicine is three orders of magnitude lower than for DEA, and five orders of magnitude lower than for formate, reflecting the greater tendency for MDEA to degrade to DEA and formate than to bicine. The activation energies (E_a) for DEA and bicine regressed to 85 kJ/mol, and the activation energy for formate regressed to 107 kJ/mol.

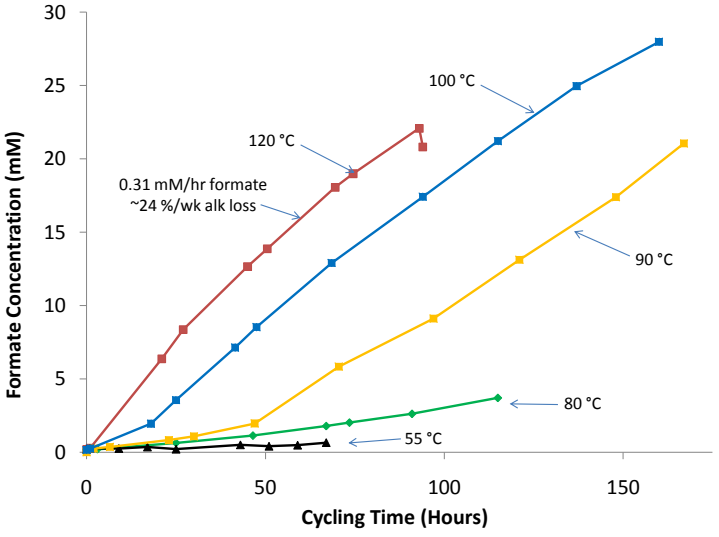

Figure 3 Formate measured with oxidative reactor at 55 °C and thermal reactor varied from 55 to 120 °C

Table 1 - Cycling Experiment Results (7 m MDEA)

Expt	T_{th} (°C)	Stir Rate (rpm)	Purge Gas	Alk Loss (mM/hr)	MDEA Loss (mM/hr)	DEA Prod Rate (mM/hr)	Formate Prod (mM/hr)	Formate w/ Hydrolysis (mM/hr)	Bicine (mM/hr)
C-8	120	1440	N_2/CO_2	1.7	1.9	0	0.013	0.001	0
C-9	120	0	N_2/CO_2	3	4.1	0	0.024	0.002	0
C-13	120	1440	Air/CO_2	0.76	0.24	0.37	0.084	0.08	0.061
C-14	90	1440	Air/CO_2	0.76	0.22	0.08	0.044	0.058	0.062
C-18	120	1440	O_2/CO_2	0.74	0	0.39	0.047	0.044	0.088
C-4	120	520	O_2/CO_2	2.8	3.4	NM	0.17	0.15	NM
C-5	120	1000	O_2/CO_2	4.3	8.5	NM	0.37	0.57	NM
C-1	120	1440	O_2/CO_2	5.2	8.8	NM	0.59	0.98	0.48
C-2	55	1440	O_2/CO_2	1.4	~0.0	NM	0.0052	~0	~0
C-15	90	1440	O_2/CO_2	1.82	2.37	~0	0.15	0.23	0.27
C-7*	120	1440	O_2/CO_2	5.4	5	1.8	0.22	0.29	0.35
C-3	55	1440	O_2/CO_2	1.5	0.9	0	0.0018	0.01	0.05
C-11	80	1440	O_2/CO_2	1.3	0.91	0	0.034	0.057	0.11
C-12	90	1440	O_2/CO_2	2.5	2.87	1.55	0.12	0.15	0.13
C-10	100	1440	O_2/CO_2	3	4.1	1.64	0.18	0.31	0.22
C-6	120	1440	O_2/CO_2	5.3	4.6	2.56	0.31	0.34	0.34

$$S = \frac{\Delta[\mathrm{Pr}]}{\Delta[O_2]} \tag{1}$$

$$\Delta[\mathrm{Pr}] = S * P_{O_2} * Q * t * \frac{1 - e^{-\left(\frac{k * V_{TR}}{Q}\right)}}{H_{O_2} * V_{total}} \tag{2}$$

Figure 4 presents the measured and predicted product formation rates vs. 1/T (K) for the components formate and bicine based on the regressed values of E_a and k_o. The predicted product formation rates approximately match the measured rates over the entire temperature range for formate, with only a slight under-prediction in the middle of the range (80 to 90 °C). For bicine, the match is poor at all but the highest temperatures, which is expected based on the regressed value for S (~4,900). In general, the model provides a better fit for formate than was provided by using a simple rate-law model by compensation for the complete consumption of dissolved oxygen at the higher temperatures in ISDA. The failure of the model to accurately predict formation rates for bicine may also be a result of bicine forming as a degradation product of something other than MDEA in a secondary reaction.

The amount of DEA produced per pass in the system is estimated as 0.7 mM when cycled from 55 to 120 °C, whereas the amount of MDEA degraded was estimated at 1.3 mM per pass. Using dissolved oxygen solubility in water data [8] at 60 °C, we determined that approximately 0.57 mM dissolved oxygen is available, implying a stoichiometric ratio between oxygen available and MDEA consumed per pass of ~0.5. Assuming that all of the MDEA loss was associated with oxidative degradation, the 1.3 mM per pass represents an upper limit of amount of dissolved oxygen available to degrade MDEA.

Table 2 - Regressed Oxidative Model Values

	Degradation Product		
Parameter	Formate	DEA	Bicine
k_o (1/hr)	2.42	0.06	3.388E-05
E_a (J/mol)	107000	85054	85010
S	0.1	16.7	4848.2

3.2. Bubble Entrainment

Based on visual observations of entrained (undissolved) bubbles in solvent exiting the oxidative reactor in early experiments, we sequentially reduced the stir rate in this reactor and observed proportional reductions in formate production (Figure 5). We then installed a bubble removal vessel immediately downstream of the oxidative reactor with 0.24-inch stainless steel unstructured packing to coalesce small entrained bubbles into larger bubbles which could easily escape the solvent before being pumped to the heat exchanger. The formate production rate (0.31 mM/hr) measured with entrained bubble removal (C-6) at full stir rate (1440 rpm) demonstrated that oxidative degradation became dependent primarily on dissolved oxygen, a process governed by the solubility limit of oxygen in solvent at the conditions prevalent in the oxidative reactor (55 °C). All subsequent experiments were conducted with the bubble removal vessel installed in the ISDA. The practical implication of this finding is

that full-scale absorber/stripper systems will need to be designed to minimize the entrainment of dissolved gases as solvent is passed out of the absorber unit. System leaks to the surrounding atmosphere will need to be eliminated to ensure that air is not introduced to the solvent.

3.3. Dissolved Oxygen

In experiments C-8 and C-9, we replaced the 98 % O_2/2 % CO_2 purge gas in the headspace of the oxidative reactor with 98 % N_2/2 % CO_2 gas at 100 cc/min in order to understand the role of thermal degradation in MDEA in the ISDA in the absence of accelerated oxidative degradation. With the exception of the purge gas, all conditions in C-8 were similar to those in C-6. Comparison of experimental results reveals that the alkalinity and MDEA loss were cut in half or better, but the rates of formate and bicine production were reduced by an order of magnitude. No DEA production was observed in experiment C-8 with the 98 % N_2/2 % CO_2 purge gas. These results indicate that DEA is primarily formed through an oxidative degradation process, as evidenced by a production rate of 2.56 mM/hr in experiment C-6.

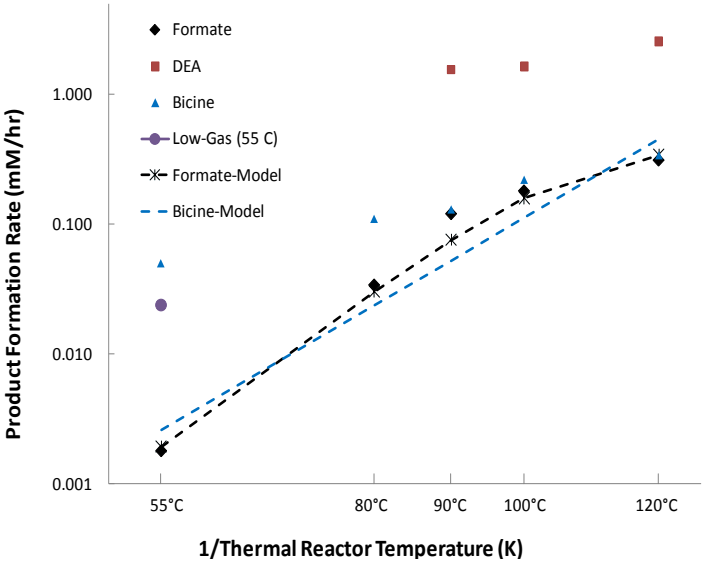

Figure 4 Measured vs. modeled formate rates in cycled 7 m MDEA

In a further effort to understand the role of dissolved oxygen in causing oxidative degradation, and how easily this process could be minimized, a modified bubble removal vessel was constructed of an 8-inch tall (1.25-inch diameter) glass bottle fitted with a fritted stone sparge tube inserted in the lid and reaching the bottom of the vessel. A 2 L/min N_2 gas purge was introduced to the solvent as it passed through this vessel to strip dissolved oxygen from the solvent before being pumped to the cross-exchanger. All other conditions of the experiment were held the same as in previous experiments, including the use of 98 % O_2/2 % CO_2 purge gas in the headspace of the oxidative reactor and a thermal reactor temperature of 120 °C.

The formate production rate (Figure 6) was reduced to 0.05 from 0.31 mM/hr, whereas the MDEA loss rate was reduced from 4.6 mM/hr to a negligible rate, indicating that the oxidation rate was reduced to a rate comparable to that expected when the thermal reactor (stripper) was operated at 80 °C or less. The results of this experiment reaffirm our ability to implement stripping to remove dissolved oxygen and reduce oxidative degradation in alkanolamine solvents.

3.4. Oxidation Inhibitor

Experiments C-7 and C-15 were conducted at conditions similar to C-6 and C-12 (120 and 90 °C, respectively, in the thermal reactor) with the exception that 100 mM of Inhibitor A was added to the solvent. At 120 °C (C-7), the bicine production rate listed in Table 1 was comparable to the rate observed in experiment C-6, indicating that the inhibitor was not effective in the cycling system. At 90 °C, the bicine production rate slightly increased with the inhibitor. The formate production rates are included in Figure 6 and indicate that Inhibitor A had little or no effect at 90 or 120 °C. In general, the data confirm that the inhibitor was ineffective at reducing the rate of oxidative degradation in solvents cycled at these conditions.

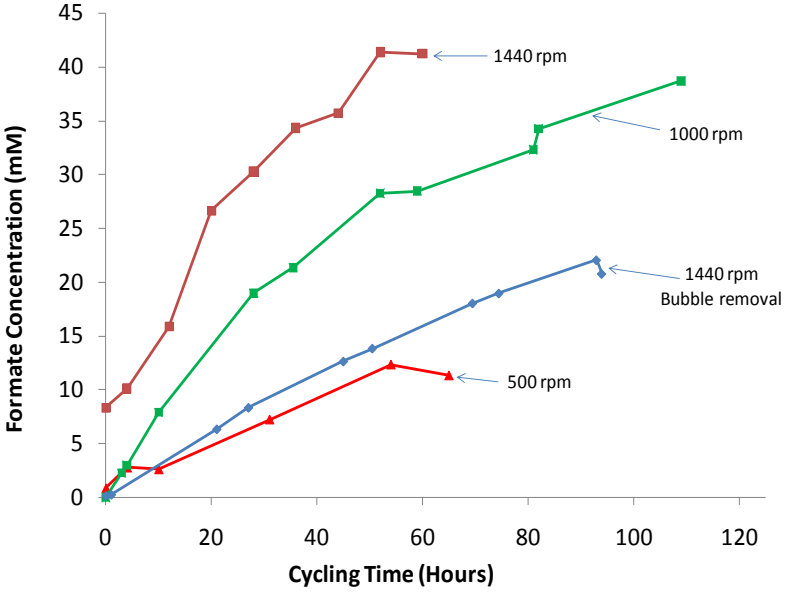

Figure 5 Formate measured in 7 m MDEA cycled from 55 to 120 °C

4. Conclusions

The primary degradation products identified in aqueous 7 m MDEA loaded to 0.1 mol CO_2/mol alkalinity and degraded in the ISDA were DEA, bicine and formate. DEA and bicine represented 43 and 9 % of carbon loss, respectively, after the solvent was cycled for 167 hours.

The rate of MDEA loss was measured as 8.8 mM/hr when 7 m MDEA was cycled from 55 to 120 °C in ISDA in the initial design, which allowed bubble entrainment. When entrained bubbles were removed from the solvent, the loss rate was approximately cut in half (4.6 mM/hr), and the formate production rate was reduced to 0.31 mM/hr. When dissolved oxygen was stripped from cycled MDEA with N_2 gas at 2 L/min, the MDEA loss rate was below detection, and the formate production rate was reduced to 0.05 mM/hr. The MDEA loss rates and degradation product formation rates measured in solvent cycled in ISDA highlight the need for designers of commercial CO_2 scrubbing systems in flue gas post-combustion applications to address dissolved and entrained oxygen accelerating oxidative degradation of aqueous amine solvents. Entrained and dissolved oxygen removal through stripping before amines enter the steam stripping unit (regenerator) is recommended to avoid high temperature oxidation.

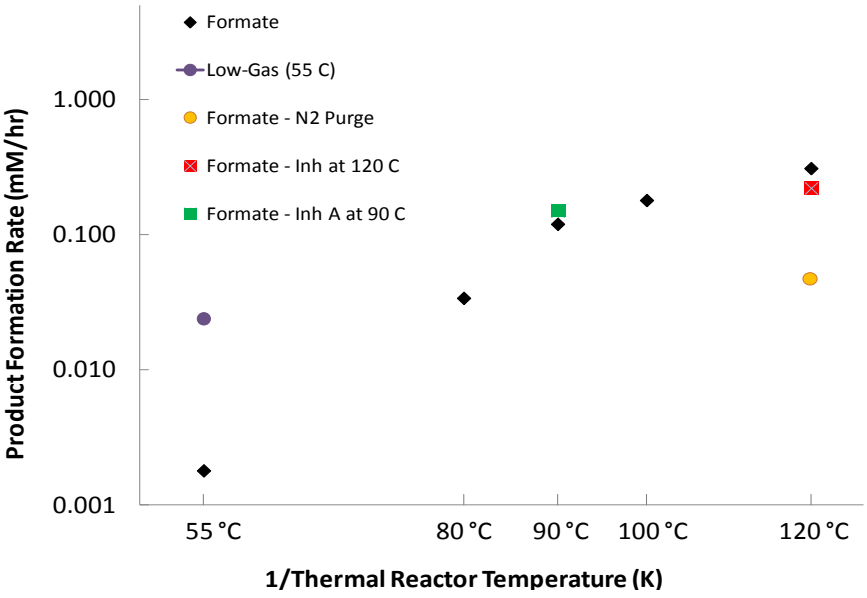

Figure 6 Formate production with/without 100 mM Inhibitor A in cycled 7 m MDEA

An oxygen solubility limit exists at a thermal reactor temperature of 120 °C which can be expressed as an apparent upper limit of dissolved O_2 available to degrade ~1.3 mM MDEA/pass. A simple rate-law model for oxidative degradation over-predicts product formation rates above 100 °C due to accelerated oxidative degradation and an apparent dissolved oxygen solubility limit. We developed an oxidative degradation model which compensates for the complete consumption of dissolved oxygen in the thermal reactor at higher temperatures. The model assumes that all oxidative degradation is occurring in the thermal reactor following PFR behavior. We compensated for complete oxygen consumption with a factor (S) which correlates moles of degradation product produced per moles of oxygen consumed. We regressed values of S, E_a, and k_o for formate of 0.1, 107 kJ/mol, and 2.4 1/hr, respectively. The predicted rates of formate production approximately match the measured rates over the entire measured temperature range of 55 to 120 °C.

When 7 m MDEA cycled from 55 to 120 °C with 98 % N_2/2 % CO_2 as the purge gas, the measured MDEA loss rate was 2 to 4 mM/hr, compared to 4.5 mM/hr when the purge gas was 98 % O_2/2 % CO_2, indicating that, in the absence of oxygen, thermal degradation is causing solvent and alkalinity loss.

When 7 m MDEA cycled from 55 to 90 and 120 °C with 100 mM Inhibitor A, the additive was ineffective at reducing the rate of oxidative degradation, as evidenced by similar formate, bicine and DEA rates measured without the inhibitor with all other conditions held the same.

5. References

[1] Astarita, Gianni and D. Savage and A. Bisio, Gas Treating With Chemical Solvents, J. Wiley & Sons, New York, 1983.
[2] Chakravarti, Shrikar and Amitabh Gupta, "Carbon Dioxide Recovery Plant", Patent Appl. No. 09/774,031, filed January 31, 2001.
[3] Appl, Max and U. Wagner, and H. Henrici, and K. Kuessner, and K. Volkamer, and E. Fuerst, "Removal of CO_2 and/or H_2S and/or COS from Gases Containing these Constituents", Patent Appl. No. 177,615, filed August 13, 1980.
[4] Rochelle, Gary T., Oral Presentation to IUPAC International Meeting, Glasgow, Scotland, August 2009.
[5] Sexton, Andrew, "Amine Oxidation in CO2 Capture Processes", PhD. Dissertation, The University of Texas at Austin, January 2008.
[6] Freeman, Stephanie and J. Davis, and G. T. Rochelle, "Degradation of aqueous piperazine in carbon dioxide capture". International Journal of Greenhouse Gas Control. In print 2010.
[7] Bedell, S. and C.M. Worley, G.Z. Padilla, and A.L. Day, "Methyldiethanolamine (MDEA) Oxidation in Flue Gas CO_2 Capture", presentation paper for SOGAT 4th International CO_2 Forum, Abu Dhabi, April 1, 2010.
[8] Baranenko, V.I., and L.N. Fal'kovskii and V.S. Kirov and L.N. Kurnyk and A.N. Musienko and A.I. Pionkovskii, "Solubility of Oxygen and Carbon Dioxide in Water", Atomnaya Energiya, Vol. 68, No. 4, pp. 291-294, April 1990.

Available online at www.sciencedirect.com

ScienceDirect

Energy Procedia 00 (2010) 000–000

Energy Procedia

www.elsevier.com/locate/XXX

GHGT-10

Optimal operation of flexible post-combustion CO_2 capture in response to volatile electricity prices

Stuart M. Cohen[a,*], Gary T. Rochelle[b], Michael E. Webber[a]

[a]*Department of Mechanical Engineering, The University of Texas at Austin, 1 University Station C2200, Austin, TX, 78712, USA*
[b]*Department of Chemical Engineering, The University of Texas at Austin, 1 University Station C0400, Austin, TX, 78712, USA*

Elsevier use only: Received date here; revised date here; accepted date here

Abstract

Flexibly operating post-combustion carbon dioxide (CO_2) capture in response to electricity prices should improve overall CO_2 capture economics. Optimization and rule-based models are used to simulate a 500 megawatt coal-fired facility that adjusts the operating point of its amine CO_2 scrubbing system to maximize profits in response to volatile electricity prices. Between CO_2 prices of 20 and 70 U.S. dollars per metric ton (USD/tCO_2), a flexible capture system that vents CO_2 while increasing power output can maintain significant CO_2 emissions reductions while improving annual operating profits by up to 10% over inflexible capture. The benefits of venting diminish at high CO_2 prices, but a solvent storage system that permits high CO_2 absorption during partial-load stripping and compression achieves a 9–29% profit advantage at 30–100 USD/tCO_2. Profit improvements with flexibility appear insensitive to CO_2 capture ramping limitations. This case study also suggests that solvent storage should only be large enough to take advantage of high electricity prices for 15–30 minutes each day.

Keywords: CO_2 capture, chemical absorption and stripping, electricity, flexibility

1. Introduction to flexible CO_2 capture

Most analyses of carbon dioxide capture and sequestration (CCS) assume the carbon dioxide (CO_2) capture system always operates at the full gas load of the power plant, but flexible operation could improve CO_2 capture economics [1, 2]. Post-combustion amine scrubbing with 90% CO_2 removal is well-suited for flexible operation due to its relative independence from the power system [3, 4]. In a coal-based retrofit, stripping CO_2 requires that 30–50% of the steam be extracted between the intermediate and low pressure (IP and LP) turbines [5, 6]. CO_2 stripping and compression result in 20–30% net electrical output reduction [7].

A flexible system, however, allows the CO_2 stripping steam to be sent to an LP turbine to produce electricity. The resulting drop in CO_2 flow exiting the stripper then reduces CO_2 compression energy requirements. A prior case study of the Electric Reliability Council of Texas (ERCOT) electric grid found that reducing CO_2 capture load at peak electricity demand can eliminate the need to replace the generation capacity lost to CO_2 capture energy requirements with minimal increase in CO_2 emissions [8]. Partial- or zero-load CO_2 capture during high electricity

* Corresponding author. Tel.: +1-512-232-2754.
E-mail address: stuart.cohen@mail.utexas.edu.

prices could also improve operating profits, though CO_2 emissions might increase [9]. Systems that respond very quickly could also allow the facility to earn payments for providing grid reliability services [3].

There are two general concepts for flexible CO_2 capture. The configuration shown in Figure 1A simultaneously and equally reduces steam and rich solvent flow to the stripper during partial- or zero-load operation [9]. Power output increases, but redirecting rich solvent to the absorber reduces the CO_2 removal rate. CO_2 emissions might increase, but incremental capital cost is negligible if the base plant is already sized to accept the additional steam, as with a retrofit. An alternative configuration (Figure 1B) enables continued high CO_2 removal when stripping and compression load is reduced by feeding the absorber from a lean solvent storage tank and depositing rich solvent into another tank. At times such as low electricity price periods, CO_2 stored in rich solvent can be stripped and compressed in larger stripping and compression equipment sized to treat both the current stream and stored solvent. CO_2 emissions remain low, but the capital costs of solvent inventory, storage tanks, and larger stripping and compression equipment are significant.

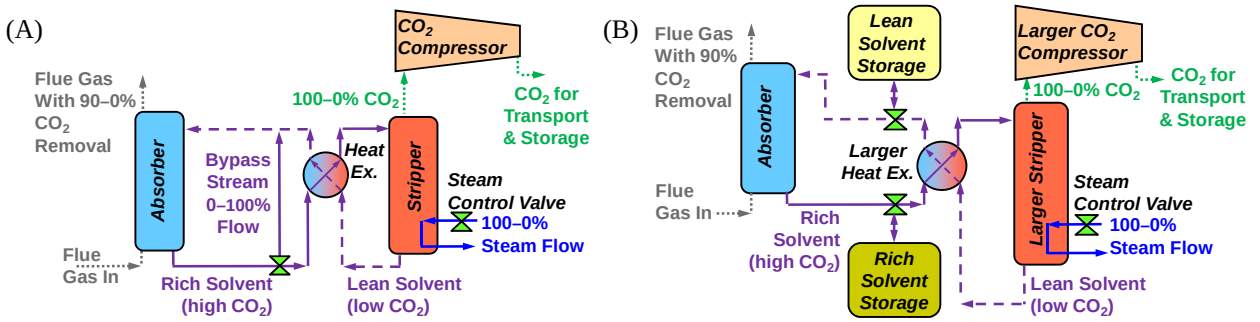

Figure 1: Flexible CO_2 capture might entail venting additional CO_2 emissions during reduced capture load (A), or solvent storage could allow continued high CO_2 removal with stripping and compression systems at partial- or zero-load (B).

Previous work studied the value of the venting-only configuration in Figure 1A using a first-order electricity dispatch model that sets electricity prices equal to the marginal cost of the most expensive plant dispatched at a given time [9, 10]. Actual electricity prices do not necessarily correspond to the marginal costs of a given facility, so the current work uses historical electricity price data to study the implications of flexible CO_2 capture in response to volatile electricity prices. An optimization model constructed within the General Algebraic Modeling System (GAMS) compares profit-maximizing operation of a single coal-fired facility with no CO_2 capture, inflexible CO_2 capture, and flexible CO_2 capture with and without a solvent storage system. A best-case scenario assuming perfect knowledge of all future electricity prices is compared to operation in response to day-ahead price forecasts, and a rule-based MATLAB model is also created to analyze operation without any price foreknowledge.

2. Methodology

This study analyzes a 500 megawatt (MW) coal-fired unit operating in response to 2008 ERCOT electricity prices posted each 15-minutes, so all monetary values are 2008 USD [11]. Large coal-fired facilities can influence electricity price, but this analysis assumes the plant is a price-taker. ERCOT electricity prices are most strongly influenced by natural gas-fired facilities, so the effect of CO_2 price on electricity prices is approximated by adding the emissions costs of an average ERCOT gas-fired facility [12, 13].

In this work, “base plant load” refers to the fraction of maximum gross power plant output, independent of CO_2 capture energy. “Absorber load” is the ratio of the current quantity of CO_2 removed to the total quantity removed with the base plant at full load. “Stripper load,” which implies CO_2 compressor load, is the ratio of the current stripping steam flow to the steam required to treat all rich solvent stream with the absorber and base plant at full-load. Thus, absorber load cannot exceed base plant load; 50% absorber and base plant load means the absorber treats all flue gas being produced. Additional CO_2 is vented only when the base plant load exceeds absorber load.

In this analysis, an inflexible CO_2 capture system must treat all flue gas exiting the boiler, so absorber, stripper, and base plant load must always be equal, though all systems may reduce load simultaneously. Inflexible scenarios imply regulatory, not process, rigidity. With venting-only flexible CO_2 capture, absorber and stripper load must be

equal but can be simultaneously reduced below the base plant load. If solvent storage is available, absorber load may exceed stripper load while excess rich solvent is sent to storage, and stripper load may exceed absorber load when stripping and compressing CO_2 from the stored rich solvent. Stripper load can then surpass 100% with enough stripping/compression capacity and available LP steam. This study assumes a CO_2 capture retrofit where 100% stripper load requires 40% of the LP steam from a turbine that has a 10% minimum load [5, 14]. Without equipment size limitations, stripper load could achieve 225%. However, stripping and compression systems are sized based on the time required to completely fill an empty rich solvent tank at 0% stripper load and 100% absorber load, assuming daily cycling of the storage system. For example, if the maximum number of hours in "full storage mode" is four, stripping and compression systems are sized for the average load in the remaining 20 hours, 120%.

2.1. Profit maximization model for perfect price foreknowledge and day-ahead forecasting

A mixed-integer linear programming (MILP) model is created in the GAMS platform to find the base plant, absorber, and stripper loads that maximize profit given one year of electricity prices. The model also includes binary variables that designate when base plant startups occur and whether the base plant is on or off in each interval. There are constraints on minimum load, maximum load, and load per time ramp limit for the base plant, absorber, and stripper. With solvent storage, a CO_2 flow balance governs the net quantity of CO_2 stored in rich solvent each interval, and the maximum quantity of stored CO_2 is limited by solvent capacity (difference between rich and lean loading), solvent physical properties, and storage facility size. Without CO_2 capture, the profit objective function includes startup costs and variable costs of fuel, CO_2 emissions, and other base plant variable operation and maintenance (VOM) costs. With CO_2 capture, there are additional costs for solvent makeup, caustic for solvent reclaiming, waste disposal of solvent degradation products, CO_2 transport and storage, and additional water use for the CO_2 capture system. This analysis assumes no operating cost penalty for flexibly operating CO_2 capture.

Perfect price foreknowledge is simulated by using CO_2 price-adjusted historical electricity prices directly. Day-ahead price forecasting is modeled by optimizing operation for pseudo-forecasted prices but calculating profits using historical prices. Pseudo-forecasted prices are generated by removing outliers from historical data and smoothing the result until prices achieve a forecast mean square error (FMSE) of 13.0 USD per megawatt-hour (MWh) and mean absolute percent error (MAPE) of 9.0%, values which are reasonably close to the 5–7 USD/MWh FMSE and 10–12% MAPE achieved with accurate day-ahead price forecasting models [15, 16]. With solvent storage, the model also requires the quantity of CO_2 stored in rich solvent to return to a specified value at the end of each day.

2.2. Rule-based model for no price foreknowledge

Some price prediction is necessary with solvent storage to plan when to store and regenerate rich solvent, but a venting-only flexible CO_2 capture system could simply operate in response to the most recent price signal. Venting-only flexible capture without price foreknowledge is analyzed using a rule-based MATLAB model that includes constraints on the CO_2 capture system ramp rate and the maximum load of the base plant and CO_2 capture system. This model does not include base plant ramp limits, base plant minimum load, or startup costs, so the GAMS model must be run with limited constraints to enable direct comparison. Assuming CO_2 prices are high enough for short-run marginal costs of electricity production (SRMC) to be lowest with full-load CO_2 capture, the model chooses to turn the base plant off if the electricity price falls below the SRMC at full-load CO_2 capture. If the electricity price is high enough for additional electricity sales at partial-load CO_2 capture to offset increased CO_2 emissions costs, capture load will decrease. Between these two price thresholds, the facility will move towards full-load base plant and CO_2 capture operation.

2.3. Default input parameters

Default input parameters are tabulated for the base power plant (Table 1), electricity market (Table 2), and CO_2 capture system (Table 3). Base plant heat rate in million British thermal units per MWh (MMBTU/MWh) and CO_2 emissions rate in metric tons (t) of CO_2 per MWh (tCO_2/MWh) are averages across all ERCOT coal-fired plants and are assumed constant across base plant and capture load [13]. Base plant minimum output, ramp limit, and startup cost are estimated from literature [17-19]. Ramp limits are assumed the same in either direction for each component, and absorber and stripper ramp limits are assumed equal. The study uses the average coal price for electricity

generators in 2008 and a default CO_2 price sufficiently high for lower SRMC at full-load CO_2 capture [20]. Coal and CO_2 prices are kept constant throughout the year. The CO_2 capture system uses a 30 wt % monoethanolamine (MEA) solvent with steam requirements, energy performance, CO_2 removal, and capacity are taken from literature [5, 9, 21]. CO_2 capture energy performance is assumed constant across absorber and stripper load [9]. The default solvent storage capacity has been suggested as a reasonable storage size, and the day-end stored CO_2 level is the average day-end CO_2 level under optimal plant operation with perfect price foreknowledge [4].

Table 1: Default base power plant input parameters

Parameter	*Units*	*Value*
Maximum output	MW	500
Minimum output	MW	150
CO_2 emissions rate	tCO_2/MWh	1.03
Heat rate	MMBTU/MWh	10.8
Ramp limit	%/minute	4
Startup cost	USD/startup	10,000

Table 2: Default electricity market input parameters

Parameter	*Units*	*Value*
Coal price	USD/MMBTU	1.54
CO_2 price	USD/tCO_2	50
CO_2 emissions rate of average ERCOT gas-fired plant	tCO_2/MWh	0.43

Table 3: Default CO_2 capture system input parameters

Parameter	*Units*	*Value*
Solvent, MEA	Wt %	30
Design CO_2 removal	Fractional	0.9
CO_2 capture energy	MWh/tCO_2	0.269
Fraction of LP steam extracted for full-load capture	Fractional	0.4
Solvent capacity (rich minus lean loading)	mol CO_2/ mol MEA	0.12
Ramp limit	%/minute	5
Volume of solvent storage tank (if applicable)	m^3	66,400
Day-end stored CO_2 level for day-ahead forecasting cases	tCO_2	1,314

3. Results & discussion

3.1. Operating modes with flexible CO_2 capture

Figure 2 illustrates different operating modes by plotting optimal CO_2 capture load and net power output fraction (net output divided by maximum output) across two sample days, January 6 and June 12, 2008. With venting-only flexible CO_2 capture (Panel A), the base plant ramps down when electricity prices fall below 52 USD/MWh, its SRMC at full-load CO_2 capture. On Jan. 6, low prices persist long enough to justify a full shutdown and incur startup costs at 7:00. Between 12:45 and 19:30 on June 12, capture load falls to zero when electricity prices exceed the 136 USD/MWh required for revenue from selling an extra 125 MW to offset costs of venting additional CO_2. At 52–136 USD/MWh, the base plant and CO_2 capture systems tend to operate at full-load with a 375 MW net output.

Figure 2B demonstrates operation with a solvent storage system. When prices are relatively low, absorber load is 100% while stripper load is 120% in order to strip and compress CO_2 from stored rich solvent. Absorber load exceeds stripper load when electricity prices are relatively high and increased power output is desirable. The base plant still ramps down below prices of 52 USD/MWh, but increased stripping capacity reduces net minimum power output and allows the plant to avoid startup costs and remain online before 7:00 on Jan. 6. During the first portion of the June 12 high price times 12:45–19:30, both absorber and stripper load fall to 0%, meaning CO_2 is being vented despite the existence of a solvent storage system. Though full storage mode is utilized during many of the highest price times, CO_2 venting might sometimes be economically justified in order to withhold storage capacity for later or return to a specified CO_2 level at a particular time.

3.2. Comparison of annual performance with default input parameters

Table 4 contains aggregate annual results for several scenarios. Columns *(1)–(3)* compare all three price foreknowledge cases for the venting-only flexible CO_2 capture configuration when base plant minimum load, ramp limits, and startup costs are ignored to maintain consistency with the MATLAB model. Though annual output is nearly the same, profits are over 4% greater with perfect or no knowledge than when using day-ahead forecasting. Reactive operation is nearly as profitable as having perfect price foreknowledge because CO_2 capture can ramp quickly in response to irregular high price spikes ignored during day-ahead forecasting.

Columns *(4)–(7)* compare CO_2 capture configurations under the most realistic conditions: day-ahead price forecasting and all base plant constraints. At 50 USD/tCO_2, annual operating profits are quite low without CO_2 capture; adding inflexible capture improves profits by nearly 16%. Relative to inflexible capture, venting-only flexible capture improves profits by 6%, and 66,400 m^3 solvent storage capacity improves profits by nearly 13%. CO_2 emissions are greater with flexible capture than with an inflexible system, but emissions still fall by over 72% from than the no-capture case, with solvent storage achieving a 79% reduction. Because the base plant is utilized nearly 30% more often with CO_2 capture, more CO_2 is captured in all capture scenarios than is emitted in the no-capture case. With perfect price foreknowledge, operating profits at the facilities in columns *(4)–(7)* improve by 1–4%, indicating that improved price forecasts would enhance profits, but only slightly.

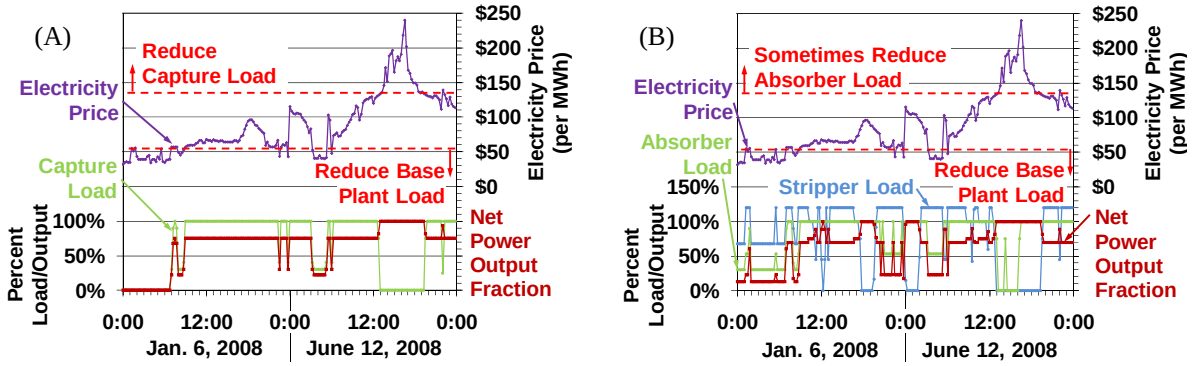

Figure 2: The operation of a facility with flexible CO_2 capture depends on electricity price levels and trends as well as whether a solvent storage system is available (B) or not (A). Default input parameters (Tables 1-3) are assumed.

Table 4: CO_2 capture flexibility improves a facility's operating economics while still drastically reducing CO_2 emissions, and economic benefits improve with the addition of a solvent storage system. Default input parameters (Tables 1-3) are assumed.

Scenarios		*(1)*	*(2)*	*(3)*	*(4)*	*(5)*	*(6)*	*(7)*
CO_2 capture flexibility		Venting only	Venting only	Venting only	No capture	Inflexible	Venting only	Solvent storage
Price foreknowledge		None	Day-ahead	Perfect	Day-ahead	Day-ahead	Day-ahead	Day-ahead
Base plant constraint set		Limited	Limited	Limited	All	All	All	All
Model results	*Units*							
Annual output to grid	million MWh	2.55	2.55	2.55	2.20	2.54	2.62	2.65
Annual CO_2 emitted	million tCO_2	0.646	0.610	0.659	2.27	0.350	0.619	0.482
Annual CO_2 captured	million tCO_2	2.742	2.792	2.727	0	3.147	2.875	3.108
Annual operating cost	million USD	$144.9	$144.4	$145.6	$164.0	$139.4	$148.9	$146.8
Annual operating profits	million USD	$131.1	$125.7	$131.6	$101.7	$117.8	$124.9	$133.0
CO_2 capture capacity factor when base plant is on	percent	89.9%	91.2%	89.5%	n/a	100%	91.4%	96.2%
Base plant capacity factor	percent	79.7%	75.1%	74.8%	50.1%	77.2%	77.2%	79.3%
Avg. CO_2 emissions rate	tCO_2/MWh	0.254	0.239	0.258	1.03	0.137	0.237	0.182

3.3. Sensitivity to CO_2 price

CO_2 price was varied from 0 to 100 USD/tCO_2 for the most realistic case that uses all base plant constraints and day-ahead price forecasting. Figure 3 shows annual CO_2 emissions at each CO_2 price for each CO_2 capture configuration to demonstrate CO_2 capture utilization and the resulting environmental impact. Corroborating previous work, prices below 20 USD/tCO_2 do not justify CO_2 capture operation, so CO_2 emissions with flexible capture equal those without CO_2 capture [9]. Solvent storage systems sit mostly idle at these low CO_2 prices. From 20 to 70 USD/tCO_2, venting CO_2 with flexible capture becomes less common until CO_2 capture is utilized nearly 100% of the time at 70 USD/tCO_2 and above. Any emissions above the inflexible case reflect CO_2 venting, so solvent storage reduces, but does not eliminate, CO_2 venting at intermediate CO_2 prices. Emissions trends with inflexible and no CO_2 capture correspond to changes in the base plant capacity factor.

Figure 4 shows annual operating profits with each capture configuration at each CO_2 price. Because electricity prices increase with CO_2 price by the emissions cost of an average ERCOT gas-fired facility, changes in operating profits with CO_2 price reflect the CO_2 emissions rate of the plant relative to 0.43 tCO_2/MWh. As CO_2 price increases, profits fall monotonically without CO_2 capture and rise monotonically with inflexible CO_2 capture. Profits with venting-only flexible capture are greater than those with inflexible and no-capture by as much as 10% during the 20 to 70 USD/tCO_2 transition period, but a facility with solvent storage maintains an economic advantage at any CO_2 price above the minimum required for CO_2 capture operation. The profit improvement with solvent storage over inflexible CO_2 capture decreases slightly with CO_2 price, but remains over 9% at 100 USD/tCO_2.

3.4. The importance of CO_2 capture ramping ability

Flexible CO_2 capture scenarios were studied for ramp rates of 0.25–8%/min., with 8%/min. being fast enough for the stripper to ramp from 0 to 120% load in one pricing interval (Figure 5). Any improvement over the profits earned with inflexible capture is nearly constant above 1%/min., and more than half the benefit is realized with 0.25%/min. Recalling the base plant ramp limit of 4%/min., these data suggest that flexible CO_2 capture can improve profits even with a very low ramp limit below that of the base plant. However, the importance of capture ramp limit might change with electricity market conditions, and ramp limits will likely be important for providing grid reliability services.

3.5. Cost/benefit analysis of solvent storage

A retrofitted venting-only flexible CO_2 capture system entails negligible incremental capital cost, but the operating profit advantage with solvent storage must be weighed against the capital cost of the solvent storage system. This tradeoff is investigated by using the annual profit improvement over inflexible capture in a cash flow analysis to determine the net present value (NPV) over a 20-year book life for solvent storage systems sized for 0.5–6 hours in full storage mode. Day-ahead price forecasting is assumed. Capital costs are depreciated on a 20-year modified accelerated cost recovery system (MACRS) half-year convention schedule, profits are taxed at 38%, and future cash flows are discounted by a 10.3% inflation-adjusted discount rate [22].

The capital cost for solvent storage is divided into the cost of additional solvent inventory, storage tanks, and larger stripping and compression equipment. Solvent inventory cost is calculated using the parameters in Table 3 and MEA at 2.52 USD/kg [5]. Storage tank capital costs are determined from a cost curve for large field-erected tanks after scaling by the appropriate Chemical Plant Indices [23, 24]. A baseline cost of stripping and compression systems for an inflexible CO_2 capture facility is scaled by the maximum stripper load raised to a conservative 85% economy of scale factor [25].

For each storage system size, Figure 6 plots additional operating profits and capital costs along with the resulting NPV. Capital cost is dominated by MEA inventory and larger stripping/compression equipment, which make up 56–59% and 31–37% of the total, depending on system size. Additional profits increase with storage system size, but rapidly increasing capital costs allow a storage system sized for just 22.5 minutes in full storage mode to achieve the greatest NPV. However, solvent inventory cost depends strongly on the design solvent capacity and MEA price, and stripping and compression equipment might already be oversized in the original plant design, so larger storage systems could be optimal at facilities with lower capital costs or different design and market specifications.

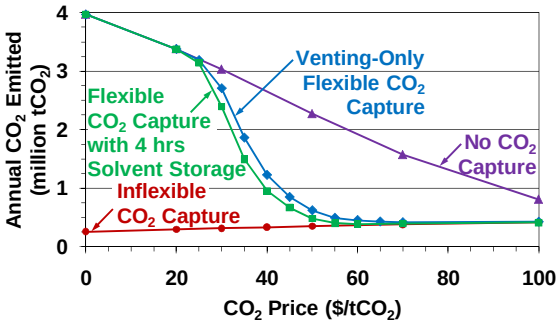

Figure 3: Solvent storage allows greater utilization of CO_2 capture systems at intermediate CO_2 prices.

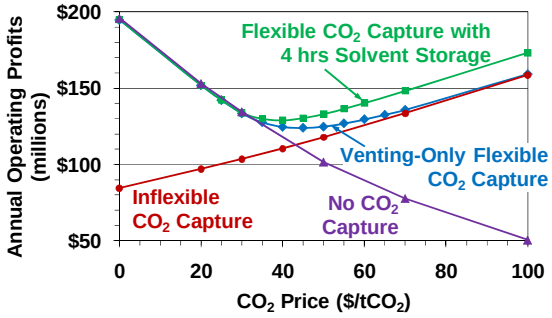

Figure 4: Annual operating profits depend on the plant's emissions costs relative to those of price-setting gas-fired plants, but profits are always best with solvent storage.

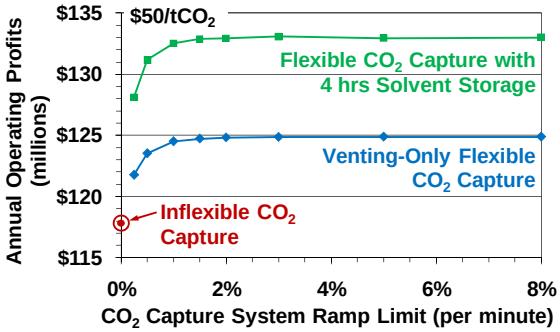

Figure 5: CO_2 capture system ramp limits must be extremely low to negate the economic benefit of flexibility.

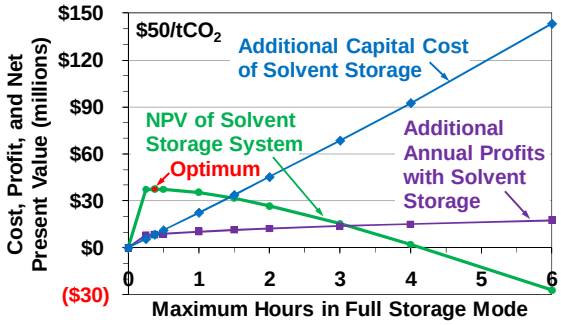

Figure 6: Though annual profits increase with solvent storage capacity, small storage systems have the greatest investment value.

4. Conclusions

Optimization and rule-based models are created and used to study profit-maximizing operation of a facility with flexible CO_2 capture with and without solvent storage under varying degrees of electricity price foreknowledge. At intermediate CO_2 prices, a coal-fired facility with flexible CO_2 capture can improve operating profits by up to 10% relative to an inflexible system by venting CO_2 when additional electricity sales offsets increased emissions costs. Within this CO_2 price regime, flexible capture systems with solvent storage may choose to vent CO_2 and reserve storage capacity for other times. The value of venting CO_2 disappears at high CO_2 prices, but a flexible CO_2 capture system with solvent storage maintains a 9–29% operating profit advantage over inflexible capture at any CO_2 price above the minimum required for CO_2 capture operation. Under the conditions studied, the operating profit improvement from flexible CO_2 capture exists for any reasonable CO_2 capture system ramp limit, and electricity price foreknowledge is only important with solvent storage to allow operators to plan when to store and regenerate rich solvent. CO_2 emissions are greater with flexible CO_2 capture than with inflexible capture, but CO_2 emissions remain far below those without CO_2 capture at CO_2 prices that justify capture operation. At CO_2 prices where venting occurs, CO_2 emissions are lower with solvent storage than with venting-only CO_2 capture because the increased operating flexibility with solvent storage allows greater overall CO_2 capture utilization.

In a retrofit application, venting-only flexible CO_2 capture incurs negligible capital cost, but any operating profit benefits of solvent storage must be weighed against the capital cost of the storage system, which is dominated by the cost of solvent inventory and larger stripping and compression equipment. In this case study, the most valuable solvent storage system is only large enough to take advantage of a few high price periods per day, but optimal storage size is expected to be sensitive to solvent and equipment capital cost parameters and accounting procedures.

5. References

[1] H. Chalmers, IEA GHG Workshop on Operating Flexibility of Power Plants with CCS, in: IEA GHG, 2010.
[2] E. S. Rubin, C. Chen, and A. B. Rao, Cost and performance of fossil fuel power plants with CO_2 capture and storage, in: Energy Policy 35 (2007) 4444-4454.
[3] H. Chalmers, M. Lucquiaud, J. Gibbins, M. Leach, Flexible operation of coal fired power plants with postcombustion capture of carbon dioxide, in: Journal of Environmental Engineering (2009).
[4] M.R.Haines, J. E. Davison, Designing Carbon Capture power plants to assist in meeting peak power demand, in: 9th International Conference on Greenhouse Gas Control Technologies, Elsevier, Washington DC, 2009, pp. 1457-1464
[5] USNETL, Cost and Performance Baseline for Fossil Energy Plants, in: J. M. Klara (Ed.) Bituminous Coal and Natural Gas to Electricity, vol 1, 2007.
[6] J. R. Gibbins, R. I. Crane, Scope for reductions in the cost of CO_2 capture suing flue gas scrubbing with amine solvents, in: Proceedings of the Institution of Mechanical Engineers - Part A - Power & Energy 218 (2004) 231-239.
[7] G. T. Rochelle, E. Chen, S. Freeman, D. V. Wagener, Q. Xu, A. Voice, Aqueous Piperazine as the New Standard for CO_2 Capture Technology, in: Austin, TX, 2010.
[8] S. M. Cohen, G. T. Rochelle, M. E. Webber, Turning CO_2 Capture On & Off in Response to Electric Grid Demand: A Baseline Analysis of Emissions and Economics, in: ASME Journal of Energy Resources Technology 132 (2010).
[9] Sepideh Ziaii, Stuart Cohen, Gary T. Rochelle, Thomas F. Edgar, M. E. Webber, Dynamic operation of amine scrubbing in response to electricity demand and pricing, in: 9th International Conference on Greenhouse Gas Technologies, Elsevier, Washington, DC, 2008.
[10] S. Cohen, J. Fyffe, G. T. Rochelle, M. E. Webber, The Effect of Fossil Fuel Prices on Flexible CO_2 Capture Operation, in: ASME 3rd International Conference on Energy Sustainability, San Francisco, CA, 2009.
[11] ERCOT, Balancing Energy Services Market Clearing Prices for Energy Annual Report, in: MCPER_MCPEL_2006.xls (Ed.) 2006.
[12] PE-Ltd., 2008 State of the Market Report for the ERCOT Wholesale Electricity Markets, in: Potomac Economics, Ltd., 2009.
[13] USEPA, Emissions & Generation Resource Integrated Database (eGRID), in: eGRID2007_Version_1_1, 2008.
[14] Mathieu Lucquiaud, Hannah Chalmers, J. Gibbins, Capture-ready supercritical coal-fired power plants and flexible post-combustion CO_2 capture, in: 9th International Conference on Greenhouse Gas Control Technologies, Elsevier, Washington, DC, 2008.
[15] G. Li, C.-C. Liu, J. Lawarree, M. Gallanti, A. Venturini, State-of-the-art of electricity price forecasting, in: CIGRE/IEEE PES, 2005. International Symposium, 2005, pp. 110-119.
[16] G. Li, C. C. Liu, C. Mattson, J. Lawarree, Day-Ahead Electricity Price Forecasting in a Grid Environoment, in: Power Systems, IEEE Transactions on 22 (2007) 266-274.
[17] H. Chalmers, J. Gibbins, Initial evaluation of the impact of post-combustion capture of carbon dioxide on supercritical pulverised coal power plant part load performance, in: Fuel 86 (2007) 2109-2123.
[18] J. H. Mortensen, T. Moelbak, P. Andersen, T. S. Pedersen, Optimization of boiler control to improve the load-following capability of power-plant units, in: Control Engineering Practice 6 (1998) 1531-1539.
[19] C. K. Pang, H. C. Chen, Optimal short-term thermal unit commitment, in: Power Apparatus and Systems, IEEE Transactions on 95 (1976) 1336-1346.
[20] USEIA, Average Cost of Coal Delivered for Electricity Generation by State, Year-to-Date through March 2009 and 2008 (Dollars per Million Btu), in: epmxlfile4_10_b.xls (Ed.) USDOE, 2009.
[21] B. Oyenekan, Modeling of Strippers for CO_2 capture by Aqueous Amines, in: Chemical Engineering, vol Ph.D., The University of Texas at Austin, Austin, 2006, p. 291.
[22] NETL, Carbon Capture and Sequestration Systems Analysis Guidelines, in: USDOE (Ed.) 2005.
[23] M. S. Peters, K. D. Timmerhaus, R. E. West, Plant Design and Economics for Chemical Engineers, McGraw-Hill Professional, Boston, Massachusetts, 2002.
[24] CES, Chemical Engineering Plant Cost Index (CEPCI), in: Chemical Engineering Science 116 (2009) 1/3.
[25] K. S. Fisher, et. al., Advanced Amine Solvent Formulations and Process Integration for Near-Term CO_2 Capture Success, in: Trimeric Corp, 2007.

Available online at www.sciencedirect.com

ScienceDirect

Energy Procedia 00 (2010) 000–000

Energy Procedia

www.elsevier.com/locate/XXX

GHGT-10

Modeling piperazine thermodynamics

Peter Frailie[a], Jorge Plaza[a], David Van Wagener[a], Gary T. Rochelle[a]1*

[a]*The University of Texas at Austin, 1 University Station C0400, Austin, TX 78757, USA*

Elsevier use only: Received date here; revised date here; accepted date here

Abstract

A thermodynamic model in Aspen Plus® was developed to predict properties of piperazine (PZ)/H_2O and PZ/H_2O/CO_2. A sequential regression was performed to represent recently acquired loaded and unloaded heat capacity, CO_2 solubility, CO_2 activity coefficient, speciation, and unloaded and loaded amine volatility data. The resulting model is able to predict each of these properties over operationally significant loading and temperature ranges (0.20—0.40 mol CO_2/mol alkalinity and 40 ^oC—160 ^oC). The predicted heat of absorption for 8 m PZ solution at 0.35 mol CO_2/mol alkalinity between 40 ^oC and 160 ^oC was 65±4 kJ/mol CO_2. The temperature dependence of the heat of absorption was predicted using three analytical methods, each of which predicted different trends but similar ranges between 40 ^oC and 160 ^oC. The sequential regression methodology has also been applied to methyl-diethanolamine (MDEA) and MDEA/PZ. Ultimately this thermodynamic model will be modified in Aspen Plus® to predict kinetic and transport data as well, and the resulting model will be used to design and optimize a post-combustion absorption/stripping process.

Keywords: carbon dioxide; piperazine; modeling

1. Introduction

This work focuses on the development of a piperazine (PZ) thermodynamic model in Aspen Plus® for the evaluation and optimization of a post-combustion absorber/stripper. Previous studies have modeled PZ thermodynamics, but each attempt has been limited by either a lack of available experimental data or the modeling methods employed. Several of these modeling methods introduce thermodynamic inconsistencies, which can lead to conflicting or inaccurate predictions. FORTRAN models developed by Bishnoi [1] and Cullinane [2] calculated equilibrium constants using a polynomial expression rather than thermodynamically significant quantities such as Gibbs free energies of formation (ΔG^o_f), enthalpies of formation (ΔH^o_f), and heat capacities (C_P^o). This introduces a thermodynamic inconsistency when calculating quantities such as heat capacities and heats of absorption, which share a fundamental interdependence with

* Gary T. Rochelle. Tel.: +1-512-471-7230; fax: +1-512-471-7060.
E-mail address: gtr@che.utexas.edu.

speciation. Activity-based PZ/H_2O and PZ/H_2O/CO_2 models developed by Hilliard [3] and Dugas [4] in Aspen Plus® do not have this inconsistency, but these models only consider PZ concentrations at or below 5m. This model accurately predicts recently acquired experimental data for CO_2 solubility, PZ volatility, heat capacity, activity coefficient of CO_2, and speciation over operationally significant temperature, loading, and amine concentration ranges using thermodynamically consistent methods. This model will be identified as 5deMayo version 1.

2. Methods and Theory

2.1 PZ/H_2O Regression

Unloaded amine volatility and heat capacity data was fit by adjusting PZ heat capacity, infinite dilution activity coefficient of PZ in H_2O, and Henry's constant of PZ in H_2O. Modeling PZ as a Henry's component provides a better set of handles for fitting PZ volatility. Even though a plant will never operate with unloaded PZ it is important to fix the model predictions at these conditions to avoid extreme or inexplicable behavior, which could indirectly affect the ability to fit data within the operational loading range. All parameters concerning the PZ/H_2O were held constant during all subsequent regressions.

2.2 PZ/H_2O/CO_2 Regression

There are two equations that may be used to calculate equilibrium constants in Aspen Plus®: (1) a temperature-dependent polynomial and (2) an expression based on $\Delta G^o_{f,rxn}$, $\Delta H^o_{f,rxn}$, and $\Delta C_P{}^o_{rxn}$. These expressions are shown below as Equations 1 and 2, respectively.

$$\ln K_{eq} = A + \frac{B}{T} + C\ln T + DT \tag{1}$$

$$-\ln K_{eq} = \frac{\Delta G^o}{RT} = \frac{\Delta G^o_0 - \Delta H^o_0}{RT_0} + \frac{\Delta H^o_0}{RT} + \frac{1}{T}\int_{T_0}^{T}\frac{\Delta C^o_P}{R}dT - \int_{T_0}^{T}\frac{\Delta C^o_P}{R}dT \tag{2}$$

The major advantage of using Equation 2 is that it maintains thermodynamic consistency between speciation and properties calculated directly from speciation. Equation 2 will always be used in this study. Before regressing CO_2 solubility and loaded heat capacity data, the pKa of PZ from 20 °C to 80 °C was fit by adjusting the ΔG^o_f, ΔH^o_f, and $C_P{}^o$ of PZH^+. The pKa values in the literature [5] had to be converted from a symmetric to an asymmetric activity coefficient reference state. The method for accomplishing this conversion can be found in Hilliard [3].

With these values held constant, CO_2 solubility and heat capacity data for 2 m to 12 m PZ between 40 °C and 160 °C were regressed by adjusting ΔG^o_f, ΔH^o_f, and $C_P{}^o$, for $PZCOO^-$, $PZ(COO)_2{}^{2-}$, and H^+PZCOO^-, as well as activity coefficients for all true species. Because Aspen Plus® cannot model zwitterions, H^+PZCOO^- was treated as a Henry's component with a Henry's constant on the order of 10^{-9}. Previous studies [3] have treated H^+PZCOO^- as a cation with a charge of 10^{-5}, but this led to two major problems: (1) a significant charge imbalance as the concentration of H^+PZCOO^- increased rapidly at high loadings and (2) a constant activity coefficient of 1. Treating H^+PZCOO^- as a Henry's component corrects these errors by giving it a zero charge.

2.3 CO_2 Activity Coefficient Regression

Aspen Plus® cannot directly regress activity coefficients. A user-supplied subroutine had to be used to adjust parameters and incorporate them into the model. The experimental data used was for an 8 m PZ solution between 25 °C and 60 °C at loadings of 0.25 and 0.40 mol CO_2/mol alkalinity. Because the concentration of free CO_2 in the liquid phase is so low, adjusting the activity coefficient of CO_2 did not affect the model predictions for other PZ/H_2O/CO_2 data sets.

CO_2 activity coefficients were inferred from N_2O solubility measurements using Equation 3.

$$\frac{H_{(N_2O/soln)}}{H_{(N_2O/H_2O)}} \approx \gamma_{CO_2/soln} \tag{3}$$

2.4 Calculating Heat of Absorption

There are three methods for calculating the heat of absorption of CO_2: (1) applying the Gibbs-Helmholtz equation to CO_2 solubility curves, (2) calculating heat duty when CO_2 is absorbed in an Aspen Plus® flash block, and (3) integrating the change in the partial heat capacity of CO_2 from a reference temperature with a known heat of absorption to another temperature of interest. Equation 4 is the Gibbs-Helmholtz equation.

$$\frac{d \ln f_{CO_2}}{d \, 1/T} = \frac{-\Delta H_{ABS}}{R} \tag{4}$$

Methods 1 and 2 should predict similar values for the heat of absorption if thermodynamically consistent methodology is used in Aspen Plus®. Method 3 is based on Equation 5, which is derived from the mass and energy balance depicted in Figure 1. Because it must always be referenced to another value for the heat of absorption, Method 3 can only be used to determine temperature dependence. For this study, the heat of absorption at 80 °C predicted by the Gibbs Helmholtz Method 1 will be used as the reference point for Method 3.

$$\Delta H_{ABS}(T) = \Delta H_{ABS}(T_{ref}) + \int_{T_{ref}}^{T} \left(\overline{C_P^{\,L}}_{CO_2} - \overline{C_P^{\,IG}}_{CO_2} \right) dT \tag{5}$$

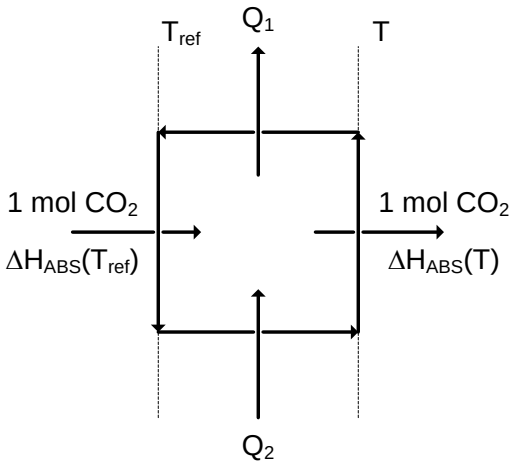

Figure 1: Mass and energy flow diagram used to derive Equation 5.

3. Results and Discussion

Figure 2 compares CO_2 solubility from Aspen Plus® predictions (lines) and experimental data (points) for 3.6, 5, 8, and 12 m PZ between 40 °C and 160 °C. Experimental data between 40 °C and 100 °C were collected by Dugas [4], and data between 120 °C and 160 °C were collected by Xu [6]. Figure 1 suggests that the solubility of CO_2 in PZ is a strong function of temperature and loading, and it is a weak function of amine concentration. This result is expected with solvents such as PZ, which produce large amounts of carbamate throughout operationally significant loading ranges [4].

Figure 3 compares Aspen Plus® predictions and experimental points [7] for 8 m PZ heat capacity between 40 °C and 150 °C at loadings of 0.21, 0.29, and 0.40 mol CO_2/mol alkalinity. Solution heat capacity tends to increase with temperature and decrease with loading. The increase with temperature may be attributed to La Chatelier's principle, which states that a system in equilibrium will shift to counteract any imposed change in temperature, partial pressure, volume, or concentration until equilibrium is re-established. By increasing its heat capacity, the solution is more resistant to temperature changes.

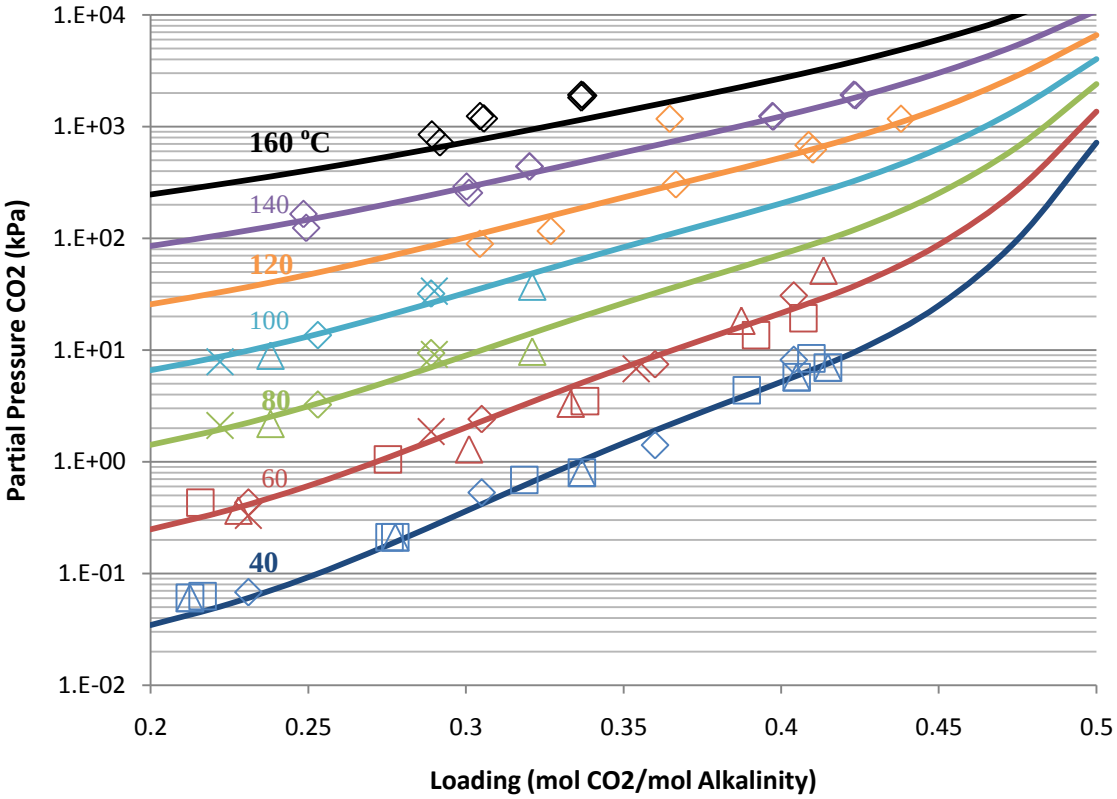

Figure 2: Partial Pressure of CO_2 as a function of loading for 3.6 m (□), 5 m (Δ), 8 m (◊), and 12 m (x) PZ between 40 °C and 160 °C, curves calculated from AspenPlus® model. Data from [4,6].

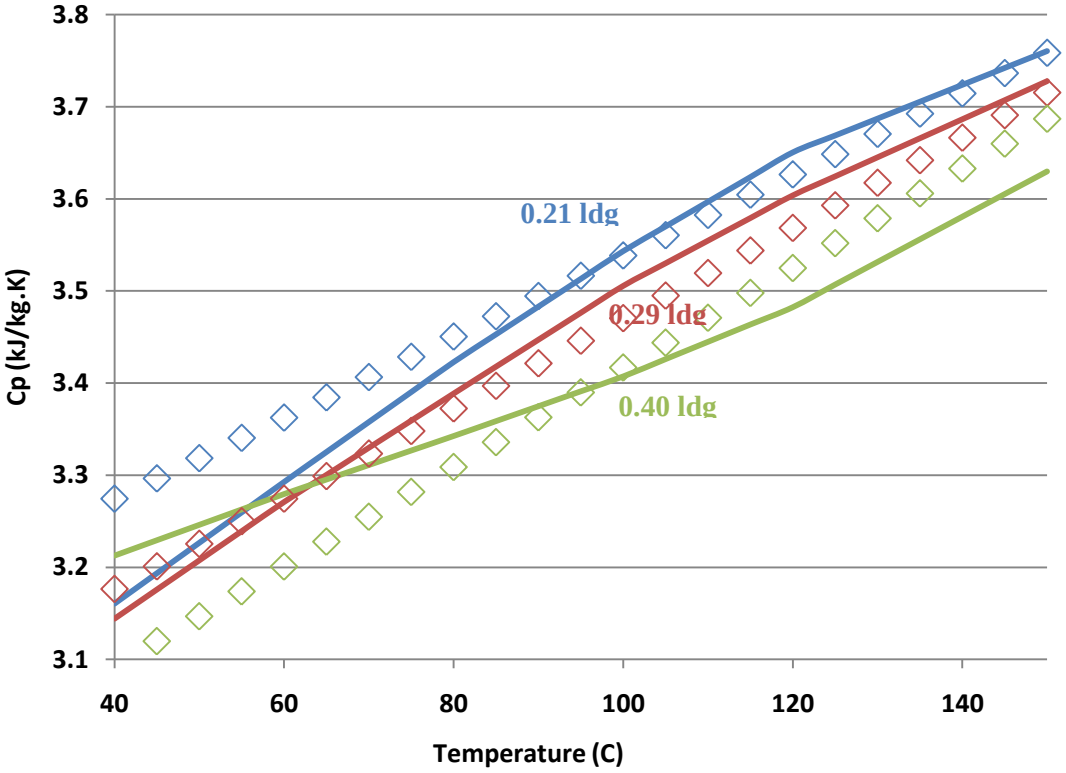

Figure 3: Experimental (points) and Aspen Plus® predictions (lines) for C_P of 8 m PZ between 40 °C and 150 °C at loadings of 0.21, 0.29, and 0.40 mol CO_2/equiv PZ. Data from [7].

The parameters used to regress the PZ/H_2O and $PZ/H_2O/CO_2$ data can be found in Table 1.

Table 1: Parameters used for the PZ/H_2O and $PZ/H_2O/CO_2$ regressions

Parameter	Species	Std. Dev.	Units
	PZ/H_2O		
$C_p^o/1$	PZ	1.2E+5	J/kmol.K
$C_p^o/2$	PZ	350	J/kmol.K
$\tau_{mm}/1$	H_2O/PZ	1.8	N/A
$\tau_{mm}/1$	PZ/H_2O	0.10	N/A
$\tau_{mm}/3$	H_2O/PZ	0.018	N/A
Henry/1	PZ/H_2O	0.96	N/A
Henry/2	PZ/H_2O	310	K
	$PZ/H_2O/CO_2$		
ΔG^o_f	H^+PZCOO^-	1.2E+5	J/kmol
ΔH^o_f	H^+PZCOO^-	3.7E+10	J/kmol
$C_p^o/1$	H^+PZCOO^-	8,610	J/kmol.K
$C_p^o/2$	H^+PZCOO^-	0.0028	J/kmol.K
ΔG^o_f	$PZCOO^-$	2.6E+05	J/kmol
ΔH^o_f	$PZCOO^-$	3.7E+10	J/kmol
$C_p^o/1$	$PZCOO^-$	8,278	J/kmol.K
$C_p^o/2$	$PZCOO^-$	0.0052	J/kmol.K
ΔG^o_f	$PZ(COO)_2^{2-}$	3.7E+10	J/kmol
ΔH^o_f	$PZ(COO)_2^{2-}$	3.73E+10	J/kmol
$C_p^o/1$	$PZ(COO)_2^{2-}$	5,002	J/kmol.K
$C_p^o/2$	$PZ(COO)_2^{2-}$	0.0054	J/kmol.K
$C_p^o/1$	PZH^+	11,700	J/kmol.K
$C_p^o/2$	PZH^+	37.1	J/kmol.K
$\tau_{ca/m}/1$	$H^+PZCOO^-/(PZH^+,PZCOO^-)$	0.46	N/A
$\tau_{ca/m}/1$	$(PZH^+,PZCOO^-)/H^+PZCOO^-$	0.040	N/A
$\tau_{ca/m}/1$	$H^+PZCOO^-/[PZH^+,PZ(COO)_2^{2-}]$	0.57	N/A
$\tau_{ca/m}/1$	$[PZH^+, PZ(COO)_2^{2-}]/H^+PZCOO^-$	0.20	N/A
$\tau_{ca/m}/1$	$H^+PZCOO^-/(PZH^+,HCO_3^-)$	0.44	N/A
$\tau_{ca/m}/1$	$(PZH^+, HCO_3^-)/H^+PZCOO^-$	0.29	N/A
$\tau_{mm}/1$	H_2O/H^+PZCOO^-	0.018	N/A
$\tau_{mm}/1$	H^+PZCOO^-/H_2O	0.0029	N/A
$\tau_{mm}/2$	H_2O/H^+PZCOO^-	5.9	K
$\tau_{mm}/2$	H^+PZCOO^-/H_2O	4.0	K
$\tau_{mm}/3$	H_2O/H^+PZCOO^-	0.0083	N/A
$\tau_{mm}/5$	H_2O/H^+PZCOO^-	0.021	N/A
$\tau_{mm}/5$	H^+PZCOO^-/H_2O	0.015	N/A

All activity coefficient tau parameters not mentioned in Table 1 were set to Aspen Plus® default values for the $PZ/H_2O/CO_2$ regression. Because Aspen Plus® is not configured to regress speciation data and the model was not generating any HCO_3^-, two of the $\tau_{ca/m}$ parameters in Table 1 [$H^+PZCOO^-/(PZH^+,HCO_3^-)$ and $(PZH^+,HCO_3^-)/H^+PZCOO^-$] were adjusted manually to generate HCO_3^- at higher loadings.

The final speciation result is shown in Figure 4. Because proton NMR is unable to distinguish between a species and its protonated counterpart (i.e. PZ vs. PZH^+, $PZCOO^-$ vs. H^+PZCOO^-), only the concentrations of $PZ(COO)_2^{2-}$ and HCO_3^- were known with any precision. Those concentrations are represented by the two points at a loading of 0.4 [8]. These measurements were made with C^{13} and proton NMR of 8 m PZ loaded with $C^{13}O_2$ at 40°C.

Figure 5 compares the Gibbs-Helmholtz and calorimetric predictions for the heat of absorption of loaded 8 m PZ. Unlike previous studies, which use Equation 1 to represent equilibrium constants, the two methods for calculating heat of absorption seem to be consistent. At the operational ranges for temperature (40 °C—160 °C) and loading (0.3—0.4) the average heat of absorption is about 65 kJ/mol CO_2.

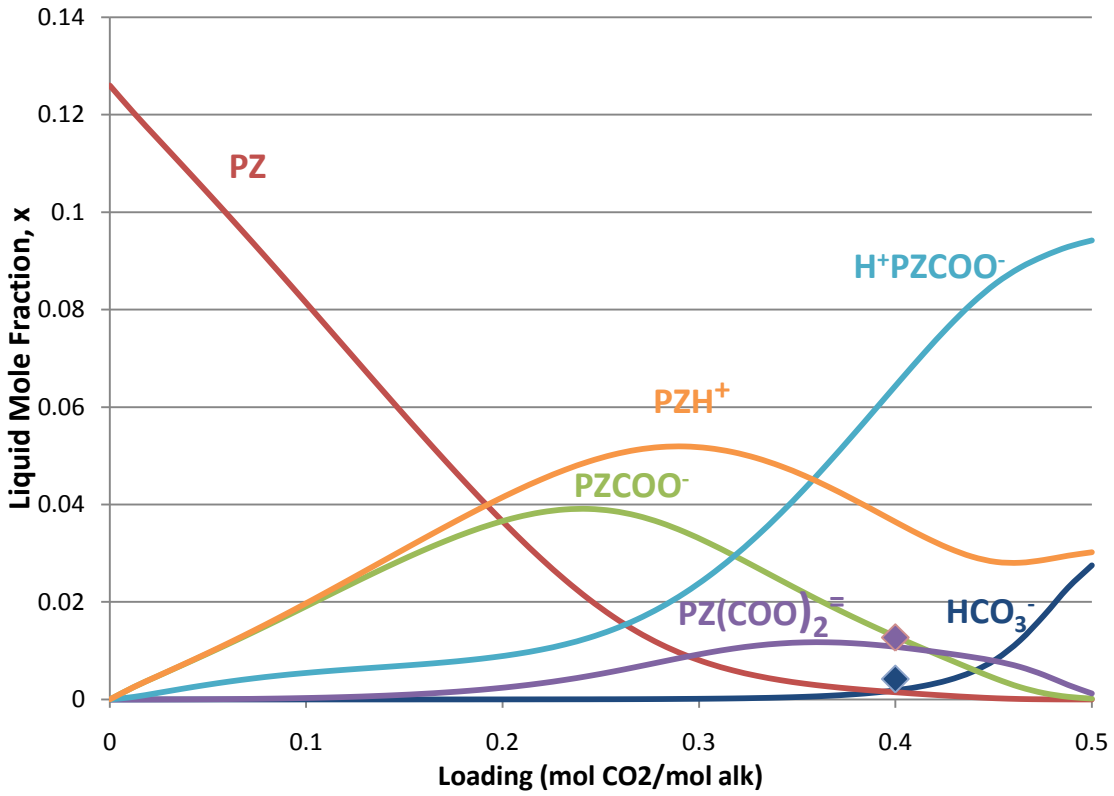

Figure 4: Aspen Plus® predictions (lines) and NMR data (points) for speciation of 8m PZ at 40 °C.

Figure 6 examines the temperature dependence of the heat of absorption of an 8 m PZ solution at a loading of 0.35 mol CO_2/mol alkalinity predicted by the Gibbs-Helmholtz equation, calorimetry, and mixture heat capacity. While all three methods predict different temperature dependence, the spread of the values is quite narrow. All three methods between 40 °C and 160 °C predict heats of absorption between 61 and 69 kJ/mol CO_2.

Figure 7 compares the Aspen Plus® predictions and experimental points [9] for the activity coefficient of CO_2 in loaded 8 m PZ. Just as with MDEA [10], the activity coefficient of CO_2 increases with loading and decreases with temperature. Both of these trends may be attributed to the effects of temperature and loading on the ideality of the liquid phase. Aspentech supplied a FORTRAN subroutine for the regression of CO_2 activity coefficients.

Figure 8 compares the Aspen Plus® predictions and experimental data for loaded [7] and unloaded [11] 8 m PZ volatility between 40 °C and 60 °C. As the loading approaches 0.5 the volatility drops off rapidly for all temperatures. This trend is easily understood after examining Figure 4. According to stoichiometry, in the absence of HCO_3^- and CO_3^{2-} production all of the PZ will be consumed at a loading of 0.5. Both Aspen Plus® predictions and NMR data suggest that HCO_3^- and CO_3^{2-} are only present at small concentrations. Therefore, the drop in PZ partial pressure can be directly attributed to the depletion of free PZ.

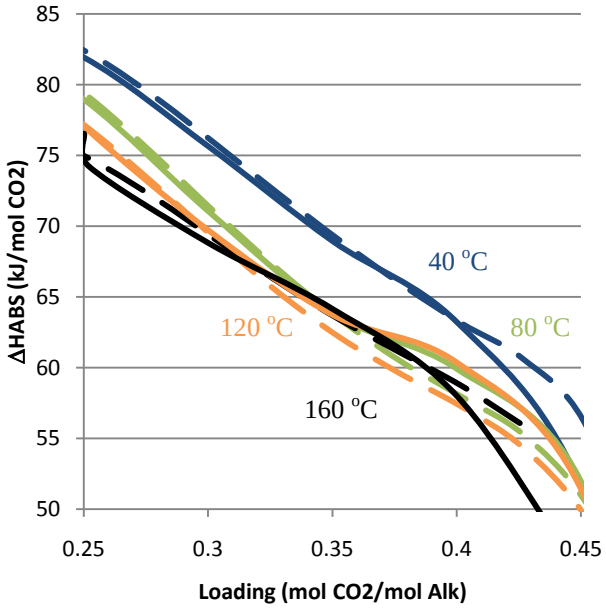

Figure 5: Comparison of Gibbs-Helmholtz (dashed lines) and calorimetric (solid lines) predictions for heat of CO_2 absorption of 8 m PZ at 40 °C to 160 °C.

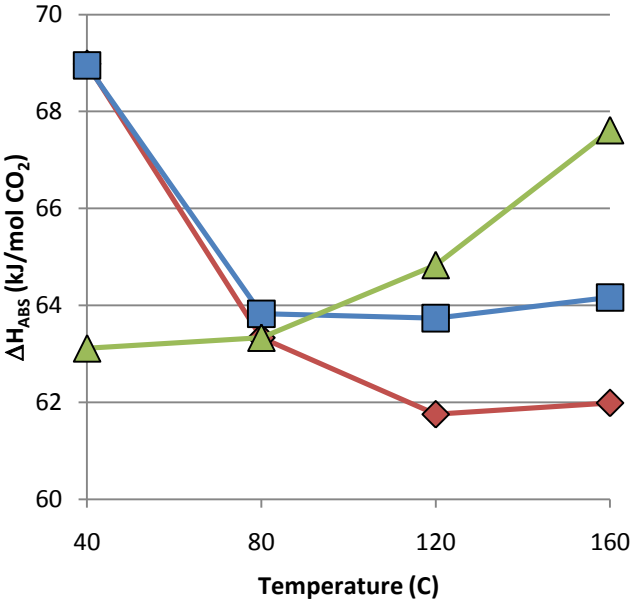

Figure 6: Comparison of Gibbs-Helmholtz (◊), calorimetric (□), and C_P (Δ) predictions for the heat of CO_2 absorption of 8 m PZ at 0.35 mol CO_2/mol alkalinity between 40 °C and 160 °C.

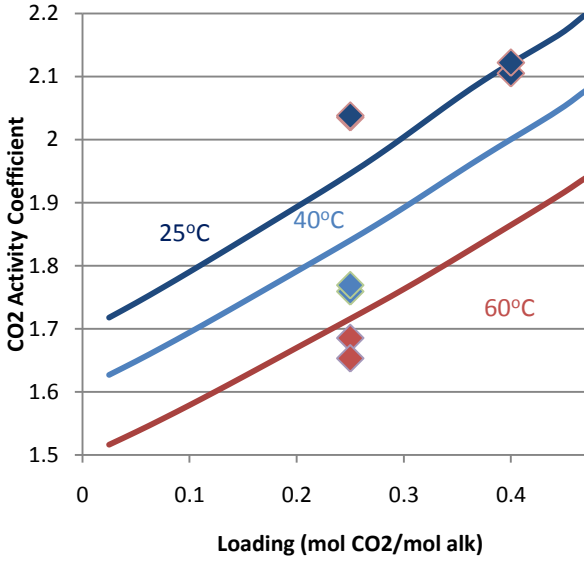

Figure 7: Aspen Plus® predictions (lines) and experimental data (points) for the activity coefficient of CO_2 in a loaded 8 m PZ solution between 25 °C and 60 °C. Data Provided by Svendsen [9].

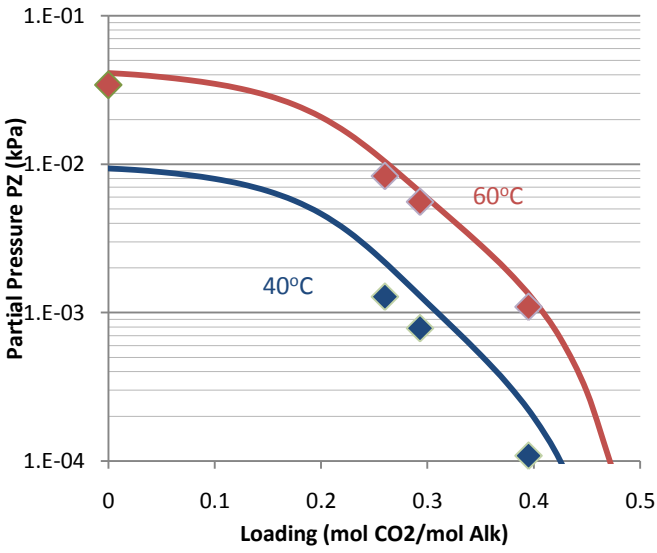

Figure 8: Experimental [7,11] (points) and Aspen Plus® predictions (lines) for volatility of 8 m PZ between 40 °C and 60 °C.

4. Conclusions

Heat capacity, CO_2 solubility, loaded and unloaded amine volatility, speciation, and CO_2 activity coefficient data were incorporated into Aspen Plus® for solutions of 2—12 m PZ. The model adequately predicts each of these quantities over operationally significant loading and temperature ranges (0.20—0.40 and 40 °C—160 °C). Modeling H^+PZCOO^- as a Henry's component eliminated both charge balance and activity coefficient issues experienced with previous models. Just as with other carbamate forming amines, the solubility of CO_2 in PZ solutions is a strong function of

temperature and loading, and it is a weak function of amine concentration. The discrepancy between the Gibbs-Helmholtz and calorimetric heat of absorption predictions has been minimized by using thermodynamically consistent methodology. Predicted values for the heat of absorption between 40 ^{o}C and 160 ^{o}C suggest that the heat of absorption is approximately 65±4 kJ/mol CO_2 at a loading of 0.35 over that temperature range. The same sequential regression methodology used to construct this model can be and has been applied to other amines.

5. Acknowledgements

This work was supported by the Luminant Carbon Management Program. Aspen Technology provided the Aspen Plus® software and a FORTRAN subroutine to regress CO2 Activity coefficients. Hallvard Svensen at NTNU provided the data on N_2O solubility. Thu Nguyen provided the speciation measurements with NMR. The Aspen Plus® model, experimental methods, and data of Marcus Hilliard provided the starting point for this model development.

6. References

[1] Bishnoi, S. *Carbon Dioxide Absorption and Solution Equilibrium in Piperazine Activated Methyldiethanolamine*. The University of Texas at Austin. Ph.D. Dissertation. 2000.

[2] Cullinane, JT. *Thermodynamics and Kinetics of Aqueous Piperazine with Potassium Carbonate for Carbon Dioxide Absorption*. The University of Texas at Austin. Ph.D. Dissertation. 2005.

[3] Hilliard, MD. *A Predictive Thermodynamic Model for an Aqueous Blend of Potassium Carbonate, Piperazine, and Monoethanolamine for Carbon Dioxide Capture from Flue Gas.* The University of Texas at Austin. Ph.D. Dissertation. 2008.

[4] Dugas, RE. *Carbon Dioxide Absorption, Desorption, and Diffusion in Aqueous Piperazine and Monoethanolamine.* The University of Texas at Austin. Ph. D. Dissertation. 2009.

[5] Hetzer HB, Robinson RA Bates RG. Dissociation Constants of Piperazinium Ion and Related Thermodynamic Quantities from 0 to 50^{o}. *J. Phys. Chem.* 1968 ;72(6): 2081—2086.

[6] Xu, Q., Rochelle, GT, Total pressure and CO_2 solubility and high temperature in aqueous amines, GHGT-10, 2010.

[7] Freeman SA, Dugas RE, Van Wagener DH, Nguyen T, Rochelle GT. CO_2 Capture with Concentrated, Aqueous Piperazine. IJGCC 2010, 4, 119-124.

[8] Nguyen, T. NMR measurements for 8 m PZ, personal communication, 2010.

[9] Svendsen, H. N_2O solubility in Piperazine/CO_2/H_2O, personal communication, 2009.

[10] Rinker EB, Ashour SS, Sandall OC. Physical Property Data Important in Modeling H_2S and CO_2 Absorption into Aqueous DEA, MDEA and Blends of DEA and MDEA. *Gas Processors Association*. RR-158. December 1997.

[11] Nguyen, T., Hilliard, M., Rochelle, GT. Amine Volatility in CO_2 Capture. doi:10.1016/j.ijggc.2010.06.003, IJGGC 2010.

Available online at www.sciencedirect.com

ScienceDirect

Energy Procedia 00 (2010) 000–000

Energy Procedia

www.elsevier.com/locate/XXX

GHGT-10

Thermal degradation of piperazine and its structural analogs

Stephanie A. Freeman and Gary T. Rochelle

The Unversity of Texas at Austin, 1 University Station C0400, Austin, TX, 78712 USA

Elsevier use only: Received date here; revised date here; accepted date here

Abstract

The resistance of concentrated, aqueous piperazine (PZ) to thermal degradation is a critical characteristic that recommends PZ as a solvent for amine based absorption/stripping for CO_2 capture from coal fired flue gas. Seven structural analogs of PZ were thermally degraded in an effort to discover the structural reasons for the enhanced resistance of PZ. Four comparisons are developed that look at the effect of changing heteroatoms (PZ, piperidine (PD), and morpholine (Mor)), ring size in monoamines (pyrrolidine (Pyr), PD, and hexamethyleneimine (HMI)), ring size in diamines (PZ and homopiperazine (HomoPZ)), and methyl substitution (PZ, 1-methylpiperazine (1-MPZ), and 2-methylpiperazine (2-MPZ)). In 6-member heterocycles with one amino function, both Mor and PD had decreased degradation rates compared to PZ, likely because the additional amino function in PZ enhances nucleophilic attack reactions. In monoamines, the expected chemical stability predicted for 5-, 6-, and 7-membered alkane rings closely predicted the thermal degradation rates of these heterocycles. Both Pyr and HMI were degraded quickly producing polymers while the 6-membered PD was stable. Increasing the size of the PZ ring by the addition of one methylene group greatly enhanced the thermal degradation rate. HomoPZ loss 99% of its initial concentration after 4 weeks at 175 °C while PZ lost only 30%. Methyl substitution increased the rate of amine degradation as both 1-MPZ and 2-MPZ degraded faster than PZ at 150 °C. Unexpectedly, a methyl on the amino group (1-MPZ) enhanced degradation more than a methyl on the carbon in the α-position to the amino group (2-MPZ). An apparent first order rate constant was calculated for the thermal degradation of these structural analogs and compared to other amines of interest in CO_2 capture.

Keywords: piperazine, CO_2 capture, amine degradation, thermal degradation, heterocycle

1. Introduction

Concentrated piperazine (PZ) has been demonstrated as an effective solvent for CO_2 capture using an amine-based absorption/stripping process [1]. Previous work has concluded that concentrated PZ has fast CO_2 absorption rates, high CO_2 capacity, low volatility, and limited degradation under absorption/stripping process conditions [1-3]. All of these characteristics are highly desirable for potential CO_2 capture solvents. The drawbacks to a concentrated PZ system are high viscosity, high potential amine cost, and the possibility for solid precipitation.

One of the most important advantages of concentrated PZ over other well-studied, baseline alkanolamine solvents such as monoethanolamine (MEA), 2-amino-2-methyl-1-propanol (AMP), or methyldiethanolamine (MDEA) is its exceptional resistance to thermal degradation. PZ has been found to be resistant to degradation up to 150 °C, well above the standard stripper operating conditions [3]. At higher temperatures, PZ begins to degrade at rates similar to alkanolamines at temperatures between 100 and 135 °C.

The goal of this study was to elucidate structural reasons for the resistance of PZ to thermal degradation. PZ is 6-membered ring with two secondary amino functions. Six-membered cyclic alkanes are known to be stable due to minimized angle or torsional strain and six-member heterocycles, such as PZ, would benefit as well [4]. PZ does not have an alcohol function, which is known to enhance thermal degradation through well know pathways [5-7]. It is also lacking any steric hindrance from alkane or hydroxyl groups on the amine or α-carbon that would interfere with reactions at the position of the amino function.

Thermal degradation of seven structural analogs of PZ was performed to determine the structural characteristics that provide thermal resistance. The structures of the eight amines, piperazine (PZ), 1-methylpiperazine (1-MPZ), 2-

methylpiperazine (2-MPZ), piperidine (PD), morpholine (Mor), pyrrolidine (Pyr), hexamethyleneimine (HMI), and homopiperazine (HomoPZ), are shown in Figure 1. The structures are arranged to demonstrate the comparisons developed in this paper. The effect of changing a secondary heteroatom, ring size in monoamines, ring size in diamines, and methyl substitution are each analyzed using thermal degradation data of the amines indicated in Figure 1.

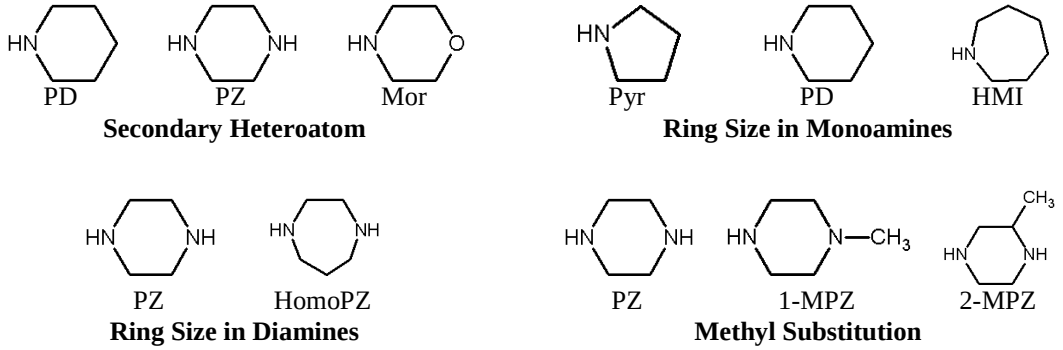

Figure 1: Structures of Amines Investigated in Thermal Screening

2. Methods and Materials

2.1. Chemicals and Solution Preparation

Piperazine (PZ, IUPAC name: 1,4-diazacyclohexane, CAS 110-85-0, 99% purity, Sigma-Aldrich Corportation, St. Louis, MO), 1-methylpiperazine (1-MPZ, CAS 109-01-3, >99%, Acros Organics N.V., Geel, Belgium), 2-methylpiperazine (2-MPZ, CAS 109-07-9, ≥99% purity, AK Scientific Inc., Mountain View, CA), homopiperazine (HomoPZ, CAS 505-66-8, 98% purity, Acros Organics), pyrrolidine (Pyr, CAS 123-75-1, >99% purity, Sigma-Aldrich), piperidine (PD, CAS 110-89-4, 99% purity, Sigma-Aldrich), hexamethyleneimine (HMI, IUPAC name: Azepane, CAS 111-49-9, 99% purity, Acros Organics), morpholine (Mor, CAS 110-91-8, 99% purity, Sigma-Aldrich), and carbon dioxide (CO_2, CAS 124-38-9, 99.5% Purity, Matheson Tri-Gas, Inc., Basking Ridge, NJ) were obtained commercially at the indicated purities.

Amine solutions were prepared gravimetrically as detailed previously using analytical grade water [1, 3]. CO_2 gas was sparged through aqueous amine and H_2O solutions using a gas washing bottle until the desired CO_2 concentration was achieved gravimetrically. Solutions were prepared with amine concentrations of 8 molal (m, mole amine per kilogram water) and CO_2 concentrations (CO_2 loading) of 0.3 mole CO_2 per mole alkalinity, where alkalinity is defined as the concentration of amino functions at 8 m amine. A mortar and pestle was used to crush 2-MPZ into manageable pieces and heat was used to melt HomoPZ before each was mixed with water. PZ, 2-MPZ, and HomoPZ solutions required slight heating before CO_2 addition to completely solubilize the amine. The remaining amines are liquids at room temperature and miscible with water.

2.2. Total Alkalinity and CO_2 Concentration

The total alkalinity was measured using an acid titration described in detail previously [1, 3, 8]. Experimental samples are titrated to an end point pH of 2.4 using 0.1 N H_2SO_4 and a Titrando automatic titrator (Metrohm, Riverview, FL). Multiple equivalence points were detected and the equivalence point near a pH of 3.8-4.0 corresponded to the total amine concentration for PZ and PZ derivatives. The volume of acid used to reach this equivalence point was used to calculate the total moles of alkalinity present in each sample. The alkalinity was only assumed to correlate with the total amine concentration in the initial sample. After degradation, deviation was seen between the amine concentration quantified through cation ion chromatography and the total alkalinity.

The CO_2 loading, or CO_2 concentration, was confirmed using a total inorganic carbon (TIC) assay that has been described previously [1, 3, 8]. Phosphoric acid is used to liberate CO_2 from solution while an infrared detector (Horiba Instruments Inc., Spring, TX) is used to quantify CO_2 concentration. A calibration curve generated from an inorganic carbon standard (Ricca Chemical Company, Pequannock, NJ) was used to calculate CO_2 concentrations.

2.3. Thermal Degradation in Stainless Steel Cylinders

Thermal degradation experiments took place in cylinders constructed from (1/2)-inch OD 316 stainless steel tubing and two Swagelok® end caps (Arthur Fluids System Technologies, Austin, TX) as described previously [3, 5]. Amine solution was used to fill multiple cylinders, allowing less than 0.5 mL of headspace, which were then sealed, and placed in forced convention ovens maintained at the experimental temperature. Sampling of an experiment occurred by

removing a single cylinder from the oven at the designated time point. Amine losses are reported as the percent of amine lost compared to the initial amine concentration as analyzed using cation ion chromatography.

2.4. Cation Ion Chromatography (IC)

Cation Ion Chromatography (IC) was used to identify and quantify amines in solution as previously described [3, 9, 10]. A Dionex ICS-2500 Ion Chromatography System with AS40 autosampler, LC25 chromatography oven, CD25 conductivity detector, and GP50 gradient pump was used (Dionex Corporation, Sunnyvale, CA). The mobile phase contained varying concentrations of methanesulfonic acid in analytical grade water. Separation occurred in an IonPac CG17 guard column (4×50mm) and IonPac CS17 analytical column (4×250 mm). The system contained a 4-mm Cationic Self-Regenerating Suppressor (CSRS) to remove anionic species before cationic species are detected with the CD conductivity detector. Chromeleon software on the attached computer analyzes the conductivity output and controls the entire system. The cation IC was used to quantify PZ, 1-MPZ, 2-MPZ, HomoPZ, Pyr, PD, HMI, Mor, ethylenediamine (EDA), and other amine degradation products.

2.5. Anion Ion Chromatography (IC) and Detection of Amides

Anion IC was used to identify and quantify negatively charged degradation products in solution. A Dionex ICS-3000 modular Dual Reagent-Free IC (RFIC) system with AS autosampler, EG40 Eluent Generator, SP/DP Dual Pump, and DC Detector/Chromatography Module was used (Dionex Corporation). The mobile phase contained varying concentrations of potassium hydroxide in analytical grade water generated from the EG40 Eluent Generator. Separation occurred in an IonPac AG15 guard column (4×50mm) and IonPac AS15 analytical column (4×250 mm). The system contains a 4-mm Anionic Self-Regenerating Suppressor (ASRS) to remove cationic species before anionic species are detected with a conductivity cell. Two carbonate removal devices, a Continuously Regenerated Anion Trap Column (CR-ATC) and Carbonate Removal Device (CRD), are in place to remove excess carbonate species from the samples. Chromeleon software on the attached computer analyzes the conductivity output and controls the entire system. The anion IC was used to quantify formate, acetate, glycolate, oxalate, and sulfate in this study.

Amides were quantified by hydrolysis to their corresponding amine and carboxylic acid as described previously [3, 9]. Experimental samples were hydrolyzed with 5N sodium hydroxide at a one-to-one ration (by mass) and allowed to react for at least 24 h to ensure complete reversal of amide formation. Amide reversal in neat solutions occurs rapidly, in less than four hours, so experimental samples were assumed to be completely treated within 24 hours. Hydrolyzed samples were analyzed for anion concentrations where the increase in concentration over the original samples represents the acid portion of the original amide (i.e., formyl or oxalyl compounds). The total formate is reported throughout this manuscript at it refers to the sum of the formate and formyl amides, or the total formate concentration after alkaline treatment.

3. Results and Discussion

3.1. Effect of Heteroatom in 6-Membered Rings (PD, PZ, and Mor)

The effect on thermal degradation of changing the heteroatom in a six-member ring containing one amino function was investigated by degrading PD, PZ, and Mor at 175 °C. This analysis compares the degradation rate achieved when the methylene group in the 4 position on PD is changed to an amino group (PZ) or oxygen (Mor). The fraction of the initial amine remaining after 10 weeks of degradation at 175 °C is shown in Figure 2. For all three amines, total formate was a dominant degradation product and is shown in Figure 3. For PZ and PD, the standard deviations in the total formate concentration are not visible in Figure 3 but were ± 3.6 mmol/kg at 5 weeks and ± 1.4 mmol/kg at 6.1 weeks, respectively.

Table 1: pK_a Values at 298 K

Molecule	$pK_{a,1}$	$pK_{a,2}$	Reference
PD	11.22	-	[11]
PZ	9.71 - 9.73	5.33 - 5.41	[12-14]
Mor	8.36	-	[15, 16]
Pyr	11.12-11.27	-	[11, 17]
HMI	11.07	-	[18]
HomoPZ [a]	10.09	6.67	[16]
1-MPZ	9.14	4.63	[14]
2-MPZ	9.57	5.24	[14]

[a] Values listed for HomoPZ are at 303 K

Mor and PD both degraded more slowly than PZ. These are the first amines to be found to be more thermally resistant than PZ although Mor has been previously identified as thermally stable [5]. The presence of a second amino function in the 6-member ring appears to increase the degradation rate of PZ. The presence of multiple amino functions allows for more nucleophilic attack within the solutions, increasing degradation. This is especially important since PZ is unique in that even when PZ has reacted with CO_2 to form protonated PZ (H^+PZ) and PZ carbamate ($PZCOO^-$), there is

another amino group that can be an attacking nucleophile or be subject to nucleophilic attack.

The pK_a values for the amines studied in this paper are shown in Table 1. The pK_a values reported for PD, PZ, and Mor in Table 1 indicate that PZ has an intermediate base strength with PD having the highest pK_a for the amino group. From the low pK_a value of Mor, it was expected that it would act as a weak attacking group and have a lower degradation rate than PZ. Although PD has a higher pK_a than PZ, indicating it is a stronger base, the higher degradation rate in PZ is likely just due to the additional amino function available for nucleophilic attack reactions whereas PD has a portion of its molecules tied up as protonated PD (H^+PD) and PD carbamate ($PDCOO^-$) after reaction with CO_2.

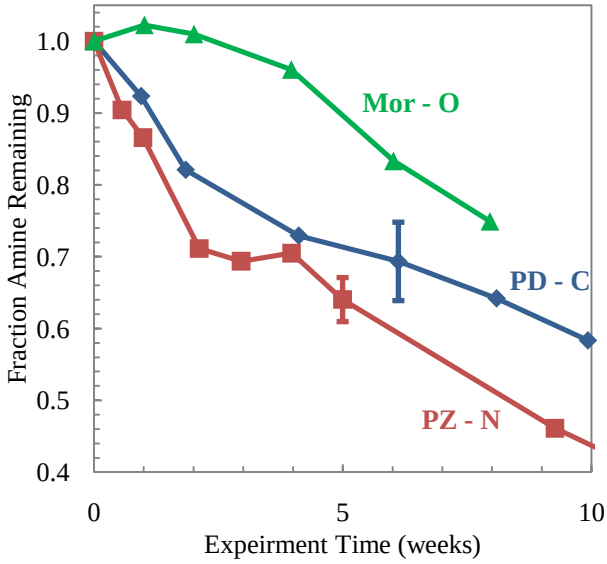

Figure 2: Amine loss in thermal degradation of 6-membered rings with varying heteroatoms at 175 °C

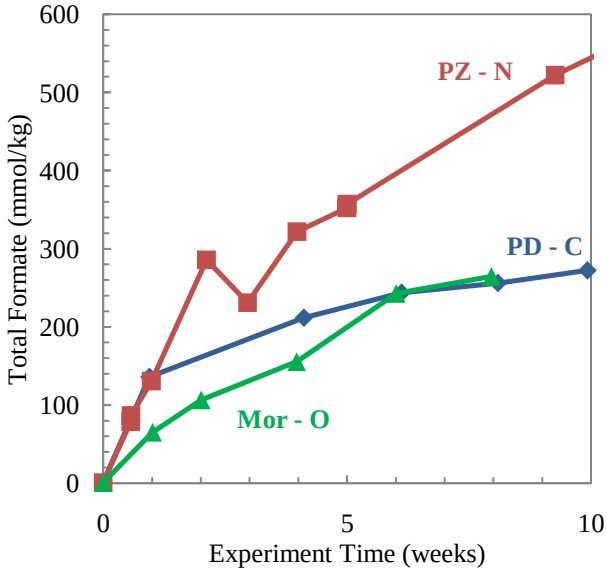

Figure 3: Production of total formate in thermal degradation of 6-membered rings with varying heteroatoms at 175 °C

3.2. Effect of Ring Size in a Monoamine (Pyr, PD, and HMI)

The effect of ring size on thermal degradation of a monoamine was investigated by degrading Pyr, PD, and HMI at 175 °C. The fraction of the initial amine remaining after 10 weeks at 175 °C is compared in Figure 4. In Figure 4, the standard deviation for the Pyr and HMI experiments were ± 0.003 and ± 0.005 mmol/kg, respectively at 6.1 weeks, but are not visible. For all three amines, total formate was one of the dominant degradation product identified and the concentration is compared in Figure 5. On Figure 5, the standard deviation for Pyr and PD data were also not visible in the figure but were ± 0.68 and ± 1.42 mmol/kg, respectively at 6.1 weeks.

The most thermally stable amine of the three, as expected, is PD. PD is a six membered ring analogous to PZ with one amino group replaced with a methylene group. The saturated nature of all three of these molecules lends itself to instability compared with their saturated and aromatic counterparts, and the effect of ring size differentiates the amines further. Both Pyr and HMI degrade faster than both PD and PZ at the experimental temperature. It is well known that 5- and 7-membered rings are not as stable as 6 membered rings and the thermal stability of these amines follows suit. Comparing the simplest cyclic alkanes, cyclopentane, cyclohexane, and cycloheptane, cyclohexane is considered to be free of strain while the cyclopentane and cycloheptane have 6.2 and 6.1 kcal/mol of torsional strain, respectively [4]. In amine heterocycles, the 7-membered HMI appears to be the least stable, losing nearly all the initial amine after one week of degradation compared to only 55% and 8% loss of Pyr and PD, respectively.

The production of total formate (Figure 5), a major degradation product for all three amines, does not track with the amount of amine lost for each. PD produced the most formate while the least amount of amine was lost. HMI produced more formate than Pyr, despite losing more amine overall. Degraded solutions of both Pyr and HMI were found to contain polymeric substances. This was not observed in PD or PZ. The mechanism for thermal degradation is certainly quite different from previous amines studied, especially MEA and PZ, and the presence of polymeric substances after degradation does not lend itself for further study in the field of CO_2 capture.

The difference in the ratio of formate produced to amine lost indicates stark differences in the mechanisms responsible for amine loss and formate production in each case. In PD, the ratio of total formate produced for amine lost is approximately 0.15 at the final time point while that of Pyr and HMI were 0.03 and 0.04, respectively. The mechanisms for HMI and Pyr degradation appear vastly different than that of PD and proceed to the generation of polymers while PD degradation likely proceeds similar to PZ with oxidation/reduction reactions or nucleophilic attack and substitution reactions.

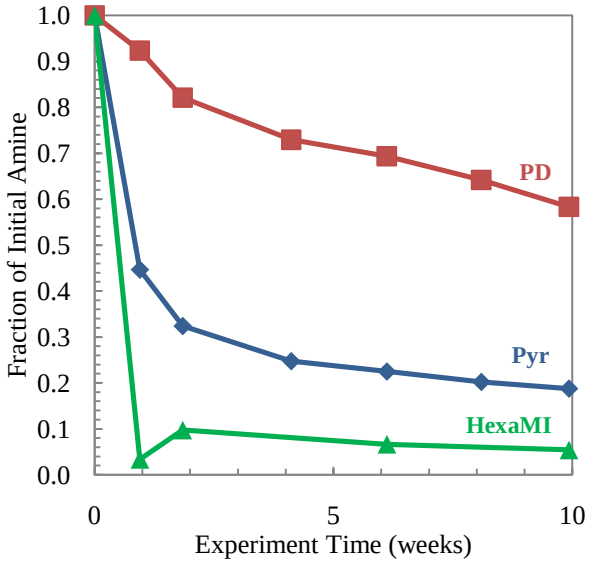

Figure 4: Amine loss in thermal degradation of monoamines at 175 °C

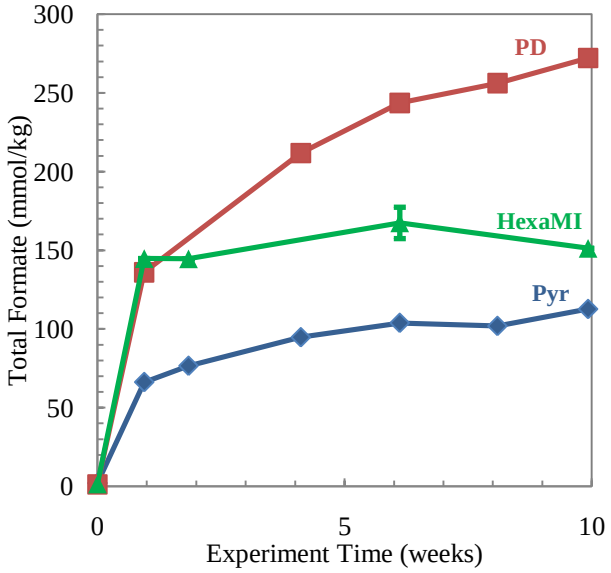

Figure 5: Production of total formate in thermal degradation of monoamines at 175 °C

3.3. Effect of Ring Size in a Diamine (PZ and HomoPZ)

The effect of ring size on thermal degradation of a diamine was investigated by thermally degrading PZ and HomoPZ at 175 °C. The loss of amine and production of total formate is shown in Figures 6 and 7. In the PZ data set, the standard deviation of the total formate at 5 weeks is ± 3.6 mmol/kg, but is not visible in Figure 7. HomoPZ degrades rapidly in comparison with PZ, losing essentially all the initial amine within 4 weeks at this temperature. PZ has lost only about 30% of the initial amine after the same amount of time. For the production of degradation products, total formate is a dominant product for both amines. PZ produces nearly twice as much as the maximum formate concentration in HomoPZ. In HomoPZ, formate appears to be an intermediate because it is initially produced and then reacts away, reaching its maximum concentration after 1 week. All previous work on PZ showed steady increases of total formate, indicating it was a final product of degradation [3].

The addition of one methylene group to a PZ molecule (HomoPZ) weakens the structure and the thermal resistance seen in PZ is lost. The degradation also proceeds through a different mechanism, as demonstrated by the presence of formate and formyl amides as intermediates, rather than final products. Although there are few data points in the region where HomoPZ is initially being degraded, the data indicates that the reaction is not first order in amine, as has been hypothesized for PZ thermal degradation [3].

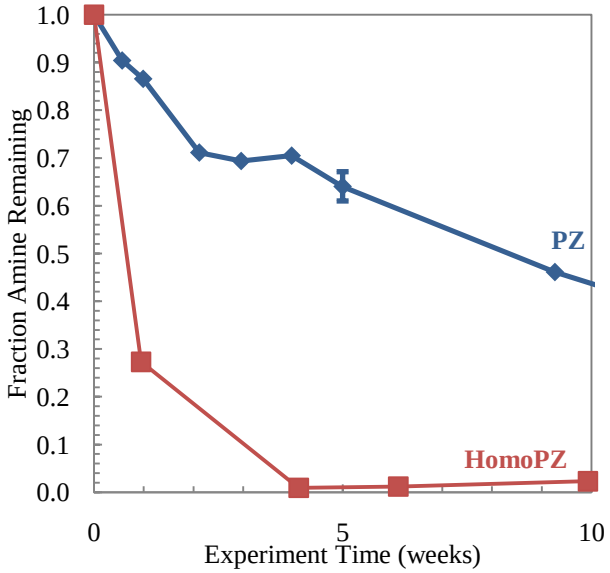

Figure 6: Amine loss in thermal degradation of diamines at 175 °C

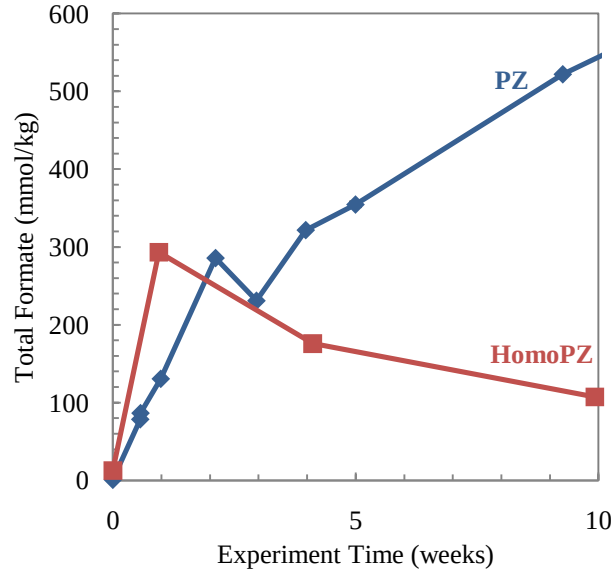

Figure 7: Production of total formate in thermal degradation of diamines at 175 °C

3.4. Methyl Substituted PZ (PZ, 1-MPZ, 2-MPZ)

The effect of methyl substitution on the thermal degradation of PZ was investigated by degrading PZ, 1-MPZ, and 2-MPZ at 150 °C. The presence of the methyl group at either the 1 or 2 position was assessed through the loss of amine and the generation of degradation products. The fraction of initial amine remaining after 30 weeks of degradation at 150 °C is shown below in Figure 8. The standard deviation for the fraction of amine in the PZ and 2-MPZ experiments at 14 weeks are not visible in Figure 8 but were both ± 0.007. A common degradation product between the three amines was the production of formate and formyl amides. The total formate is compared in Figure 9. The standard deviation for the total formate concentration in the PZ and 2-MPZ experiments at 14 weeks were also not visible and are ± 5.8 and ± 0.9 mmol/kg, respectively.

The addition of a methyl group at either the 1 or 2 position on the molecule decreases the thermal resistance of the PZ molecule. Both 1-MPZ and 2-MPZ shown enhanced degradation rates compared to PZ at 150 °C. Unexpectedly, 1-MPZ degraded faster than 2-MPZ, indicating the presence of a methyl group directly on the amino function enhanced degradation. Secondary amines (PZ and 2-MPZ) are considered, in general, to be stronger bases than tertiary amines (1-MPZ) and this is demonstrated by the lower pK_a values in 1-MPZ shown in Table 1. The pK_a values for 2-MPZ shown in Table 1 indicate that the presence of a methyl group on the carbon α to the amino function has reduced the basicity of the molecule only slightly compared with PZ. Resistance to thermal degradation appears to be positively associated with increasing base strength as with these three amines. The lower pK_a values found in 1-MPZ predict faster degradation while the higher pK_a of 2-MPZ and PZ correspond to decreasing degradation rates.

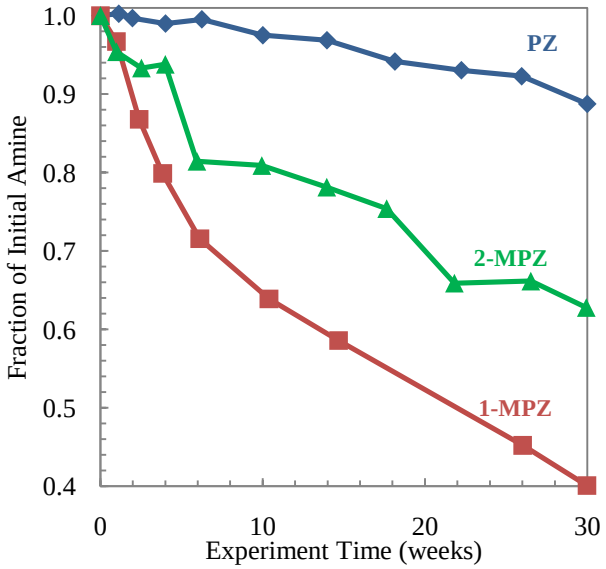

Figure 8: Amine loss in thermal degradation of methyl substituted PZ at 150 °C

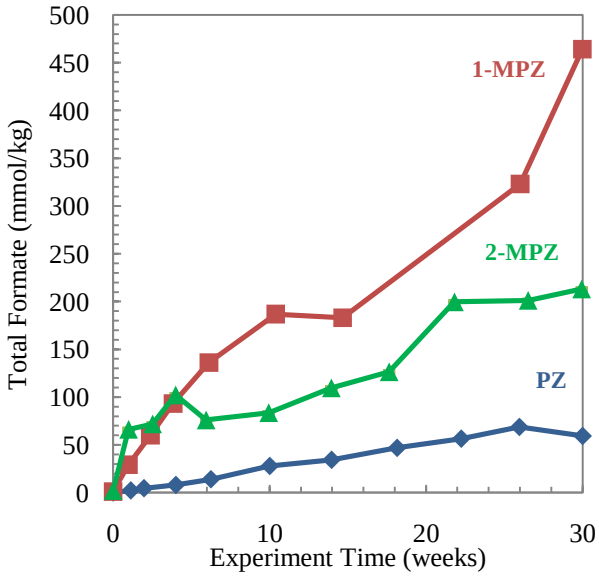

Figure 9: Production of formate in thermal degradation of methyl substituted PZ at 150 °C

3.5. Summary of Results

In order to summarize the thermal degradation data presented in this paper, a rate constant, k_1, has been calculated for each amine based on the change in amine concentration with respect to time. It is clear from the degradation profiles shown in previous sections that all the amines discussed here do not follow first order kinetics in amine loss, as PZ has be hypothesized to do [3]. However, in an attempt to compare the amines on the same basis, an apparent first order rate constant was calculated for each amine. For PZ, PD, Mor, 1-MPZ, and 2-MPZ, a first order loss of amine was assumed and k_1 was calculated from all the data shown as described previously [3]. For Pyr, HMI, and HomoPZ, where amine loss is initially drastic and certainly not first order in amine, the initial rate demonstrated after 1 week of degradation was used to calculate a k_1.

A summary of the calculated k_1 values for thermal degradation are compared for the amines discussed in this manuscript in Table 2. Previously reported data for PZ degradation at 135 °C is included [3]. Values of k_1 for other amines that are of interest to CO_2 capture applications are also included in Table 2 for comparison purposes. Data for 7 m MEA, 7 m AMP, 7 m Diglycolamine® (DGA®), 7 m N-(2-hydroxyethyl)piperazine (HEP), and 7 m diethylenetriamine (DETA) were reported previously by Davis (2009) [5]. Data for ethylenediamine (EDA) and 2-piperidineethanol (2-PE) were reported previously by Shan (2010) and data for MDEA and the blend of MDEA and PZ were reported previously by Closmann (2009) [19, 20]. Data for thermal degradation of MAPA were obtained from unpublished work of Vevelstad (2010) [21].

Mor and PD were the only amines found to have slower degradation rates, and therefore lower k_1 values, than PZ at

175 °C. Pyr, HMI, and HomoPZ all had higher k_1 values than PZ at 175 °C, while HMI had the highest k_1 calculated thus far at that temperature. At 150 °C, 1-MPZ and 2-MPZ were found to have similar k_1 values that were both 4-6 times higher than that of PZ. PZ and its methyl substituted analogs, 1-MPZ and 2-MPZ, all had lower k_1 value than both AMP and MEA. The k_1 values for MEA and AMP were found to be at least 2.3 and 22 times higher, respectively, than the next closest PZ-based amine at 150 °C, 1-MPZ.

Table 2: Apparent first order rate constant for thermal degradation of potential CO_2 capture amines

Solvent	Amine (m)	CO_2 Loading (mol/mol alk)	k_1 (10^{-9} s^{-1})		
			135 °C	150 °C	175 °C
Morpholine (Mor)	8	0.3	-	-	50
Piperidine (PD)	8	0.3	-	-	84
Piperazine (PZ)	8	0.3	1.2	6.1	140
2-Methylpiperazine (2-MPZ)	8	0.3	-	25	-
1-Methylpiperazine (1-MPZ)	8	0.3	-	36	-
2-Amino-2-methyl-1-propanol (AMP)	7	0.4	21	86	-
Methyldiethanolamine (MDEA)/PZ	7/2	0.1	21/190 [a]	88/1021 [a]	-
Diglycolamine® (DGA®)	7	0.4	35	-	-
N-(2-Hydroxyethyl)piperazine (HEP)	7	0.4	46	-	-
Methyldiethanolamine (MDEA)	7	0.1	55	-	-
2-Piperidineethanol (2-PE)	8	0.4	80	293	-
Pyrrolidine (Pyr)	8	0.3	-	-	1000 [b]
Homopiperazine (HomoPZ)	8	0.3	-	-	1300 [b]
Hexamethyleneimine (HMI)	8	0.3	-	-	1700 [b]
Monoethanolamine (MEA)	7	0.4	134	807	8500 [c]
Ethylenediamine (EDA)	8	0.4	168	-	-
3-(Methylamino)propylamine (MAPA)	9	0.4	313		
Diethylenetriamine (DETA)	7	0.4	991	-	-

[a] Rates provided are for each of the amines in the blend, respectively

[b] k_1 values for Pry, HomoPZ, and HMI were estimated from the initial rate after one week of degradation

[c] First order rate constant is estimated for 7 m MEA at 175 °C from lower temperature data

4. Conclusions

The resistance to thermal degradation demonstrated by PZ has been further explored by investigating the thermal degradation characteristics of its structural analogs. In a 6-membered heterocycle with one nitrogen, the presence of carbon, nitrogen, or oxygen as the second heteroatom affected the degradation rate at 175 °C. Oxygen as the second heteroatom (Mor) had the lowest degradation rate. Nitrogen as the second heteroatom (PZ) had a higher degradation rate compared to both carbon (PD) and oxygen (Mor). PD and Mor are the only amines that have ever showed a lower degradation rate than PZ.

In 5-, 6-, and 7-membered rings with one amino function, as in Pyr, PD, and HMI, the degradation rate was lowest in the 6-membered PD at 175 °C. This was expected with the reduced torsional strain and overall stability of 6-membered rings, which is believed to extend to heterocycles. Between Pyr and HMI, The 5-membered Pyr was shown to be more stable than the 7-membered HMI. The generation of total formate, one of the major degradation products for all three did not track with the degradation, indicating that different mechanisms are responsible for the degradation of each amine. Polymeric substances were found in degraded Pyr and HMI indicating the mechanism for amine loss in these solutions is likely the production of polymer in alkaline conditions.

Increasing the size of the PZ ring by one methylene group greatly increased the thermal degradation rate at 175 °C. HomoPZ lost 99% of its initial amine after 4 weeks, while PZ lost only 30% during the same time. The 7-membered heterocyclic HomoPZ is much less stable compared to the 6-member heterocyclic PZ.

Methyl-substituted PZ displayed unique behavior during degradation at 150 °C. Attaching a methyl group at the α-position to the amino group (2-MPZ) accelerated degradation compared to PZ. The presence of the methyl group on the amino group (1-MPZ) greatly accelerated the degradation compared to PZ and even more than 2-MPZ. The addition of the methyl group directly to the amino function (1-MPZ) provides the lowest pK_a values for the tertiary amine compared with the other two secondary amines and the fastest degradation rate.

The comparison of apparent k_1 values between amines provides a way to generalize high temperature degradation on a similar basis. Mor, PD, and PZ are highly resistant amines that can survive temperatures well above normal stripper operating conditions. 2-MPZ, 1-MPZ, AMP, MDEA/PZ, DGA®, HEP, MDEA, and 2-PE are all moderately resistant to thermal degradation and allow for a variety of applications based on other valuable characteristics of each solvent.

Pyr, HomoPZ, and HMI degrade easily and the unique degradation mechanisms in each, including the production of polymeric products, do not lend themselves to CO_2 capture. MEA, EDA, MAPA, and DETA have been found to be the least thermally resistant amines and require low temperature applications in order to fully utilize the advantageous solvent characteristics of each.

5. Acknowledgements

The authors would like to acknowledge the Luminant Carbon Management Program at the University of Texas at Austin for funding this research. The authors would also like to sincerely thank Solrun Vevelstad for her yet to be published thermal degradation data for MAPA.

References

[1] Freeman SA, Dugas R, VanWagener D, Nguyen T, Rochelle GT. Carbon dioxide capture with concentrated, aqueous piperazine. Int. J. Greenh. Gas Con. 2010; 4(2): 119-124.

[2] Dugas R, Rochelle GT. Absorption and desorption rates of carbon dioxide with monoethanolamine and piperazine. Absorption and desorption rates of carbon dioxide with monoethanolamine and piperazine. 2009; 1(1): 1163-1169

[3] Freeman SA, Davis J, Rochelle GT. Degradation of aqueous piperazine in carbon dioxide capture. Int. J. Greenh. Gas Con. 2010; 4(5): 756-761.

[4] McMurry J. Organic Chemistry. 5th ed. Pacific Grove: Brooks/Cole; 2000.

[5] Davis J. Thermal Degradation of Aqueous Amines Used for Carbon Dioxide Capture. The University of Texas at Austin, Austin, TX, 2009.

[6] Kennard ML, Melsen A. Mechanisms and Kinetics of Diethanolamine Degradation. Ind. Eng. Chem. Fund. 1985; 24(2): 129-140.

[7] Dawodu OF, Meisen A. Degradation of alkanolamine blends by carbon dioxide. Can. J. Chem. Eng. . 1996; 74(6): 960-966.

[8] Hilliard MD. A Predictive Thermodynamic Model for an Aqueous Blend of Potassium Carbonate, Piperazine, and Monoethanolamine for Carbon Dioxide Capture from Flue Gas. The University of Texas at Austin, Austin, TX, 2008.

[9] Sexton AJ. Amine Oxidation in CO_2 Capture Processes. The University of Texas at Austin, Austin, TX, 2008.

[10] Sexton AJ, Rochelle GT. Reaction Products from the Oxidative Degradation of Monoethanolamine. Ind. Eng. Chem. Res. 2009; (in print).

[11] Searles S, Tamres M, Block F, Quarterman LA. Hydrogen Bonding and Basicity of Cyclic Imines. J. Am. Chem. Soc. 1956; 78: 4917-4920.

[12] Hamborg ES, Versteeg GF. Dissociation Constants and Thermodynamic Properties of Amines and Alkanolamines from (293 to 353) K. J. Chem. Eng. Data. 2009; 54(4): 1318-1328.

[13] Hetzer HB, Robinson RA, Bates RG. Dissociation Constants of Piperazinium Ion and Related Thermodynamic Quantities from 0 to 50°C. J. Phys. Chem. 1968; 72(6): 2081-2086.

[14] Khalili F, Henni A, East ALL. pK(a) Values of Some Piperazines at (298, 303, 313, and 323) K. J. Chem. Eng. Data. 2009; 54(10): 2914-2917.

[15] Hall HK. Field and Inductive Effects on the Base Strengths of Amines. J. Am. Chem. Soc. 1956; 78(11): 2570-2572.

[16] Pagano JM, Golberg DE, Fernelius WC. A Thermodynamic Study of Homopiperazine, Piperazine, and N-(2-Aminoethyl)-Piperazine and their Complexes with Copper (II) Ion. J. Phys. Chem. 1961; 65: 1062-1064.

[17] Albert A, Serjeant EP. The determination of ionization constants: A laboratory manual. Edinburg: Chapman and Hall; 1971.

[18] Perrin DD. Dissociation constants of organic bases in aqueous solution. London: Buttersworth; 1965.

[19] Closmann F, Nguyen T, Rochelle GT. MDEA/Piperazine as a solvent for CO_2 capture. Energy Proceedia. 2009; 1(1): 1351-1357.

[20] Zhou S, Chen X, Nguyen T, Voice Alexander K, Rochelle Gary T. Aqueous Ethylenediamine for CO_2 Capture. ChemSusChem. 2010; (In Print).

[21] Vevelstad S. Thermal Degradation of 3-(Methylamino)propylamine (MAPA). Personal Communication to S. A. Freeman. 2010.

Available online at www.sciencedirect.com

ScienceDirect

Energy Procedia 00 (2010) 000–000

Energy Procedia

www.elsevier.com/locate/XXX

GHGT-10

Volatility of aqueous amines in CO_2 capture

Thu Nguyen[a], Marcus Hilliard[b], Gary Rochelle[a]

[a]*The University of Texas at Austin, Luminant Carbon Management Program, Department of Chemical Engineering, 1 University Station C0400 Austin, TX 78712, USA*

[b]*The Dow Chemical Company, USA*

Elsevier use only: Received date here; revised date here; accepted date here

Abstract

The volatility of amines in amine-water was measured using a hot gas FTIR. The amine partial pressures are reported as their respective Henry's constants. At infinite dilution in water, Henry's constants are in the order: methyldiethanolamine (MDEA) < 2-aminoethoxyethanol (DGA©) < piperazine (PZ) < 2-Methyl Piperazine (2-MPZ) < 3-methylamino propylamine (MAPA) < ethylenediamine (EDA) < monoethanolamine (MEA) < 1,2-diaminopropane (DAP) < 1-Methyl Piperazine (1-MPZ) < 2-amino-2-methyl-1-propanol (AMP). The amine Henry's constant at 40 °C is correlated to molecular group contributions: $\ln H_{40\ ^\circ C} = 4.19 - 1.65(N) - 0.21(NH) - 1.55(R\text{-}O\text{-}R) + 0.7(\text{Non Cyclic C-}CH_3) + 2.63(\text{Cyclic N-}CH_3)$, where the number of each functional group is defined as: N = tertiary nitrogen, NH = secondary amine, R-O-R = ether, Non Cyclic C-CH_3 = C-CH_3 in a straight chained amine, Cyclic N-CH_3 = N-CH_3 in a cyclic amine. Predictions of Henry's constants at 40 ˚C by the UNIFAC-DMD model in AspenPlus overestimate most measured values up to an order of magnitude except in the case of MEA.

Keywords: amine volatility; MEA; PZ; AMP; MDEA

1. Introduction

Thermodynamic studies of amine-water systems are important for many reasons. First, the need to understand how the volatility of different amines changes with loading, from an unloaded to nominal lean and rich loading conditions, is a key industrial interest that arises in the selection of a suitable CO_2 capture solvent and in the design of the water wash unit. Secondly, volatility measurements are essential to thermodynamic modeling of binary amine-water systems, which are then integrated into more complex models. Finally, there is an ongoing scientific interest in understanding the molecular interactions of species in nonideal amine-water systems.

While there are published measurements on the VLE of amine-water systems, only a few of them measure the vapor phase mole fraction of the amine. Lenard et al. [1] measured the gas phase composition of MEA in binary aqueous solution (343K and 363K) using gas chromatography. These data were represented using a three parameter Redlich-Kister expansion. Pappa et al. [2] made isobaric T-x-y measurements for the AMP-H_2O system at 66.7, 80.0, and 101.3 kPa using a modified Swietoslawski ebulliometer with sample compositions being determined using a standard curve of refractive index for this system at 25 ˚C. Kim et al. [3] also used this ebulliometer technique to determine the total pressure along with the liquid and vapor mole fractions of MEA, MDEA, and MAPA. Cai et al. [4] measured isobaric VLE at 101.3 kPa and 66 kPa (373K - 443K) using the standard curve of refraction index

versus mole fraction of the binary mixture at 20 ºC. The liquid phase activity coefficients were calculated with the UNIFAC group contribution model as published by Larsen et al. [5]. These data are in the high temperature range, and therefore are considered outside of the scope of our low temperature application.

This work presents the volatility of 10 different amines in binary amine-water systems as measured by a hot gas FTIR. The amines that were investigated were: monoethanolamine (MEA), piperazine (PZ), methyldiethanol-amine (MDEA), diglycolamine (DGA), ethylene diamine (EDA), 1-methyl piperazine (1-MPZ), 2-methyl piperazine (2-MPZ), 2-amino-2-methyl-1-propanol (AMP), 1,2-diaminopropane (DAP), and 3-methylamino propylamine (MAPA). These results were obtained at 40 – 70 ˚C and atmospheric pressure as typical in absorber operation for CO_2 capture. This work aims to explore the interactions between amine and water which determine volatility and to generalize these molecular interactions with a group contribution correlation. This approach differs from UNIFAC in that it focuses exclusively on amines in water with the use of a much smaller set of group contribution parameters. Also, the amine behavior in water is quantified by Henry's constants rather than activity coefficients.

2. Materials & Methods

2.1. Solution Preparation

Approximately 500 – 525 g of solution was prepared by dissolving pure, analytical-grade amine in water to achieve the desired molality (m, gmol amine/kg water). High concentrations of PZ were heated to dissolve anhydrous solid PZ in water. The purity grades of chemicals used were 99 % or greater.

2.2. Amine Concentration

The amine concentration was determined by acid titration with an automatic Titrando series titrator with automatic equivalence point detection. A 300X diluted sample was titrated with 0.1 N H_2SO_4 to a pH of 2.4. The amount of acid needed to reach the equivalence point at a pH of 3.9 was used to calculate the total amine concentration. The reproducibility of this method is about 1%.

2.3. Amine Volatility

Amine volatility was measured in a stirred reactor coupled with a hot gas FTIR analyzer (Fourier Transform Infrared Spectroscopy, Temet Gasmet Dx-4000) as shown in Figure 1. This was the same method and apparatus used by Nguyen et al. [6] and Hilliard [7] to measure amine volatility and CO_2 partial pressure in loaded solutions.

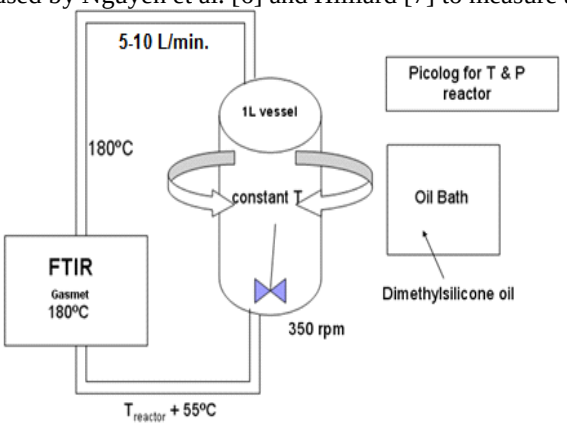

Figure 1. FTIR System for amine volatility

The 1L glass reactor was agitated at 350 rpm ± 5 rpm. Temperature in the reactor was controlled to ±0.1 °C by circulating dimethylsilicone oil. The reactor was insulated with thick aluminum insulation. The temperature inside the reactor was measured with a platinum resistance thermometer with an accuracy of ± 0.01 °C. Vapor from the headspace of the reactor was circulated at a rate of ~5-10 L/min. by a heated sample pump to the FTIR through a heated Teflon line. Both the line and analyzer were maintained at 180 ºC to prevent possible condensation or adsorption of amine. The FTIR measured amine and water concentration in the gas. The relative standard uncertainty in the vapor phase measurement was reported to be ±2 % by Goff [8]. After the gas passed through the FTIR, it was returned to the reactor through a heated line maintained ~ 55 ºC hotter than the reactor. With the 55°C difference, the measured water concentrations were found to remain consistent, within 0.5 %-1 %, between continuous instrument samplings at a given temperature. Upon completion of a given experiment, approximately 25 mL of liquid sample was taken to verify the amine concentration using acid titration.

FTIR calibration for each amine was performed with a syringe pump, a manual needle valve, and a stainless steel injection chamber. A known nitrogen flow rate, typically 2 SLPM, is introduced to the calibrator at room temperature via a mass flow controller. The syringe pump injects a known and very precise flow of the target amine

to be calibrated into the nitrogen flow in a heated injection chamber kept at 180 °C. This produces a continual flow of a known concentration calibration gas that is flown into the FTIR analyzer at 180 °C. A spectrum of a known mixture of the target gas and N_2 is measured and saved as a reference calibration. Calibration was performed at each concentration of interest. If the target amine is a solid at room temperature, it was necessary to dilute it in deionized water up to the point where it is soluble. The diluted amine-water mixture was then injected into the heated chamber. In this case, the water component was subtracted from the overall spectra leaving the target amine as the remaining residual spectra. The amine residual was then saved as a reference calibration. PZ was calibrated by this method because it is a solid at room temperature.

3. Data

In an amine-water system, the Henry's constant of the amine is a quantitative measure of amine volatility and can be correlated to molecular structure. As the mole fraction of amine (x_{amine}) approaches zero, the Henry's constant is defined by

$$H_{amine}(T) = P_{amine} / x_{amine} = \gamma^{\infty}_{amine} * P^{sat}_{amine} \quad (1)$$

In this work the Henry's constant is approximated as the ratio of amine partial pressure to amine mole fraction in solutions of 0.3 to 2 m amine. This value can also be determined by taking the product of the amine activity coefficient at infinite dilution and the amine saturation pressure. At these concentrations and 40 to 70 ˚C, the amine partial pressures are typically less than 30 Pa. Table 1 gives the measured amine and water partial pressures and the calculated Henry's constants of the amines.

Table 1. Henry's Constants of Amines (MEA data from Hilliard [7])

T (C)	P_{amine} (Pa)	P_{H2O} (Pa)	H_{amine} (Pa)		T (C)	P_{amine} (Pa)	P_{H2O} (Pa)	H_{amine} (Pa)
2.86 m MDEA					**0.204 m DGA**			
40	0.59	6935	12.7		50	0.18	12257	33.4
50	0.81	11156	16.2		55	0.22	15645	40.8
55	0.91	14271	18.1		60	0.27	18435	50.1
60	1.24	18191	23.3		65	0.33	22322	61.2
65	1.70	22613	31.8		70	0.59	27404	110
70	2.40	29045	44.5					
1.95 m PZ					**3.5 m MEA**			
40	1.51	6797	43.4		40	4.19	6940	70.7
50	2.79	11195	80.3		46	5.88	8690	99.2
60	6.35	16892	183		49	7.29	9760	135
70	14.2	30786	409		56	11.2	13600	189
					60	13.2	17100	223
					65	18.2	19900	321
0.5 m MAPA					**0.48 m EDA**			
40	0.53	8977	59.3		40	0.56	7694	62.7
45	0.72	11622	80.9		45	0.87	9692	97.5
50	1.01	15830	113		50	1.26	12590	141
55	1.33	20038	149		55	1.87	15688	210
60	2.28	25749	255		60	2.74	18485	307
65	3.41	31661	382					

0.95 m 2-MPZ					0.3 m DAP			
40	0.81	6758	48.2		40	0.61	6453	114
45	1.26	8674	75.0		45	1.14	8439	212
50	2.13	10850	127		50	1.54	10821	287
55	2.87	13685	171		55	2.11	13899	392
60	4.46	17798	265		60	3.02	17870	563
65	7.24	21681	431		65	4.01	22536	748
70	10.6	33589	630					
1.05 m 1-MPZ					**0.29 m AMP**			
40	2.65	6871	143		40	1.55	7486	288
45	4.94	8822	266		45	2.23	9682	414
50	7.51	12333	405		50	3.55	12278	662
55	11.6	14637	628		55	4.99	15672	929
60	18.7	18631	1010		60	7.09	18367	1320
65	29.1	23671	1566		65	10.2	22360	1896
					70	15.1	27550	2806

4. Results

4.1 Experimental Validation of FTIR Method

Figure 2 shows that MEA partial pressures obtained from the FTIR method agree very well with those of Kim et al. [3]. Kim used ebulliometry to obtain MEA and H_2O volatility.

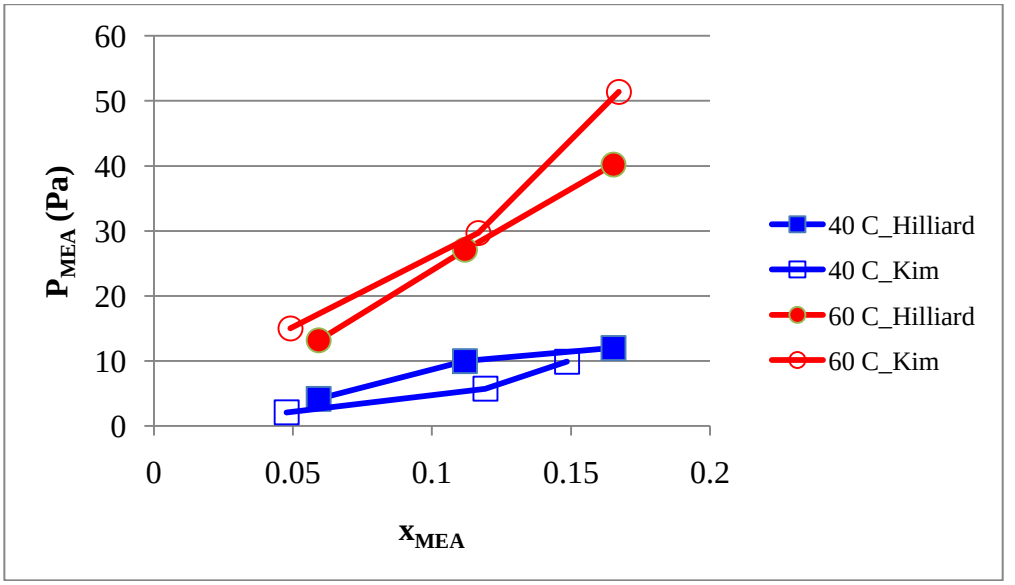

Figure 2. MEA Partial Pressures for 3.0 m, 7.0 m, 11.0 m, 23.8 m MEA-H_2O at 40 ˚C and 60 ˚C

The data obtained between runs were reproducible within the expected ±2% error. The detection limit of the FTIR is approximately 1 ppm for amines.

4.2. Amine Volatility Analysis

The volatilities of the amines are correlated with molecular groups and structural shapes. Amines having one or more polar groups, such as amine, hydroxyl, and ether groups, tend to be less volatile due to favourable interactions with water. The presence of one or more methyl groups in a structure contributes to non-polarity or greater volatility as is the case of AMP. As a second order effect, the presence of an N-CH_3 contribution in a straight chained amine, or a C-CH_3 contribution in a cyclic amine, correlates to lower volatility, respectively. Finally, to a small extent, the cyclic amines appear to be less volatile than straight chain amines. Table 2 shows the 10 amines studied in order of increasing Henry's constants at 40 ˚C.

The amine Henry's constant at 40 °C is given as a function of the various polar and non-polar group contributions as shown in equation (2).

$$\ln H_{amine,40\,^{\circ}C} = [4.19\ (\pm 0.09)] - [1.65(\pm 0.17)](N) - [0.21(\pm 0.07)](NH) - [1.55(\pm 0.17)](R\text{-}O\text{-}R) + [0.7(\pm 0.08)](\text{Non Cyclic C-}CH_3) + [2.63(\pm 0.21)](\text{Cyclic N-}CH_3) \quad (2)$$

The UNIFAC-DMD method in AspenPlus was also used to estimate the amine Henry's constants at 40 ˚C. Structural information for UNIFAC group contribution estimates was available for most amines with the exception of 1-MPZ and 2-MPZ. The vapor pressures of many amines had to be estimated in Aspen using the Mani method in conjunction with experimental normal boiling point. Table 2 also shows the Heat of amine absorption estimated from the Henry's constant as a function of temperature by the Gibbs-Helmholz equation.

Table 2. A Comparison of Measured Amine H Constant at 40 ˚C to Values Estimated by Eq. (2) and by UNIFAC-DMD

Amine	Structure	B.P. (C)	H (Pa)	$H_{pred.}$ (Pa)	H_{UNIFAC} (Pa)	- ΔH_{amine} (kJ/mol)
MDEA	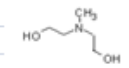	245	12.7	12.7	43.6	57
DGA	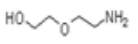	223	(13.9)	13.9	216	37
PZ		146	43.4	43.5	887	67
2-MPZ		155	48.2	43.5	221	77
MAPA	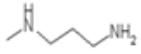	139	59.3	53.5	388	66
EDA	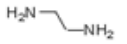	117	62.7	66	25.8	68
MEA		170	70.7	66	72.7	53
DAP	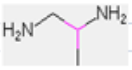	119	114	133	308	57
1-MPZ	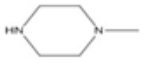	138	143	143	335	79
AMP	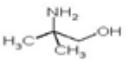	166	288	267	634	68

While many of the amine H constants were overestimated by UNIFAC-DMD, the H constant for MEA was accurately predicted within a small margin of error. This result is expected as the MEA-H_2O system is well-studied with adequate supporting data. Also there is not a perfect correlation between the amine normal boiling points and

their Henry's constants. This result is rather surprising as it indicates that one amine may be more volatile than another in its pure form but the opposite is true when each amine is in water.

Figure 3 shows the amine Henry's constants from 40 to 70 ˚C with the corresponding heats of absorption.

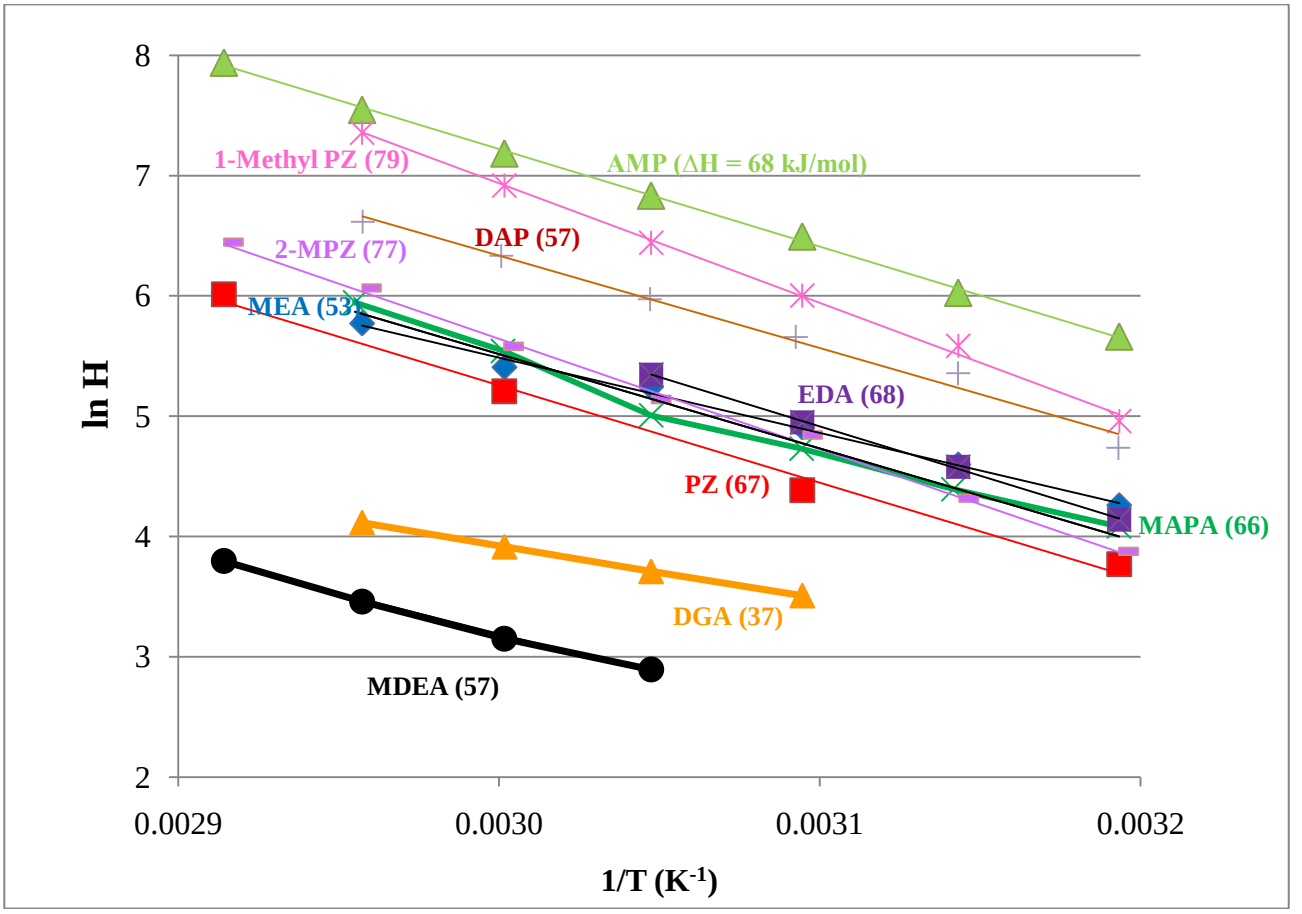

Figure 3. Aqueous Amine Volatility and Estimated Amine Heat of Absorption

5. Conclusions

Amine volatility in water is ranked in the order: MDEA < DGA < PZ < 2-MPZ < MAPA < EDA < MEA < DAP < 1-MPZ < AMP. The amine partial pressures in binary aqueous systems were less than 30 Pa in the range of 40 to 70 ˚C. The measured amine Henry's constants at 40 ˚C, as obtained from FTIR technique, varied from 12.7 Pa to 288 Pa. The Henry's constant predictions by the UNIFAC-DMD model, within AspenPlus, overestimated these values in most cases, with the exception of MEA. An empirical correlation was developed to estimate the amine Henry's constants at 40 ˚C given the number of tertiary amine groups, secondary amine groups, ether group, non-cyclic C-CH_3 contribution, and cyclic N-CH_3 contribution present in an amine structure. The estimated heats of absorption of the amines were ~37 – 80 kJ/mol over the temperature range studied.

6. References

[1] J. Lenard , R. Rousseau, A. Teja, Vapor-Liquid Equilibria for Mixtures of 2-aminoethanol + water, AIChE Symposium Series. 86 (1990).
[2] G. Pappa, C. Anastasi, E. Voutsas, Measurement and thermodynamic modeling of the phase equilibrium of aqueous 2-amino-2-methyl-1-propanol solutions. Fluid Phase Equilibria. 243 (2006) 193-197.
[3] I. Kim, H.F. Svendsen, E. Borresen, Ebulliometric Determination of Vapor-Liquid Equilibria for Pure Water, Monoethanolamine, N-Methyldiethanolamine, 3-(Methylamino)-propylamine, and Their Binary and Ternary Solutions, J. Chem. Eng. Data. 53 (2008) 2521-2531.

Add graphs comparing our data to the Kim MDEA and MAPA data.

[4] Z. Cai, R. Xie, Z. Wu, Binary Isobaric Vapor-Liquid Equilibria of Ethanolamines + Water, J. Chem. Eng. Data. 41 (1996) 1101 – 1103.

[5] B.L. Larsen, P. Rasmussen, A. Fredenslund, A Modified UNIFAC Group Contribution Model for Prediction of Phase Equilibria and Heats of Mixing, Industrial & Engineering Chemistry Research. 26 (1987) 2274-2286.

[6] T. Nguyen, M. Hilliard, G.T. Rochelle, Amine Volatility in CO_2 Capture, International Journal of Greenhouse Gas Control. 4 (2010) 707-715.

[7] M. Hilliard, A Predictive Thermodynamic Model for an Aqueous Blend of Potassium Carbonate, Piperazine, and Monoethanolamine for CO_2 Capture from Flue Gas. Ph.D. Dissertation, The University of Texas, Austin, 2008.

[8] G.S. Goff, Oxidative Degradation of Aqueous Monoethanolamine in CO_2 Capture Processes: Iron and Copper Catalysis, Inhibition, and O_2 Mass Transfer. Ph.D. Dissertation, The University of Texas, Austin, Texas, 2005.

Available online at www.sciencedirect.com

ScienceDirect

Energy Procedia 00 (2010) 000–000

Energy Procedia

www.elsevier.com/locate/XXX

GHGT-10

Modeling pilot plant results for CO_2 capture by aqueous piperazine

Jorge M. Plaza[a], Gary T. Rochelle[a]1*

[a]*The University of Texas at Austin, 1 University Station C0400, Austin, TX 78712, USA*

Elsevier use only: Received date here; revised date here; accepted date here

Abstract

Concentrated aqueous piperazine has been proposed as a possible evolutionary step from monoethanolamine (MEA) as a solvent for post-combustion capture. High concentration piperazine (>5 m) has volatility similar to MEA but provides CO_2 absorption rate and capacity that is almost double that of 7 m MEA. It is also more resistant to oxidative and thermal degradation and can be used up to 150°C. In order demonstrate these benefits a one month pilot plant campaign was conducted in November 2008 at The University of Texas at Austin with 5 m, 8 m and 9 m PZ.
An absorber model for concentrated PZ was developed in Aspen Plus® RateSep™ . The model was validated with the pilot plant results and served to assess the quality of the pilot plant data using the reconciliation tool in Aspen Plus®. The model simulates the temperature profile of the absorber. Loadings are matched within 0.03 and the deviation of the removal fraction is no more than 0.03. The absorber model was used to study intercooling and determine optimum conditions for its implementation. Based on pilot plant data and model results 90% CO_2 removal can be achieved with 8 m piperazine, 9 meters of packing, and intercooling with a loading shift from 0.32 (lean) to 0.39(rich) mol CO_2/mol alkalinity and steam heat rate in the stripper of 148 kJ/mol CO_2 and an equivalent work of 33.6 kJ/mol CO_2

Keywords: Carbon dioxide, absorption, piperazine, pilot plant

1. Introduction

Concentrated Piperazine (PZ) has been suggested as a possible improvement to the industry standard monoethanolamine (MEA) for CO_2 capture from flue gas. Freeman et al.[1] showed that 8 m PZ has a volatility similar to MEA but the advantage of faster kinetics (more than twice) and higher capacity (double) than MEA. It is also more resistant to oxidative and thermal degradation (degrades at temperatures higher than 150°C). PZ has previously been used as a promoter to increase absorption rates and capacity in solvents. It has been blended with K_2CO_3 [2-4] and with MDEA for natural gas sweetening [5, 6]. Freeman et al. [1] showed that 8 m PZ can be used without solids precipitation at the optimum loading range of 0.3 to 0.4 mol CO_2/mol alkalinity. This greater PZ concentration requires the implementation of a new model. Frailie et al.[7] describe the development of the thermodynamic framework for concentrated PZ. This framework was used to implement a kinetic representation for concentrated PZ based on work by Dugas[8] and Cullinane[2]. Once the kinetic framework was established, an absorber model was built for a PZ pilot plant campaign at The University of Texas at Austin. The model uses a FORTRAN subroutine to implement the Tsai

* Gary T. Rochelle. Tel.: +1-512-471-7230; fax: +1-512-471-7060.
E-mail address:gtr@che.utexas.edu

[9] interfacial area correlation and a viscosity correlation used to fit the data by Freeman et al. [1]. The absorber model was used to reconcile pilot plant data, validate the model, and analyze the performance of the solvent.

2. Initial pilot plant data evaluation

A simple evaluation of the absorber data was performed to estimate the overall gas-side mass transfer coefficient (K_G) at isothermal conditions with a log mean driving force by the equation:

$$K_G = \frac{N_{CO_2}}{a_{eff} V_p LMPD} \quad (1)$$

The effective packing area, a_{eff} was calculated by the Tsai et al.[9] correlation. The total CO_2 flux, N_{CO2}, was estimated from the reported gas CO_2 inlet and outlet. V_p is the packing volume. LMPD is the log mean of the inlet and outlet CO_2 partial pressure driving force. Figure 1 shows the resulting K_G as a function of the arithmetic average between inlet and outlet CO_2 equilibrium pressures. K_g data from the pilot plant campaign were consistent with the values of k_g' obtained by Dugas[8] in the wetted wall column. The K_G with the PZ solvents is 4 to 5 times greater than results with 7 m MEA and 5 m K^+/2.5 m PZ

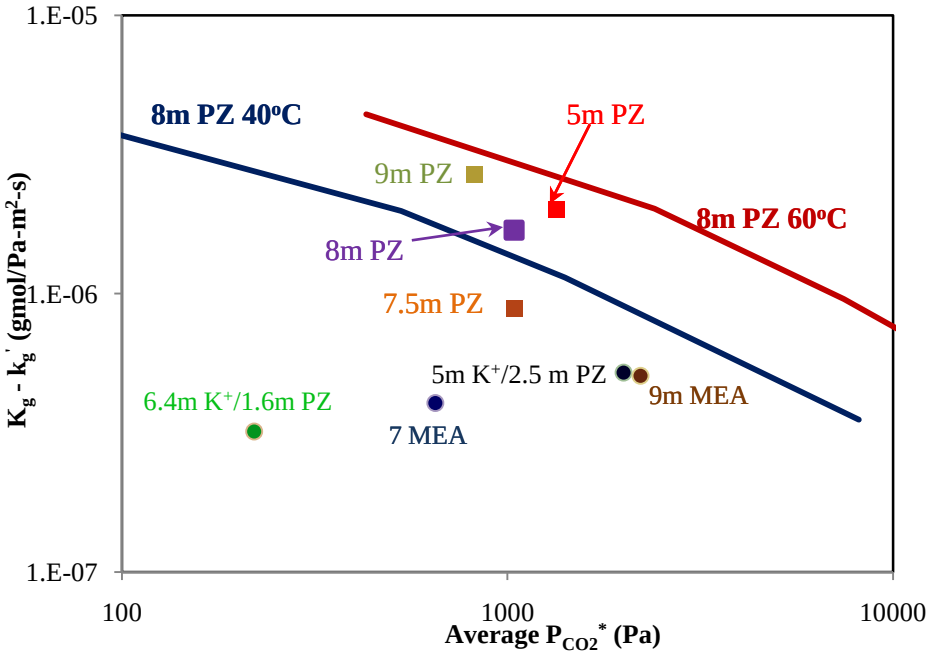

Figure 1. Comparison between K_G and kg' data for concentrated PZ. Lines are kg' data by Freeman et al.[1] Circles are data from other campaigns and solvents. [4, 8, 10, 11]

3. Kinetic model development

A wetted wall column (WWC) model was developed in Aspen Plus® RateSep™. It uses the thermodynamic framework by Fraile et al.[7] and FORTRAN subroutines for liquid and gas mass transfer coefficients, and interfacial area implemented by Dugas [8]. These subroutines include correlations found in Cullinane [2]. For the gas film transfer coefficient (k_g):

$$k_g = \frac{1.075}{RT} D_{CO_2}^{0.15} d^{0.7} \left(\frac{v}{h}\right)^{0.85} \quad (1)$$

where: R is the gas constant
D_{CO2} is the diffusion coefficient of CO_2
d is the hydraulic diameter of the WWC
v is the linear velocity of the gas
h is the height of the contact cylinder in the WWC

The liquid film transfer coefficient is defined taking into account that the WWC experiments are conducted at conditions for which the dimensionless penetration distance (η) is less than 0.01. The penetration distance is defined as:

$$\eta = D_{CO_2} h \left(\frac{2}{3^{4/3}}\right) \left(\frac{W}{Q}\right)^{4/3} \left(\frac{\rho g}{\mu}\right)^{1/3} \quad (2)$$

where: W is the circumference of the contact cylinder
Q is the volumetric flow rate of the liquid

ρ is the liquid density
g is the gravity constant
μ is the liquid viscosity

For these conditions the liquid mass transfer coefficient (k_L^0) follows equation 3. Here *A* is the gas-liquid contact area.

$$k_L^0 = \frac{Q}{A}\sqrt[3]{\frac{\eta}{\pi}} \tag{3}$$

Gas and liquid specifications were taken from WWC experimental data in Dugas [8]. Reported flux data was used to obtain the kinetic constants (k_n) in the activity (a) based reactions in the WWC (Table 1). The reverse rates are calculated from the equilibrium constant (K_{eq}) for each reaction as :

$$k_{n-r} = \frac{k_{n-f}}{K_{eq}} \tag{4}$$

Kinetic constants in Aspen Plus® RateSep™ are represented by the power law equation. The experimental data were used to generate the pre-exponential factor (k_o) and energy of activation (E_a) in the power law:

$$k_n = k_0\left(\frac{T}{298.15}\right)^n exp\left(\frac{-E_a}{R}\left(\frac{1}{T}-\frac{1}{298.15}\right)\right) \tag{5}$$

Figure 2 shows the flux fit between reported data by Dugas [8] and the WWC model with the calculated kinetic constant values. Results match reported flux data within 20% for 40, 60, and 80 °C as seen in Figure 1. However, deviation increases for 100 °C. This might be related to other phenomena taking a larger role in the absorption/desorption process such as the diffusion of reactants and products.

Table 1 Kinetic expressions used in the PZ model

Reaction	Rate Expression	
$2\,PZ + CO_2 \rightarrow PZH^+ + PZCOO^-$ (6)	$r = k_{1-f}a_{PZ}a_{CO_2}a_{PZCOO^-}$	(6a)
	$r = k_{1-r}\frac{a_{PZH^+}a^2_{PZCOO^-}}{a_{PZ}}$	(6b)
$2\,PZCOO^- + CO_2 \rightarrow PZ(COO^-)_2 + H^+PZCOO^-$ (7)	$r = k_{2-f}a^2_{PZCOO^-}a_{CO_2}$	(7a)
	$r = k_{2-r}a_{H^+PZCOO^-}a_{PZ(COO^-)_2}$	(7b)
$PZCOO^- + CO_2 + H_2O \rightarrow HCO_3^- + H^+PZCOO^-$ (8)	$r = k_{3-f}a_{PZCOO^-}a_{CO_2}$	(8a)
	$r = k_{3-r}\frac{a_{H^+PZCOO^-}a_{HCO_3^-}}{a_{H_2O}}$	(8b)
$PZ + H^+PZCOO^- \leftrightarrow PZH^+ + PZCOO^-$	Equilibrium*	(9)

*Reaction 7 is included as an equilibrium reaction.
Subscripts *f* and *r* refer to the direction of the reaction (forward and reverse respectively)

4. Pilot plant absorber modeling

The resulting kinetic values and the developed thermodynamic framework[7] were used to implement an absorber model in Aspen Plus® RateSep™ for the pilot plant at The University of Texas at Austin. The absorber at the pilot plant has a diameter of 0.427 m and was packed with 6.10 m of Mellapak 2X divided into two equal beds. It was fed at the bottom with a blend of air and recycled $CO_2$from the stripper. The lean solvent was introduced at the top of the column. Total packing was represented in the model using 30 segments with counter current flow. The liquid mass transfer film was divided into 20 segments optimized to adequately capture the absorption enhancement effect of the amine. Heat loss was neglected.

The analyzed pilot plant campaign data consisted of 12 runs with constant volumetric gas flow (≈ 0.165 actual m^3/s) and a CO_2 content around 12%. Amine concentration varied from 5 m to 9 m with most data around 8 m.. Lean loading, and solvent flow rate were also varied. Table 2 summarizes the conditions of the analyzed pilot plant runs.

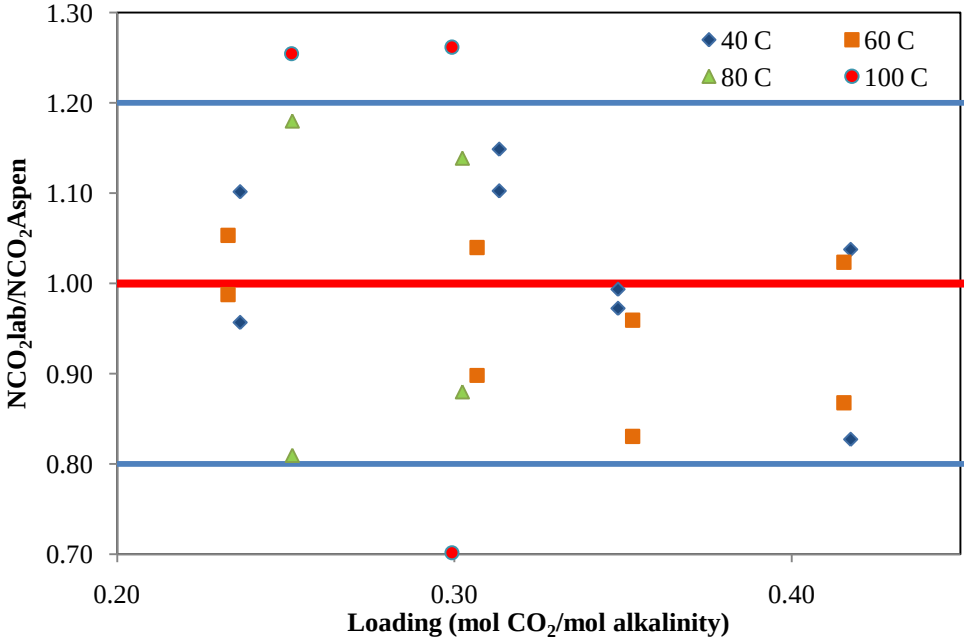

Figure 2 Comparison of flux calculated by the Aspen model and flux measured in the wetted wall column.

Table 2. Pilot plant conditions for the concentrated PZ campaign at The University of Texas at Austin. Absorber packing height = 6.1 m Mellapak 2X . Diameter = 0.427 m. Gas flow rate ≈0.165 actual m^3/s.

PZ concentration	L/G	Loading (mol CO_2/mol alkalinity)		Removal
(m)	(mol L/mol G)	Lean	Rich	(%)
7.46	5.5	0.285	0.340	85.9
7.88	5.5	0.308	0.370	66.6
9.18	4.9	0.254	0.330	87.9
7.82	4.3	0.284	0.360	68.2
8.22	6.0	0.302	0.360	77.1
8.06	5.6	0.305	0.360	73.7
7.85	6.7	0.267	0.340	92.2
7.67	5.7	0.331	0.380	48.7
4.81	7.1	0.316	0.380	60.7
4.95	6.8	0.274	0.360	88.6
4.88	5.5	0.257	0.360	78.3
4.64	4.8	0.262	0.380	66.8

Independent streams of PZ, CO_2 and water were created in the model and mixed to generate the reported solvent conditions. Nitrogen, oxygen, water and CO_2 streams were mixed to generate the inlet gas conditions. The model accuracy and quality of the data were evaluated using the parameter estimation tool in Aspen Plus® RateSep™. This tool adjusts experimental data and results to close material and energy balances and match CO_2 removal. The level of necessary adjustment is an indicator of the quality of the data and the accuracy of the model. Table3 shows the range of adjustment of the variables and parameters required to close material and energy balances. The interfacial area factor was the only manipulated model parameter. It corrected the effective interfacial area calculated using the correlation by Tsai et al[9]

The interfacial area was reduced 2% to fit the data. To close the material balance, rich and lean loadings were adjusted no more than 0.03 and no less than 0.01. Removal fraction was increased by 0.008 to 0.03. CO_2 gas outlet gas concentrations were matched to less than 4% deviation. Temperatures were adequately represented with exception of a couple of outliers. Figures 3 and 4 show the temperature profile for two runs in the PZ campaign. The temperature bulge was correctly located. Its location depends on the values for the L/G. Higher solvent flow rates move the bulge towards the bottom of the column (figure 4) and reduce its temperature.

Table 3 Pilot plant reconciliation results. 6.10 m absorber packing, 0.427 m diameter.

Variable	Specified standard deviation	Reconciled variation range	Variable	Specified standard deviation	Reconciled variation range
Area Factor	±1.0	Not applicable	T (°C)**		
Inlet liquid flow (kg/s)			Inlet Gas	±3	0.2 to 9.5
PZ	5%	-4.0% to 2.6%	Inlet Solvent	±3	-6.6 to -3.1
CO_2	5%	-2.9% to 3.9	Outlet Gas	±3	-0.19 to 2.6
H_2O	5%	-2.6% to 3.2%	Z/Z_{Total}		
Lean ldg (mol CO_2/mol alkalinity)	*	-0.01 to 0.03	0.14	±3	3.0 to 10.7
Rich ldg (mol CO_2/mol alkalinity)	±0.03	0.0004 to 0.03	0.34	±3	2.3 to 15.6
Gas mol flow (kmol/s)			0.50	±3	0.3 to 5.8
CO_2	5%	-0.2% to 8.9%	0.64	±3	-2.4 to 6.4
H_2O	5%	0.0% to 0.2%	0.72	±3	-5.9 to 2.0
N_2	5%	-3.5% to 0.04%	0.84	±3	-17.8 to -1.2
O_2	5%	-0.9% to 0.01%	0.90	±3	-19.3 to -0.5
y_{out}	5%	-0.0005 to 0.0006	1.06***	±3	-2.5 to 0.02
Removal fraction	5%	0.008 to 0.02	1.08***	±3	-3.8 to -1.3

* Lean loading was not specified directly. It was entered as individual streams of PZ, CO_2 and water.
** Z/Z_{Total} = 1 is the bottom of the column.
*** Z/Z_{Total} greater than 1 refers to thermocouples located below the packing bed.

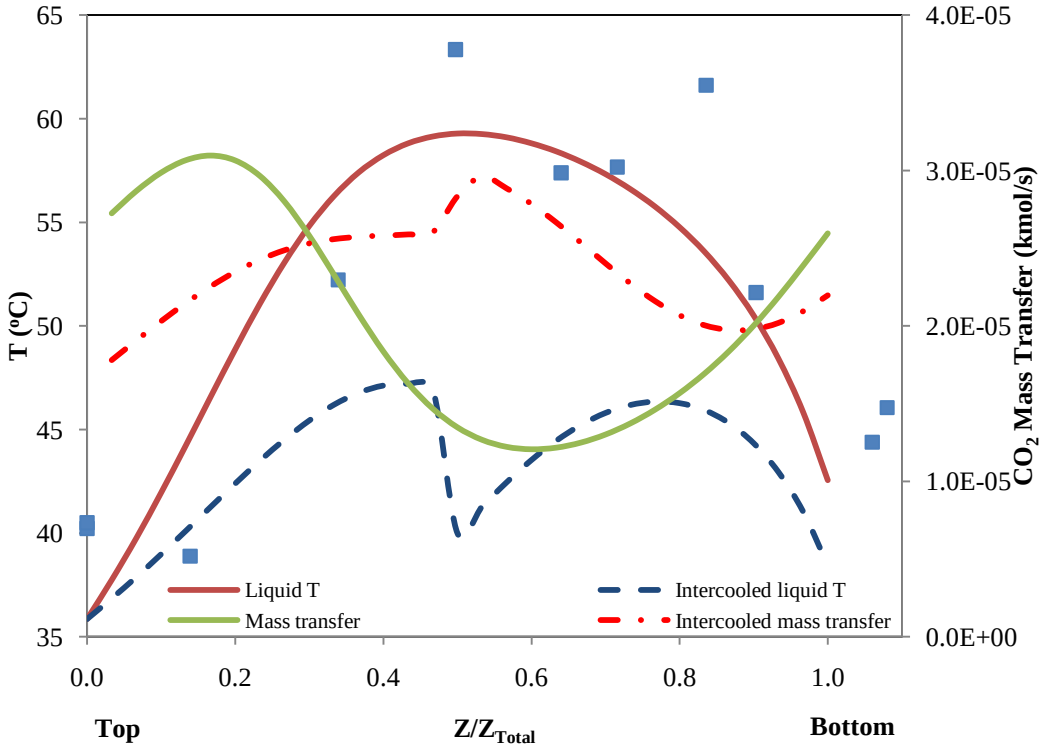

Figure 3. Liquid temperature and CO_2 mass transfer profiles for L/G = 4.5 mol/mol , 7.5 m PZ. Lean loading = 0.29. Points are pilot plant temperature data. Intercooling was placed at Z/Z_{Total}=0.5 and specified to reach 40°C. It increased CO_2 removal from 69.8% to 80.4%.

5. Performance analysis

The validated model predicted the expected performance of the absorber as a function of lean loading and L/G. (Figure 5). An additional analysis introduced an intercooling heat stream in the middle of the column (Z/Z_{Total}=0.5) to set stage temperature to 40°C. Results show that intercooling offers a benefit for all studied cases by increasing rich loading and removal. However, the benefit is negligible for conditions with low lean loading and high L/G. This result is similar to that observed by Plaza et al. for K_2CO_3/PZ [12]. Following the 90% and 80% removal curves on figure 5 it is possible to define the critical L/G region for this system. As in Plaza et al. [12] the critical L/G is located at the discontinuity observed for rich loading at constant removal. Figures 3 and 4 show the resulting profiles. Figure 3 is located near the

critical L/G so the CO_2 mass transfer approaches a pinch at the temperature bulge location ($Z/Z_{Total} \approx 0.5$). Intercooling breaks the pinch and reduces the magnitude of the bulge. Figure 4 is a high L/G case. The bulge has a lower magnitude and is not located near the mass transfer pinch.

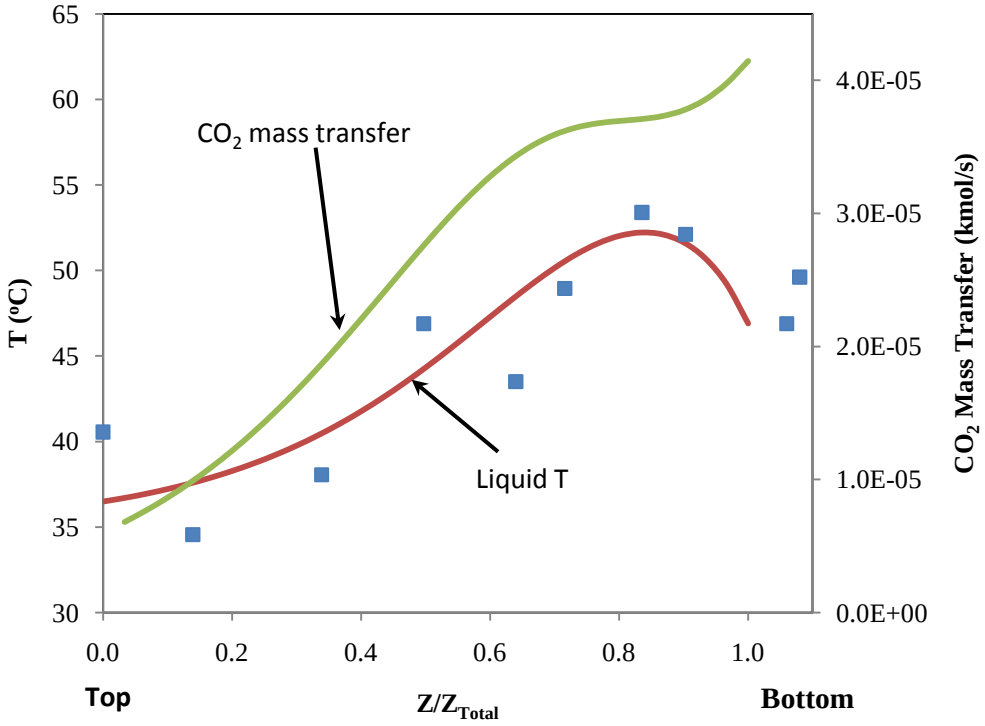

Figure 4 Liquid Temperature and CO_2 mass transfer profiles for L/G = 6.8 , 7.6 m PZ. Lean loading = 0.28 rich loading= 0.35. Points are temperature pilot plant data CO_2 removal 93.2%.

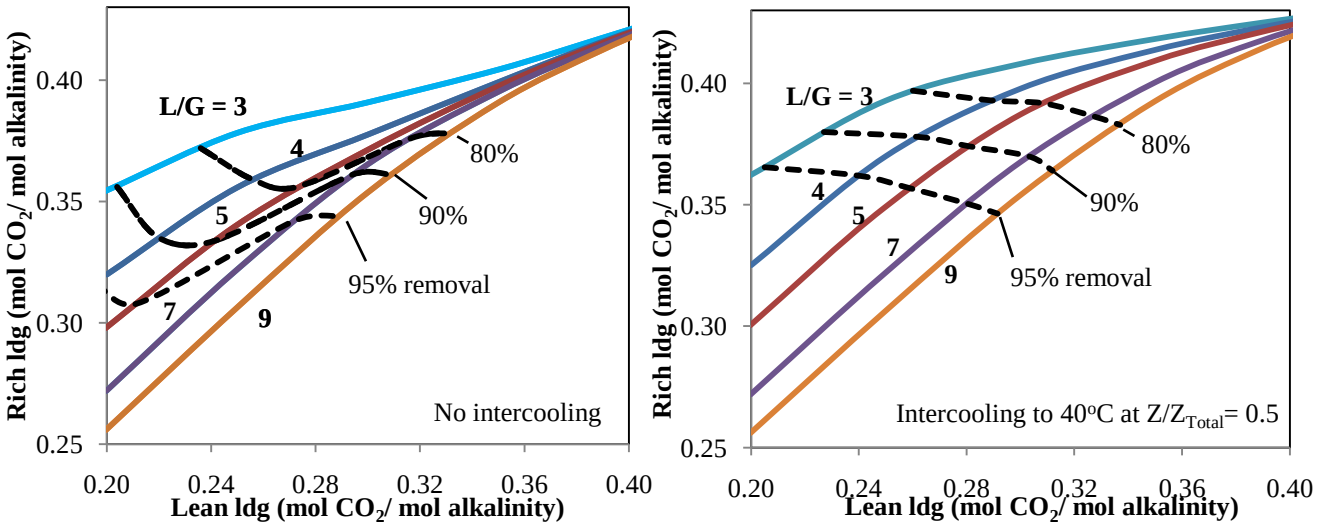

Figure 5. Effect of solvent lean loading on rich loading for 6.1 m Mellapak 2X . diameter 0.427 m, 8 m PZ. y_{CO2} = 0.12. Inlet gas and liquid T = 40° C. Constant gas flow rate = 0.165 actual m^3/s.

Table 4 is summarizes conditions for 90% removal using concentrated PZ. It combines pilot plant results with the intercooling analysis. The stripper heat rates are based on pilot plant conditions for a stripper at 138 kPa. The equivalent work is calculated following the methodology by Van Wagener[11] and assuming final product CO_2 compression to 15 MPa.

Table 4. Conditions to obtain 90% CO_2 removal using concentrated PZ . Absorber with 6.1 m of Mellapak 2X and 0.427 m diameter. Intercooling of liquid to 40°C

PZ concentration (m)	L/G (mol L/mol G)	Loading (mol CO_2/mol alkalinity)		Steam heat rate (kJ/mol CO_2)*	Equivalent work (kJ/mol CO_2)	Intercooling?
		Lean	Rich			
9	4.9	0.266	0.360	148	37.4	NO
8**	5.4	0.272	0.361	148	40.1	
8	5.9	0.294	0.374	136	35.6	YES
8***	6.7	0.320	0.389	137	33.6	

*Equivalent work obtained calculated using pilot plant conditions and the method by Van Wagener[11] assuming final compression to 15 MPa. For the intercooled systems values were extrapolated taking into account rich and lean loadings.

** Reported CO_2 removal for this case is 87.7%

***Conditions for this run require 9 m of packing height.

Plaza et al.[12] proposed an approximation of the critical L/G for the absorption of CO_2 that required the heat of absorption of the solvent and heat capacity values for gas and liquid:

$$\left(\frac{L}{G_i}\right)_c = \left(1 + (1-R)Y_{in}^{CO_2} + Y_{out}^{H_2O}\right)\left(\frac{Cp_{out}^G}{Cp_{in}^L}\right) + \frac{\left(Y_b^{CO_2} - (1-R)Y_{in}^{CO_2}\right)h_{abs}\big|_{T_b} + \left(Y_{out}^{H_2O} - Y_b^{H_2O}\right)h_{vap}\big|_{T_b}}{Cp_{in}^L(T_{in}^L - T_b)} \quad (10)$$

where: $(L/G)_c^i$ is the critical ratio of liquid to inert gas species;
Y^{H2O}, Y^{CO2} are the fractions of water and carbon dioxide respectively to inert species in the gas stream (n^{CO2}/G^i, n^{H2O}/Gi).
R is the specified removal.

Using this relation to predict the critical L/G and the methodology in Plaza et al.[12] for the analyzed system gave similar results to the observed in Figure 5 . The critical L/G for 8m PZ was predicted at 4.2 (mol L/mol G) for 90% removal and 4.4 (mol L/mol G) for 80%. The temperature bulge magnitude was also predicted within 5% of the value observed in Figure 3 (65°C)

6. Conclusions

- Pilot plant results show that it is possible to obtain 90% removal using 6.1 m of Mellapak 2X packing and concentrated PZ. The developed model is capable of predicting the necessary conditions to reach 90% removal using intercooling. (Table 4). Intercooling is capable of reducing the equivalent work by 11% since it allows the absorber to operate at higher loading values that translate in a reduction in stripper energy requirements. An additional 3 m of packing in absorber can reduce the equivalent work to 33.6 kJ/mol CO_2 which is almost 18% less than the reported value for the pilot plant for 9 m MEA by Van Wagener.[11]

- Reconciled pilot plant results demonstrate that the model is capable of simulating absorber operation. Loadings and removal fraction were matched (less than 0.03 difference). Temperature profiles were adequately traced and the temperature bulge location was closely approximated. The interfacial area factor used was equal to 0.98 showing and adequate prediction of the effective area using Tsai et al.[9].

- Intercooling is capable of increasing absorber removal by as much as 10% when the absorber is designed close to the critical L/G. The critical L/G region for this system is near 4 mol/mol as was observed in Figure 5 and in the profiles in Figure 3 where the mass transfer pinch is located close to the temperature bulge.

- This observed critical L/G (figure 5) was compared to the predicted value using the proposed equation by Plaza et al.[12] with satisfactory results. The equation predicted a value of 4.2 (mol/mol) for 90% and 4.4 (mol/mol) for 80% removal. The temperature bulge was also predicted within 5% for the critical L/G.

- The WWC model is capable of generating kinetic values for CO_2 absorption using concentrated PZ. The reported laboratory CO_2 flux data are matched with a ±20% deviation (Figure 2). Model results above 80 °C show a higher deviation from experimental data due to additional phenomena becoming predominant at these conditions, possibly the increase of diffusion effects of reactants and products.

- Preliminary evaluation of the reported pilot plant data (Figure 1) shows that the K_G is located within the expected values based on the laboratory results. This serves as a first validation of the data obtained.

7. Acknowledgements

This work was supported by the LSPower Pilot Plant Initiative and the Luminant Carbon Management Program. AspenTech provided Aspen Plus® with RateSep™. Special thanks to Dr. Frank Seibert and the staff at J.J Pickle Research Campus of The University of Texas at Austin for their operational support during the pilot plant campaign and to Stephanie Freeman for tabulating the pilot plant data.

8. References

[1] Freeman, SA; Dugas, R; Van Wagener, DH; Nguyen, T; Rochelle, GT, Carbon dioxide capture with concentrated, aqueous piperazine. International Journal of Greenhouse Gas Control **2010,** 4, (2), 119-124.
[2] Cullinane, JT. Thermodynamics and Kinetics of Aqueous Piperazine with Potassium Carbonate for Carbon Dioxide Absorption. Ph.D. Dissertation, The University of Texas at Austin, Austin, Texas, 2005.
[3] Oexmann, J; Hensel, C; Kather, A, Post-combustion CO2-capture from coal-fired power plants: Preliminary evaluation of an integrated chemical absorption process with piperazine-promoted potassium carbonate. International Journal of Greenhouse Gas Control **2008,** 2, (4), 539-552.
[4] Chen, E. Carbon Dioxide Absorption into Piperazine Promoted Potassium Carbonate using Structured Packing. Ph.D. Dissertation, The University of Texas at Austin, Austin, Texas, 2007.
[5] Appl, M; Wagner, U; Henrici, HJ; Kuessner, K; Volkamer, K; Fuerst, E Removal of CO_2 and/or COS from Gases Containing these Constituents 1982.
[6] Asprion, N; Grossmann, C Method for Removal of Acid Gases from a Glass Flow. 2004.
[7] Fraile, PT; Plaza, JM; Van Wagener, DH; Rochelle, GT, Modeling Piperazine Thermodynamics. In *International Conference on Greenhouse Gas Technologies*, Amsterdam, The Netherlands, 2010.
[8] Dugas, R. Carbon Dioxide Absorption, Desorption and Diffusion in Aqueous Piperazine and MEA. Ph.D. Dissertation, The University of Texas at Austin, Austin, Texas, 2009.
[9] Tsai, R; Seibert, F; Eldridge, B; Rochelle, GT, Influence of Viscosity and Surface Tension on the Effective Mass Transfer Area of Structured Packing. Energy Procedia **2008,** 1, 1197-1204.
[10] Dugas, R. Pilot Plant Study of Carbon Dioxide Capture by Aqueous Monoethanolamine. Master, The University of Texas at Austin, Austin, Texas, 2006.
[11] Plaza, JM; Van Wagener, D; Rochelle, GT, Modeling CO2 capture with aqueous monoethanolamine. Int. J of Greenhouse Gas Control **2010,** 4, (2), 161-166.
[12] Plaza, JM; Chen, E; Rochelle, GT, Absorber Intercooling in CO_2 Absorption by Piperazine Promoted Potassium Carbonate. AIChE J. **2009,** 56, (4), 905-914.

Available online at www.sciencedirect.com

ScienceDirect

Energy Procedia 00 (2010) 000–000

Energy Procedia

www.elsevier.com/locate/XXX

GHGT-10

UT/SRP CO_2 Capture Pilot Plant – Operating Experience and Procedures

F. Seibert[a]*, E. Chen[b], M. Perry[a], S. Briggs[a], R. Montgomery[a], G. Rochelle[b]

[a]*University of Texas at Austin, Separations Research Program, 10100 Burnet Rd., Bldg 133, Austin, TX 78758*
[b]*University of Texas at Austin, Department of Chemical Engineering, 1 Univeristy Station C0400, Austin, TX 78712*

Elsevier use only: Received date here; revised date here; accepted date here

Abstract

The Separations Research Program (SRP) pilot plant is located at The University of Texas (UT) Pickle Research Campus and has been operated as a carbon capture facility since 2002. The semi-works scale pilot facility uses air and 3-14 mol% CO_2 as flue gas as it applies the latest advancements in carbon dioxide recovery technology. The capacity of the pilot plant is approximately 15 m^3/min of gas and 130 liters/min of solvent. Past experimental studies include solvent performance characterization using potassium carbonate with piperazine, monoethanolamine, concentrated piperazine and other proprietary solvents. In recent years, the pilot plant has been utilized to determine the mass transfer and hydraulic characteristics of various structured and random packings using amine-based solvents for CO_2 absorption.

In 2002, the UT/SRP began developing improved measurement techniques and operating procedures to ensure reliable process control and closure of material and energy balances. Past experience and learning with the UT/SRP pilot plant is currently being utilized for the design and operation of several future pilot plants that will process actual coal-fired flue gas. The purpose of the presentation is to provide a brief description of the UT/SRP CO_2 capture pilot plant capabilities, innovative operational procedures and instrument accuracies. The objectives of this paper are to discuss SRP pilot plant experience including: process description, operations and control, key equipment, measurement methods including novel techniques, overall process performance, and future work.

Keywords: CO_2 capture; pilot plant, design, operation

1. Introduction

A computer controlled, state-of-the-art carbon dioxide capture pilot plant is located at The University of Texas Pickle Research Campus. Originally constructed in 1986 at a cost of $2 million (US), this multi-use pilot facility was originally used for distillation, liquid extraction and reactive separations. Starting in 2002, the pilot plant was upgraded through a series of carbon dioxide capture campaigns. A recent photo of the pilot plant is shown in Figure 1. Approximately $3 million (US) was invested to optimize the capability for carbon dioxide studies between 2002 and 2010. The investment includes a recent $425,000 (US) project supported by Emerson Process Management to upgrade the SRP control system and control room. The pilot plant is well instrumented and controlled with a DeltaV control system. The plant consists of three integrated systems, 1) absorber, 2) stripper with related heat exchange

equipment and 3) a make-up and recycle carbon dioxide system. A process flow diagram (Figure 2) and a brief description of each system are provided.

Figure 1. SRP CO_2 capture pilot plant

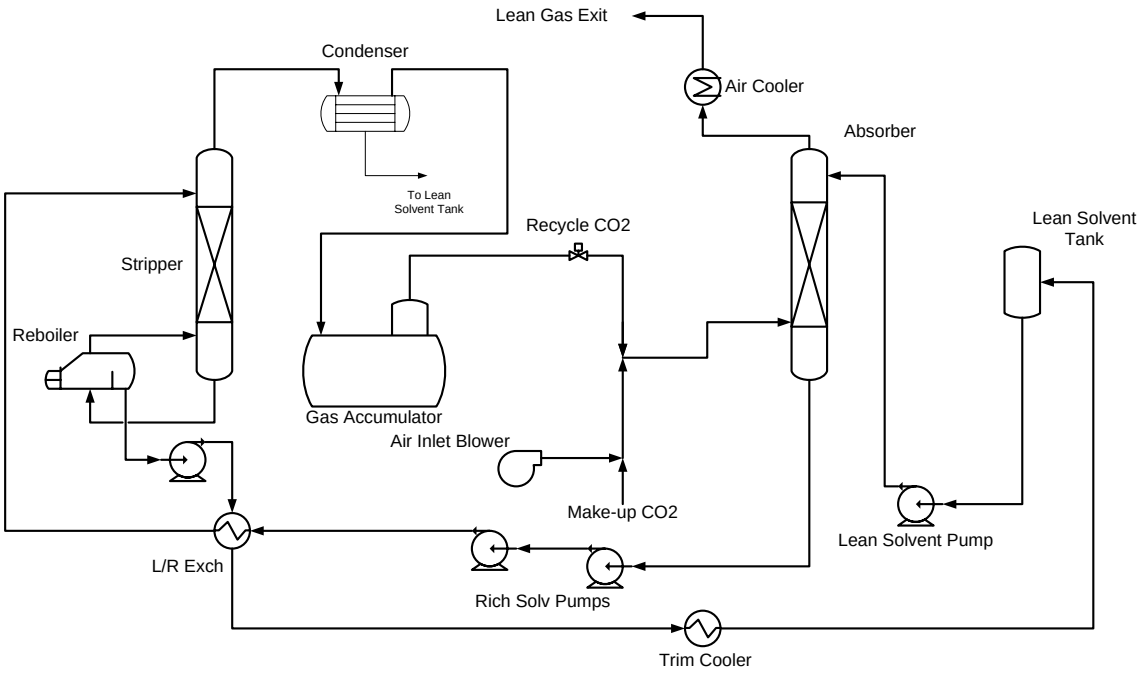

Figure 2. Process flow diagram of the SRP CO_2 capture pilot plant

2. Process Description

2.1. Absorber System

The absorber system is composed of a 4,000 liter feed tank, 5.5 kW centrifugal pumps, 30 kW blower, absorption column, air cooler and knock-out drum. The carbon steel absorption column is 42.7 cm in diameter (ID), approximately 10.7 m tall and is capable of providing two 3.07 m beds of packing. Lean amine solvent is pumped from an unheated feed tank to the top of the absorber and discharged into an orifice pipe distributor. In the middle of the column, liquid is collected on the chimney tray that feeds a second orifice pipe distributor, redistributing liquid to the lower bed of packing. The rich amine solvent leaving the column is pumped to a second booster pump and then sent to the cold side of a plate and frame cross-exchanger associated with the stripping system. The rich amine is maintained at an elevated pressure (400-500 kPa) to prevent flashing of carbon dioxide within the cross exchanger.

The lean and rich amine flow rates are measured using advanced Coriolis mass flow meterswith density and temperature readout capabilities. Ambient air is compressed with a 30 kW blower and fed into the sump section of the absorber. Recovered carbon dioxide from the stripping system and make-up carbon dioxide from the bulk storage tank are blended at the discharge of the blower to provide a simulated flue gas containing the desired composition. The entering gas is heated and humidified by the falling liquid below the packing. The gas flows upward and counter-currently contacts the falling liquid film on the packing surface. Carbon dioxide diffuses from the gas and into the liquid film. The gas travels through the two upcomer pipes on the chimney tray to the upper bed. The gas stream flows upward contacting the falling liquid film on the packing surface and then exits out the very top of the absorber. The SRP absorber does not currently provide a wash-section. Future work may incorporate a wash section by utilizing an adjacent PVC column. The exiting air is fed to a low pressure drop chilled-water air cooler. Condensed water/solvent drains from the knock out drum to the absorber feed tank while the cooled air is vented to the atmosphere.

The inlet air flow is measured with an annubar meter and is corrected for carbon dioxide concentration. Accurate air flow measurements require turbulent flow in the pipe and adequate run lengths before and after the annubar. The outlet air flow rate is not measured. The pressure drop across each bed is measured with two differential pressure transmitters ranged from 0-75 mbar and 0-7.5 mbar. The absorber sump liquid level is measured with a differential pressure transmitter. The impulse tubing of these differential pressure transmitters is purged with a small flow of nitrogen to prevent condensation in the legs of the tubing. Multiple remote temperature monitoring points are located along the column. The inlet and outlet concentrations of carbon dioxide are measured with an online Vaisala probe. The inlet and outlets Vaisala probes provide a range of 0 – 20 mol% carbon dioxide and are installed in the air piping prior to the absorber column and downstream the air cooler located at the column exit. In both cases, the Vaisala probe is located in a stream with less than 100% humidity. Liquid sample compositions are usually determined by titration. The water content within the solvent is performed using a Karl Fischer auto-titration system.

2.2. Stripping Column Configuration

The stripping system is composed of a cross exchanger, packed stripping column, kettle reboiler, condenser feed pumps and a trim cooler. The stripper is usually operated at a pressure of 165 kPa. The carbon steel stripping column is 42.7 cm in diameter (ID), approximately 10.7 m tall and is filled with two beds of packing. The metallurgy associated with the remainder the stripping system is composed of 304 or 316 SS with the exception of the reflux accumulator that is carbon steel. Rich solvent is pumped from the absorber to the cold side of the plate and frame cross exchanger. Two cross exchanger sizes have been utilized in past SRP studies. One model (160 ft^2) is used for low viscosity solvents and a second (440 ft^2) for high viscosity solvents. These cross exchangers proved capable of achieving a 6 to 8°C approach. The rich amine is heated with the hot lean solvent leaving the stripper. The hot rich amine solution is flashed just before entering the stripper. A special gas/liquid separator within the top of the tower provides non-frothy liquid to a trough drip tube liquid distributor. The flashed carbon dioxide and water (and solvent) vapor exits the top of the stripper and enters a chilled-water shell and tube condenser (237 ft^2). The

condensed water and solvent are returned to the absorber feed tank by pressure difference. The non-condensed carbon dioxide is fed to a horizontal accumulator system and also serves to control the stripper pressure. The falling and spreading liquid contacts rising vapor through the top 3 m bed of packing. The liquid is recollected on a chimney tray and then fed to a second trough drip tube distributor feeding the lower 3 m bed of packing. The redistributed liquid falls and spreads through the packing as a wetted film contacting the rising vapor. The liquid enters the column sump which is connected to a kettle type reboiler (210 ft^2) through an equalization line. Saturated steam at 1.1 MPa is supplied to the tube side of the reboiler to generate stripping vapor. The heat and flowing vapor is used to liberate and remove the carbon dioxide from the liquid solvent. The regenerated solvent, referred to as the stripper lean amine, exits the column bottom and is fed to the hot side of the cross exchanger. The cooled sipper lean amine flow is measured with an advanced Coriolis mass flowmeter with density and temperature readout capabilities. The stripper lean amine is fed to the absorber feed tank.

2.3. CO_2 Recovery and Make-Up

The overhead vapor leaving the stripper is condensed using a shell and tube chilled water stainless steel heat exchanger. The condensed water and residual solvent are sent to a 200 liter carbon steel reflux accumulator. Carbon dioxide exits the vent from the condenser and reflux accumulator and is fed to the 3,800 liter horizontal accumulator. An air-actuated control valve is used to control the stripper pressure. Essentially pure carbon dioxide exits the horizontal accumulator through the control valve and is fed to the discharge of the air blower. A CO_2 flowmeter is located on the upstream side of the pressure control valve and provides an independent measurement of the carbon dioxide absorption rate. Makeup carbon dioxide is transferred from a 5,000 kg bulk carbon dioxide storage to the discharge of the blower. The makeup carbon dioxide is metered using an advanced Coriolis flow meter and an air actuated control valve.

3. Key Measurements and Control

A number of key measurements are obtained to judge the quality of the pilot plant data including absorber carbon dioxide material balances (transfer rates), stripper heat loss, and stripper heat balance. The online inferred measurement of carbon dioxide dissolved in the solvent was found to be extremely valuable in the control of the absorption/stripping process.

3.1 Absorber Carbon Dioxide Material Balance

The SRP carbon dioxide capture pilot plant offers versatile operation, and it is capable of equipment modifications as well as additions of skid mounted equipment. The pilot plant routinely obtains absorber carbon dioxide transfer material balances in the range of 93-98% and stripper energy balances of 96-99%. For a recent study of a concentrated piperazine solvent, typical examples of CO_2 transfer material balances are shown in Table 1. The corresponding energy balance for this run was 98.3 %.

Table 1. Typical Material Balance. (Based on 2008 Run 5 with Concentrated Piperazine)

Parameter	Value, kg/hr	Deviation from Average
CO_2 transfer into the solvent[1]	236	5.8%
CO_2 transfer out of the air[2]	208	6.7%
CO_2 leaving the stripper[3]	224	0.5%
Average CO_2 transfer rate and deviation	223	4.3%

[1] Measured from averaged inlet and outlet flowrates and titrations
[2] Measured from averaged inlet gas flowrate and inlet and outlet Visala CO_2
[3] Measured from averaged flow transmitter off horizontal accumulator

3.2 Heat loss

While the stripper is insulated with calcium silicate, heat loss at elevated temperatures and pressure must be accounted for. Heat loss experiments were carried out prior to the carbon dioxide absorption using water and operating at total reflux. The difference in reboiler duty and condenser duty was assumed to be a result of heat loss. The heat loss was determined to be a function of the average internal column temperature and the ambient temperature shown in equation 1. The coefficient, C_f, represents the product overall heat transfer coefficient and the column surface area. It should be noted that the coefficient doubles in the presence of rain. The heat loss is usually 10-20% of the total heat supplied to the reboiler.

$$Q_{loss} = C_f \ (T_{col} - T_{amb}) \qquad (1)$$

Where C_f = 0.18 for reboiler duties greater than 160 KW
= 0.15 for reboiler duties less than 160 KW
Q_{loss} = heat loss, KW
T_{col} = average temperature within the stripper, F
T_{amb} = ambient temperature, F

3.3 Stripper Heat Balance

An energy balance around the stripper routinely achieved 95-99% balances. The heat balance was calculated from the equation 2.

$$Heat\ Balance = \left(\frac{Q_{cond} + Q_{loss} + Q_{abs} + Q_{bot} + Q_{gas} - Q_{feed}}{Q_{reb}} \right) * 100 \qquad (2)$$

Where Q_{cond} = sensible heat removed the condenser cooling water
Q_{loss} = estimated heat loss
Q_{abs} = total heat of absorption of carbon dioxide
Q_{bot} = sensible heat leaving column bottoms prior to cross exchanger
Q_{gas} = sensible heat of carbon dioxide leaving condenser
Q_{feed}= sensible heat of rich amine entering stripper and leaving cross exchanger, no phase change is assumed.
Q_{reb} = reboiler heat duty

3.4 Carbon Dioxide Loading Control

SRP's early campaigns suffered from not knowing the real-time carbon dioxide loading concentrations. Plant runs tended to have significant upsets as a result. Lab studies indicated that the carbon dioxide concentration could be inferred from an accurate measurement of the liquid density. Thus carbon dioxide concentrations in the lean and rich amine could be estimated from the solvent densities and temperatures provided by the advanced Coriolis mass flowmeters. The solvent density was observed to vary linearly with density. These data were correlated and the resulting models were placed into our process control system (DeltaV). The correlations were checked against titrations of actual samples. In general, a small correction factor was added to the laboratory correlation. The correlations for carbon dioxide with 30 wt% MEA are given below and were programmed into our DeltaV control system. One would expect that the correlations to be adjusted slightly for each advanced Coriolis mass flow meter. The applications of the estimated online carbon dioxide loading values greatly improved the control of the carbon dioxide capture pilot plant relative to the earlier carbon capture pilot plant campaigns.

For 30% MEA,

Lean Amine

$$X_{CO2} = ((1028.5 * SG\_in - 1031.7) * 0.001 + 0.00036 * T\_in - 0.0374) * 0.92$$

Rich Amine

$$X_{CO2} = ((1028.5 * SG\_out - 1031.7) * 0.001 + 0.00036 * T\_out - 0.0374) * 0.93$$

Stripper Lean Amine

$$X_{CO2} = ((1028.5 * SGF\_in - 1031.7) * 0.001 + 0.00036 * TF\_in - 0.0374) * 0.94$$

Where: SG = specific gravity of the solvent measured at the MicroMotion flowmeter
T = temperature measured by the advanced Coriolis flowmeter, °F
X_{CO2} = weight fraction of CO2 in solvent

4. Operational Experience

4.1 Once Through vs. Recycled Air

The SRP currently feeds air spiked with carbon dioxide on a once-through basis. In earlier operations, the air was recycled. Unstable operations and fluctuating air flow were observed with the recycled air. Carbon dioxide transfer material balances were poorer in the recycled operation. However, in the current once-through operation the solvent is exposed to a higher concentration of oxygen. Typical SRP carbon dioxide capture pilot campaigns are usually less than three weeks, so oxidative solvent degradation is not an important issue.

4.2 Saturated vs Unsaturated Inlet Air

Attempts to humidify the inlet air by re-vaporizing condensed water from the stripper were made in early campaigns which ultimately lead to significant problems with inlet gas temperature control, inlet carbon dioxide measurements, solvent concentration, and carbon dioxide material balances. These problems were eliminated by feeding unsaturated air to the absorber.

4.3 Process Dynamics

The process dynamics of the absorber/stripper is quite interesting in that the stripper response is relatively slow while the absorber is quite fast. This is a result of the liquid inventory which is far greater in the stripper. While the process dynamics were not studied in detail, consistent trends were observed. Run conditions were typically changed by modifying either the liquid and/or the gas rate by 10-15%. Under these conditions, the pilot plant typically required 1-1.5 hours to approach steady state. In some runs, the lean loading was modified 25%. Under these conditions, the plant generally required 2-4 hours approach steady state.

4.4 Corrosion Inhibitors

A vanadium based corrosion inhibitor was used in SRP's early campaigns involving piperazine and potassium carbonate, and these runs suffered from significant foaming. This may not be attributed to the inhibitor but also the high surface area (330 m^2/m^3) structured packing utilized in the study. Rinse water used to remove residual solvent resulted in considerable cost and was treated as hazardous due to the heavy metal content. The inhibitor did not prevent a carbon steel reboiler tube leak observed immediately following the campaign during a hydrocarbon distillation test. The carbon steel reboiler was replaced with a 304 SS unit. Corrosion inhibitors were no longer used in subsequent tests. No corrosion problems have been observed since the replacement of reboiler tube sheet. It should be noted that the SRP pilot plant only operates in the carbon dioxide capture mode for 20-30% of the year and all of the piping and heat exchangers are constructed of stainless steel.

4.5 Absorber Processing Rates

The processing rates of the SRP absorber were generally constrained between providing adequate liquid density for gas/liquid contact area and flooding. Typical liquid superficial velocities ranged from 250 to 900 liters/m^2-min.

Typical superficial gas velocities ranged from 40 to 120 meters/min. The SRP system is capable of liquid flowrates of 150 liters/min and gas flowrates of 25 m^3/min.

4.6 Packing Mass Transfer Efficiency for Carbon Dioxide Absorption

The height of a transfer unit will be considerably higher than distillation values generally reported by the packing vendors. Pilot tests are recommended to obtain design values. The HTUog will vary considerably with packing and solvent type. HTUog values measured by the SRP are often in the range of 2 m to 6 m.

4.7 Foaming

Foaming has been observed with the SRP carbon dioxide capture testing. While fundamental studies have not been performed, several trends have been observed. Foaming appeared more often during testing with aged solvents and high surface area structured packings. Again pilot tests should be performed to identify potential problems with foaming and the identification of proper procedure to minimize or eliminate foaming.. Foaming tended to reduce column capacity by 100%.

4.8 Stripper Flashing Feed

The hot rich amine leaving the cross exchanger will consist of two phases, gas and liquid . The two-phase mixture will resemble a frothy, foamy liquid and should not be fed to a standard liquid distributor. At the SRP, this mixture has been fed to standard trough distributor and was observed to overflow the distributor leading to poor liquid distribution and stripper performance. Care must be taken to provide liquid only to the distributor which will require separation of the flashed gas from the liquid. This may be accomplished using a flash tank prior to entering the stripper and a special flashing feed distribution system. At present, the SRP uses a novel and potentially patentable device to separate the gas and liquid as it enters the stripper.

5. Future Work

In late 2010, a skid-mounted, high temperature two-stage flash stripping system will be studied and compared with the traditional packed stripping column using concentrated piperazine. The semi-works scale two-stage flash stripping system will be studied to validate recent process simulation studies. A photo of the multi-stage flash stripping system is shown in Figure 3. The thermal stability of concentrated piperazine permits high temperature regeneration (150 °C) and the high temperature two-stage flash process produces CO_2 at significantly higher pressures (17 and 11 bar). The higher regeneration pressure reduces the capital and operating costs of the compressor required for sequestration (150 bar). In addition, two flash tanks should be more cost effective than a packed column.

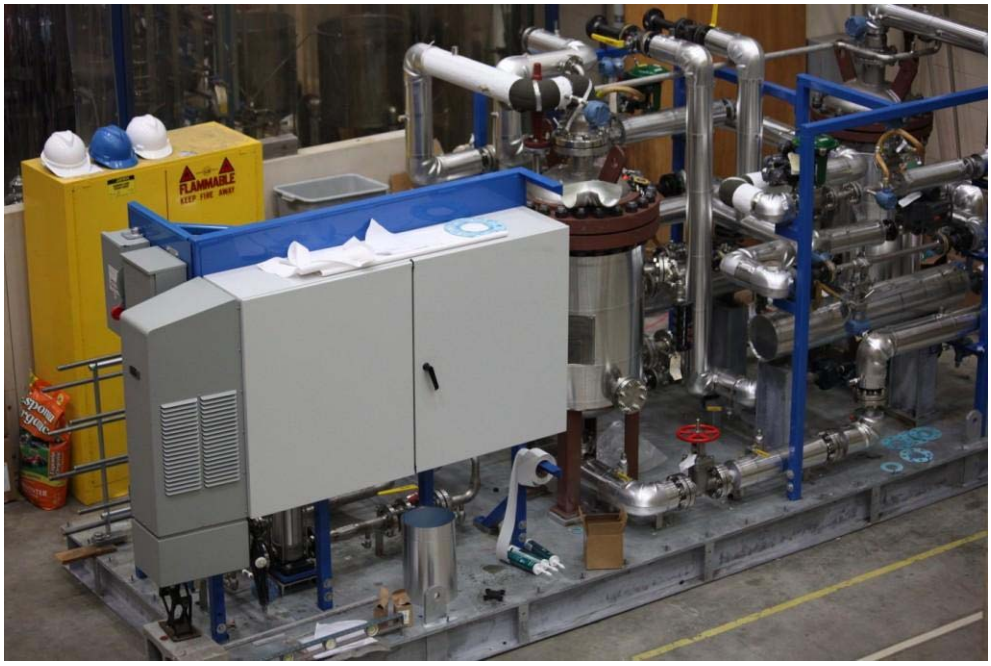

Figure 3. High temperature two-stage flash stripping system

The effect of absorber intercooling will also be studied by the SRP in late 2010. Collected liquid from the absorber chimney tray will be cooled and returned to the liquid distributor feeding the lower bed. Process simulations have shown that intercooling can enhance performance for processes with large temperature bulges.

The correlation of carbon dioxide concentration with liquid density has proven extremely valuable in the operation of the absorber and stripper. Future work supported by Emerson Process Management is ongoing to correlate amine concentration with pH. The initial results appear promising for the inferred online measurement of amine concentration with accurate measurements of pH.

Wireless instruments provided by Emerson Process Management are also being studied and offer the advantage in eliminating the need for conduit. Wireless instruments are also nicely suited for the testing of skid-mounted system.

Acknowledgements
The authors acknowledge the support of the Luminant Carbon Management Program, CO_2 Capture Pilot Plant Program, Process Science and Technology Center, the Separations Research Program, Raschig-Jaeger and Emerson Process Management.

Available online at www.sciencedirect.com

ScienceDirect

Energy Procedia 00 (2010) 000–000

Energy Procedia

www.elsevier.com/locate/XXX

GHGT-10

Stripper configurations for CO_2 capture by aqueous monoethanolamine and piperazine

David H. Van Wagener[a], Gary T. Rochelle[a]1*

Department of Chemical Engineering, The University of Texas at Austin, 1 University Station C0400, Austin, TX 78712, USA

Elsevier use only: Received date here; revised date here; accepted date here

Abstract

Absorption/stripping with aqueous amines is a competitive technology for CO_2 capture from coal-fired power plants. A major challenge is reducing the energy requirement in the stripper, which has contributions from the reboiler(s), pumps, and compressors. In this study, the effects of flowsheet complexity and solvent choice were explored. Five flowsheets were stimulated in Aspen Plus® using 9 m MEA and 8 m PZ. Although the absorber was not modeled, the rich loadings used for the two solvents accounted for the faster CO_2 reaction rate of PZ in the absorber. The simulations demonstrated that increased configuration complexity improved the efficiency of the absorber by 5%-8%, depending on the solvent, operating temperature, and rich loading. The best improvement from the simple stripper was observed with the interheated column. The improvements were attributed to better reversibility of the more complex flowsheets. Furthermore, 8 m PZ consistently had a lower energy requirement than 9 m MEA. Configurations with packed columns exhibited improvements in energy consumption of 9%-11%.

Keywords: carbon dioxide; monoethanolamine; piperazine; stripper; complexity

1. Introduction

CO_2 capture is becoming an important topic to improve the environmental friendliness of heavily used energy sources like coal- and natural gas-fired power plants. Absorption/stripping by aqueous amines is considered the best option due to its proven applicability with the industry-standard solvent of monoethanolamine (MEA). Although 7 m MEA is proven technology, 9 m MEA has also been shown to be a feasible solvent [1]. Additionally, 8 m concentrated piperazine (PZ) is expected to improve overall performance with properties like higher resistance to oxidative and thermal degradation, higher reaction rate with CO_2, and more efficient stripping for regeneration [2]. In addition to the new solvent, advanced configurations have previously been explored [3]. The advanced configurations reduce energy usage by increasing the reversibility and decreasing the exergy loss [4]. The advanced

* Corresponding author. Tel.: +1-512-471-7230; fax: +1-512-471-7060.
E-mail address: gtr@che.utexas.edu.

process arrangements were used with a new model of concentrated PZ to determine the potential overall improvement over a base case with MEA.

2. Process Model

2.1. Thermodynamic model

A rigorous thermodynamic model was difficult to develop due to the large number of species present in the H_2O-PZ-CO_2 system, including a non-volatile zwitterion. A model for PZ has been developed [5], and its structure is based on the ΔG, ΔH, Cp, and τ method of specification in the electrolyte non-random two-liquid (e-NRTL) activity coefficient model used by Hilliard [6]. In the Aspen Plus® regression of this model, a large database of thermodynamic properties was used, including CO_2 solubility, amine vapor pressure, enthalpy of absorption, heat capacity, and NMR speciation.

2.2. Stripper representation

The simulations used Aspen Plus®, and their scope included the stripping vessels, rich and lean pumps, cross exchanger, and multistage, intercooled compressor. Several variables were held constant across all simulations to permit adequate comparison between solvents and configurations. The simulations were run with a constant rich CO_2 loading, and lean loading was varied and optimized. A 5°C cold side approach was specified on the main cross exchanger, and the reboiler(s) also had a 5°C approach. In configurations with multiple pressure stages, equal vapor production on a molar basis was maintained. By stipulating equal steps across the pressure stages, the most reversible operation was preserved to improve efficiency. Also in an effort to enhance reversibility, the analysis used a constant maximum temperature in the regenerator, which consequently resulted in variable pressures at different lean loadings. Finally, the outlet pressures of the pumps were specified to consistently account for frictional and gravitational losses in the pipes. These approximations considered 50 kPa of pressure drop in the cross exchange, and an appropriate amount of head to reach the elevation gain in configurations with packed columns.

Configurations with packed columns used a height of 5 m, which was enough packing to maintain a rich end pinch for all runs. Since all runs were pinched, they could be compared on a common level. IMTP#40 random packing was used with the Onda correlations for mass transfer coefficient and interfacial area and with the Chilton and Colburn correlation for heat transfer coefficient. Both of these correlations are standard options in Aspen Plus®. The reactions within the column were specified as equilibrium, assuming that the chemical reaction during desorption was fast enough that the mass transfer was the limiting step. The diameter of the column was always specified to have a maximum fractional capacity of 0.8. Configurations with flash tanks were modeled with thermal and chemical equilibrium.

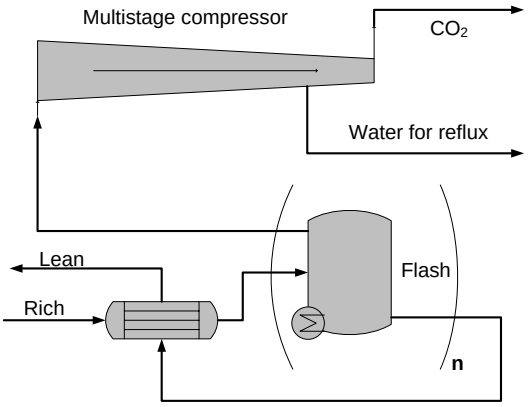

Figure 1: Multi-Stage Heated Flash (1SF and 2SF)

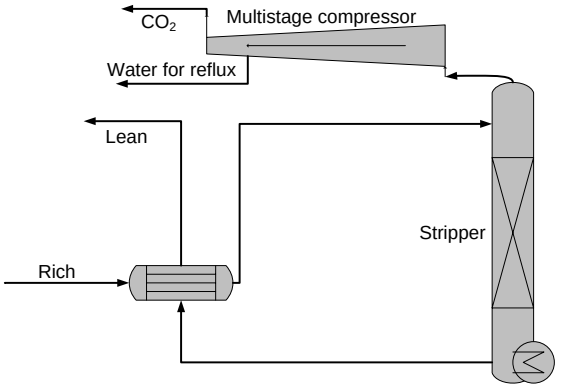

Figure 2: Simple Stripper (SS)

2.3. Configurations

The main goals of this study were to address the effect of configuration complexity on process efficiency and how this effect differed between MEA and PZ. Five configurations were explored, and they are described in Figures 1 to 4. The 1- and 2-stage flash configurations were derivations of the multi-stage flash arrangement (Figure 1). These configurations would be cheaper to construct as compared to the simple stripper (Figure 2). The adiabatic flash configuration (Figure 4) was an attempt to improve the efficiency of heat recovery by taking a small step down in pressure to approach absorber conditions, which consequently reduced the temperature and flashed off some CO_2 and water vapor. Without precooling, this low-pressure vapor was compressed to the main column pressure before returning it to the bottom of the stripper. This configuration introduced an additional pressure stage without adding an extra heating element. The interheated column also introduced complexity into the base case flowsheet (Figure 3). It had promise to improve the efficiency by approaching continuous heat exchange along the length of the packed column. The interheating occurred in the middle of the column and heated 80% of the solvent with an approach temperature of 5K. A continuously heated column would have the smallest exergy loss within the scope of the column itself.

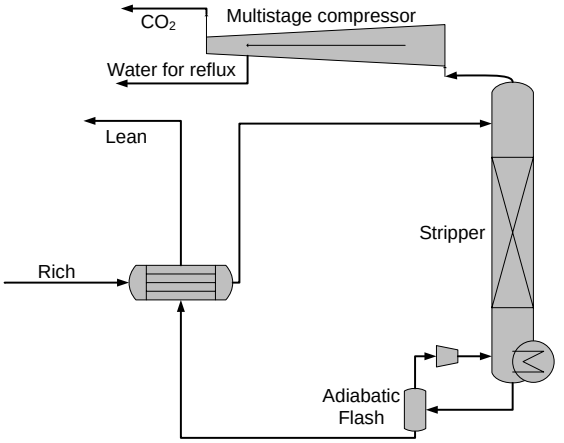

Figure 4: Packed Column with Adiabatic Lean Flash (ALF)

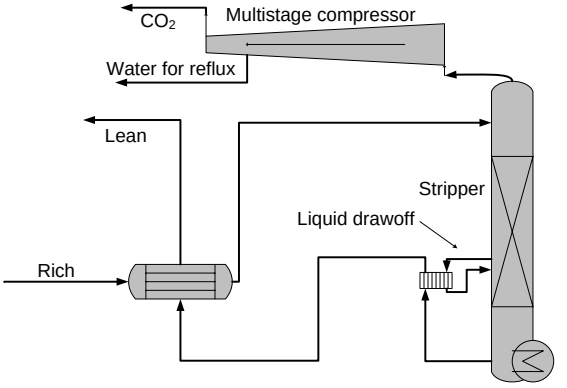

Figure 3: Interheated Column (IHC)

2.4. Absorber performance approximation

In order to appropriately compare the performance of the stripper using 9 m MEA and 8 m PZ, it was desired to determine a rich loading for each solvent which accounted for the difference in reaction rates in the absorber. The overall reaction rate constant k_g' combined the kinetic and mass transfer effects and can be used to calculate CO_2 flux with the gas side driving force between the bulk gas and interface concentrations:

$$\boldsymbol{N_{CO_2} = k'_g\left(P_{CO_2} - P^i_{CO_2}\right)} \quad (1)$$

Data for k_g' in MEA and PZ was tabulated by Dugas [7] as a function of P^*_{CO2} at 40°C, which was directly indicative of the loading of the solution. The rate constant was also measured with varying temperature and solvent concentration, both of which had little effect (between 40°C and 60°C). This data was correlated to give k_g' as a function of P^*_{CO2} at 40°C for MEA using 40°C and 60°C data for 7 m, 9 m, 11 m, and 13 m MEA. A similar correlation was derived for PZ using 40°C and 60°C data for 2 m PZ, 5 m PZ, and 8 m PZ. The final correlation for each is shown below:

$$\boldsymbol{MEA}: \quad \boldsymbol{ln\, k'_g = -0.40 \cdot ln\, P^*_{CO_2,40°C} - 14.35} \quad (2)$$

$$\boldsymbol{PZ}: \quad \boldsymbol{ln\, k'_g = -0.41 \cdot ln\, P^*_{CO_2,40°C} - 13.44} \quad (3)$$

Next, corresponding rich and lean loadings sets for MEA and PZ were calculated which balanced the log mean fluxes, thereby indicating roughly equivalent absorber performance for the two solvents while using identical packing heights. Loading was defined in this work as the ratio of CO_2 moles per mole of alkalinity. This definition accounted for the presence of two amine groups on the PZ molecule. The lean loading was specified to match 10% of the rich equilibrium partial pressure since 90% removal in the absorber is expected.

Table 1: Rich and Lean Loadings for MEA and PZ to Match Log Mean Flux in Absorber

MEA rich		MEA lean		PZ rich		PZ lean	
P^*_{CO2} (kPa)	ldg	P^*_{CO2} (kPa)	ldg	P^*_{CO2} (kPa)	ldg	P^*_{CO2} (kPa)	ldg
5.0	0.50	0.50	0.45	8.4	0.42	0.84	0.33
1.5	0.48	0.15	0.40	5.0	0.40	0.50	0.31

Prior work [8] used a common rich and lean loading set for MEA corresponding to 5 kPa/0.5 kPa of P^*_{CO2} at 40°C. Table 1 shows that these loadings for MEA correspond to loadings for PZ which provide 8.4 kPa/0.84 kPa P^*_{CO2} at 40°C. It is expected that a more realistic loading set for PZ is 5 kPa/0.5 kPa, so this pair and the corresponding set for MEA will be used for the simulations. These estimates assume an isothermal absorber at 40°C.

2.5. Multistage compressor correlation

The multistage compressor block in Aspen Plus® (MCOMP) had convergence issues due to the high final pressure, small presence of solvent in the vapor, and use of the complex e-NRTL property method. To avoid its questionable behavior affecting the simulations, a correlation for the compressor work was separately developed to incorporate into the final energy requirement. An Aspen simulation with an isolated MCOMP block was run with the SRK property method and a feed consisting of CO_2 saturated with water at 40°C. Each vapor stream was intercooled to 40°C with water knockout between compression stages. The minor presence of solvent was ignored since it would have a negligible contribution to the total work requirement. The inlet pressure of the CO_2/H_2O mixture was varied from 0.8 to 20 bar. For each inlet pressure, the minimum number of compression stages was used to maintain a compression ratio no greater than 2. The outlet pressure was held constant at 150 bar. The compressor polytropic efficiency was taken to be 80%. The pressure drop per stage was assumed to be 20% of the suction pressure.

The final regressed form of the multistage compressor correlation was:

$$W_{comp}\left(\frac{\text{kJ}}{\text{gmol CO2}}\right) = \begin{cases} 4.572\ ln\left(150/P_{in}\right) - 4.096, & P_{in} \le 4.56 \text{ bar} \\ 4.023\ ln\left(150/P_{in}\right) - 2.181, & P_{in} > 4.56\ bar \end{cases} \quad (4)$$

where P_{in} is the compressor feed vapor coming from the highest pressure stage in bar.

3. Results

Equivalent work was used to compare the performance between the different configurations and solvents. Equivalent work (kJ/gmol CO_2), calculated as in equation 5 below, uses the total heat duty (Q_i, in kJ/gmol CO_2), temperature of heat source (T_i), pump work, and compressor work to calculate a total work requirement on an electricity basis. The pumps and compressors would be run with electricity directly drawn from the power plant, and the reboiler(s) uses steam that could otherwise generate electricity in the plant turbines. The net work of the lean pump was neglected if the stripper pressure was higher than the required outlet pressure to pump the solvent back to the top of the absorber. The equation uses the 5 K driving force for the reboiler(s). The sink temperature (T_{sink}) was assumed to be 313K. Pump efficiency was 72%, and compressor work was calculated by equation 4.

$$W_{eq} = \sum_{i=1}^{n_{reboilers}} 0.75 Q_i \left(\frac{T_i + 5K - T_{sink}}{T_i + 5K}\right) + W_{pumps} + W_{comps} \quad (5)$$

A numerical system was developed to rank the configurations by complexity level. The stripper section of each flowsheet was evaluated, and each of the following counted for one complexity point:

- Reboiler/heat exchanger
- Vessel
- Packing

The complexity levels for all configurations are listed in Table 2. As an example, the simple stripper had a complexity level of 3 because it contained one at each of the above complexity types: reboiler, vessel, and packing. The adiabatic lean flash had an additional credit over the other configurations because moving the first compressor stage down into the stripper eliminated the need for a precooler.

Table 2: Configuration Abbreviations and Complexity Levels

	Configuration	Complexity
1SF	1-Stage flash	2
SS	Simple Stripper	3
ALF	Stripper with adiabatic lean flash	3
2SF	2-Stage flash	4
IHC	Interheated column	5

3.1. MEA results

The 5 configurations listed in section 2.3 were evaluated using 9 m MEA. Simulations were run with two different rich loadings as suggested by section 2.4: 0.50 mol CO_2/mol MEA corresponding to 5 kPa P^*_{CO2} at 40°C, and 0.48 corresponding to 1.5 kPa P^*_{CO2} at 40°C. High temperature yields the best performance in the stripper due to greater CO_2 pressure, but the maximum temperature considered for MEA was 120°C due to elevated thermal degradation rates at higher temperatures [9]. Temperatures lower than 120°C were not of interest in this study, so only the reboiler temperature of 120°C was used for MEA. The work requirement and optimum lean loading for each configuration at the two rich loadings is detailed in Table 3.

Table 3: Work Requirement for Configurations Using 9 m MEA. Heating to 120°C and Lean Loading adjusted to minimize equivalent work.

Configuration	Equivalent Work	Lean Loading	Equivalent Work	Lean Loading
	kJ/mol CO_2	*mol CO_2/mol alk*	*kJ/mol CO_2*	*mol CO_2/mol alk*
	0.5 rich ldg		*0.48 rich ldg*	
1SF	34.9	0.41	37.2	0.39
SS	34.0	0.39	36.1	0.36
ALF	33.6	0.39	35.4	0.36
2SF	33.5	0.39	35.5	0.38
IHC	32.5	0.37	34.2	0.35

The lean loading was optimized for each configuration to minimize equivalent work. Every case demonstrated an overstripped optimum lean loading, where the P^*_{CO2} at 40°C was less than 10% of the rich equilibrium partial pressure. This result would be fortunate news for the design of the absorber because the lower lean loading would provide a greater driving force for absorption and reduce the size of the column. The best case scenario with a 0.5 rich loading improved the optimum performance of each configuration by 5% to 9%, with the greatest influence on the 2-stage flash. The performance typically improved with increased complexity. All configurations except the 1-stage flash showed improvement over the simple stripper base case. The best performance for both rich loadings was with the interheated column, demonstrating a 7.8% and 4.6% improvement over the simple stripper using rich loadings of 0.48 and 0.50, respectively.

3.2. PZ results

Similar to the MEA simulations, the 5 configurations were evaluated using 8 m PZ. PZ has a fast reaction rate with CO_2 and should be expected to achieve a high rich loading in the absorber. However, it was uncertain whether a rich loading with an equilibrium partial pressure higher than 5 kPa was feasible. Therefore, a rich loading of only 0.40, corresponding to 5 kPa P^*_{CO2} at 40°C, was used. PZ demonstrates a higher resistance to thermal degradation than MEA, and its ceiling temperature is 150°C [2]. It was also desired to observe the performance of PZ in a process designed for MEA with reboiler temperature(s) of 120°C. For these reasons, PZ was evaluated using 120°C and 150°C. The work requirement for each configuration at the two operating temperatures is detailed in Table 4.

Table 4: Energy Requirement with 8 m PZ. 0.4 Rich Ldg, 0.31 Lean Ldg (*= 0.28 Lean Ldg)

Configuration	Equivalent Work	
	kJ/mol CO_2	
T (°C)	*150*	*120*
1SF	36.1	39.2
SS	33.1	33.7
ALF	32.3	32.9
2SF	34.1	35.7
IHC	30.9*	31.8

The lean loading was optimized for each configuration. However, the optimal lean loading demonstrated understripping in many cases, where the P^*_{CO2} at 40°C of the solution with the optimal lean loading was greater than 10% of the rich equilibrium partial pressure. Some cases, particularly those with high complexity and/or high operating temperature, yielded a saturated optimum lean loading which was equal to the 90% removal spec. The only case which had an optimum lean loading that was overstripped was the interheated column at 150°C. The equivalent work reported for each configuration in Table 4 was for the saturated lean loading except for the interheated column at 150°C which had an optimum lean loading of 0.28. As described in section 3.1, optimum cases with overstripping would be ideal for the absorber to achieve the desired performance and rich loading. The improvement in the equivalent work between 120°C and 150°C was marginal, only 1% to 3% for the cases with optimized lean loadings, but the tabulated values with lean loadings at saturation or lower demonstrated a 2% to 8% improvement. Additionally, the reduced capital cost of the multistage compressor would favor operating at the elevated temperature of 150°C. The effect of complexity on the equivalent work was still noticeable, with a 5% and 6% maximum improvement over the simple stripper base case for 120°C and 150°C, respectively.

3.3. Comparison of MEA and PZ Performance

The use of 8 m PZ with a rich loading of 0.4 in the place of 9 m MEA with a rich loading of 0.48 yielded a 3%-11% improvement depending on the configuration. When changing only the solvent, the simple stripper showed the greatest improvement of 11%, followed by the interheated column with an improvement of 10%, and the adiabatic lean flash had the third-best improvement of 9%. The 1- and 2-stage flash configurations did not benefit much by using 8 m PZ, demonstrating only a 4% and 3% improvement, respectively. Table 5 summarizes the results of important solvent/configuration combinations. The total equivalent work was separated into its three components as used by equation 5: heating work, pump work, and compression work.

Table 5: Noteworthy Solvent/Configuration Combinations

System	Equivalent Work	Lean Ldg	Pressure	Reb duty	Q work	Pumps	Comp
	kJ/mol CO_2	*mol/mol*	*bar*	*kJ/mol CO_2*			
MEA - SS - 0.5 rldg	34.0	0.39	5.1	131	21.1	1.5	11.5
MEA - SS - 0.48 rldg	36.1	0.36	3.9	137	21.9	1.6	12.6
MEA - 2SF - 0.48 rldg	35.5	0.38	7.1 / 4.4	145	23.1	1.5	10.8
PZ - SS - 150C	33.1	0.31	9.3	112	22.6	1.5	9.0
PZ - 2SF - 150C	34.1	0.31	13.4 / 9.4	120	24.2	1.8	8.1
PZ - IHC - 150C	30.9	0.28	7.6	100	20.1	1.0	9.8

Various mechanisms within the stripper dictated the improvement of each combination. Changes in compression and pump work were straightforward. Compression work decreased due to any increase in the pressure of the vessel(s), and pump work increased due to any increase in the pressure of the vessel(s). However, pump work also decreased with reduced lean loading due to increased capacity and decreased solvent circulation rate. Several mechanisms directed changes in the heating work. First, increased reboiler temperature raised the heating work since the steam used would be of higher quality. Next, improved solvent capacity decreased the heat duty since less solvent would need to be heated to balance the temperature approach across the cross exchanger. Finally, the difference in the heats of desorption of CO_2 of the solvents would affect the amount of heat duty dedicated to desorption. The improvements of each combination in Table 5 can be explained using these mechanisms. 8 m PZ consistently performed better than 9 m MEA, mostly due to the fact that it could be operated at 150°C. At the

higher temperature, the vessel pressures were significantly higher in the PZ cases, drastically reducing the compression work.

A comparison which demonstrated another major difference between the two solvents was the difference between the simple stripper and 2-stage flash. The flash configuration was capable of reducing the work requirement with MEA, but the performance worsened when transitioning from the simple stripper to 2-stage flash with PZ. Comparing the changes in work components for this modification with each solvent, it was apparent that PZ was not able to effectively use the 2-stage flash because it did not experience as significant of a drop in compression work as compared to MEA. Coupled with a slightly greater effect on both heat work and pump work, the 2-stage flash did not prove to be a better option with PZ. The Gibbs-Helmholtz relation suggests that the low heat of desorption of PZ yields a low CO_2 partial pressure in the stripper compared to an equal change in temperature with MEA. The partial pressure of water is roughly the same for the two solvents at equally high temperature, so the selectivity for CO_2 is lower with PZ than for MEA. Heat of desorption has previously been linked to improving performance for this reason [8]. Configurations using PZ need to effectively utilize the latent heat contained in the stripping steam which otherwise escapes with the CO_2, eventually becoming wasted heat as the steam is knocked out in the condenser preceding the multistage compressor.

Table 5 clarifies the source of improvement with the interheated column. First, since the heat contained in the lean stream was more effectively recycled to the column, the reboiler duty decreased, so the heating work also decreased. Next, the column pressure was lower with the lower lean loading, so the rich pump pressure change decreased by 15%. The lower optimum lean loading caused the solvent rate to decrease by 25%, so the overall decrease in rich pump work was 33%. The compression work increased by 9% due to the lower column pressure, but the other savings resulted in a much more efficient configuration.

Table 6: Rich/Lean Loadings Accounting for Varying Reaction Rates

Solvent	Rich		Lean	
	P^*_{CO2} *(kPa)*	*ldg*	P^*_{CO2} *(kPa)*	*ldg*
MEA	1.5	0.479	0.09	0.360
PZ	4.5	0.394	0.45	0.308

Finally, the difference in optimum lean loadings between MEA and PZ needed to be addressed. As previously pointed out, the process optimally utilized overstripping for MEA, but only typically 90% removal for PZ. The rich loadings of 0.48 and 0.4 for MEA and PZ, respectively, were calculated to be an accurate comparison in section 2.4 when paired with the respective lean loadings corresponding to 90% removal. The magnitude of k_g' increases with decreasing loading. Since MEA optimized with lower lean loading, the log mean CO_2 flux in the absorber would be greater, so the rich and lean loadings for PZ needed to also be lower to similarly increase its log mean flux in the absorber. Table 6 summarizes the final set of rich and lean loadings for 9 m MEA and 8 m PZ. The optimized runs in section 3.1 demonstrated optimum lean loadings from 0.35 to 0.37, so a representative value of 0.36 was selected. The new calculated loadings for PZ were not significantly different than the originally selected values. Consequently, the simple stripper at 150°C had an energy requirement of 33.57 kJ/mol CO_2, only 0.4 kJ/mol CO_2 (1.4%) greater than the requirement with a rich loading of 0.4. Approximately the same change could be expected for the other configurations.

4. Conclusions

With both MEA and PZ, greater complexity in the stripper usually resulted in better energy efficiency due to a closer approach to a reversible process. The improvement over the simple stripper depended on the solvent, rich loading, and reboiler temperature, but the interheated column consistently required 4.8% to 7.8% less equivalent work.

8 m PZ consistently had a lower energy requirement than 9 m MEA when using a rich loading which accounted for the faster reaction rate of PZ in the absorber. The simple stripper and complex configurations with packed columns demonstrated substantial improvement of 9%-11% better energy performance with PZ. The multi-stage flash configurations were 3%-4% better with PZ.

Increasing the stripping temperature of 8 m PZ from 120°C to 150°C reduced the work requirement by 1% to 3%.

Reducing the rich loading of the MEA runs to a more conservative value of 0.48 reduced the efficiency of each configuration by 2%-9%. The configuration least affected by the loading change was the interheated column.

5. Acknowledgments

This work was supported by the Luminant Carbon Management Program. AspenTech provided Aspen Plus®.

6. References

[1] Plaza, J.M., Van Wagener, D.H., Rochelle, G.T. Modeling CO2 capture with aqueous monoethanolamine. IJGGC 4(2): 161–6. 2010.

[2] Freeman, S.A., Dugas, R., Van Wagener, D.H., Nguyen, T., Rochelle, G.T. Carbon dioxide capture with concentrated, aqueous piperazine. IJGGC 4(2): 119-24. 2010.

[3] Van Wagener, D.H., Rochelle, G.T. Stripper Configurations for CO2 Capture by Aqueous Monoethanolamine. Chem. Eng. Res. Des. 2010. *Submitted*.

[4] Leites, I.L., Berchenko, V.M. Application of the Second Law of Thermodynamics for Optimization of Absorption Processes to Decrease the Energy Consumption. ENSEC International Conference. Cracow, Poland, 1993.

[5] Frailie, P.T., Plaza, J.M., Van Wagener, D.H., Rochelle, G. Modeling piperazine thermodynamics. Proceedings of the 10th International Conference on Greenhouse Gas Control Technologies; Energy Procedia, Amsterdam, The Netherlands, 2010.

[6] Hilliard, M.D. A Predictive Thermodynamic Model for an Aqueous Blend of Potassium Carbonate, Piperazine, and Monoethanolamine for Carbon Dioxide Capture from Flue Gas. Ph.D. Dissertation. The University Of Texas at Austin. 2008.

[7] Dugas, R., Rochelle, G. Absorption and desorption rates of carbon dioxide with monoethanolamine and piperazine. Proceedings of the 9th International Conference on Greenhouse Gas Control Technologies; Energy Procedia, Washington, DC, USA, 2009.

[8] Oyenekan, B.A., Rochelle, G.T. Alternative Stripper Configurations for CO2 Capture by Aqueous Amines. AIChE Journal 53 (12): 3144-54. 2007.

[9] Davis, J., Rochelle, G. Thermal degradation of monoethanolamine at stripper conditions. Proceedings of the 9th International Conference on Greenhouse Gas Control Technologies; Energy Procedia, Washington, DC, USA, 2009.

Available online at www.sciencedirect.com

ScienceDirect

Energy Procedia 00 (2010) 000–000

Energy Procedia

www.elsevier.com/locate/XXX

GHGT-10

Oxidation of amines at absorber conditions for CO_2 capture from flue gas

Alexander K. Voice, Gary T. Rochelle*

Department of Chemical Engineering, Luminant Carbon Management Program, University of Texas, 1 University Station C0400, Austin, TX 78712, USA

Elsevier use only: Received date here; revised date here; accepted date here

Abstract

Eleven amines that are suitable for CO_2 capture by an amine scrubbing system have been evaluated for their stability in the presence of oxygen. Six amines produced measureable quantities of ammonia in the order: 1,2-diamino-propane (DAP) > monoethanolamine (MEA) > ethylene diamine (EDA) > 3-methylamino-1-propylamine (MAPA) > potassium glycinate (GLY) > potassium taurinate (TAU). Five other amines produced no detectable ammonia (<0.2mmol/kg/hr): piperazine (PZ), 1-methyl-piperazine (1-MPZ), diglycolamine (DGA®), 2-amino-2-methyl-propanol (AMP), and 1-methyl-diethanolamine (MDEA). The effect of temperature on ammonia production from aqueous MEA in the presence of Inh. A was also measured. The activation energy of ammonia production varied from 86 kJ/mol with no inhibitor to 133 kJ/mol with 200 mM Inh. A. At 55°C, ammonia production was reduced by 74-99% with 50-200 mM Inh. A.

Keywords: Oxidative degradation; amine screening; ammonia rates; activation energy.

1.0 Introduction

Aqueous monoethanolamine (MEA) is the baseline solvent for carbon dioxide capture from flue gas by absorption-stripping. MEA is an attractive solvent, because it is relatively cheap, has a fast reaction rate with CO_2, and has a high heat of absorption. Unfortunately, MEA solutions are corrosive to metal surfaces, prone to oxidation by oxygen in the flue gas, and polymerize with CO_2 at temperatures above 120°C [1, 2]. Degradation can contribute up to 10% of the total cost of a CO_2 capture process [3].

The overall degradation rate is a combination of thermal degradation and oxidative degradation. The lean amine enters the absorber at approximately 40°C. However the heat of absorption of CO_2 causes a temperature bulge in the middle or top of the absorber, which may reach 70°C [4]. At these conditions, dissolved oxygen will react with MEA to produce ammonia and other products. Dissolved oxygen that does not react in the absorber will react in the cross exchanger or the stripper, where the temperature is 100-120°C. When the MEA enters the cross exchanger, stripper, and reboiler, it will also begin to react irreversibly with CO_2 to form substituted ureas and diamines at the high temperature [1, 2]. Degradation products, which can act as chelating agents, are more corrosive than the neat MEA solution, which can cause iron concentrations as high as 160 ppm (2.9 mM) [5]. These metals are catalytically active and promote oxidative degradation when they come in contact with oxygen. Metals such as Cu and V, which can be added as corrosion inhibitors, have also been shown to catalyze oxidation of MEA [6, 7, 8]. Thus, the degradation rate by oxidation alone in a commercial process can be confounded by other factors.

Oxidative degradation can be decoupled from thermal degradation by conducting experiments at low temperatures (40-70°C) where no thermal degradation is observed. Known amounts of metal salts are added to simulate the conditions of an industrial absorber, where some corrosion is inevitable. Under these conditions, oxidation of MEA probably proceeds by a free radical mechanism (Figure 2). The process may be initiated by the oxidation of ferrous to ferric forming a free radical [9]. Free radicals in solution can abstract a hydrogen atom from the alpha carbon of MEA. The MEA radical then reacts with molecular oxygen to produce an MEA-peroxide radical. The MEA-peroxide radical can go on to react with another molecule of MEA to produce the MEA peroxide, which can react again to produce two

free radicals [10, 11, 12]. Termination occurs by the reaction of two free radicals to form molecular products. Decomposition of the MEA peroxide can produce formaldehyde, ammonia, and hydroxyacetaldehyde.

$Fe^{2+} + O_2 \rightarrow Fe^{3+} + HO\bullet$ Initiation

$MEA + R\bullet \rightarrow MEA\bullet$ Propagation
$MEA\bullet + O_2 \rightarrow MEAOO\bullet$
$MEAOO\bullet + MEA \rightarrow MEAOOH + MEA\bullet$
$MEAOOH \rightarrow MEAO\bullet + \bullet OH$
$MEAOOH + MEA \rightarrow MEA\bullet + MEAO\bullet + H_2O$

$MEAOO\bullet \rightarrow\rightarrow 2\ CHO + NH_3$ Ammonia Production
$MEAOO\bullet \rightarrow\rightarrow HOCH_2CHO + NH_3$

Ammonia is expected to be a primary oxidation product of MEA [6,7,8,13,14,15,16,17], thus it can be used as a marker for MEA oxidation.

2.0 Previous Studies on MEA Oxidative Degradation

2.1 Studies on Ammonia Production from MEA Solutions

Kindrick et al. [16] studied the relative resistance to oxidation of commercially available amines for use in a submarine atmosphere purification system. 2.5 N amine solutions were contacted with 1000 L of 50% O_2 with 50% CO_2 at a rate of 100 mL/min and a temperature of 80°C. Ammonia leaving the reactor was condensed and quantified. Solutions were also analyzed before and after for total alkalinity, total primary amine, and total nitrogen (Table 1). AMP (2-amino-2-methyl-propanol) and MDEA (n-methyl-n,n-diethanolamine) showed significant resistance to oxidation. MEA and its derivatives oxidized in the order of MMEA (n-methyl-n-ethanolamine) > DEA (n,n-diethanolamine) > MEA > DGA (2-(2-aminoethoxy)-2-ethanol) > TEA(n,n,n-triethanolamine).

Table 1. Summary of selected amines screened in [16] for oxidative stability

Amine	Alkalinity Loss (%)	Primary Amine Loss (%)	Total Nitrogen Loss (%)	NH_3 Rate (mM/hr)
MEA	46	44	11	0.4
DGA	33	24	10	0.7
AMP	4	13	4	1.0
MDEA	2	--	1	0.1
DEA	61	--	16	1.0
TEA	6	--	0	0.2
MMEA	80	--	11	1.1

Hofmeyer [17] studied oxidative degradation of 20% wt MEA at 75°C in the presence of 1atm O_2. In these experiments, the solution alkalinity decreased at a rate of 37 mM/hr. NH_3 accounted for 40% (15mmol/L/hr) of the lost alkalinity.

Blachly and Ravner [8] studied the production of NH_3 from MEA solutions in the presence of various dissolved metals (iron, nickel, chromium, and copper) as well as a number of inhibitors. Of those tested, only EDTA (ethylenediamine tetra-acetic acid) and bicine reduced NH_3 production from MEA solutions at 55°C in the presence of metals. At 98°C, only the combination of both inhibitors reduced NH_3 production, while at 138-148°C, no inhibiting effect was observed.

A series of studies at the University of Texas [6, 7, 15] examined the rates of ammonia production from 7 m MEA solutions in the presence of various metals. These experiments were performed at 55°C with 0-2% CO_2 in air, and using a gas rate of 5-9 LPM with 350 ml of solution. Ammonia evolution rates and volatile MEA losses in the gas phase were continuously monitored by a hot gas FTIR analyzer.

Chi [15] confirmed the findings of Blachly and Ravner, demonstrating that the NH_3 rate from MEA solutions increased with additions of iron (Fe^{2+} or Fe^{3+}), and that EDTA and bicine are both effective inhibitors. NH_3 rates were 6-8 times faster in the presence of CO_2 at 0.4 loading, and two times faster in 12 m MEA than 2.5 m MEA.

Goff [6] expanded on this work by studying the effect of several catalysts and inhibitors on the ammonia rate, as well as varying the oxygen and MEA concentration. Copper was found to be a potent catalyst for ammonia production at concentrations as low as 0.1 mM. The NH_3 rate increased with higher MEA concentration, and showed a linear dependence on oxygen concentration. Of the inhibitors tested, Inh. A was the most effective. Addition of 100 mM Inh. A reduced the NH_3 rate by a factor of 10 in the presence of Cu and by a factor of 1.5 in the presence of Fe [18].

Sexton [7] sought to identify additional nitrogen-containing degradation products and close the MEA material balance. He oxidized MEA in the presence of Fe and Cu and analyzed both the gas and liquid phase. NH_3 was the only significant gas phase degradation product detected. NO, NO_2, N_2O, and methylamine were not detected in significant

quantities. In the liquid phase, HEF [1-(2-hydroxyethyl)-formamide] and HEI [1-(2-hydroxyethyl)-imidazole] were determined to be significant nitrogen-containing oxidation products. MEA loss in the liquid phase was found by the difference between the amount detected in the initial and final samples using cation chromatography. The MEA loss was found by subtracting vapor phase losses (detected using the FTIR analyzer) from the liquid phase losses. In the presence of iron only, NH_3 accounted for at least 90% of the lost MEA. Rates for NH_3 and amine loss from previous work are summarized in Table 2.

Table 2. Previous Oxidative Degradation Experiments on MEA

Author	Catalyst (mM)	Rate (mmol/kg/hr)	Conditions
Chi	0.1 Fe^{2+} added	1.0 (NH_3)	55°C, 21kPa O_2
Chi	1.0 Fe^{2+} added	1.5, 1.6, 1.6 (NH_3)	
Goff	1.0 Fe^{2+} added	1.7 (NH_3)	55°C, 21kPa O_2, 2kPa CO_2
Goff	0.1 Fe^{2+} added	1.4, 2.0, 2.0 (NH_3)	
Sexton	1.0 Fe^{2+} added	1.7, 1.7 (NH_3) 1.9, 2.0 (MEA)	55°C, 15kPa O_2, 2kPa CO_2
Hofmeyer	no metals added	36 (alkalinity)	75°C, 100kPa O_2
Kindrick	0.5-1.0 Fe (metal coil)	0.4 (NH_3) 1.7 (total N) 6.8 (alkalinity) 6.7 (primary amine)	80°C, 50kPa O_2
Blachly and Ravner	0.5 Fe	0.2 (NH_3)	80°C, 21kPa O_2, 1kPa CO_2

2.2 Studies on Inhibitor A

Goff showed that Inh. A was effective at reducing ammonia production from MEA under a variety of conditions [6, 18]. These included rich and lean loading, as well the presence of iron and copper. Goff showed that addition of 100 mM Inh. A to 7 m MEA was enough to significantly reduce the ammonia rate. Goff also demonstrated that Inh. A was a more effective inhibitor than several other reaction inhibitors, including hydroquinone, manganese, ascorbic acid, sodium sulphite, and formaldehyde. EDTA, as well as several other chelating agents and stable salts, were also found to be inferior to Inh. A, in terms of the reduction in ammonia observed for a given amount of inhibitor.

Sexton used an accelerated degradation test and liquid phase analysis to determine the effectiveness of Inh. A at reducing amine loss (as opposed to simply limiting NH_3 production) and production of degradation products in MEA solutions. 7 m MEA with 100 mM Inh. A had no detectable amine loss after ten days of oxidation, compared with a loss of nearly 30% of the MEA after less than one week from the uninhibited solution. Furthermore, no degradation products were observed in the inhibited solution (with the exception of ~1mM formate), whereas the uninhibited solution had high concentrations of 1-(2-hydroxyethyl-formamide) (380 mM), 1-(2-hydroxyethyl)-imidazole (280 mM), and heat stable salts [7].

3.0 Experimental Procedures

3.1 High Gas Flow Degradation Apparatus

Amine oxidation was carried out in a 1L jacketed glass reactor with five sampling ports. The ports were used to control and monitor the experiment by measuring the temperature of the reactor, providing a continuous supply of makeup water, pumping gas from the reactor to the analyzer, and agitation to the reactor. The temperature of the reactor was set using a circulating temperature bath with dimethyl silicone oil as the heat transfer fluid. A platinum resistance thermometer inserted into the reactor was used to monitor temperature. A centrifugal pump provided a continuous supply of make-up water to the reactor at a rate of 0.29-1.22mL/min, depending on the temperature of the reactor. The water balance was maintained by periodic visual inspection of the reactor and adjustment of the pump rate as needed. In-house air was blended with high-purity carbon dioxide to 2% using two mass flow controllers and supplied to the reactor at a dry gas rate of 5SLPM. Gas exiting the reactor was analyzed by a hot gas Fourier-transform infrared (FTIR) spectrometer. The solution was continuously agitated at 1440 RPM using an agitator and stainless-steel swivel paddle stir rod, which entered through the top of the reactor. The apparatus is essentially the same as that described in Goff and Sexton [6, 7], with the exception that the air pre-saturator was not used. Instead, makeup water was supplied directly to the reactor, which allowed for better control of the water balance while varying the reactor temperature.

3.2 Typical Experimental Run

Amine screening for oxidative degradation was carried out by addition of 350 mL amine solution to the high gas flow (HGF) apparatus. All amines were commercially available—solutions were prepared by addition of Millipore de-ionized water to the amine and subsequent loading with high purity carbon dioxide. The concentration was selected based on the solubility limit of the amine in the loaded aqueous solution, as well as the practical concentration for use in

a carbon capture facility, and the availability of previous data. Metal catalysts were added as their sulfate salts in dilute sulfuric acid solution after the ammonia rate had reached a steady state. In early experiments, only 1.0 mM of Fe^{2+} was added to the solution. Later, a mixture of 0.4 mM Fe^{2+}, 0.1 mM Cr^{3+}, and 0.05 mM Ni^{2+} was used instead. After the ammonia rate had returned to steady state, 100 mM of Inh. A was added to the solution. Inh. A was tested in most cases where significant ammonia production was observed.

To determine the temperature dependence of the ammonia rate from MEA solutions, the reactor temperature was initially set to 40°C. Air (98%) and CO_2 (2%) were sparged into the reactor at a dry gas rate of 5 SLPM. Gas exiting the reactor was pumped to the FTIR analyzer. The water balance was maintained by periodic visual inspection of the liquid level in the reactor and manual addition of water or adjustment of the pump rate when necessary. The total mass of solution was measured before and after each experiment, and the average of the two numbers was used for calculation of the NH_3 rate. The difference in the two numbers, due to water balance issues, was typically less than 10%. The system was allowed 12-24 hours to reach steady state before adjusting the temperature. In some cases, the system did not reach steady state after more than 24 hours, in which case the rate was determined two hours after the last temperature change.

3.3 Liquid-Phase Analysis

Liquid samples were taken at the start and end of each experiment. The total alkalinity of the samples was determined by titration with 0.2 N sulfuric acid. The amine concentration was determined by cation chromatography using aqueous methane-sulfonic acid as the eluent. Heat stable salts were detected by anion chromatography using aqueous sodium hydroxide as the eluent. Amides of formate and oxalate were quantified by treatment of 0.5 mL of sample with 1.0 mL of 5 N NaOH, followed by detection of the resulting carboxylic acid using anion chromatography. The result is reported as "total formate" or "total oxalate." This technique has been used previously to detect amides in degraded amine solutions [7,19].

3.4 Gas-Phase Analysis

Gas leaving the reactor was passed through a mist eliminator into a heated line at 180°C. The gas went through a heated pump into the FTIR analyzer. The analyzer continuously measured the IR absorbance spectrum of the gas passing through and averaged them together every five minutes. The analyzer was calibrated to detect a variety of expected degradation products, including NH_3, NO, NO_2, formaldehyde, acetaldehyde, methanol, and methylamine. However only NH_3 was produced in detectable quantities at steady state. Water, CO_2, and volatile amine were also recorded for each experiment. The inversion transition peak, which occurs at ~900-1000cm^{-1} was the major peak used for NH_3 quantification. Further details of this method have been described previously [6].

4.0 Results

4.1 Amine Screening for Ammonia Production Rates

Results for the stability of commercially viable amines for CO_2 capture studied in this work are summarized in Table 2. For amines where the ammonia rate did not reach steady state after several days, the initial rate (rate after two hours of contact with air) is reported. Many of the amines in this study were stable in the presence of oxygen, or fragmented to form nitrogen-containing compounds other than ammonia.

Table 3. Ammonia Production Rates from Amine Solutions at 55°C, 21kPa O_2/2kPa CO_2, 1440RPM, 350mL solution volume, 5SLPM dry gas rate. Experiments ranged from 2-7 days to achieve a steady state for NH_3 production from the neat solution, in the presence of metal, and in the presence of Inh. A.

Amine	Structure	Conc. (m)	NH_3 Rate (mmol/kg/hr)	Catalyst (mM)	Inh. A Effect
1,2-diamino-propane (DAP)	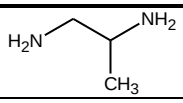	8.0	2.68	SS metals	no effect
monoethanolamine (MEA)	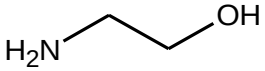	7.0	1.55	SS metals	reduce
ethylene diamine (EDA)	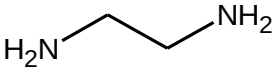	8.0	0.78	1.0 Fe	reduce
N-methyl-1,3-propanediamine (MAPA)	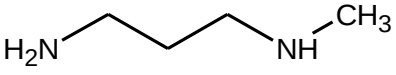	8.0	0.47	SS metals	reduce
Potassium glycinate (GLY)	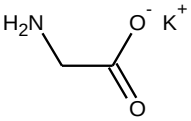	3.6	0.16	1.0 Fe	no effect

Potassium taurinate (TAU)	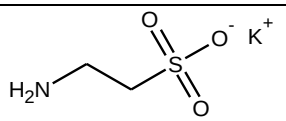	1.9	0.02	1.0 Fe	reduce
2-(2-aminoethoxy)-2-ethanol (DGA®)	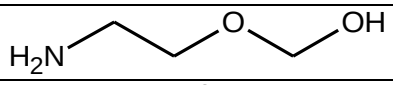	17.7	<0.02	1.0 Fe	increase*
2-amino-2-methyl-1-propanol (AMP)	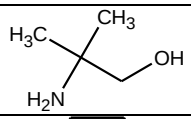		<0.02	1.0 Fe	not tested
Piperazine (PZ)	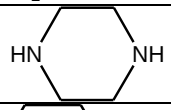	8.0	<0.02	1.0 Fe	not tested**
N-methyl-piperazine (NMPZ)	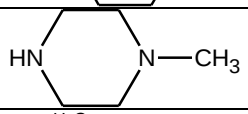	8.0	<0.02	1.0 Fe	not tested
N-methyl-diethanolamine (MDEA) / PZ	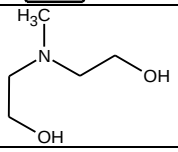	7.0 / 2.0	<0.02	1.0 Fe	not tested***

*DGA® produced ammonia in a separate experiment at 70°C (Figure 3) where Inh. A increased the ammonia rate.
**Inh. A may be effective with 8 m PZ, because it has been shown to reduce foaming in oxidized PZ solutions [20].
*** Inh.A was not effective in 7 m MDEA at 90°C [21].

Amines that produced ammonia were tested for their response to Inh. A. When Inh. A was effective, a single addition of 100 mM resulted in an immediate and significant drop in NH_3 production (Figures 1, 2, and 3). This was the case for EDA, MEA, MAPA, and TAU. In the case of DGA®, ammonia production actually increased from 6.1 to 10 mmol/kg/hr (Figure 2).

The liquid phase analysis (Table 4) indicates that amine loss and alkalinity loss are generally in agreement with one another. Volatile losses often account for a significant amount of amine loss or alkalinity loss, whereas ammonia losses are comparatively small. Heat stable salts detected in final samples are also reported in Table 4. In general, heat stable salts are observed in solutions that produced ammonia. A notable exception to this is MAPA, which produced a significant amount of ammonia but did not produce any heat stable salts.

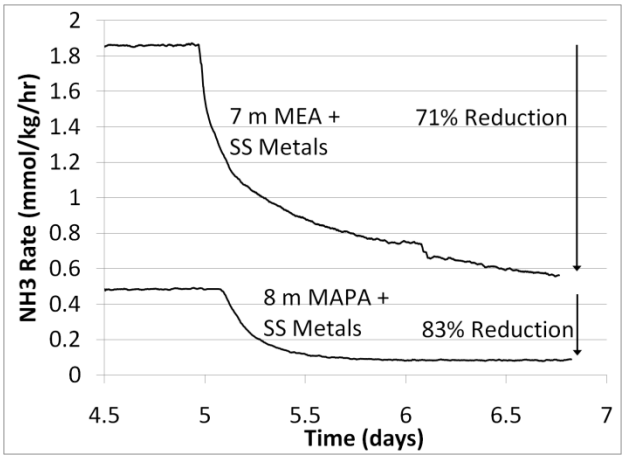

Figure 1. NH_3 production with 100 mM Inh. A at 55°C from 7 m MEA and 8 m MAPA with 0.4 mM Fe/0.1 mM Cr/0.05 mM Ni

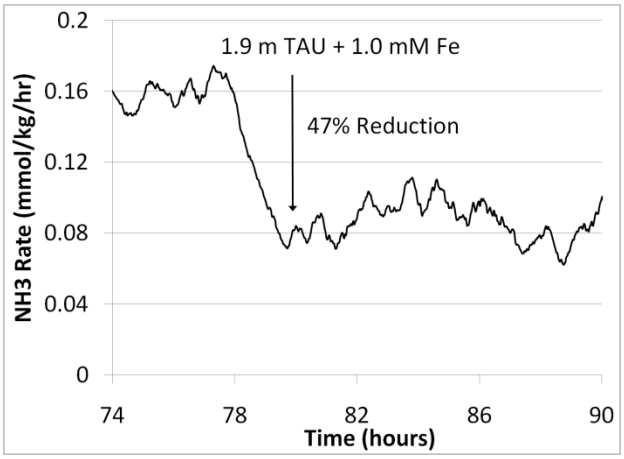

Figure 2. NH_3 production with 100 mM Inh. A from 1.9 m TAU with 0.4mM Fe/0.1mM Cr/ 0.05 mM Ni at 55°C

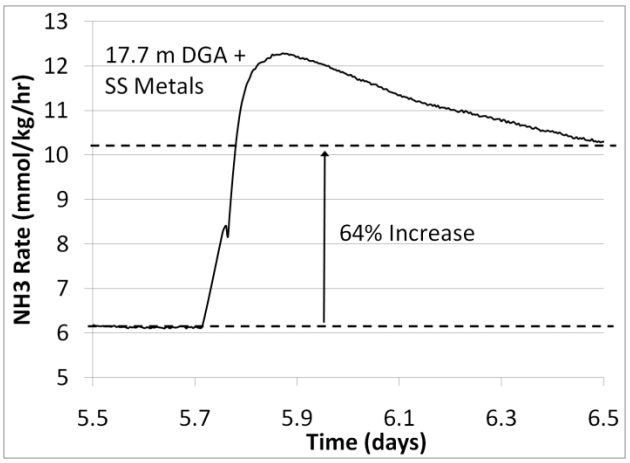

Figure 3. Ammonia production with 100 mM Inh. A from 17.7 m DGA® in the presence of 0.4 mM Fe, 0.1 mM Cr, and 0.05 mM Ni

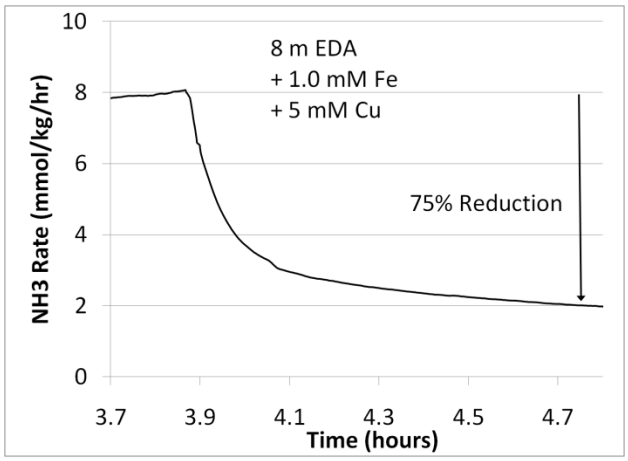

Figure 4. Effect of 100 mM Inh. A on ammonia production from 8 m EDA in the presence of 1.0 mM Fe and 5.0 mM Cu

Table 4. Liquid phase analysis for amines screened in the HGF apparatus. 55°C, 21 kPa O_2/2 kPa CO_2, 1440 rpm, 350 mL solution volume, 5 SLPM dry gas rate

Amine	Time (days)	Amine Loss (mmol/kg)	Alkalinity Loss (mmol/kg)	Volatile Loss (mmol/kg)	Total Formate (mmol/kg)	Total Oxalate (mmol/kg)	Nitrate (mmol/kg)	Nitrite (mmol/kg)
DAP	6.8	500	600	190	5	0	1	1
MEA	6.8	400	400	280	57	13	4	9
EDA	6.0	400	400	30	42	1	2	2
MAPA	7.3	300	400	80	<0.5	<0.5	<0.5	0
GLY	2.8	--	--	--	4	1	0	8
TAU	3.8	--	--	--	1	0	0	0
DGA®	3.5	0	300	30	3	0	0	0
AMP	3.0	700	700	930	<0.5	<0.5	<0.5	<0.5
PZ	7.3	<50	<50	80	1	<0.5	<0.5	<0.5
NMPZ	4.9	2300	2300	2070	1	<0.5	<0.5	<0.5
MDEA/PZ	6.2	300/0	300	40/50	<0.5	<0.5	<0.5	<0.5

4.2 Inhibition of Oxidative Degradation by Inh. A

Inh. A has been shown to reduce NH_3 production and amine loss from MEA solutions [6]. In this work, NH_3 rates were measured for MEA in the presence of 0.4 mM Fe^{+2}, 0.1 mM Cr^{+3}, 0.05 mM Ni^{+2}, and at various temperatures and concentrations of Inh. A (Figure 5). The ammonia production exhibits a strong dependence on temperature and Inh. A. In this experiment, addition of 50 mM of Inh. A (74% reduction) had the same effect as decreasing the temperature from 55°C to 40°C (80% reduction). The NH_3 rate was typically allowed 12-24 hours to reach steady state. If the system had not reached steady state at this point, the rate was assessed at a pseudo steady state two hours after any perturbation was made to the system (Figure 6). At 70°C steady state was often not observed, even after running the experiment for several days. In particular, when Inh. A was present at 70°C, the NH_3 rate dropped dramatically over the course of several days. This may be due to high volatility losses from the batch system, which would alter the MEA concentration over time. It is also possible that Inh. A becomes more active over a long time-scale at 70°C, further reducing the ammonia rate.

The NH_3 rate is dramatically reduced by as little as 50 mM of Inh. A. Additions of larger amounts further reduce the NH_3 rate although the returns are diminished for concentrations over 100 mM. The activation energy was substantially higher in the presence of Inh. A, indicating that a different mechanism controls the reaction when the inhibitor is present. The high activation energy in the presence of Inh. A indicates that a combination of intercooling and inhibitor may provide the most optimal condition for limiting degradation.

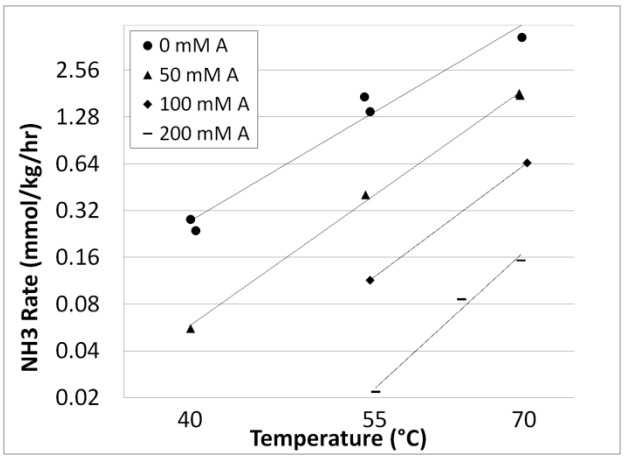

Figure 5. Ammonia Rates from 7 m MEA at various temperatures in the presence of 0.4 mM Fe, 0.1 mM Cr, 0.05 mM Ni, and Inh. A.

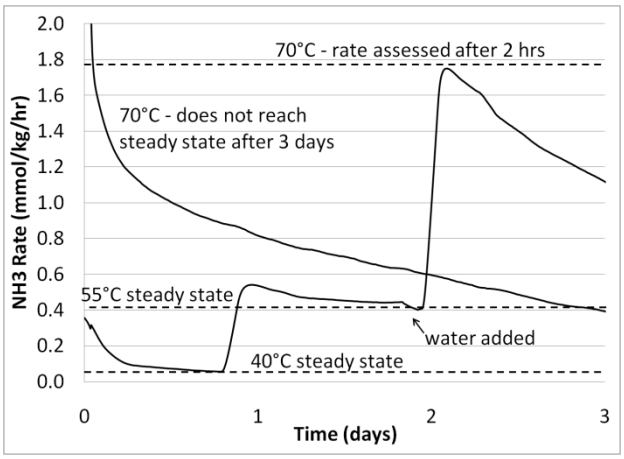

Figure 6. Ammonia Rates at three temperatures in two experiments with 7 m MEA, 0.4 mM Fe, 0.1 mM Cr, 0.05 mM Ni, and 50 mM Inh. A

Table 6. Activation Energy with Summary with Inh. A. 0.4 mM Fe, 0.1 mM Cr, and 0.05 mM Ni in the HGF: 21kPa O_2/2kPa CO_2, 1440 RPM, 350 mL solution volume, 5 SLPM dry gas rate.

Inh. A (mM)	Reduction at 40°C (%)	Reduction at 55°C (%)	Reduction at 70°C (%)	Activation Energy (kJ/mol)
0	--	--	--	86
50	78	74	57	102
100	--	93	84	113
200	--	99	96	133

The liquid-phase analysis of all experiments with Inh. A shows that the alkalinity loss and amine loss are generally in agreement (Table 7). The majority of lost alkalinity or amine is accounted for by gas-phase nitrogen—this was primarily volatile losses, which were often much greater than ammonia losses. The highest concentrations of formate, oxalate, nitrate, and nitrite detected were in the solution with no Inh. Added, which was oxidized for more than three days (Table 8). No heat stable salts were detected in solutions that contained 100-200 mM Inh. A. Even with 50 mM Inh. A, significantly less formate is observed considering the experimental conditions: when MEA was inhibited with 50 mM Inh. A and degraded at 70°C, the final sample had nearly half the amount of formate as the uninhibited solution, despite the latter being a shorter experiment at lower temperature.

All experiments were conducted at constant reactor gas composition (2% CO_2 in air). Therefore, the effect of temperature on the ammonia rate is complicated by the effect of loading, which goes down at higher temperature for a given partial pressure of CO_2. Previous work [6] has shown that lean (0.15 loading) solutions degrade faster than rich (0.4 loading) ones.

5.0 Conclusions

Aside from MEA, several other amines were discovered to produce ammonia when contacted with oxygen in the presence of a metal catalyst at low temperature. All of the amines that produced ammonia were primary amines. Of the primary amines, only DGA® and AMP did not produce ammonia at 55°C (although DGA produced a significant amount at 70°C). The potassium salts of two amino acids, glycine and taurine, were among the primary amines found to be susceptible to oxidative degradation. Besides MEA, Inh. A was found to be effective in reducing ammonia production from MAPA, taurine, and EDA.

The rate of ammonia production from MEA solutions was determined to be very sensitive to temperature. For an uninhibited or an inhibited system, significant benefit from reduced degradation can be achieved by intercooling the absorber, or running a higher liquid rate. Since all experiments were run at constant gas composition (2% CO_2 in air) the activation energy calculated in this work has an imbedded change in loading. Future experiments will increase the CO_2 concentration at higher temperatures to study the effect of temperature at constant loading.

Table 7. Effect of Inh. A on oxidation of 7 m MEA. 0.4 mM Fe, 0.1 mM Cr, and 0.05 mM Ni in the HGF: 21kPa O_2/2kPa CO_2, 1440RPM, 350mL solution volume, 5SLPM dry gas rate.

Inh. A (mM)	T(C)	Time (days)	Amine Loss (mol/kg)	Alkalinity Loss (mol/kg)	NH_3 (mmol/kg)	Volatile Loss (mol/kg)

0	40, 55	0.9	0.3	0.2	9	15
0	40, 55, 70	3.2	0.6	0.5	145	430
50	40, 55, 70	4.4	0.6	0.6	82	564
50	70	4.9	1.2	1.2	65	1174
100	40, 55, 70	2.9	0.3	0.2	14	329
200	55, 63, 70	0.7	0.0	0.0	3	38

Table 8. Heat stable salts in oxidized 7 m MEA solutions with Inh. A. 0.4 mM Fe, 0.1 mM Cr, and 0.05 mM Ni. Reactor gas was 2% CO_2 in air supplied at a rate of 5SLPM.

Inh. A (mM)	T (C)	Time (days)	Formate (mmol/kg)	Oxalate (mmol/kg)	Nitrate (mmol/kg)	Nitrite (mmol/kg)
0	40, 55	0.9	1	0	0	1
0	40, 55, 70	3.2	23	6	3	7
50	40, 55, 70	4.4	4	0	2	2
50	70	4.9	13	3	2	2
100	40, 55, 70	2.9	<0.5	<0.5	<0.5	<0.5
200	55, 63, 70	0.7	<0.5	<0.5	<0.5	<0.5

6.0 References

[1] Davis, JD. Thermal Degradation of Aqueous Amines used for Carbon Dioxide Capture. Ph.D. Dissertation. Austin, TX: The University of Texas at Austin; 2009.
[2] Polderman LD, Dillon CP, Steele AB, Why Monoethanolamine Solutions Breaks Down in Gas-Treating Service. Oil Gas J 1955; 54(No. 2):180-3.
[3] Rao AB, Rubin ES. A Technical, Economic, and Environmental Assessment of Amine-Based CO2 Capture Technology for Power Plant Greenhouse Gas Control. Environmental Science and Technology 2002; 36(20):4467-75.
[4] Plaza, JM, Rochelle, GT. Absorber intercooling in CO_2 Absorption by piperazine promoted potassium carbonate. AIChE J, 2009.
[5] Hall WD, Barron JG. Solving Gas Treating Problems – A Different Approach. Presented at the Laurance Reid Gas Conditioning Conference. Norman, OK; 1981
[6] Goff, GS. Oxidative Degradation of Aqueous Monoethanolamine in CO2 Capture Processes: Iron and Copper Catalysis, Inhibition, and O_2 Mass Transfer. Ph.D. Dissertation. Austin, TX: The University of Texas at Austin; 2005.
[7] Sexton, AJ. Amine Oxidation in CO2 Capture Processes. Ph.D. Dissertation. Austin, TX: The University of Texas at Austin; 2008.
[8] Blachly CH, Ravner H. The Stabilization of Monoethanolamine Solutions for Submarine Carbon Dioxide Scrubbers. NRL Report 6189. Washington , DC: Naval Research Laboratory; 1964.
[9] Stumm W, Lee GF. Oxygenation of Ferrous Iron. Ind Eng Chem 1961, 53, 143-146.
[10] Kovtun GA, Aleksandrov AL. Oxidation of Aliphatic Amines by Molecular Oxygen in the Liquid Phase-Commnunication 1-Kinetic principles of the uninhibited and inhibited oxidation of primary and secondary amines. Izv Akad Nauk SSSR, Sev Khim 1973; 10:2208-11
[11] Kovtun GA, Aleksandrov AL. Oxidation of Aliphatic Amines by Molecular Oxygen-Communication 4-Regeneration of Inhibitors in Tertiary Amines Undergoing Oxidation. Izv Akad Nauk SSSR, Sev Khim 1974; 1274-9
[12] Denisov ET. Cyclic mechanisms of chain termination in the oxidation of organic compounds. Russ Chem Rev 1996; 65 (6):505-20.
[13] Dennis WH Jr, Hull DH, Rosenblatt H. Oxidation of Amines. IV. Oxidative Fragmentation. J Org Chem 1967; 32(12): 3783-87
[14] Petryaev EP, Pavlov AV, Shadyro OI. Homolytic Deamination of Amino Alcohols. Zh Org Khim 1984; 20:29-34.
[15] Chi QS. Oxidative Degradation of Monoethanolamine. Masters Thesis. Austin, TX: The University of Texas at Austin; 2000.
[16] Kindrick RC, Atwood K, Arnold MR. The Relative Resistance to Oxidation of Commercially Available Amines. Girdler Report No. T2.15-1-30; 1950.
[17] Hofmeyer BG, Scholten HG, Lloyd, WG. Contamination and Corrosion in Monoethanolamine Gas Treating Solutions. Am Chem Soc, Div Petrol Chem, Preprints-Symposia 1956; 1(2):91-9.
[18] Goff, GS and Rochelle, GT. Oxidation Inhibitors for Copper and Iron Catalyzed Degradation of Monoethanolamine in CO_2 Capture Processes. Ind Eng Chem Res 2006; 45(8):2513-21.
[19] Koike L, Barone JS, Godinho OES, Aleixo LM, Reis FAM. N-formyl-diethanolamine: A new artefact in diethanolamine solutions. Chem Ind-London 1987; 626-7.
[20] Chen X, Freeman S, Rochelle GT. Foaming of Aqueous Piperazine and Monoethanolamine for CO2 Capture. Submitted to Int J Greenh Gas Con 2010.
[21] Closmann F, Rochelle GT. Degradation of aqueous MDEA by temperature and oxygen cycling. Poster presentation. Submitted to Int J Greenh Gas Con 2010.

Available online at www.sciencedirect.com

ScienceDirect

Energy Procedia 00 (2010) 000–000

Energy Procedia

www.elsevier.com/locate/XXX

GHGT-10

Accurate screening of amines by the Wetted Wall Column

Xi Chen, Fred Closmann, Gary T. Rochelle*

Department of Chemical Engineering, The University of Texas at Austin, 1 University Station C0400, Austin, Texas 78712, USA

Elsevier use only: Received date here; revised date here; accepted date here

Abstract

To screen amine solvents accurately for CO_2 capture, a Wetted Wall Column (WWC) was used to measure equilibrium CO_2 partial pressure and CO_2 absorption/desorption rate at variable CO_2 loading from 40 to 100 ℃. The solvents included 10 m diglycolamine (DGA®), 4.8 m 2-amino-2-methyl-propane (AMP), 8 m N-methyl-1,3-propanediamine (MAPA), 7 m/2 m and 5 m/5 m methyldiethanolamine (MDEA)/piperazine (PZ). With a semi-empirical VLE model assuming a lean/rich CO_2 loading corresponding to 500 Pa/5000 Pa CO_2 partial pressure, cyclic capacity and heat of CO_2 absorption was determined. Liquid film mass transfer coefficients are reported for each solvent, which allows estimation of packing area required for 90% removal via a simple absorber design. The results show that the capacity of DGA® and MAPA is 10–20% less than 7 m MEA with a 5 to 15% slower rate. 4.8 m AMP has a capacity twice as great as 7 m MEA, but the rate is lower by 45%. 7 m/2 m MDEA/PZ has a similar capacity to 8 m PZ but slightly slower rate. 5 m /5 m MDEA/PZ has a capacity 20% greater than 8 m PZ and a comparable rate. The heat of CO_2 absorption in the primary amines is about 80 kJ/mol CO_2. The value for PZ and its blend with MDEA is about 70 kJ/mol CO_2.

Keywords: Amine screening; Absorption/desorption rates; Cyclic capacity; Heat of CO_2 absorption.

1. Introduction

Amine solvents for CO_2 capture require high absorption/desorption rate, high capacity for CO_2, low degradation rate, and low volatility. A high heat of CO_2 absorption is also required to reduce overall energy consumption in amine regeneration and CO_2 compression [1, 2]. Efforts in amine screening have been reported by many researchers [3-8]. Most of them measure relative absorption/desorption rate by simple CO_2 sparging, which lacks the ability to estimate amine performance in a real absorber. Furthermore, cyclic capacity and heat of absorption at practical conditions are rarely available in these studies.

A wetted wall column (WWC) has been extensively utilized to study kinetics between amines and CO_2. However, few of these studies use practical levels of CO_2 loading and amine concentration [9-13]. Because it closely approximates mass transfer between gas and liquid on real packing, a WWC provides an excellent platform to evaluate new amine solvents.

In this study, CO_2 solubility and the absorption/desorption rate in five amine solvents, 10 m DGA®, 4.8 m AMP, 8 m MAPA, 7 m/2 m and 5 m/5 m MDEA/PZ were measured in a WWC at 40 ℃ to 100 ℃ with variable CO_2

* Corresponding author. Tel.: +1-512-471-7230; fax: +1-512-475-7824.
E-mail address: gtr@che.utexas.edu.

loading. The CO_2 loading (α, mol/mol alkalinity) was chosen to give a CO_2 partial pressure at 40 °C of 500 Pa to 5000 Pa to cover the expected range for post-combustion capture from a coal-fired power plant. Equilibrium CO_2 partial pressure (P_{CO2}^*) and liquid film mass transfer coefficient (k_g') were measured at each condition. The obtained solubility data was modelled with a semi-empirical correlation, which enables calculation of cyclic capacity and heat of CO_2 absorption.

2. Experimental methods and materials

A schematic of the entire WWC apparatus is shown in Figure 1. Details of the WWC are shown in Figure 2. This is the same apparatus and method as used by Bishnoi [14], Cullinane [12], Dugas [13], and Chen et al. [15].

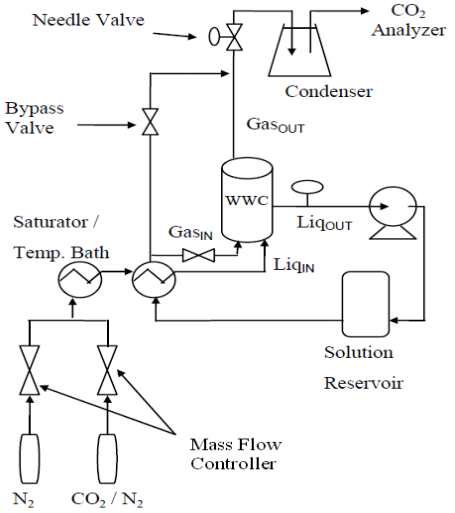

Figure 1. Flow sheet of the WWC apparatus.

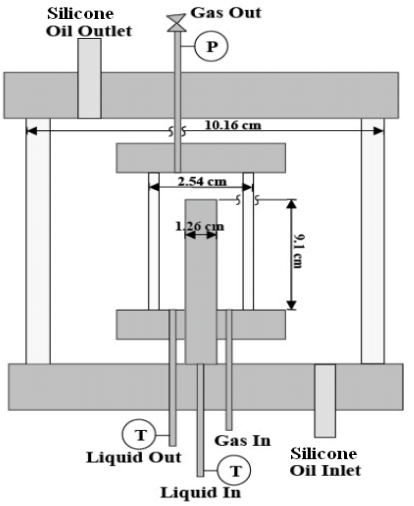

Figure 2. Detailed view of the WWC.

A CO_2/N_2 mixture was fed into the WWC by mass flow controllers at 5×10^{-3} standard m^3/min. The inlet partial pressure of CO_2 was varied from zero to about double the equilibrium pressure. The gas mixture was saturated with water and further heated by an oil bath before entering the WWC chamber from the bottom. Liquid in a one-liter reservoir was pumped through the middle of the column and overflowed from the top. Then it evenly distributed along the outer surface of the column and exited the bottom, counter-currently contacting the gas. The liquid was recirculated at 2.4×10^{-4} m^3/min. The total pressure of the system was regulated between 0.2 MPa to 0.7 MPa with a needle valve at the gas outlet. The gas exiting from the top was directed through a condenser and a desiccation unit to remove water and amine vapor. The outlet CO_2 concentration was measured continuously by an infrared CO_2 analyzer (Horiba 2000). The bypass valve allows direct measurement of inlet CO_2 concentration.

Typically six inlet CO_2 partial pressures were selected for each CO_2 loading and temperature (T), as shown in Figure 3. Three of them are greater than the equilibrium CO_2 partial pressure of the solution, leading to absorption of CO_2 and positive flux; while the other three correspond to desorption. CO_2 flux and driving forces between gas and liquid, which are determined from the difference of inlet and outlet CO_2 concentration, can be correlated by a line. The slope of the line represents the overall mass transfer coefficient (K_G):

$$K_G = \frac{N_{CO_2}}{P_{CO_2,g} - P^*_{CO_2}} \tag{1}$$

where N_{CO2} is CO_2 flux and $P_{CO2,g}$ is CO_2 partial pressure in the bulk gas.

The line is shifted along the abscissa axis by adjusting P_{CO2}^* until it almost crosses the original point, where the driving force is zero and no flux should be observed. In this way, P_{CO2}^* is determined as a function of loading and temperature.

A pre-determined correlation for gas film mass transfer coefficient (k_g) [14] is combined with the experimental results for K_G to calculate liquid film mass transfer coefficient (k_g'):

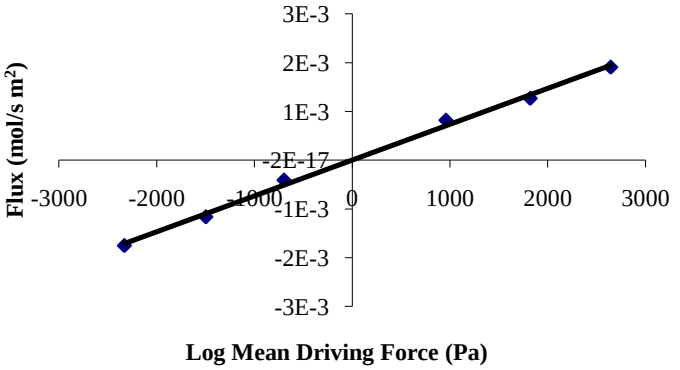

Figure 3. Flux as a function of log mean driving force between gas and liquid for 10 m DGA® at 60 ℃ and CO_2 loading of 0.4 mol/mol alkalinity.

$$\frac{1}{k_g^{'}} = \frac{1}{K_G} - \frac{1}{k_g} \tag{2}$$

k_g' is the CO_2 flux normalized by CO_2 partial pressure driving force between gas-liquid interface and bulk liquid. It is dependent on reaction kinetics, CO_2 solubility and diffusivity of reactants and products. Therefore k_g' is an inherent property of the amine solvent. If amine concentration can be assumed to be constant across the reaction boundary, the following approximation is valid:

$$k_g^{'} \approx \frac{\sqrt{D_{CO_2} k_2 [Am]_b}}{H_{CO_2}} \tag{3}$$

D_{CO2}, diffusivity of CO_2 in amine solution; k_2, second-order reaction rate constant; $[Am]_b$, free amine concentration in bulk solution; H_{CO2}, Henry's constant of CO_2 in amine solution.

DGA® (98%, Acros), AMP (99%, Acros), MAPA (99%, Alfa Aesar), MDEA (99%, Huntsman), PZ (anhydrous, 99%, Alfa Aesar) were used without purification for preparation of aqueous solution. CO_2 loading was determined by total inorganic carbon analysis [16]. Amine concentration was confirmed by amine titration [16].

3. Results and Discussion

3.1 CO_2 solubility

CO_2 solubility data in DGA® and AMP show good agreement with literature data (Figure 4 and Figure 5). A semi-empirical model (Equation 4), which assumes P_{CO2}^* (Pa) is only a function of CO_2 loading (α) and T (K), was used to fit the solubility data for each amine. Parameters for different amines are given in Table 1. With this model, lean and rich CO_2 loading corresponding to 500 and 5000 Pa at 40 °C were determined. The difference between lean and rich loading gives cyclic capacity of CO_2 for each amine.

$$\ln P_{CO_2}^* = a + b/T + c\alpha + d\alpha/T + e\alpha^2 \tag{4}$$

The heat of CO_2 absorption (ΔH_{abs}) is obtained using the Gibbs-Helmholtz equation:

$$\Delta H_{abs} = -R\frac{d(\ln P_{CO_2}^*)}{d(1/T)} = -R\cdot(b + d\cdot\alpha) \tag{5}$$

ΔH_{abs} is only dependent on CO_2 loading under the current model. ΔH_{abs} at the CO_2 loading corresponding to P_{CO2}^* = 1500 Pa is reported as an average value.

CO_2 solubility data for MAPA and MDEA/PZ are shown in Figure 6. In MAPA, free amine is depleted as CO_2 loading approaches 0.5 and P_{CO2}^* increases rapidly with loading. Therefore the CO_2 capacity of MAPA from 500 Pa to 5000 Pa is relatively small. In Figure 7, the solubility data for MDEA/PZ are compared to those from Bishnoi et al. [17] and Derks et al. [18] for 7.8 m MDEA/1.2 m PZ. Increases in the PZ fraction increase CO_2 solubility because PZ carbamate is a more stable form of CO_2.

Table 1. Regressed value of parameters for solubility model used in this work

Amine	a	b	c	d	e
7 m MEA	36.61±2.80	-11152±896	-7.46±8.36	2389±2636	26.69±2.58
8 m PZ	34.52±2.09	-10676±683	-10.10±7.27	7596±2370	14.43±3.27
10 m DGA®	53.57±5.61	-16434±2081	-48.85±15.13	14762±5798	34.28±11.18
8 m MAPA	53.45±9.84	-14517±3234	-78.86±25.91	9035±8009	103.75±17.99
4.8 m AMP	35.47±0.87	-10080±299	1.70±2.80	3258±966	-4.89±1.11
7m/2m MDEA/PZ	33.94±0.76	-9694±277	2.30±4.98	8054±1918	-29.46±3.88
5m/5m MDEA/PZ	34.68±1.76	-10792±602	6.98±7.97	8746±2612	-31.49±6.39

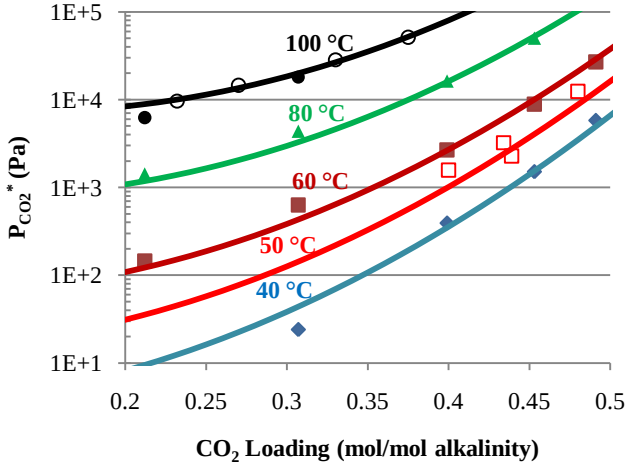

Figure 4. CO_2 solubility in 10 m DGA®. Filled points: experimental data; Solid lines: model prediction (Eq. 4); Open points: 14.3 m DGA® at 50 ℃ (square) and 100 ℃ (circle) from Ref. [19].

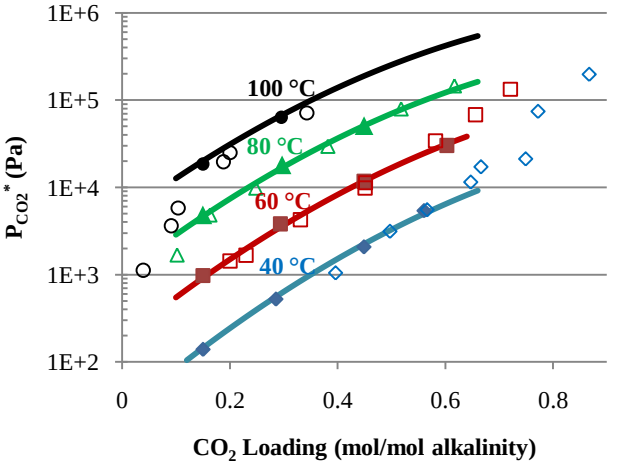

Figure 5. CO_2 solubility in 4.8 m AMP. Filled points: experimental data; Solid lines: model prediction (Eq. 4); Open points: Ref. [20].

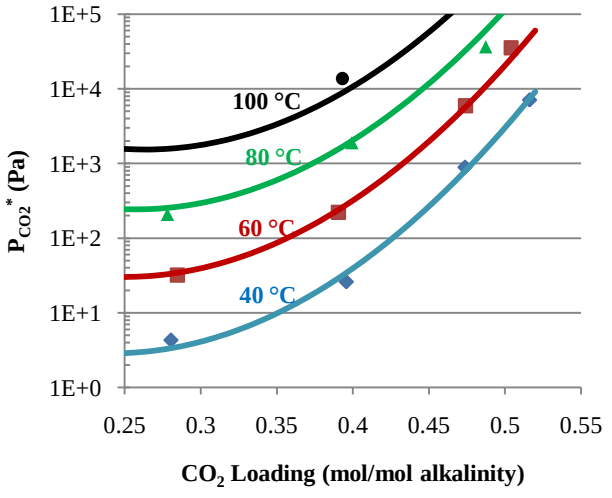

Figure 6. CO_2 solubility in 8 m MAPA. Filled points: experimental data; Solid lines: model prediction.

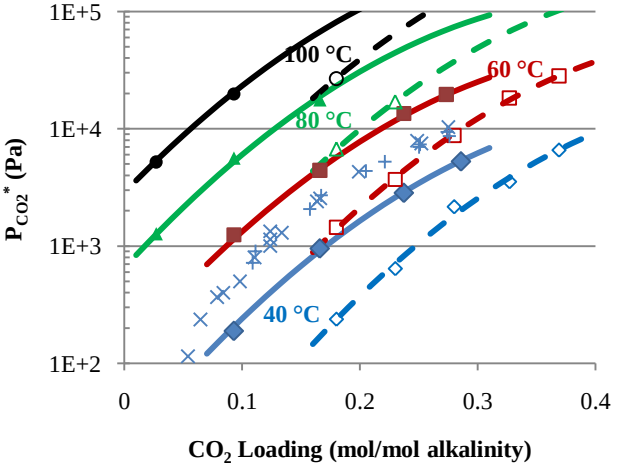

Figure 7. CO_2 solubility in MDEA/PZ. Filled points: experimental 7 m/2 m; Solid lines: model 7/2; Open points: experimental 5 m/5 m; Dashed lines: model 5/5; 7.8 m /1.2 m PZ at 40 ℃ by Bishnoi et al. [17] (×) and Derks et al. [18] (+).

3.2 Absorption/desorption rate

The rate data for the amines are shown in Figure 8 to Figure 11. k_g' values are shown as a function of P_{CO2}^* at 40 ℃, a surrogate for loading. In general, an increase in T leads to equal or smaller k_g', with exceptions seen in AMP. This can be explained by Equation 3. Although D_{CO2} and k_2 both increase with T, H_{CO2} increases simultaneously. The change in k_g' depends on how these factors offset each other. Using the P_{CO2}^* instead of CO_2 loading as the x-axis also allows direct comparison of rates on the same basis for different amines. Data for 8 m PZ and 7 m MEA at 40 ℃ by Dugas et al. [13] are shown for comparison. As can be seen, CO_2 absorption in PZ is about 1.5 to 2 times faster than MEA. DGA® has a comparable rate to MEA from 20 Pa to 1000 Pa, presumably because that they are both unhindered primary amines. Although the reaction kinetics of AMP with CO_2 is approximately 10 times slower than MEA [21, 22] due to the steric hindered amino group, CO_2 absorption rate of AMP is found to be as high as half of MEA. A stoichiometric ratio of 1 mol CO_2/mol AMP results in higher free amine concentration, which compensates for small k_2. MAPA is a faster solvent than MEA at lean CO_2 partial pressure but much slower at the rich end.

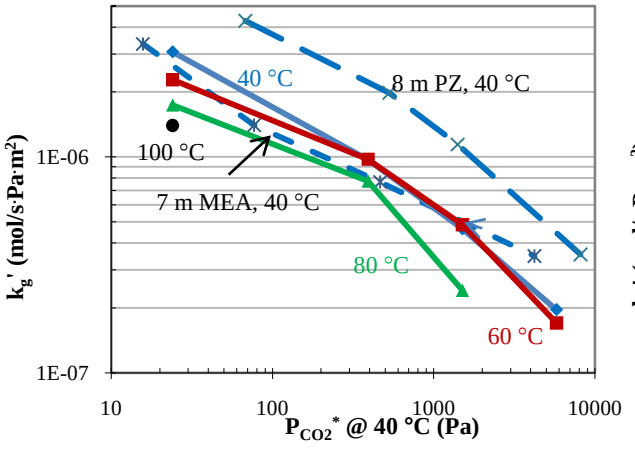

Figure 8. Liquid mass transfer coefficient (k_g') of 10 m DGA® (solid lines). The data is compared with k_g' for 7 m MEA (short dashed line) and 8 m PZ at 40 ℃ (long dashed line) [13].

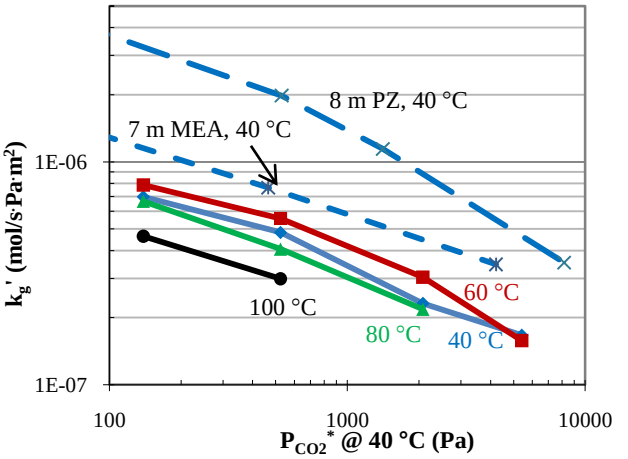

Figure 9. k_g' of 4.8 m AMP (solid lines).

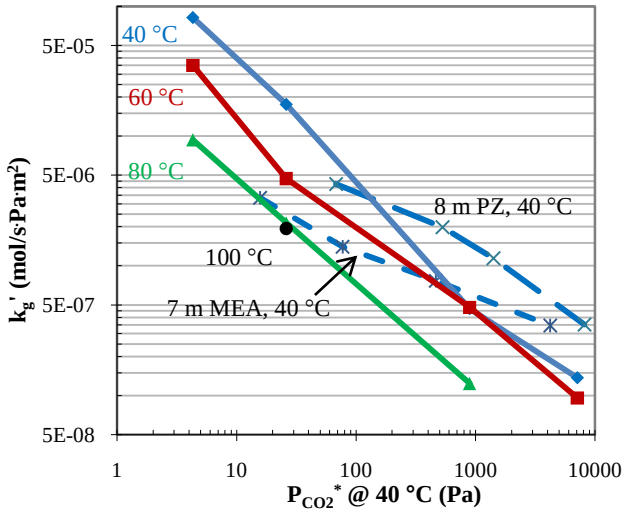

Figure 10. k_g' of 8 m MAPA (solid lines).

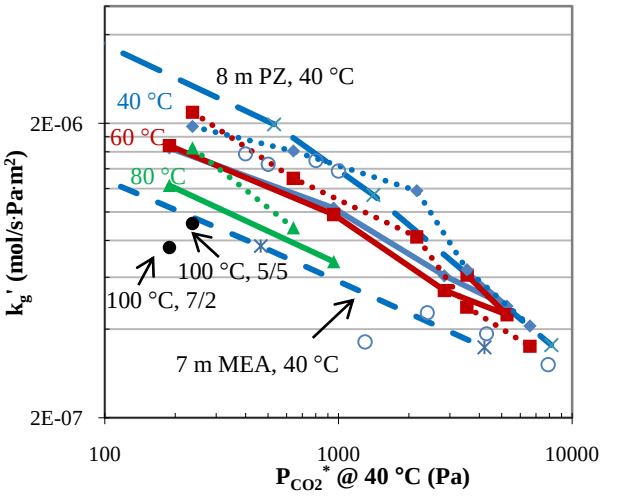

Figure 11. k_g' of 7 m/2 m (solid lines) and 5 m/5 m MDEA/PZ (dotted lines). Open circles: 7.8 m /1.2 m MDEA/PZ at 40 ℃ [17].

7 m/2 m MDEA/PZ is slightly slower than 8 m PZ at lean loading but similar at rich loading. This means PZ can greatly enhance CO_2 absorption rate even at a lower fraction. 5 m/5 m MDEA/PZ has a faster rate than 7/2 at all the temperatures. It also has a similar performance to PZ at 40 °C. kg' reported by Bishnoi et al. for 7.8 m/1.2 m MDEA/PZ [17] is greater than that for 7/2 and slightly less than 5/5 at lean loading, but slower than either 7/2 or 5/5 at rich end. In the blend, MDEA catalyzes the formation of PZ carbamate and becomes protonated, therefore there is still abundant free PZ available to react with CO_2, retaining higher absorption rate. All the solubility and rate data are given in Table 2.

Table 2. Equilibrium CO_2 partial pressure (P_{CO2}^*, kPa) and liquid film mass transfer coefficient (k_g', 10^{-7} mol/(s Pa m^2)) at varied CO_2 loading (α, mol/mol alkalinity) and temperature (T, ℃)

T	α	P_{CO2}	k_g'
10 m DGA®			
40	0.307	0.02	30.7
	0.399	0.39	9.7
	0.453	1.51	4.6
	0.491	5.79	2.0
60	0.212	0.15	37.1
	0.307	0.63	22.8
	0.399	2.67	9.8
	0.453	8.87	4.9
	0.491	26.9	1.7
80	0.212	1.42	31.4
	0.307	4.36	17.4
	0.399	16.3	7.7
	0.453	50.1	2.4
100	0.212	6.25	24.5
	0.307	18.0	14.0

T	α	P_{CO2}	k_g'
4.8 m AMP			
40	0.15	0.14	7.0
	0.28	0.52	4.8
	0.44	2.08	2.3
	0.56	5.41	1.7
60	0.15	0.98	7.9
	0.29	3.81	5.6
	0.44	11.7	3.0
	0.60	30.2	1.6
80	0.15	4.85	6.7
	0.29	18.2	4.1
	0.44	51.0	2.2
100	0.15	18.5	4.6
	0.29	63.6	3.0

T	α	P_{CO2}	k_g'
8 m MAPA			
40	0.280	0.00	817.
	0.396	0.03	175.
	0.474	0.89	4.7
	0.516	7.12	1.4
60	0.285	0.03	350.
	0.390	0.22	47.0
	0.474	5.92	4.8
	0.504	35.3	1.0
80	0.278	0.21	93.5
	0.399	1.89	21.4
	0.487	36.4	1.2
100	0.393	13.8	19.4

T	α	P_{CO2}	k_g'
7 m MDEA/2 m PZ			
40	0.093	0.19	16.5
	0.166	0.95	10.3
	0.237	2.84	6.1
	0.286	5.26	4.8
60	0.093	1.25	16.8
	0.166	4.41	9.8
	0.237	13.5	5.4
	0.273	19.6	4.5
80	0.027	1.27	27.6
	0.093	5.62	12.3
	0.166	17.6	6.8
10 0	0.027	5.21	16.3
	0.093	19.8	7.6
5 m MDEA/5 m PZ			
40	0.18	0.24	19.5
	0.23	0.64	16.1
	0.28	2.16	11.8
	0.33	3.54	6.4
	0.37	6.59	4.1
60	0.18	1.45	21.8
	0.23	3.70	13.0
	0.28	8.77	8.2
	0.33	18.3	4.8
	0.37	28.2	3.5
80	0.18	6.73	16.5
	0.23	16.9	8.8
10	0.18	26.7	9.1

3.3 Cyclic capacity and heat of CO_2 absorption

The calculated values for lean/rich CO_2 loading, capacity, and heat of absorption are given in Table 3. The capacity of 7 m/2 m MDEA/PZ is same as 8 m PZ, while that of the 5/5 blend is about 25% higher than 8 m PZ. If the total amount of alkalinity in each solvent is taken into account, it can be seen that the addition of MDEA to PZ effectively increases the CO_2 capacity while maintaining the fast kinetics associated with PZ. Tertiary amines like MDEA cannot form carbamate with CO_2. Instead, 1 mol MDEA reacts with 1 mol CO_2 to produce bicarbonate and protonated MDEA. 4.8 m AMP has a CO_2 capacity two times as great as that of MEA and about 20% higher than PZ, even at a lower amine concentration. This is attributed to the hindered nature of AMP. However the CO_2 capacity of 10 m DGA® and 8 m MAPA are only about half of 8 m PZ and slightly smaller than 7 m MEA.

The heat of CO_2 absorption for PZ and its blend with MDEA is about 70 kJ/mol CO_2. ΔH_{abs} for AMP is slightly higher than PZ. All of the primary amines, MEA, DGA® and MAPA, have a value slightly greater than 80 kJ/mol CO_2, presumably because of the greater heat of reaction in carbamate formation.

3.4 Application of rate data

Accurate measurement of absorption rates makes it possible to accomplish simple absorber design. k_g' values at P_{CO2}^* = 500 Pa and 5000 Pa at 40 °C for each amine are interpolated/extrapolated from available data. These two values represent the rate of mass transfer at the top and bottom of an isothermal absorber operated at 40 °C. The CO_2 flux is then equal to k_g' times the driving force. An average value of k_g' is generated by dividing the log mean flux by the log mean driving force at the top and bottom (Equation 6):

$$k'_{g,avg} = \frac{Flux_{CO_2,LM}}{(P_{co_2,gas} - P^*_{co_2})_{LM}} = \frac{(Flux_{CO_2,top} - Flux_{CO_2,bottom}) / \ln(Flux_{CO_2,top} / Flux_{CO_2,bottom})}{[(P_{co_2,top} - P^*_{co_2,lean}) - (P_{co_2,bottom} - P^*_{co_2,rich})] / \ln(\frac{P_{co_2,top} - P^*_{co_2,lean}}{P_{co_2,bottom} - P^*_{co_2,rich}})} \quad (6)$$

This value reflects the average absorption rate over the whole absorber column. The packing area (A_p) required for unit volumetric flow rate of flue gas (V_g) can also be estimated with the assumption of 90 % CO_2 removal.

$$A_p / V_g = \frac{90\% \times 12\% \times P / RT}{Flux_{CO_2,LM}} \quad (7)$$

The average value of k_g' as well as A_p/V_g are shown in Table 3. 8 m PZ has the fastest CO_2 mass transfer rate, corresponding to the least packing area requirement, 1800 $m^2/(m^3/s)$. 7 m MEA is only 50% as fast as PZ, which doubles the required packing area. 5 m /5 m MDEA/PZ has a similar rate to PZ, while 7/2 is roughly 15% slower. CO_2 absorption in 10 m DGA® and 8 m MAPA are slower than in MEA by 5–15%. 4.8 m AMP, as the slowest solvent, requires a packing area up to 6300 $m^2/(m^3/s)$.

Table 3. Overview of properties for all the amines tested. PZ and MEA [13] and N-methyl PZ and 2-methyl PZ data [15] are also included.

Amine	Lean/Rich loading (mol CO_2/mol alkalinity)	Cyclic CO_2 Capacity (mol/kg (water+amine))	$-\Delta H_{abs}$ @P_{CO2} =1.5kPa (kJ/mol)	$k_g'_{avg}$@40°C ($\times 10^7$mol/s Pa m^2)	A_p/V_{fg} (10^3 $m^2/(m^3/s)$)
8 m PZ	0.31/0.39	0.79	70	8.5	1.8
8 m N-methyl PZ	0.16/0.26	0.83	67	8.4	1.8
5m/5m MDEA/PZ	0.21/0.35	0.99	70	8.3	1.8
7m/2m MDEA/PZ	0.13/0.28	0.80	68	6.9	2.2
8 m 2-methyl PZ	0.27/0.37	0.93	72	5.9	2.6
7 m MEA	0.45/0.55	0.47	82	4.3	3.5
10 m DGA®	0.41/0.49	0.38	81	3.6	4.2
8 m MAPA	0.47/0.51	0.42	84	3.1	4.8
4.8 m AMP	0.27/0.56	0.96	73	2.4	6.3

4. Conclusions

The measurements of CO_2 solubility and absorption/desorption rates with the Wetted Wall Column enable the extraction and comparison of CO_2 capacity, heat of absorption, and mass transfer rates in different amine solvents. The primary amines studied, DGA® and MAPA, along with MEA, suffer from low CO_2 capacity and absorption rates. However, their high heat of absorption would help lower the energy requirement and could offset their disadvantages. 4.8 m AMP has a high CO_2 capacity, but its application as a CO_2 capture solvent could be hindered by its low CO_2 absorption rate. MDEA blended with PZ shows great promise with its high CO_2 capacity and absorption rate, if compromised with the relatively lower heat of absorption.

The packing area for unit volume of flue gas is estimated in a simple absorber design. Fast amines such as 5 m /5 m MDEA/PZ, only require 1/2 to 1/3 of the packing area that would be needed for slow solvents like DGA®, MAPA, and AMP. Therefore a fast amine would greatly reduce the column size and capital cost.

5. Acknowledgement

The authors acknowledge the support of the Luminant Carbon Management Program.

6. References

[1] Oyenekan BA, Rochelle GT. Energy Performance of Stripper Configurations for CO_2 Capture by Aqueous Amines. Ind. Eng. Chem. Res. 2006; 45(8): 2457-2464.
[2] Oexmann J, Kather A. Minimising the regeneration heat duty of post-combustion CO_2 capture by wet chemical absorption: The misguided focus on low heat of absorption solvents. 2009; 4(1): 36-43.
[3] Hook RJ. An Investigation of Some Sterically Hindered Amines as Potential Carbon Dioxide Scrubbing Compounds. Ind. Eng. Chem. Res. 1997; 36(5): 1779-1790.
[4] Mimura T, et al. Evaluation of alkanolamine chemical absorbents for CO_2 from vapor-liquid equilibrium measurements. Kagaku Kogaku Ronbunshu 2005; 31(4): 237-242.
[5] Singh P, Niederer JPM, Versteeg GF. Structure and activity relationships for amine based CO_2 absorbents-I. Int. J. Greenhouse Gas Control 2007; 1(1): 5-10.
[6] Singh P, Versteeg GF. Structure and activity relationships for CO_2 regeneration from aqueous amine-based absorbents. Process Saf. Environ. Prot. 2008; 86(5): 347-359.
[7] Singh P, Niederer JPM, Versteeg GF. Structure and activity relationships for amine-based CO_2 absorbents-II. Chem. Eng. Res. Des. 2009; 87(2): 135-144.
[8] Puxty G, et al. Carbon Dioxide Postcombustion Capture: A Novel Screening Study of the Carbon Dioxide Absorption Performance of 76 Amines. Environ. Sci. Technol. 2009; 43(16): 6427-6433.
[9] Al-Juaied M, Rochelle GT. Absorption of CO_2 in aqueous blends of diglycolamine and morpholine. Chem. Eng. Sci. 2006; 61(12): 3830-3837.
[10] Pacheco MA, Kaganoi S, Rochelle GT. CO_2 absorption into aqueous mixtures of diglycolamine and methyldiethanolamine. Chem. Eng. Sci. 2000; 55(21): 5125-5140.
[11] Bishnoi S, Rochelle GT. Absorption of carbon dioxide in aqueous piperazine/methyldiethanolamine. AIChE J. 2002; 48(12): 2788-2799.
[12] Cullinane JT, Rochelle GT. Carbon dioxide absorption with aqueous potassium carbonate promoted by piperazine. Chem. Eng. Sci. 2004; 59(17): 3619-3630.
[13] Dugas R, Rochelle G. Absorption and desorption rates of carbon dioxide with monoethanolamine and piperazine. Energy Procedia 2009; 1(1): 1163-1169.
[14] Bishnoi S, Rochelle GT. Absorption of carbon dioxide into aqueous piperazine: reaction kinetics, mass transfer and solubility. Chem. Eng. Sci. 2000; 55(22): 5531-5543.
[15] Chen X, Rochelle GT. Aqueous Piperazine Derivatives for CO_2 Capture: Accurate Screening by a Wetted Wall Column. Submitted to Chem. Eng. Res & Des. 2010.
[16] Freeman SA, et al. Carbon dioxide capture with concentrated, aqueous piperazine. Energy Procedia 2009; 1(1): 1489-1496.
[17] Bishnoi S. Carbon dioxide absorption and solution equilibrium in piperazine activated methyldiethanolamine Department of Chemical Engineering 2000; Ph.D. Dissertation.
[18] Derks PWJ, Hogendoorn JA, Versteeg GF. Experimental and theoretical study of the solubility of carbon dioxide in aqueous blends of piperazine and N-methyldiethanolamine. J. Chem. Thermodyn. 2009; 42(1): 151-163.
[19] Martin JL, Otto FD, Mather AE. Solubility of hydrogen sulfide and carbon dioxide in a diglycolamine solution. J. Chem. Eng. Data 1978; 23(2): 163-4.
[20] Li M-H, Chang B-C. Solubilities of Carbon Dioxide in Water + Monoethanolamine + 2-Amino-2-methyl-1-propanol. J. Chem. Eng. Data 1994; 39(3): 448-52.
[21] Alper E. Reaction mechanism and kinetics of aqueous solutions of 2-amino-2-methyl-1-propanol and carbon dioxide. Ind. Eng. Chem. Res. 1990; 29(8): 1725-8.
[22] Saha AK, Bandyopadhyay SS. Kinetics of absorption of CO_2 into aqueous solutions of 2-amino-s-methyl-1-propanol. Chem. Eng. Sci. 1995; 50(22): 3587-98.

Available online at www.sciencedirect.com

ScienceDirect

Energy Procedia 00 (2010) 000–000

Energy Procedia

www.elsevier.com/locate/XXX

GHGT-10

Total Pressure and CO_2 Solubility at High Temperature in Aqueous Amines

Qing Xu, Gary Rochelle [1]*

Department of Chemical Engineering, The University of Texas at Austin, 1 University Station, Austin, TX 78712, USA

Elsevier use only: Received date here; revised date here; accepted date here

Abstract

Total pressure was measured in CO_2 loaded aqueous monoethanolamine, piperazine, 1-methyl-piperazine, 2-methyl-piperazine, and diglycolamine® at 82 to 191°C from 115 to 2819 kPa. CO_2 solubility is estimated from these data. Empirical models have been developed to predict the CO_2 partial pressure of these amine solutions from 40 to 160°C. The heat of CO_2 absorption derived from these models varies from 66 kJ/mol for piperazine and its derivatives to 71 and 73 kJ/mol for monoethanolamine and diglycolamine and does not vary significantly with temperature.

Keywords: CO_2 capture, CO_2 solubility, aqueous amine, high temperature, high pressure.

1. Introduction

Amine scrubbing will be an important technology for CO_2 capture form coal-fired power plants. Various aqueous amines have been used for absorption. 7 m (molal, gmol/ kg water, 30 wt %) monoethanolamine (MEA) is considered the baseline solvent. Previous studies have shown that concentrated piperazine (PZ) is very promising, because of greater CO_2 capacity and absorption rate and greatly reduced thermal and oxidative degradation [1].

Improved energy performance can be achieved by elevating the stripping temperature and pressure [2]. MEA is not thermally resistant so the stripper temperature cannot exceed 120 ℃. However, PZ, diglycolamine (DGA) and PZ derivatives can be used up to 150 ℃ without significant degradation. Therefore thermodynamic data at high temperature will be especially useful in the design of stripper, multi-stage flash, reclaimer and other high temperature processes. Mid-temperature thermodynamics can also be interpolated from high and low temperature data.

For MEA, CO_2 solubility at high temperature is available from Jou et al. in 30 wt% MEA up to 150°C and 20,000 kPa [3]. These data will be compared to the CO_2 solubility in MEA in this work to validate the experimental methods. There is little data available for PZ, DGA and PZ derivatives at high temperature and pressure.

* Corresponding author. Tel.: +1-512-471-7230; fax: +1-512-475-7824.
E-mail address: gtr@che.utexas.edu.

2. Experimental Methods

2.1 Apparatus

2.1.1 Calorimeter

The first measurements of total pressure were performed using a 400 mL stainless steel calorimeter (by Parr Instrument) as the equilibrium cell (Figure 1). Pressure was measured with a Validyne® DP15 transducer, calibrated by heating water and correlating the readings with known water vapor pressures from DIPPR [4]. The voltage of the heating tape was manually controlled by a power controller to maintain selected temperature. An Omega® K type thermocouple was installed inside the thermal well and an Omega® 4001A was used as the temperature indicator.

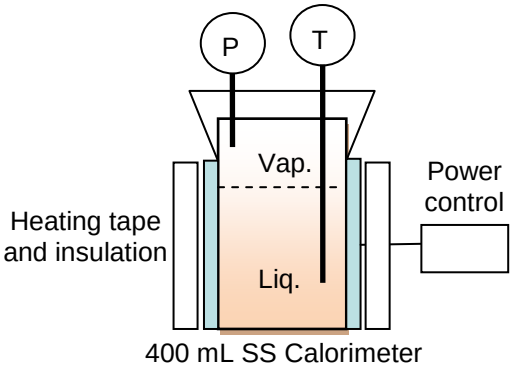

Figure 1: Total Pressure Measurement with a Calorimeter

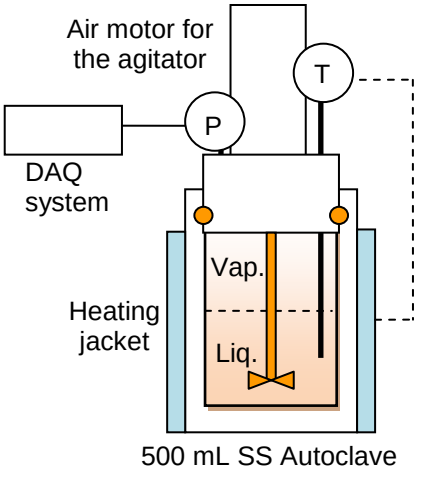

Figure 2: Total Pressure Measurement with an Autoclave

2.1.2 Autoclave

As shown in Figure 2, a 500 mL stainless steel autoclave (ZipperClave®, by Autoclave Engineers) was used as the equilibrium cell for most of the measurements. Closure was effected by a resilient spring member inserted through a circumferential groove in the body and cover [5]. A magnetic hollow shaft agitator (MAG075, MagneDrive II Series, by Autoclave Engineers) was used to get equilibrium without leaking to the atmosphere. A compressed air motor (2AM-NCC-16, by Gast®) provided agitation from 100 to 2500 rpm. The agitator circulates both liquid and vapor phases. Temperature was controlled by a Fuji Electric PXZ-4 temperature controller, with connection to a K-type thermocouple placed inside the thermal well of the autoclave. A pressure transducer (Druck® PTX 611, 0-30 bar absolute) was connected to a signal converter and a data logger used for to record data. The pressure indicator was calibrated by a dead weight pressure tester (S/N 19189/278, by Budenberg Volumetrics, INC.).

The 1 run with MEA and 3 runs with PZ were conducted in the calorimeter. The autoclave was used in all the other experiments. The results do not show obvious differences between the two apparatuses.

2.2 Procedure

Before each run, 300 to 330 mL of CO_2 loaded aqueous amine was prepared and added into the equilibrium cell. To avoid the effects of O_2, N_2 was used to purge air and then the cell was sealed. The initial pressure of N_2 and temperature were recorded for correction. Then the cell was heated. Recording of both temperatures and pressures started at around 100 ℃. After holding at temperature for at least 30 min or until the pressure did not change for 10 min, the system was assumed to be at equilibrium. The solution was heated to about 160 ℃ (or higher for PZ) and then cooled down to 100 ℃. Data were taken during both heating and cooling processes to make the interval 10 ℃ in general. Liquid samples were collected before and after each experiment at room temperature and analyzed by total inorganic carbon analyzer and acid titration.

2.3 Analytical Methods

Total Inorganic Carbon (TIC)

The concentration of CO_2 in solution was determined by TIC analysis. The liquid samples collected before and after each run were diluted by a factor of 100. About 10–15 μL diluted sample was injected into a CO_2 analyzer (Model 525, Horiba PIR 2000). Details can be found in Appendix B.2 of Hilliard [6].

Acid Titration

The total alkalinity of solution was determined by acid titration using a Metrohm-Peak 835 Titrando equipped with an automatic dispenser, Metrohm-Peak 801 stirrer, and 3M KCl pH probe. Details are available in Appendix A.3 of Hilliard [6] and Appendix F of Sexton [7].

2.4 Chemicals

CO_2 is CP (Clinical Purity) 99.5% by Matheson TriGas. MEA is 99% by Acros Organics. PZ is 99% by Sigma-Aldrich. 1-methyl-piperazine (1MPZ) is 99+% by Acros Organics. 2-methyl-piperazine (2MPZ) is 99% by AK Scientific. Diglycolamine (DGA®) is 99% by Huntsman. DDI water was used for solution preparation.

3. Results and Discussion

The total pressure of amine-H_2O-CO_2 system is $P_t=P_{meas}-P_{N2}$, where P_{meas} is the measured pressure and P_{N2} is the N_2 partial pressure; N_2 was assumed to be an ideal gas so $P_{N_2} = P_{0,N_2} \cdot T(K)/T_0(K)$, 0 stands for the initial condition.

$$P_{CO_2} = P_t - P_{H_2O} - P_{amine} = P_t - P^*_{H_2O} \cdot x_{H_2O} - P^*_{amine} \cdot x_{amine} \quad (1)$$

P_{H2O} and P_{amine}: partial pressure of water and amine.

P^*_{H2O} and P^*_{amine}: pressure of pure water and pure amine at T, from DIPPR [4].

The mole fractions $x_{H2O}+x_{amine}=1$, assuming there is water and total amine but no free CO_2 in the solution. For PZ derivatives and DGA, P_{amine} was ignored. Liquid analysis gives the total CO_2 loading at room temperature, from which high temperature liquid loadings were corrected by the estimated amount of CO_2 in the vapor.

3.1. Results

Table 1 lists the measured total pressure and calculated CO_2 partial pressure over aqueous MEA, PZ, 1MPZ, 2MPZ, PZ/2MPZ and DGA. CO_2 loading is defined as the mol CO_2/mol alkalinity.

Table 1: CO_2 Solubility and Total Pressure in MEA, PZ, 1MPZ, 2MPZ, PZ/2MPZ and DGA

Amine m	T ℃	Loading	P_{CO2} kPa	P_t kPa	Amine m	T ℃	Loading	P_{CO2} kPa	P_t kPa	Amine m	T ℃	Loading	P_{CO2} kPa	P_t kPa
MEA														
6.97	100	0.424	101	191	6.86	166	0.420	1568	2216	6.86	129.9	0.313	77	220
6.97	100	0.425	86	176	6.82	100	0.388	34	125	6.86	131.9	0.313	73	217
6.97	110	0.424	138	266	6.82	110	0.387	61	190	6.86	141.4	0.311	131	279
6.97	110	0.424	123	251	6.82	120	0.387	62	241	6.86	142.3	0.310	145	293
6.97	120	0.422	237	415	6.82	120	0.385	108	287	6.86	150.2	0.308	213	366
6.97	120	0.423	192	370	6.82	129	0.382	176	412	6.86	152.0	0.307	236	390
6.97	130	0.419	352	594	6.82	131	0.383	153	403	6.86	159.0	0.303	332	490
6.97	130	0.421	292	535	6.82	140	0.378	289	614	6.87	100	0.501	167	258
6.97	140	0.414	613	937	6.82	140	0.377	308	633	6.87	120	0.492	387	565
6.97	140	0.417	464	788	6.82	150	0.371	463	892	6.87	140	0.477	764	1089
6.97	150	0.406	1062	1490	6.82	150	0.369	500	929	6.87	150	0.467	1008	1437
6.86	101	0.475	95	189	6.82	160	0.361	724	1281	6.87	160	0.457	1302	1859
6.86	111	0.472	171	303	6.82	160	0.361	732	1289	6.85	100	0.520	233	324
6.86	121	0.467	283	467	6.82	170	0.348	1090	1805	6.85	120	0.508	512	691
6.86	130	0.461	448	691	6.82	170	0.350	1051	1766	6.85	140	0.489	964	1289
6.86	139	0.450	716	1032	6.86	100.5	0.315	16	146	6.85	150	0.478	1259	1688
6.86	140	0.452	683	1008	6.86	101.1	0.315	12	143	6.85	160	0.464	1626	2184
6.86	149	0.440	997	1414	6.86	109.0	0.314	36	169	6.87	120	0.370	63	241
6.86	150	0.439	1012	1440	6.86	111.3	0.315	22	157	6.87	140	0.364	217	542
6.86	160	0.424	1427	1984	6.86	120.4	0.314	50	189	6.87	150	0.358	368	797
6.86	161	0.424	1442	2013	6.86	121.8	0.314	45	184	6.87	160	0.351	569	1126
PZ														
7.78	110	0.312	125	251	7.94	100	0.417	322	410	8.00	110.0	0.444	881	1006
7.78	110	0.312	125	251	7.94	101	0.418	277	369	8.00	112.2	0.444	891	1026

Amine m	T ℃	Loading	P_{CO2} kPa	P_t kPa	Amine m	T ℃	Loading	P_{CO2} kPa	P_t kPa	Amine m	T ℃	Loading	P_{CO2} kPa	P_t kPa
7.78	120	0.311	211	385	7.94	110	0.413	478	604	8.00	117.8	0.440	1067	1228
7.78	120	0.311	211	385	7.94	111	0.414	447	576	8.00	120.0	0.438	1175	1348
7.78	130	0.311	268	505	7.94	120	0.410	623	797	8.00	128.3	0.433	1423	1647
7.78	130	0.310	343	579	7.94	120	0.409	682	856	8.00	129.4	0.431	1507	1738
7.78	140	0.308	517	833	7.94	130	0.404	898	1134	8.00	140.5	0.424	1901	2221
7.78	140	0.308	546	863	7.94	130	0.403	945	1181	8.00	140.6	0.423	1928	2248
7.78	150	0.304	894	1311	7.94	139	0.398	1228	1534	8.00	146.7	0.418	2203	2583
7.78	150	0.305	864	1281	7.94	140	0.397	1243	1558	4.93	100.6	0.292	20	115
7.78	160	0.301	1247	1788	7.94	146	0.393	1452	1825	4.93	108.9	0.291	31	157
7.43	100	0.311	79	168	7.94	150	0.389	1646	2062	4.93	110.6	0.291	40	174
7.43	110	0.311	41	167	7.94	150	0.389	1639	2055	4.93	120.0	0.290	60	242
7.43	110	0.310	115	242	7.94	157	0.384	1911	2411	4.93	130.0	0.289	105	353
7.43	119	0.310	146	315	7.75	100	0.373	174	263	4.93	138.9	0.287	152	473
7.43	120	0.310	95	270	7.75	110	0.371	281	407	4.93	140.0	0.286	176	507
7.43	130	0.308	285	522	7.75	120	0.367	444	618	4.93	150.0	0.283	273	709
7.43	130	0.309	195	433	7.75	120	0.364	577	751	4.93	150.0	0.283	295	732
7.43	140	0.306	531	849	7.75	130	0.359	798	1034	4.93	159.4	0.278	447	1005
7.43	140	0.307	427	745	7.75	134	0.361	723	989	4.93	160.6	0.277	457	1032
7.43	150	0.302	877	1296	7.75	140	0.357	913	1229	4.93	169.4	0.271	665	1381
7.43	150	0.304	653	1072	7.75	140	0.353	1085	1401	4.93	170.0	0.269	711	1436
7.43	160	0.298	1317	1861	7.75	150	0.345	1505	1922	4.93	180.0	0.261	991	1909
7.43	160	0.301	974	1518	7.75	151	0.347	1415	1844	4.93	180.6	0.260	1035	1967
7.43	169	0.297	1374	2054	7.75	160	0.337	1919	2460	4.93	191.1	0.248	1436	2615
7.93	120	0.328	116	290	7.75	160	0.337	1892	2433	4.96	100.0	0.372	76	169
7.93	125	0.328	124	327	7.93	110	0.368	223	348	4.96	100.6	0.371	103	198
7.93	130	0.327	229	465	7.93	119	0.365	390	558	4.96	109.4	0.370	140	268
7.93	139	0.325	441	748	7.93	121	0.367	304	483	4.96	110.0	0.369	170	301
7.93	140	0.325	440	756	7.93	129	0.360	609	838	4.96	120.0	0.367	243	425
7.93	149	0.321	780	1184	7.93	137	0.357	760	1050	4.96	120.6	0.366	272	458
7.93	150	0.321	777	1193	7.93	139	0.354	901	1208	4.96	130.0	0.363	388	636
7.93	160	0.317	1238	1778	7.93	146	0.350	1106	1479	4.96	130.6	0.362	415	667
7.93	161	0.318	1181	1737	7.93	150	0.346	1316	1731	4.96	140.0	0.358	578	909
7.93	167	0.311	1831	2473	7.93	152	0.345	1369	1807	4.96	140.0	0.357	607	938
7.92	110	0.306	37	162	7.93	161	0.337	1816	2369	4.96	148.3	0.352	823	1240
7.92	120	0.304	89	262	7.93	163	0.334	1934	2516	4.96	150.0	0.351	835	1271
7.92	130	0.303	135	371	7.86	118.5	0.251	28	193	4.96	160.0	0.344	1149	1715
7.92	130	0.303	156	392	7.86	129.9	0.251	59	295	4.96	160.6	0.342	1194	1769
7.92	140	0.301	256	571	7.86	131.1	0.250	100	344	4.96	170.0	0.334	1538	2264
7.92	140	0.300	291	607	7.86	140.9	0.249	124	449	4.96	170.6	0.333	1580	2317
7.92	150	0.297	460	876	7.86	141.1	0.248	166	492	4.96	175.0	0.329	1775	2593
7.92	150	0.296	510	926	7.86	149.5	0.247	252	663	7.92	100	0.416	301	390
7.92	160	0.292	723	1263	7.86	151.5	0.247	237	670	7.92	110	0.413	471	597
7.92	160	0.289	849	1389	7.86	159.8	0.244	417	955	7.92	120	0.408	679	853
7.92	170	0.283	1160	1852	7.86	163.4	0.243	447	1036	7.92	130	0.402	971	1207
7.92	170	0.282	1251	1943	7.86	171.9	0.239	664	1388	7.92	140	0.395	1302	1618
7.92	174	0.278	1421	2183	7.86	173.2	0.237	749	1497	7.92	150	0.387	1709	2125
7.94	81	0.422	94	137	7.86	180.5	0.234	957	1844	7.92	160	0.378	2192	2732
7.94	82	0.421	126	171	7.86	182.9	0.231	1093	2030	7.80	120	0.300	64	238
7.94	89	0.421	151	210	7.86	191.8	0.224	1482	2623	7.80	140	0.297	220	537
7.94	90	0.419	197	258	8.00	100.0	0.448	711	800	7.80	150	0.294	374	791
7.94	94	0.419	200	271	8.00	100.6	0.451	596	686	7.80	160	0.289	602	1142
1MPZ														
7.76	120	0.192	225	399	7.76	160	0.170	1282	1823	7.66	140	0.224	1289	1606
7.76	130	0.188	381	617	7.66	100	0.246	244	333	7.66	150	0.215	1744	2161
7.76	140	0.183	616	932	7.66	120	0.238	630	804	7.66	160	0.205	2272	2814
7.76	150	0.178	903	1320	7.66	130	0.232	917	1154					
2MPZ														
7.61	120	0.279	145	319	7.61	160	0.258	1126	1668	6.69	140	0.363	1247	1569
7.61	130	0.276	262	499	6.69	100	0.389	205	295	6.69	150	0.353	1709	2133
7.61	140	0.272	449	766	6.69	120	0.379	571	748	6.69	160	0.340	2269	2819
7.61	150	0.266	715	1133	6.69	130	0.372	859	1100					
PZ/2MPZ, m is the total moles of PZ and 2MPZ per kg water. PZ and 2MPZ have approximately the same concentration.														

Amine m	T ℃	Loading	P_{CO2} kPa	P_t kPa	Amine m	T ℃	Loading	P_{CO2} kPa	P_t kPa	Amine m	T ℃	Loading	P_{CO2} kPa	P_t kPa
7.63	120	0.306	142	316	7.63	160	0.288	1011	1554	7.86	140	0.376	1201	1517
7.63	130	0.303	252	489	7.86	100	0.397	227	315	7.86	150	0.369	1585	2001
7.63	140	0.300	427	744	7.86	120	0.389	576	750	7.86	160	0.359	2084	2624
7.63	150	0.295	673	1091	7.86	130	0.384	837	1073					
DGA														
9.55	100	0.410	57	144	9.55	150	0.375	975	1380	9.60	130	0.463	990	1220
9.55	120	0.402	252	421	9.55	160	0.361	1359	1885	9.60	140	0.450	1329	1637
9.55	130	0.396	417	647	9.60	100	0.488	356	442	9.60	150	0.437	1699	2104
9.55	140	0.387	662	970	9.60	120	0.473	732	901	9.60	160	0.421	2150	2676

3.2 Empirical Models

Empirical models were regressed based on the data in this work and low temperature literature data for each amine. Literature data includes: 40-100°C MEA data by Hilliard [6], Dugas et al. [8] and Jou et al. [3]; 40-120°C PZ data from Hilliard [6], Dugas et al. [8], Ermatchkov et al. [9] and Nguyen et al [10]; 40-100°C 1MPZ, 2MPZ, PZ/2MPZ and DGA data by Chen et al. [11, 12].

Table 2: Empirical Correlation of CO_2 Partial pressure (P_{CO2}, Pa) with loading (α, gmol CO_2/equiv. alkalinity) and T (K). $\ln P_{CO_2}(\text{Pa}) = a - b\frac{1}{T} + c\alpha + d\alpha^2 + e\frac{\alpha}{T} + f\frac{\alpha^2}{T}$

Amine	a	b	c	d	e	f	R^2
MEA	39.3 ±0.6	12155 ±194	0	-(19.0 ±3.6)	1105 ±410	12800 ±1444	0.994
PZ	35.5 ±0.3	11065 ±127	0	-(22.4 ±3.1)	4702 ±418	11699 ±1365	0.993
1MPZ	35.2 ±0.7	10344 ±234	-(6.4 ±3.5)	0	9741 ±1197	0	1.000
2MPZ	39.8 ±0.8	12554 ±262	-(19.6 ±3.2)	-(8.1 ±2.6)	14509 ±917	0	0.999
PZ/2MPZ	41.2 ±0.8	12998 ±238	-(27.0 ±2.8)	7.3 ±2.4	14684 ±746	0	1.000
DGA	28.1 ±1.3	7572 ±376	67.8 ±10	-(115 ±18)	-(25209 ±3383)	50113 ±6361	0.998

Figure 3 shows a favorable comparison of the MEA data with data by Jou et al.[3].

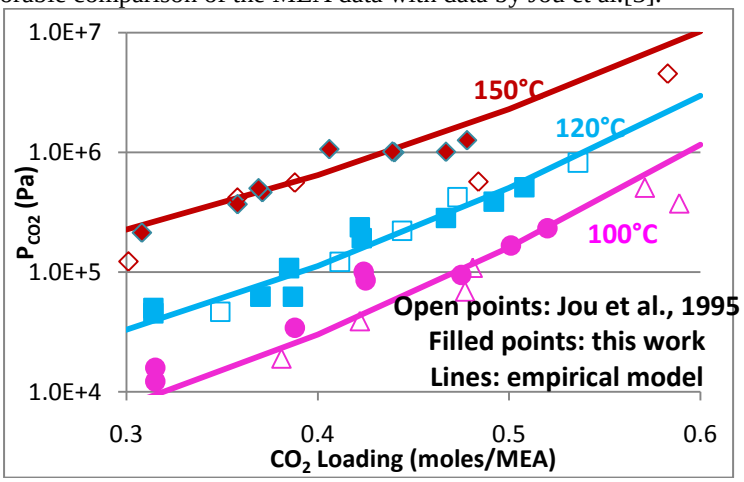

Figure 3: Comparison of CO_2 Solubility in MEA at 100, 120 and 150°C with Jou et al. [3]

Figures 4 through 9 show the temperature and loading dependence of CO_2 solubility in MEA, PZ, 1MPZ, 2MPZ, PZ/2MPZ and DGA, respectively.

In Figure 4 the data is compared with the MEA Aspen model prediction by Hilliard [6]. The Hilliard model is good for 60-120°C within 0.2-0.5 loading. At higher than 140°C, it over predicts the CO_2 partial pressure.

In Figure 5 the data is compared with the PZ Aspen model prediction by Frailie et al. [13]. The Frailie model predicts well for 40-160°C with 0.2-0.45 loading. At higher than 0.45 loading, there is no experimental data and the model prediction is higher than the empirical correlation.

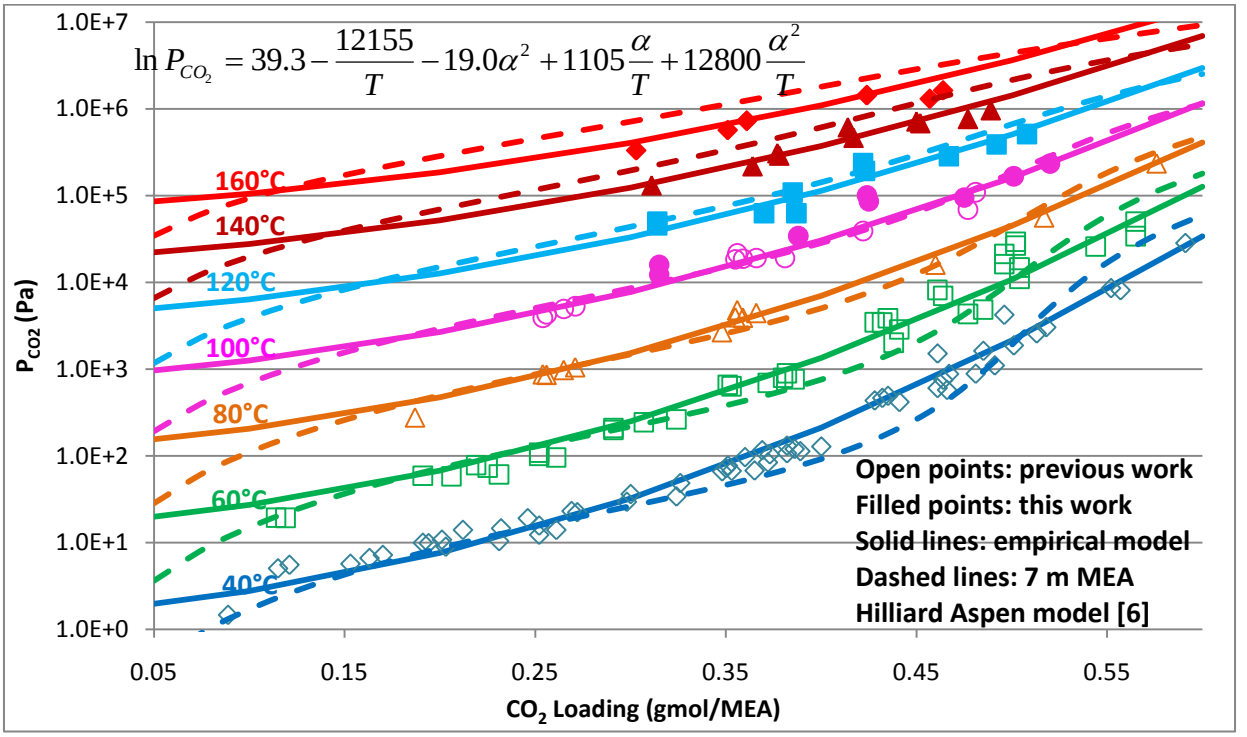

Figure 4: CO_2 Solubility in 3.5-13 m MEA, Previous Work by Hilliard [6], Dugas et al. [8] and Jou et al.[3].

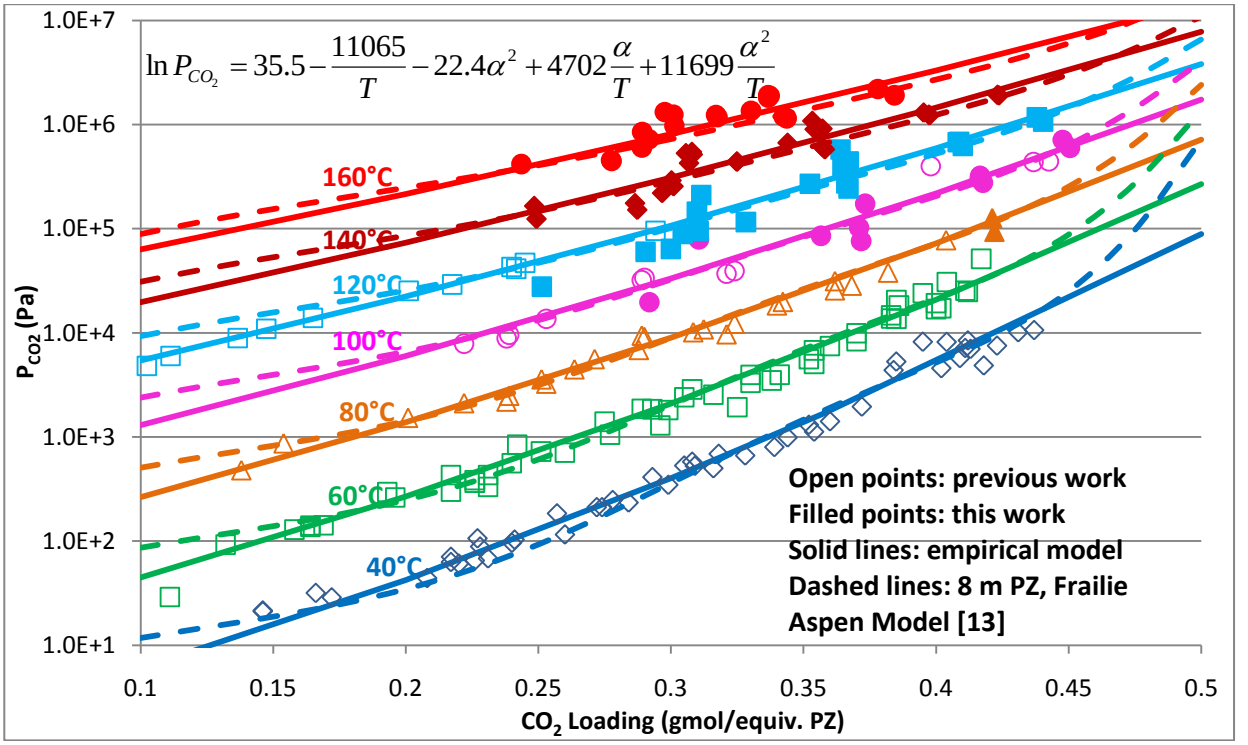

Figure 5: CO_2 Solubility in 0.9-12 m PZ, Previous: Hilliard [6], Dugas [8] Ermatchkov [9] & Nguyen [10]

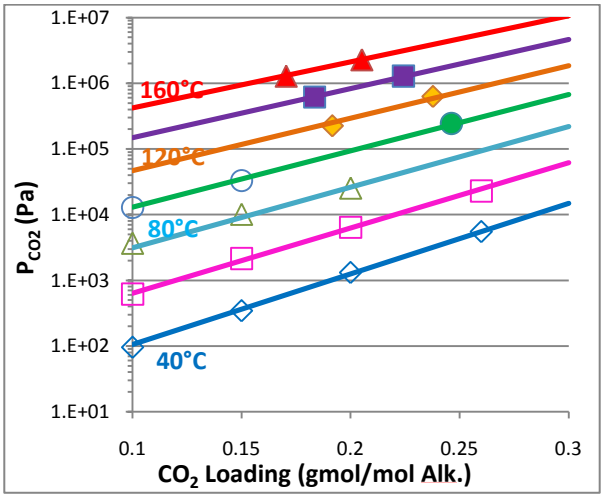

Figure 6: CO_2 Solubility in 1MPZ
Filled points: this work; Open pts: [11]; curves:

$$\ln P_{CO_2} = 35.2 - \frac{10344}{T} - 6.4\alpha + 9741\frac{\alpha}{T}$$

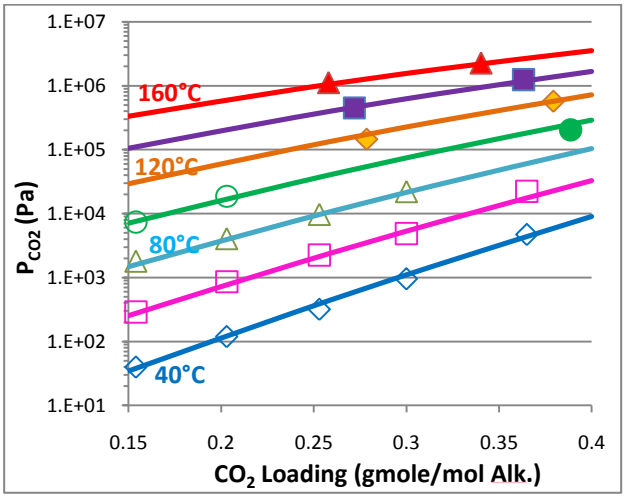

Figure 7: CO_2 Solubility in 2MPZ
Filled points: this work; Open pts: [11]; curves:

$$\ln P_{CO_2} = 39.8 - \frac{12554}{T} - 19.6\alpha + 14509\frac{\alpha}{T} - 8.1\alpha^2$$

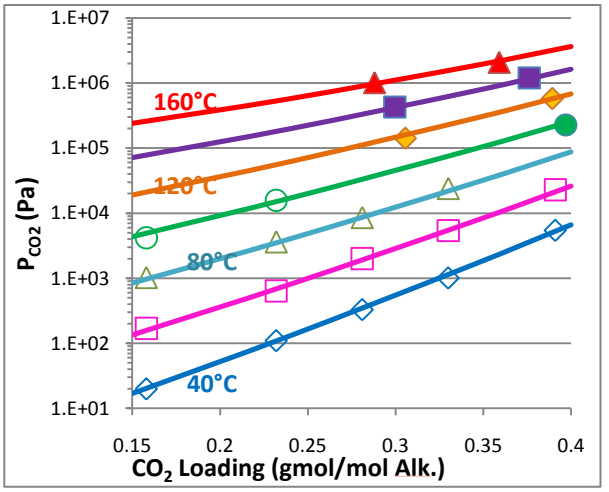

Figure 8: CO_2 Solubility in PZ/2MPZ
Filled points: this work; Open pts: [11]; curves:

$$\ln P_{CO_2} = 41.2 - \frac{12998}{T} - 27.0\alpha + 14684\frac{\alpha}{T} + 7.3\alpha^2$$

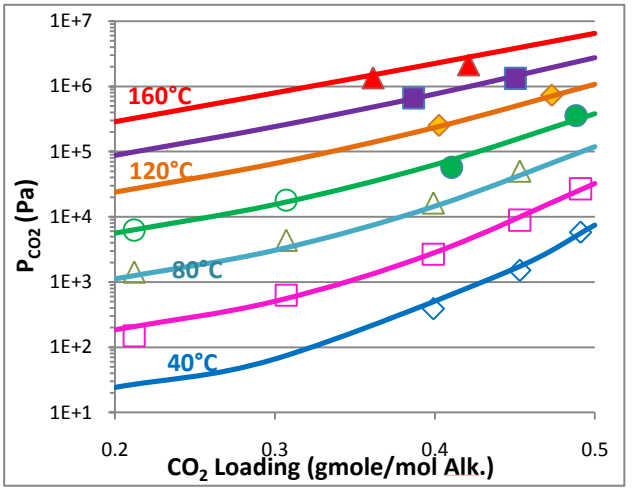

Figure 9: CO_2 Solubility in DGA
Filled points: this work; Open pts: [12]; curves:

$$\ln P_{CO_2} = 28.1 - \frac{7572}{T} + 67.8\alpha - 25209\frac{\alpha}{T} - 115\alpha^2 + 50113\frac{\alpha^2}{T}$$

3.3 Heat of Absorption of CO_2 into Aqueous Amines

According to the Gibbs-Helmholtz Equation, $\left(\frac{\partial ln P_{CO_2(g)}}{\partial \frac{1}{T}}\right)_{P,x} \approx -\frac{\Delta H_{abs}}{R}$, ΔH_{abs} is the heat of absorption of CO_2 into aqueous amines. Table 3 gives ΔH_{abs} derived from the empirical models. Within the precision of these measurements and estimates, the heat of CO_2 absorption is independent of temperature and amine concentration, but varies with CO_2 loading. The statistics of the empirical regression suggest that the heat of absorption is determined with a precision of 2 to 4 kJ/mol.

4. Conclusions and recommendations

CO_2 solubility data was obtained using total pressure measurements. Empirical models as a function of temperature and loading were developed for CO_2 solubility from 40 to 191°C in aqueous MEA, PZ, 1MPZ, 2MPZ, PZ/2MPZ and DGA. The high temperature CO_2 solubility data for MEA is comparable with that by Jou et al. [3]. The high temperature data is also compatible with previous low temperature data. For MEA and PZ, amine concentration does not have obvious effects on the CO_2 solubility. The heat of CO_2 absorption derived from these models varies from 66 kJ/mol for PZ and its derivatives to 71 and 73 for MEA and DGA and does not vary significantly with temperature.

Table 3: Comparison of the Heat of Absorption of CO_2

Solvent	ΔH_{abs} (J/mol CO_2)	ΔH_{abs} (kJ/mol CO_2)*	Mid-loading**
3.5–13 m MEA	$-R(-12155+1105\alpha+12800\alpha^2)$	71±4	0.486
0.9–12 m PZ	$-R(-11065+4702\alpha+11699\alpha^2)$	66±2	0.353
7.7–8 m 1MPZ	$-R(-10344+9741\alpha)$	69±3	0.207
6.7–8 m 2MPZ	$-R(-12554+14509\alpha)$	66±3	0.314
4/4 m PZ/2MPZ	$-R(-12998+14684\alpha)$	66±3	0.341
9.6–10 m DGA	$-R(-7572-25209\alpha+50113\alpha^2)$	73±3	0.447

*: The heat of absorption of CO_2 at mid-loading.
**: The loading where P_{CO2} is 1.5 kPa at 40 °C, calculated from the empirical models.

Acknowledgements

This work was supported by the Luminant Carbon Management Program. Some experiments were conducted by the undergraduate assistants Martin Metzner and Mychal Zipper.

References

[1] Freeman SA, Dugas R, Van Wagener D, Nguyen T, Rochelle GT. Carbon dioxide capture with concentrated, aqueous piperazine. IJGCC, 2010, 4, 119-124.
[2] Rochelle GT. Amine Scrubbing for CO_2 Capture. Science, 2009, 325, 1652-1654.
[3] Jou, F.-Y.; Mather, A. E.; Otto, F. D., The solubility of CO_2 in a 30 mass percent monoethanolamine solution. The Canadian Journal of Chemical Engineering, 1995, 73, 140-146.
[4] DIPPR, 1998-Provo, UT: BYU DIPPR, Thermophysical Properties Laboratory, 1998-Version 13.0.
[5] Autoclave Engineers®, Zipperclave® 500&1000 mL stirred reactor, http://www.autoclaveengineers.com/ae_pdfs/SR_500_1000_Zip.pdf
[6] Hilliard MD. A Predictive Thermodynamic Model for an Aqueous Blend of Potassium Carbonate, Piperazine and Monoethanolamine for CO_2 Capture from Flue Gas. The University of Texas. Ph.D. Dissertation. 2008.
[7] Sexton AJ. Amine Oxidation in CO_2 Capture Processes. The University of Texas. Ph.D. Dissertation. 2008.
[8] Dugas R., Rochelle GT. Absorption and desorption rates of carbon dioxide with monoethanolamine and piperazine. GHGT-9, Washington D.C. 2008.
[9] Ermatchkov V., Kamps A. P-S., Speyer D. and Maurer G. Solubility of carbon dioxide in aqueous solutions of piperazine in the low gas loading region. J. Chem. Eng. Data, 2006, 51 (5), 1788-1796.
[10] Nguyen T., Hilliard M., Rochelle GT. Amine Volatility in CO_2 Capture. IJGCC. 2010, in press.
[11] Chen, X., Rochelle GT. Aqueous Piperazine Derivatives for CO_2 Capture: Accurate Screening by a Wetted Wall Column. Chem. Eng. Res. Des. 2010, submitted.
[12] Chen, X., Closmann, F., Rochelle GT. Accurate Screening of amines by the Wetted Wall Column. GHGT-10, 2010.
[13] Frailie, PT., Plaza, JM., Van Wagener, DH., Rochelle, GT. Modeling piperazine thermodynamics, GHGT10. 2010.

Available online at www.sciencedirect.com

ScienceDirect

Energy Procedia 00 (2010) 000–000

Energy Procedia

www.elsevier.com/locate/XXX

GHGT-10

Optimum Design and Control of Amine Scrubbing in Response to Electricity and CO_2 prices

Sepideh Ziaii[a] , Gary T. Rochelle[a,]* , Thomas F. Edgar[a]

[a]Chemical Engineering Department, University of Texas, Austin, Texas 78712, USA

Elsevier use only: Received date here; revised date here; accepted date here

Abstract

This paper presents steady state and dynamic modelling of post combustion CO_2 capture using 30 wt% MEA integrated with models of CO_2 compression and the steam power cycle. It uses multivariable optimization tools to maximize hourly profit of a 100 MWe coal-fired power plant. Steady state optimization for design provided optimum lean loading and CO_2 removal as a function of price ratio (CO_2 price / electricity price). The results indicated that for price ratio between 2.1 and 7, the plant should be designed at removal between 70% and 98% and lean loading in the range of 0.22–0.25. Dynamic optimization determined the operation of the capture system in response to two partial load scenarios (reboiler steam load reduction and power plant boiler load reduction) and provided optimum set points for steam rate, solvent circulation rate and stripper pressure control loops. Maximum profit is maintained by allowing the stripper pressure to drop and implementing a ratio control between solvent and steam rate (and flue gas rate for partial boiler load operation).

Keywords: Dynamic modeling; Absorption; Stripping; Optimization; Control

1. Introduction

Dynamic modelling of a process is a helpful tool that is commonly used not only for analyzing the dynamic behaviour and designing simple control strategies but also for optimizing the operation of the plant in response to possible disturbances. However, this strategy has not been previously employed for optimizing the operation and control of CO_2 absorption plants with aqueous amines. In the few works found on dynamic modelling (Kvamsdal et al. [1]; Ziaii et al. [2]), the dynamic simulation of CO_2 capture was used to investigate the dynamic behaviour

of the absorber and stripper separately in response to the partial load operational scenarios. Lawal et al. [3] analyzed the effects of possible upstream disturbances on the dynamic responses of a combined model of the absorber and regenerator. Several works have focused on reducing overall energy consumption of the capture and/or improvement of absorption performance [4-6]. Since those studies are based on steady state analysis of the plant running continuously at full capacity, they cannot provide insight into dynamic and control performance of the system during transitional operation.

This study presents a fully integrated model of an absorber/stripper using monoethanolamine(MEA) for CO_2 capture. The model was, developed in Aspen Custom Modeller (ACM) and also included an approximation of steady state models of CO_2 compression and power cycle steam turbines to account for the interaction of these components with capture during dynamic operation. This paper, presents the implementation of steady state multivariable optimization tool of ACM® to optimize the most important design parameters, lean loading and CO_2 removal. In an economical study presented by Abu Zahra et al. [7], the lean loading and amine concentration were optimized based on minimization of cost of electricity for a plant designed at 90% removal, which included the terms of total capital cost, operating cost and energy cost. The analysis neglected the effects of capital cost and operating cost of the power plant, capture, and only considered energy cost by using power plant hourly profit as the cost function.

The second part of this study presents the implementation of a multivariable dynamic optimization tool, which is tied with dynamic simulation of the MEA plant, to find final optimum set points for the control loops when two main possible dynamic scenarios are applied. This optimization maximized the power plant profit at the time when the new steady state is reached. The scenarios considered in this study were introduced as possible operational cases in previous work [1, 3, 8]. The first operational scenario is a partial load reboiler steam operation in response to the variation of electricity or CO_2 market conditions. This scenario indicates when the operation of flexible capture is economical, and is discussed in detail in the paper authored by Ziaii et al. [8]. The second one represents the variation of the load of power plant boilers, which can directly affect the operation of the capture.

2. Model development

A model of CO_2 absorption/stripping with 30 wt% monoethanolamine (MEA) was created in a flow sheet of ACM®. The model includes dynamic rate-based models of packed columns (absorber and stripper), simplified steady state models for the heat exchangers, general performance curves for multi-stage CO_2 compressor and pumps and an approximate steady state model for the steam turbine. The stages for steam turbines (HP, IP, and LP) with the extracted steam was extracted for solvent regeneration from the IP/LP crossover of the three-stage steam turbine (HP, IP, and LP). Each stage the turbines was represented with the ellipse law with design conditions reported by Lucquiaud [9]. The flue gas from 100 MWe coal- fired power

plant enters the absorber with 13% CO_2. Figure 1 gives the flow sheet of the absorption/stripping process with specified design conditions.

3. Steady state and dynamic optimization

This work uses power plant profit ($/hour) as the objective function for steady state and dynamic optimization:

$$profit(\$/hr) = Elec.price(\$/kWh) \times Elect.gen.(kW) + CO_2 price(\$/ton) \times removedCO_2(ton/hr) \quad (1)$$

Where the electricity generation is the total work produced by steam in the power cycle, minus lost work due to CO_2 capture and compression. It is also assumed that the total work produced by steam is only a function of total steam rate in the steam cycle and varies proportionally with that variable. The influence of factors such as turbine inlet/outlet conditions is neglected. Equation 2 calculates the lost work of CO_2 capture and compression:

$$W_{lost} = 0.75 Q_{reb}\left(\frac{T^{sat}(P_{ext}) - T_{sink}}{T^{sat}(P_{ext})}\right) + W_{comp} + W_{pumps} \quad (2)$$

The FEASOPT method in ACM® was connected to the steady state model of the MEA plant and operated at steady state to maximize the profit by adjusting the lean loading and CO_2 removal. Other independent process variables were set at their design specification as shown in Figure 1. Optimization was performed with the ratio of CO_2 price to the electricity price varying from 2 to 7($/ton CO_2)/(cents/kWh)). This steady state optimization provides optimum design curves for lean loading and removal as a function of price ratio.

Dynamic optimization was used to find optimum operating curves for manipulated variables to maximize the final power plant profit as the disturbance occurs. Four valves (figure 1) were used to control. The valve on the lean solution is manipulated to control the reboiler level. The other three valves regulate the steam rate, solvent rate, and the stripper vapor rate. The operating curves provided by dynamic optimization give the optimum final values of the controlled variables so that they can be used to establish a set point.

The FEASOPT method performed multivariable dynamic optimization and ultimately optimized the set point paths of steam rate, solvent rate, and stripper pressure simultaneously over a range of variations in disturbances for two dynamic scenarios:

1. Partial steam load operation in flexible capture with a price ratio of 2 to 5.
2. Partial boiler load operation in a variable load power plant with the same simultaneous relative decrease in both flue gas rate and power cycle steam rate up to 70% of the full load.

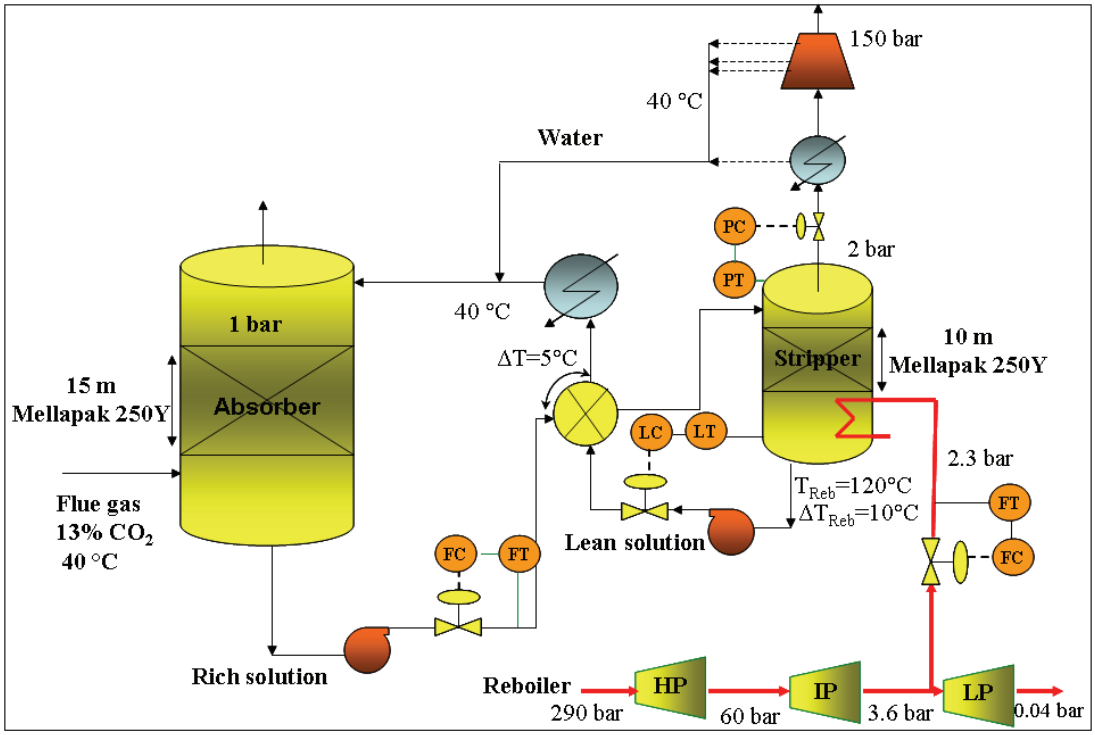

Figure 1: MEA absorption/stripping integrated with power cycle and CO_2 compression system along with control valves

4. Results and Discussion

4.1. Optimization in Response to the Price Ratio

Steady state optimization was performed to optimize design variables (lean loading and CO_2 removal) for different values of price ratios. Then dynamic optimization was carried out for a case study designed at a specific point on the optimum design curve (price ratio = 2.6, removal = 90.1%, lean loading = 0.225) to find the optimum operating curve as the price ratio varies. This means that if the controller set points move on the optimum operating curves as the price ratio varies, we can make the highest profit at the new steady state condition. Figure 2 illustrates the design and operating curves of CO_2 penetration versus price ratio. CO_2 penetration is defined as the fraction of the CO_2 in the flue gas that is released to the atmosphere:

$$CO_2\,penetration = 1 - CO_2\,removal \qquad (3)$$

As shown in Figure 2, for price ratio of 2 to 3 the rate of the reduction is much higher relative to the higher price ratio. The design curve shows a large change around price ratio = 2.1, which means that there are two local optima around this point, at 53% and 70% removal. The optimum operating curve deviates from the design curve specifically when the new price ratio is higher than the initial price ratio because of using different specifications in steady state and dynamic

simulation for the liquid level in the absorber sump. Even at the design point (price ratio = 2.6) the optimum operating point does not lie on the design curve. No significant deviation is seen between the design and operating curves for lean loading for the selected case study (Figure 3).

Considering the design curve, at medium and high price ratio where the system is designed at removal higher than 70%, the optimum lean loading is lower than 0.25, while at low level of removal (≤ 53%), the optimum lean loading greater than 0.39. Figure 4 illustrates how the optimum lean loading moves from low to high as removal increases. Comparing the equivalent work curve of 90% removal to 70% and 53%, we can see a flat minimum area at lower removal so that the global minimum can easily change from low to high as the removal varies slightly. That is why the optimum lean loading changes significantly around price ratio = 2.1.

One of the variables that was optimized during dynamic optimization is pressure at the top of the stripper. The results suggest that in order to stay on maximum profit and minimum energy lost, the pressure valve should be kept wide open and the stripper pressure should be allowed to drop as the steam rate reduces.

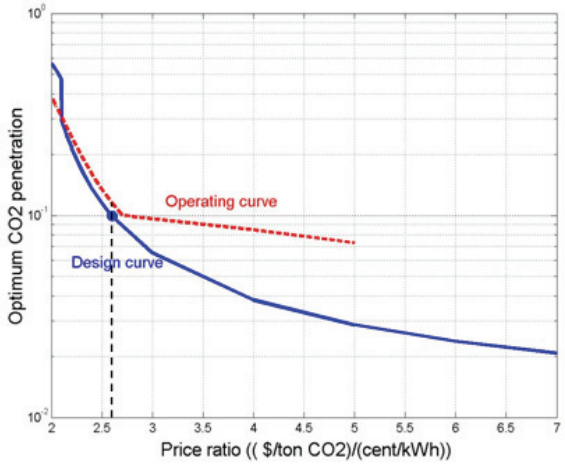

Figure 2: CO_2 penetration at the optimum design and operating conditions, H_{abs}=15m, H_{strip} = 10m, cross heat exchanger ΔT_{design} = 5°C, reboiler ΔT_{design}=10°C, reboiler T_{design} = 120°C, τ_{sumps}=2 min

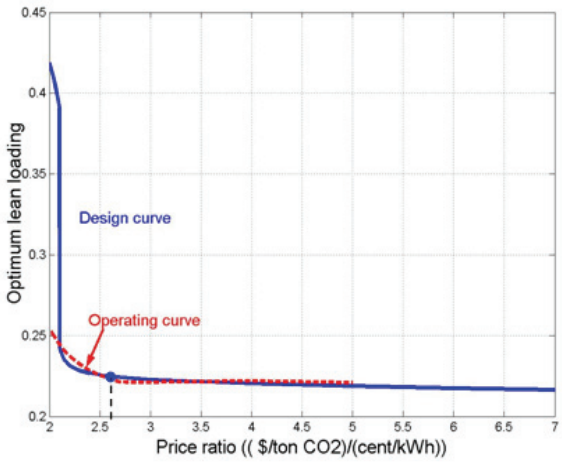

Figure 3: Lean loading at the optimum design and operating conditions, H_{abs}=15m, H_{strip} = 10m, cross heat exchanger ΔT_{design}=5 °C, reboiler ΔT_{design} = 10°C, reboiler T_{design} =120°C, τ_{sumps} =2 min

At the optimum operating conditions the optimum solvent rate is a linear function of the steam rate. Although the slope of the line deviates slightly from one, we can use a ratio control on the steam rate and solvent rate and still stay close to the optimum path. (Figure 5)

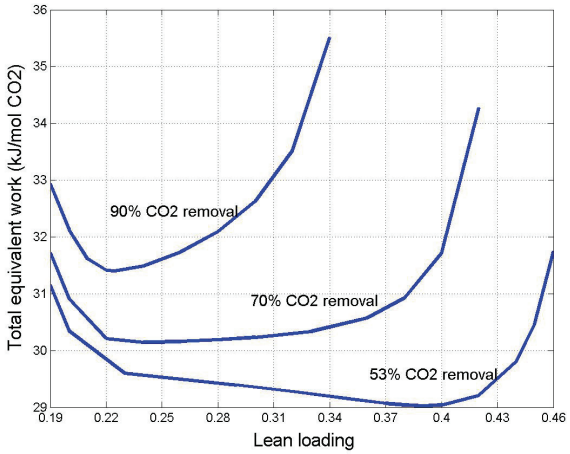

Figure 4: Capture total lost work versus at optimum design conditions, H_{abs}=15m, H_{strip} = 10m, cross heat exchanger ΔT_{design} = 5 °C, reboiler ΔT_{design} = 10 °C, reboiler T_{design} = 120 °C

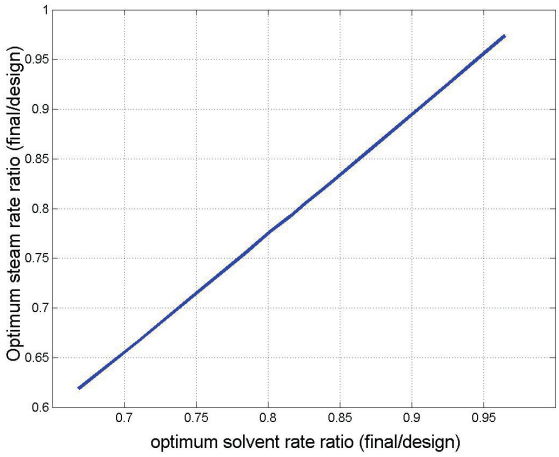

Figure 5: Steam flow at optimum operating conditions, plant designed at price ratio=2.6 (removal=90% and lean loading=0.225), H_{abs}=15m, H_{strip} = 10m, cross heat exchanger ΔT_{design} = 5 °C, reboiler ΔT_{design} = 10 °C, reboiler T_{design} =120 °C, τ_{sumps} = 2 min

4.2. Optimization in Response to the Partial Boiler Load Operation

When the boiler load decreases, the flow of flue gas directed to the absorber and total steam rate entering the first stage of steam turbine decreases. Variation of steam rate in the power cycle leads in changing the rate and the pressure of extracted steam entering the reboiler, which can influence the stripper operation. In the simulation, we assumed that both flue gas rate and total steam rate vary proportionally with the boiler load.

The simulation and optimization of this dynamic scenario is performed for the plant designed initially at 90.1% removal and 0.225 lean loading. As in partial steam load operation, optimizing the pressure shows that keeping the pressure valve always wide open. Therefore allowing the stripper pressure to drop with decreasing steam rate is the most energy efficient and profitable strategy for partial boiler load operation.

Figure 6 indicates that optimum steam rate and solvent rate vary linearly with the boiler load. The deviation of the slope of the solvent rate from 1 is slightly more than steam rate. Since the deviation of slopes of solvent and steam rates are not significant, placing a ratio control among flue gas rate, steam rate, and solvent rate will keep the plant close to the optimum path.

Both optimum removal and lean loading increase as boiler load decreases (Figure 7). From a process control perspective, the current results indicate that keeping L/G constant in both

absorber and stripper is a control strategy that enables the plant to run close to the optimum path during variable load operation of power plant.

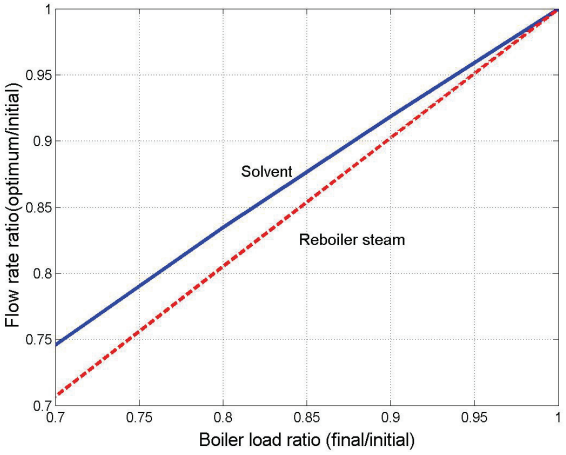

Figure 6: Optimum steam rate and solvent rate (normalized by initial rates) with variable boiler load, H_{abs}=15m, H_{strip} = 10m, cross heat exchanger ΔT_{design} = 5 °C, reboiler ΔT_{design} = 10 °C, reboiler T_{design} = 120 °C, τ_{sumps} = 2 min

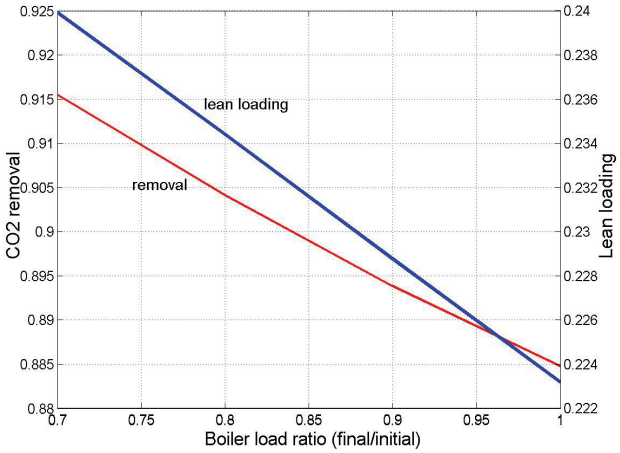

Figure 7: Optimum CO_2 removal and lean loading with variable boiler load, H_{abs}=15m, H_{strip} = 10m, cross heat exchanger ΔT_{design} = 5 °C, reboiler ΔT_{design} = 10 °C, reboiler T_{design} = 120 °C, τ_{sumps} = 2 min

5. Conclusions

The dynamic model of the absorption/stripping process was integrated with the first order approximation model of the power plant steam turbines. By doing so, the variation of steam pressure at the IP/LP crossover point is taken into account in dynamic simulation. After implementing the multivariable steady state optimization tools of ACM® , power plant profit was maximized to optimize lean loading and CO_2 removal at different values of price ratio (CO_2 price/electricity price) for design purposes. As a result, for price ratio between 2.1 and 7, the plant should be designed at removal between 70% and 98% and lean loading in the range of 0.22–0.25. For a price ratio lower than 2 , the plant should be designed at high lean loading (≥ 0.39).

Two important operational scenarios were dynamically simulated: partial reboiler steam load and partial boiler load operations. After implementing the multivariable dynamic optimization tools of ACM® to maximize profit, solvent rate, steam rate, and stripper pressure were optimized. The results show that for both scenarios, keeping the pressure valve wide open and allowing the stripper pressure to swing is found to be the most profitable strategy. For reboiler steam partial load operation, a linear relationship exists between the optimum solvent rate and reboiler steam rate with the slope very close to 1. For boiler partial load operation, a linear

relationship exists between the optimum solvent rate and reboiler steam rate with the boiler load (or flue gas rate). The slope of the line is relatively close to 1. This significant observation leads to a practical application in which the ratio control between the solvent rate and steam rate in scenario 1 and ratio control among the solvent rate, steam rate, and flue gas rate in scenario 2 can be proposed as optimum strategies in response to the discussed disturbances.

6. Acknowledgments

This work was supported by the Luminant Carbon Management Program at the University of Texas at Austin.

7. References

- [1] Kvamsdal HM, Jakobsen JP, Hoff KA. Dynamic modelling and simulation of a CO_2 absorber column for post-Combustion CO_2 capture. Chem Eng & Proc. 2009; 48:135–144.
- [2] Ziaii S, Rochelle GT, Edgar TF. Dynamic modeling to minimize energy use for CO_2 capture in power plants by aqueous Monoethanolamine. Ind Eng Chem Res. 2009; 48(13):6105–6111.
- [3] Lawal A, Wang M, Stephenson P, Koumpouras G, Yeung H. Dynamic modeling and analysis of post-combustion CO_2 chemical absorption process for coal-fired power plants. Fuel 2010, doi:10.1016/j.fuel.2010.05.030.
- [4] Freguia, S, Rochelle GT. Modeling of CO_2 capture by aqueous monoethanolamine. AICHE J 2003**;** 49(7):1676-1686.
- [5] Oyenekan BA , Rochelle GT, Energy performance of stripper configurations for CO_2 capture by aqueous amines, Ind Eng Chem Res. 2006; 45(8): 2457–2464.
- [6] Plaza JM, Van Wagener D, Rochelle GT. Modeling CO_2 capture with aqueous Monoethanolamine. International Journal of Greenhouse Gas Control 2009; 1(1):1171–1178.
- [7] Abu-Zahra MRM, Niederer JPM, Feron PHM, Versteeg GF. CO_2 capture from power plants: Part II. A parametric study of the technical performance based on monoethanolamine. International Journal of Greenhouse Gas Control 2007; 1(2):135–142.
- [8] Ziaii S, Cohen S, Rochelle GT, Edgar TF, Webber ME. Dynamic operation of amine scrubbing in response to electricity demand and pricing. International Journal of Greenhouse Gas Control 2009; 1(1):4047–4053.
- [9] Lucquiaud M, Steam cycle options for capture-ready power plants, retrofits and flexible operation with post combustion CO_2 capture. Ph.D. Dissertation, Imperial College London, 2010.